AEC RESEARCH AND DEVELOPMENT REPORT

DECLASSIFIED

CLASSIFICATION CHANGED TO:

By Authority of: *ACC P-20-62*

By: *M. Young 2.8.63*

AIRCRAFT NUCLEAR PROPULSION PROJECT

QUARTERLY PROGRESS REPORT

FOR PERIOD ENDING DECEMBER 31, 1957

OAK RIDGE NATIONAL LABORATORY
operated by
UNION CARBIDE CORPORATION
for the
U.S. ATOMIC ENERGY COMMISSION

ORNL-2440
C-84 — Reactors-Special Features of Aircraft Reactors

This document consists of 324 pages.
Copy /25 of 273 copies. Series A.

Contract No. W-7405-eng-26

AIRCRAFT NUCLEAR PROPULSION PROJECT

QUARTERLY PROGRESS REPORT

For Period Ending December 31, 1957

A. J. Miller, Project Coordinator

DATE ISSUED

APR 15 1958
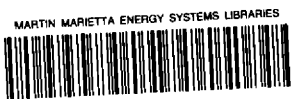
FOREWORD

This quarterly progress report of the Aircraft Nuclear Propulsion Project at ORNL summarizes the progress that was made in the development of circulating-fuel reactors and records the status of work now under way on other ANP programs at the Laboratory under its contract W-7405-eng-26. The report is divided into five major parts: 1. Aircraft Reactor Engineering, 2. Chemistry, 3. Metallurgy, 4. Radiation Damage, and 5. Shielding.

With the cancellation of work on circulating-fuel reactors as of October 1957, program emphasis has shifted to research in support of the work of other organizations participating in the national ANP effort. The major fields of the ORNL effort are now shielding, materials research and development, and investigations of components of reactors and of systems designed for the nuclear propulsion of aircraft.
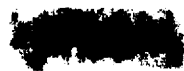
ANP PROJECT QUARTERLY PROGRESS REPORT

SUMMARY

PART 1. AIRCRAFT REACTOR ENGINEERING

1.1. Reactor and Facility Construction

A summary of the status of the ART-ETU program at the time it was cancelled is presented. Reference is made to comprehensive reports that have been prepared on the various aspects of the development work. Much of the operations planning had been done, and reference is made to documents containing detailed operating procedures. All outside contract work on the facility in which the ART would have been operated had been completed. A pictorial summary of that work is presented, as well as cost summaries.

1.2. Component Development and Testing

Tests of actual and prototype ETU and ART components and systems have been terminated or are being completed before being terminated. The experiments designed for establishing a detailed pump sparging procedure were finished. The reactor fuel pump rotary element that was being operated in a new gamma-irradiation facility at the MTR was shut down for repair of an ion chamber, and during further inspection it was found that other repairs were needed. This test will be resumed, since this experimental study of the effect of irradiation on bearings, seals, and lubricants is of general interest.

An ART-type fuel pump that is operating at service temperatures with NaF-ZrF_4-UF_4 (50-46-4 mole %, fuel 30) has accumulated 3350 hr of continuous operation. This pump is to be operated for an additional 3000 hr under induced cavitation in order to determine the effect on the impeller. An identical pump is being operated with NaK in order to study the effect of the type of fluid being pumped.

Operation of a fuel pump in an endurance test was terminated after a total operating time of 4410 hr. Replacement of the lower seal would have permitted further operation, but this test is not to be resumed.

Operating data on electromagnetic flowmeters were obtained in a primary NaK pump loop, and a split-purge arrangement for the shaft annulus is being tested as a means of obtaining long-time trouble-free operation of the lower seal. A Fulton-Sylphon bellows lower seal on an auxiliary NaK pump was found to have operated successfully for 936 hr with an average leakage of 16 cm^3/day. Approximately 8700 hr of high-temperature operation of primary NaK pumps with NaK has been accumulated, and the accumulated operating time for auxiliary NaK pumps with NaK is 5100 hr.

A sodium pump equipped with the thermal barrier designed to protect the bearing-housing region from thermal and radiation damage and also equipped with a simulated ETU type of lubricating and cooling oil system was found to operate quite successfully in a high-temperature test. The system was operated a total of 3800 hr, of which 2600 hr were without interruption.

The heat exchanger and radiator development testing program is being concluded with a thermal cycling test of a 20-tube semicircular heat exchanger designed to simulate the ART main heat exchanger tube geometries. The heat exchanger has completed 155 cycles of the proposed 300-cycle program. A tube in ART test radiator No. 2 failed after a total of 181 thermal cycles, which was six times the number of thermal cycles proposed for the ART radiators.

Measurements made on the second quarter-scale outer core shell model, which was subjected to 339 thermal cycles, are being analyzed in order to determine whether dimensional changes occurred. The shell is being prepared for a creep buckling test at 1500°F. A welded shell is to be tested in order to determine the reliability of that type of construction.

Zirconium fluoride vapor traps designed for use in the ETU were found to be satisfactory with minor modifications. The additional changes that would be required for satisfactory ART operation were established.

1.3. Instrumentation and Controls Development

The ART control rod drive system, which was successfully operated under simulated ART conditions for 3000 hr, was disassembled and examined. There were no indications of wear and

no sodium deposits on rod drive parts located above the surface of the molten sodium.

In metering tests made in the aluminum north head mockup just prior to termination of the ART program, it was demonstrated that the purged-dip-tube continuous level indicator could detect changes in level in the fuel expansion tank with an accuracy of ±5% at design speed and flow conditions. Turbulence prevented absolute level measurements. Considerable work remained to be done in determining the dynamic characteristics of the measuring system under ART conditions. A resistance type of fuel level indicator was designed as a possible alternate to the purged dip tube, and it is to be tested further. In preliminary experiments the performance of the indicator was in reasonable agreement with the calculated performance.

Construction work on the resistance-type level transducers that were to be used in the NaK pump bowls of the ART and ETU was terminated with the completion of a total of 22 units. Design work was completed on all the continuous level probes required for the ETU and the ART in the sodium expansion tank, the sodium auxiliary tank, and the NaK-furnace-circuit drain tank. Tests to determine the error introduced by an unwetted level probe were continued.

On-off level probes with brazed, rather than welded, copper-Inconel junctions at the tip were installed in a NaK system. After a sufficiently long operating period these probes will be examined in order to evaluate the use of the braze method of construction. Sixteen on-off probes installed in the gas pots of two NaK systems have each operated at high temperatures for 3000 hr without a failure.

The program of tests of 2- and $3\frac{1}{2}$-in. magnetic flowmeters was cancelled. The data obtained in the operation of 20 such flowmeters are being processed and analyzed. Indications are that the accuracy of these flowmeters was well within the specified ART and ETU requirements. The fifteen $\frac{3}{8}$-in. magnetic flowmeters that had been delivered for installation on ETU cold traps, as well as parts for 15 more units, will be packaged and stored.

Examination of experimental turbine-type flowmeters indicated the need for further modifications. The bearing radial clearance was increased, as was the clearance between the downstream end of

the rotor body and the positioner. In addition, the over-all blade diameter was reduced to give greater clearance between the blades and the housing. Units that incorporate these modifications have operated in excess of 350 hr at temperatures ranging from 1200 to about 1600°F.

In further tests, six strain-gage pressure transmitters of 0- to 100-psig range indicated an average output-input deviation of 0.4% of full scale over their operating pressure range from ambient temperature to 1400°F. This accuracy compares favorably with the accuracies of other pressure transmitters.

Drift testing of thermocouples was continued, and reports are being prepared that describe the design and testing of ART thermocouples. One report will cover fabrication techniques and the results of aging tests in fuel, sodium, and NaK, and the other will give the results of aging tests in air.

1.4. Engineering Design Studies

Work on the applied mechanics and stress analysis problems of the ART was discontinued. Reports have been prepared that describe the techniques used and summarize the results. The results that had been checked by component tests were found to be valid.

1.5. Design Physics

The design of the ART was based on extensive reactor physics studies that were largely completed. The problems studied are described, and reference is made to reports that give the details of the work.

1.6. Materials and Components Inspection

A summary of the quantities and types of materials and components inspected is presented. The various inspection methods used include visual, dye penetrant, radiographic, ultrasonic, eddy current, and others.

1.7. Heat Transfer Studies

Several additional tests were completed in the high-frequency thermal-cycling loop. In this pulse-pump apparatus the fuel mixture $NaF-ZrF_4-UF_4$ (56-39-5 mole %) is used as the circulating fluid and helium is the pulsing and cover gas. For these recent tests, the Inconel test sections were made up of welded pieces of tubing and pipe that

were approximately 0.5 in. in inside diameter but varied in wall thickness from 0.029 to 0.250 in. A cursory examination of the data indicated that the severity of cracking as a result of thermal cycling increased with increasing wall thickness and with proximity to a weld. This study is being continued. Similar experimental investigations with the use of a pressurized system were discontinued.

Tests of a full-scale plastic ART core model that was divided into three flow regions by installing two annular shell liners were also discontinued. The data obtained, which consist primarily of Pitot traverse measurements and dye-injection movies, are being assembled. Summary reports were prepared on previous experimental studies of flow through quarter-scale models of the ART core, including the screen-packed core and header arrangement, and on the phosphorescent-particle technique for velocity-profile visualization.

Forced-convection heat transfer studies with KCl-LiCl flowing in a heated tube were discontinued after some tests of stainless steel test sections. A summary report has been prepared on the inconclusive results obtained in these tests.

An experimental system is being designed for the study of forced-convection heat transfer with molten lithium flowing in metal tubes. The test section will be constructed of stainless steel and will be instrumented for measurements of wall temperatures, fluid flow rates, and mixed-mean temperatures.

A study of the effect of screens in a diverging annular channel on the thermal structure of a volume-heated fluid is being continued. Also, a system is being constructed for an experimental study of heat transfer from an internally heated liquid metal (mercury, initially). An empirical relation for forced-convection volume-heat-source heat transfer with liquid metals was devised.

Preliminary data on burnout heat fluxes for water in nucleate boiling have confirmed the concept that source-vortex flow would delay the burnout condition to a higher heat flux. The higher burnout values obtained were not counterbalanced by excessively large power expenditures.

Equipment is being designed and assembled for a study of flow distribution in the coolant annuli of the Tower Shielding Reactor II (TSR-II). The data obtained will be combined with heat-generation rates in order to determine the redistribution of flow required to approximate a flat exit-water temperature profile.

The thermal conductivity of fuel 30 was redetermined, and measurements were made of the enthalpies and heat capacities of the eutectic mixtures $LiCl\text{-}SrCl_2$ and $LiCl\text{-}BaCl_2$.

PART 2. CHEMISTRY

2.1. Phase Equilibrium Studies

Extensive studies of phase equilibria in fused-salt mixtures have been made over a period of years in order to provide information needed for the selection of fuel and coolant mixtures for use in aircraft reactor systems. Reference is made to detailed reports on these studies.

A comparison of the Russian and ORNL investigations of the $NaF\text{-}ThF_4$ system is presented. It has been found that unclassified Russian reports presently represent the predominant number of contributions to the literature of phase equilibrium studies of fused-salt mixtures. Since 1946 more than 200 Russian reports have been issued concerning the phase equilibria of oxide, silicate, chloride, nitrate, and fluoride systems.

A disproportionation reaction was found to interfere with investigations of phase equilibria in the $NaF\text{-}CrF_2$ system. Various efforts to produce pure $NaF\text{-}CrF_2$ samples that are free of Cr^{+++} have been unsuccessful.

The upper operating temperature for the thermal-gradient quenching apparatus has, through equipment modifications, been raised from 850 to 1300°C. In the revised apparatus a single, traveling, recording thermocouple was substituted for 18 monitoring thermocouples; the furnace was redesigned to permit the sample tubes to be protected by a static helium atmosphere during brazing; and a roller crimping machine was adapted for use in sample preparation in order to minimize sample tube expansion during heating.

Results of the use of the petrographic microscope for the routine inspection of solidified fuel mixtures are described. In such examinations, oxygen-containing compounds are detected and variations from a nominal composition are revealed.

An optical method is described for the determination of equilibrium paths and tie lines in ternary

fused-salt systems. Application of the method to the LiF-ThF$_4$-UF$_4$ system is demonstrated.

2.2. Chemical Reactions in Molten Salts

The results of a study of the disproportionation of UF$_3$ in fused-salt fuel mixtures are presented. Nonacidic fuel solvents that contain a high concentration of fluoride donor constituents, such as alkali fluorides, were found to increase the extent of disproportionation by complexing the acidic UF$_4$ (fluoride acceptor). The ease of alloy formation between the uranium formed and the container metal also noticeably influences the extent of the disproportionation. Less disproportionation occurred in copper vessels than in nickel vessels, and tantalum and molybdenum were found to be even more resistant than copper to alloying with the uranium formed. It was also found that UF$_3$ was oxidized by the alkali fluorides.

In comparison with UF$_4$-containing fuels, the UF$_3$-containing fuels exhibit a marked improvement in initial corrosion attack at high temperatures. Unfortunately, however, the difficulties arising from the deposition of uranium by disproportionation prevented the easy exploitation of UF$_3$ as a solution to corrosion problems.

Analyses of the results of determinations of the activity coefficients of FeF$_2$ and of NiF$_2$ in molten NaF-ZrF$_4$ (53-47 mole %) are presented. The numerical values of the activity coefficients of FeF$_2$ are, at 800, 700, and 600°C, 1.46, 2.20, and 3.28, with respect to the pure crystalline solid; 0.64, 0.66, and 0.66, with respect to liquid FeF$_2$; and unity, with respect to the standard state of reference at infinite dilution.

The results of similar studies of NiF$_2$ gave very large discrepancies between the calculated and experimental equilibrium constants and very high values of the activity coefficients. It is clear from the values of the activity coefficients that when NiF$_2$ is dissolved in NaF-ZrF$_4$ (53-47 mole %) it behaves in a manner vastly different from that predicted by the free energies of formation for solid NiF$_2$. It is postulated that the values available for the free energies of formation of solid and liquid NiF$_2$ are not accurate.

Solubilities and activity coefficients of NiF$_2$ as functions of solvent composition in NaF-ZrF$_4$ mixtures are being measured in an effort to locate the positions of the maximums of the activity coefficient and the solubility. The present results indicate that the effective Z/R average of the solvent may correspond closely to that predicted by the previously proposed acid-base scale. An observation that the value of the activity coefficient of the NiF$_2$ solute is not dependent on the solubility has verified a previous conclusion that the precipitating phase is not NiF$_2$.

A summary of the results of studies of the reduction of UF$_4$ by chromium in various fluoride reaction mediums is presented, as well as data for the reaction of UF$_4$ with various other metals, including Inconel, in which the activity of chromium is much less than unity. In all solvents studied the chromium concentration decreased as the UF$_3$ concentration increased. The implications of the studies are analyzed in terms of the corrosion mechanism. Molybdenum was the only metal found to have stability in the NaF-LiF-KF-UF$_4$ mixture, and accordingly nickel-molybdenum alloys would be expected to resist corrosion by this fused salt. In the ZrF$_4$-based melts, molybdenum, niobium, and tungsten appear to be stable toward UF$_4$. Tantalum and vanadium appear to offer no advantage over chromium for either type of melt.

Extensive study of the reduction of FeF$_2$ by chromium in molten fluorides has indicated that the behavior is far from ideal. An analysis of Cr^{++}-to-Fe^{++} ratios obtained from equilibrium quotients determined by the filtration method and a comparison with activity coefficients obtained from the standard free energies of formation indicates that equilibrium was not attained in these experiments. It is apparent that the filtration method is not capable of establishing the Cr^{++}-to-Fe^{++} ratio in these reaction mediums at 600°C.

The results of experimental studies of the temperature coefficient of the equilibrium

$$2UF_4 + M \rightleftharpoons 2UF_3 + MF_2$$
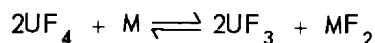
when molten-salt mixtures are used as the reaction mediums, were used as a basis for a thermodynamic interpretation of equilibrium data on the corrosion of iron and chromium by molten-salt fuels. The discussion covers the tendency toward mass transfer. It was expected from the similarity of the compounds CrF$_2$ and FeF$_2$ that their solution behaviors would be similar and that any difference would be governed by the difference of their $\Delta H°$ values. Experimental data proved this supposition to be invalid, and it must be concluded that some of the data are incorrect or that CrF$_2$ and FeF$_2$ have entirely different solution behavior.

A summary of the results obtained thus far in the determination of the solubilities of various noble gases in a number of different solvents is presented. In all the cases investigated, Henry's law was found to apply, and the solubilities were found to increase with temperature. For the same solvent, the solubilities of the gases decreased with increasing solute gas size. Variations in solvents showed corresponding gas solubilities to be approximately the same in two related ZrF_4-bearing solvents, but the solubility of helium in NaF-KF-LiF was found to be less than half that in the ZrF_4-bearing solvents.

The solubility of HF in mixtures in the NaF-ZrF_4 system has been determined as a function of temperature, pressure, and melt composition, and a summary of the results is presented. In all cases the solubility decreases with increasing temperature. Also, the Henry's law constants for the HF solubility illustrated a constant heat of solution over the experimental temperature range used for each composition.

Experimental studies of the solubilities of fission-product fluorides in molten NaF-ZrF_4 mixtures were made. It was found that varying the ratio of sodium to zirconium in the solvent had a considerable effect on the solubility of CeF_3. The solubility of YF_3 in NaF-ZrF_4 (53-47 mole %) was found to follow a pattern similar to the patterns obtained for the rare earths. The solubility values for CeF_3 and SmF_3 in combination in NaF-ZrF_4 (53-47 mole %) were found to be substantially the same as those found previously with NaF-ZrF_4-UF_4 (56-40-4 mole %) as the solvent.

Measurements were made of the solubility of BaO in KF-LiF (50-50 mole %). The results of three experiments unexpectedly showed the solubility to be quite high. This study is related to a systematic investigation of the possibilities of removal of fission-product fluorides from NaF-KF-LiF base mixtures. A comparison study of the reaction of CeF_3 and UF_4 with CaO in KF-LiF eutectic was also made. The precipitation of cerium as Ce_2O_3 suggests the possible separation of tetravalent metals, as oxides, from the trivalent fission products. Alternatives would be to precipitate uranium oxide and leave the fission products in solution or to precipitate the rare earths as oxides and leave the uranium in the solvent.

The results of a determination of chromium diffusion coefficients in Inconel–molten salt systems are described. This investigation was undertaken because experiments carried out over the past few years on the migration of metal as a result of temperature gradients in a molten-salt environment suggested that the over-all migration rate is controlled by the diffusion rates within the metal.

An analysis of steady-state chromium migration in thermal-convection loops is described. Information available from the many thermal-convection loops operated to date is correlated in order to develop a method whereby the amount of chromium transported can be estimated as a function of loop operating time, and the extent of corrosion to be expected at any time can be predicted.

Measurements of the activities of the metallic components of container materials for fused-salt fuels have been made in order to study the effects of composition and temperature on the activities and thus on the corrosion resistance of container alloys. The activity of chromium in nickel-chromium alloys (Inconel) has been studied, and the results of studies of the nickel-molybdenum system are presented. In future work the chromium-molybdenum system is to be studied, as well as the ternary system nickel-molybdenum-chromium, which includes the INOR alloys developed by the Metallurgy Division.

The possibility of dissolving stainless steel fuel elements in molten fluorides, with the resultant advantage of adaptability to the present volatility method for fuel reprocessing, prompted some exploratory experiments. In general it appears that a practical process could be evolved for removing the uranium from the steel and leaving a constant nonaccumulative heel in the reactor vessel. This heel could be flushed out periodically with a dummy salt mixture.

In experiments for studying the oxidation of sodium and potassium mixtures it was found that the variables could not be controlled sufficiently to establish any quantitative effect of original composition on the Na-to-K ratio in the mixed oxides. The data show, however, a significant decrease in the ratio of Na to K in the mixed oxides upon an increase in the potassium content of the original alkali metal mixture from 49 to 77 wt %.

2.3. Physical Properties of Molten Materials

Methods used for vapor pressure studies of molten salts are described, and the results obtained in these studies are summarized. Reference is made to a concurrent effort to measure vapor pressures that was carried out at Battelle Memorial Institute.

Future vapor pressure investigations of fused fluorides of reactor interest will involve systems containing BeF_2. Difficulty will be encountered at BeF_2 concentrations of less than 75 mole % because vapor-phase compounds will contribute appreciably to the total pressure. It will be necessary to obtain partial pressures. Methods for these measurements are being developed.

A mass spectrometric study of salt vapors is also being planned in order to obtain an understanding of the nature of dimeric and trimeric molecules in the vapor of alkali halides. Polymer formation can cause components of salt mixtures to be even more volatile as part of an associated species than the pure component is, in some cases. A preliminary study is described for which potassium chloride was chosen as a suitable material with which to develop the method.

The results of surface tension determinations on molten salts by three different methods are compared. The methods used were the sessile-drop technique, the maximum-bubble-pressure technique, and a tensiometer technique. During the course of these experiments it has become apparent that further information is needed on the wetting characteristics of fluoride salts.

2.4. Production of Purified Mixtures

A summary of experience in the synthesis for use in ANP chemistry studies of compounds that were not available commercially is presented. Of particular interest were fluorides of the metals being considered as container materials for various fuels and the products of their reactions with constituents of proposed fuels. Corrosion products found in fuels were identified by comparison of their x-ray diffraction patterns and optical crystallographic properties with those of synthesized compounds. Fluorides of the fission products were prepared for use in the study of their effects on the fuel mixtures of interest.

Summaries are presented of the experience in the preparation of fuel for the Aircraft Reactor Experiment and of the establishment and operation of pilot-scale and production-scale purification apparatus.

2.5. Analytical Chemistry

Work was terminated on the development of an instrument which would serve to monitor the exhaust gases from the ART by detecting traces of NaK in air. The instrument was based on the measurement of the absorption of sodium resonance radiation by sodium atoms. It is thought to be applicable to the detection of a concentration of sodium in air that would be equivalent to the introduction of a total volume of 6 cm^3 of NaK per hour to the exhaust gases. This corresponds roughly to an increment of 10 ppb of NaK across the NaK-to-air radiators. The test model showed that the response of the instrument to small increments in the concentration of sodium in air samples was almost instantaneous, and the model was satisfactorily stable and reliable in all respects. Other methods of detection which were evaluated during feasibility studies included photometric smoke detectors, emission spectrography, flame photometry, and surface ionization detectors. These methods were not considered to be as promising as the resonance radiation absorption technique because they either lacked adequate sensitivity or presented technological complications that would make their application to the ART extremely difficult.

The apparatus for the determination of oxygen in fluoride salts with potassium bromotetrafluoride was put into operation. The gas-measuring system of the apparatus was calibrated to a precision of about 2% with oxygen. The method was also tested on samples of yttrium oxide and is being used routinely for the determination of oxygen in yttrium fluoride. The precision of the method with respect to yttrium fluoride appears to be less than 5%.

PART 3. METALLURGY

3.1. Nickel-Molybdenum Alloy Development Studies

The developmental work on nickel-molybdenum-base alloys for use as reactor structural materials in contact with the fused salt fuel NaF-KF-LiF-UF (11.2-41-45.3-2.5 mole %, fuel 107) at normal

operating temperatures of 1650°F and above is summarized. The various alloys studied fell into three general categories: solution-hardening, precipitation-hardening, and dispersion-hardening alloys. The alloys were evaluated in terms of fabricability, mechanical properties, corrosion resistance, weldability, and aging characteristics. The results of the evaluations showed that the solid solution-hardening alloys most nearly met the specifications. Extensive work has been done in order to establish the final composition of the alloy selected on this basis (INOR-8) and to produce commercial quantities of the alloy.

Since the chromium content of INOR-8 was expected to limit the peak metal-salt interface temperature to the range 1650 to 1700°F, an alloy designated INOR-9 was being investigated. In this alloy the chromium is replaced with niobium, which does not corrode in fuel 107. Preliminary data on the properties of this alloy are presented.

3.2. Mechanical Properties Studies

The mechanical properties of the various materials to be used in circulating-fuel aircraft reactors have been investigated during the past several years. Fairly complete design data were obtained for Inconel, the structural alloy that was being used for the ART, for beryllium, the moderator material, and for various shielding materials. Basic information on the behavior of metals was also obtained in order to be able to predict the safe operating life of various components under a variety of operating conditions.

In the investigation of Inconel it was found that, in the fused-salt environment, the fine-grained material is stronger than the coarse-grained material at 1300°F but weaker at 1500°F and above. It was also found that, in order to improve the strength of Inconel without impairing its fabricating characteristics, it was feasible to add carbon through carburization of finished tubing.

It was found in the beryllium investigations that data obtained on a laboratory scale could be reliably applied to large-scale pressings.

Methods for interpolating and extrapolating the available data on mechanical properties have been explored, and several relationships have been found that have merit. Empirical equations based on specific data are available for Inconel.

Tests of both rod and tube specimens of Inconel were made in order to evaluate the effect of

strains that would be produced by thermal cycling during reactor operation. The results obtained in tests in which the strain was mechanically induced compared favorably with those of a supporting investigation at the University of Alabama in which thermally induced strains are being studied. The effects of temperature, grain size, environment, specimen geometry, and cycle frequency are summarized.

The shielding materials that have been investigated included an 80% Mg–20% Li alloy, an alloy of very pure lead with 0.06% copper, and a lead-lithium alloy.

3.3. Welding and Brazing Studies

A production facility for the manufacture of brazing-alloy rings according to techniques and procedures developed by the Metallurgy Division was set up by the Engineering and Mechanical Division. Approximately 750,000 rings were produced by the graphite-mold technique, and a production rate of 60,000 to 70,000 rings per day was achieved. Production of these rings at ORNL became necessary because the fabricator of the ART radiators could not obtain satisfactory brazing-alloy rings.

A procedure was developed for fabricating thermocouples for high-temperature service that involves brazing an end cap to the shield and thermocouple wires. This procedure replaces a welding technique used previously. Closures made by the welding technique were frequently rejected because of cracks and pores in the weld zone. Closures that are satisfactory as to both integrity and consistency in the distance between the end of the seal and the thermocouple junction are made by the use of the new brazing procedure.

An investigation of optimum methods for fabricating the tube-to-tube-sheet joints of the ART fill-and-drain tank was completed. A unique method for brazing the unit was developed that may be applicable to tube-to-tube-sheet joints of other types of heat exchangers.

Investigations were started of methods for welding niobium. Fusion welds were tested in simple bend tests and found to be ductile. Experiments are being carried out in order to determine differences in the weldability of arc-cast and powder-metallurgy niobium. Filler wires for welding niobium are also being tested. Both butt welds and tubing saddle welds have been

fabricated in an argon-atmosphere dry box by using the tungsten-arc process and zirconium-niobium filler wire. Impurities in the welding atmosphere have been found to have an embrittling effect.

Brazing tests were made on carburized Inconel tubes. The desired fine-grained structure was retained. Extensive grain growth would have occurred in conventional Inconel subjected to the same brazing cycle.

3.4. Corrosion and Mass Transfer Studies

In continuing screening tests of new brazing alloys, Handy and Harman brazing alloys No. 91 (91.25% Ni–4.5% Si–2.9% B) and No. 93 (93.25% Ni–3.5% Si–1.9% B) were found to have good corrosion resistance to NaF-ZrF$_4$-UF$_4$ (53.5-40-6.5 mole %, fuel 44) when tested in seesaw apparatus at a hot-zone temperature of 1500°F for 100 hr.

In similar screening tests, iron-base brazing alloys are being exposed to lithium as they became available. (High-nickel-content alloys have very limited corrosion resistance to lithium.) An 86% Fe–5% Si–5% Cu–4% B brazing alloy showed good corrosion resistance under static conditions but only fair resistance in seesaw-furnace tests at 1500°F for 100 hr.

Inconel welds made with nitrogen as the shield gas were tested for comparison with welds made with helium as the shield gas. The corrosion resistance of the welds made in nitrogen was about the same as that of Heliarc welds.

Several cermet-metal joints formed by fusion or brazing of TiC-Ni, WC-Co, and WTiC$_2$-Co cermets to metals were found to be corrosion resistant to molten sodium and to NaF-ZrF$_4$-UF$_4$ (50-46-4 mole %, fuel 30) in 100-hr exposures at 1500°F. These cermet-metal joints were developed to permit these types of cermets to be joined to Inconel by brazing.

An examination was made of the rare-earth-oxide ceramic cylinders that constituted a prototype ART control rod and which were exposed to molten sodium for 3000 hr in a rigorous test of the control rod drive system. Some of the ceramic pieces were broken as a result of rather large thermal changes. There was no detectable corrosion of the ceramic cylinders by the sodium. Despite the breakage of some of the cylinders, the rod would have been satisfactory for ART operation because there was no change in the location of the cylinders.

Extensive grain-boundary penetration was found in the hot-leg areas of niobium thermal-convection loops in which lithium was circulated. These tests were conducted in a vacuum chamber. This penetration is thought to be due to attack on impurity phases, such as carbides, in the grain boundaries. Experiments are planned in which various grades of niobium will be tested in order to determine what factors control grain-boundary penetration.

A forced-circulation loop is being designed for studying lithium-niobium systems. The niobium tubing of the loop is to be protected from air oxidation by a continuous outer sheath of type 310 stainless steel.

A summary of the results of the extensive corrosion tests that were made of Inconel exposed to fused fluorides and to sodium and NaK is presented.

3.5. Materials Fabrication Research

An investigation of the recrystallization of niobium and the effects of recrystallization on recovery and on tensile properties was made. Except for the large grain size of recrystallized arc-cast material, no significant differences were found between arc-cast and powder-metallurgy material. Work has been initiated on fabrication of material for use in forced-circulation corrosion-testing loops. Attempts to fabricate tubing by extrusion of compacted pellets were unsuccessful because of failures in the tube walls during tube reducing. Billets of arc-cast material are being secured and will be extruded to produce tube blanks for redrawing. Methods for the protection of pump parts and other odd-shaped sections of a niobium loop from oxidation during testing are being investigated. Sprayed coatings of brazing alloy appear to offer a possible solution to the problem.

Further development of equipment has provided means for producing yttrium sponge of increasing purity. Analysis of a recent batch of sponge detected only 1000 ppm of oxygen, and a sample of this sponge after arc-melting was reduced 37% in area by cold-swaging.

Equipment is being prepared to make possible the direct transfer of the molten fluoride charge

into the reaction retort in order to eliminate con-
tamination from handling. Molten-state transfer of
the lithium reductant is now being practiced.

The work on the neutron shield and the shield
plug for the ART fuel pumps was completed, and
a report describing the development work was
prepared.

The tensile strength and ductility of core material
for tubular control rods were determined from
extruded specimens. These specimens were pre-
pared from especially processed Lindsay oxide
and had somewhat greater ductility than previously
tested material.

Developmental work was initiated at the request
of GE-ANP on high-density BeO bodies for use
as moderating material. Very fine particles of
BeO are being obtained by the controlled cal-
cination of $BeSO_4$.

Rods of MgO and of BeO were extruded to
provide rod insulators with four longitudinal
holes. Rods of this type are required for thermo-
couple assemblies.

Methods are being developed for hydriding dense
yttrium metal when it becomes available. Reactor-
grade zirconium, which is available and which
responds to hydrogen in much the same manner
as yttrium does, is being used in developing the
hydriding process.

3.6. Metallographic Examinations of Engineering Test Components After Service

The results of examinations of the ART pro-
totype test radiator No. 1, which failed immediately
after reaching full power in its first controlled
thermal cycle, are presented. Data on fin-to-tube
joint braze integrity and the degree of oxidation
of the fin collar are compared with similar data
on other radiators. Incomplete melting of the
braze alloy rings was found in several instances.
Corrosion and mass transfer were negligible, as
was expected in view of the short operating period.
It is concluded that the tube failure which per-
mitted the NaK leak could have been the result
of at least three things: reaction with an in-
sulating material, damage to the tube during
fit-up and brazing, and the presence of stringers
across the tube wall.

Test radiator No. 2, which failed during the
182nd thermal cycle, was also disassembled and
sectioned. Forty tubes from the damaged area
were examined, and only one was found that

showed signs of incipient failure. The evidence
of incipient failure was similar to that found
previously in creep test specimens.

3.7. Nondestructive Testing

The inherent accuracy of the new eddy-current
thickness gage was increased by the replacement
of the previously used variable-frequency signal
generator with drift-free transistor oscillators. Small
cup cores that will produce symmetrical electro-
magnetic fields and will decrease the size of
the field are being constructed to improve eddy-
current cladding-thickness determinations.

Preliminary use of a closed-circuit television
system for direct x-ray imaging has given en-
couraging results. The technique for use of this
system is similar to that used in conventional
radiography. The greatest area of usefulness of
the system will be in the inspection of thin
sections through which high-intensity radiation can
reach the photoconductive target.

Routine inspection of tubing, pipe, and plate
was performed by using immersed-ultrasound and
eddy-current techniques. A special lot of Hastelloy
B was found to be among the best tested to date.

PART 4. RADIATION DAMAGE

4.1. Radiation Damage

Examinations of the four forced-circulation loops
that were operated in the MTR with fused fluoride
fuels as the circulated fluids have been completed.
The final items examined were the impeller
housings of the pumps used in loops 4, 5, and
6. No evidences of erosion were found on the
impellers.

Examinations were continued of the moderator
materials that were irradiated in the second ex-
posure in the MTR. No cracking or flaking of
the graphite slug that was encased in nickel was
evident, and the dimensions of the slug after
irradiation were essentially the same as those
prior to irradiation. Metallographic examination re-
vealed no reaction between the nickel and the
graphite. When the zirconium hydride slug that
was encased in molybdenum was being sectioned,
the casing separated from the slug, and thus it
appears that there was no bonding. The molyb-
denum was very brittle. Metallographic studies of
these specimens are continuing in an investigation
of significant differences between irradiated and
control capsules.

The out-of-pile tests that correspond to the MTR tube-burst tests were completed. The times to rupture were two to five times longer than in the MTR tests, but were of the order of a factor of 4 shorter than in tests conducted by the Metallurgy Division under similar conditions. Further investigation has revealed that the fused-quartz insulation used in these in-pile and out-of-pile tests caused changes in the calibration of the Chromel-Alumel thermocouples that were operating in a helium atmosphere. These changes gave higher temperatures than those indicated. The higher temperatures partially account for the shorter times to rupture, but they do not entirely account for the loss of ductility being greater in the in-pile tests than in the out-of-pile tests. Results of extensive tests in the LITR are also reported. The tube-burst specimens have exhibited the low ductility found in the MTR test specimens.

Disassembly of the vertical in-pile loop which circulated fused salt fuel in the LITR for 235 hr was completed, and various parts are being examined and analyzed. The lubricant was found to have decomposed and become waxlike.

An Inconel capsule and two Hastelloy B capsules were examined that had been irradiated in the MTR in contact with fused salt fuel. The Inconel was attacked 1 to 2 mils in 304 hr at 1500°F; the power density was 6000 w/cm^3. There were thin films on the surfaces of the Hastelloy B capsules, but the corrosion was negligible. Attempts are being made to identify the film and to determine the mechanism of deposition.

In an investigation of irradiation effects in photoconductive detectors, both neutron and gamma-irradiation have been found to decrease the photoresponse of PbS cells, and the decrease is proportional to the total integrated flux. There is threshold damage that seems to depend upon the dimensions of the sample, which, if exceeded, completely destroys the cell. Below threshold the cell recovers in a first-order process. The photoresponse at 24,000 Å and above fails before that at shorter wavelengths. In addition to a decrease in response, the noise level increases with irradiation.

A state-of-the-art survey of irradiation effects in semiconductor barriers is presented to unify the material presented in previous progress reports

and to establish a reference of current concepts. With this survey as a basis, subsequent reports will present a coherent picture of the progress being made in these investigations.

PART 5. SHIELDING

5.1. Shielding Theory

For most calculations of neutron scattering in air, isotropic scattering in the center-of-mass system is assumed, although it does not represent the actual case. For purposes of comparison, a calculation was performed in which anisotropic scattering was assumed. The results from the calculations indicate that the isotropic scattering method of calculation is conservative.

Another calculation was performed to determine the spectra of bremsstrahlung radiation resulting from the degradation of electrons in sodium iodide and in air. The assumptions made, the equations used, and the results obtained are presented.

A third calculation was prompted by the need of aircraft shield designers to know the production of secondary gamma rays by neutron interactions in air. The problem was idealized to that of determining the dose rate and angular distribution of gamma rays at a detector located an arbitrary distance from a neutron source. The source and the detector were considered to be embedded in an infinite volume of air. The source was taken to be either a point isotropic source of monoenergetic neutrons or a point source which emitted a mono-energetic line beam of neutrons at an angle θ_0 with respect to the source-detector axis. For a point isotropic source and a 50-ft separation distance, it was found that the dose rate varies with the neutron source energy approximately as $E^{-1/3}$. When curves for various monoenergetic line-beam sources and a 65-ft separation distance were plotted as a function of θ_0, they were relatively flat over the region from 30 to 180 deg, and they became flatter as the source energy increased. Since aircraft reactor shields are usually designed so that most of the neutron leakage is from the rear, the results of the line-beam calculations indicate that a knowledge of the exact surface distribution of low-energy neutrons is of less importance than a knowledge of the energy spectrum and total neutron leakage.

5.2. Lid Tank Shielding Facility

A second group of tests of advanced shielding materials was performed in conjunction with the Pratt & Whitney ANP shield design effort. In this group of tests particular emphasis was placed on a study of the production of secondary gamma rays in a gamma-ray shield of depleted uranium. In most cases, slabs of nickel and stainless steel were placed between the fission source and the uranium. Borated water was always used as the neutron shield behind the uranium.

Another series of tests with advanced shielding materials was performed at the request of General Electric. These tests, again, were designed for a study of the production of secondary gamma rays in gamma-ray shields. The materials used in this series of tests were Hevimet (largely tungsten), stainless steel, and depleted uranium. Lithium hydride was also included in most of the configurations tested, and, since it is highly reactive with water, oil rather than water was used as the neutron shield.

5.3. Tower Shielding Reactor II

The mechanical design of the Tower Shielding Reactor II (TSR-II) has been modified slightly to provide more clearance for the thermal expansion that will occur at the highest operating powers. A second mockup of the control mechanism has been constructed and is undergoing testing. Additional nuclear calculations have been performed, from which it has been found that the control plates could be worth 6% in k. The critical mass, which was found to be 8.2 kg of U^{235}, will be checked with further calculations and in a mockup experiment with dummy fuel elements and uranium solutions. The design of the water cooling system is approximately 95% complete.

5.4. Tower Shielding Facility

Gamma-ray measurements in various crew-shield mockups at the Tower Shielding Facility have indicated an intensity which is greater than that expected from scattered gamma rays alone. This prompted a study of the production of secondary gamma rays in air, both those resulting from thermal-neutron capture in nitrogen and those resulting from inelastically scattered fast neutrons. For this study an experiment was performed in which a beam of neutrons from the reactor irradiated a cone of air, and the gamma rays resulting from neutron interactions within the cone were observed by a gamma-ray spectrometer several feet away. The ratio of the nitrogen capture gamma rays observed by the detector to other gamma rays observed was varied by covering the reactor neutron beam with boron-impregnated Plexiglas for some of the measurements. The difference between the measurements was then used to separate the pulse-height spectrum associated with nitrogen capture gamma rays from the spectrum associated with other sources. In this report the spectrum which remained after the subtraction of the capture-gamma-ray spectrum was presumed to be due to inelastically scattered fast neutrons; however, contributions from other sources, such as air-scattered gamma rays, must be considered. The results of the experiment are to be compared with theoretical calculations of the pulse-height spectra to be expected from neutron interactions with air, as well as from scattered gamma rays.

CONTENTS

PART 3. METALLURGY

PART 4. RADIATION DAMAGE

PART 5. SHIELDING

Part 1

AIRCRAFT REACTOR ENGINEERING

1.1. REACTOR AND FACILITY CONSTRUCTION

W. F. Boudreau   A. P. Fraas

H. W. Savage

STATUS OF THE ART-ETU PROGRAM AT TIME OF TERMINATION

A. P. Fraas

The Aircraft Reactor Test was designed as a 60-Mw circulating-fuel reactor having a major portion of the features essential to an aircraft propulsion reactor. The details of the design have been reported, as they were developed, in previous reports in this series, and they were summarized in a design report.[1] Diagrams of the reactor and the cell in which it was to operate are presented in Figs. 1.1.1, 1.1.2, and 1.1.3. At the time of termination of the program, a full-scale, non-nuclear engineering test unit (ETU) that essentially duplicated the ART was being fabricated and assembled. The ETU was to demonstrate the feasibility of fabrication and assembly, and, in high-temperature operation, to test the effects of the complex thermal and pressure stresses expected during nuclear operation. The complex geometry, the wide variety of stresses, and the difficulty of predicting the magnitude and direction of thermal warping and distortion had indicated the need for a comprehensive test on a non-nuclear assembly. Upon completion of the planned tests, the ETU was to have been disassembled and thoroughly examined before operation of the ART.

At the time of cancellation, the design, the shop drawings, and much of the component testing and fabrication had been completed. All outside contract work on the facility in which the ART was to operate had been completed, and work was to have started on the installation of the process piping.

The analysis of the design of the ART was completed except for a number of thermal stress analysis problems intimately related to test work which was in progress. Sufficient analytical and test work had been completed to indicate that the design was adequate to carry the basic pressure stresses and a modest number of thermal cycles. The design objective was a nominal life of 300 thermal cycles, whereas the operating program

anticipated only 30 full thermal cycles; thus a factor-of-10 margin was provided to ensure a high degree of reliability. The results of the analytical design studies agreed surprisingly well, in most instances, with the results of tests of components, for example, heat exchangers. It was expected that the programmed tests would have confirmed the results of analytical studies of the designs of other components.

Much of the extensive program of component testing had been completed. The performance testing of the pumps was finished, together with much of the extensive endurance test program. The fuel-to-NaK heat exchanger component test work was largely completed, except for some tests on circular-arc tube bundles designed to simulate in considerable detail the geometry of the full-scale reactor.

Difficulties were experienced with leaks caused by thermal stresses in the prototype NaK-to-air radiators that were tested, but design modifications were made which, it was believed, would give an acceptable arrangement. Tests of the modified radiators were to have been started shortly after the program was cancelled. The reflector cooling circuit was completely worked out and checked in flow tests. The core hydrodynamics had posed many problems, but tests were made in the fall of 1957 on a combination of screens which was found to be effective in suppressing local temperature fluctuations. The control-rod drive mechanism had been thoroughly tested and found to be satisfactory in extensive endurance tests. The principal area in which component test work remained to be done was in structural tests of the thin shells. This work had been delayed by difficulties in fabricating these shells, but analytical and preliminary test work on models indicated that the shell designs were satisfactory.

Much of the fabrication of the first set of parts was completed. The pumps were available; the basic parts of the north head were finished, including the sodium-to-NaK heat exchangers, and the assembly work was 70% completed. The island beryllium and core shell assembly was completed, and the beryllium for the reflector was machined and ready for assembly, as were the

---

[1] A. P. Fraas and A. W. Savolainen, *Design Report on the Aircraft Reactor Test*, ORNL-2095 (Dec. 7, 1956).

1
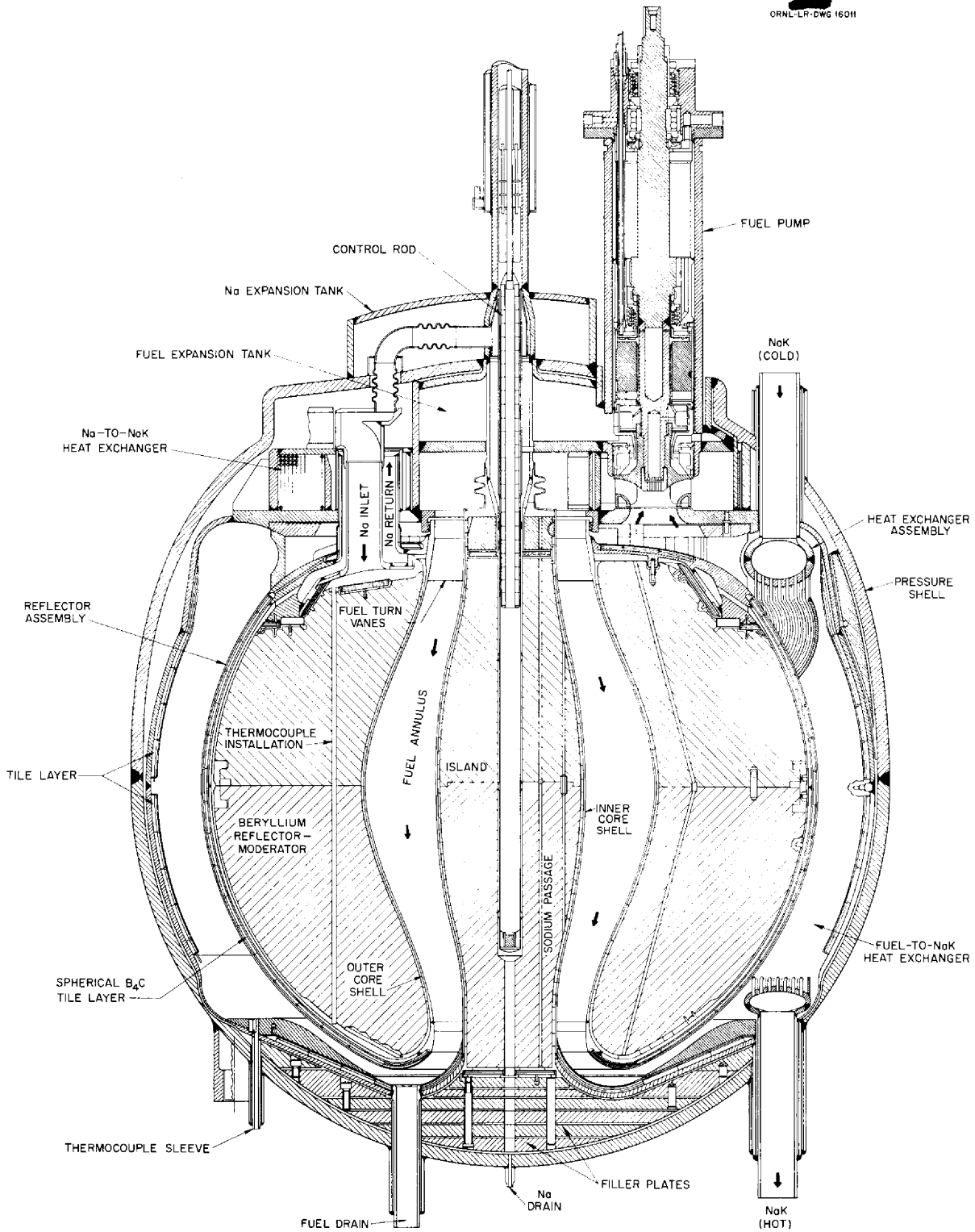
ORNL-LR-DWG 16011

Fig. 1.1.1. Vertical Section Through Reactor Assembly.

Labels on figure:
- CONTROL ROD
- Na EXPANSION TANK
- FUEL EXPANSION TANK
- Na-TO-NaK HEAT EXCHANGER
- Na INLET
- Na RETURN
- REFLECTOR ASSEMBLY
- THERMOCOUPLE INSTALLATION
- TILE LAYER
- FUEL TURN VANES
- BERYLLIUM REFLECTOR-MODERATOR
- FUEL ANNULUS
- ISLAND
- SPHERICAL B₄C TILE LAYER
- OUTER CORE SHELL
- SODIUM PASSAGE
- INNER CORE SHELL
- THERMOCOUPLE SLEEVE
- FUEL DRAIN
- Na DRAIN
- FILLER PLATES
- FUEL PUMP
- NaK (COLD)
- HEAT EXCHANGER ASSEMBLY
- PRESSURE SHELL
- FUEL-TO-NaK HEAT EXCHANGER
- NaK (HOT)

ORNL-LR-DWG 16457

TYPICAL LiOH CAN

CONTROL ROD

ALUMINUM TANK

18-in.-THICK BORATED WATER SHIELD

FUEL PUMP DRIVE HYDRAULIC MOTORS

HEXAGONAL CANS FILLED WITH LiOH

PARAFFIN

REACTOR SUPPORT PADS

ALUMINUM TANK

SUPPORT FOR WATER SHIELD

HANGER RODS
SUPPORTING LEAD SHIELD

4.3-in.-THICK LEAD
GAMMA-RAY SHIELD

1/2-in.-THICK
AIR GAP

10-in.-THICK BORATED
WATER SHIELD

STEEL SUPPORT STRUCTURE FOR
THE REACTOR ASSEMBLY AND THE
LEAD AND WATER SHIELDS

ALUMINUM TANK

33-in.-THICK BORATED
WATER SHIELD

REACTOR
PRESSURE SHELL
ASSEMBLY

COOLING WATER PASSAGES,
3/4-in.-OD TUBES ON
4-in. CENTERS

1/2-in.-THICK
THERMAL INSULATION

HEXAGONAL CANS FILLED WITH LiOH

3-in.-THICK LEAD GAMMA-RAY SHIELD

1/2-in.-THICK THERMAL INSULATION

FUEL DRAIN LINE

Fig. 1.1.2. Vertical Section Through Lead-Water Shield.

ORNL-LR-DWG 15056

2 0 2 4 6 8
FEET
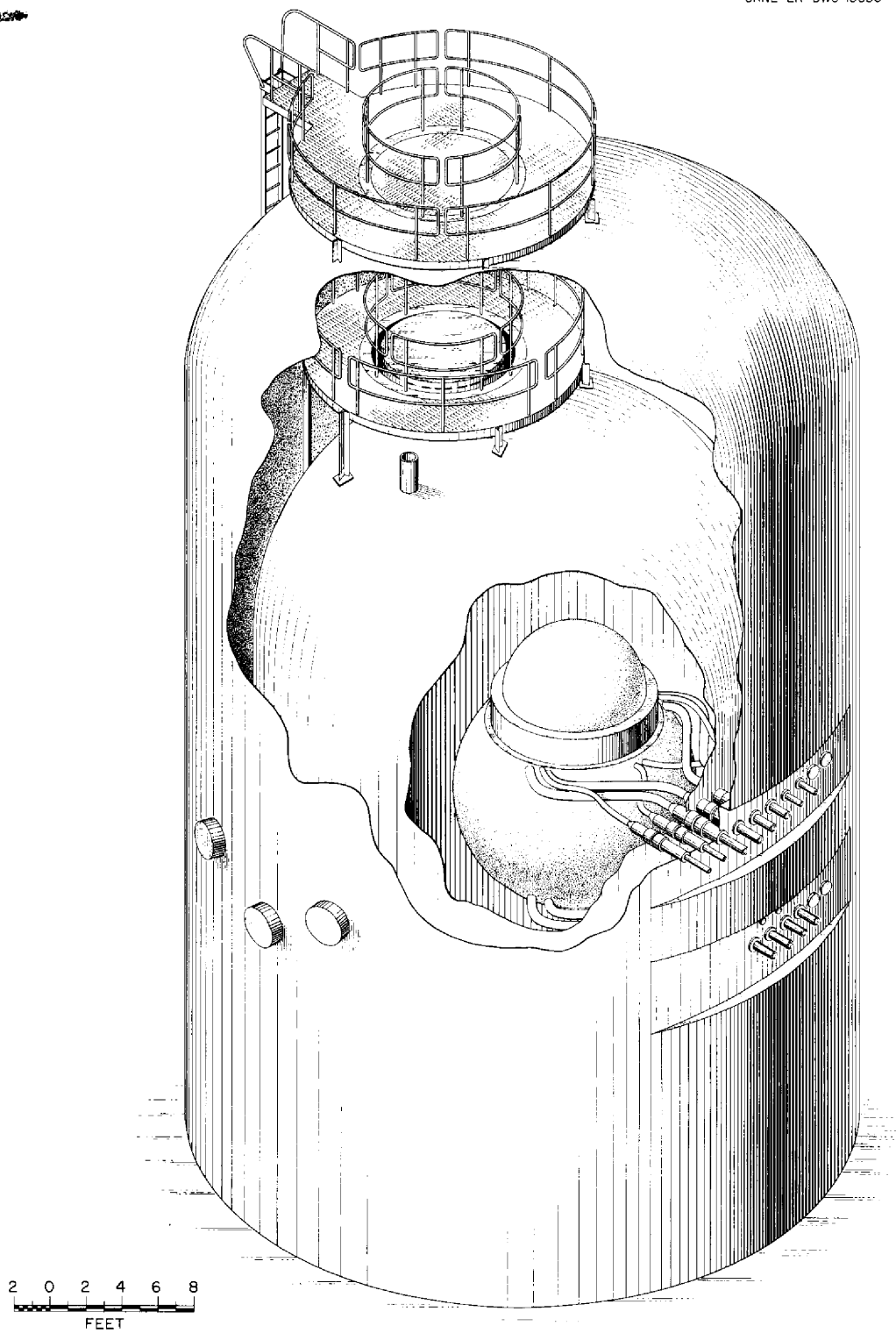
Fig. 1.1.3. Reactor Assembly Cell.

boron-bearing parts for the boron curtain. A proto-type main fuel-to-NaK heat exchanger tube bundle had been completed and was found to meet specifications. The remaining tube bundles were expected at the rate of two per month. The forging for the pressure shell was being machined.

The ART design presented some difficult problems in the fabrication of thin-walled Inconel shells, particularly in connection with the core shells and the thin, hemispherical shells for jacketing the boron. Various techniques, including hydrospinning, pressing, and machining from forgings and pressings, were investigated. Hydrospinning was found to be unsatisfactory, but the core shells were machined readily to the desired tolerances from pressings and were ready for assembly. It was found that the large-diameter thin-walled hemispherical shells could not be fabricated by hydrospinning, but similar parts were made (with dies built for a missile application) which showed that these parts could be fabricated by hydraulic pressing. New dies for the ART parts were scheduled for completion in November 1957.

Construction work on the facility for the ETU was under way in the experimental engineering building. The ART facility in which the second reactor assembly was to be tested was, as stated above, completed and ready for the installation of process piping. A summary description of the construction of the facility is given in a subsequent section. Plans had been completed for training operating crews, and operating procedures were being prepared. These items are also described in a subsequent section.

CANCELLATION OF FABRICATION AND CONSTRUCTION ACTIVITIES

W. F. Boudreau

Arrangements were made, immediately after notification was received to cancel work on the ETU and the ART, to halt construction and fabrication activities in the Oak Ridge area and at the various vendors' plants. All work was terminated in a manner that preserved tooling, materials, and partially completed components in a condition suitable either for the future resumption of the work or for adaptation to other uses. The ETU and the ART facilities were put into standby condition pending a determination of their usability for other purposes.

Termination reports have been prepared which summarize the reactor and facility construction activities. The first of these, which describes the construction and procurement work for the ETU and ART reactors and the ETU facility, has been essentially completed except for material which is to be prepared by the vendors of heat exchangers, radiators, and other equipment. In addition to descriptions of the various problems encountered in construction, assembly, and procurement, and the solutions that were found for them, this report will contain a brief analysis and summary of expenditures for the various phases of the work.

A summary report on the planning for removal and disassembly of the ART has also been prepared.[2] This document contains a great deal of information that can be expected to be of value to other projects, in particular, sections concerning methods for making accurate dimensional measurements on highly radioactive parts and methods for dissecting a relatively large and complex object by remote means.

SUMMARY OF ART AND ETU OPERATIONS PLANNING

D. B. Trauger

W. B. Cottrell   S. M. DeCamp
C. W. Cunningham   R. E. MacPherson

The ETU-ART Operations Group was established in the spring of 1956 to review the reactor flow sheets and general design from an operational standpoint, to prepare preliminary procedures for reactor operation, and, eventually, to train personnel and to operate the reactors. To augment the few people who could be made available for this work and to utilize experience and information from the various groups within the project, a committee was formed to assist in the preparation of procedures. The Operating Committee studied ART and ETU operational problems and conditions, and preliminary drafts of ART operating procedures were prepared. The initial procedures constituted, essentially, a basic philosophy of operation. With the pattern thus established, the activities of the Committee were completed, and the Operations Group went forward with the task of preparing detailed procedures.

[2]A. A. Abbatiello and F. R. McQuilkin, *ART Removal and Disassembly*, ORNL-2464 (in preparation).

The reactor flow sheets and control circuitry were used as the bases for the detailed operating procedures. At the time of cancellation of the program, most of the flow sheets were complete and up to date. Systematic tabulations of various components, such as thermocouples and valves, were made to clarify the requirements and to check the flow sheet nomenclature. An instrument tabulation was prepared which specified the service and requirements that every instrument was to fulfill.

Preparation of procedures served as a final check on the over-all design. The procedures prepared first included reactor disassembly, maintenance, operation of certain auxiliary equipment, pump startup, and filling and draining of the reactor. The studies of procedures led to numerous design changes; for example, the review of disassembly requirements alone revealed 45 necessary or desirable changes, while the fill-and-drain system studies resulted in the elimination of unnecessary equipment. Particular attention was given to radiation levels and other conditions to be expected where maintenance was likely to be required during operation. At the time of termination of the project, consideration had been given to procedures for most of the normal operating situations of both the ETU and ART.[3-6] In addition to the procedures pertaining specifically to sched-

uled reactor operation, separate procedures were to be prepared for servicing and maintaining instruments and other equipment and for complex maintenance, such as the replacement of a pump or a radiator.

Procedures for an operation such as the ART could not be developed in such detail that an operator unacquainted with the device could be expected to perform a safe and satisfactory operation. Therefore, a program of operator training was planned to provide the necessary background.

SUMMARY OF ART FACILITY CONSTRUCTION

F. R. McQuilkin

Lump sum contract work on the ART facility was completed. This work was contracted in four stages, as determined by the design program. The first stage, package 1, included major building alterations, additions to existing buildings, cell installation, installation of main air duct, installation of a 1500-kva substation, and installation of 480-v main switch-gear. The second stage, package A, included installation of auxiliary service piping. The third stage, package 2, included installation of diesel-generators and facility, electrical motor control centers, spectrometer room electrical system, and the spectrometer air-conditioning system. The fourth stage, package 3A, included installation of an electrical system for supplying power to the pipe and equipment heaters, a dry-air plant and facility, NaK pump motor controllers, a lube-oil fill-and-waste system, and a hydraulic system for louver operation. Tables 1.1.1, 1.1.2, and 1.1.3 present pertinent information concerning all ART lump sum contract work performed at the 7503 building.

---

[3]*ETU Operations: Status Report*, ORNL CF-57-10-7 (in press).

[4]*ART Operations: Status Report*, ORNL CF-57-10-9 (in press).

[5]*ETU Operating Procedures*, ORNL CF-57-10-8 (in press).

[6]*ART Operating Procedures*, ORNL CF-57-10-10 (in press).

Table 1.1.1. Contract Cost Summary

Total Lump Sum Contract Cost		$1,096,390.42
Contract AT-(40-1)-1952		881,852.25
Package 1, phase I	$607,526.68	
Package 1, phase II	274,325.67	
Package A	50,351.62	
Contract AT-(40-1)-1954		214,538.17
Package 2	71,557.67	
Package 3A	142,980.50	

Table 1.1.2 Contract AT-(40-1)-1952 Summary

Total Contract Cost		$881,852.25
Phase I — package 1	$557,175.06	
Phase II — package 1	274,325.57	
Package A	50,351.62	
Package 1		
Initial total contract cost	765,835.00	
Phase I, construction of additions to Building 7503	501,462.00	
Phase II, construction of 7503 cell (operational)	264,373.00	
Final total contract cost		831,500.63
Phase I	557,175.06	
Phase II	274,325.57	
Total number of contract deviations	45	
Official starting date	8-23-55	
Official scheduled completion date	8-1-56	
Actual completion date	10-9-56	
Contract liquidated damages rate		
Phase I	$100/day	
Phase II	$300/day	
Liquidated damages charged	None	
Reason liquidated damages charge not invoked	Contract deviations plus equipment delivery delays resulting from Westinghouse strike	
Prime contractor	V. L. Nicholson Co.	
Major subcontractors		
Electrical	Davis-Longsworth Electrical Corp.	
Mechanical	John F. Humphrey Co.	
Cell installation	Chicago Bridge & Iron Co.	
Designed by	K-25 Plant Engineering Dept.	
Approximate number of drawings	118	

<div align="center">Table 1.1.2 (continued)</div>

Package A

Initial contract price	$50,351.62	
Final contract price		$ 50,351.62
Official starting date	4-10-56	
Official scheduled completion date	6-29-56	
Actual completion date	9-26-56	
Prime contractor	V. L. Nicholson Co.	
Major subcontractors		
Electrical	Davis-Longsworth Electrical Corp.	
Mechanical	John F. Humphrey Co.	
Designed by	ORNL Engineering Department	
Approximate number of drawings	18	

<div align="center">Table 1.1.3. Contract AT-(40-1)-1954 Summary</div>

Total Contract Cost		$214,538.17
Package 2	$ 72,557.67	
Package 3A	142,980.50	
Package 2		
Initial contract price	58,400.00	
Final contract price		71,557.67
Total number of contract deviations	8	
Official starting date	1-25-56	
Official scheduled completion dates		
Part 1	6-22-56	
Part 2	1-27-57	
Actual completion dates		
Part 1	6-22-56	
Part 2	2-22-56	
Liquidated damage rate	$100/day	
Liquidated damage charged	None	

Table 1.1.3 (continued)

Reasons liquidated damages not invoked	Government-furnished diesel-generators were damaged in shipment and caused extensive equipment delivery delay. Contract extension was granted for excessive amount of time beyond the contractor's control required for performance of the specified diesel tests.
Contractor	Rentenbach Engineering Co.
Major subcontractors	
Electrical	Broadway Electrical Service Co.
Mechanical	Hicks-Ingle Co.
Designed by	ORNL Engineering Department
Approximate number of drawings	15

Package 3A

Initial contract price	$114,434.00	
Final contract price		$142,980.50
Capital expenditures	118,394.71	
Operational expenditures	24,585.79	
Total number of deviations	6	
Official starting date	12-7-56	
Official scheduled completion dates		
Initial	4-25-57	
Final	8-21-57	
Actual completion date	8-20-57	
Liquidated damage rate	$100/day	
Liquidated damage charged	None	
Contractor	Rentenbach Engineering Co.	
Major subcontractors		
Electrical	Broadway Electrical Service Co.	
Mechanical	Hicks-Ingle Co.	
Designed by	ORNL Engineering Department	
Approximate number of drawings	34	

A pictorial resume of the facility construction activity is presented with the following series of pictures which were taken at various stages of the construction program: Figure 1.1.4 shows a portion of building 7503 as it existed at the start of construction of the ART facility. When this picture was taken in September, some remodeling had been started. Figure 1.1.5 is an early view looking into the south side of the building. In the foreground can be seen the concrete reinforcing steel for the absorber pit and the cell foundation. In the background can be seen the forms required for the control-tunnel wall. Figure 1.1.6, which was taken in January 1956, shows the structural steel required for additions to the building. On the left can be seen the switchhouse. The foreground shows the stack foundation and the top of the absorber pit. Figure 1.1.7, which was made in January 1956, shows the early stages of cell and water vessel fabrication. Figure 1.1.8, also made in January 1956, shows the cell foundation and the first portion of the water tank that was installed. Figure 1.1.9 shows the status of the cell installation during the early part of March 1956. Figure 1.1.10 is a close-up view of the water vessel and cell which was taken in the latter part of March 1956. In the foreground can be seen the cell and a portion of the water vessel. In the background is the top section of the water vessel. Figure 1.1.11 was photographed during vacuum leak-testing of the cell in June 1956. It shows the cell water vessel in place as it would have been during ART operation. Figure 1.1.12 is a view looking into the main air duct. It was photographed in June 1956. Figure 1.1.13, which was also taken in June 1956, shows the 480-v switchgear. Figure 1.1.14, which was taken in October 1956, shows the cell after the head had been removed and placed in a storage area. This view represents the status of the cell after contract work was completed. Figure 1.1.15 was photographed in May 1956. It shows a portion of package A service piping in the auxiliary equipment room. Figure 1.1.16 was photographed in April 1956 and is a view looking at the west side of the building. In the right foreground can be seen the foundation for the diesel-generator building, which was installed under the package 2 contract. Figure 1.1.17 is a view of one of the two sections of the motor control center installed by the package 2 contractor. This was photographed in June 1956. Figure 1.1.18 is a view showing the five diesel generators which were installed by the package 2

contractor. This was photographed in July 1956. Figure 1.1.19, which was photographed in April 1957, shows portions of the electrical heater distribution panels which were installed by the package 3A contractor. Figure 1.1.20, which was also photographed in April 1957, shows the dry air station which was installed by the package 3A contractor. Figure 1.1.21 was also photographed in April 1957 and shows the regulator pit in the north basement and some of the induction voltage regulators installed by the package 3A contractor. Figure 1.1.22 shows the NaK pump motor controllers which were installed by the package 3A contractor. Figure 1.1.23 was photographed in August 1957. It shows a portion of the louver hydraulic operating system. Figure 1.1.24, which was photographed after construction activity ceased in August 1957, is a view looking south toward the building. In the foreground can be seen the diesel-fuel storage tank which was installed by the package 1 contractor. The transformer in the center of this view was also installed under the package 1 contract. On the right can be seen the "Braden" type building which houses the five diesel-generator units. It was constructed by the package 2 contractor. On the left can be seen the process water tank which was part of the existing ARE facility. Figure 1.1.25, which also was photographed in August 1957 after construction had ceased, is a view looking toward the southwest corner of the building. In the left background can be seen the diesel-generator house and in the left foreground is the compressor house. In the center is the blower house. In the right foreground is the vent house, stack, and top of the absorber pit. The generator house was installed by the package 2 contractor; the compressor house was installed by the package 3A contractor; and the blower house, vent house, absorber pit, and stack were installed by the package 1 contractor.

ORNL forces had painted the spectrometer tubes, installed tracks for the collimator dolly and the neutron spectrometer dolly, fabricated one set of heat barrier doors, vacuum leak-tested the lube-oil waste system, installed the unit heater in the switchhouse, and painted miscellaneous piping and structural steel.

A termination report on the construction of the ART facility has been prepared.[7]

---

[7] F. R. McQuilkin *et al.*, *Termination Report for Construction of the ART Facility*, ORNL-2465 (in press).
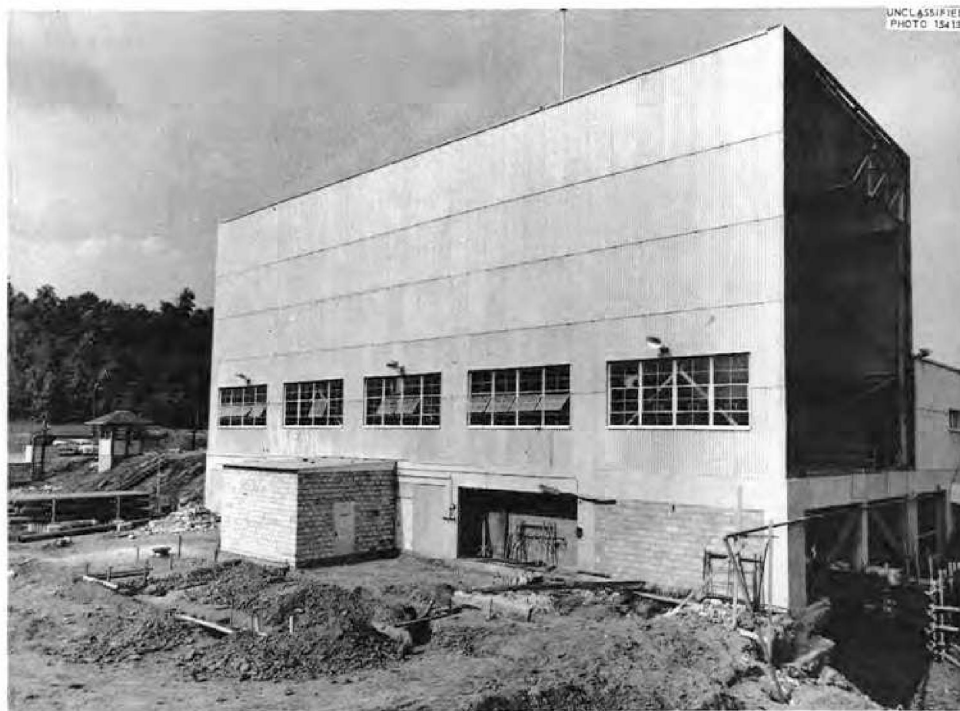
Fig. 1.1.4. Status of Construction at ART Building in September 1955.
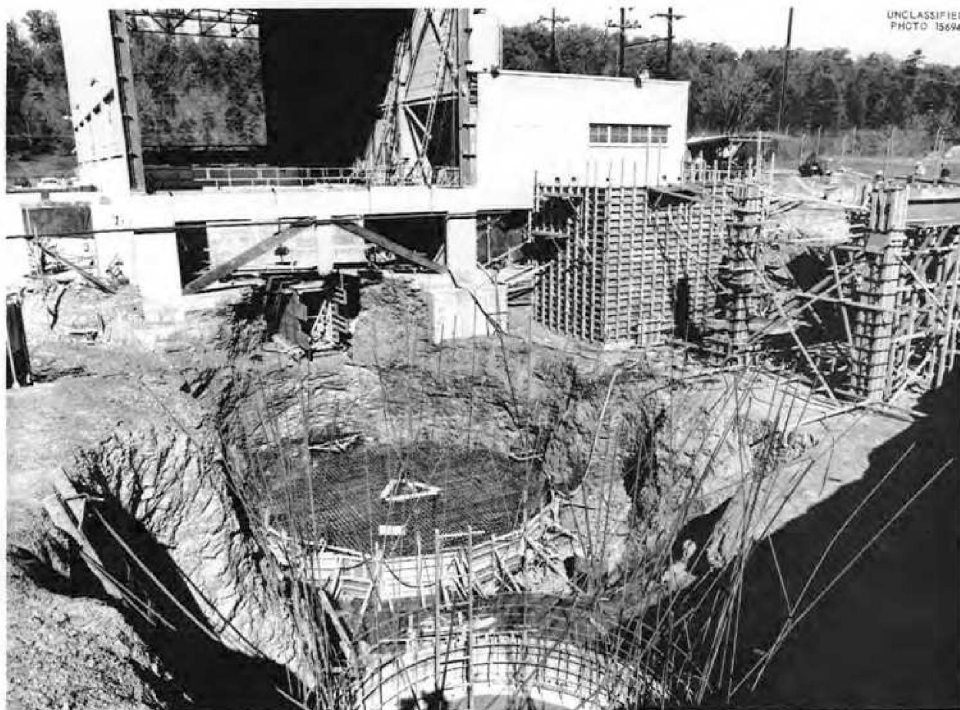
Fig. 1.1.5. Early Work on Absorber Pit and Cell Foundation.
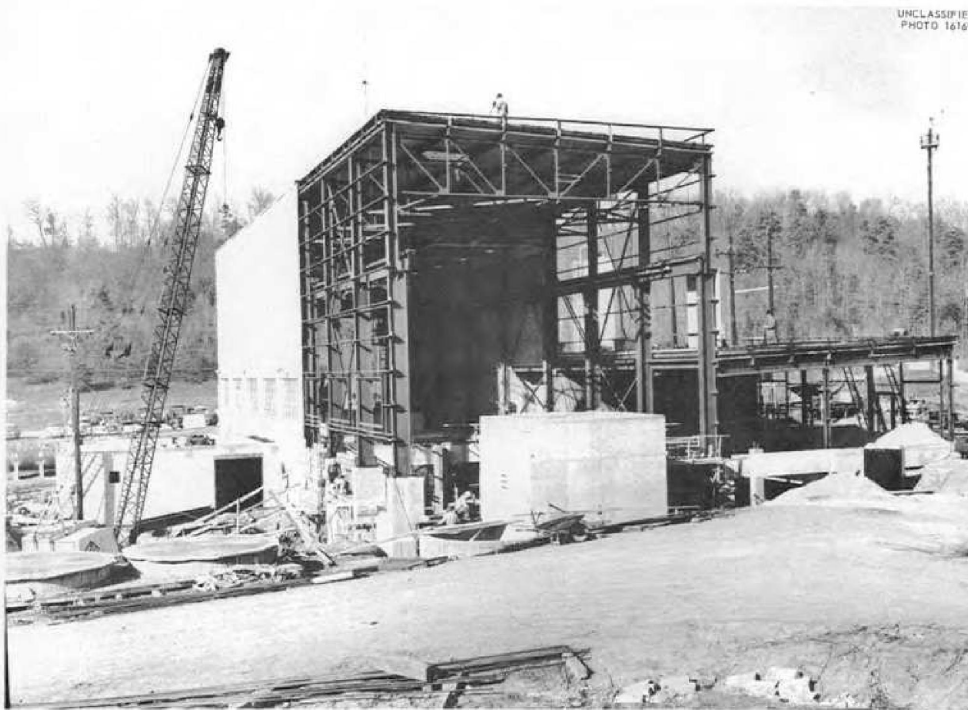
Fig. 1.1.6. Structural Steel for Additions to Building. January 1956.

Fig. 1.1.7. Cell Fabrication. January 1956.
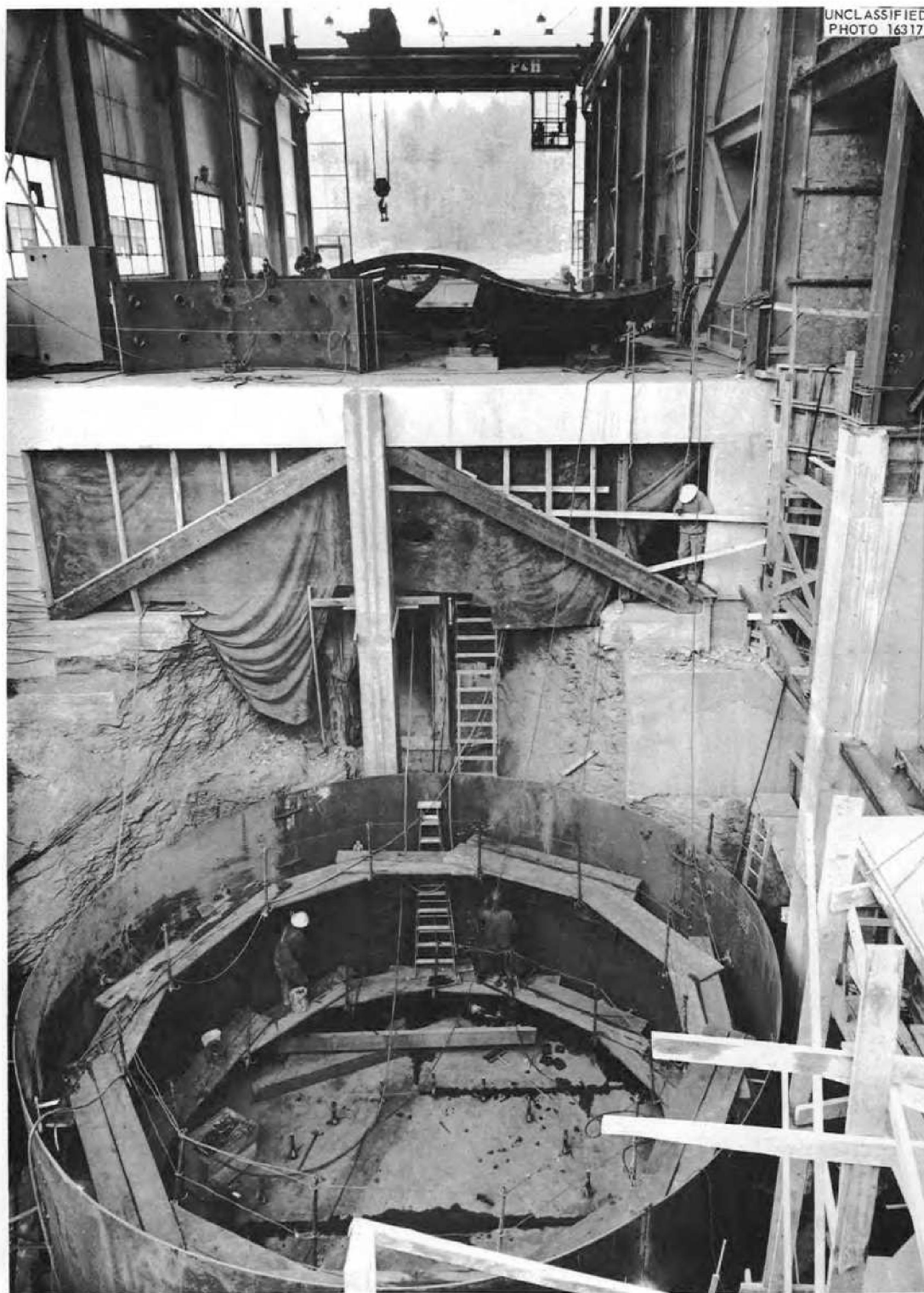
Fig. 1.1.8. Cell Foundation and Portion of Water Tank. January 1956.
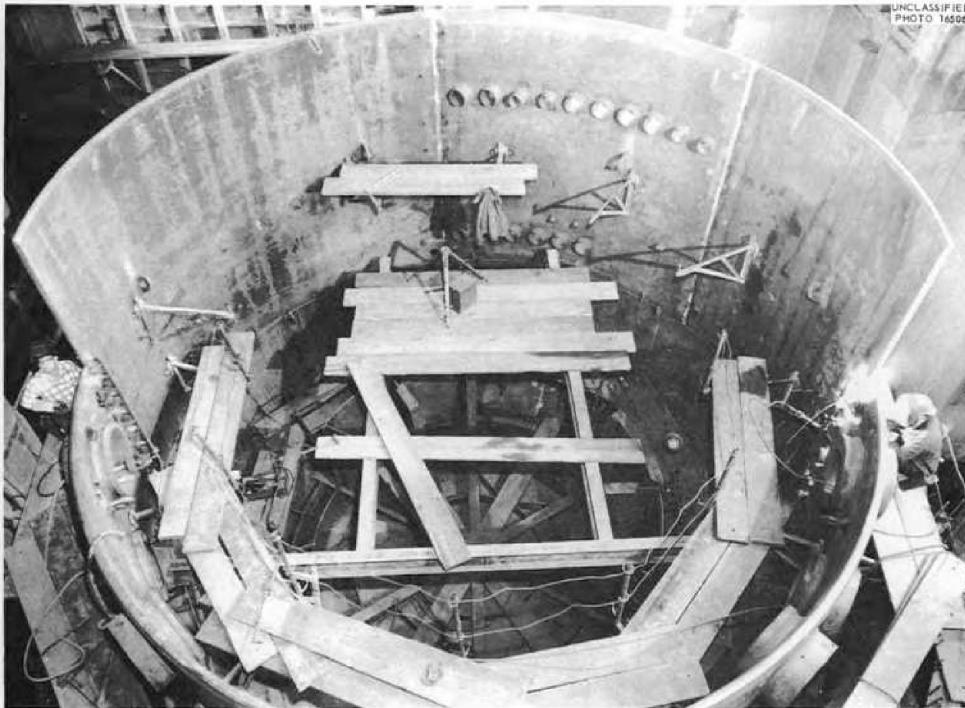
Fig. 1.1.9. Status of Cell Installation in Early Part of March 1956.

Fig. 1.1.10. Status of Cell Installation in Late March 1956.
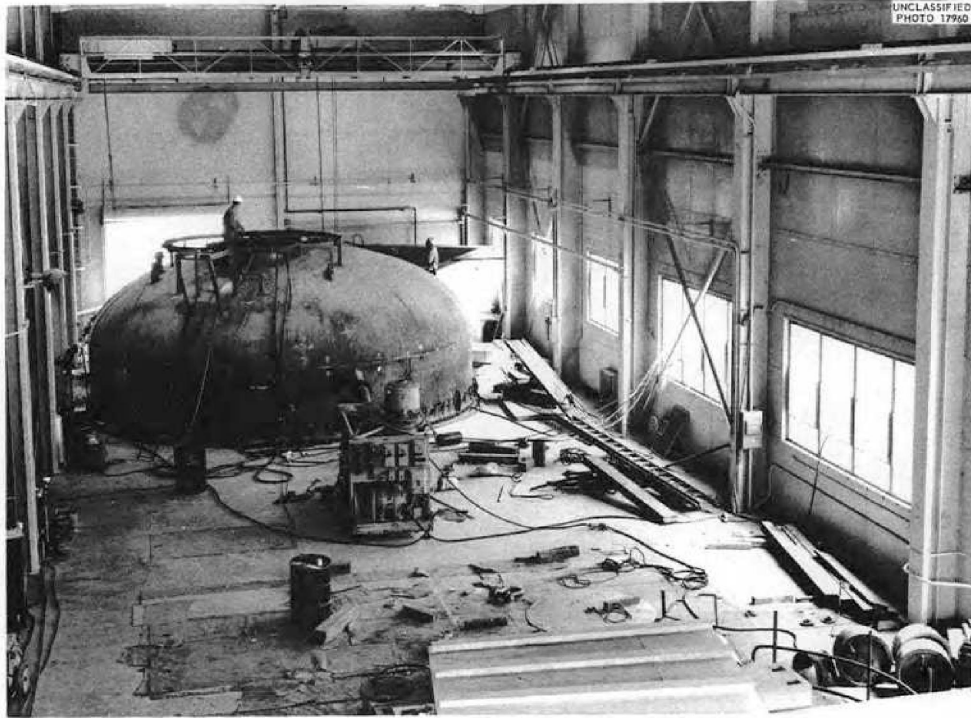
Fig. 1.1.11. Vacuum Leak Testing of Cell in June 1956.
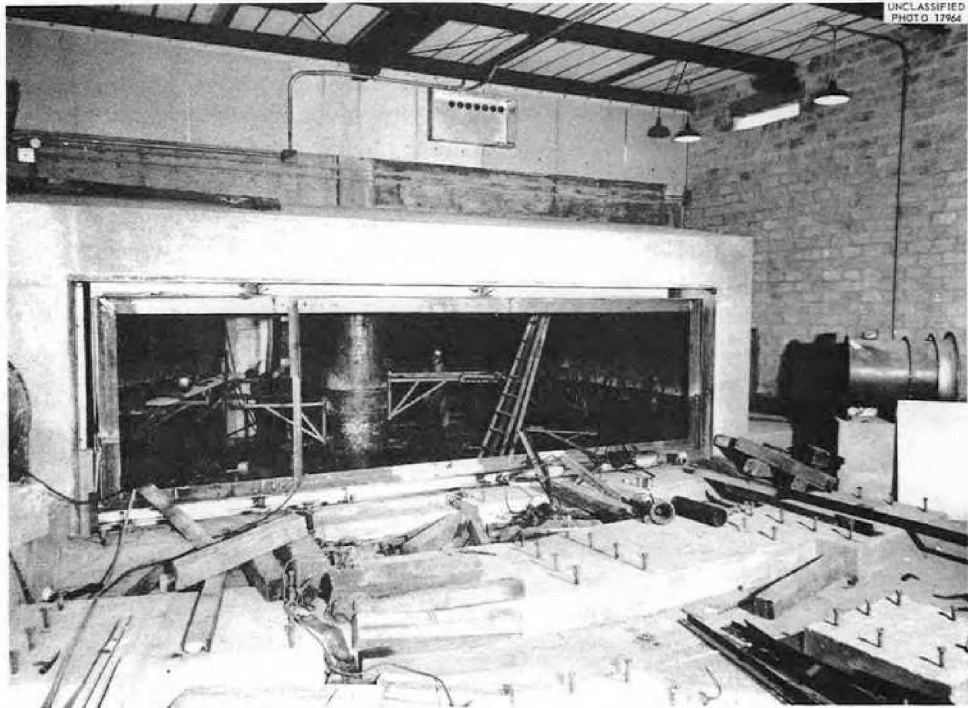
Fig. 1.1.12. Status of Main Air Duct in June 1956.
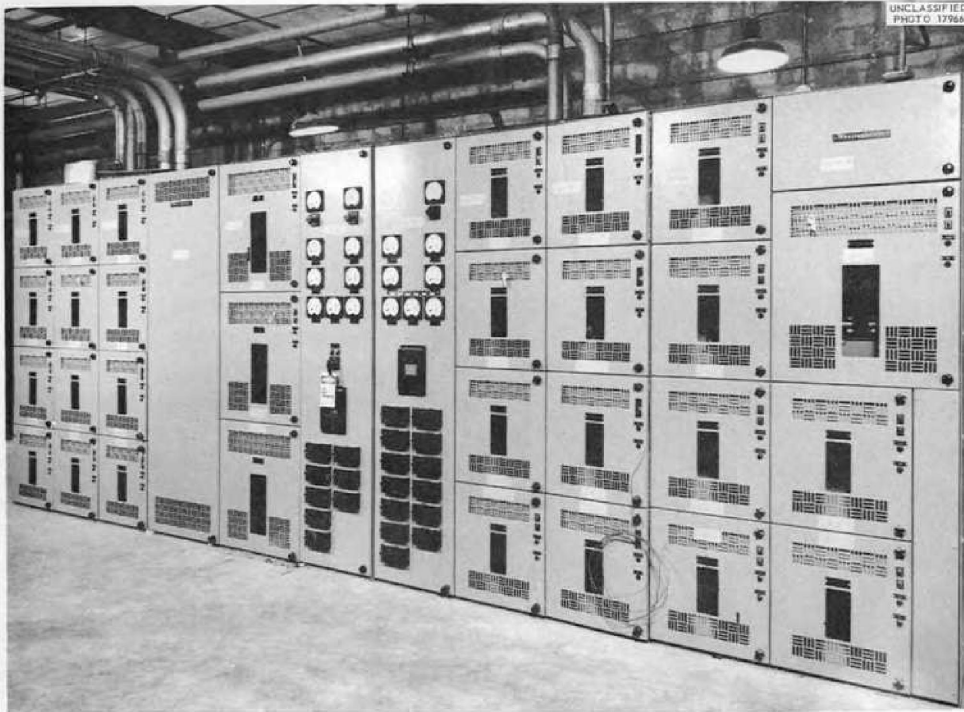
Fig. 1.1.13. The 480-v Switchgear Installation in June 1956.
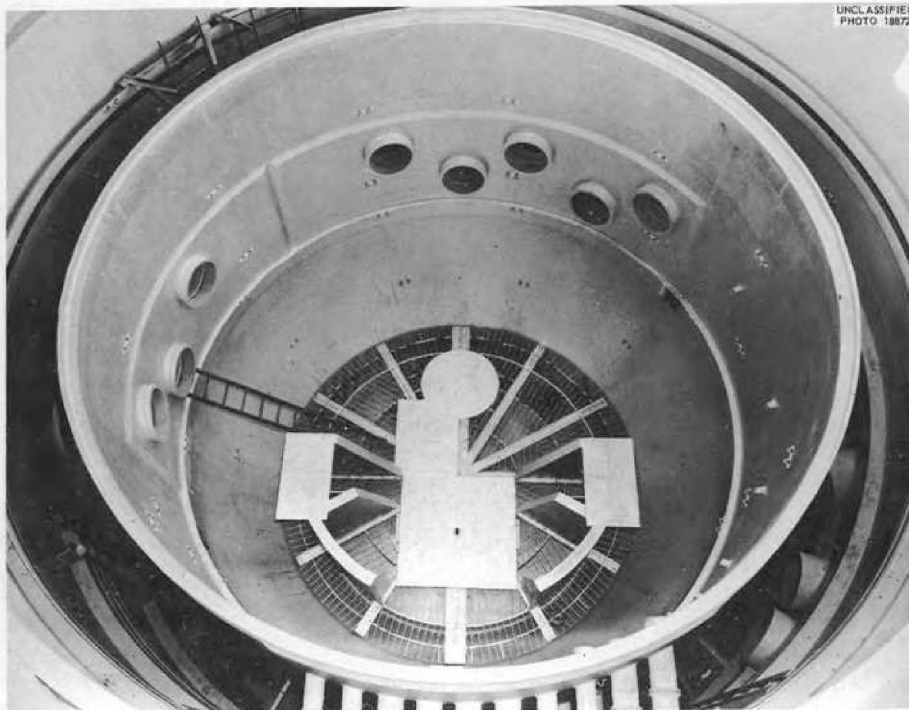
Fig. 1.1.14. Inside of Cell. October 1956.
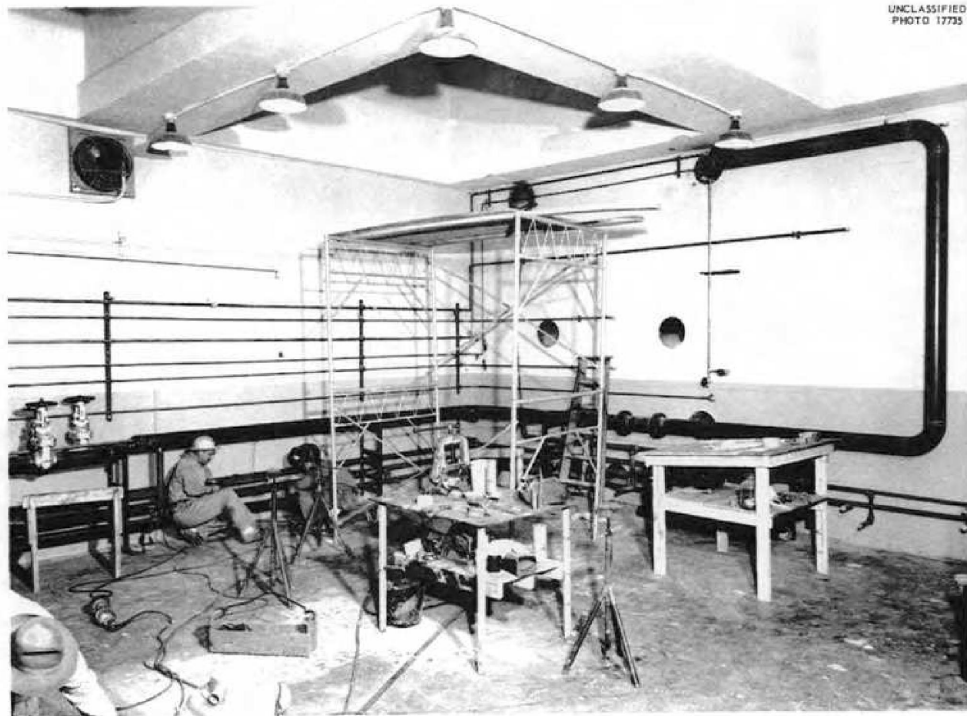
Fig. 1.1.15. Service Piping in Auxiliary Equipment Room. May 1956.

Fig. 1.1.16. View of Building Showing Foundation of Diesel-Generator Building in Right Foreground. April 1956.

Fig. 1.1.17. A Section of the Motor Control Center. June 1956.
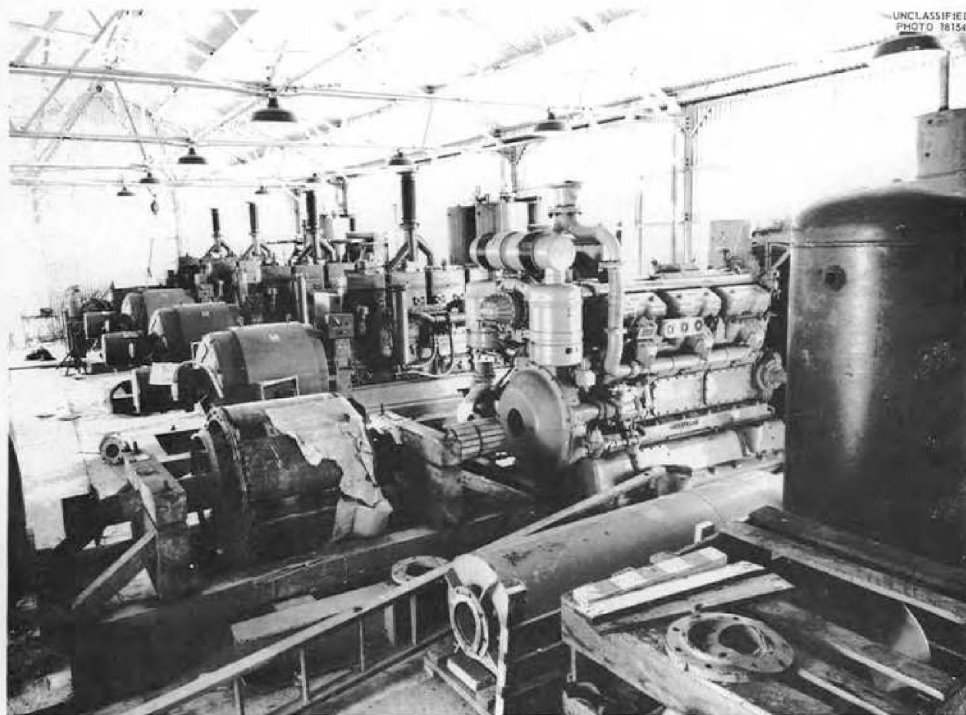
Fig. 1.1.18. Diesel Generators. July 1956.
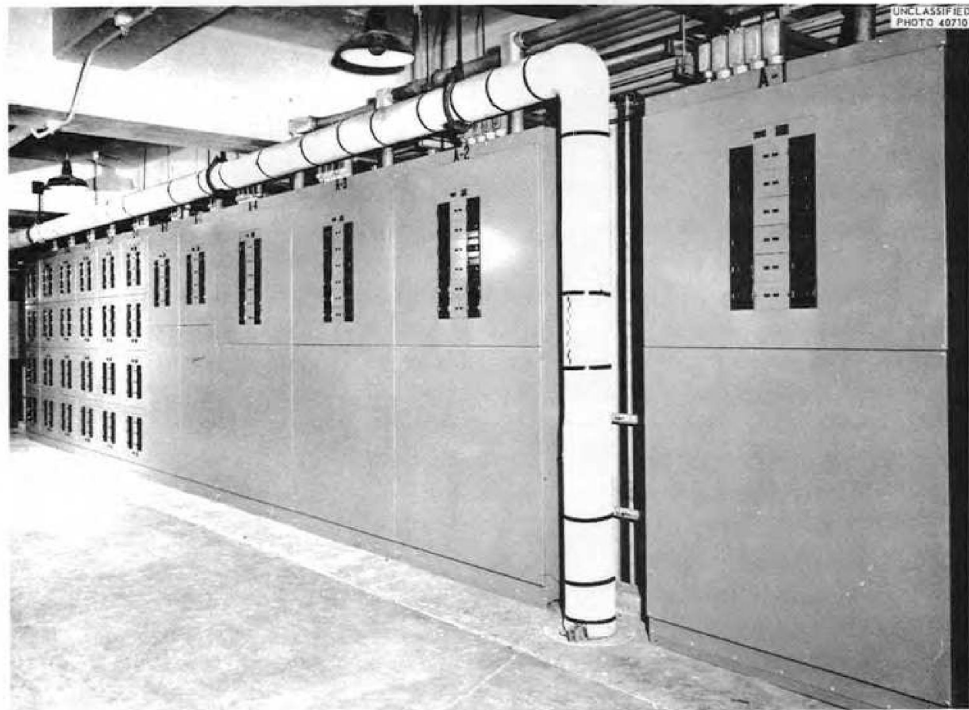
Fig. 1.1.19. Electrical Heater Distribution Panels. April 1957.

Fig. 1.1.20. Dry-Air Plant. April 1957.

Fig. 1.1.21. Remotely Controlled Induction Voltage Regulators. April 1957.
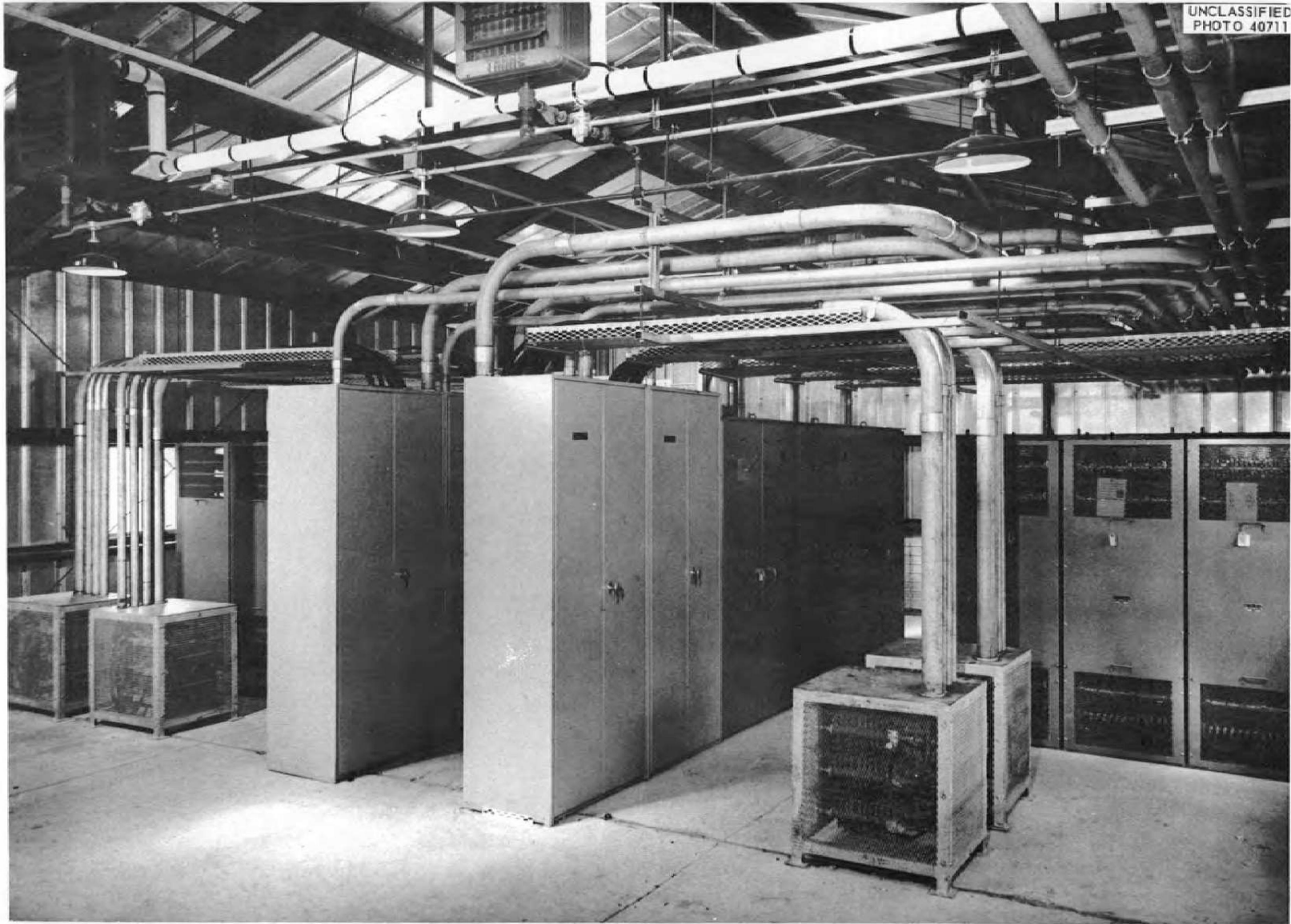
Fig. 1.1.22. NaK Pump Motor Controllers. April 1957.
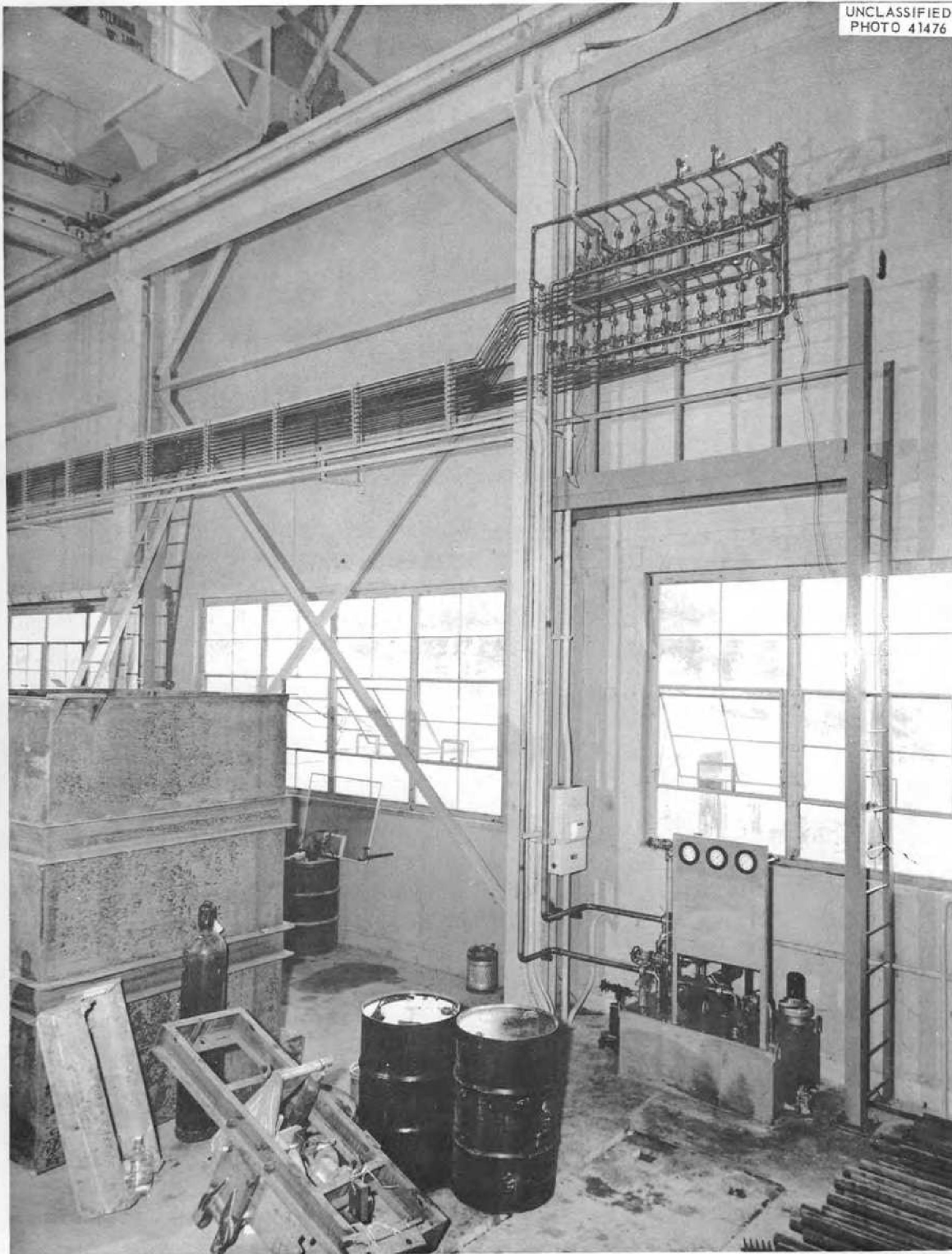
Fig. 1.1.23. Portion of Louver Hydraulic Operating System. August 1957.

Fig. 1.1.24. Status of Facility as of August 1957. View looking south.
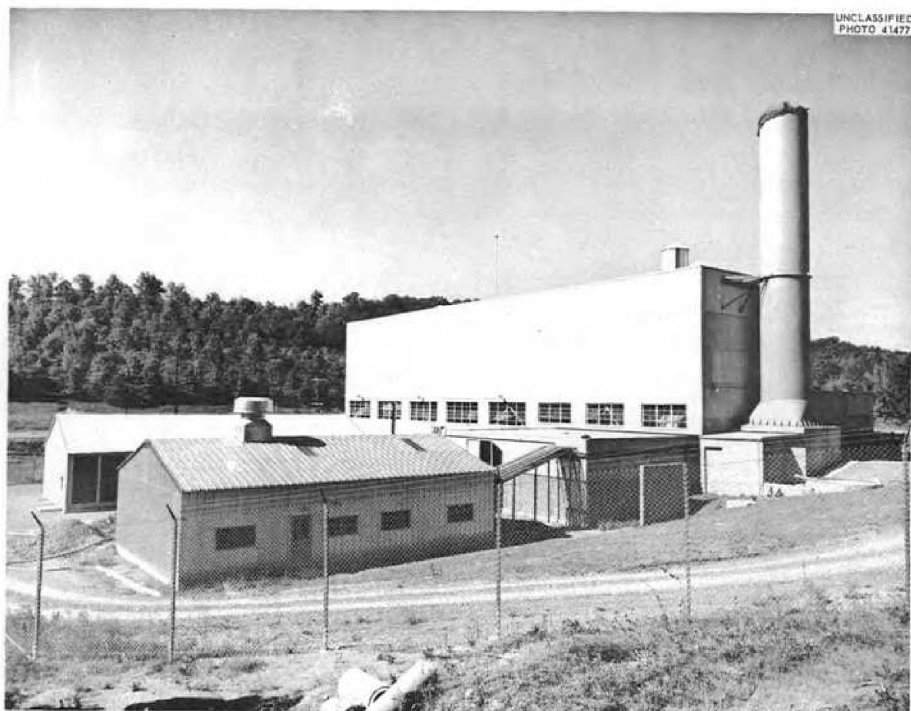
Fig. 1.1.25. Status of Facility as of August 1957. View looking toward southwest corner of building.

1.2. COMPONENT DEVELOPMENT AND TESTING

H. W. Savage

The experimental engineering activities associated with the development and testing of components for the ART and ETU systems are being terminated gradually with the objective of obtaining the maximum information that will be of value in further aircraft reactor developments. Equipment and test stands for which no more essential tests were planned or from which the data to be obtained were applicable only to the ART or ETU have been disassembled. Parts that could be used elsewhere were salvaged and stored. All outstanding orders for equipment in this category were cancelled.

Test components that had been completed in the shop, or almost completed, from which information of general interest can be obtained are being tested as test facilities become available. Similarly, tests that were under way at the time of cancellation of the ART-ETU program will be completed if they provide data of value to other ANP programs. Summary reports on the major test programs are being prepared as the work is completed.

A forced-circulation niobium-lithium loop is being designed in which to evaluate system components and metallurgical developments. Construction of the loop will be initiated when the niobium becomes available. Thermal-convection loops will also be operated. A development program will be carried out on valves, bearings, pump seals, and the other components that will be required in an operating system. Secondary programs will include the testing of equipment for the continuous processing of lithium to achieve and maintain the required purity in an operating system.

PUMP DEVELOPMENT TESTS

W. F. Boudreau   A. G. Grindell

Bearing, Seal, and Lubricant Tests

D. L. Gray

The tests described previously[1] that were being conducted in order to establish a detailed pump sparging procedure for use during ETU and ART operation were completed. Detailed reports covering these tests and previous bearing and seal developments are being prepared.

As mentioned in the previous report,[1] the reactor fuel pump rotary element that was being operated in a new gamma-irradiation facility at the MTR was shut down for repair of a defective ion chamber. The chamber was found to be inoperative because of the deterioration of the Teflon used to insulate the high-voltage element. The system has now been modified so that dose rates can be determined from flux readings taken external to the test capsule. A subsequent attempt to resume operation of the rotary element was halted by ruptures of two pressure-measuring devices. Inspection has revealed that the hydraulic drive system has failed somewhere inside the sealed unit, but it is not yet known whether the hydraulic line is plugged or the motor is defective. The unit will be examined and repaired. Another attempt will be made to resume the experiment when the repairs have been made.

Aluminum North Head Water Tests

J. W. Cooke[2]

Terminal reports[3,4] are being prepared that will give details of the water tests of the ART fuel and sodium systems. These tests were performed with the use of an aluminum mockup of the ART north head.

Fuel Pump High-Temperature-Performance Tests

P. G. Smith   W. E. Thomas

The loop in which high-temperature performance tests are being run of an ART-type fuel pump with $NaF-ZrF_4-UF_4$ (50-46-4 mole %, fuel 30) as the circulated fluid operated throughout the quarter and has accumulated a total of 3350 hr of continuous operation. The loop is presently

---

[1]D. L. Gray and W. K. Stair, *ANP Quar. Prog. Rep. Sept. 30, 1957*, ORNL-2387, p 32.

[2]On assignment from Pratt & Whitney Aircraft.

[3]J. W. Cooke, *Terminal Report of the Aluminum North Head Twin MF Pump Water Test Stand*, ORNL CF-57-12-4 (in press).

[4]J. W. Cooke, *Terminal Report of the Aluminum North Head Twin MN (Moderator Coolant) Pump Water Test Stand*, ORNL CF-57-12-5 (in press).

running with the pump suction pressure reduced sufficiently to induce cavitation so that the effect on the impeller can be determined. The pump has operated at 1200°F for 1200 hr at the cavitation conditions (2.5 psig pump surge pressure, 645 gpm, and 2700 rpm), and the test is scheduled for termination at the end of 3000 hr under these conditions.

An identical fuel pump was placed in operation with NaK (56-44%) in order to obtain information on the effect of the type of fluid being pumped. Preliminary data indicate that the head is 2 to 4 ft higher than in water and fuel tests. A total of 350 hr of continuous operation of this pump has been accumulated. Investigations are under way to determine the cause of the difference in head, and, in further tests, cavitation effects will be studied.

Fuel Pump Endurance Tests

P. G. Smith

Operation of the fuel pump endurance test was resumed, and 860 hr of additional operation was accumulated to bring the total operating time to 4410 hr. The test was terminated when leakage of oil from the lower seal exceeded prescribed limits. Examination of the pump indicated that replacement of the lower seal would have permitted further operation; however, the tests of this pump are not to be resumed. A report on the details of the test operation of the pump has been issued.[5]

Primary and Auxiliary NaK Pump Development

D. L. Gray

Operation of primary NaK pump loop No. 1 at elevated temperatures was resumed in order to observe the effects on the lower seal area of operating without a purge flow down the shaft annulus. Shortly after startup, the NaK in the loop had to be drained so that a leaking drain valve could be replaced. The loop was then restarted and operated for approximately 1172 hr prior to a scheduled shutdown on November 7, 1957. Operation of this loop will be resumed for testing preheating procedures and for tests at temperatures above 1500°F.

Data on electromagnetic flowmeters were obtained in primary NaK pump loop No. 2, and at

[5]P. G. Smith, *MF Pump Endurance Test — 860 Hours*, ORNL CF-57-12-3 (Dec. 31, 1957).

the same time, a test was started on a split-purge arrangement for the shaft annulus in an attempt to obtain long-time trouble-free operation of the lower seal. The helium purge supply is brought directly to the pump shaft annulus and a portion of the gas flows down and through the pump tank and into the off-gas system. The remainder of the gas flows upward into the catch basin to perform the function of sparging the lower seal oil leakage. A scheduled shutdown to remove the flowmeters halted the split-purge test after 953 hr; the rotary element is to be moved to the auxiliary NaK pump test stand No. 1 and the test will be resumed. Approximately 8700 hr of hot testing with NaK have been accumulated in the two primary NaK pump test stands.

On August 16, 1957, an auxiliary NaK pump with a Fulton-Sylphon bellows type of lower seal was installed in auxiliary NaK pump loop No. 2 for testing. When the test was stopped for a scheduled shutdown on November 5, approximately 936 continuous hours of operation had been accumulated. The seal had operated successfully with an average leakage of 16 cm^3/day. Testing of this pump will not be resumed.

Performance tests were completed on the auxiliary NaK pump operating in loop No. 1. The pump in this loop had operated approximately 2048 hr with an estimated 200 hr at 1500°F. The pump has been removed from this test stand and is being replaced with the pump from the primary NaK pump loop No. 2, except that the original auxiliary NaK pump impeller will continue to be used. A total of 5100 hr of operation at elevated temperatures with NaK has been accumulated on the two auxiliary NaK pump test stands.

Sodium Pump Endurance Tests

W. F. Boudreau   P. G. Smith

The Inconel thermal barrier that was designed to protect the bearing-housing region of the ART sodium pumps from thermal and radiation damage was subjected to tests in the sodium pump endurance test stand. The test was performed with sodium at 1250°F and with the pump rotating at 3500 rpm. For this test, the expansion tank cover and the instrumented section of the pump barrel were insulated.

A typical set of temperature data obtained from the pump barrel and from the barrel and barrier arrangement is presented in Fig. 1.2.1.

THERMOCOUPLE NO.	TEMPERATURE (°F)
11	1252
14	770
15	938
16	430
17	240
56	275
57	295
58	317
59	365
60	450
61	475
62	525
63	560
64	640
65	652
66	672
67	708
68	722
69	750
70	765
71	812
72	818
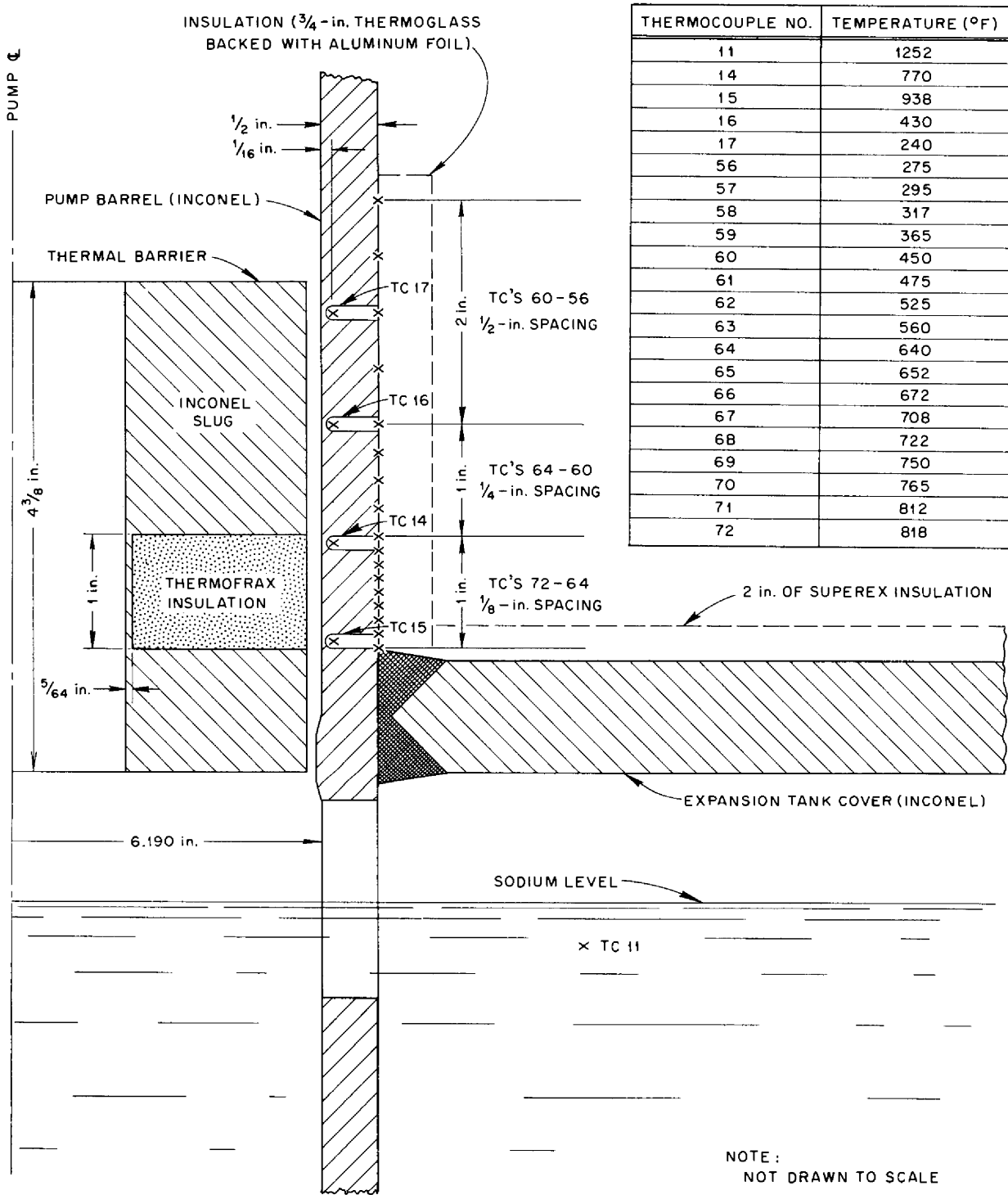
Fig. 1.2.1. Sodium Pump Thermal Barrier Test.

The temperature data are plotted in Fig. 1.2.2 to give the temperature profiles along the outside and the inside of the pump barrel.

The test system was operated for 400 hr, and the test was terminated because of an apparent high leakage rate from the lower seal. The test was not resumed because of termination of the ART program.

This test stand was equipped with a lubricating and cooling oil system which simulated that to be used in the ETU. The results of tests on this system are described in a separate report.[6] This system was tested for a total of 3800 hr of which 2600 hr were without interruption.

UNCLASSIFIED
ORNL–LR–DWG 27001
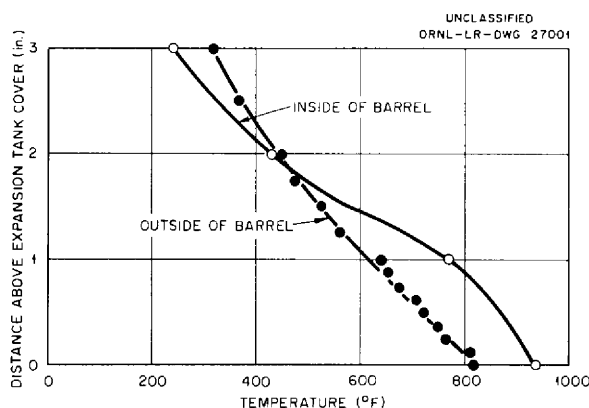
Fig. 1.2.2. Sodium Pump Barrel Temperature Profile.

REACTOR COMPONENT DEVELOPMENT TESTS

Heat Exchanger and Radiator Development Tests

R. E. MacPherson   J. C. Amos
R. L. Senn   D. R. Ward

The heat exchanger and radiator development testing program is currently being concluded with a thermal cycling test of a 20-tube semicircular heat exchanger designed to simulate the ART main heat exchanger tube geometries. The heat exchanger has completed 155 cycles of the proposed 300-cycle program. A report is being prepared that will summarize the results of the over-all ANP heat exchanger development program.[7]

The radiator development program was concluded with the termination of ART test radiator No. 2 because of failure of a radiator tube after a total of 181 thermal cycles. The number of cycles imposed on this radiator was six times the maximum number of thermal cycles proposed for the ART radiators.

Details for testing of this radiator and ART test radiator No. 1 are presented in a spearate report.[8] Details of the development testing of smaller 500-kw units of the same basic design have also been summarized in a separate report.[9]

Outer Core Shell Thermal Stability Tests

W. B. McDonald   E. R. Storto
J. C. Amos   R. L. Senn

The second quarter-scale outer core shell model, which was subjected to 339 thermal cycles, has been measured, and the measurements are being analyzed to determine whether dimensional changes occurred during testing. The test shell is currently being readied for an extended creep buckling test at 1500°F with an external helium gas pressure of 52 psi.

A third quarter-scale core shell is being fabricated by welding together oversize sections of a complete shell and bringing the shell to proper dimensions by final machining. This shell will be subjected to thermal-cycling tests similar to those described previously in order to obtain data on the structural reliability of the welded shell construction. This method of shell construction was one of those proposed as a means of meeting the rigid dimensional tolerances required for the ART core shells.

Fabrication of a shell-buckling rig for testing full-scale shells is 95% complete. This apparatus will be shipped to Pratt & Whitney Aircraft, where tests will be made on ART core shells.

[6]P. G. Smith, *Simulated ETU Reactor Pump Lube and Cooling Oil System Test*, ORNL CF-57-10-60 (Oct. 10, 1957).

[7]J. C. Amos *et al.*, *ANP Heat Exchanger Development, 1955 Through 1957*, ORNL-2439 (in preparation).

[8]J. C. Amos and D. R. Ward, *Performance and Endurance Tests of ART NaK-to-Air Test Radiators Nos. 1 and 2*, ORNL CF-58-1-2 (in press).

[9]R. E. MacPherson and R. J. Gray, *ART Prototype Radiators — Development Program and Metallurgical Results*, ORNL-2436 (in preparation).

Zirconium Fluoride Vapor Traps

D. B. Trauger   J. A. Conlin
A. G. Smith[10]

Developmental work on ZrF_4 vapor traps for use in the ART system has been terminated. The trap, shown in Fig. 1.2.3 and described previously,[11] was tested and found to be satisfactory for ETU operation with the addition of a conical inlet to reduce heat losses by convection and radiation to the cooling tubes and the inclusion of a retainer web to prevent filter material from being blown out of the trap.

Additional modifications were to be made to assure that the unit would be satisfactory for

---

[10]On assignment from Pratt & Whitney Aircraft.

[11]M. H. Cooper, *ANP Quar. Prog. Rep. March 31, 1957*, ORNL-2274, p 61.

ART operation. Further, it was essential to final design considerations that the quantity, density, and conductivity of the expected deposits be determined precisely. The quantity and density would affect the trap size, and the conductivity would affect the size of the tubes in the second section. A detailed report on the vapor trap developmental work is being prepared.[12]

IN-PILE EXPERIMENTATION

D. B. Trauger   J. A. Conlin

An in-pile loop in which ART operating conditions could be simulated was designed, and three such loops were operated as supporting research for the ART program. The loops provided information needed for final choice of the

---

[12]M. H. Cooper *et al.*, *Zirconium Fluoride Vapor Traps*, ORNL-2245 (in preparation).

Fig. 1.2.3. Component Parts of ZrF_4 Vapor Trap.

materials of construction and fuel compositions proposed for the ART. The three loops were operated in the MTR with varying degrees of success. The results indicated no measurable effect of radiation on the corrosion resistance of the structural material or on the stability of the fuel. Some work in support of an advanced ART reactor design was being considered at the time of the termination of the ART program. This work will be described in a forthcoming report.[13]

---

[13]D. B. Trauger *et al.*, *Circulating Fluoride Fuel In-Pile Loop*, ORNL-2444 (in preparation).

1.3. INSTRUMENTATION AND CONTROLS DEVELOPMENT

E. R. Mann   C. S. Walker   R. G. Affel

ART CONTROL ROD DRIVE TEST
C. S. Walker

The test of the ART control rod drive system, as stated previously,[1] was terminated after 3000 hr of successful operation with the control rod thimble at or above the design temperature of 1100°F. The drive mechanism operated through 1780 full stroke cycles.

Before the termination of the test on September 17, 1957, electrical leakage resistance measurements were taken with the system temperature maintained as in the test in order to determine whether sodium deposition had reduced insulation resistances. The leakage resistance to ground and the leakage resistances between isolated conductors which penetrated the tank that enclosed the rod drive mechanism were measured. All these leakage resistances were above 4×10^6 ohms and were acceptable in each case. The lowest resistance measured between the open contacts of the limit switches exceeded 10^9 ohms.

The sodium was drained from the control rod thimble, and the drive mechanism was completely dismantled and carefully examined. There were no indications of wear; the backlash in the gears had not increased beyond that in the original assembly. No sodium deposition could be found on the rod drive parts that were located above the surface of the molten sodium. The speed of operation of the rod had not changed during the test, and thus there was apparently no binding or increase in friction between moving parts.

The heat exchanger which surrounded the thimble at the upper surface of the sodium was found to have a deposit of scale on all areas that were in contact with water. This deposit was 0.018 in. thick, and chemical analysis indicated it was practically all calcium, with small quantities of magnesium and zinc. A porous ceramic water filter in the effluent water line was found to contain a sizable quantity of rust.

A chemical analysis of the oil in the gear box showed no significant amount of sodium or rare earths. This further indicates that no deposition

---

[1]E. R. Mann and C. S. Walker, *ANP Quar. Prog. Rep. Sept. 30, 1957*, ORNL-2387, p 54.

of sodium occurred on the cool portions of the drive machinery.

The only troubles encountered during the test stemmed from equipment external to the rod drive itself; namely, difficulty with regulation of the water flow through the sodium-to-water heat exchanger, and faults in the temperature recording apparatus. The rod drive mechanism successfully completed the test.

Samples of the sodium were taken for analysis and the control rod was disassembled for examination. Details of the results of the sodium analysis and rod examination are presented in Chap. 3.4 of this report.

ART FUEL-EXPANSION-TANK CONTINUOUS LEVEL INDICATOR
R. F. Hyland

In the early stages of ART design it became apparent that a method would have to be developed for continuous measurement of the level in the reactor fuel expansion tank. The level indicator was required to function continuously in a fuel 30–helium environment in an Inconel container in the temperature range of 1000 to 1500°F and a gas pressure of 15 psig. The range of level indication was 0 to 5 in. The indication was to be accurate to ±2% (percentage of maximum level) and reproducible to ±1%. The minimum life of the device was to be 1000 hr of continuous operation.

Any portion of the device that was above the fuel level in the expansion tank was to be cooled because there would be severe beta heating during power operation of the reactor. The device was to be operable under the extremely turbulent fuel flow conditions that would exist during power operation. Turbulence of the type to be expected is illustrated in Fig. 1.3.1, which presents two pictures taken during water tests of the aluminum north head mockup. Penetrations through the top of the north head were to be kept to a minimum because of the complexity of the system in that area and the number of layers that would have to be penetrated to reach the fuel expansion tank, as
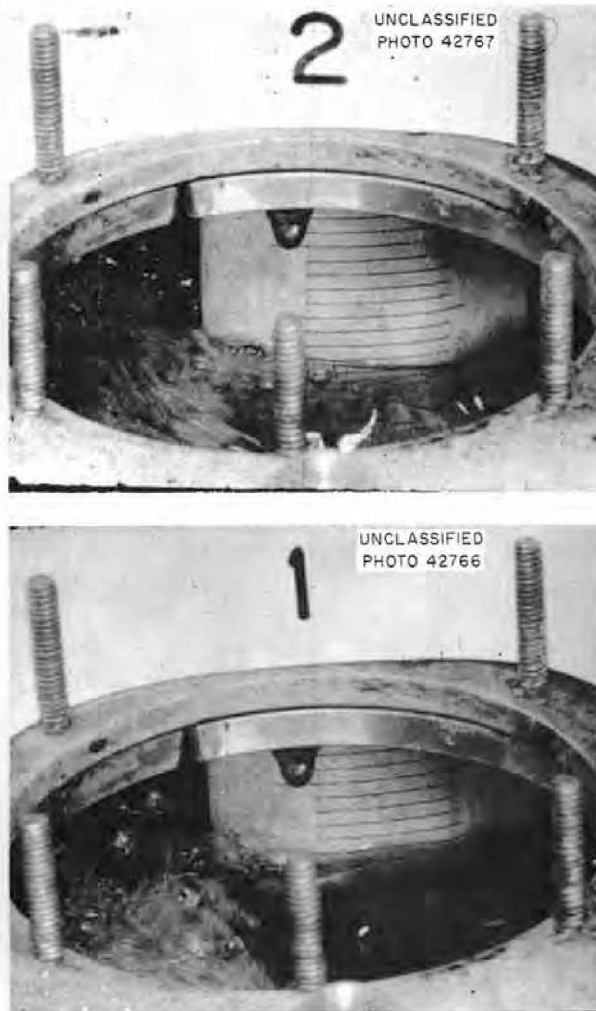
Fig. 1.3.1. Two Views of Fuel Expansion Tank of Aluminum North Head Mockup During Simulated Power Operation with Water as the Circulated Fluid. (Secret with caption)

shown in Fig. 1.3.2. The level sensor and any seals or stuffing boxes used were to be leaktight, as determined with a mass spectrometer, to preclude leakage of radioactive gases.

An appraisal was made of known level-measuring techniques, and it was apparent that, because of its basic simplicity, the conventional purged-dip-tube level-measuring device offered a possible solution to the problems. Penetrations through the top of the reactor north head could be avoided by entering the side of the fuel expansion tank, as shown in Fig. 1.3.3, and the beta heating problem could be avoided by entering the tank below the

fuel level. The use of a multiple-pass Heliarc-welded dip tube penetration would remove the seal problem, and the use of materials that were not subject to radiation damage would assure the lifetime required. On the basis of this study, static tests with fuel and dynamic tests with water and with fuel were initiated. These tests were not completed because of the termination of the ART experiment; however, a summary of the the test results obtained is presented below.

Continuous measurement of nonturbulent fuel levels in the temperature range 1150 to 1500°F and a level range of 0 to 5 in. with an accuracy of ±2%, a reproducibility of 1.5%, and a sensitivity of 0.03 in. of fuel was demonstrated. Typical results of these tests are presented graphically in Fig. 1.3.4. Dip tube life averaged approximately 1500 hr before plugging occurred. The plugs were of two general types: zirconium dioxide and other metallic oxide deposits in the bottom of the dip tube or fuel vapor deposits in the region of the dip tube that was below the melting temperature of the fuel. Several of the zirconium dioxide plugs were traced to contamination of the helium purge gas with oxygen and moisture, and it is felt that this type of plug could be eliminated by controlling the oxygen and moisture content of the gas. The fuel vapor deposits were readily melted out of the dip tubes and could undoubtedly be eliminated completely by preheating the purge gas. The all-welded Taylor Instrument Companies model X333RD differential-pressure level sensor which was being tested appeared to be satisfactory for reactor service, contingent upon individual units passing mass spectrometer leak checks.

Metering tests conducted with the use of the aluminum north head mockup demonstrated that with both pumps at design speed (2700 rpm), the system at design flow (645 gpm), and the dip tubes properly placed, changes in level could be detected with an accuracy of ±5%. Determination of an absolute level under these simulated reactor operating conditions proved to be impossible. As shown in Fig. 1.3.1, the water in the expansion tank was extremely turbulent, and, of course, the turbulence caused appreciable level oscillations. Attempts to establish an average level reference by using high-speed photography were inconclusive because of the difficulty of photographing the expansion tank through the small viewing port provided.

ORNL-LR-DWG 27019
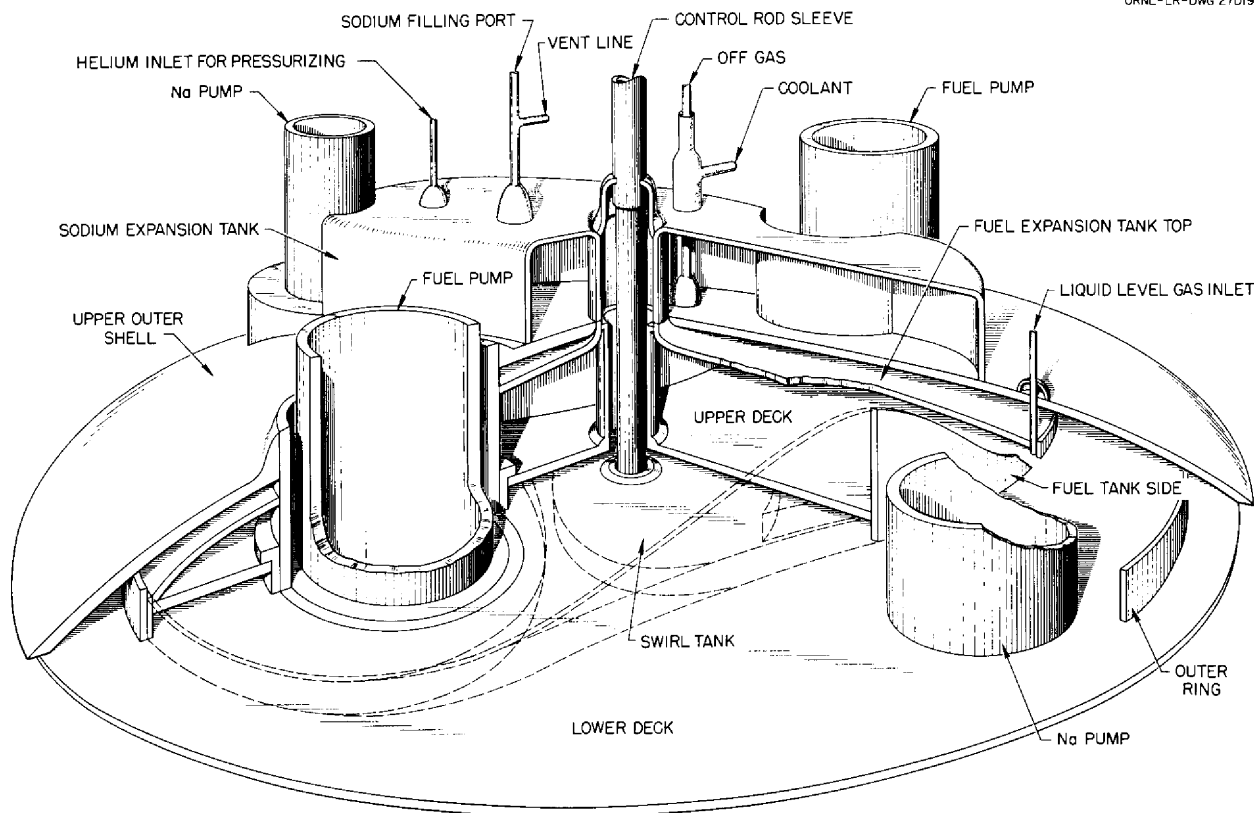
Fig. 1.3.2. ART North Head Showing Fuel Expansion Tank Region.

Since the level-measuring system depends upon the sensing of the fuel pressure, the level indication is dependent on the fluid density. The magnitude of the density effect is shown in Fig. 1.3.5. If the reactor operating temperature of 1150°F is taken as the point of zero error, a level error range of +2.5 to −5.7% exists in the temperature range 1000 to 1500°F. This error could be eliminated by installing a separate temperature- (and thus density-) measuring system. The signal from this system would be multiplied by the signal from the level-measuring system to produce a signal corresponding to the true level.

Considerable work remained to be done in determining the dynamic characteristics of the measuring system under ART conditions. The planned test program included installation and testing in water in the aluminum north head test rig of shielded dip tubes of the type to be used in the ART and similar testing in fuel in the ETU. Details of the tests described here are available in a separate report.[2]

---

[2]R. F. Hyland, *ART Fuel Expansion Tank Continuous Level Indicator*, ORNL CF-58-2-1 (in press).

ORNL—LR—DWG 27020

TO ALL WELDED DIP CELL

REACTOR PRESSURE SHELL

FUEL EXPANSION TANK ROOF

FUEL LEVEL

LEVEL SENSOR TUBE

SIDE OF FUEL EXPANSION TANK

HELIUM FLOW

LEVEL SENSOR SHIELD

FUEL EXPANSION TANK FLOOR

HEAT EXCHANGER
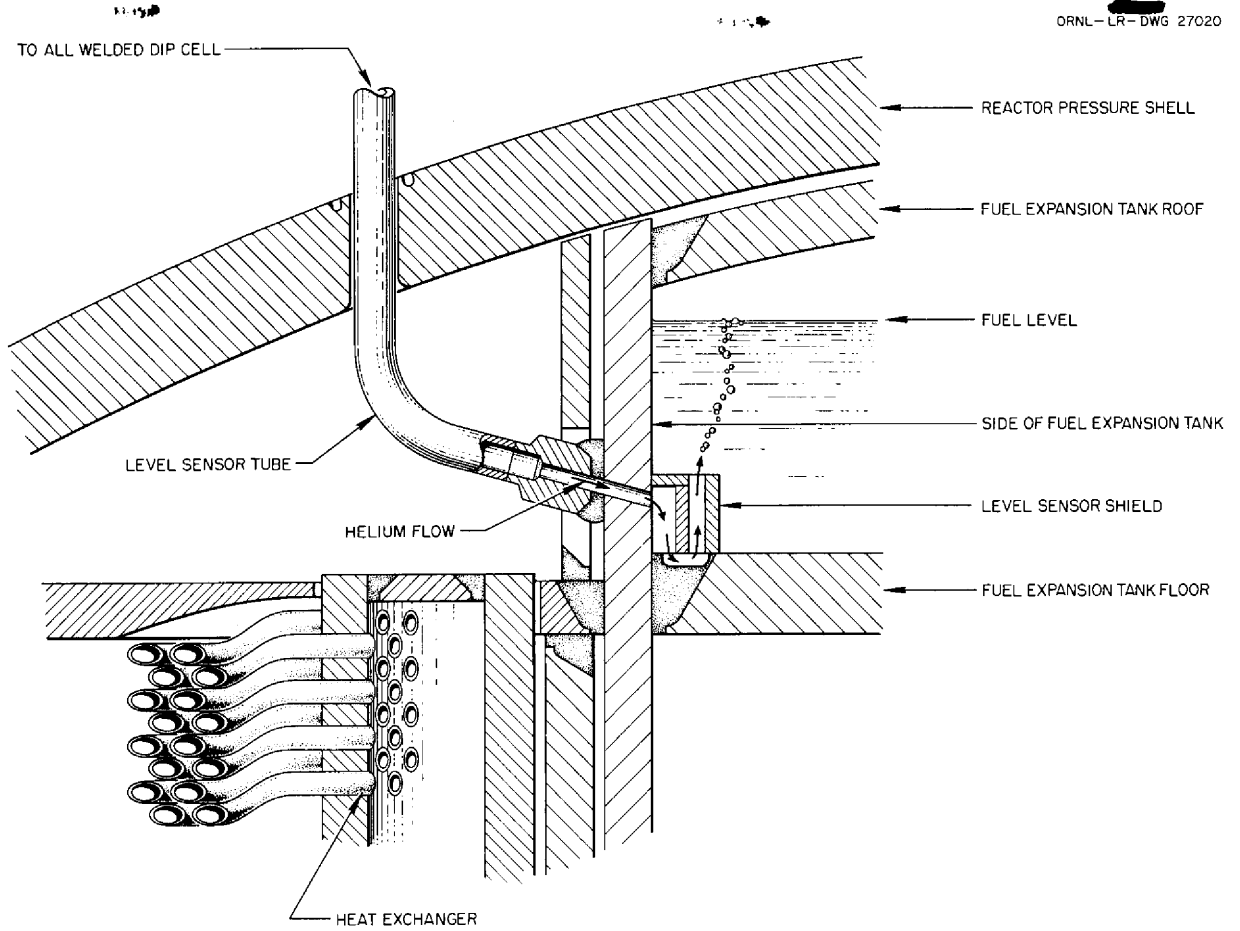
Fig. 1.3.3. Dip Tube Installation in Reactor North Head.

ORNL—LR—DWG 27021

LEVEL INDICATOR S1
LEVEL INDICATOR S2

DECREASING LEVEL

INCREASING LEVEL

MEASURED LEVEL ERROR (in. OF FUEL)

MEASURED LEVEL ERROR (% OF MAXIMUM LEVEL)

REFERENCE LEVEL (in. ON CALIBRATING PROBE)
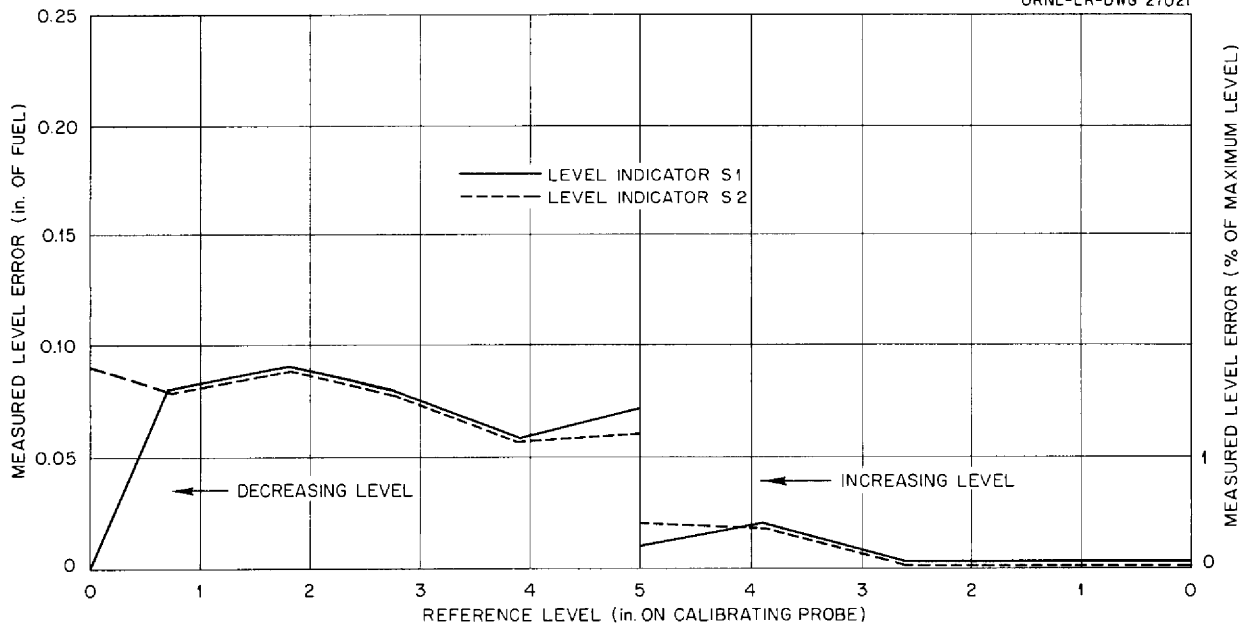
Fig. 1.3.4. Results of Level-Measuring Tests in Nonturbulently Flowing Fuel.

33
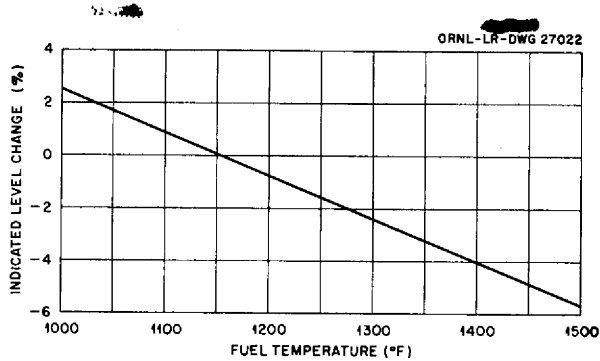
Fig. 1.3.5. Effect of Fuel Density, as Indicated by Fuel Temperature, on Accuracy of Purged-Dip-Tube Level Measurements.

Fig. 1.3.6. Electrical Diagram of Resistance-Type Fuel Level Probe.

RESISTANCE-TYPE FUEL LEVEL INDICATOR

T. V. Blalock   R. F. Hyland

A resistance-type fuel level indicator was designed as a possible alternate to the purged dip tube described in the previous section. The operation of this level element depends on a resistance change that is a function of fuel level. A schematic electrical diagram of the system is shown in Fig. 1.3.6.

In Fig. 1.3.6, R is the current adjusting potentiometer, R_L is the lead resistance, R_c is a temperature-compensation resistance, R_f is the fuel resistance between the Inconel rod and the $1\frac{1}{2}$-in. Inconel pipe (Fig. 1.3.7), R_t is the Inconel tube resistance, r_f is a resistance representing the shorting-out effect of the fluid on the Inconel tube, and R_T is the total input resistance of the parallel section of the level element.

In reference to Fig. 1.3.6, if $R \gg 2R_L + R_T$, the current I will depend primarily on R, and therefore the level element can be supplied with a constant current. The output voltage must be measured with an instrument of high input impedance, such as a vacuum-tube voltmeter or a Brown recorder. The current flows from the source through the compensating resistance R_c to junction B. From this junction the current has three possible parallel paths. The first path is through the Inconel rod, the fuel, the $1\frac{1}{2}$-in. pipe, and the $\frac{1}{4}$-in. plate to junction C; the second path is through the Inconel tube and the $\frac{1}{4}$-in. plate to junction C; and the third path is through the fuel, the Inconel tube, and the $\frac{1}{4}$-in. plate to junction C.

As the fuel level rises, the current flow through the fuel between the Inconel rod and the $1\frac{1}{2}$-in. pipe will become less inhibited because of the increase in the flow-path cross-sectional area. The resistance of the rod and pipe to this current flow will be negligible compared with the fuel resistance. At zero level the element output will be given by the product of the supply current and the Inconel tube resistance, since the resistance R_f will be infinite for nonimmersion. The maximum output will occur at zero level, and the output will decrease as the level increases. The resistance R_c is a function of temperature only, and R_f and r_f are functions of both temperature and level.

The slope of the resistivity curve of the fused salt mixture is negative; that is, the resistivity decreases with increasing temperature. The resistivity of Inconel is almost constant over the temperature range under consideration (1100 to 1600°F), and therefore R_t can be assumed to be constant. It follows then that R_T will be a function of R_r and r_f and will decrease with increasing temperature.

An increase in fuel temperature will have the same effect on the output as an increase in level if the system is not temperature compensated. One method of temperature compensation is described below. The element is to be compensated at a fluid height, h, so that a temperature excursion from T_1 to T_2 will produce no change in output. If the compensating resistance (R_c) is placed in series with R_T, the temperature-compensation

ORNL—LR—DWG 27024
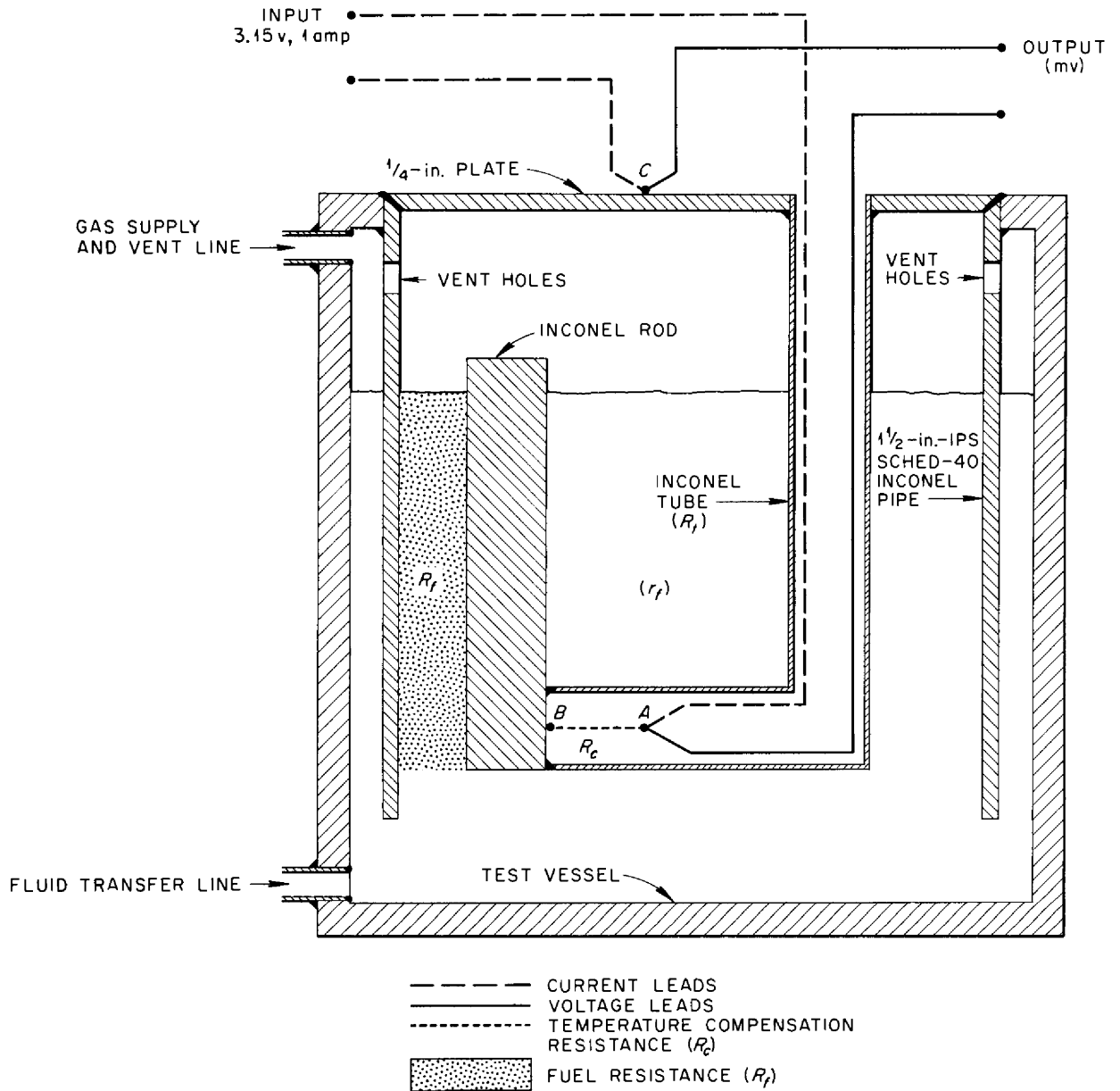
Fig. 1.3.7. Fabrication Diagram of Resistance-Type Fuel Level Probe.

criterion will be satisfied if

(1) $\dfrac{V_{R_{c_1}} - V_{R_{c_2}}}{T_1 - T_2} = -\left(\dfrac{V_{R_{T_1}} - V_{R_{T_2}}}{T_1 - T_2}\right)$

or

(2) $\dfrac{\Delta V_{R_c}}{\Delta T} + \dfrac{\Delta V_{R_T}}{\Delta T} = 0 \qquad$ for $\Delta T = T_2 - T_1$.

As stated previously, $\Delta V_{R_T}/\Delta T$ is negative, and therefore $\Delta V_{R_c}/\Delta T$ must be positive and the resistivity curve of the compensating resistor must have a positive slope.

A short length of A-nickel wire can be used for R_c and its dimensions can be arrived at as follows:

$V_{R_c} = IR_c = I\,\dfrac{\rho_c}{A_c}\,l_c$,

$V_{R_T} = IR_T$,

$V_{R_{c_1}} = I\,\dfrac{l_c}{A_c}\,\rho_{c_1} \qquad$ at temperature T_1 ,

$V_{R_{c_2}} = I\,\dfrac{l_c}{A_c}\,\rho_{c_2} \qquad$ at temperature T_2 ,

$V_{R_{T_1}} = IR_{T_1} \qquad$ at temperature T_1 ,

$V_{R_{T_2}} = IR_{T_2} \qquad$ at temperature T_2 ,

$I\,\dfrac{l_c}{A_c}\,\rho_{c_1} - I\,\dfrac{l_c}{A_c}\,\rho_{c_2} = -\,(IR_{T_1} - IR_{T_2})$,

(3) $\dfrac{l_c}{A_c} = \dfrac{R_{T_1} - R_{T_2}}{\rho_{c_2} - \rho_{c_1}}$,

where

ρ_c = specific resistance of compensating wire,

l_c = length of compensating wire,

A_c = area of compensating wire.

Two resistance-type level elements without temperature compensation were fabricated (Figs. 1.3.8 and 1.3.9) and are being used to experimentally determine the resistance-level characteristics of the element and to observe polarization and other effects not included in the design calculations. The elements are of a rugged all-welded design with no seals or stuffing boxes. They are designed for a maximum fuel temperature of 1600°F and a maximum allowable working pressure of 5 psig. Calculated performance curves for these elements, both temperature compensated and uncompensated, are shown in Fig. 1.3.10. These curves are based upon a constant current of 1 amp through the measuring element.

INCONEL PIPE

INCONEL TUBE

INCONEL ROD   INTERNAL STRUCTURE
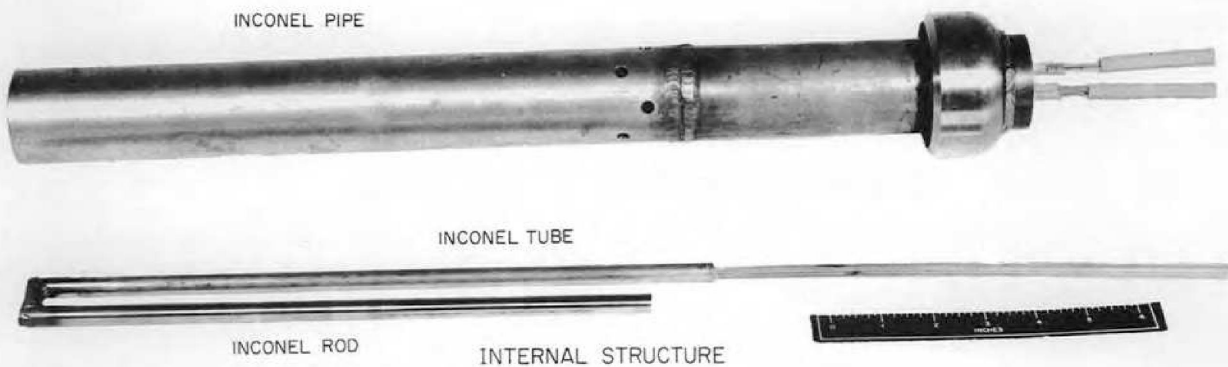
Fig. 1.3.8. Component Parts of Resistance-Type Fuel Level Probe. (Secret with caption)

UNCLASSIFIED
PHOTO 29726

Fig. 1.3.9. Assembled Resistance-Type Fuel Level Probe. (Secret with caption)

ORNL-LR-DWG 27025
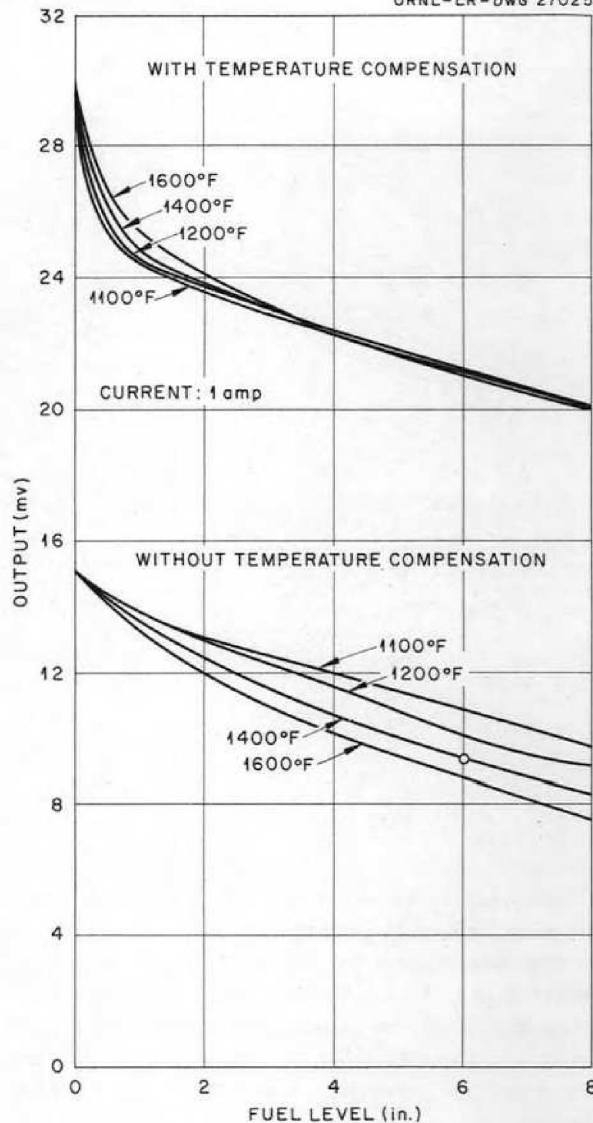
Fig. 1.3.10. Calculated Performance Characteristics of Resistance-Type Fuel Level Indicator.

A test rig designed to test two level elements simultaneously was fabricated in accordance with the flow diagram shown in Fig. 1.3.11. The liquid level was varied by a helium-forced exchange of fuel between the two vessels. The initial readout of the level signal was accomplished with a Hewlett-Packard model 400H vacuum-tube voltmeter. A sliding probe which completed a lamp circuit when contacted by the fuel was used for calibration.

ORNL-LR-DWG 27026

SOLENOID VALVE SWITCH MAY BE
REPLACED BY A REPEAT CYCLE
TIMER FOR AUTOMATIC CYCLING.

KEY

▶◀ THROTTLING VALVE

▶◀ THREE WAY VALVE
DARKENED PORT CLOSED
▽ DESIGNATES COMMON PORT

ᒐᒑᒐ ELECTRIC HEATERS
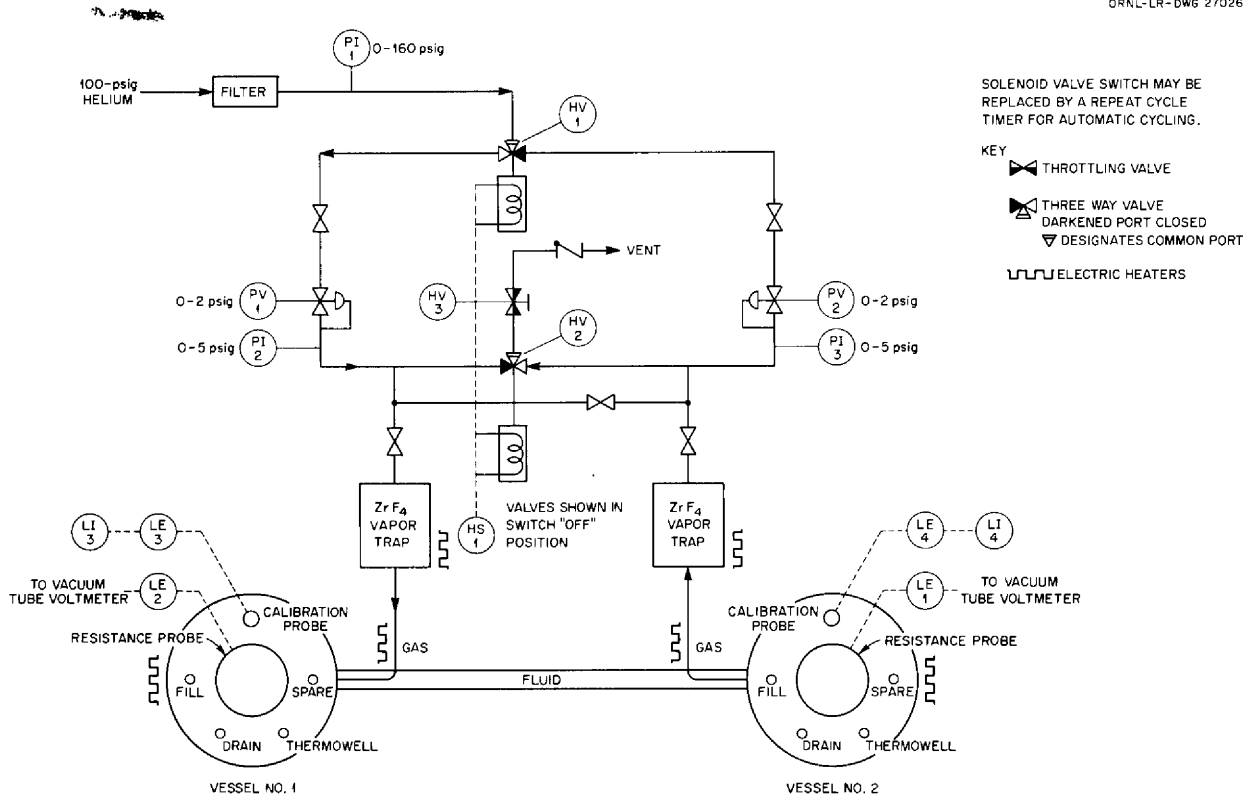
Fig. 1.3.11. Diagram of System for Testing Resistance-Type Fuel Level Probes.

Preliminary experimentally determined performance characteristics of an uncompensated element are shown in Fig. 1.3.12. The actual performance of the probe was in reasonable agreement with the calculated performance. A family of curves suitable for designing temperature compensation into the element is now being obtained.

LIQUID-METAL-LEVEL TRANSDUCERS

G. H. Burger   R. E. Pidgeon, Jr.[3]

At the time of suspension of the ETU-ART program, a total of 22 resistance-type level transducers for the NaK pump bowls had been constructed in the ORNL machine shop. An acceptable, reasonably simple construction technique had been devised for the production of reliable units. Considerable difficulty was experienced earlier in the fabrication of these

transducers that had resulted in internal electrical shorts and a high rejection rate.

Design work was completed on all the continuous level probes required for the ETU and ART for use

ORNL-LR-DWG 27027
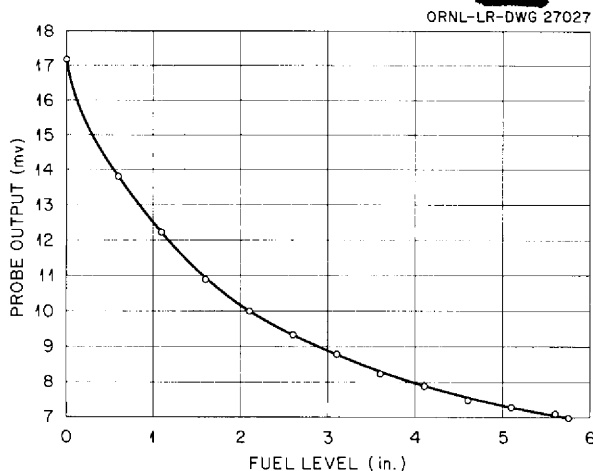
Fig. 1.3.12. Preliminary Experimental Performance Characteristics of Resistance-Type Fuel Level Probe.

---

[3]On loan from Radio Corp. of America.

in the sodium expansion tank, the sodium auxiliary tank, and the NaK-furnace-circuit drain tank. All work was cancelled for construction and testing of these level probes. During this quarter, two level-element testing rigs were rebuilt that had been damaged because of NaK leaks in the system (Fig. 1.3.13), and the test program was resumed in order, primarily, to determine the error introduced by an unwetted level probe. Before this type of level probe is wetted by NaK there is contact resistance between the surface of the probe and the NaK that results in the indicated level being lower than the actual level.

As part of the wetting investigation, three newly fabricated NaK-pump-bowl tranducers were cleaned with emery cloth and rinsed with alcohol just prior to installation in the test facility. The NaK was heated and then raised to approximately 4 in. on one of the probes with the NaK at 300°F and on two of the probes with the NaK at 400°F. The results of the first level change of approximately 4 in. on each level probe are given in Table 1.3.1.

After the level changes above, the probes were submerged and calibrated at the test temperature. With the NaK at 300°F, the indicated level for the 18 points measured was between 0.15 and 0.28 in. below the actual level. For the test with NaK at 400°F the indicated level for the 18 points was between 0 and 0.1 in. below the actual level. Further wetting tests are being made at other temperatures, and the results will be included in a final report.

Four level transducers were installed in a life testing facility. Two of these transducers were previously operated for 3480 hr and the other two were operated previously for 2440 hr. These units

are shown in Fig. 1.3.14 before installation in the life testing facility. It is planned to continue the life tests indefinitely.

ON-OFF LEVEL PROBES

G. H. Burger   R. E. Pidgeon, Jr.

Plans for construction and testing of the ETU and ART on-off level probes described previously[4] were cancelled, but similar probes were constructed for instrumenting test rigs. These probes differed from those built previously in that the copper-and-Inconel junction at the tip of the probe was brazed instead of being welded in an attempt to eliminate weld failures. These new probes were installed in the NaK systems, but they have not yet operated long enough for an evaluation of them to be made.

Sixteen on-off probes installed in the gas pots of two NaK system test loops have each operated for 3000 hr without a probe failure. These probes have usually operated with the NaK temperature below 800°F. The control circuit associated with the on-off probes installed in one test loop failed because of in-gassing of the pump. Apparently, during operation of the loop, the NaK level reached the high-level probe in the throat of the gas pot, and the control circuit acted to lower the level. When the level had dropped to below the high-level probe, the sensitive relay across the probe failed to energize and allowed helium to be forced into the loop. The relay failed to operate because the "pull-in" voltage of the relay had increased and the level probe current was adjusted too low. The

[4]G. H. Burger and R. E. Pidgeon, Jr., *ANP Quar. Prog. Rep. Sept. 30, 1957,* ORNL-2387, p 58.

Table 1.3.1. Results of Tests of Especially Cleaned Level Probes

NaK Temperature (°F)	Time After Initial Level Change (hr)	Level Error (in.)	Indicated Accuracy (% of actual level)
300	0	0.31	92.9
	7	0.28	93.5
400	0	0.17	95.6
	21	0.16	96
400	0	0.13	96.6
	21	0.13	96.6

Fig. 1.3.13. A Pot of a Level-Element Testing Rig Showing Oxide Deposits Resulting from a NaK Leak.

Fig. 1.3.14. Liquid-Metal-Level Transducers That Were Installed in a Life-Testing Facility After Having Operated for 3480 or 2440 hr.

on-off control circuit of the other test loop has operated without failure and without maintenance or readjustment. These level probes and their circuitry will be discussed in a detailed final report.

MAGNETIC FLOWMETERS

G. H. Burger   C. L. Pearce, Jr[5]

The 2- and $3\frac{1}{2}$-in. magnetic flowmeter calibration and test program, as described in the previous report,[6] was terminated. The data obtained from the operation of 20 such flowmeters in pump test loops are being processed and analyzed, and the findings will be discussed in a final report.

The loop tests were terminated on November 5, 1957, and the instrument panels have been dismantled. The flowmeters are being removed from

the loops and will be cleaned and crated for storage. The total operating times accrued on the 2-in. units are given below:

No. of Units	Accumulated Operating Time for Each Unit (hr)
4	1038
4	1916
2	2935

For the $3\frac{1}{2}$-in. units the operating times were as follows:

No. of Units	Accumulated Operating Time for Each Unit (hr)
4	770
4	2368
2	3138

---

[5]On loan from Radio Corp. of America.

[6]G. H. Burger and C. L. Pearce, Jr., *ANP Quar. Prog. Rep. Sept. 30, 1957*, ORNL-2387, p 58.

41

There was no obvious deterioration in performance of any of the flowmeters during the periods indicated.

As mentioned in the previous report,[6] an apparent drop in sensitivity of the second lot of units installed in the test loop was observed in conjunction with plugging of the loop flow-control valve at low loop temperatures. An attempt to relate the apparent nonlinearity of the units in this lot with a high oxide level was unsuccessful, since the effect remained after the oxide level of the loop was reduced. It was subsequently found that a slightly bent pen on the venturi differential-pressure flow recorder, which employs a square-root differential-pressure chart, was responsible for the apparent shift in sensitivity. The bent pen caused a fixed error in the differential pressure, which appeared as an error in the square root of the differential pressure that increased as the flow decreased. The lower flows, as read from the chart, showed the effect of the slight shift in pen position more than the higher flows. The effect of this error appeared as a shift in sensitivity in the calculations. It appears therefore that the linearity of the units will be better than 1%, as stated in a previous report. The data which have been analyzed indicate that all the units that were calibrated may be expected to provide flow accuracy well within the specified ART and ETU requirements over the entire flow and temperature range prescribed in the flowmeter specifications. The indications are that, upon completion of data processing and analysis, an expected accuracy may be assigned that will be somewhat higher than that specified.

A total of fifteen $\frac{3}{8}$-in. magnetic flowmeters for ETU cold traps had been assembled and delivered for installation in the ETU. The units, as noted in a previous report, were delivered without the magnet attached to permit easier handling for installation in the systems. In addition to these fifteen units, parts for 15 more units for the ART were completed but not assembled. All completed and incomplete units will be packaged and stored for future disposition.

As noted in a previous report, it was not planned to calibrate the $\frac{3}{8}$-in. units. However, temperature tests were made on the units to determine magnet flux changes with magnet temperature and to determine temperatures of the pipe in the air gap in order to check for loop cold spots which could

cause plugging during operation. It was found that the flux changed by approximately 3.9% when the magnet was heated from room temperature to 365°F. It was also found that, with the insulated section of pipe at 610 to 1722°F, the section of pipe through the air gap was at 262 to 680°F when it was insulated with approximately 2 in. of Fiberfrax and the flow pipe was held in each mounting clamp by a series of four corrugated clamps.

Based upon tests on the large flowmeters and the flux data obtained during the $\frac{3}{8}$-in. flowmeter tests, it was expected that the accuracy of the units could be predicted to well within the required ±15% specified for ETU and ART operation, without the need for magnet flux and temperature monitoring. It was also expected that, with proper insulation of the magnet air gap, the problem of plugging because of cold spots could be eliminated and yet the magnet would remain cool enough for proper operation at the specified fluid temperatures.

TURBINE FLOWMETERS

G. H. Burger

The 1-in. turbine flowmeter designated No. 2-Rev. 3, which was described previously,[7] was, as stated previously,[8] installed in a forced-circulation gas-fired Inconel loop containing $NaF-ZrF_4-UF_4$ (50-46-4 mole %, fuel 30) for calibration and for an endurance test of 3000 hr. Operation of the loop was started on January 8, 1957, and the turbine operated satisfactorily for about 340 hr. An investigation then showed that the unit was not operating, but it was not removed from the loop until the loop was drained. At that time the loop had operated for 5538 hr at temperatures ranging from 1200 to 1300°F.

An examination of the unit upon its removal from the loop showed that the bearing shaft on the end of the large turbine had broken and allowed the unit to drop and bend; the turbine therefore ceased to rotate. No oxidation other than that found after previous operation in NaK was apparent. No reason for the broken shaft was apparent, but it is thought that the break was probably an indirect

[7] G. H. Burger, *ANP Quar. Prog. Rep. Dec. 31, 1956,* ORNL-2221, p 25.

[8] G. H. Burger, *ANP Quar. Prog. Rep. March 31, 1957,* ORNL-2274, p 26.

result of the small diameter of the shaft and the brittleness of the material.

Two similar 1-in. flowmeters, designated No. 4-Rev 0 and No. 5-Rev 0, were calibrated with water and were installed in a forced-circulation gas-fired Inconel loop containing NaK that was being operated in order to test pressure transducers. This test loop is similar to those used previously except that it can operate with much higher flow rates. Unit No. 5-Rev 0, which is shown in Fig. 1.3.15, differed from Unit No. 4-Rev 0 in that its turbine had 10 blades, whereas the turbine of Unit No. 4 had five blades. The results of the water calibration of the units are presented in Fig. 1.3.16.

The two turbines were installed in series, and the loop was filled October 2, 1957, at 200°F. The loop operation was started at approximately room temperature, and was held at room temperature for approximately 120 hr before the temperature was raised to 1000°F at a slow rate. Unit No. 5-Rev 0 ceased to operate properly after 162 hr, but Unit No. 4-Rev 0 continued to operate. Unit No. 5 could be started momentarily by varying the pump

speed but would cease to operate after a very short operating period. After the loop had been operating for a total of 500 hr, the temperature was again raised with the intention of reaching 1200°F. At 1150°F, Unit No. 4 also stopped, but the temperature was quickly dropped to 1125°F and the unit
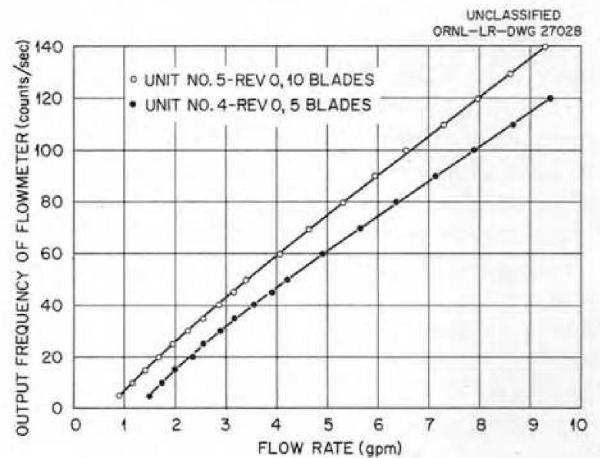
Fig. 1.3.16. Calibration Data Obtained with Water for Turbine Flowmeters No. 4-Rev 0 and No. 5-Rev 0.
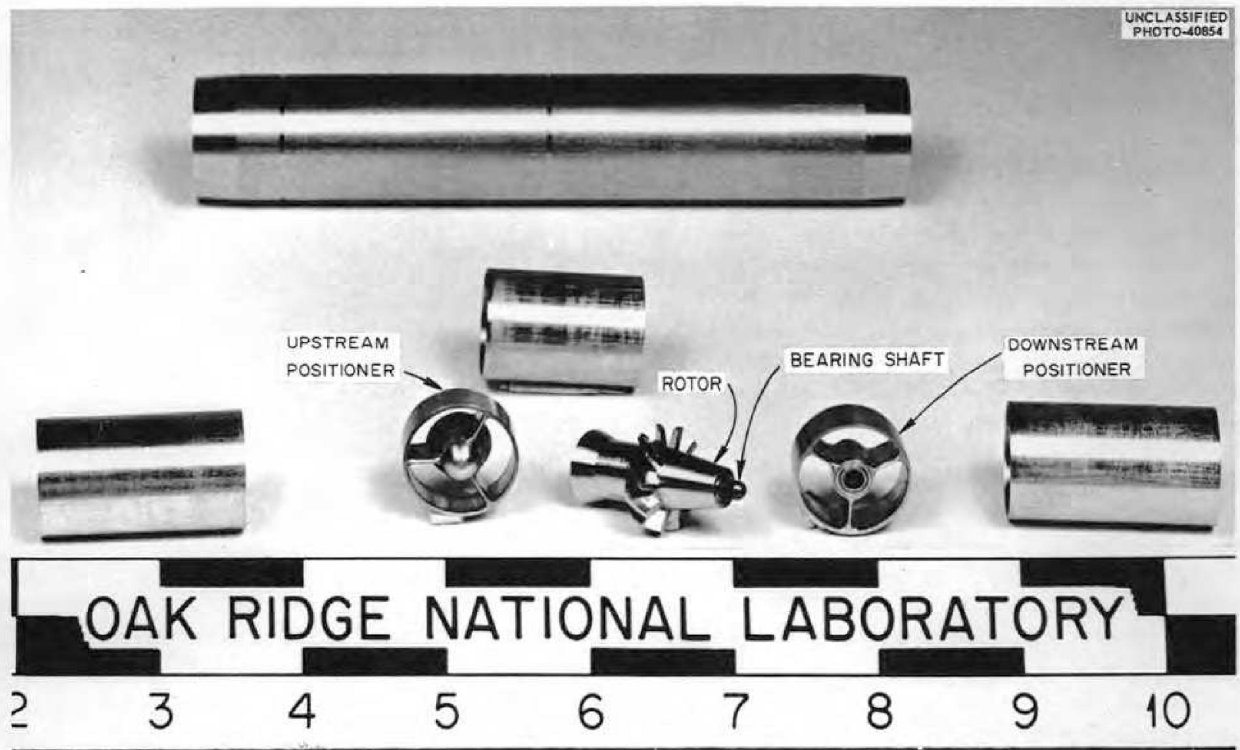
Fig. 1.3.15. Turbine Flowmeter No. 5-Rev 0.

again started operating and continued operating for approximately 100 hr at 1100°F. The loop temperature was then again raised, very slowly, to 1200°F. This time the unit operated in a normal manner and continued operating until the loop was shut down after 644 hr for removal of a defective pressure transducer that was being tested.

During the operating period, the flow rate was varied from 1.5 to 8.9 gpm. The turbine rotational speed varied from 300 to 3300 rpm, with 300 rpm being the lowest running speed of the turbine because of bearing friction and blade or rotor drag in the fluid. It was noted during the test that the output frequency of the unit became increasingly nonlinear below 4 gpm. This was not unexpected, since the unit was operating from below to just within the design flow range of from 5 to 50 gpm for 1-in. turbine flowmeters. No particular effort was made to achieve linearity or accuracy to a high degree, since the major objective of the tests was to determine the operating life of the units at various flow rates and temperatures.

After the loop was drained for removal of the pressure transducer, it was decided to remove the turbine flowmeters for examination and repair or modification, if necessary. The examinations showed that the bearings were in excellent condition, with no signs of oxidation, and the turbines rotated freely. Further examination disclosed, however, that the downstream thrust of Unit No. 5 was sufficient to wear slightly the end of the downstream shaft and thus allow the rotor body to contact the positioner body and cause the unit to drag and stop. It is evident that increased temperatures would aggravate this condition because of the increased softness of the Inconel. Unit No. 4 did not show this type of wear to so great an extent, since it was only a five-blade unit, and it therefore continued to operate.

Based upon the examination of the units, the bearing radial clearances were increased, the clearance between the downstream end of the rotor body and positioner was increased to 0.030 in. when the rotor was fully positioned in the downstream direction, and the number of blades was reduced to five on Unit No. 5 in order to reduce downstream thrust. In addition, the over-all blade diameter was reduced to give greater clearance between the blades and turbine housing and thus reduce the chances of jamming as a result of dirt

or oxide plugs in the loop. The units were then reassembled and reinstalled in the test loop without water calibration. Since the units were not recalibrated, the accuracy is not expected to be as good as before, but the linearity should be about the same. The flow rates indicated by the turbine and magnetic flowmeters in the system are plotted against pump speed in Fig. 1.3.17. It may be noted that the linearity of both the turbine flowmeters is quite good when compared with that of the magnetic flowmeter, which is known to be linear. It may also be noted that there is considerable error in the flow rates indicated by the turbine flowmeters in comparison with the rates given by the magnetic flowmeter. This was expected, as explained above, since the units were not recalibrated and are still operating near the lower limit of the design operating range.
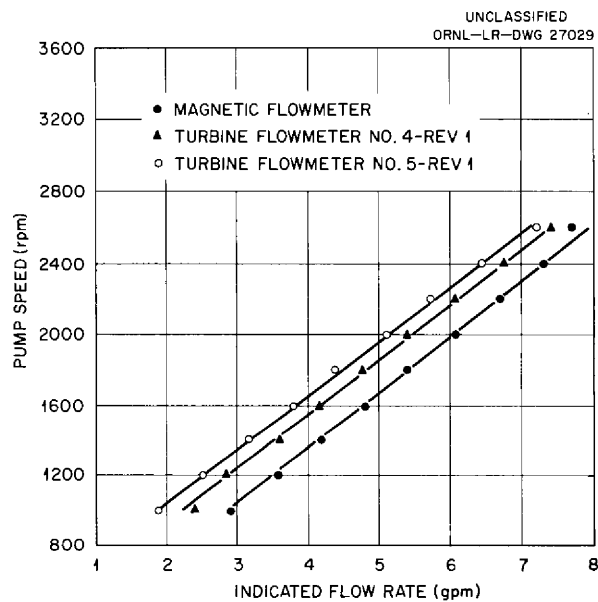
Fig. 1.3.17. Comparison of Flow Rates Indicated by Two Turbine Flowmeters and a Magnetic Flowmeter in a Test Loop Circulating NaK at 1200°F.

Since the units were reinstalled in the test loop they have operated in excess of 350 hr at temperatures ranging from 1200 to approximately 1600°F. It has been demonstrated during these tests that the units can be stopped at high temperatures and then restarted. It thus appears that self-welding of the bearings is not a problem. A detailed report on turbine flowmeter development and testing is to be prepared.

PRESSURE TRANSMITTERS

C. M. Burton

Additional tests were made of strain-gage pressure transmitters designed for use at high temperatures. In these pressure transmitters the process pressure acts on a diaphragm, which transmits the pressure to a NaK-filled capillary tube, which, in turn, transmits the pressure to a Bourdon spring. The Bourdon spring is linked to an unbonded strain gage, which is connected electrically in the form of a Wheatstone bridge. Similar strain gages have been used extensively in aircraft instrumentation work.

Primary pressure sensors of the same type but with pneumatic means for signal transmission were tested previously and are being used to obtain important pressure measurements in experimental test facilities. The possibility of leakage of radioactive material through pneumatic tubing in the event of an explosion, however, has directed attention toward instrumentation with electrical transmission. The condition of the electrical readout equipment can be periodically checked by switching to a calibrated resistor which should have a predetermined "synthetic" reading.

The strain-gage bridge is energized with a 5-v d-c supply, which can be unregulated if the voltage-ratio type of measuring equipment is used to determine the millivolt signal. This type of readout equipment is commercially available as a slightly modified form of the familiar electrical self-balancing potentiometer.

Under test conditions, six strain-gage pressure transmitters of 0- to 100-psig range indicated an average output-input deviation of 0.4% of full scale over their operating pressure range from ambient temperature to 1400°F. This accuracy compares favorably with the accuracies of other pressure transmitters. Two of these pressure transmitters are now being tested in a NaK loop under more severe conditions.

ART THERMOCOUPLES

J. T. DeLorenzo

Sheathed Thermocouples

Inconel-sheathed thermocouples (0.250-in.-OD sheath, MgO insulation) with hot-junction closure welds made by the Heliarc welding process are still being tested, with approximately 2000 hr of additional exposure time having been accumulated since the previous report. Eighteen Chromel-Alumel thermocouples, with closure welds that passed dye-penetrant and x-ray inspection, have now completed over 8000 hr of operation at 1500°F in sodium. The operating temperature has been reduced approximately once a week to 1300 and to 1100°F for readings at these temperatures. Since the last report,[9] no major shifts in performances have been observed. Three of the seven assemblies that earlier exhibited a slight downward shift have started slight upward drifts. Four of the seven assemblies with slow upward drifts have finally drifted approximately 2°F out of tolerance at the 1100°F test temperature. (An accuracy of $\pm\frac{3}{4}$ of 1% over the range of 530 to 2300°F is claimed by the vendor of the material being tested.) One assembly that showed a sharp downward drift at about 3000 hr has continued to drift downward and is well out of tolerance. All assemblies other than the five mentioned above are presently operating within the vendor's tolerance. The data for all 18 assemblies are summarized in Table 1.3.2.

Thirteen similar specimens and three platinum, platinum–10% rhodium units have now completed over 6000 hr of operation at 1500°F in NaF-ZrF$_4$-UF$_4$ (50-46-4 mole %, fuel 30). Readings at approximately one-week intervals were also taken at 1300 and 1100°F. No major shifts in performance have occurred over the past 2000 hr of operation. All thermocouples except one are now showing upward drift trends but are still within the vendor's tolerance. The data for these 16 thermocouples are summarized in Table 1.3.3.

The effect of nuclear radiation on the resistance of the magnesium oxide insulation was checked by inserting three samples of the sheathed material in hole HB-3 of the LITR. Two samples were maintained at a constant temperature of 1200°F and the third sample was not heated (gamma heating raised its temperature to 450°F). The samples were irradiated for three weeks, and a preliminary examination has revealed that no significant immediate effect was produced by radiation – a 10 to 30% decrease in resistance was observed in going from zero power to full

[9]J. T. DeLorenzo, *ANP Quar. Prog. Rep. Sept. 30, 1957*, ORNL-2387, p 61.

reactor power. Further, no significant drift in resistance was noted during the three-week interval of the test. An upward drift that was noted during the first 48 hr of the test was believed to be a result of additional drying of the magnesium oxide.

Table 1.3.2. Results of Drift Tests of Inconel-Sheathed Chromel-Alumel Thermocouples In Sodium

Test Period (hr)	Thermocouple Reading (°F)[a]	
	Deviation[b]	Spread[c]
Test Temperature: 1500°F		
0	5.2	6.6 to 3.0
1000	5.1	6.6 to −0.2
2000	5.4	7.4 to 0.8
3000	4.3	7.0 to −6.5
4000	4.4	7.8 to −11.5
5000	2.4	8.5 to −10.0
6000	1.9	11.5 to −17.8
7000	0.8	8.0 to −20.0
8000	0.7	9.9 to −27.5
Test Temperature: 1300°F		
0	7.3	8.8 to 6.0
1000	8.1	10.0 to 5.0
2000	5.7	8.0 to 2.0
3000	4.7	8.5 to −3.8
4000	1.5	8.0 to −8.5
5000	3.8	9.7 to −6.0
6000	2.7	9.0 to −10.5
7000	3.5	10.1 to −14.4
8000	0.9	9.2 to −23.0
Test Temperature: 1100°F		
0	6.8	8.1 to 5.5
1000	6.9	8.2 to 4.8
2000	6.2	8.0 to 3.4
3000	6.9	8.5 to 1.5
4000	4.2	9.5 to −14.0
5000	4.9	10.0 to −4.0
6000	4.6	9.5 to −5.0
7000	4.2	10.6 to −13.0
8000	4.2	10.5 to −3.1

[a]Nineteen assemblies were tested (one was removed after 5000 hr); each assembly contained two thermocouples and was aged 24 hr at 1350°F in helium prior to testing.

[b]Deviation of the average of the thermocouple readings from the test temperature.

[c]Maximum spread of the thirty-eight readings obtained.

Tests have revealed the extreme susceptibility of magnesium oxide to water absorption. Considerable baking was necessary to insure dryness of the material prior to the tests.

Well Thermocouples

Drift tests on well thermocouples designed for temperature measurement of high-velocity, high-temperature (1400 gpm, 1100 to 1500°F) liquid metals in Inconel piping were continued; over 2000 hr of testing has been completed. The ten thermocouples (two per well) employed in these tests were fabricated from 20 AWG, solid, Chromel-Alumel wire (accuracy, $\pm\frac{3}{8}$ of 1% over range of 530 to 2300°F) and were welded, with Heliarc welding techniques, to the bottom of the well. The test environment is static liquid NaK at 1500°F. The temperature of the system is reduced to 1300 and 1100°F weekly for readings at these temperatures.

No major shifts in drift have occurred since the start of the tests. All the thermocouples appear to be operating within the tolerance given above. The very close agreement between the two thermocouples in any given well is surprising, and the maximum deviation for all five units is 1°F. The variation in readings between wells can possibly be explained by the high temperature differences that exist in the region of the wells. The data taken to date are summarized in Table 1.3.4.

All the work done on the design and testing of ART thermocouples will be summarized in two ORNL reports to be issued soon. One report will cover the fabrication techniques used and the results of aging tests on Chromel P–Alumel and platinum, platinum–10% rhodium systems in fuel, sodium, and NaK, in addition to the results of rapid heating tests. The second report will describe all aging tests in air on Chromel P–Alumel and platinum, platinum–10% rhodium systems; this report will also include some recent aging information on thermocouple systems made of iron-constantan, British-made Chromel P–Alumel, Kanthal alloys, Driver-Harris 242-33 alloys, and Chromel P–Alumel systems with a titanium oxygen getter.

Table 1.3.3. Results of Drift Test of Sheathed Thermocouples in Fuel 30

Test Period (hr)	Chromel-Alumel Assemblies[a] Aged 24 hr		Chromel-Alumel Assemblies[b] Aged 200 hr		Pt, Pt−10% Rh Assemblies[c]	
	Deviation[d] ($^\circ$F)	Spread[e] ($^\circ$F)	Deviation[d] ($^\circ$F)	Spread[e] ($^\circ$F)	Deviation[d] ($^\circ$F)	Spread[e] ($^\circ$F)
Test Temperature: 1500°F						
0	1.9	4.0 to −0.5	2.9	3.0 to 2.8	−1.0	2.5 to −3.0
1000	2.7	6.0 to 0.0	5.1	5.5 to 4.8	0.4	1.0 to 0.0
2000	2.4	6.5 to −10.5	7.3	8.0 to 7.5	−0.6	1.0 to −3.0
3000	0.2	6.5 to −17.0	8.4	8.8 to 8.0	−1.4	1.0 to −4.2
4000	0.7	7.5 to −14.5	8.0	8.5 to 7.5	0.7	2.5 to −5.0
5000	2.0	7.6 to −10.5	8.4	9.2 to 7.6	0.4	1.8 to −1.1
6000	1.4	6.0 to −10.0	9.5	9.7 to 9.2	1.0	1.2 to −3.0
Test Temperature: 1300°F						
0	7.0	8.0 to 5.0	6.9	7.0 to 6.9	−0.1	1.8 to −3.8
1000	4.3	7.6 to −0.5	6.9	7.4 to 6.5	−1.2	0.0 to −2.1
2000	2.5	8.0 to −6.2	7.8	8.0 to 7.6	−0.6	1.2 to −3.0
3000	1.9	8.5 to −12.0	8.8	9.2 to 8.5	−0.8	1.2 to −3.0
4000	3.8	8.2 to −5.5	8.8	9.4 to 8.2	−0.6	1.8 to −3.5
5000	3.6	8.4 to −8.5	9.1	9.6 to 8.5	0.3	2.1 to −1.5
6000	2.3	7.3 to −9.0	8.4	8.8 to 8.0	0.1	2.5 to −1.2
Test Temperature: 1100°F						
0	4.2	5.4 to 3.0	4.6	4.8 to 4.5	−2.1	−0.2 to −4.2
1000	5.2	7.8 to 3.5	6.4	6.8 to 6.0	−0.3	0.4 to −0.9
2000	2.8	8.2 to −5.0	7.7	8.2 to 7.2	−0.5	1.2 to −1.5
3000	2.4	8.0 to −10.5	8.3	8.6 to 8.0	−0.3	1.2 to −2.0
4000	2.7	7.8 to −9.5	8.1	8.6 to 7.5	1.0	2.8 to −1.0
5000	4.7	8.5 to −6.5	8.7	10.0 to 7.5	1.5	2.9 to 0.2
6000	6.1	10.2 to −4.5	10.6	11.4 to 9.7	3.1	5.4 to 3.3

[a]Eight assemblies were tested; each assembly contained two thermocouples and was aged 24 hr at 1350°F in helium prior to testing.

[b]Two assemblies were tested; each assembly contained two thermocouples and was aged 200 hr at 1350°F in helium prior to testing.

[c]Three assemblies were tested; each assembly contained two thermocouples.

[d]Deviation of the average of the thermocouple readings from the test temperature.

[e]Maximum spread of the thermocouple readings.

47

Table 1.3.4. Results of Drift Tests of Well Thermocouples in NaK

Test Period (hr)	Well No. 1		Well No. 2		Well No. 3		Well No. 4		Well No. 5	
	Deviation[a] (°F)	Spread[b] (°F)	Deviation[a] (°F)	Spread[b] (°F)	Deviation[a] (°F)	Spread[b] (°F)	Deviation[a] (°F)	Spread[b] (°F)	Deviation[a] (°F)	Spread[b] (°F)
				Test Temperature: 1500°F						
0	2.2	0.8	−2.2	0.2	1.0	0.7	−4.3	1.4	−0.4	0.2
1000	1.5	1.0	−3.2	0.4	0.9	0.2	−4.2	1.2	−0.9	0.1
2000	4.5	1.0	−1.5	0.2	3.7	0.5	−0.3	0.5	3.4	0.0
				Test Temperature: 1300°F						
0	3.1	0.8	0.0	0.1	−3.5	0.1	−5.6	0.6	−4.5	1.0
1000	2.7	0.8	−1.5	0.1	2.9	0.0	−2.3	0.1	2.4	0.0
2000	4.0	0.7	−0.6	0.2	3.6	0.6	−2.6	0.9	2.9	0.1
				Test Temperature: 1100°F						
0	−1.4	1.1	−4.1	0.4	−1.8	0.4	−1.7	1.4		
1000	2.5	0.5	0.7	0.5	3.0	0.7	−3.7	0.4	−1.3	0.1
2000	4.8	0.4	1.3	0.2	3.4	0.4	−1.5	0.5	2.6	0.4

[a]Deviation of the average of the two thermocouple readings from the test temperature.
[b]Spread between the two thermocouple readings.

1.4. ENGINEERING DESIGN STUDIES

A. P. Fraas

APPLIED MECHANICS AND STRESS ANALYSIS

R. V. Meghreblian

Summaries and final reports on the applied mechanics and stress analysis problems of the ART have been prepared. The reports that have been prepared and issued include an analysis of the north-head pressure-stress distribution,[1] a description of a general relaxation method for determining two-dimensional temperature distributions on an IBM-650,[2] an analysis of a thermal cycling experiment performed on beryllium by using volume heat sources,[3] the results of a study of the temperature distribution at the junction of shell V (lower) and shell VI,[4] the results of the stress analysis of controlled structural tests

performed on the IHE-8B heat exchangers,[5] and a summary description of the core shell-liner experiment.[6]

Reports were also completed on the temperature distribution in the ART reflector-moderator assembly,[7] on the stress analysis of the radiators,[8] and on the thermal stress analysis of the ART heat exchanger channels and header pipes.[9] Two memoranda were also prepared on general methods for analyzing plates and shells.[10,11]

[1]S. E. Moore, *ART North Head Analysis*, ORNL CF-57-10-114 (in press).

[2]D. M. Miller, *Relaxation Calculations by Machine for Two-Dimensional Heat Conduction Problems*, ORNL CF-57-11-4 (Nov. 1, 1957).

[3]S. E. Moore, *Canned Cylindrical Beryllium Specimen with Internal Heating*, ORNL CF-57-10-109 (Oct. 30, 1957).

[4]D. M. Miller, *Temperature Profile of Shell V Lower—Shell VI Connection*, ORNL CF-57-11-9 (Nov. 1, 1957).

[5]D. L. Platus, *Summary of IHE-8B Heat Exchanger Stress Analysis*, ORNL CF 57-12-7 (in press).

[6]D. H. Platus, *Summary of Core-Shell-Liner Experiment*, ORNL CF-57-1-134, Addendum (Dec. 11, 1957).

[7]D. L. Platus, D. M. Miller, and R. V. Meghreblian, *ART Reflector Temperature Distribution*, ORNL-2425 (Nov. 2, 1957).

[8]D. H. Platus, *ORNL Tube-Fin Radiator Stress Analysis*, ORNL-2441 (in press).

[9]D. L. Platus, *Thermal Stress Analysis of the ART Heat Exchanger Channels and Header Pipes*, ORNL-2442 (in press).

[10]B. L. Greenstreet and D. M. Miller, *An Extension of the Esslinger Shell Relationships to Include Effects of Axial Load and Temperature*, ORNL CF-57-11-65 (Nov. 19, 1957).

[11]F. J. Stanek, *Stress Analysis of Flat Circular Plates*, ORNL CF-57-11-111 (Nov. 25, 1957).

1.5. DESIGN PHYSICS

A. M. Perry

The reactor physics problems associated with the design of the ART were the same as those that arise in the design of any reactor, but there were major shifts in relative importance. Typical problems that were studied included critical core size, or critical mass of fuel; reactivity effects of temperature, poisons, control rods, and so forth; radiation heating of various parts of the reactor; activation or neutron-induced changes in the composition of various materials; and shielding.

For a fused-salt reactor, the problem of critical mass may be viewed in a somewhat different perspective than for a fixed-fuel reactor. Since the concentration of fissionable material can be readily adjusted to achieve criticality or the desired excess reactivity, the urgent problem is not so much to know in advance exactly how much fuel the reactor will require, as to be assured that the melting point of the fuel, which depends upon the uranium concentration, will remain within acceptable limits for any foreseeable additions of UF_4 to the fuel.

The criticality problem for the ART was initially one of finding a suitably compact core geometry, while at the same time keeping the UF_4 concentration within acceptable limits. The work of the Laboratory on this problem[1-3] was augmented by a contract with the Curtiss-Wright Corporation for a parametric survey[4] of fuel concentration and core power distribution, upon which the physical dimensions of the ART core and reflector were finally based. The composition and thickness of the core shell were shown to have a decisive influence on critical fuel concentration;[4,5] this was confirmed

by the room-temperature critical experiments.[6] While the analysis indicated a negative temperature coefficient of reactivity, the marked dependence of critical concentration on the core shell thickness caused some concern that the reactor might in fact have a positive moderator temperature coefficient, and led to the performance of a high-temperature critical experiment[7] which proved the moderator coefficient to be negative. The experiment was based on an exact mockup of the design core. Nevertheless, there were a number of differences, such as the absence of reflector cooling and deviations in the outer boundary of the reflector, whose cumulative effect on critical concentration proved to be quite significant.[8] The required concentration of UF_4 in the ART fuel, including allowance for reactivity changes during the core life, was expected to be about 5 to 5.5 mole %, in contrast to the critical concentration in the high-temperature critical experiment of 2.84 mole %.

A major problem in the circulating-fuel reactor is activation of the secondary coolant. While the thermal neutrons leaving the reflector can be effectively absorbed in a boron-containing layer between the reflector and the heat exchangers, some activation remains because of higher energy neutrons absorbed in the sodium resonance at 2.9 kev, or moderated in the heat exchanger, and because of delayed neutrons emitted in the heat exchanger. The problems of determining the level of sodium activity and of finding a satisfactory means of keeping the activity as low as possible have been examined extensively, both analytically[9] and experimentally.[10]

The total Na^{24} activity expected in the ART secondary coolant loop was 1000 curies. It was evident, however, that the level of activity could

[1]A. P. Fraas and C. B. Mills, *A Reflector-Moderated Circulating Fuel Reactor for an Aircraft Power Plant,* ORNL CF-53-3-210 (March 27, 1953).

[2]C. S. Burtnette, M. E. LaVerne, and C. B. Mills, *Reflector-Moderated-Reactor Design Parameter Study,* ORNL CF-54-7-5 (Nov. 8, 1954).

[3]M. E. LaVerne and C. S. Burtnette, *ANP Quar. Prog. Rep. June 10, 1954,* ORNL-1729, p 32.

[4]H. Reese, Jr., S. Strauch, and J. T. Mihalczo, *Geometry Study for an ANP Circulating Fuel Reactor,* WAD-1901 (Sept. 1, 1954); C. B. Mills and H. Reese, Jr., *Design Study of an ANP Circulating Fuel Reactor,* WAD-1930 (Nov. 30, 1954).

[5]W. K. Ergen, *ANP Quar. Prog. Rep. June 10, 1955,* ORNL-1896, p 20.

[6]A. D. Callihan *et al., ANP Quar. Prog. Rep. March 10, 1955,* ORNL-1864, p 43.

[7]A. D. Callihan *et al., ANP Quar. Prog. Rep. Sept. 10, 1955,* ORNL-1947, p 58.

[8]A. M. Perry, *ANP Quar. Prog. Rep. Sept. 10, 1955,* ORNL-1947, p 33.

[9]H. W. Bertini, *ANP Quar. Prog. Rep. March 10, 1956,* ORNL-2061, p 28.

[10]J. B. Dee *et al., ANP Quar. Prog. Rep. Dec. 10, 1955,* ORNL-2012, pp 204, 209.

be very substantially reduced – perhaps by a factor of 5 or more – in an aircraft reactor.

Closely related to the NaK activity is the activity of material activated in the heat exchangers and carried to the radiators by mass transfer in the NaK stream. In the case of the ART, the activity in the radiators after shutdown and removal of the NaK was expected to be about 1 curie, and the dose rate 1 ft from the radiator surface was expected to be about 1 r/hr, due mostly to Co^{60} (ref 11).

A major area of investigation in reactors with high power density is the heating of structural components by gamma radiation and neutrons. Calculations showed that, in the ART, the heating of the reflector, the core shells, the north head structures, and many other components would be substantial, especially from gamma radiation, and special provisions were provided for cooling them. A complete summary of the radiation heating calculations may be found in two topical reports;[12,13] several aspects of the problem have been discussed in progress reports, that is, heating in the vicinity of the pressure vessel,[14] the north head,[15] the off-gas system,[16] and in the beryllium and core shells.[17,18]

The control rod in the ART illustrates the usual considerations of depletion of the active material and of internal heating to a marked degree.[19] It was found[20,21] that a $1\frac{3}{8}$-in.-OD annular rod, $\frac{1}{4}$ in. thick, would be adequate if composed of rare-earth oxide at $\frac{1}{3}$ to $\frac{1}{2}$ the normal density, with the voids occupied by metal or sodium to achieve high thermal conductivity. The reactivity value of the control rod was determined entirely by critical experiments.[7]

Most of the considerations affecting the shielding requirements for the ART are described in the *Report of the 1953 Summer Shielding Session.*[22] Additional studies relating particularly to the shielding of various components included the NaK pipes,[23] fuel drain line,[23] fuel overflow line,[23] vapor traps,[23] and the fill-and-drain tank.[24]

[11]A. M. Perry, *ANP Quar. Prog. Rep. March 10, 1956,* ORNL-2061, p 30.

[12]H. W. Bertini *et al., Basic Gamma-Ray Data for ART Heat Deposition Calculations,* ORNL 2113 (Oct. 3, 1956).

[13]H. W. Bertini *et al., Radiation Heating in the ART,* ORNL-2429 (to be published).

[14]H. W. Bertini, *ANP Quar. Prog. Rep. June 10, 1956,* ORNL-2106, p 28.

[15]H. W. Bertini and D. L. Platus, *ANP Quar. Prog. Rep. June 10, 1956,* ORNL-2106, p 34.

[16]R. B. Stevenson, *ANP Quar. Prog. Rep. June 10, 1956,* ORNL-2106, p 35.

[17]R. B. Stevenson, *ANP Quar. Prog. Rep. Sept. 10, 1956,* ORNL-2157, p 31.

[18]C. M. Copenhaver, *ANP Quar. Prog. Rep. Dec. 31, 1956,* ORNL-2221, p 15; R. B. Stevenson, *ANP Quar. Prog. Rep. Dec. 31, 1956,* ORNL-2221, p 16.

[19]W. K. Ergen and H. W. Bertini, *ANP Quar. Prog. Rep. March 10, 1955,* ORNL-1864, p 26.

[20]W. Fader, *ANP Quar. Prog. Rep. June 10, 1955,* ORNL-1896, p 22.

[21]W. Fader and A. M. Perry, *ANP Quar. Prog. Rep. Sept. 10, 1955,* ORNL-1947, p 33.

[22]E. P. Blizard and H. Goldstein (eds.), *Report of the 1953 Summer Shielding Session,* ORNL-1575 (July 12, 1954).

[23]H. W. Bertini, C. M. Copenhaver, and A. M. Perry, *ANP Quar. Prog. Rep. June 30, 1957,* ORNL-2340, p 71.

[24]H. W. Bertini, *ANP Quar. Prog. Rep. Sept. 30, 1957,* ORNL-2387, p 80.

1.6. MATERIALS AND COMPONENTS INSPECTION

A. Taboada

MATERIALS INSPECTION

Approximately 4000 requests were received for the inspection of materials for the ART-ETU program. The total quantities inspected and the rejection rates are given in Table 1.6.1. At the time of suspension of the program 61,243 ft of CX-900 Inconel tubing was being inspected or was awaiting inspection.

WELD INSPECTION

The weldments inspected were made almost entirely by the inert-gas shielded-arc method and were predominantly of Inconel material. Visual, dye penetrant, and radiographic inspection techniques were used for the inspection of all thin-walled tubing and other critical weldments where complete reliability was essential. Such

Table 1.6.1. Total Quantities of Materials Inspected for the ART-ETU Program and the Rejection Rates

Item	Type	Quantity Inspected	Quantity Rejected	Rejection Rate (%)
Tubing	Regular Inconel	32,000 ft	5,000 ft[a]	15.5
	Regular Inconel	54,000 ft	54,000 ft[b]	100.0
	CX-900 Inconel	73,000 ft	18,225 ft[c]	25.0
	Stainless steel of various types	813 ft	266 ft	33.0
	Incoloy	70 ft	0 ft	0.0
	Hastelloy (tubing and small pipe)	1,390 ft	816 ft[d]	59.0
	INOR-8	128 ft	5 ft[d]	4.0
Pipe	Regular Inconel	12,300 ft	1,329 ft[a]	11.0
	CX-900 Inconel	1,470 ft	70 ft	5.0
Plate and sheet	CX-900 Inconel	1,574 ft^2	198 ft^2[e]	12.5
	Other	7,350 ft^2	257 ft^2	3.5
Rod and bar	CX-900 Inconel	50 ft	0 ft	0.0
	Other	2,381 ft	139 ft	6.0
Fittings	Machined adapters, reducers, ells, pipe caps, etc.	600 ft	43 ft	7.0

[a]Used for test loop applications; rejected for defects greater than 5% of the wall thickness or cracks.

[b]Rejected on the basis of a random 10% sampling inspection.

[c]Reactor heat exchanger and radiator tubing rejected for defects greater than 2% of wall thickness. Of the rejected tubing 8700 ft was returnable to vendor and 6150 ft was salvageable.

[d]Rejected for gross defects only.

[e]High rejection rate resulted from poor surface condition.

welds are designated C in the summary presented in Table 1.6.2. Weldments which did not require radiography, either because of inaccessibility or because the weldment did not require complete reliability, are designated CN in Table 1.6.2. Heavy section weldments on test loop pipes were also designated CN.

The ANP welding performance record from December 1954 to September 1957 is summarized in Table 1.6.2. Prior to December 1954, non-qualified welders had been used, and rejection rates approached 40%. The culmination of this work was the ETU assembly welding. Two hundred and fifty-six weldments were made, of which 40, or 15.5%, were rejected. The ETU weld rejection rate at termination was approximately 8%.

Table 1.6.2. Total Quantities of Weldments Inspected for the ART-ETU Program and the Rejection Rates

Period	C-Type Weldments			CN-Type Weldments		
	Quantity Inspected	Quantity Rejected	Rejection Rate (%)	Quantity Inspected	Quantity Rejected	Rejection Rate (%)
1954 to Oct. 1955	1,358	275	20	276	44	14.5
Oct. 1955 to Oct. 1956	11,067	1,318	12	1,163	31	2.5
Oct. 1956 to Sept. 1957	3,244	573	18	11,292	130	1.0
	15,669	2,166		12,731	205	

1.7. HEAT TRANSFER STUDIES

H. W. Hoffman

THERMAL-CYCLING RESEARCH

Pulse-Pump System

J. J. Keyes   A. I. Krakoviak
J. E. Mott[1]

Several additional tests were completed in the high-frequency thermal-cycling loop[2] with the fuel mixture $NaF-ZrF_4-UF_4$ (56-39-5 mole %) as the circulating fluid and helium as the pulsing and cover gas. A Milton Roy pump with a $1\frac{1}{2}$-in.-dia piston and a 4-in. stroke was used to generate approximately sinusoidal pressure oscillations at frequencies of 0.4 and 1.0 cps. These pulsations were transmitted to the fuel in the pulse chamber so as to force alternate hot and cold slugs of liquid through the test section. Outside wall temperatures and, in one case, fluid stream temperatures were measured instantaneously; the inside wall temperature amplitude was estimated by using data from previous water tests. The test sections were constructed of Inconel tubing and pipe that was approximately 0.5-in. in inside diameter and varied in wall thickness.

The test conditions and results for runs 3 through 5 are given in Tables 1.7.1 and 1.7.2,

---

[1]On assignment from Pratt & Whitney Aircraft.

[2]A complete description of this experimental system may be found in the following ANP Quarterly Progress Reports: ORNL-2157, p 56, ORNL-2221, p 54, and ORNL-2274, p 53.

and the geometries of the test pieces, as well as the direction of flow and the location of the samples taken for metallographic study, are shown in Fig. 1.7.1. The photographs of Fig. 1.7.2 show the results of examination of the test piece from run 5. In Fig. 1.7.2a some surface cracks are visible in the transition section near the entrance of the heavy-walled test piece (sample e). An approximately 0.070-in. crack in the wall of the same test piece at a position 3 in. downstream of the entrance (sample b) is shown in Fig. 1.7.2b. The total failure of the Inconel pipe in the vicinity of a weldment (sample c) may be seen in Fig. 1.7.2c.

A cursory examination of the data indicates that the severity of cracking as a result of thermal cycling increases with increasing pipe wall thickness and with proximity to a weld. This study is being continued on a limited basis.

The basic investigation of thermal transients at a solid-fluid interface was continued, with an experimental study in which the conditions of an adiabatic infinite wall were approximated. The results, obtained for three different film heat-transfer coefficients ranging between 2500 and 5000 $Btu/hr \cdot ft^2 \cdot °F$, have validated the theoretical analysis. A memorandum giving a detailed description of the experimental system and a discussion of the results has been issued.[3]

---

[3]J. E. Mott, *An Investigation of Thermal Transients at a Solid-Fluid Interface*, ORNL CF-57-10-122 (Oct. 25, 1957).

Table 1.7.1. Conditions of High-Frequency Thermal Cycling Tests of Inconel Pipe

Test No.*	Average Fluid Temperature (°F)	Maximum Temperature Difference Between Hot and Cold Streams (°F)	Frequency of Temperature Oscillations (cps)	Total Time** (hr)	Total Cycles	Total Fluid Flow Rate (gpm)
3	1360	288	1.0	99.5	360,000	
4	1387	454	1.0	250.0	900,000	
5	1412	493	0.4	135.0***	195,000	5.8

*Tests 1 and 2 were considered cleaning and "shakedown" runs and therefore inconclusive.

**Neglecting isothermal time.

***Estimated time at failure.

Table 1.7.2. Results of High-Frequency Thermal-Cycling Tests of Inconel Pipes

Test No.	Sample Designation	Wall Thickness (in.)	Measured Temperature Amplitude on Outside Pipe Wall (°F)	Estimated Temperature Amplitude on Inside Pipe Wall (°F)*	Results of Metallographical Examination of Test Piece and/or Adjacent Piping
3	a	0.091	±64	±68, ±95	Moderate to heavy void formation to a depth of 2 mils; some intergranular cracks or attack
3	b	0.029	±64	±68, ±95	Very light and scattered void formation to a maximum depth of 2 mils
4	a	0.133	Not measured	±90, ±112	Heavy subsurface void formation to a depth of 3 mils
4	b	0.091	Not measured	±125, ±150	Heavy intergranular cracks to a depth of 20 to 80 mils found immediately above and below welds
4	c	0.065	Not measured	±125, ±150	Moderate intergranular cracks which appeared to produce spalling
4	d	0.029	±85	±93, ±125	Very few general and intergranular voids to a depth of 3 mils
5	a	0.133	±20	±150, ±200	Moderate intergranular cracks, especially near weld
5	b	0.250	±7	±150, ±200	Heavy intergranular cracks to a depth of 72 mils
5	c	0.091	±68	±100, ±175	Moderate intergranular cracks with heavy cracks in heat-affected zone of weld where failure occurred
5	d**	0.133	±15	±100, ±175	Light intergranular cracks to a depth of 2 to 3 mils

*First value calculated from outside surface temperature; second value calculated from fluid temperature amplitude by using the η ratio.
**Subjected to conditions of tests 3 through 5.
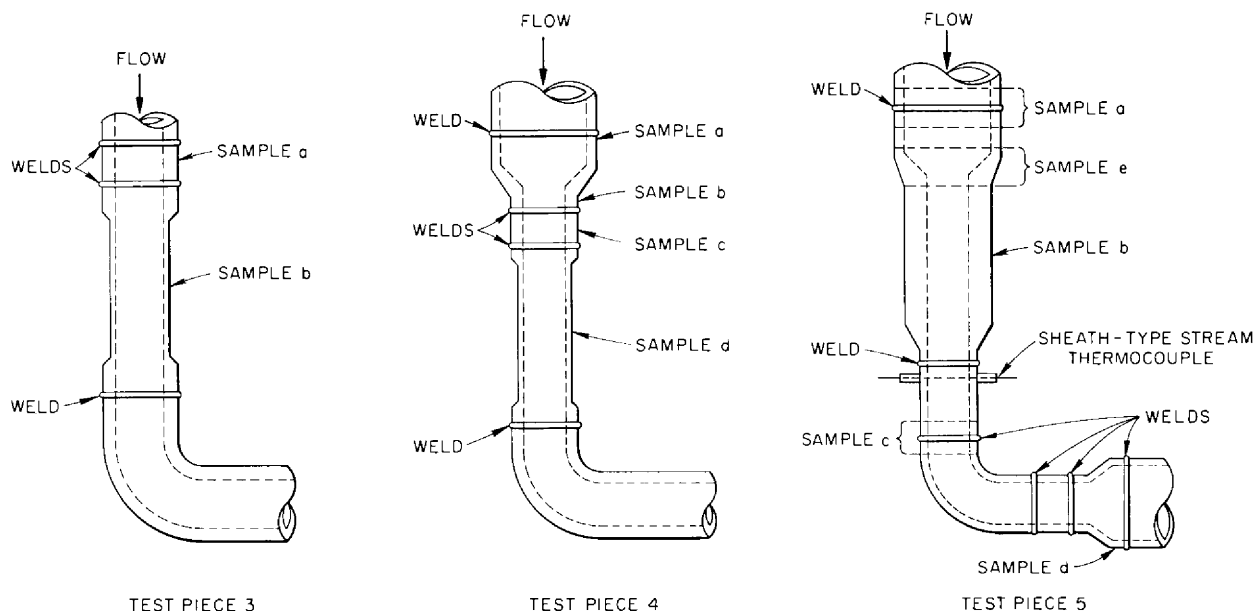
Fig. 1.7.1. Schematic Diagram of Test Pieces and Sample Locations.

Pressurized System

H. W. Hoffman   D. P. Gregory[1]

The experimental investigation of the effect of thermal-stress cycling on Inconel tubes filled with flowing $NaF-ZrF_4-UF_4$ (50-46-4 mole %) with the use of a pressurized flow system was discontinued. A report summarizing the results of this experimental study is being prepared.[4]

ART HYDRODYNAMICS

G. L. Muller[1]   F. E. Lynch
W. J. Stelzman

The investigations of the mechanics of the ART core fluid flow for which the full-scale plastic core model was being used have been terminated. The tests of the core that was divided into three flow regions by installing two annular shell liners[5] were not completed. A discussion of the design has been prepared by Platus.[6] The mass of data obtained in the course of these studies is being assembled and annotated for future publication. The data consist primarily of Pitot traverse measurements and dye-injection movies.

No further work has been done on the experimental studies of flow through quarter-scale models of the ART core. A complete report on this work has been prepared.[7] Work done on the screen-packed core and header combination while simulating single and dual pump operation will be reported in a later memorandum.

A report describing the phosphorescent-particle technique for velocity-profile visualization is also being prepared.[8]

FUSED SALT HEAT TRANSFER

S. I. Cohen   H. W. Hoffman

Forced-convection heat transfer studies with KCl-LiCl (41.2-58-8 mole %) flowing in a heated tube were continued. The results obtained are

[4]H. W. Hoffman and D. P. Gregory, *An Experimental Study into the Effects of Surface Thermal Cycling on Inconel in a Fluoride Fuel Environment*, ORNL-2435 (to be published).

[5]W. J. Stelzman, *ANP Quar. Prog. Rep. Sept. 30, 1957*, ORNL-2387, p 96.

[6]D. H. Platus, *Summary of Core-Shell-Liner Experiment*, ORNL CF-57-1-134, Addendum (Dec. 11, 1957).

[7]G. L. Muller, J. O. Bradfute, and F. E. Lynch, *Investigation of Fluid Flow in the ART and Other Reflector-Moderated Reactor Cores*, ORNL-2199 (in press).

[8]F. E. Lynch, L. D. Palmer, and G. M. Winn, *Instantaneous Velocity Profile Measurement by Photography*, ORNL-2257 (to be published).
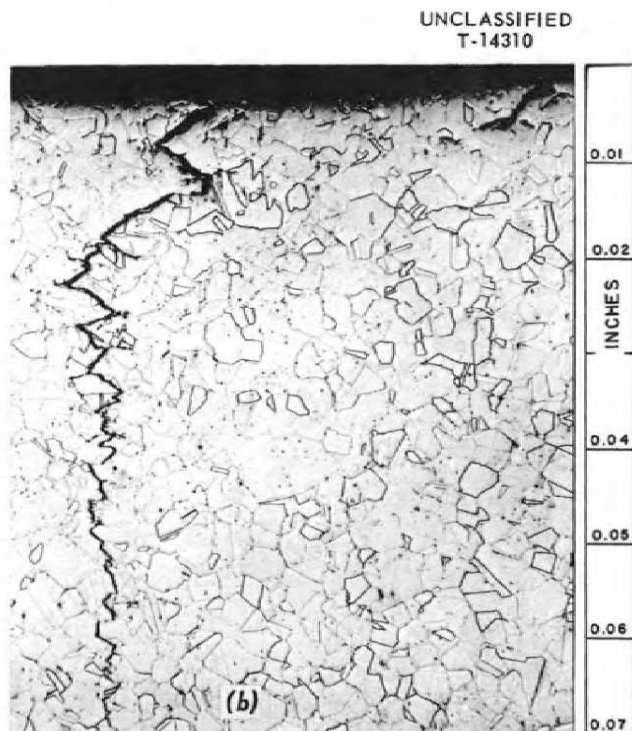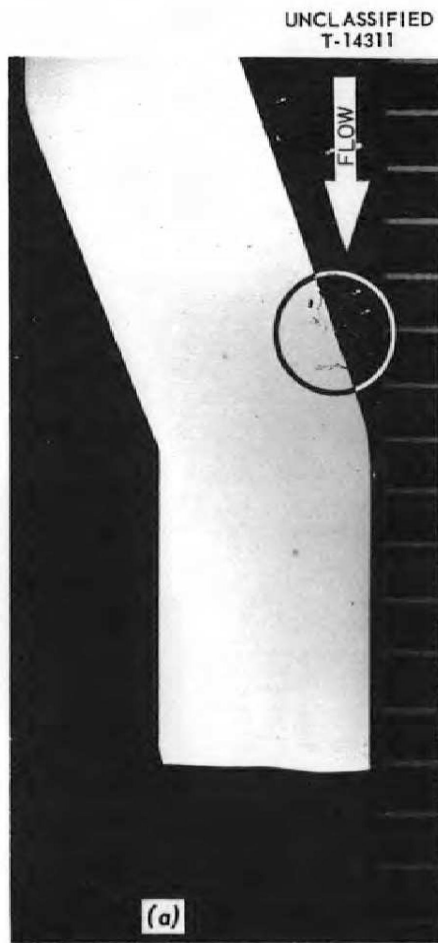
Fig. 1.7.2. Effect of High-Frequency Thermal Cycling on Inconel in an $NaF-ZrF_4-UF_4$ (56-39-5 Mole %) Environment — Test Run 5. (a) Inlet transition section; sample location e. 4X. (b) Section from sample location b; crack extends about 0.070 in. into 0.250-in. wall. 50X. (c) Exit region; sample location c; $\frac{3}{8}$-in. sched-40 pipe. 4X. (Secret with caption)

presented graphically in Fig. 1.7.3 in terms of the heat transfer parameter $N_{Nu}/N_{Pr}^{0.4}$ The data, which cover the Reynolds modulus range between 6,000 and 18,000, were obtained for both type 347 stainless steel and Inconel test sections.
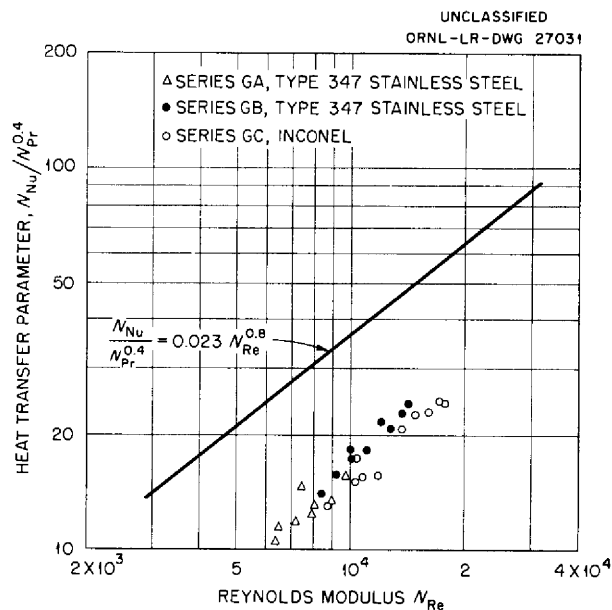
Fig. 1.7.3. Heat Transfer Characteristics of KCl-LiCl (41.2-58.8 Mole %).

The data of the first experiment (series GA) for a type 347 stainless steel tube fell approximately 55% below the general heat transfer correlations for standard fluids. These results were corroborated in succeeding tests with a new type 347 stainless steel test section (series GB) and with an Inconel test section (series GC). An analysis of the system indicated that the observed deviations might result from the use of incorrect thermal conductivity values in evaluating the data and/or the existence of high thermal resistance films at the salt-metal interface.

The thermal conductivity value used for the salt in the analyses of the data was obtained by averaging the preliminary value of 0.8 Btu/hr·ft·°F experimentally determined by Powers[9] and the value of 1.2 Btu/hr·ft·°F predicted on the basis of correlations by Gambill.[10] No attempt was

made to weight the data from either of these sources. To completely explain the observed discrepancy in the heat transfer parameter, a decrease in the thermal conductivity of the salt to a value of 0.3 Btu/hr·ft·°F would be needed. On the basis of previous experimental measurements of the thermal conductivity of fused salts, a change of this magnitude (0.8 to 0.3 Btu/hr·ft·°F) between preliminary and final values is not anticipated. Thus, incorrect thermal conductivity values can provide only a partial explanation of the experimental results.

It was found in earlier work with NaF-KF-LiF (11.5-42-46.5 mole %) in Inconel systems[11] that a reaction occurred between the salt and the metal to form a film of high thermal resistance at the salt-metal interface. Visual observation of the inside surface of the test section from series GA did disclose a very thin reddish-brown surface deposit. Spectroscopic and x-ray analyses of this film material have been inconclusive. Thus, the question as to whether this film is due to a surface reaction or to deposition from an impure salt mixture remains unresolved. Work on this program has been discontinued, and the results are summarized in a series of reports.[11-14]

MOLTEN LITHIUM HEAT TRANSFER

N. D. Greene

Preliminary designs are being prepared of an experimental system for the study of forced-convection heat transfer with molten lithium flowing in metal tubes. The loop proposed will consist of a gas-sealed pump, a magnetic flow-meter, a test section, and an air-cooled heat sink. In order to mitigate the difficulties and hazards encountered in earlier studies with lithium, an effort will be made to keep the volume

[9]W. D. Powers, unpublished data.

[10]W. R. Gambill, *Prediction of the Thermal Conductivity of Fused Salts*, ORNL CF-56-8-61 (Aug. 10, 1956).

[11]H. W. Hoffman and J. Lones, *Fused Salt Heat Transfer. Part II: Forced Convection Heat Transfer in Circular Tubes Containing NaF-KF-LiF Eutectic*, ORNL-1777 (Feb. 1, 1955).

[12]H. W. Hoffman, *Turbulent Forced Convection Heat Transfer in Circular Tubes Containing Molten Sodium Hydroxide*, ORNL-1370 (Oct. 3, 1952).

[13]H. W. Hoffman and S. I. Cohen, *Fused Salt Heat Transfer. Part III: Forced-Convection Heat Transfer in Circular Tubes Containing the Salt Mixture NaNO$_2$-NaNO$_3$-KNO$_3$*, ORNL-2433 (in preparation).

[14]H. W. Hoffman, S. I. Cohen, and D. P. Gregory, *Experimental Determination of Forced-Convection Heat Transfer with Several Fuel and Coolant Mixtures*, ORNL CF-58-1-1 (in preparation).

of liquid metal to a minimum. The lithium will be maintained at approximately 700°F, and the Reynolds modulus in the test section will be at least 50,000.

The test section will be constructed of type 347 stainless steel tubing having an inside diameter of approximately $\frac{3}{16}$ in. Heat will be generated electrically in the tube wall by the passage of a high amperage current. The heat generation in the lithium can be reduced to approximately 7.6% of the total for a tube wall thickness of $1\frac{1}{32}$ in. Test section wall temperatures, fluid flow rates, and mixed-mean temperatures will be measured.

VOLUME-HEATED SYSTEMS

ART-Type Core With Screens

N. D. Greene

The study of the effect of screens in a diverging annular channel on the thermal structure of a fluid under volume-heat-source conditions is being continued on a limited scale. Four screens of varying radial solidity have been fabricated and are currently being installed in the test model. These screens were designed to increase the resistance in the high-velocity regions of the flow so as to force the fluid into the lower velocity region near the outer wall.

Liquid-Metal Experiment

G. L. Muller

Construction of the system described previously[15] for the experimental investigation of heat transfer in a liquid metal (mercury) with internal heat generation has been essentially completed. The test-section electrical-power leads and instrumentation are now being installed. The three flow-measuring orifices have been calibrated with mercury by using a weigh tank. Differential pressure cells and a recorder were used to measure the orifice pressure drop. A few minor leaks around valve stems and pump shaft seals have been corrected.

An attempt has been made to obtain a universal relation for forced-convection volume-heat-source

heat transfer with liquid metals. The empirical equation

$$(1) \quad \frac{k(t_w - t_m)}{Wr_w^2} = T = \frac{1}{79 + 0.226\, N_{Pe}^{0.92}},$$

where

t_w = wall temperature,

t_m = mean fluid temperature,

k = thermal conductivity,

W = power density,

r_w = tube radius,

N_{Pe} = Peclet modulus (the Reynolds-Prandtl product),

was found to describe the analytical results previously reported[16] to within ±15% over the limits $0 \leq N_{Pr} \leq 0.1$ and $N_{Re} \geq 10{,}000$. The entire turbulent range ($N_{Re} \geq 5000$) can be represented to a lesser degree of accuracy (approximately ±30% at low N_{Re}) by the equation

$$(2) \quad \frac{k(t_w - t_m)}{Wr_w^2} = T = \frac{1}{65 + 0.24\, N_{Pe}^{0.915}}$$

The results obtained previously are compared in Fig. 1.7.4 with results of analyses made by Poppendiek and Palmer.[17] It may be seen that for values of the Peclet modulus above 1000 the agreement is excellent.

HEAT TRANSFER WITH VORTEX FLOW

W. R. Gambill   N. D. Greene

Previous experiences with source-vortex flow of fluids in forced-convection heating (no phase change) indicated that such a flow field might be of particular value in a boiling system. It was felt that, in comparison with other types of flow fields, the gravitational acceleration produced by the rotating fluid would keep a concave heated surface freer of bubbles at a given heat flux by providing an increased buoyant driving force for inward radial bubble migration. Delay of the burnout condition to a higher heat flux

---

[15]G. L. Muller, *ANP Quar. Prog. Rep. Sept. 30, 1957,* ORNL-2387, p 106.

[16]G. L. Muller, *ANP Quar. Prog. Rep. June 30, 1957,* ORNL-2340, p 102.

[17]H. F. Poppendiek and L. D. Palmer, *Forced Convection Heat Transfer in Pipes with Volume Heat Sources Within the Fluids,* ORNL-1395 (Dec. 17, 1952).
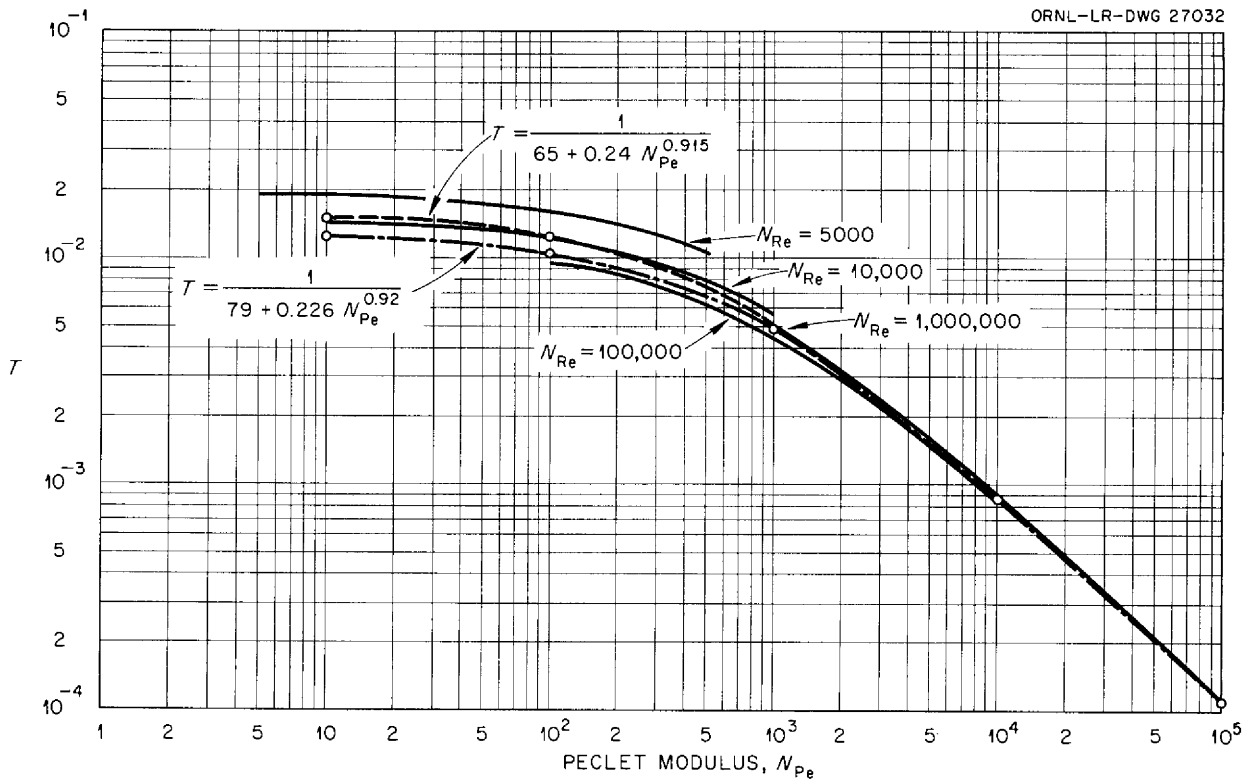
Fig. 1.7.4. Correlation of Liquid-Metal Volume-Heat-Source Forced-Convection Heat Transfer Data.

value was foreseen as the primary advantage of this phenomenon.

These early concepts have been justified to a considerable extent by preliminary data taken for the burnout heat fluxes for water in nucleate boiling, both subcooled throughout and with small net steam generation. These data are presented in Table 1.7.3. Comparisons of these burnout heat flux values with literature data for straight-through linear water flow at the same conditions of axial fluid velocity, L/D, exit pressure level, and exit subcooling (defined as saturation temperature minus actual liquid temperature, at exit), indicate approximately a 500% superiority for the vortex case. A typical comparison is shown in Table 1.7.4, where test No. 5 by Gunther[18] is compared with vortex flow run No. 4, for which the pertinent experimental conditions were almost the same.

---

[18]F. C. Gunther, *Trans. Am. Soc. Mech. Engrs.* **73**, 115–123 (1951).

If all Gunther's conditions were identical with those of ORNL run No. 4, it is estimated that his flux value would be 2.3×10^6 Btu/hr·ft², at the most; thus the advantage for the vortex case would be 378%. Gunther's values were chosen for comparison here because they are consistently among the highest reported in the literature and should give a conservative evaluation. Gunther's data were obtained for a rectangular flow passage within which was suspended a thin (0.004-in.) electrically heated metal strip or wafer that was cooled on both sides. This geometry gave considerably higher burnout values for linear water flow than those obtained in similar tests with straight, round tubes.

The high burnout values reported are not counterbalanced by an inordinately large power expenditure, as is indicated by the ratio designated P_f/P_q in Table 1.7.3. The ratio values given, in per cent, are the ratios of power input required for fluid flow across the test section to the heat absorption rate of the water in the same power units. As may be seen the heat

Table 1.7.3. Results of Investigation of Burnout Heat Fluxes for Water in Nucleate Boiling

Run No.	Axial Fluid Velocity (fps)	Degree of Subcooling at Exit (°F)	Inlet Static Pressure (psig)	Inside Diameter, D_i (in.)	Outside Diameter (in.)	Heated Length, L (in.)	L/D_i	Material	Exit Quality (%)*	P_f/P_q (%)**	Burnout Heat Flux (Btu/hr·ft²)
1	12.1	36	93	0.275	0.300	3.063	11.14	Copper	0	0.26	5,940,000
2	11.8	0	94	0.275	0.300	3.187	11.60	Copper	1.24	0.19	8,240,000
3	12.35	0	99	0.275	0.2875 (inlet) 0.300 (exit)	2.875	10.44	Copper	1.49	0.20	9,690,000
4	13.61	72	100	0.250	0.300	1.20	4.80	Inconel	0	0.43	10,980,000
5	13.18	135	248	0.300	0.375	3.05	10.16	Copper	0	0.37	8,630,000
6	16.3	150	248	0.250	0.270 (inlet) 0.281 (exit)	2.25	9.00	Inconel	0	0.39	10,810,000
7	24.0	49	285	0.250	0.270 (inlet) 0.278 (exit)	1.625	6.50	Inconel	0	1.01	17,250,000

*Percentage of water in steam at exit.

**Ratio (expressed in percentage) of power input required for fluid flow across test section to heat absorption rate of the fluid in the same power units.

Table 1.7.4. Comparison of Heat Transfer Data for Vortex Flow and Straight-Through Linear Flow

Condition	Vortex Flow*	Straight-Through Flow**
Axial water velocity, fps	13.6	12.3
Exit pressure, psia	15.0	14.4
Exit subcooling, °F	72	71
L/D_i	4.8	6
Burnout heat flux, Btu/hr·ft²	11.0×10^6	2.0×10^6

*Data obtained by Gambill and Greene (see Table 1.7.3).

**Data obtained by Gunther (ref 18).

absorption rate ranges from 99 to 526 times the test-section flow power.

An interesting observation was made recently in connection with runs 6 and 7. In run 6, the exit pressure level was held at 100 psig (rather than atmospheric as in all the other runs), but little change was noted in the burnout heat flux. In run 7, however, a maximum inlet pressure was generated for the maximum flow rate and gravitational field, and the very high burnout heat flux attained indicates that velocity effects are more important than pressure effects. These studies have been reported in greater detail in a recently issued ORNL memorandum.[19]

TOWER SHIELDING REACTOR II (TSR-II) HYDRODYNAMICS

W. R. Gambill

Detailed design work is nearly completed on an enclosure assembly for a full-scale model of a quarter segment of the TSR-II to be used in hydrodynamic studies. The data on the flow distribution in the coolant annuli will be combined with calculated heat-generation rates to determine the magnitude of redistribution of flow necessary to approximate a flat exit–water temperature profile. In these tests the exit annulus gap and the radial location of the control assembly at the core center will both be varied. The necessary pumps and instrumentation are being obtained concurrently with design work on the enclosure.

PHYSICAL PROPERTIES

W. D. Powers

Thermal Conductivity

The variable-gap thermal-conductivity device modified to include a heat meter of larger area

---

[19]W. R. Gambill and N. D. Greene, *A Study of Burnout Heat Fluxes Associated with Forced-Convection, Subcooled, and Bulk Nucleate Boiling of Water in Source-Vortex Flow*, ORNL CF 57-10-118 (Oct. 29, 1957).

has been used to redetermine the thermal conductivity of the fuel mixture $NaF\text{-}ZrF_4\text{-}UF_4$ (50-46-4 mole %, fuel 30). A preliminary value of 1.3 Btu/hr·ft·°F has been obtained that is to be compared with the previous values that range from 0.8 to 1.6 Btu/hr·ft·°F. This study will be completed after replacement of several defective components in the circuit that supplies power to the apparatus.

Enthalpy and Heat Capacity

Final results have been obtained for the enthalpies and heat capacities of the eutectic mixtures $LiCl\text{-}SrCl_2$ (52-48 mole %) and $LiCl\text{-}BaCl_2$ (70-30 mole %). The wide discrepancies in enthalpy between duplicate samples reported previously[20] were resolved by making improvements in the technique for mixing the two dry salts. The equations describing the enthalpies and heat capacities of these two mixtures are as follows:

$LiCl\text{-}SrCl_2$ (52-48 mole %)

Solid (99 to 493°C)

$$H_T - H_{30°C} = -3.52 + 0.140T +$$
$$+ (4.25 \times 10^{-5}) T^2$$
$$c_p = 0.140 + (8.50 \times 10^{-5}) T$$

Liquid (550 to 852°C)

$$H_T - H_{30°C} = -39.8 + 0.356T -$$
$$- (8.15 \times 10^{-5}) T^2$$
$$c_p = 0.356 - (16.3 \times 10^{-5}) T$$

Fusion (525°C estimated)

$$H_L - H_S = 43$$

$LiCl\text{-}BaCl_2$ (70-30 mole %)

Solid (100 to 502°C)

$$H_T - H_{30°C} = -4.57 + 0.146T +$$
$$+ (2.50 \times 10^{-5}) T^2$$
$$c_p = 0.146 + (5.00 \times 10^{-5}) T$$

Liquid (551 to 850°C)

$$H_T - H_{30°C} = -6.67 + 0.278T -$$
$$- (3.93 \times 10^{-5}) T^2$$
$$c_p = 0.278 + (7.85 \times 10^{-5}) T$$

Fusion (511°C)

$$H_L - H_S = 49$$

In the expressions above

H = enthalpy in cal/g,

c_p = heat capacity in cal/g·°C,

T = temperature in °C.

To date the enthalpies, heat capacities, and heats of fusion have been determined for five chloride mixtures containing lithium chloride. In a manner analogous to that previously used for fluoride-containing mixtures,[21] it has been possible to correlate these three properties for the chloride salts, and the results for the five mixtures are presented on a gram-atom basis in Table 1.7.5. It may be seen that the maximum deviation of any salt mixture from the average for the five salts is 9%. The values per gram are obtained by multiplying the listed per-gram-atom quantities by the factor N/M, where $N = \Sigma x_i N_i$ and $M = \Sigma x_i M_i$, x_i being the mole fraction of the ith component; N_i, the number of atoms in the ith component; and M_i, the molecular weight of the ith component.

[20]W. D. Powers, *ANP Quar. Prog. Rep. Sept. 30, 1957,* ORNL-2387, p 108.

[21]W. D. Powers and G. C. Blalock, *Enthalpies and Heat Capacities of Solid and Molten Fluoride Mixtures,* ORNL-1956 (Jan. 11, 1956).

Table 1.7.5. Properties of Binary Eutectics with Lithium Chloride

Second Component	LiCl (mole %)	$\bar{M}$	$\bar{N}$	$\bar{M}/\bar{N}$	Enthalpy per gram-atom		Heat Capacity per gram-atom		Heat of Fusion per gram-atom
					Solid at 300°C	Liquid at 700°C	Solid at 300°C	Liquid at 700°C	
NaCl	72	46.89	2.00	23.45	6.78	8.23	1750	6760	2020
KCl	59	55.59	2.00	27.79	6.56	9.03	1860	6960	1830
CaCl$_2$	62	68.46	2.38	28.77	6.76	8.31	1650	6560	1750
SrCl$_2$	52	98.15	2.48	39.58	6.56	9.55	1670	6690	1700
BaCl$_2$	70	92.16	2.30	40.07	6.45	8.94	1660	6770	1960
				Average	6.62	8.81	1720	6750	1850
	Maximum deviation from average				3%	8%	8%	3%	9%

Part 2

CHEMISTRY

W. R. Grimes

2.1. PHASE EQUILIBRIUM STUDIES[1]

C. J. Barton   R. E. Moore   R. E. Thoma

SUMMARY OF SALT SYSTEM INVESTIGATIONS

R. E. Thoma

Comprehensive studies of phase equilibria in fused-salt mixtures have been made over a period of years. These studies have been relevant to (1) selections of fused-salt fuels, solvents, and fuel-enriching mixtures, (2) development of fuel reprocessing techniques, (3) considerations of molten-salt secondary coolants, (4) structural metal corrosion, (5) crystal structure relationships, and (6) basic investigations of the phenomena involved in fused-salt phase equilibria.

A nearly current report of the status of fused-salt phase equilibrium diagrams was published recently,[2] and an extensive discussion of the equilibrium relationships in some of the more complex systems which have been investigated will be available soon.[3] Continued phase equilibrium studies have provided, during the quarter, sufficient data for essentially complete diagrams of the following systems: $KF-UF_4$, $RbF-UF_4$, $NaF-HfF_4$, $LiF-ThF_4$, $NaF-ThF_4$, $NaF-LiF-BeF_2$. For the most part, reliable liquidus lines or surfaces are well known for the systems that have been reported,[2] but for many systems only tentative conclusions can be drawn regarding the subliquidus phase relationships.

The search for improved fuel mixtures for aircraft reactor use has been directed to areas of low-melting-point regions of fluoride salt diagrams. Characteristic features of most fluoride salt diagrams that have strongly influenced the selections of fuel systems have been the high melting temperatures (800 to 1000°C) of $3MF \cdot XF_4$ and $2MF \cdot XF_4$ compounds, where MF is an alkali fluoride and XF_4 is ZrF_4, UF_4, or ThF_4. These high-melting-point compounds and related high-temperature liquidus compositions in ternary

systems have frequently precluded otherwise useful mixtures for fuels.

COMPARISON OF RUSSIAN AND ORNL INVESTIGATIONS OF THE $NaF-ThF_4$ SYSTEM

R. E. Thoma

A search for low-melting fuels requires a knowledge of binary phase diagrams for alkali fluorides and quadrivalent fluorides. An example which affords a comparison of published Russian fused-salt data with the type of information developed for ANP fuels is the system $NaF-ThF_4$. The Russian phase diagram of the $NaF-ThF_4$ system[4] is presented in Fig. 2.1.1, and the results of ORNL studies are given in Fig. 2.1.2. In the ORNL investigations, because of the need for a complete understanding of fuel behavior, all the phase equilibria, including those below the solidus, received attention. In Fig. 2.1.1, Emelyanov and Eustyukhin have interpreted thermal analysis data to indicate that in the vicinity of 20 mole % ThF_4 the incongruent melting temperature of $4NaF \cdot ThF_4$ is 648°C, that the $4NaF \cdot ThF_4 - 2NaF \cdot ThF_4$ eutectic temperature is 620°C, that $4NaF \cdot ThF_4$ decomposes into NaF and $2NaF \cdot ThF_4$ at 606°C, and that the α-$2NaF \cdot ThF_4$ to β-$2NaF \cdot ThF_4$ inversion occurs at 568°C. At ORNL, results of x-ray diffraction and optical examination of samples from thermal-gradient quenching experiments have shown that, for the above cases, no transition occurs at 648°C, that the $4NaF \cdot ThF_4 - 2NaF \cdot ThF_4$ eutectic temperature is 606°C, and that $4NaF \cdot ThF_4$ decomposes into NaF and $2NaF \cdot ThF_4$ at 568°C.

Emelyanov and Eustyukhin have assigned equilibrium polymorphism to the compound $2NaF \cdot ThF_4$, apparently wholly on the basis of the Zachariasen[5] indication that two crystal modifications of this compound exist. ORNL data show that there are two forms of $2NaF \cdot ThF_4$; however, the hexagonal δ form is either metastable or has equilibrium existence below 400°C.

---

[1]The petrographic examinations reported here were performed by T. N. McVay, Consultant, and R. A. Strehlow, Chemistry Division. The x-ray examinations were performed by R. E. Thoma, Chemistry Division.

[2]R. E. Thoma and W. R. Grimes, *Phase Equilibrium Diagrams for Fused Salt Systems*, ORNL-2295 (June 24, 1957).

[3]J. E. Ricci, *Guide to the Phase Diagrams of the Fluoride Systems*, ORNL-2396 (to be published).

[4]V. S. Emelyanov and A. I. Eustyukhin, *Atomnaya Energ.* 1, No. 5, 80 (1956).

[5]W. H. Zachariasen, *J. Am. Chem. Soc.* 70, 2147–51 (1948).

ИССЛЕДОВАНИЕ СИСТЕМ РАСПЛАВЛЕННЫХ СОЛЕЙ НА ОСНОВЕ ФТОРИДА ТОРИЯ

ThF_4. Это указывает, что при 606° С со-
единение Na_3ThF_7 распадается, образуя
NaF и соединение Na_2ThF_6. При 568° С
происходит полиморфное превращение
α-—β-Na_2ThF_6. Соединение Na_2ThF_6 (в
точке с 33,3 мол.% ThF_4) плавится с от-
крытым максимумом при температуре 708° С.
Эвтектическая смесь соединений Na_4ThF_8 и
Na_2ThF_6 плавится при 620° С и содержит
24 мол.% ThF_4.

830° С происходит перитектическая реак-
ция разложения химического соединения
$NaTh_2F_9$ (66,7 мол.% ThF_4), состав которого
подтверждается, в частности, тем, что теп-
ловой эффект при 830° имеет максимальную
величину в точке около 67 мол.% ThF_4
и вблизи этого состава исчезает эффект плав-
ления эвтектики при 750° С.

Таким образом, в системе NaF ThF_4
имеется четыре химических соединения:
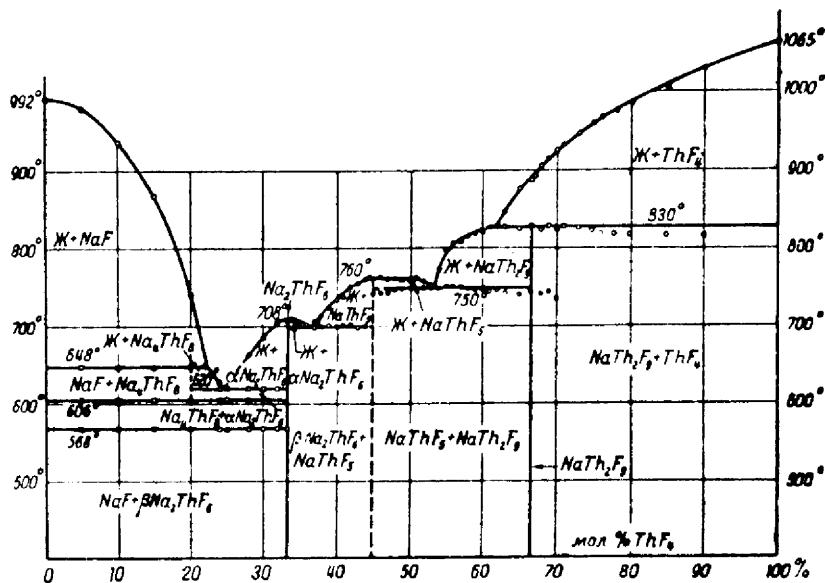
Рис. 1. Система $NaF—ThF_4$.

Далее линия ликвидуса постепенно по-
нижается до следующей эвтектической точки
при 700° С и 36—37 мол.% ThF_4. Начиная
с 36,5 мол.% ThF_4 и далее, тепловой эф-
фект плавления эвтектики уменьшается
и исчезает около 50 мол.% ThF_4.

По совокупности данных термического
и микроструктурного анализа следует, что
в области около 50 мол.% ThF_4 существует
химическое соединение предположительного
состава $NaThF_5$, имеющее весьма пологий
максимум. Линия ликвидуса от соединения
$NaThF_5$ незначительно понижается до эвтек-
тики при 750° С и 53,5 мол.% ThF_4 и далее
резко поднимается вверх, претерпевая при
830° С и 62 мол.% ThF_4 излом, после кото-
рого она плавно поднимается до 1065° С
(температура плавления чистого ThF_4). При

Na_4ThF_8, Na_2ThF_6, $NaThF_5$ и $NaTh_2F_9$. Со-
единение Na_4ThF_8 существует в двух модифи-
кациях: α-Na_4ThF_8, β-Na_4ThF_8, и, повиди-
мому, в расплавленном состоянии; соеди-
нения Na_4ThF_8 и $NaTh_2F_9$ распадаются по
перитектическим реакциям. Эти данные
подтверждают структурные исследования
Захариазена [1]. Соединение предположи-
тельного состава $NaThF_5$ имеет в области
от 44 до 50 мол.% ThF_4 очень пологий
максимум на линии ликвидуса, по которому
трудно установить точный состав.

Исследование системы $KF — ThF_4$

Было изготовлено и исследовано [5], [6]
свыше 40 сплавов через интервал 2—3 мол.%
ThF_4. На основании этих исследований была
построена диаграмма состояния системы

Fig. 2.1.1. The System NaF-ThF_4 According to Emelyanov and Eustyukhin.
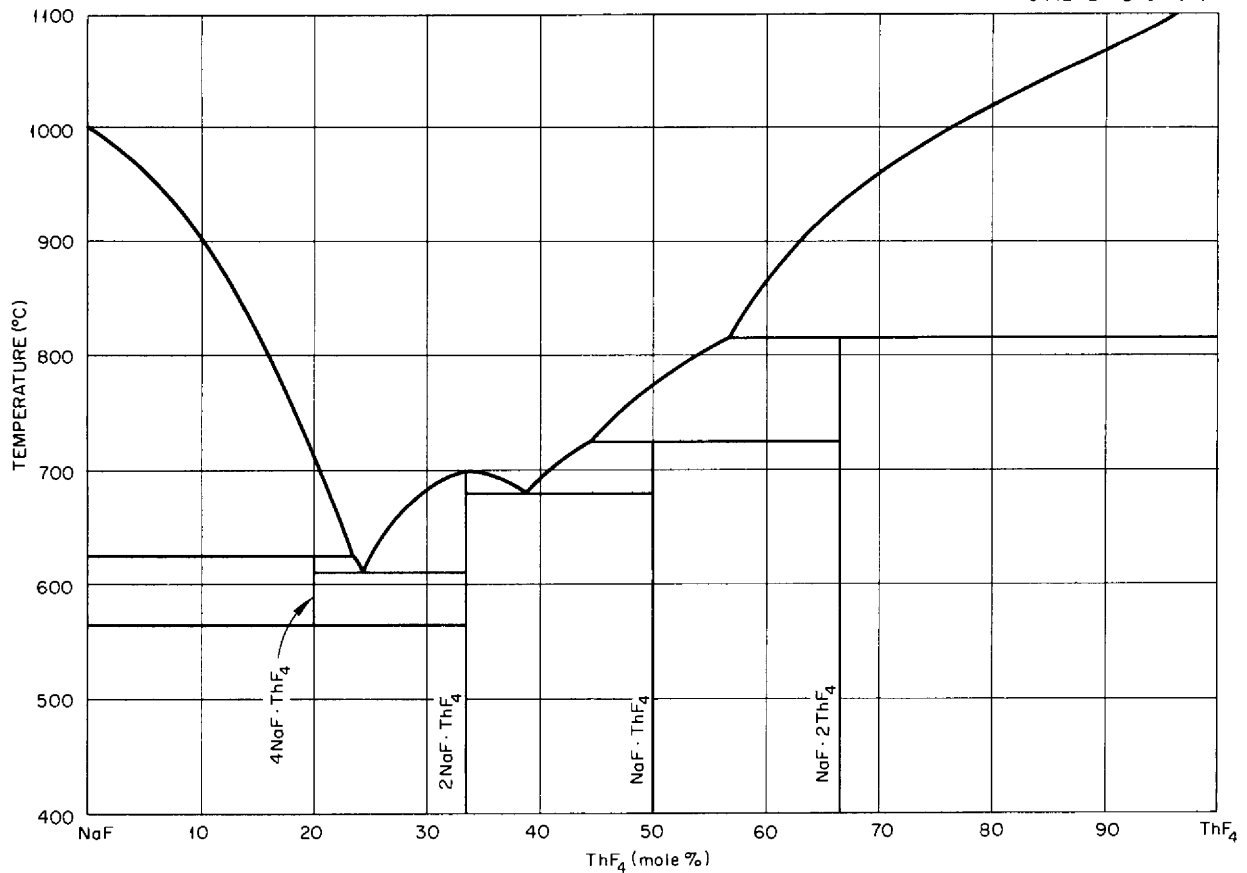
Fig. 2.1.2. ORNL Data on the NaF-ThF$_4$ System.

The Russian diagram shows a congruently melting compound NaF·ThF$_4$. ORNL data show that the compound NaF·ThF$_4$ melts incongruently to NaF·2ThF$_4$ and liquid.

Unclassified Russian reports presently represent the predominant number of contributions to the literature of phase equilibrium studies of fused salt mixtures. Since 1946 more than 200 Russian reports have been issued[6] concerning the phase equilibria of oxide, silicate, chloride, nitrate, and fluoride systems.

Most Russian phase work is done with thermal analysis and differential thermal analysis techniques. Phase identification is accomplished for the most part with x-ray diffraction. No reports

indicate the use of the thermal-gradient quenching techniques or of routine petrographic examinations.

THE SYSTEM NaF-CrF$_2$

H. A. Friedman   C. F. Weaver

Phase equilibria in the NaF—structural metal fluoride systems NaF-CrF$_2$, NaF-FeF$_2$, and NaF-NiF$_2$ have been studied in an effort to elucidate the corrosion process as it is related to these materials. Phase diagrams for the systems NaF-FeF$_2$ and NaF-NiF$_2$ have been reported.[7]

No fused-salt melts from thermal analysis experiments or from thermal-gradient quenching experiments have produced pure NaF-CrF$_2$ samples that are free of Cr^{+++}. A variety of means has been

[6]A. G. Bergman, K. A. Evdokimova, and O. F. Bogush, *Izvest. Sektora Fiz.-Khim. Anal., Inst. Obshchei Neorg. Khim., Akad. Nauk S.S.S.R.* **27,** 419—56 (1956).

[7]H. A. Friedman and B. S. Landau, *ANP Quar. Prog. Rep. June 30, 1957,* ORNL-2340, p 128.

employed to minimize the effects of the disproportionation reaction

$$3CrF_2 \rightleftharpoons 2CrF_3 + Cr^{\circ}$$
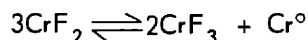
in these phase equilibrium studies. Even the inclusion of 20 to 30 wt % chromium metal powder dispersed through samples for thermal-gradient quenching has not suppressed the forward reaction sufficiently for $NaF-CrF_2$ phase equilibrium data to be derived.

APPARATUS FOR HIGH-TEMPERATURE THERMAL-GRADIENT QUENCHING EXPERIMENTS

H. A. Friedman

A design modification of the apparatus[8,9] used in thermal-gradient quenching experiments has permitted the feasible upper operating temperature limit to be raised from 850 to 1300°C. Previous difficulties encountered with quenching apparatus when operated routinely at 900 to 1000°C included the frequent need for replacement of the 18 thermocouples which monitored the thermal gradient, the rupture of the sample tube because of oxidation corrosion, uncertainties as to temperature constancy of the sample because of discontinuous monitoring, and sample tube expansion during heating.

In the revised apparatus a single, traveling, recording thermocouple was substituted for the 18 monitoring thermocouples. The furnace was redesigned to permit the sample tubes to be protected by a static helium atmosphere during heating. The use of a roller crimping machine contributes to minimizing sample tube expansion.

The apparatus, shown schematically in Fig. 2.1.3, now consists of a round nickel block 10 in. in length and 2 in. in diameter, which is supported in a $2\frac{1}{2}$-in. tube furnace that has a platinum wound core. Interchangeable gears allow a choice of excursion times for the traveling thermocouple. A complete thermocouple travel cycle of 2 hr is usually employed in using this apparatus.

The roller and crimping machine (Fig. 2.1.4) is designed so that a 6-in.-long, 0.10-in.-OD, 0.010-in.-wall nickel tube containing a sample

to be quenched is flattened and crimped at $\frac{1}{4}$-in. intervals. The sample tubes are sealed by welding after they have been rolled and crimped. Sample tubes prepared in this manner have better heat transfer characteristics than those of the tubes used previously. Much less expansion of the tubes during heating occurs because the void space is also reduced in the crimping process.

PETROGRAPHIC ANALYSES OF FUEL MIXTURES

R. A. Strehlow

The petrographic microscope has been used on a routine basis for the inspection of solidified fuel mixtures.[10] This type of examination is performed to detect the presence of oxygen-containing compounds and, for some samples, to determine any variance from the nominal composition. Mixtures of $NaF-ZrF_4$, $NaF-ZrF_4-UF_4$, $LiF-NaF-KF-UF_4$, and related compositions have formed the bulk of samples submitted for inspection. An illustration of the results obtained with the technique used in the inspection of these samples is given here for $NaF-ZrF_4$ mixtures containing about 50% ZrF_4.

Mixtures in the $NaF-ZrF_4$ system which contain between 46.2 and 57.1 mole % ZrF_4 will contain some $3NaF \cdot 4ZrF_4$ which will, in general, occur in the slowly cooled melt and will be dispersed in eutectic aggregates that also contain $7NaF \cdot 6ZrF_4$. The aggregate frequently will exhibit a brown cast, which has been attributed to hydration of $3NaF \cdot 4ZrF_4$. Better crystallized $3NaF \cdot 4ZrF_4$ has been observed in samples containing about 56 mole % ZrF_4. The material present as the matrix in the eutectic aggregates is the compound with the reported formula of $7NaF \cdot 6ZrF_4$.

This compound occurs as the primary phase in mixtures containing from 46.2 to 49 mole % ZrF_4. It is characterized as a crystalline uniaxial substance that is optically negative with $N_o = 1.502$ and $N_e = 1.508$, where N_o and N_e refer to the ordinary and extraordinary indices of refraction of uniaxial crystals.

Compositions containing about 50 mole % ZrF_4 which have been cooled at intermediate rates occasionally contain $NaF \cdot ZrF_4$ as a nonequilibrium phase that is uniaxial positive with $N_o = 1.417$ and

[8]C. J. Barton *et al.*, *ANP Quar. Prog. Rep. Dec. 10, 1954*, ORNL-1816, p 57.

[9]C. J. Barton *et al.*, "Phase Equilibria in the Systems $LiF-UF_4$ and $NaF-UF_4$," *J. Am. Ceram. Soc.* (in press for issuance in Feb. 1958).

[10]The techniques described were developed over a period of several years by T. N. McVay, G. D. White, H. Insley, and B. S. Landau.
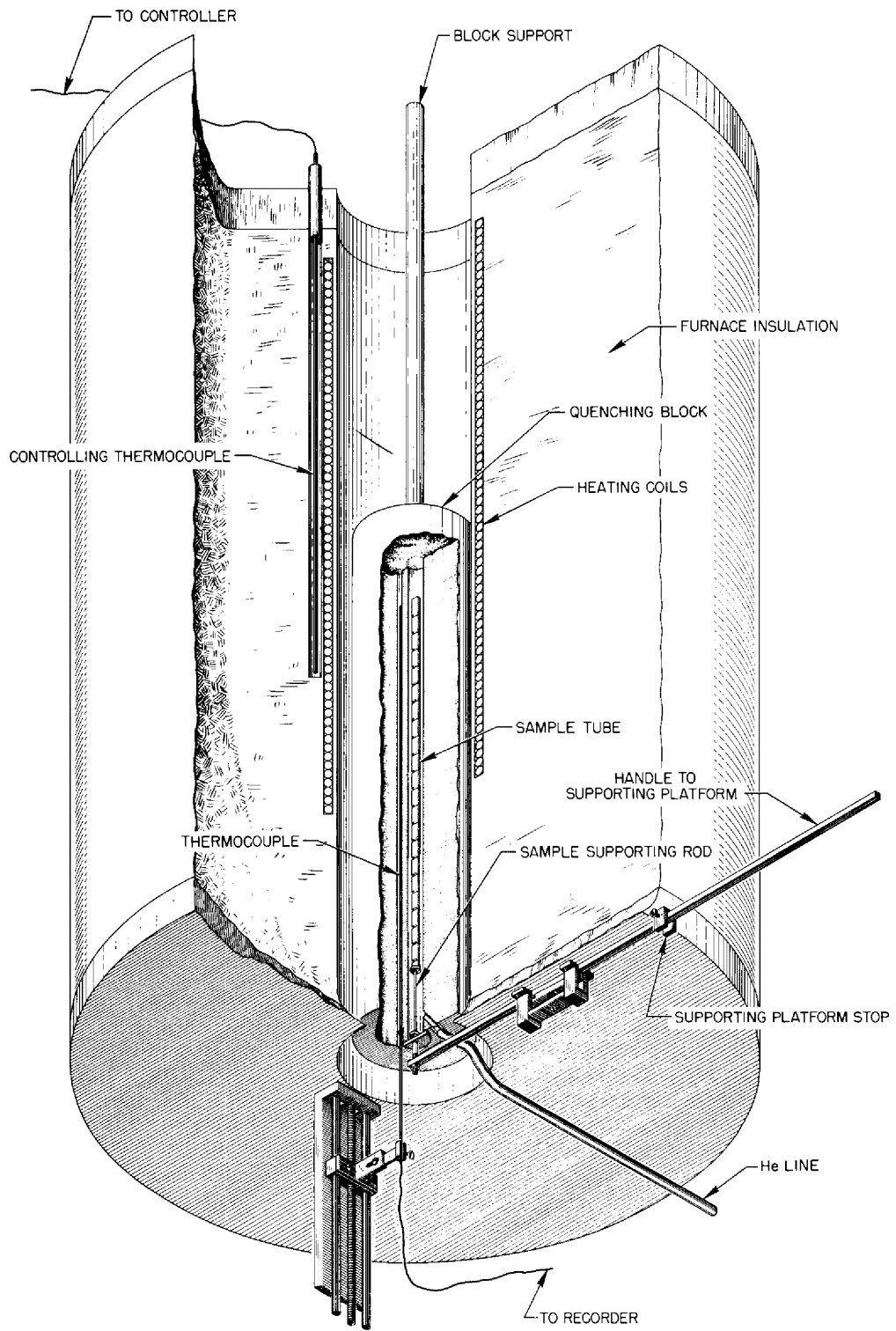
Fig. 2.1.3. Thermal-Gradient Quenching Apparatus.
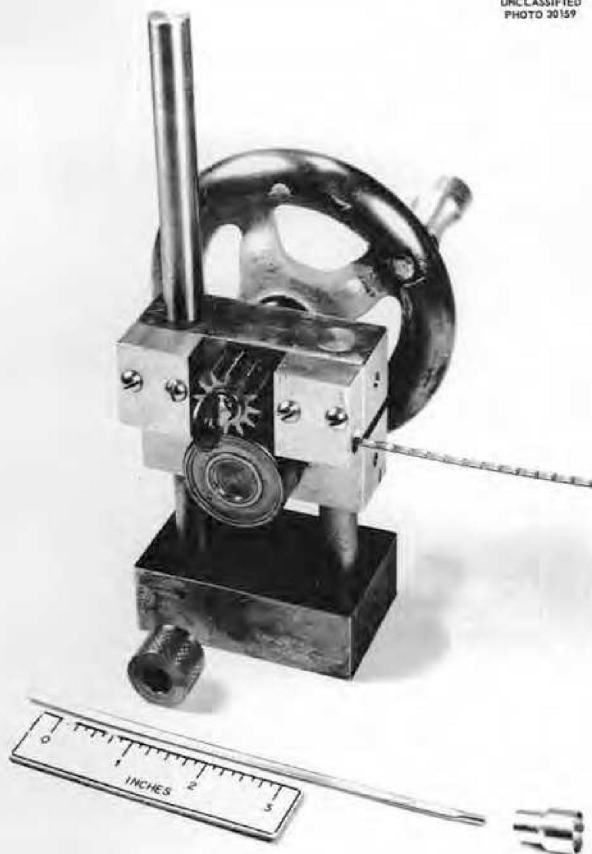
Fig. 2.1.4. Rolling and Crimping Machine for Preparing Thermal-Gradient Quenching Samples.

$N_e = 1.446$. This is rare, however, in slowly cooled fuel mixtures.

At higher NaF concentrations than 53.8 mole %, crystals of the solid solution between $7NaF \cdot 6ZrF_4$ and $3NaF \cdot 2ZrF_4$ are observed which are, in general, poorly crystallized and which may be distinguished from $7NaF \cdot 6ZrF_4$ crystals by their lowered indices of refraction, their crystalline character, and their poor extinction when examined with crossed polarizing disks.

Oxygen will, in general, be observed as the oxyfluoride, which is uniaxial negative with indices of refraction greater than 1.54 to 1.7 and which frequently crystallizes as hexagonal plates. Zirconium oxide has been observed, and it is easily seen in samples of this type because of its pronounced angular cleavages, frequent high birefringence, and very high refractive indices (higher than 2.13).

The addition of UF_4 may introduce, as a new material, a UF_4-ZrF_4 solid solution which occurs in mixtures containing less than 50 mole % NaF and is biaxial negative ($2V = 50$ deg)[11] with marked birefringence and refractive indices of around 1.6. If UO_2 is present it is optically isotropic and garnet red in color. Partial reduction of UF_4 to UF_3 results in a yellow-brown cast to the otherwise green crystals.

AN OPTICAL METHOD FOR THE DETERMINATION OF EQUILIBRIUM PATHS AND TIE LINES IN TERNARY FUSED-SALT SYSTEMS

C. F. Weaver

Systems Without Solid Solution

If the liquidus temperatures and the boundary curves in a ternary phase equilibrium system are known, and if there is no solid solution, all the tie lines for any over-all composition and temperature can be drawn. The tie lines will then describe the equilibrium path (a straight line) and indicate the composition of the liquid in equilibrium with a primary phase as a function of temperature and over-all composition.

Systems With Solid Solution

If there is solid solution, knowledge of the liquidus temperatures and the boundary curves is insufficient to allow the tie lines to be drawn. The difference between the case without solid solution and the case with solid solution lies in properties of the primary phase. In the case of no solid solution, the composition of the primary phase is given on the phase equilibrium diagram, and it is independent of temperature. In the case of solid solution, the composition of the primary phase is not specified on the phase equilibrium diagram. In addition the composition of the primary phase is, in general, a function of temperature.

Under certain conditions the composition of the primary phase as a function of temperature can be determined experimentally for each over-all composition. This information together with the liquidus temperatures can be used to draw the tie lines. As in the case of no solid solution, the tie lines will describe the equilibrium path (in general, a curved line) and indicate the composition of the

---

[11]In this expression, $2V$ refers to the acute angle between the axes in biaxial crystals.

liquid in equilibrium with a primary phase as a function of temperature and over-all composition.

Index of Refraction vs Solid Solution Composition

If a series of fused-salt solid solutions of known composition are prepared, their indices of refraction can be measured by means of a microscope and suitable immersion oils. A hypothetical plot of index of refraction vs composition for a continuous fused-salt solid solution between A and B is given in Fig. 2.1.5.
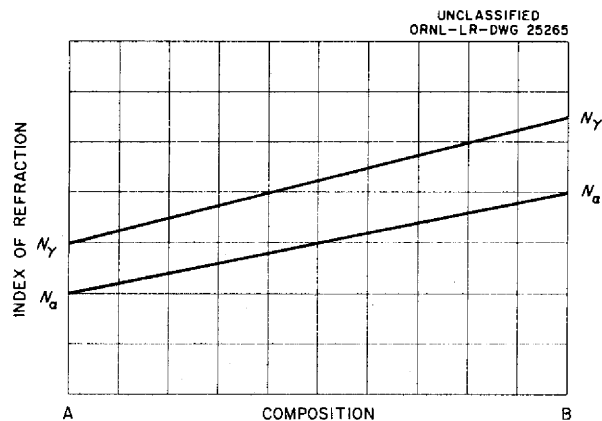
Fig. 2.1.5. Hypothetical Plot of Index of Refraction vs Composition for a Continuous Fused-Salt Solid Solution Between A and B.

In general, when the solid solution AB appears in the system of interest its composition is not immediately known. It is readily apparent that the composition can be determined from Fig. 2.1.5, if the indices of refraction for the solid solution AB are measured. In order to avoid ambiguity, plots such as Fig. 2.1.5 must contain no maximums or minimums. Further it should be noted that the accuracy of the determination increases with the slope of the curve of index of refraction vs composition of the solid solution.

Composition as a Function of Temperature

The composition of the solid solution AB must be determined, as described above, for a series of temperatures at a given over-all composition P in order to obtain the information needed for constructing the equilibrium paths. The composition of AB is plotted vs temperature, as in Fig. 2.1.6,

and the curve is valid, of course, only at point P. Hence a series of such curves must be constructed to suitably cover the primary phase area of interest.

Constructing Tie Lines and Equilibrium Paths

If the over-all composition is considered to be that shown in Fig. 2.1.7 and it is assumed that Fig. 2.1.6 gives the solid solution composition
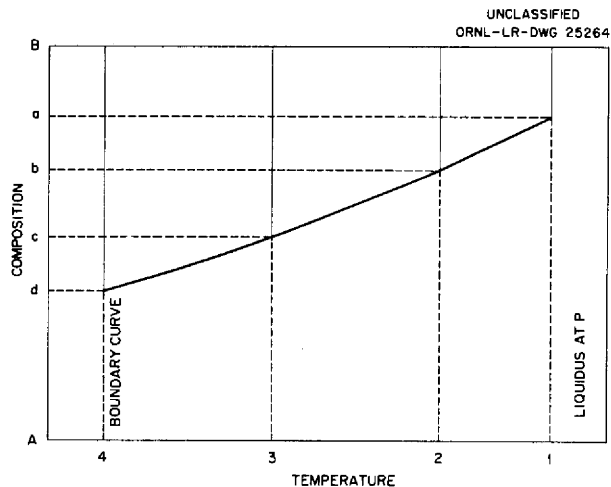
Fig. 2.1.6. Composition of AB vs Temperature for Point P.
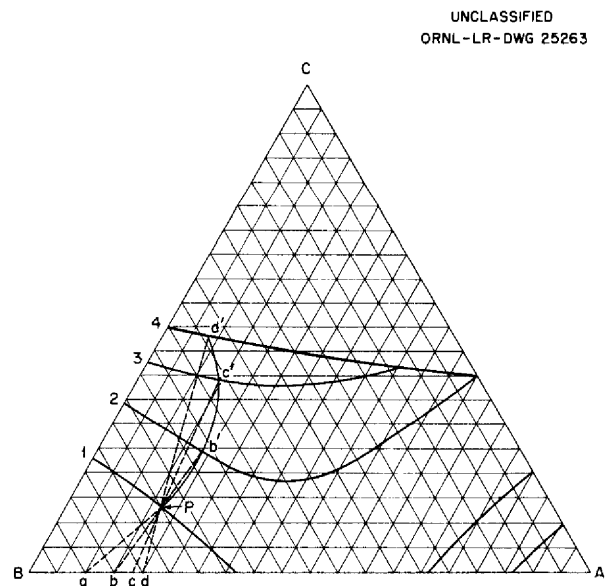
Fig. 2.1.7. Over-All Composition of Ternary System ABC.

vs temperature plot for P, at temperature 1 the composition of AB solid solution is a, the composition of the liquid is P, and the tie line is Pa. Likewise for temperatures 2, 3, and 4, the composition of AB solid solution is b, c, and d, the composition of the liquid is b', c', and d', and the tie lines are $b'b$, $c'c$, and $d'd$, respectively. The locus of all points such as P, b', c', and d' is the equilibrium path.

The System LiF·ThF$_4$·UF$_4$

The system LiF-ThF$_4$-UF$_4$ appears to contain three continuous solid solutions: UF$_4$-ThF$_4$, LiF·4UF$_4$-LiF·4ThF$_4$, and 7LiF·6UF$_4$-7LiF·6ThF$_4$. In the UF$_4$-ThF$_4$ solid solution the plot of index of refraction vs composition has a small slope. As previously mentioned, tie lines cannot be accurately determined when the slope of the plot is small. In the remaining two solid solutions, however, the slopes are sufficient for the determination of tie lines. These solid solutions offer ample opportunity for a study of the tie lines and equilibrium paths, and such studies have been initiated.

2.2. CHEMICAL REACTIONS IN MOLTEN SALTS

F. F. Blankenship   L. G. Overholser
R. F. Newton   G. M. Watson

THE PREPARATION OF UF₃ AND ITS STABILITY IN MOLTEN FLUORIDE MIXTURES

F. F. Blankenship

The use of UF_3 in fuel mixtures was found to be impractical because disproportionation occurred and uranium metal deposited on the container surfaces. The work that led to this conclusion and the results of investigations of methods for eliminating or avoiding disproportionation are summarized here. The mechanism for disproportionation has been ascertained and means for controlling it are suggested. Petrographic and x-ray diffraction examinations were used in this study to characterize phases in solidified melts,[1] and liquid compositions were, in general, defined by synthesis or by filtration and chemical analysis.[2,3]

The UF_3 compound may be prepared in solution by various redox reactions or by electrolysis, but, when large quantities were needed for corrosion studies, solid UF_4 was used as the starting material. The reaction

$$(1) \qquad 3UF_4 + U^\circ \rightleftharpoons 4UF_3$$

was used to produce routinely kilogram batches of 99% UF_3. Essentially complete reaction of stoichiometric mixtures of UF_4 and U° was obtained in 48 hr at 900°C.[4]

The equilibrium pressure of UF_4 above UF_3 as a result of disproportionation by the reverse reaction in Eq. 1 was measured at temperatures between 1270 and 1400°C in tantalum-lined vapor pressure apparatus. The results obtained are represented by the expression[5]

$$\log p \text{ (mm Hg)} = -\frac{4187}{T} + 3.945 \ ,$$

where T is in degrees Kelvin. The equilibrium values thus obtained indicated that crystalline UF_3 is more stable than published estimates of the free energies of formation would indicate. In contrast, UF_3 was found to disproportionate in molten fluoride solvents to a much greater extent than it did in the solid-crystal form. Partially complete phase diagrams were prepared[6] that were useful in approximating the solubility behavior of UF_3 in binary mixtures of alkali fluorides. The solubility of UF_3 in NaF-ZrF₄ and in NaF-BeF₂, which are mixtures of interest as reactor fuels, is 1 to 2 wt % U at 600°C.[7]

Nonacidic fuel solvents that contain a high concentration of fluoride donor constituents, such as alkali fluorides, were found to increase the extent of disproportionation by complexing the acidic UF_4 (fluoride acceptor). The ease of alloy formation between the uranium formed and the container metal also noticeably influences the extent of the disproportionation.[8] Less disproportionation occurred in copper vessels than in nickel vessels, and tantalum and molybdenum were found to be even more resistant than copper to alloying with the uranium formed.

It was also found that UF_3 was oxidized by the alkali fluorides. The reaction was particularly noticeable with mixtures containing KF:

$$(2) \qquad UF_3 + KF \longrightarrow UF_4 + K^\circ$$
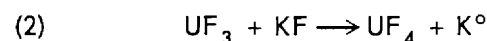
For example,[9] when a solution containing 21.4 wt % U as UF_3 in the LiF-NaF-KF eutectic (46.5-11.5-42 mole %) was heated under helium in copper apparatus, about one-third of the UF_3 was lost by disproportionation in 2 hr at either 650 or 750°C; the amount of UF_3 oxidized by KF at the same time increased from 7 to 18%. Sufficient reduction in the helium pressure caused a rapid increase in the

[1] H. Insley *et al.*, *Optical Properties and X-Ray Diffraction Data for Some Inorganic Fluoride and Chloride Compounds*, ORNL-2192 (Oct. 23, 1956).

[2] R. J. Sheil and B. H. Clampitt, *ANP Quar. Prog. Rep. March 10, 1955*, ORNL-1864, p 53.

[3] M. B. Panish, *ANP Quar. Prog. Rep. June 10, 1955*, ORNL-1896, p 69.

[4] B. J. Sturm and E. E. Ketchen, *ANP Quar. Prog. Rep. March 10, 1955*, ORNL-1864, p 66.

[5] S. Langer, *ANP Quar. Prog. Rep. June 10, 1955*, ORNL-1896, p 64.

[6] C. J. Barton *et al.*, *ANP Quar. Prog. Rep. Sept. 10, 1954*, ORNL-1771, p 56.

[7] L. M. Bratcher *et al.*, *ANP Quar. Prog. Rep. March 10, 1955*, ORNL-1864, p 50.

[8] C. J. Barton and B. H. Clampitt, *ANP Quar. Prog. Rep. Sept. 10, 1955*, ORNL-1947, p 78.

[9] B. H. Clampitt, *ANP Quar. Prog. Rep. March 10, 1956*, ORNL-2061, p 97.

rate of disappearance of U^{+++}. The sharp increase in the rate occurred at a pressure corresponding to the bubble pressure of potassium. The small apparent temperature coefficient of the disproportionation in such experiments was probably the result of the process being limited, after an initial rapid deposition of uranium, by the slow rate of diffusion of uranium into copper.

In comparison with UF_4-containing fuels, the UF_3-containing fuels exhibit a marked improvement in initial corrosion attack at high temperatures.[10] Moreover, the use of UF_3 in conjunction with UF_4 could provide reserve reducing capacity to compensate for any tendency of the fuel to become more oxidizing during burnup. Unfortunately the difficulties arising from the deposition of uranium by disproportionation prevent the easy exploitation of UF_3 as a solution to corrosion problems. However, even in the UF_4 fuels, some UF_3 always appears as a product of the oxidizing action of UF_4, and the fate of this UF_3 is of interest in connection with long reactor lives.

ACTIVITY COEFFICIENTS OF FeF_2 AND OF NiF_2 IN MOLTEN NaF-ZrF_4

C. M. Blood

The activity coefficients[11,12] of FeF_2 and of NiF_2 in NaF-ZrF_4 (53-47 mole %) were determined by comparing the values of the equilibrium quotients of the reaction

$$MF_2(d) + H_2(g) \rightleftharpoons M^\circ(s) + 2HF(g)$$
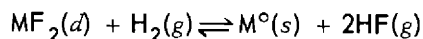
with the corresponding values of equilibrium constants calculated from the tabulated[13] free energies of formation of FeF_2, NiF_2, and HF. Experimental values for the equilibrium quotients for the reactions of FeF_2 and of NiF_2 were shown to be independent of concentration. For the FeF_2 reaction the values of K_x are 2.6 ± 0.2, 0.63 ± 0.04, and 0.097 ± 0.007 atm at 800, 700, and 600°C, respectively. These values are in essential agreement with equilibrium constants calculated from

the standard free energies of formation of pure solid and supercooled FeF_2 at these temperatures. Accordingly, the activity coefficients for FeF_2 in this solvent are near unity, regardless of the choice of standard state. The numerical values of the activity coefficients of FeF_2 are, at 800, 700, and 600°C, 1.46, 2.20, and 3.28 with respect to the pure crystalline solid, 0.64, 0.66, and 0.66 with respect to liquid FeF_2, and unity with respect to the standard state of reference at infinite dilution.

Equilibrium quotients for the NiF_2 reduction have been determined to be $21,900 \pm 2,000$, $15,300 \pm 700$, $11,000 \pm 600$, and $7,600 \pm 400$ atm, as compared with the values 10.9, 7.4, 4.8, and 3.1 calculated from the free energies of formation of pure solid NiF_2 at 625, 600, 575, and 550°C, respectively. The corresponding constants calculated for liquid NiF_2 are 43.8, 33.6, 25.2, and 18.4. The very large discrepancies between the calculated and experimental constants give rise to very high values of the activity coefficients of NiF_2. By using the solid as the standard state the numerical values of the activity coefficients were found to be 2009, 2076, 2292, and 2468 at 625, 600, 575, and 550°C, respectively. With supercooled liquid NiF_2 as the standard state, the corresponding values of the activity coefficients are 500, 455, 436, and 413.

It is clear from the values of the activity coefficients that when NiF_2 is dissolved in NaF-ZrF_4 (53-47 mole %) it behaves in a manner vastly different from that predicted by the free energies of formation for solid NiF_2. This is somewhat surprising in view of the agreement shown to exist between the calculated and experimental behavior of FeF_2 in the same solvent. Accordingly, the results of these investigations confirm that the tabulated values of the free energies of formation of solid FeF_2, the tabulated melting point, and the estimated heat of fusion are adequate to predict the behavior of FeF_2 in the solvent NaF-ZrF_4 (53-47 mole %). On the other hand the corresponding values for NiF_2 are not at all suitable to describe its behavior in the same solvent.

In the case of FeF_2 the experimentally determined free energy of formation at 600°C for the standard state of reference at infinite dilution was -135.4 kcal/mole, as compared with the tabulated values -137.5 and -134.5 for the solid and liquid states, respectively. Thus the experimental value for FeF_2 was found to be between the predicted values for the solid and the liquid states. On the

[10]J. H. DeVan and E. A. Kovacevich, *ANP Quar. Prog. Rep. Dec. 10, 1955*, ORNL-2012, p 107.

[11]C. M. Blood and G. M. Watson, *ANP Quar. Prog. Rep. March 10, 1956*, ORNL-2061, p 84.

[12]C. M. Blood, *ANP Quar. Prog. Rep. Sept. 30, 1957*, ORNL-2387, p 117.

[13]L. Brewer *et al., Natl. Nuclear Energy Ser. Div. IV 19B*, pp 65, 110 (1950).

other hand, the experimentally determined free energy of formation of the standard state of reference for NiF_2 was found, at 600°C, to be −114.6 kcal/mole, while the tabulated value for the solid state is −127.9. As has been pointed out elsewhere,[14] at first glance it appears that the value of the free energy of formation of the solid NiF_2 is in error by approximately 13 kcal. It is known, however, that the solubility of NiF_2 is quite low in in this solvent,[15] 0.17 mole % at 600°C; and, if the saturating phase is pure NiF_2, an activity coefficient of 588 would be required to give unit activity at saturation. Since the saturating phase is not pure NiF_2 but rather a complex fluoride, it is only possible to predict from the solubility an upper limit of 588 for the activity coefficient for solid NiF_2 as the standard state. The upper limit of 588 corresponds to a value of −125.7 for the free energy of formation of NiF_2. Conversely, it may be stated that the upper limit at 600°C of the free energy of formation for solid NiF_2 is −125.7 kcal/mole, as given by its solubility, the experimental K_x, and the tabulated free energy of formation for gaseous HF. The magnitude of a more reasonable value will now be considered.

In order to obtain an activity coefficient in the neighborhood of unity with supercooled liquid NiF_2 as the standard state, the free energy of formation must be approximately −114.6 kcal/mole at 600°C. The free energy of formation of solid NiF_2 at 600°C, based on an assumed free energy of formation of liquid NiF_2 of −114.6, may be computed according to the equation

$$\Delta F^{\circ}_{NiF_2(s)} = \Delta F^{\circ}_{NiF_2(l)} - \Delta F_{Melting} .$$

If the heat of fusion is assumed to be independent of temperature, then

$$\Delta F^{\circ}_{NiF_2(s)} = \Delta F^{\circ}_{NiF_2(l)} - \Delta S_M (T_M - T) ,$$

where $\Delta S_M = \Delta H_f / T_M$, the entropy of fusion, and T_M is the melting point of solid NiF_2.

In previous calculations,[12] a heat of fusion of 8000 cal/mole and a melting point of 1300°K for NiF_2 were assumed, as suggested by Brewer.[13]

These values give a free energy of formation for solid NiF_2 of −117.2 kcal/mole. However, some recent work indicates that the melting point of NiF_2 is greater than 1500°C (ref 16). If the entropy of fusion for FeF_2 (8000/1375 = 5.82 eu) is assumed for NiF_2, but a melting point of 1800°K is used, a value of −120.0 kcal/mole is obtained as a reasonable estimate of the free energy of formation of solid NiF_2 at 600°C.

SOLUBILITIES AND ACTIVITY COEFFICIENTS OF NiF₂ AS FUNCTIONS OF SOLVENT COMPOSITION IN NaF-ZrF₄ MIXTURES

C. M. Blood

It has been postulated[17,18] that the activity coefficients of a solute in a fluoride solvent will reach a maximum at the isoelectric point or when the charge-to-distance ratio of the solute's positive ion is equal to the average or effective charge-to-distance (Z/R) ratio of the positive ions of the solvent mixture. As the composition of the solvent is changed and its charge-to-distance ratio is made to differ from that of the solute, negative deviations from ideality become greater. On this basis a tentative acid-base scale for predicting isoelectric points of solutes in $NaF-ZrF_4^*$ melts was prepared.[18] Since not much experimental evidence is available on the effect of solvent composition on solute activity coefficients, the proposed plot is only tentative, since no proven way exists to obtain the effective Z/R of the solvent as a function of composition. In an effort to provide quantitative information, hydrogen-reduction equilibrium quotients of NiF_2 were measured in various $NaF-ZrF_4$ mixtures. Activity coefficients were calculated, but, since no satisfactory value of the free energy of formation of either solid or liquid NiF_2 is available, the data are presented (Table 2.2.1) as the ratio of the activity coefficient of NiF_2 in the solvent indicated to the activity coefficient of NiF_2 in $NaF-ZrF_4$ (53-47 mole %). In addition, the solubility data are given as a function of solvent composition.

[14]M. Blander and F. F. Blankenship, *ANP Quar. Prog. Rep. Sept. 30, 1957*, ORNL-2387, p 121.

[15]C. M. Blood, *ANP Quar. Prog. Rep. June 10, 1956*, ORNL-2106, p 99.

[16]H. A. Friedman, private communication to C. M. Blood.

[17]R. F. Newton and F. F. Blankenship, *ANP Quar. Prog. Rep. March 31, 1957*, ORNL-2274, p 123.

[18]D. G. Hill and F. F. Blankenship, *ANP Quar. Prog. Rep. March 31, 1957*, ORNL-2274, p 126.

Table 2.2.1. Equilibrium Quotients, Activity Coefficient Ratios, and Solubilities of NiF_2 in NaF-ZrF_4 Mixtures at 600°C

Solvent Composition (mole % ZrF_4)	Equilibrium Quotient	Activity Coefficient Ratio*	Solubility (ppm Ni)
	$\times 10^3$		
57	4.6	0.30	450
52	9.2	0.60	540
47	15.3	1.00	980
44	18.5	1.21	1380
40	25.3	1.65	

*Based on activity coefficient of NiF_2 in NaF-ZrF_4 (53-47 mole %).

The experimental measurements of the 40 mole % ZrF_4 mixture have not been completed, and the data given in Table 2.2.1 for this composition may be revised. It is proposed to make measurements on the solvent containing 37 mole % ZrF_4 in an effort to locate the positions of the maximums of the activity coefficient and solubility. The present results indicate that the effective Z/R average of the solvent may correspond closely to that predicted by the proposed acid-base scale.[18] It may also be noted that the value of the activity coefficient of the NiF_2 solute is not dependent on the solubility; this confirms a previous conclusion that the precipitating phase is not NiF_2.

REDUCTION OF UF_4 BY CHROMIUM IN MOLTEN FLUORIDES

J. D. Redman

The possible use of Inconel or stainless steel as a material for containing UF_4-bearing fluoride mixtures raised numerous questions as to the effect of corrosion attack in the temperature range 600 to 800°C. The most active metal present in these alloys is chromium, and consequently any fundamental information relating to the interaction of chromium with UF_4 dissolved in representative fluoride mixtures should be applicable to an understanding of the corrosion of the alloys by the fluoride melts.

A summary of the results of studies of the reduction of UF_4 by chromium in various fluoride reaction mediums is presented here, and data for the reaction of UF_4 with various other metals are given in the next section. Some data are also given for the reaction of UF_4 with Inconel, in which the activity of chromium is much less than unity.

As might be expected, the reaction of UF_4 with chromium is influenced by the reaction medium employed. The reaction which occurs in the ZrF_4- and BeF_2-bearing melts studied may be written as

$$2UF_4 + Cr° \rightleftharpoons 2UF_3 + CrF_2$$
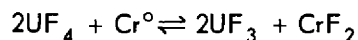
The valency of the chromium compound has been established through numerous experiments, and it has also been demonstrated experimentally that the solubility of the uranium and chromium compounds involved is considerably greater than the concentrations encountered in these studies. The equilibrium quotient, K_x, defined as

$$K_x = \frac{N_{UF_3}^2 \cdot N_{CrF_2}}{N_{UF_4}^2},$$

where N denotes mole fraction, may be evaluated for this system by adding a known concentration of UF_4 to chromium and determining the resulting concentration of Cr^{++}. Side reactions that arise from impurities (H_2O, HF, Fe^{++}, Ni^{++}) must be eliminated or suppressed to such a degree that the chromium blank is small compared with the total chromium measured. The blanks in these studies ranged from 150 to 250 ppm Cr.

A filtration method was used in which the melt was equilibrated under designated conditions and a sample was withdrawn through a sintered-nickel filter and analyzed for chromium. Nickel apparatus was used in most cases, because early experimental work demonstrated that nickel is stable toward UF_4 dissolved in fluoride mixtures. Equilibrium is attained in these systems fairly rapidly, 3 hr being sufficient in virtually all cases, although a longer period of heating was utilized for some studies.

The data given in Table 2.2.2 demonstrate that the equilibrium quotient, K_x, is essentially constant over the range of concentrations of UF_4 and UF_3 studied with NaF-ZrF_4 (50-50 mole %) as the

Table 2.2.2. Equilibrium Quotients for the Reaction $2UF_4(d) + Cr(c) \rightleftharpoons 2UF_3(d) + CrF_2(d)$
in $NaF\text{-}ZrF_4$ (50-50 mole %) at 600 and 800°C

Conditions of Equilibration		Original Concentration (mole %)		Equilibrium Chromium Concentration (ppm)	Equilibrium Quotient,* K_x
Temperature (°C)	Time (hr)	UF_4	UF_3		
					$\times 10^{-4}$
600	3 or 5	4.1		2220 ± 120	3.2 ± 0.8
	5	3.0	0.82	950	4
	5	2.0	1.7	155	3
	5	0.89	2.5	30	5
800	3 or 5	4.1		2550 ± 210	5.9 ± 1.8
	5	3.2	0.92	1120	6
	5	2.2	1.9	320	6
	5	1.3	2.8	60	6
	5	2.0		1450	4

*Standard deviations were obtained from 10 measurements at 600°C and 13 measurements at 800°C. The other values for K_x were obtained from the arithmetic mean of two to four measurements.

reaction medium. As anticipated, the chromium concentrations decrease as the UF_3 concentration increases; this suggests that the extent of attack on chromium or chromium-bearing alloys may be decreased by the addition of UF_3. The reaction has a small positive temperature coefficient; an average heat of reaction of 6 kcal in the temperature range 600 to 800°C is obtained from the values for K_x. Values of 70 and 20 were obtained for the equilibrium constants at 600 and at 800°C, respectively, by using the available values of the free energies of formation for CrF_2, UF_4, and UF_3. The corresponding equilibrium concentrations were 8100 and 7300 ppm. A comparison of these values with those given in Table 2.2.2 indicates that this system behaves in a manner that is far from ideal.

When dealing with melts in the NaF-LiF-KF system, the reaction of UF_4 with Cr° cannot be precisely defined. A mixture of Cr^{++} and Cr^{+++} results, but the ratio of the two ions has not been accurately determined. Equilibrium quotients cannot, therefore, be evaluated, but, rather, the data are presented in terms of total dissolved chromium ($Cr^{++} + Cr^{+++}$). The data obtained with NaF-LiF-KF as the reaction medium are summarized in Table 2.2.3. Again it may be observed that the

Table 2.2.3. Equilibrium Chromium Concentrations for the Reaction of Chromium with UF_4 in NaF-LiF-KF (11.5-46.5-42 mole %) at 600 and at 800°C

Conditions of Equilibration		Original Concentration (mole %)		Equilibrium Concentration*	
Temperature (°C)	Time (hr)	UF_4	UF_3	U (wt %)	Cr (ppm)
600	3	2.30		12.0	1130
	5	2.30		11.7	1050
	5	2.00	0.24	11.0	205
	12	2.00	0.24	11.4	250
800	3	2.30		11.2	2650
	5	2.30		11.5	2750
	5	2.00	0.24	11.1	1890
	12	2.00	0.24	10.8	1750
	5	1.10	1.20	10.2	140
	5	0.70	1.60	10.8	40

*Arithmetic mean of two to six measurements.

chromium concentrations decrease as the UF_3 concentration increases. The large difference in chromium concentrations at 600 and at 800°C indicates that the heat of reaction in this medium is much greater than that calculated for the reaction in $NaF-ZrF_4$ and suggests that the mass transfer of chromium is more severe in the former case.

The chromium concentrations for equilibrium with Inconel can be calculated by using an activity value of 0.1 for chromium in the alloy and the chromium concentration values given in Table 2.2.2. The values thus obtained are 1050 and 1150 ppm at 600 and at 800°C, respectively, in the reaction medium $NaF-ZrF_4-UF_4$. These concentrations are much lower than that given for equilibrium with pure chromium at 600°C and indicate that it should not be possible to deposit chromium at 600°C when $NaF-ZrF_4-UF_4$ melts of this general composition are circulated in Inconel loops with hot- and cold-leg temperatures of 600 and 800°C, respectively. Mass transfer of chromium would occur in loops of pure chromium under these conditions, and would occur in an Inconel loop if the deposited chromium were able to diffuse rapidly enough into the cold-zone material.

Similarly the data given in Table 2.2.3 may be used to calculate the equilibrium chromium concentration in the $NaF-LiF-KF-UF_4$ melt at 800°C when Inconel is the container material. Values of 1250 and 1500 ppm were obtained based on Cr^{++} and Cr^{+++}, respectively, and the equilibrium concentration is probably intermediate between the two values. Since these concentrations are greater than the value of 1100 ppm found for equilibrium with pure chromium at 600°C, Inconel in contact with the $NaF-LiF-KF-UF_4$ melt will support a higher concentration of $Cr^{++} + Cr^{+++}$ in equilibrium at 800°C than pure chromium can support at 600°C. Thus chromium would be removed from Inconel in the hot zone and deposited as essentially pure chromium in the cold zone. Since no diffusion process is required in the cold zone, the rate of attack in the hot zone would be controlled by the rate of diffusion of chromium to the metal-salt interface. The chromium concentrations that result when Inconel is contacted with UF_4 dissolved in either the $NaF-ZrF_4$ or $NaF-LiF-KF$ mixture are given in Table 2.2.4.

It may be noted that the chromium concentrations given in Table 2.2.4 are, in general, lower than

Table 2.2.4. Chromium Concentrations Resulting from the Reaction of Inconel with UF_4 in Molten Fluorides

Reaction Medium	Conditions of Equilibration		Original Concentrations (mole %)		Final Chromium Concentration (ppm)
	Temperature (°C)	Time (hr)	UF_4	UF_3	
$NaF-ZrF_4$ (50-50 mole %)	600	12	4.1		135
		5	3.1	1.0	35
	800	3	4.1		360
		5	4.1		610
		12	4.1		840
		5	3.1	1.0	210
$NaF-LiF-KF$ (11.5-46.5-42 mole %)	600	5	2.3		350
		12	2.3		310
		5	2.0	0.24	30
		12	2.0	0.24	30
	800	5	2.3		680
		12	2.3		900
		24	2.3		820
		5	2.0	0.24	480
		12	2.0	0.24	700

those for reaction with pure chromium. If 700 ppm is taken for the chromium concentration in the $NaF-ZrF_4-UF_4$ melt at 800°C and 0.1 is taken for the activity of chromium in Inconel, a value of 5×10^{-5} may be calculated for K_x. This value is about an order of magnitude less than that given in Table 2.2.2 for the equilibrium quotient obtained for pure chromium. The discrepancy undoubtedly results from an apparent equilibrium state in which the Inconel surface is depleted in chromium because of the relatively slow diffusion of chromium to the surface.

Values for the equilibrium quotients for the reaction of UF_4 with chromium at 600 and at 800°C in various reaction mediums are presented in Table 2.2.5. An examination of the data for the alkali fluoride–ZrF_4 binary mixtures containing approximately 52 mole % of alkali fluoride shows a decrease in K_x upon changing from lithium to rubidium. This behavior is attributed to the change in the cation charge-to-separation ratio, Z/R, and the resulting decrease in fluoride activity upon going from LiF to RbF while keeping a constant mole percentage of alkali fluoride. A similar effect is noted when the NaF content in the $NaF-ZrF_4$ binary is increased from 50 to 59 mole %. The results are also shown in Fig. 2.2.1, where K_x is plotted against either the cation radius or the mole percentage of NaF. The change in K_x with temperature, which is a measure of the heat of reaction, is probably a good index for the mass transfer of chromium. Thus, in considering the effect of the solvent for UF_4 on the corrosion of chromium-bearing alloys, the change in K_x must be considered, as well as the equilibrium chromium concentrations. In addition to the various fluoride

Table 2.2.5. Equilibrium Quotients for the Reaction $2UF_4(d) + Cr(c) \rightleftharpoons 2UF_3(d) + CrF_2(d)$ in Molten Fluorides

Reaction Medium	Temperature (°C)	Initial UF_4 Concentration (mole %)	Equilibrium Chromium Concentration (ppm)	K_x
LiF-ZrF$_4$ (52-48 mole %)	600	4.0	2930 ± 170	$(7.5 \pm 2.0) \times 10^{-4}$
	800	4.0	3860 ± 140	$(2.4 \pm 0.4) \times 10^{-3}$
NaF-ZrF$_4$ (53-47 mole %)	600	4.0	1730 ± 30	$(1.3 \pm 0.1) \times 10^{-4}$
	800	4.0	2160 ± 20	$(2.9 \pm 0.1) \times 10^{-4}$
KF-ZrF$_4$ (52-48 mole %)	600	4.0	1080 ± 70	$(2.4 \pm 0.5) \times 10^{-5}$
	800	4.0	1160 ± 60	$(3.2 \pm 0.7) \times 10^{-5}$
RbF-ZrF$_4$ (52-48 mole %)	600	4.0	690 ± 30	$(1.0 \pm 0.2) \times 10^{-5}$
	800	4.0	760 ± 40	$(1.5 \pm 0.4) \times 10^{-5}$
NaF-ZrF$_4$ (50-50 mole %)	600	4.1	2220 ± 120	$(3.2 \pm 0.8) \times 10^{-4}$
	800	4.1	2550 ± 210	$(5.9 \pm 1.8) \times 10^{-4}$
NaF-ZrF$_4$ (59-41 mole %)	600	3.7	1020 ± 40	$(1.5 \pm 0.2) \times 10^{-5}$
	800	3.7	1050 ± 110	$(1.7 \pm 0.7) \times 10^{-5}$
LiF-NaF-ZrF$_4$ (55-22-23 mole %)	600	2.5	540 ± 90	$(1.0 \pm 0.7) \times 10^{-6}$
	800	2.5	750 ± 60	$(3.8 \pm 1.1) \times 10^{-6}$
LiF-BeF$_2$ (48-52 mole %)	550	1.5	920	(2×10^{-6})
	650	1.5	1300 ± 220	(9×10^{-6})
	800	1.5	2060 ± 210	(7×10^{-5})
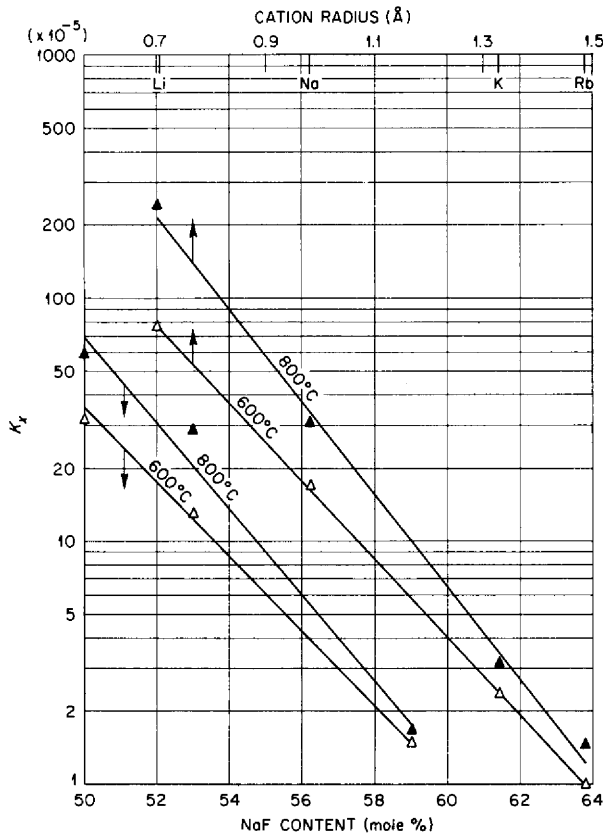
Fig. 2.2.1. Effect of Cation Radius and NaF Content of the NaF-ZrF$_4$ Reaction Medium on the Equilibrium Quotient for the Reaction of UF$_4$ with Chromium at 600 and at 800°C. (Secret with caption)

mixtures listed in Table 2.2.5, other solvents, namely, LiF-BeF$_2$-ThF$_4$ (67-23-10 mole %) and LiF-ThF$_4$ (72-28 mole %), have been studied with UF$_4$ concentrations in the range 0.1 to 0.2 mole %. The extent of reaction with chromium at these low UF$_4$ concentrations is so limited, however, that no measurable difference was found between the chromium blanks and the chromium concentrations resulting from the reaction of UF$_4$ with chromium.

REACTION OF UF$_4$ WITH VARIOUS STRUCTURAL METALS IN MOLTEN FLUORIDES

J. D. Redman

The compatibility of UF$_4$ dissolved in various fluoride mixtures with various metals having desirable structural properties, either as the metal or in alloy form, is of considerable importance in the study of molten fluoride fuels for reactors. Many of the available alloys have either a nickel or an iron base, with chromium added to impart oxidation resistance and high-temperature strength. Such alloys include Inconel and the stainless steels. Nickel is stable toward UF$_4$ dissolved in the fluoride mixtures of interest and consequently is a suitable base for alloys. Data are presented here which demonstrate that even though iron reacts with UF$_4$ the extent of the reaction is sufficiently limited that iron might also serve as a suitable base for the structural material. Data given in the previous section, in comparison with the data presented here, show conclusively that chromium is more reactive with UF$_4$ than is iron and indicate that the chromium present in Inconel and the stainless steels is the element most likely to react with UF$_4$ and therefore to play the important role in the corrosion of these alloys by UF$_4$-bearing fluoride mixtures. The possibility of replacing chromium in alloys by other elements, such as molybdenum, niobium, tantalum, vanadium, and tungsten, led to a study of the compatibility of these materials with UF$_4$ dissolved in either alkali fluoride mixtures or alkali fluoride—ZrF$_4$ mixtures.

A filtration method was employed in which the UF$_4$-bearing fluoride mixture was equilibrated in nickel equipment with the metal under study and a sample was removed through a sintered-nickel filter and analyzed for the desired metal. In the case of iron in ZrF$_4$-bearing melts the reaction is believed to proceed as

$$2UF_4 + Fe° \rightleftharpoons 2UF_3 + FeF_2$$
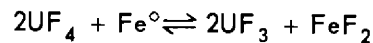
and equilibrium quotients may be evaluated from the expression

$$K_x = \frac{N^2_{UF_3} \cdot N_{FeF_2}}{N^2_{UF_4}} \, .$$

The valence states of the oxidation products of the metals other than iron have not been established, and consequently only the equilibrium metal concentrations are given.

The data presented in Table 2.2.6 show a remarkable insensitivity of iron concentration to changes in the composition of the reaction medium. It may be noted that the reaction exhibits a negative

Table 2.2.6. Data for the Reduction of UF_4 by Iron in
Molten Fluorides at 600 and at 800°C

Reaction Medium	Temperature (°C)	Fe (ppm)	K_x
LiF-ZrF$_4$ (52-48 mole %)	600	500	1.4×10^{-6}
	800	370	5×10^{-7}
NaF-ZrF$_4$ (53-47 mole %)	600	490	2×10^{-6}
	800	380	6×10^{-7}
KF-ZrF$_4$ (52-48 mole %)	600	540	3×10^{-6}
	800	320	6×10^{-7}
RbF-ZrF$_4$ (52-48 mole %)	600	490	4×10^{-6}
	800	140	5×10^{-8}
NaF-ZrF$_4$ (50-50 mole %)	600	450	1×10^{-6}
	800	310	3×10^{-7}
NaF-ZrF$_4$ (59-41 mole %)	600	530	1.5×10^{-6}
	800	450	8×10^{-7}
LiF-NaF-ZrF$_4$ (55-22-23 mole %)	600	420	6×10^{-7}
	800	625	2×10^{-6}
NaF-LiF-KF (11.5-46.5-42 mole %)	600	690	
	800	480	

temperature coefficient in all mediums except the LiF-NaF-ZrF$_4$ mixture. The results given for the LiF-NaF-KF mixture, a composition quite different from the alkali fluoride–ZrF$_4$ mixtures, indicate a negative temperature coefficient and equilibrium iron concentrations very similar to those found in the ZrF$_4$-bearing melts. In contrast to these results for iron, the behavior of chromium, as described above, follows the expected pattern in the alkali fluoride–ZrF$_4$ melts.

An examination of the data presented for various metals in Tables 2.2.7 through 2.2.11 reveals some interesting differences in the behavior of the individual metals and the effects of different reaction mediums. The only metal that shows any real stability in an NaF-LiF-KF-UF$_4$ melt is molybdenum, which undergoes rather limited attack. The attack on molybdenum by an NaF-ZrF$_4$-UF$_4$ melt is less than that of the alkali fluoride mixture,

as is, in general, the case for most of the metals studied. Niobium is not stable in the NaF-LiF-KF-UF$_4$ melt, but it is unattacked by either the NaF-ZrF$_4$-UF$_4$ or LiF-NaF-ZrF$_4$-UF$_4$ melt. Tantalum, which would be expected to behave similarly to niobium, is not stable in either type of melt. Vanadium, likewise, is not stable in any of the melts used, whereas tungsten is stable in the NaF-ZrF$_4$-UF$_4$ melt but not in the NaF-LiF-KF-UF$_4$ melt. In general, the extent of attack on the metals increases with a temperature increase from 600 to 800°C.

It is evident that only molybdenum exhibits any stability toward UF$_4$ in the NaF-LiF-KF mixture, and accordingly nickel-molybdenum alloys would be expected to resist corrosion by this type of melt. In the ZrF$_4$-based melts, molybdenum, niobium, and tungsten appear to be stable toward UF$_4$, and thus these metals or their alloys might serve as suitable container materials for this type of melt. Tantalum and vanadium appear to offer no advantage over chromium for either type of melt.

REDUCTION OF FeF$_2$ BY CHROMIUM IN MOLTEN FLUORIDES

J. D. Redman

A study has been made of the reaction

$$FeF_2 + Cr° \rightleftharpoons Fe° + CrF_2$$
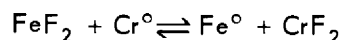
in an attempt to evaluate the equilibrium quotient

$$K_x = \frac{N_{CrF_2}}{N_{FeF_2}}$$

at 600°C in the following reaction mediums: NaF-ZrF$_4$ (53-47 mole %), KF-ZrF$_4$ (52-48 mole %), and RbF-ZrF$_4$ (52-48 mole %). Although it was known that the equilibrium quotient for this reaction was much greater than 1, it was believed that the equilibrium concentrations of Cr^{++} and Fe^{++} might be determined sufficiently accurately by the filtration method to permit an evaluation of the ratio.

If the system behaves ideally, a value of approximately 6×10^3 for K_a is obtained from the standard free energies of formation for CrF$_2$ and FeF$_2$ at 600°C, and thus essentially complete reduction of Fe^{++} by the chromium is indicated. A calculation of the Cr^{++}-to-Fe^{++} ratio from values found for K_x

Table 2.2.7. Data for the Reaction of UF_4 with Molybdenum in Molten Fluorides at 600 and at 800°C

| Reaction Medium | Conditions of Equilibration | | Found in Filtrate | | |
	Temperature (°C)	Time (hr)	Total U (wt %)	Total Mo* (ppm)	Total Ni (ppm)
NaF-ZrF$_4$ (50-50 mole %)	600	3	8.4	7	155
		3	8.6	7	135
		5	8.5	7	230
		5	8.6	9	215
	800	3	8.5	8	90
		3	8.4	8	85
		5	8.5	9	30
		5	8.6	11	85
		5	8.6	9	80
		5	8.6	9	10
NaF-LiF-KF (11.5-46.5-42 mole %)	600	3	13.3	210	85
		5	14.6	200	110
		5	11.8	325	170
	800	3	13.5	130	170
		3	13.9	105	85
		5	14.4	55	205
		5	13.9	65	145

*Blanks of 20 ppm were present at 800°C in both reaction mediums and have been subtracted from the amount found in the filtrate.

for the reaction

$$M^\circ + 2UF_4 \rightleftharpoons 2UF_3 + MF_2$$
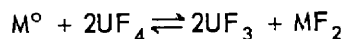
where M° is iron or chromium, in the NaF-ZrF$_4$ mixture at 600°C yielded a value of ~60, however, which suggests that the behavior is far from ideal. The corresponding values in the KF-ZrF$_4$ and RbF-ZrF$_4$ mixtures are ~10 and ~3, respectively. These values for the Cr^{++}-to-Fe^{++} ratios, if correct, should be determinable by the filtration method.

The data given in Table 2.2.12 were obtained from filtration runs in nickel equipment. In most cases the equilibration time was 5 hr. Several runs, with an equilibration period of 12 hr gave similar values and demonstrated that equilibrium was

attained within 5 hr. A comparison of the experimentally determined chromium values with the theoretical values shows that, in the case of the NaF-ZrF$_4$ and KF-ZrF$_4$ mixtures, the reaction occurs as indicated and yields a good balance between the Fe^{++} added and the Cr^{++} found, except at the higher concentrations. The abnormal behavior at the higher concentrations will be discussed below. In the data for the runs with RbF-ZrF$_4$ as the reaction medium, it may be noted that the calculated chromium values are about 10 to 20% lower than the experimentally determined values, in most cases. No experimental error could be found to explain this discrepancy, and, although there is no evidence that the valence of the iron and chromium is not 2, some abnormal behavior must occur.

Table 2.2.8. Data for the Reaction of UF_4 with Niobium in Molten Fluorides at 600 and at 800°C

Reaction Medium	Conditions of Equilibration		Found in Filtrate		
	Temperature (°C)	Time (hr)	Total U (wt %)	Total Nb* (ppm)	Total Ni (ppm)
NaF-ZrF₄ (50-50 mole %)	600	3	8.2	25	55
		3	7.9	20	60
		5	8.9	25	55
		5	8.7	25	80
	800	3	8.8	20	40
		3	8.8	20	70
		5	8.8	20	80
		5	8.6	20	85
LiF-NaF-ZrF₄ (55-22-23 mole %)	600	3	8.2	1	100
		3	8.8	1	120
		5	8.4	2	120
		5	8.9	1	45
	800	3	8.5	1	110
		3	8.6	1	110
		5	8.9	5	15
		5	8.3	4	40
NaF-LiF-KF (11.5-46.5-42 mole %)	600	3	11.2	675	20
		3	11.3	725	65
		5	11.1	655	1
		5	11.2	640	6
	800	3	10.8	1090	35
		3	10.5	1200	15
		5	11.1	1540	6
		5	11.2	1580	40
		12	11.0	1830	
		12	10.9	1470	
		12	11.0	1930	
		12	11.1	1310	
		12	11.4	1230	
		12	12.0	1360	

*Blanks present at 800°C for the various mediums were: for NaF-ZrF₄, 15 ppm; for LiF-NaF-ZrF₄, 15 ppm; for NaF-LiF-KF, 315 ppm.

Table 2.2.9. Data for the Reaction of UF_4 with Tantalum in Molten Fluorides at 600 and at 800°C

Reaction Medium	Conditions of Equilibration		Found in Filtrate		
	Temperature (°C)	Time (hr)	Total U (wt %)	Total Ta* (ppm)	Total Ni (ppm)
NaF-ZrF$_4$ (53-47 mole %)	600	5	9.4	1710	175
		5	9.4	1630	145
	800	5	9.0	2420	315
		5	9.2	2820	270
NaF-LiF-KF (11.5-46.5-42 mole %)	600	3	11.2	1320	140
		3	11.6	1220	90
		5	12.1	1150	110
		5	11.8	1150	240
	800	3	11.2	3220	170
		5	11.9	2800	80
		5	11.8	3020	180

*Blank of 130 ppm present at 800°C in the NaF-ZrF$_4$ mixture; 650 ppm present in the NaF-LiF-KF mixture at 800°C.

The reduction of Fe^{++} was essentially complete in all cases, except at the higher FeF_2 additions in the NaF-ZrF$_4$ mixture. In fact the Fe^{++} concentrations are so low that the ratio of Cr^{++} to Fe^{++} cannot be evaluated in any of the reaction mediums. A value of ~60 was calculated, as stated above, for the ratio in the NaF-ZrF$_4$ mixture, and the experimental data do not deny that it may be this large. However, for the KF-ZrF$_4$ and RbF-ZrF$_4$ mixtures, it is evident that the experimentally determined ratios, while not constant, are considerably greater than the calculated ratios of ~10 and ~3. This lack of agreement must be attributed to some uncertainty in the K_x values found for the iron and chromium reactions with UF_4.

The limited solubility of CrF_2 in the NaF-ZrF$_4$ mixture precludes the addition of large amounts of FeF_2, and thus the concentration range is rather limited. It will be noted that for runs made at 600°C with either 1 or 2% additions of Fe^{++} the results are not precise and very incomplete reduction of Fe^{++} occurred. This behavior probably results from the presence of solid phases containing NaF, ZrF_4, CrF_2, and/or FeF_2. The solid phase contains more ZrF_4 than NaF, and consequently the liquid phase is enriched with respect to NaF. The lack of precision indicates that equilibrium was not attained in these runs. It is of interest to compare these runs with similar runs made at 700°C in which the solubility of the CrF_2-bearing compound was not exceeded. Here essentially complete reduction of Fe^{++} occurred, and a stoichiometric relationship prevailed between the Fe^{++} added and the Cr^{++} found. It is apparent that the method employed is incapable of establishing the Cr^{++}-to-Fe^{++} ratio in these reaction mediums at 600°C.

Table 2.2.10. Data for the Reaction of UF_4 with Vanadium in Molten Fluorides at 600 and at 800°C

Reaction Medium	Conditions of Equilibration		Found in Filtrate		
	Temperature (°C)	Time (hr)	Total U (wt %)	Total V* (ppm)	Total Ni (ppm)
NaF-ZrF$_4$ (53-47 mole %)	600	3	7.4	460	120
		3	8.1	500	25
		5	8.8	420	25
		5	10.3	390	35
	800	3	8.3	2200	70
		3	8.3	2150	30
		5	8.3	1850	30
		5	8.3	1600	70
NaF-LiF-KF (11.5-46.5-42 mole %)	600	3	11.4	550	25
		3	11.4	750	45
		5	11.8	700	50
	800	3	11.0	1450	25
		3	10.6	1350	20
		8	12.0	1800	50
		8	11.9	1900	5

*Blank of 180 ppm present at 800°C in the NaF-ZrF$_4$ mixture; 150 ppm present in the NaF-LiF-KF mixture at 800°C.

THERMODYNAMIC INTERPRETATION OF EQUILIBRIUM DATA ON THE CORROSION OF IRON AND OF CHROMIUM BY MOLTEN-SALT FUELS

M. Blander

Considerable attention has been given to the corrosion and metal deposition caused by the temperature coefficient of the equilibrium[19]

$$(1) \qquad 2UF_4 + M \rightleftharpoons 2UF_3 + MF_2$$
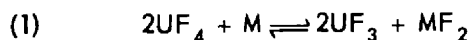
when molten-salt mixtures are used as the reaction mediums. The equilibrium constant for the reaction is

$$K_a = \frac{a_{MF_2} \, a_{UF_3}}{a_{UF_4}^2 \, a_M} ,$$

where a is the activity of the designated material, the salts are dissolved in the fuel melt, and the metal is in the container wall. Some of the differences in the behavior of structural metals are very important from the standpoint of compatibility between fuel and container. The effect of temperature,[20] for a steady-state concentration of UF_4, UF_3, and MF_2 in the melt, can be represented as

$$(2) \qquad RT^2 \, \frac{d \ln X_M}{dT} = -(\Delta H^\circ + \Delta H_s)$$

$$= -RT^2 \, \frac{d \ln K_x}{dT} ,$$

[19] W. R. Grimes, *ANP Quar. Prog. Rep. June 10, 1956*, ORNL-2106, p 96.

[20] This discussion covers only the tendency toward mass transfer. The rate is governed by this tendency, or driving force, and by a resistance to this force which is a function mainly of the diffusion coefficient of the metal in question through the container alloy being considered.

Table 2.2.11. Data for the Reaction of UF_4 with Tungsten in Molten Fluorides at 600 and at 800°C

Reaction Medium	Conditions of Equilibration		Found in Filtrate		
	Temperature (°C)	Time (hr)	Total U (wt %)	Total W* (ppm)	Total Ni (ppm)
NaF-LiF-KF (11.5-46.5-42 mole %)	600	3	11.2	950	215
		3	11.2	920	435
		5	11.6	1410	250
		5	11.2	1350	230
		5	10.5	900	
		5	11.0	1120	
	800	3	11.3	980	260
		3	11.2	920	205
		5	11.2	1480	65
		5	10.8	2150	250
		5	11.8	1260	165
		5	11.6	1210	
		5	11.8	1600	
		12	10.5	1880	115
		12	11.8	1400	
		12	11.3	1430	
NaF-ZrF$_4$ (53-47 mole %)	600	3	9.2	70	110
		5	9.0	95	45
		5	9.1	70	30
	800	3	9.2	130	40
		3	9.3	100	50
		5	8.5	95	50
		5	8.9	100	20

*Blank of 350 ppm present at 800°C in NaF-LiF-KF; <5 ppm present in NaF-ZrF$_4$.

where X_M is the equilibrium concentration of metal M in the wall, $\Delta H°$ is the heat of change of the reactants in the equilibrium reaction (Eq. 1) from their standard state (chosen here as the pure liquids for the salts and pure solid for the metal), ΔH_s is the difference between the heats of solution of the reactants and products, and K_x is the equilibrium quotient:

$$K_x = \frac{N^2_{UF_3} N_{MF_2}}{N^2_{UF_4} N_M} ,$$

where N is the mole fraction of the designated material. If $\Delta H° + \Delta H_s$ is positive the metal M will tend to transfer from the hot to the cold end of

Table 2.2.12. Data for the Reaction $FeF_2 + Cr^\circ \rightleftharpoons Fe^\circ + CrF_2$ in Molten Fluorides

Reaction Medium	Temperature (°C)	FeF$_2$ Added (ppm of Fe)	Present in Filtrate			Calculated Cr* (ppm)
			Ni (ppm)	Fe (ppm)	Cr (ppm)	
NaF-ZrF$_4$ (53-47 mole %)	600	0	55	70	165	
		0	35	60	165	
		0	85	65	155	
		0	85	65	160	
		870	60	85	960	970
		915	70	55	1,010	1,010
		970	90	50	980	1,060
		885	110	55	880	980
		2,000	110	50	2,000	2,020
		2,100	110	45	2,130	2,120
		2,000	195	75	1,960	2,020
		2,050	65	50	1,690	2,070
		4,020	20	140	4,100	3,910
		4,050	70	120	3,730	3,940
		4,100	55	150	4,170	3,980
		3,940	30	160	4,160	3,840
		6,220	20	195	5,740	5,960
		6,240	35	160	4,360	5,980
		6,150	30	125	6,380	5,900
		6,150	25	115	5,940	5,900
		10,000	50	1,320	4,460	9,400
		10,000	55	1,500	2,700	9,400
		10,000	90	2,010	2,210	9,400
		10,000	60	1,670	2,560	9,400
		20,000	55	2,140	4,620	18,700
		20,000	70	3,280	1,290	18,700
	700	6,000	40	15	5,840	5,740
		6,000	35	15	5,660	5,740
		10,000	40	20	7,700	9,400
		10,000	40	25	9,500	9,400
		20,000	75	70	18,400	18,700
		20,000	110	80	18,400	18,700

Table 2.2.12 (continued)

Reaction Medium	Temperature ($^\circ$C)	FeF$_2$ Added (ppm of Fe)	Present in Filtrate			Calculated Cr* (ppm)
			Ni (ppm)	Fe (ppm)	Cr (ppm)	
KF-ZrF$_4$ (52-48 mole %)	600	0	90	4	420	
		0	60	15	200	
		0	60	8	395	
		0	85	5	220	
		2,330	75	115	2,770	2,470
		2,330	40	120	2,170	2,470
		2,270	30	150	2,180	2,410
		6,540	45	150	6,240	6,390
		6,560	30	310	6,230	6,410
		20,000	55	35	18,400	18,700
		20,000	80	140	18,400	18,700
RbF-ZrF$_4$ (52-48 mole %)	600	0	30	90	315	
		0	40	100	215	
		0	40	85	235	
		0	35	100	280	
		990	55	100	1,300	1,180
		840	20	95	1,080	1,040
		890	20	90	1,050	1,090
		850	35	95	1,120	1,050
		1,920	110	135	2,330	2,050
		1,860	35	95	2,300	1,970
		1,900	20	90	2,360	2,030
		1,950	30	105	2,400	2,070
		4,050	35	145	4,620	4,030
		3,890	35	85	4,610	3,870
		3,900	25	90	4,670	3,880
		3,970	30	100	4,880	3,960
		6,030	50	105	7,360	5,880
		6,100	80	140	7,100	5,940
		6,100	75	95	7,320	5,940
		6,050	30	90	7,610	5,890

*Complete reduction of FeF$_2$ assumed.

the system and, if negative, from the cold end to the hot end. The most desirable condition would be for $\Delta H^{\circ} + \Delta H_s$ to be zero so that there would be no mass transfer by the proposed mechanism.

If the pure liquids involved in the reaction are chosen as the standard state, the values of ΔH° tabulated below can be obtained by using the heat content values listed in Table 2.2.13:

M	ΔH°
Cr	+9
Fe	+22
Ni	+33

Since all these values of ΔH° are positive, there would be a tendency for mass transfer to take place from the hot to the cold end of the system if the ΔH° term is not compensated for by the term ΔH_s, which involves all the heats of solution.

The term ΔH_s is given by

$$(3) \quad \Delta H_s = 2(\bar{H}_{UF_3} - H^{\circ}_{UF_3}) + (\bar{H}_{MF_2} - H^{\circ}_{MF_2}) -$$
$$- 2(\bar{H}_{UF_4} - H^{\circ}_{UF_4}) - (\bar{H}_M - H^{\circ}_M) ,$$

where H is the partial molal heat content of the material in solution and H° is the molal heat content of the pure substance. For a pure metal the last term in Eq. 3 is zero. The other terms in this expression are unknown, but if data are available

Table 2.2.13. Heat Content Data* for Reactants of the Reaction $2UF_4 + M \rightleftharpoons 2UF_3 + MF_2$

Compound	Heat of Formation, ΔH_{298} (kcal)	Heat of Fusion, ΔH_f (kcal)
UF_4	−443	5.7
UF_3	−357	8.5
CrF_2	−181	(12)**
NiF_2	−159.5	(12)**
FeF_2	−168	(12)**

*From *Selected Values of Chemical Thermodynamic Properties*, NBS Circular 500.

**Estimated by using a method discussed by Blander and Blankenship in a previous report, *ANP Quar. Prog. Rep. Sept. 30, 1957*, ORNL-2387, p 121.

they can be obtained from the equation

$$(4) \quad \left[\frac{d \ln \gamma}{d (1/T)}\right]_N = +\frac{\bar{H} - H^{\circ}}{R} ,$$

where γ is the activity coefficient based on pure liquid as the standard state and the subscript N denotes that the mole fractions are held constant. A comparison can be made of the behavior of two different pure metals, such as Cr and Fe, in any given melt composition that is relatively dilute in CrF_2 or FeF_2. Since the values for the heats of solution of UF_3 are the same for a melt dilute in CrF_2 as for a melt dilute in FeF_2, and similarly for UF_4, it follows from Eq. 2 that

$$(5) \quad RT^2 \frac{d \ln (N_{Cr}/N_{Fe})}{dT} = -\Delta H^{\circ}_{CrF_2} +$$
$$+ \Delta H^{\circ}_{FeF_2} - (\bar{H} - H^{\circ})_{CrF_2} + (\bar{H} - H^{\circ})_{FeF_2}$$
$$= \frac{RT^2 \, d \ln [K_x(Fe)/K_x(Cr)]}{dT} .$$

The values of K_x for chromium and for iron in NaF-ZrF$_4$ (53-47 mole %) at 600 and at 800°C (ref 21) are given in Table 2.2.14.

From the similarity of the compounds CrF_2 and FeF_2 it would be expected that their solution behaviors would not differ greatly and that any difference would be governed mainly by the difference of their ΔH° values. As may be seen in Table 2.2.14, these suppositions are not valid. It must be concluded either that some of the data are

21J. D. Redman, *ANP Quar. Prog. Rep. June 30, 1957*, ORNL-2340, p 135.

Table 2.2.14. Equilibrium Quotients and Heat Changes Derived from Temperature Coefficients for Chromium and Iron in NaF-ZrF$_4$ (53-47 Mole %)

	Chromium	Iron
K_x		
At 600°C	1.3×10^{-4}	2×10^{-6}
At 800°C	2.9×10^{-4}	6×10^{-7}
$\Delta H^{\circ} + \Delta H_s$	7.5 kcal	−11.3 kcal
ΔH°	9 kcal	22 kcal

incorrect or that CrF_2 and FeF_2 have entirely different solution behavior.

Speculations as to the source of the discrepancy may be made on the basis of available data and some reasonable estimates for the heats of solution. From data on the activity coefficients of FeF_2 (ref 22) based on the solid as the standard state and the estimate of the heat of fusion of FeF_2 given in Table 2.2.13, the heat of solution of FeF_2 was found to be −4 kcal/mole. Since the heat of solution of UF_4 is probably similar to that of ZrF_4 (ref 23) in the fuel melt, it is assumed to be between 2.0 and 4.3 kcal/mole. Similarly, it is likely that the heat of solution of UF_3 in the fuel melt lies in the range ±5 kcal. If these heats of solution are combined with the values of ΔH given in Table 2.2.13, a range of values for ($\Delta H° + \Delta H_s$) of +15 to +27 kcal/mole is obtained for the FeF_2 equilibrium; the apparent value of −11 kcal/mole given in Table 2.2.14 seems to be improbable. It may be considered therefore that the measured temperature coefficient of the iron equilibrium reaction appears to be unreasonable. The probable range for ($\Delta H° + \Delta H_s$) for the CrF_2 equilibrium is +2 to +14 kcal/mole. Within the broad limits of the method of estimation used here the temperature coefficient of K_x for the chromium equilibrium is not unreasonable.

SOLUBILITIES OF NOBLE GASES IN MOLTEN FLUORIDE MIXTURES

N. V. Smith

The solubilities of noble gases in molten salts have been investigated because such gases are produced in fused-salt-fueled reactors. Xenon gas is an important reactor poison, and the ease of its removal from the reactor core depends primarily on its absolute solubility in the particular fused salt mixture used as the fuel. A knowledge of the temperature dependence of the solubility was needed in order to predict in what portion of the reactor system the gas would have the greatest tendency to come out of solution.

Helium and argon gases are used as protective blankets and for sparging during reactor operations, and therefore their solubilities in fuel mixtures were also studied. It was conceivable that a portion of the reactor fuel could become saturated with these gases in one section of a reactor and supersaturated in another and that bubble formation could result. This condition could lead to undesirable perturbations in reactivity. The solubilities of helium and of argon were determined as functions of pressure and temperature.

Because of the chemical simplicity of the noble gases, the solubility relationships of these gases in molten salts may be correlated with some fundamental aspects of liquid structure and chemical composition. The variations of the solubilities, the heats and entropies of solution, and the other properties with the atomic size of the gas may perhaps be sufficiently meaningful to reveal some of the characteristics of the potential-energy functions that govern the behavior of the ionic and molecular species in the liquid.

A summary of the results obtained thus far[24-26] in the determination of the solubilities of various noble gases in a number of different solvents is presented in Table 2.2.15. In all the cases investigated, Henry's law was found to apply. In addition, the solubilities were found to increase with increasing temperature. For the same solvent, the solubilities of the gases decreased with increasing solute gas size. Variations in solvents showed corresponding gas solubilities to be approximately the same in the two related ZrF_4-bearing solvents, but the solubility of helium in NaF-KF-LiF was found to be less than half that in the ZrF_4-bearing solvents.

The heats and entropies of solution of the four gases studied in the NaF-ZrF_4 (53-47 mole %) mixture are summarized below:

Gas	ΔH (kcal/mole)	ΔS (eu)
Helium	6.2	−1.3
Neon	7.8	−0.4
Argon	8.2	−1.6
Xenon	11.1	−0.7

[22]C. M. Blood and G. M. Watson, *ANP Quar. Prog. Rep. March 10, 1956,* ORNL-2061, p 84.

[23]S. Cantor, *ANP Quar. Prog. Rep. June 10, 1956,* ORNL-2106, p 111.

[24]N. V. Smith, *ANP Quar. Prog. Rep. June 30, 1957,* ORNL-2340, p 140.

[25]N. V. Smith, *ANP Quar. Prog. Rep. March 31, 1957,* ORNL-2274, p 111.

[26]N. V. Smith, *ANP Quar. Prog. Rep. Dec. 31, 1956,* ORNL-2221, p 130.

Table 2.2.15. Henry's Law Constants for Various Noble Gases in Molten Fluoride Solvents

Solvent	Gas	K^*		
		At 600°C	At 700°C	At 800°C
		$\times 10^{-8}$	$\times 10^{-8}$	$\times 10^{-8}$
NaF-ZrF$_4$ (53-47 mole %)	Helium	21.6	29.2	42.0
	Neon	11.3	18.4	24.7
	Argon	5.06	8.07	12.0
	Xenon	1.9	3.6	6.3
NaF-ZrF$_4$-UF$_4$ (50-46-4 mole %)	Helium	20	27	41
	Xenon	2.0	4.0	6.5
NaF-KF-LiF (11.5-42-46.5 mole %)	Helium	11.3		

$^*K = c/p$ in moles of gas per cubic centimeter of melt per atmosphere.

It may be observed that the heat of solution increases with increasing atomic size of the gas. Also it is worth noting that the entropy of solution corrected to equal concentrations is negative and in all cases quite small. Because of the uncertainties of the measurements, the heats of solution are considered to be reliable only to ±1 kcal/mole and the entropy changes are reliable only to ±1 eu. Accordingly it appears that the trend in the heats of solution is real but that no particular significance should be attached to the different values of the entropy change, since as far as the experimental measurements are concerned the values listed for the entropy change are not significantly different.

SOLUBILITY OF HF IN NaF-ZrF$_4$

J. H. Shaffer

The solubility of HF in mixtures in the NaF-ZrF$_4$ system has been successfully determined as a function of temperature, pressure, and melt composition. A summary of the recent experimental results and those obtained previously[27,28] is presented in Table 2.2.16.

It may be noted that the solubility of HF, in all cases, decreases with increasing temperature.

Furthermore, as shown in Fig. 2.2.2, the Henry's law constants for the HF solubility illustrate a constant heat of solution over the experimental temperature range for each melt composition. The

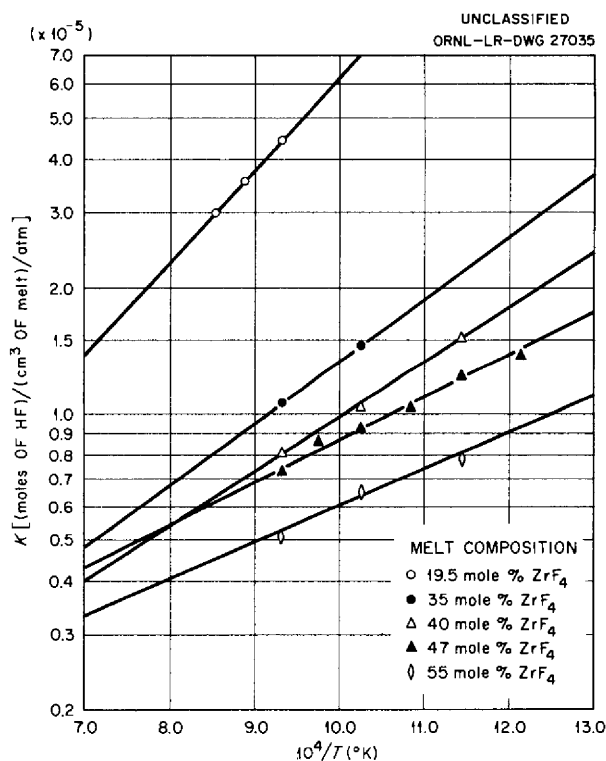Fig. 2.2.2. Temperature Dependence of Henry's Law Constants for the Solubility of HF in NaF-ZrF$_4$.

[27] J. H. Shaffer, *ANP Quar. Prog. Rep. June 30, 1957*, ORNL-2340, p 141.

[28] J. H. Shaffer, *ANP Quar. Prog. Rep. Sept. 30, 1957*, ORNL-2387, p 136.

Table 2.2.16. Solubility of HF in NaF-ZrF$_4$ Mixtures as a Function of Temperature, Pressure, and Melt Composition

Melt Composition (mole % ZrF$_4$)	Temperature (°C)	Saturating HF Pressure (atm)	Solubility (moles of HF/cm^3 of melt)	Henry's Law Constant, K*
			$\times 10^{-5}$	$\times 10^{-5}$
19.5	800	2.04	9.12	4.47
		2.12	9.26	4.38
				Av 4.43 ± 0.05
	850	1.54	5.94	3.85
		2.06	6.85	3.33
		2.07	7.33	3.55
				Av 3.58 ± 0.18
	900	1.48	4.28	2.90
		2.07	6.39	3.09
				Av 3.00 ± 0.09
35**	700			1.46 ± 0.03
	800			1.06
40**	600			1.52 ± 0.03
	700			1.03
	800			0.81 ± 0.01
47**	550			1.38 ± 0.02
	600			1.23 ± 0.04
	650			1.03 ± 0.02
	700			0.93 ± 0.02
	750			0.86 ± 0.02
	800			0.73 ± 0.01
55	600	1.14	0.96	0.83
		1.40	1.09	0.78
		1.44	1.12	0.78
		1.87	1.33	0.71
		1.92	1.53	0.80
				Av 0.78 ± 0.03
	700	1.24	0.82	0.66
		2.04	1.27	0.62
		2.36	1.60	0.68
				Av 0.65 ± 0.02
	800	1.46	0.74	0.51
		1.51	0.79	0.52
		2.46	1.22	0.49
				Av 0.51 ± 0.01

*K = c/p in moles of HF per cubic centimeter of melt per atmosphere.

**Summarized results of previously reported data are listed for K.

values for the heats of solution at each composition have been calculated from Fig. 2.2.2 and are shown graphically in Fig. 2.2.3. The composition dependence of the solubility of HF is illustrated in Fig. 2.2.4. As may be noted, the solubility of HF undergoes an inflection point at approximately 44 mole % ZrF_4, and it increases with increasing NaF concentration.

Attempts to correlate the observed changes of HF solubility with corresponding changes in solvent composition will be withheld until considerably more information is available. Experiments to measure the solubility of HF in NaF-KF-LiF (11.5-42-46.5 mole %) and in LiF-BeF$_2$ and NaF-BeF$_2$ mixtures are now under way.
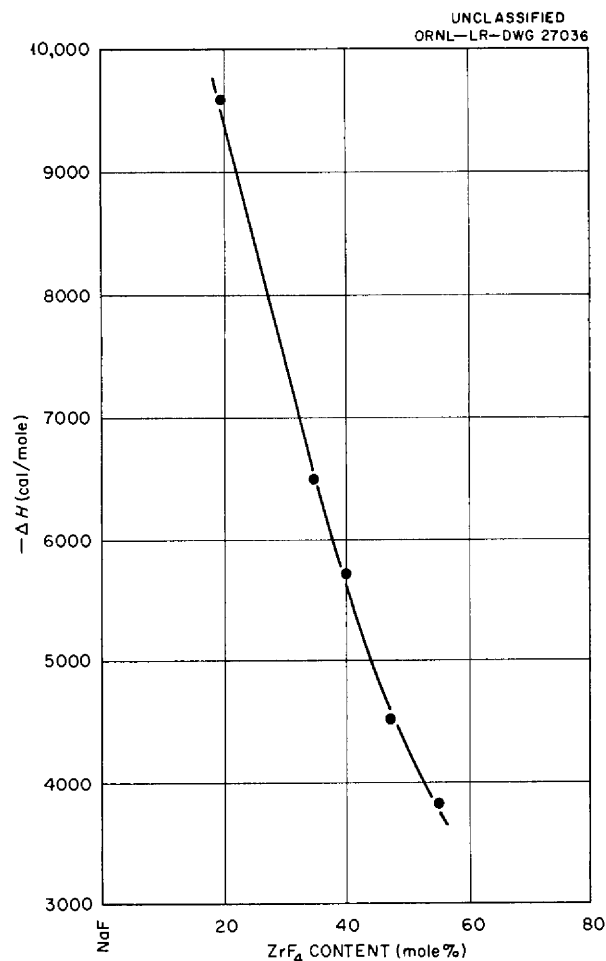

Fig. 2.2.4. Composition Dependence of Henry's Law Constants for the Solubility of HF in NaF-ZrF$_4$.

SOLUBILITIES OF FISSION-PRODUCT FLUORIDES IN MOLTEN NaF-ZrF$_4$ MIXTURES

W. T. Ward   R. A. Strehlow

Experiments have been completed in order to determine (1) the effect that varying the ratio of sodium to zirconium in the NaF-ZrF$_4$ solvent has on the solubility of CeF$_3$, (2) the solubility of YF$_3$ in NaF-ZrF$_4$ (53-47 mole %), and (3) the solubilities of CeF$_3$ and SmF$_3$ when both are present in NaF-ZrF$_4$ (53-47 mole %). The solubility measurements were made by using the radiochemical tracer techniques described previously.[29,30]

Fig. 2.2.3. Composition Dependence of the Heat of Solution of HF in NaF-ZrF$_4$.

[29] W. T. Ward, *ANP Quar. Prog. Rep. Dec. 31, 1956,* ORNL-2221, p 125.

[30] W. T. Ward, *ANP Quar. Prog. Rep. March 31, 1957,* ORNL-2274, p 105.

CeF$_3$ in NaF-ZrF$_4$

It has been found that varying the ratio of sodium to zirconium in the solvent has a considerable effect on the solubility of CeF$_3$. This effect is clearly shown in Fig. 2.2.5, in which the solubility vs temperature curves for five different NaF-ZrF$_4$ compositions are plotted. In addition to the compositions indicated on Fig. 2.2.5, the NaF-ZrF$_4$ (80.5-19.5 mole %) solvent was briefly investigated. It was found that all the 4.60 mole % CeF$_3$ that was added was soluble at temperatures from 793 to 915°C.
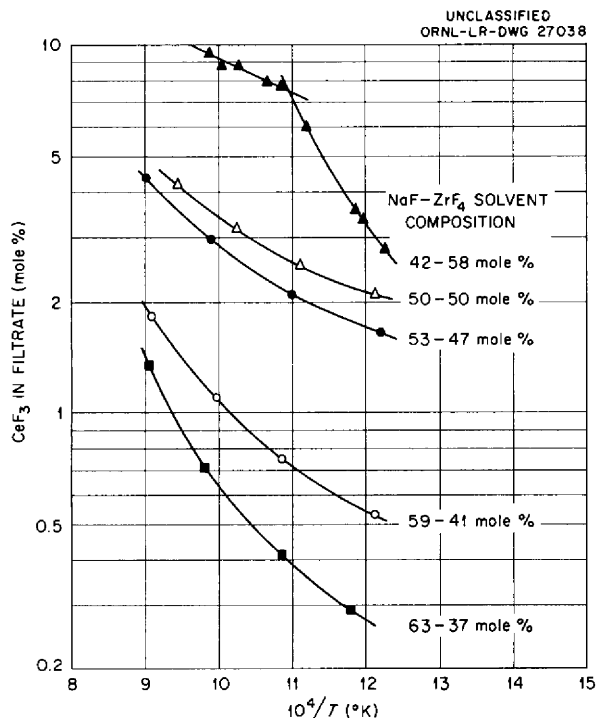

Fig. 2.2.5. Solubility vs Temperature for CeF$_3$ in Various NaF-ZrF$_4$ Mixtures.

One interesting observation is that in the solvent NaF-ZrF$_4$ (42-58 mole %) the nature of the precipitating phase changes at about 640°C, the inflection point on the curve. A plot of CeF$_3$ solubility at 600°C as a function of composition is presented in Fig. 2.2.6, and it may be noted that the curve is quite similar to that obtained earlier[31] for the solubility of UF$_3$ in NaF-ZrF$_4$. Such correlation would be expected from a consideration

[31]G. M. Watson and C. M. Blood, *ANP Quar. Prog. Rep. June 10, 1954*, ORNL-1729, p 51.
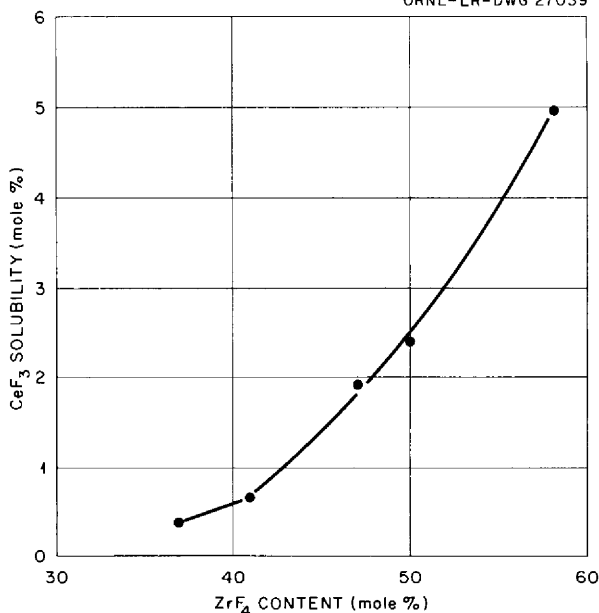
Fig. 2.2.6. Solubility of CeF$_3$ at 600°C in NaF-ZrF$_4$ Mixtures as a Function of Composition.

of the similarity of the U^{+++} and the Ce^{+++} ionic radii, that of U^{+++} being 1.03 Å and that of Ce^{+++} being 1.02 Å. It is quite likely that an inflection exists in the solubility curve at a composition near 41 mole % ZrF$_4$, since with higher NaF content the precipitating phase is not CeF$_3$ but rather NaCeF$_4$, as determined by petrographic observation.

YF$_3$ in NaF-ZrF$_4$

The solubility of YF$_3$ in NaF-ZrF$_4$ (53-47 mole %) was determined, and the results are presented in Table 2.2.17 and Fig. 2.2.7. Although some

Table 2.2.17. YF$_3$ Solubility in NaF-ZrF$_4$ (53-47 Mole %)

Filtration Temperature (°C)	Solubility	
	In wt % Y	In mole % YF$_3$
854	11.37	13.68
817	8.68	10.26
756	6.31	7.39
663	4.10	4.75
560	2.37	2.72

scattered earlier results had indicated that the plot of the log of the solubility vs the reciprocal of the temperature for YF_3 was linear, these results show a behavior pattern more similar to the patterns obtained for the rare earths.

CeF₃ plus SmF₃ in NaF-ZrF₄

The solubilities of CeF_3 and SmF_3 in combination in NaF-ZrF₄ (53-47 mole %) were measured by

UNCLASSIFIED
ORNL-LR-DWG 27040
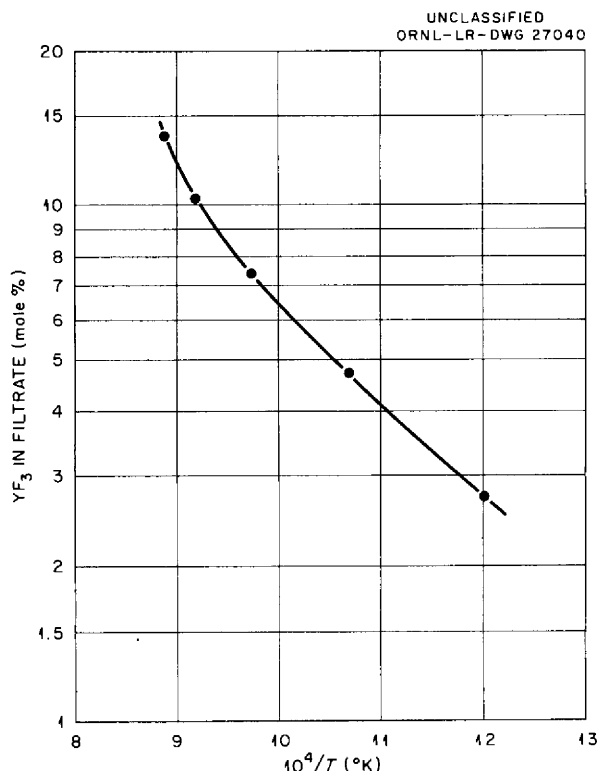
Fig. 2.2.7. Solubility vs Temperature for YF_3 in NaF-ZrF₄ (53-47 Mole %).

using the two-tracer technique described previously.[30] Filtrates were obtained over the temperature range of 550 to 800°C for two cerium-to-samarium ratios. A summary of the solubility data is presented in Table 2.2.18, along with the solubility of CeF_3 by itself in the same solvent. The solubility vs temperature relationships are illustrated in Fig. 2.2.8, where the logs of the sums of the solubilities are plotted vs the reciprocal of the temperature.

The solubility of pure SmF_3 has not yet been measured in this solvent, but, by utilizing the correlation of solubility with the cube of the ionic radius, estimates were made of the solubilities of SmF_3 at these temperatures. The values obtained are shown in Table 2.2.19.

These values are summarized in the pseudo-ternary diagram presented as Fig. 2.2.9. The rare-earth fluoride solubility behavior in this solvent is seen to be substantially the same as the behavior reported previously when the solvent was NaF-ZrF₄-UF₄ (50-46-4 mole %).[32]

SOLUBILITY OF BaO IN KF-LiF

J. H. Shaffer

The solubility of BaO in KF-LiF (50-50 mole %) is of interest in the systematic investigation of possibilities of removal of fission-product fluorides from NaF-LiF-KF base mixtures. Three experiments have been performed to obtain solubility values in which the starting barium compound, either BaF_2 or BaO, was labeled with radioactive Ba^{133}.

---

[32]R. A. Strehlow and W. T. Ward, *ANP Quar. Prog. Rep. June 30, 1957*, ORNL-2340, p 139.

Table 2.2.18. Solubilities of CeF_3 and SmF_3 in NaF-ZrF₄ (53-47 Mole %)

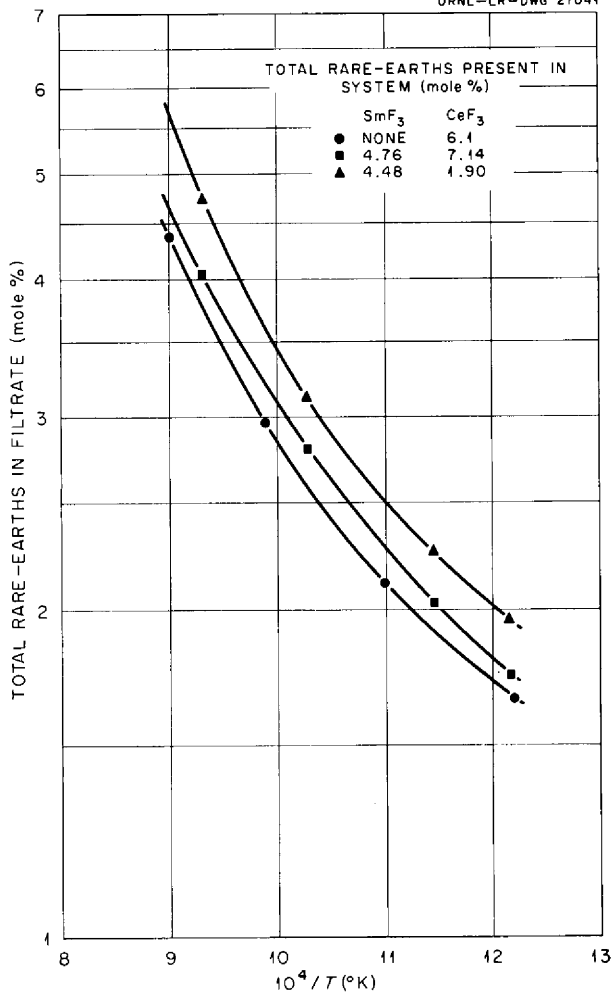| Filtration Temperature (°C)	Total Additive						
	4.48 Mole % SmF₃, 1.90 Mole % CeF₃			4.76 Mole % SmF₃, 7.14 Mole % CeF₃			6.1 Mole % CeF₃, no SmF₃
	Solubilities (mole %)			Solubilities (mole %)			Solubility of CeF₃ (mole %)
	SmF₃	CeF₃	SmF₃ + CeF₃	SmF₃	CeF₃	SmF₃ + CeF₃	
800	3.23	1.48	4.71	1.56	2.48	4.04	3.78
700	2.17	0.95	3.12	1.13	1.66	2.79	2.57
600	1.62	0.62	2.24	0.86	1.16	2.02	1.90
550	1.45	0.50	1.95	0.76	0.97	1.73	1.67

Fig. 2.2.8. Solubilities of SmF_3 and CeF_3 in NaF-ZrF_4 (53-47 Mole %) as a Function of Temperature.

Table 2.2.19. Estimates of the Solubility of SmF_3 in NaF-ZrF_4 (53-47 Mole %) Based on the Solubility of CeF_3

Temperature (°C)	Solubility of CeF_3 (mole %)	Estimated SmF_3 Solubility (mole %)
800	3.78	4.40
700	2.57	2.99
600	1.90	2.21
550	1.67	1.95
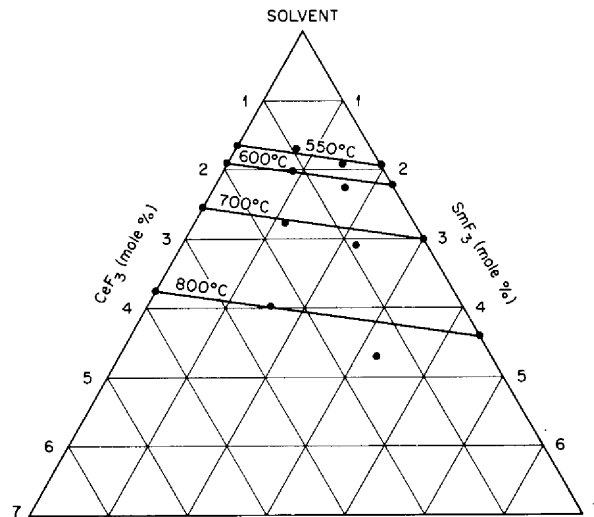
Fig. 2.2.9. Pseudoternary Diagram of the System CeF_3-SmF_3 with the Mixture NaF-ZrF_4 (53-47 Mole %) as the Solvent.

The melting point and heat of fusion of BaO are listed[33] as 1923°C and 13.8 kcal/mole, respectively. Accordingly the estimated solubility of BaO at 600°C would be quite low (less than 0.5 mole %). Since it was considered to be difficult to prepare labeled BaO free of traces of soluble impurities, such as carbonates, hydroxides, and chlorides, it was decided to prepare the BaO *in situ* from BaF_2. The soluble impurities would cause apparent solubility values of BaO to be erroneously high. This preparation was attempted in two different experiments. The first consisted in the addition to the melt of LiOH containing a known amount of labeled BaF_2. A filtrate sample was obtained prior to the addition of the LiOH, and filtrates at 700 and 600°C were obtained after the addition was completed. Since no change was noted in the concentration of barium in solution, it was decided to repeat the experiment with sodium peroxide as the precipitating agent. The results of the second experiment also showed no change in the concentration of barium in the liquid after addition of 20% and of 140% excess Na_2O_2, calculated as Na_2O.

[33]A. Glassner, *A Survey of the Free Energies of Formation of the Fluorides, Chlorides, and Oxides of the Elements to 2500°K*, ANL-5107, p 6 (Aug. 1953).

In view of the unexpected results obtained in the first two experiments, a third experiment was carried out with labeled BaO as the additive. The labeled BaO was prepared by ignition of $Ba(NO_3)_2$. Again the results showed that the solubility of BaO was quite high. The labeled BaO used was examined with the petrographic microscope and by x-ray diffraction. The results of these examinations show that the material used was high-quality BaO. The numerical results of the three experiments are summarized in Table 2.2.20.

REACTION OF CeF$_3$ AND UF$_4$ WITH CaO IN KF-LiF

J. H. Shaffer

Studies of the precipitation of cerium as Ce_2O_3 from the molten KF-LiF eutectic[34] and of the solubility of barium oxide in this solvent (see preceding section) have provided a basis for ·investigating the possible separation of tetravalent metals as oxides from the trivalent fission products of a fused-salt reactor. Alternatives to this separation are to precipitate the rare earths as oxides and leave the uranium in the solvent or to precipitate uranium oxide and leave the fission products in solution.

In the present study, 5 wt % of labeled Ce was added as CeF$_3$ to the molten KF-LiF eutectic

containing 1 mole % U as UF$_4$ at 600°C. Calcium oxide was then added in tared increments, and filtrate samples were taken approximately 2 hr after each addition. These samples were counted for radioactivity to determine the cerium concentration and were chemically analyzed for uranium. The results are shown graphically in Fig. 2.2.10.

It may be noted that the cerium concentration increases, initially, because of the removal of the uranium from solution, until the equivalence point for the uranium is reached. Upon further addition

---

[34]J. H. Shaffer, *ANP Quar. Prog. Rep. Sept. 30, 1957*, ORNL-2387, p 139.
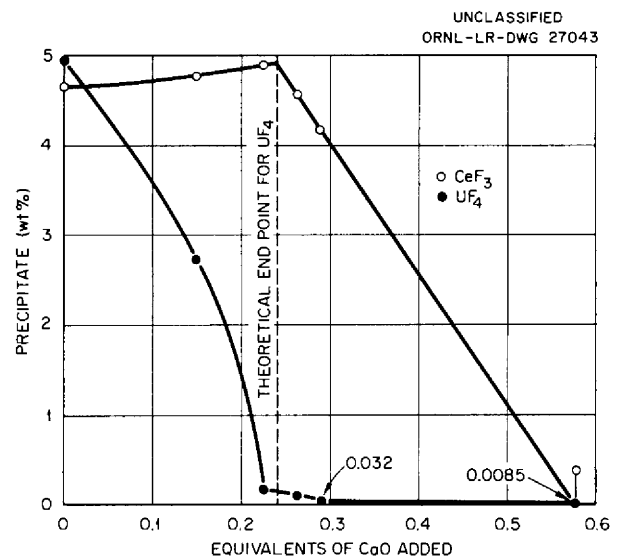
Fig. 2.2.10. Precipitation of CeF$_3$ and UF$_4$ with CaO in KF-LiF (50-50 Mole %).

Table 2.2.20. Concentration of Barium in Liquid KF-LiF After Addition of BaF$_2$-LiOH, BaF$_2$-Na$_2$O$_2$, and BaO

Additive	Temperature (°C)	Initial Barium Concentration (wt % Ba)		Final Barium Concentration (wt % Ba)	
		Calculated	Experimental	Calculated	Experimental
BaF$_2$-LiOH	600	11.4	9.85	9.93	10.45
	700			9.93	10.95
BaF$_2$-Na$_2$O$_2$ (20% excess)	600	8.28	8.1	7.82	7.6
	700			7.82	7.6
	800			7.82	7.6
BaO	600			6.94	6.6
	700			6.94	6.6
	800			6.94	6.6

of CaO the soluble cerium concentration decreases linearly to zero. The uranium concentration decreases to a value of approximately 0.1 wt % at the equivalence point. This experiment is now being repeated with the exception that the initial CeF_3 concentration has been decreased to 0.5 wt %. Another experiment is proposed in which ZrF_4 with a labeled hafnium tracer is to be substituted for the UF_4.

DETERMINATION OF CHROMIUM DIFFUSION COEFFICIENTS IN INCONEL–MOLTEN SALT SYSTEMS

R. B. Evans

The results of experiments carried out over the past few years on the migration of metal as a result of temperature gradients in a molten-salt environment have strongly suggested that the over-all migration rate is controlled by the diffusion rates within the metal. Accordingly, a thorough knowledge of solid-state diffusion phenomena is considered to be an important phase of corrosion studies. Several investigations of these phenomena have been made, but only a small portion of the work covered cases in which molten salts were involved. Therefore an investigation was initiated of the over-all mass transfer rate within isothermal systems in which Inconel is the container material and NaF-ZrF$_4$ is the salt. The diffusing metal in Inconel in this system is chromium.

Diffusion Coefficients

The diffusion coefficient is a flow-resistance parameter used in diffusion rate–time relationships. It is defined by the linear flow equation

$$(1) \qquad \frac{1}{A} \frac{\partial M}{\partial t} = -D \frac{\partial C}{\partial x} ,$$

which, if steady-state conditions are established and D is assumed to be independent of concentration, may be written as

$$(2) \qquad \frac{1}{A} \frac{\Delta M}{\Delta t} = D \frac{\Delta C}{L} ,$$

where

$\Delta M/\Delta t$ = constant rate of diffusion, g/sec,

A = area through which diffusion takes place, cm^2,

L = length, cm, of system in x direction (L is zero at the surface and increases with penetration of the metal wall),

ΔC = concentration change of diffusing material across L, $C_{x=0} - C_{x=L}$, g/cm^3,

D = diffusion coefficient, cm^2/sec.

The diffusion coefficient is a function of the temperature, the diffusing material, and the material through which diffusion takes place. It does not depend on the geometry of the flow system. It is entirely independent of the molten salt in contact with the surface of the metal, although the salt has a marked effect on ΔC and on the rate equations. Therefore it is not necessary to employ molten salts in experiments designed to determine diffusion coefficients, even though the ultimate application involves molten-salt systems.[35]

The steady-state equation (Eq. 2) is useful for discussion and forms the basis for the determination of flow constants in analogous systems (flow of heat, flow of electricity, and fluid flow in porous mediums); however, its use in solid-state diffusion studies has been discouraged because of the extremely low values of $\Delta M/\Delta t$ and D involved. The only alternative is utilization of experiments and equations based on unsteady-state flow. The basic linear flow equation for this case is

$$(3) \qquad \frac{\partial C}{\partial t} = \frac{\partial}{\partial x}\left(D \frac{\partial C}{\partial x} \right) .$$

If self-diffusion measurements are to be made, for example, diffusion of radioactive silver into pure silver,[36] and/or if the values of $\partial C/\partial x$ involved are not high, Eq. 3 may be written as[37]

$$(4) \qquad \frac{\partial C}{\partial t} = D \frac{\partial^2 C}{\partial x^2} .$$

Equation 4 is known as Fick's diffusion law.

Measurements Based on Radioactive Tracers

Tracer-Layer Method. – One method for experimentally determining diffusion coefficients for a given metal diffusing through a bar composed of the same or a different metal is based on the use of radioactive isotopes of the given metal. A very thin layer of solid labeled metal is placed, by any of various methods, on the face of a solid specimen

---

[35]It will be shown, however, that utilization of molten salts leads to a unique and simple method of indirectly determining diffusion coefficients for metals in which the salt rather than the metal is analyzed.

[36]J. C. Fischer, *J. Appl. Phy.* **22**, 74 (1951).

[37]A. C. Wahl and N. Bonner (eds.), *Radioactivity Applied to Chemistry*, Wiley, New York, 1951.

of unlabeled metal. Uniform placement ensures linear flow, and the layer is never replenished after initial placement. The specimen is then subjected to a constant temperature ($T > 600°C$) for a specified period of time during which the labeled metal diffuses into the bar. Even though the specimens may be of small dimensions, they may be considered as being infinite in length with respect to the direction and distance of labeled-metal invasion, since the rates of diffusion involved are very low.

A solution of Eq. 4 under boundary conditions[37,38] which closely approximate the described experimental condition is

$$(5) \qquad C^* = \frac{Q_0^*}{(\pi D t)^{1/2}} \ e^{-x^2/4Dt} \ ,$$

where all quantities other than Q_0^* have been previously defined, and the starred variables refer to the labeled metal. A physical interpretation of Q_0^*, g/cm^2, is somewhat difficult for the case of diffusional flow; it is analogous to an "impulse of energy" for heat or electrical flow systems. It may be thought of as being the product of the layer thickness and the layer density, the thickness being zero. The layer is put on at an infinite rate over a zero time interval.

A sketch of C^* vs x at various times t is shown in Fig. 2.2.11. The quantity $\partial C/\partial x$ at $x = 0$ is zero, and thus $\partial M/\partial t$ at $x = 0$ is zero for all $t > 0$. Also shown in Fig. 2.2.11 is a sketch of $\log C$ vs x^2 at various times. It is apparent from Eq. 5 that the slopes of the lines of this plot are equivalent to $-(4Dt)^{-1}$. Thus D may be determined from a $\log a$ vs x^2 plot. It is assumed in the sketches of

---

[38] R. V. Churchill, *Modern Operational Mathematics in Engineering*, p 117, McGraw-Hill, New York, 1944.

Fig. 2.2.11 that a has been corrected for time decay. The diffusion coefficient determined for the labeled material is essentially the diffusion coefficient for the unlabeled material.

Excellent results[39-41] have been reported for this type of experiment. In some instances, two types of diffusion occurred simultaneously.[36] The two types are (1) diffusion through the grains and (2) diffusion along the grain boundaries; the latter controls the over-all diffusion rate at lower temperatures, and a combination of the two controls the rate at higher temperatures. In instances in which both types of diffusion occur, $\log a$ vs x^2 plots tend to bend.[41,36] Such results leave considerable doubt as to the value of the over-all diffusion coefficient.

Labeled-Molten-Salt Method. — If consideration is given to a semi-infinite isothermal system wherein an alloy containing metal $M°$ is in contact (at one face) with a molten salt containing a fixed amount of MX_2, it may be seen that at equilibrium the net rate of transfer of M between the metal and the salt will be zero, although a random dynamic exchange of M will take place. If a small amount of the MX_2 were removed and replaced by an equal amount of labeled M^*X_2, the random dynamic exchange could be studied by following the exchange rate of the labeled M^*X_2. The expression which relates the quantities of interest in terms of the surface exchange reaction or "wall reaction,"

$$M° + M^*X_2 \rightleftharpoons MX_2 + M°^* \ , \ \Delta F° = 0 \ ,$$

---
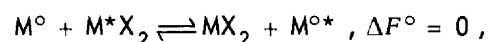
[39] W. A. Johnson, *Trans. Am. Inst. Mining Met. Engrs., Inst. Metals Div.* 143, 107 (1941).

[40] P. L. Gruzin and G. B. Fedorov, *Doklady Akad. Nauk S.S.S.R.* 105, 264 (1955).

[41] S. T. Kishkin and S. Z. Bokstein, *Proc. Intern. Conf. Peaceful Uses Atomic Energy, Geneva, 1955* 15, 87 (1955).
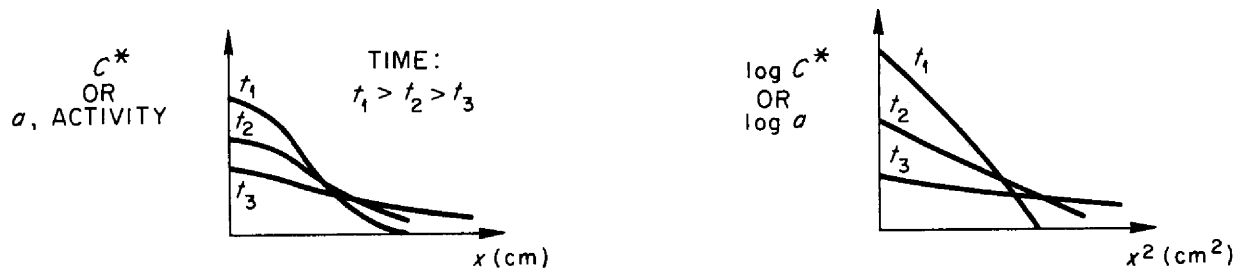
Fig. 2.2.11. Concentration of Labeled Metal at Various Times.

is

(6a)
$$K_x = \frac{[M^{\circ *}][MX_2]}{[M^{\circ}][M^*X_2]} \; .$$

The equilibrium of Eq. 6a is established within a short period of time after the M^*X_2 is added. Since

$$K_a = 1 \cong K_x \; ,$$

the concentration of $M^{\circ *}$ at the surface of the alloy at any time is given by the equation

(6b)
$$[M^{\circ *}]_{x=0} = [M^{\circ}] \frac{[M^*X_2]}{[MX_2]} \; .$$

The bracketed concentration expressions are taken to be weight fractions.

The $M^{\circ *}$ will diffuse back into the metal as time progresses and tend to deplete both the $M^{\circ *}$ at the surface and the M^*X_2 in the salt. Depletion will occur unless M^*X_2 is added to the system at a rate equal to the diffusion rate. If the latter manipulation is carried out, or if it can be assumed that M^*X_2 remains constant, $[M^{\circ *}]_{x=0}$ is constant with time. The solution of Fick's law for this case is

(7)
$$C_{M^{\circ}*} = C_{M^{\circ}*}\Big]_{x=0} \operatorname{erfc} \frac{x}{2(Dt)^{1/2}} \; ,$$

whereby

(8)
$$\frac{1}{A}\frac{dM^*}{dt}\bigg]_{x=0} = C_{M^{\circ}*}\Big]_{x=0}\left(\frac{D}{\pi t}\right)^{1/2} \; ,$$

and

(9)
$$\frac{\Delta M^*}{A} = \frac{1}{A}\int_0^t \left(\frac{dM^*}{dt}\right)_{x=0} dt$$

$$= 2\,C_{M^{\circ}*}\Big]_{x=0}\left(\frac{Dt}{\pi}\right)^{1/2} \; .$$

In Eq. 9, ΔM^* is the cumulative amount of $M^{\circ *}$ (in grams) which has passed through A (cm^2) of the metal surface at any time t (sec). The quantity $C_{M^{\circ}*}\big]_{x=0}$ is the concentration of metallic labeled M at the surface of the alloy (g/cm^3).

If ΔM^* is measured as a function of time under the conditions stated, the diffusion coefficient can be directly determined from the slopes of ΔM^* vs $t^{1/2}$ plots. These slopes are equivalent to the quantity $2\,C_{M^{\circ}*}\big]_{x=0}\,(D/\pi)^{1/2}$. The conditions set forth for the equations would be difficult to duplicate experimentally, however, since the necessity of using small sample containers and of excluding air suggests the use of sealed capsules. Continuous addition of M^*X_2 could not be accomplished, and Eq. 8 would be applicable only at early flow times. In view of the low diffusion rates involved, it is not important that the conditions cannot be duplicated experimentally. Equation 4 can be solved in such a way as to take into account depletion behavior. A rigorous solution is

$$\frac{\Delta M^*}{M^*]_{t=0}} = 1 - e^{a^2 t} \operatorname{erfc} at^{1/2} \; ,$$

where a is proportional to $D^{1/2}$. It can be shown that Eq. 9 is a first approximation to the solution for small values of t.

Diffusion coefficients obtained by the labeled-molten-salt method are of value because they are over-all diffusion coefficients, that is, coefficients that are independent of microscopic behavior within the alloy. Further, the experimental procedure is simple: the initial value of ΔM^* is taken to be the early-time depletion of M^*X_2 in the melt, and the melt is assayed at various times.

Battelle Diffusion Experiments

Isothermal capsule diffusion experiments have recently been conducted at Battelle Memorial Institute on Inconel—fused fluoride salt systems.[42] Radioactive chromous fluoride was added to the salt in order to study the combined effect of the wall reaction and the diffusion coefficient on the chromium transfer rate.

Briefly, the experimental procedure consisted of placing a series of identical Inconel capsules, each containing 2 g of salt and known amounts of labeled CrF_2, in a furnace. The capsules were removed individually at various time intervals. The salts in the capsules removed were analyzed for the amount of CrF_2 and Cr^*F_2 present. In addition, the walls of one capsule from each series of isothermal tests were sectioned by an electropolishing technique to obtain the wall distribution

[42]R. Price *et al.*, *A Tracer Study of the Transport of Chromium in Fluoride Fuel Systems*, BMI-1194 (June 18, 1957).

of labeled chromium. The data obtained are used below in a critical analysis of the proposed method for the determination of diffusion coefficients.

Data Based on Molten-Salt Analyses. — A portion of the results of the Battelle experiments is reproduced in Fig. 2.2.12. This figure indicates that (1) at low temperatures and (2) at early flow times for high temperatures the amount of labeled chromium which diffuses from the salt into the metal varies directly with the square root of the flow time. It may also be noted that as time goes on the experimental points at higher temperatures fall away from the straight-line relationship. This was to be expected because the quantities $C_{Cr^\circ*}]_{x=0}$ and $[Cr^*F_2]$ were not held constant during the experiment.

A reasonable approximation of the diffusion coefficient can be obtained, however, from the slopes of the straight lines in Fig. 2.2.12. The expression relating the slope of these lines to the diffusion coefficient can be obtained by combining

Eqs. 6 and 9. The expression is

$$(10) \quad m = \frac{\% \text{ Depletion}}{[t \text{ (hr)}]^{1/2}}$$

$$= (60)(200) \frac{A}{N_T} \rho_{Metal} \frac{[Cr^\circ]}{[CrF_2]}\left(\frac{D}{\pi}\right)^{1/2},$$

where ρ_{Metal} is the density of Inconel (g/cm^3), N_T is the amount of salt present (g), $[CrF_2]$ is the weight fraction of CrF_2 in the salt, reported as Cr^{++}, and m is the slope given on Fig. 2.2.12. This method was used to estimate values of D from the results of several capsule experiments. The experiments were divided into two groups, with the base salt for one group being NaF-ZrF$_4$ (50-50 mole %) and for the other NaF-ZrF$_4$-UF$_4$ (50-46-4 mole %). It was necessary to assume that equilibrium amounts of UF$_3$, UF$_4$, and CrF$_2$ were present in the base salt of the second group, since data on the $[UF_3]/[UF_4]$ ratios and the $[CrF_2]$ variations as functions of time were not
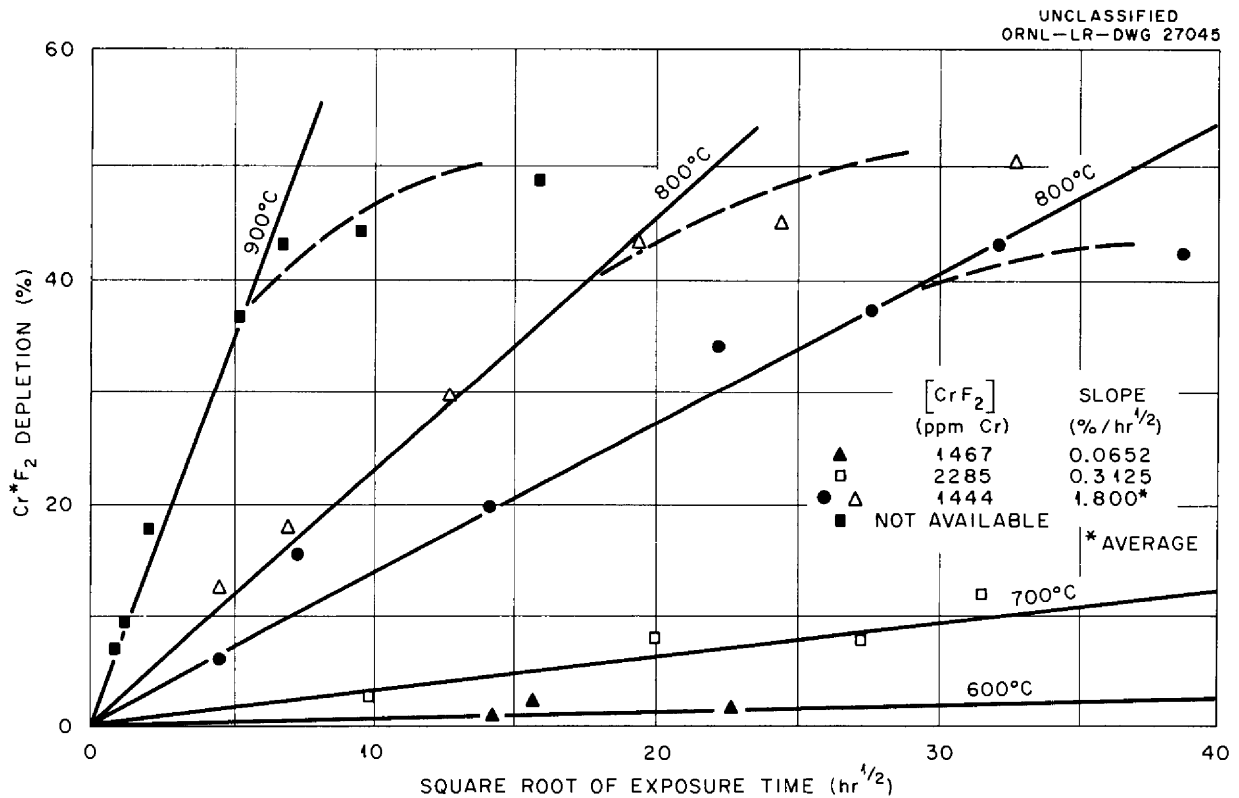
Fig. 2.2.12. Net Loss of Cr*F$_2$ Activity from NaF-ZrF$_4$-UF$_4$ (50-46-4 Mole %) Because of Cr* Diffusion into Inconel Capsule Wall. (Secret with caption)

available. The estimated values are presented in Fig. 2.2.15, which is discussed in a subsequent section of this report.

Data Based on Distribution of Labeled Metal in Wall. – The $Cr^{\circ*}$ wall distribution data formed the basis for the values of the diffusion coefficients reported by the Battelle investigators. Equation 5 was utilized for correlating the results, although the boundary condition

$$\frac{dM}{dt}\Bigg]_{x=0} = 0$$

was obviously violated by the experimental conditions. A plot of one set of the Battelle distribution data is shown in Fig. 2.2.13. The "volume" diffusion curve reported by the Battelle investigators, as well as the distribution predicted by Eq. 7, was superimposed over the data, and both curves failed to fit the data. The "average D" calculated by both equations was 10^{-13} cm^2/sec. The fact that the curve of Eq. 7 did not fit casts some doubt as to the validity of the related Eq. 9.
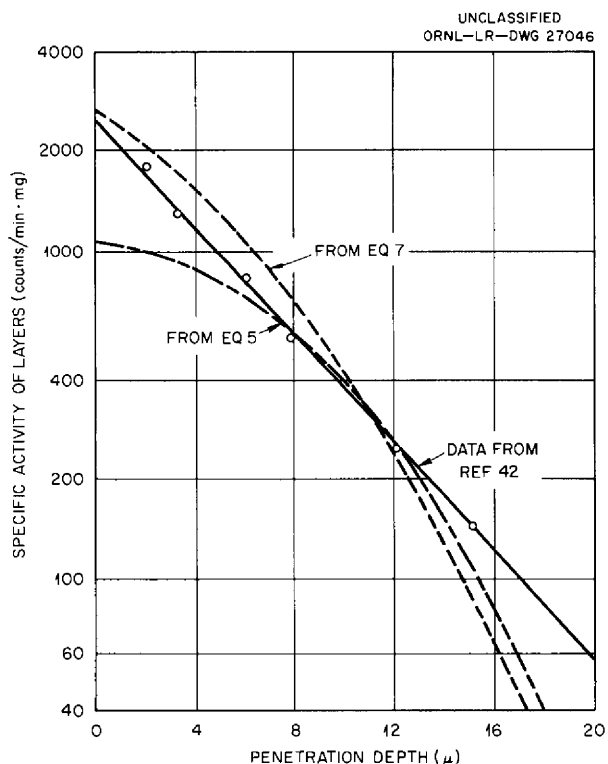
In order to evaluate the discrepancies, the value of D from the distribution data was used to construct a depletion curve. This in turn was compared with the actual depletion data obtained for the same experiment. The results are shown in Fig. 2.2.14.

Additional comparisons with chromium diffusion coefficients available in the literature[40] are presented in Fig. 2.2.15. These values are also tabulated in Table 2.2.21 along with the corresponding activation energies for diffusion. Although Eq. 7 did not fit the distribution data, it was concluded on the basis of Table 2.2.21 that Eq. 9 was suitable for estimating values of the over-all diffusion coefficient.

The magnitudes of the variations encountered in terms of amount of material transferred are not immediately apparent from plots such as Fig. 2.2.15; hence, calculated rate values are presented in Table 2.2.22 to give a "feel for the numbers" in terms of rate of diffusion and amount transferred as a function of time.

The values presented in Table 2.2.22 were calculated by using Eq. 2 for the amount of steady-state chromium diffusion which would occur over a one-year interval through a thin Inconel sheet, one face of which was backed up by a thick chromium plate, and the other face of which was continuously exposed to a fresh molten $NaF-ZrF_4-UF_4$ salt mixture at 900°C. The sheet was assumed to be 3 mils thick, with a 130-cm^2 cross-sectional area (equivalent to the area exposed in a 16-in. loop of 0.5-in. Inconel tubing). A comparison of these values suggests that the diffusion coefficients reported by the Battelle investigators yield diffusion rates which are somewhat pessimistic with respect to Inconel corrosion properties.

STEADY-STATE CHROMIUM MIGRATION IN THERMAL-CONVECTION LOOPS

R. B. Evans

The results of many investigations[43] of the corrosion of polythermal Inconel loops have shown that chromium is transported[44] from hot to cold zones by circulating $NaF-ZrF_4-UF_4$ salts. Mass transfer of chromium also occurs with other salt

UNCLASSIFIED
ORNL–LR–DWG 27046

Fig. 2.2.13. Cr^{51} Distribution in Inconel at 700°C After 739 hr of Exposure.

[43]W. D. Manly *et al.*, *Metallurgical Aspects of Molten Fluoride Reactors*, ORNL-2349 (Sept. 17, 1957).

[44]W. R. Grimes, *ANP Quar. Prog. Rep. June 10, 1956*, ORNL-2106, p 96.

UNCLASSIFIED
ORNL-LR-DWG 27047
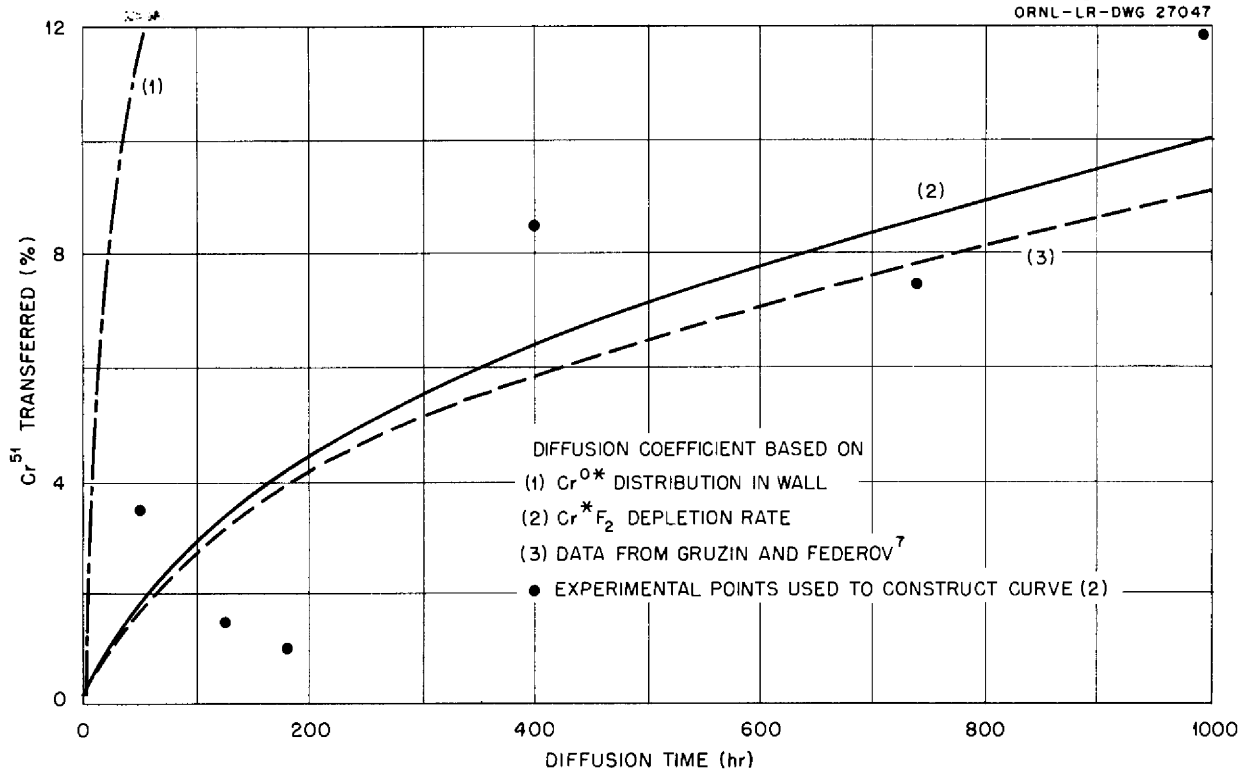
Fig. 2.2.14. Effect of Diffusion Coefficients as Determined by Various Methods on Predicted Diffusion Rates of Labeled Chromium in Inconel.

Table 2.2.21. Diffusion Coefficients for Chromium at 700°C in Various Nickel-Base Alloys from Various Sources

Type of Metal	Chromium (wt %)	Diffusion Coefficient (cm^2/sec)	Activation Energy* for Diffusion (kcal/g-at.)	Values Reported by	Data Reference
		$\times 10^{-15}$			
Ni-Cr alloy 3	20.4	3.2**	66	Gruzin and Fedorov	40
Inconel	16	3.7		Present investigation	
Pure nickel	0	71**	48	Gruzin and Fedorov	40
Inconel	16	100	41	Price *et al.*	42

$^\star D = D_0 \, e^{-E_{act}/RT}$.

**Extrapolated values.

105

ORNL-LR-DWG 27048
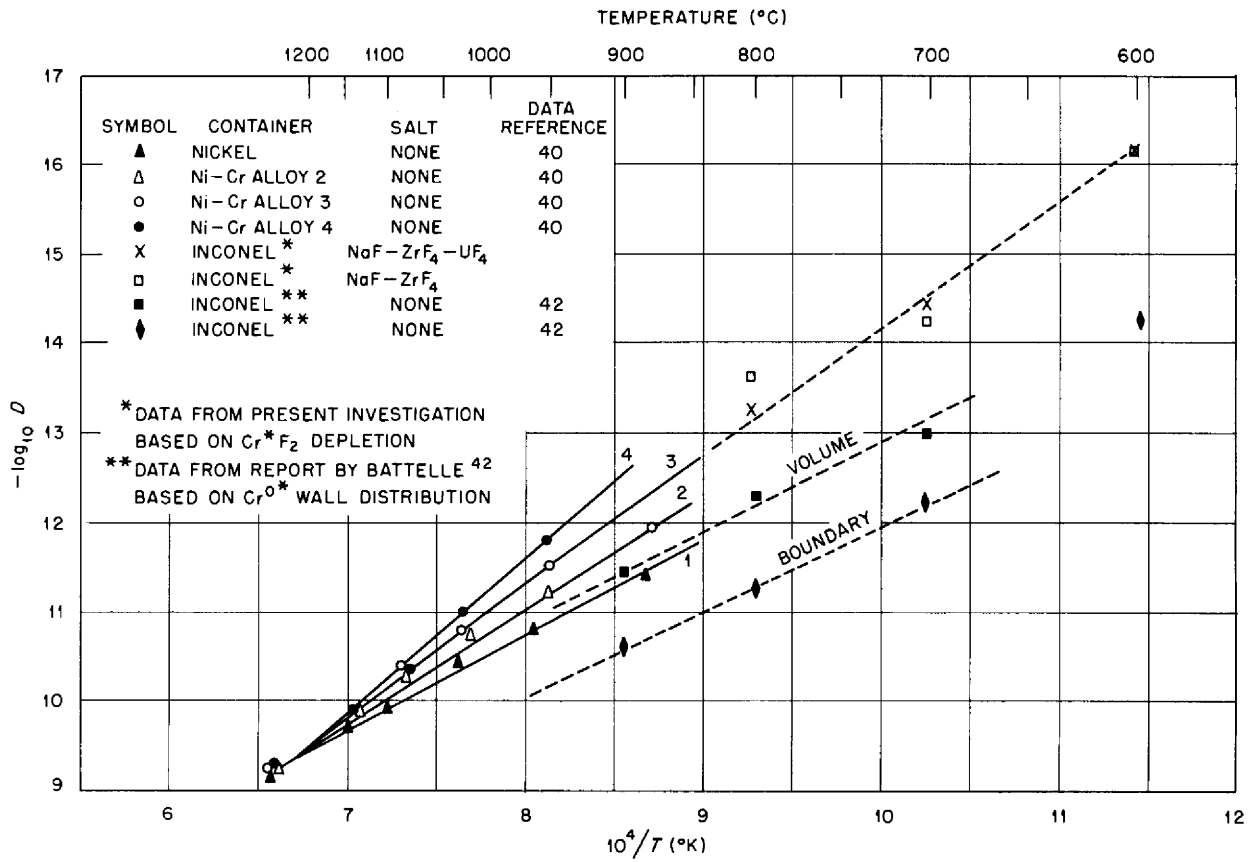
Fig. 2.2.15. Comparisons of Various Diffusion Coefficients.

Table 2.2.22. Calculated Steady-State Diffusion Rates for Chromium Through Thin Alloy Sheets at 900°C

Sheet Material	Diffusion Coefficient (cm^2/sec)	Diffusion Rate (g/sec)	Diffusion Rate $(g/year)$	Calculations Based on Coefficients Reported By	Data Reference
Inconel	$8 \times 10^{-13*}$	1.4×10^{-8}	4.5	Present investigation	
Ni-Cr alloy 3	8×10^{-13}	1.8×10^{-8}	5.7	Gruzin and Fedorov	40
Inconel**	3×10^{-12}	5.2×10^{-8}	17	Price *et al.*	42
Inconel***	2×10^{-11}	3.5×10^{-7}	110	Price *et al.*	42

*Extrapolated value.

**By volume diffusion alone.

***By boundary diffusion alone.

systems and metals; however, this report deals only with the chromium migration peculiar to the NaF-ZrF_4-UF_4 salt system contained in Inconel.

In all experiments the loops have been loaded with pure salt mixtures, that is, mixtures which did not initially contain corrosion products. Therefore the over-all transport vs time relationships observed could be broken down into three consecutive flow situations or regions. The study of each region required a separate analytical approach, since the first two regions involve unsteady-state solutions and the transport phenomena corresponding to the third and final region are governed by a quasi-steady-state situation. The analysis of the third region is relatively simple compared with the analyses of the unsteady-state regions. The final steady-state situation is of considerable interest because low migration rates occur in this region.

One objective of the present study is to develop a method whereby the amount of chromium transported can be estimated as a function of loop operating time, and thus to be able to predict the extent of corrosion to be expected at any time. This method will be applicable only for the case in which loop operation is initiated with the equilibrium concentration of the corrosion products in the salt mixture. Chromium migration behavior for this case approximates the behavior in the quasi-steady-state region, with the exception that the distribution of chromium in the wall does not depend on what might have happened during the unsteady-state period. The finding of a relatively simple method of estimating the equilibrium concentrations is a further objective of this study.

Chromium Migration Mechanism

The chromium migration process in thermal-convection loops involves two chemical changes and two transport mechanisms. Over the entire hot zone, the metallic chromium slowly diffuses from the matrix of the Inconel tubing to the salt-exposed surface. The chromium concentration gradient in the metal is the driving force for the diffusion process. The transported chromium is then oxidized at the surface according to the reaction

$$(1) \qquad Cr^\circ + 2UF_4 \rightleftharpoons 2UF_3 + CrF_2$$
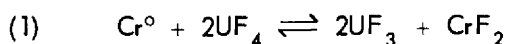
and is carried as CrF_2 to the cold zone via the circulating salt. At the cold-zone surface, the reaction is reversed, and the chromium reverts to the metallic state. The deposition process results in a chromium concentration gradient along the cold-zone surface which causes the chromium metal to diffuse into the tube walls.[45] The diffusion into or out of the walls occurs in a direction which is essentially normal to the surface and is governed by semi-infinite, linear flow relationships.

The CrF_2 concentration in the salt builds up initially with respect to time and then remains essentially constant. Thus a quasi-steady-state situation appears to exist whereby chromium is transported at very low rates and under conditions of a fixed chromium surface concentration vs loop position relationship. This idea is supported by the fact that corrosion continues even though the amounts of CrF_2, UF_4, and UF_3 in the salt remain constant.

Steady-State Migration

Based on experimental evidence alone, there is still some doubt as to whether the loops operated thus far have actually attained the quasi-steady state. Although the CrF_2 concentration remains constant, within the accuracy of the measurements, it has not been possible to make a direct, quantitative measurement of the total over-all amount of chromium transported. An irrefutable statement about the existence of a quasi-steady state cannot be made without such measurements.

Another approach to a study of the migration is to assume that the equilibrium amounts of CrF_2 and UF_3 are present in the salt before the loop and salt are subjected to the operating conditions. With this and the migration mechanism in mind, the following conditions may be specified for the resulting migration:

1. At any given time the cumulative amount of chromium which leaves the hot zone must equal the cumulative amount deposited in the cold zone. Furthermore, the over-all instantaneous rate of transfer out of the hot zone must equal the instantaneous rate of transfer into the cold zone.

---

[45]The equilibrium constants for the reaction

$$Ni^\circ + 2UF_4 \rightleftharpoons 2UF_3 + NiF_2$$
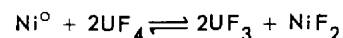
are so low compared with those for the chromium reaction that the transport of nickel by the mechanism described here may be ignored.

2. The over-all rate of transfer is diffusion controlled, since the diffusion rates are very much lower than the other rates involved.

3. There must be at least two points within the loop at which chromium is neither deposited nor depleted. In subsequent discussions, these points will be referred to as the balance points.

4. At the balance points (a) no diffusion takes place within the walls; (b) the chromium concentration at the surface is the same as the concentration in the original Inconel; (c) the circulating UF_3, UF_4, and CrF_2, the concentrations of which do not vary with loop position or time, must be in equilibrium with the original concentration of chromium in Inconel,[46] and thus the concentrations of the circulating salts are fixed by the equilibrium constants (and temperatures) at these points; and (d) the temperatures controlling the equilibrium constants must be the same.

5. The loop position vs temperature relationships are constant with respect to time. Thus the balance points must remain at fixed loop positions.

6. The concentration of chromium at any point on the tubing surface varies with loop position but not with time.

Unsteady-State Migration

As previously pointed out, unsteady-state corrosion arises in loops in which the salt initially contains UF_4 but no UF_3 or CrF_2. At zero time, t_0, the entire loop area will be a depletion zone (zero deposition zone), and it will remain so until time t_z is reached. At t_z, the CrF_2 concentration of the circulating salt will have increased to an amount Z, where Z is the concentration of CrF_2 in equilibrium with the chromium concentration of the wall surface at the position which has the lowest temperature of the loop. The balance points are then a single point at this position. As the concentration of CrF_2 in the circulating salt increases to values greater than Z, the initial balance point will develop into a growing deposition area bounded by two balance points. Steady state will be attained when the balance points become stationary and

the CrF_2 concentration in the circulating salt ceases to vary with time. The first two regions mentioned in the introduction are separated by the point Z. The last region starts when the balance points become stationary.

A very important observation can be made on the basis of the above discussion; that is, the over-all amount of chromium transferred during the unsteady-state time interval would be higher than that transferred in any identical pre-equilibrated loop which started at the same time. This observation is valid, since the depletion areas and driving forces for the unsteady-state case are greater (CrF_2 concentrations much lower) than those for the steady-state case. In addition, the degree of chromium depletion (corrosion) per unit area in the maximum-temperature portion of the loop is highest in the unsteady-state case. In other words, pre-equilibration is good operating procedure with respect to suppressing chromium migration within loops. The remainder of this discussion will deal with loops which have been pre-equilibrated at conditions close to the operating balance-point conditions.

Estimating Equilibrium Concentrations for Steady-State Loop Operation

The equilibrium (balance-point) concentrations of UF_4, UF_3, and CrF_2 can be estimated for steady-state loop operation by applying the six conditions previously outlined to a given set of loop parameters and operating conditions. Basic material data needed to carry out numerical calculations are (1) diffusion coefficients for chromium in Inconel as a function of temperature,[47] and (2) equilibrium ratios for the redox equation (Eq. 1) as a function of temperature.[48,49]

Tentative values of these variables are given in Fig. 2.2.16. The diffusion coefficients are based on extrapolations of published data and the equilibrium ratios are based on an interpolation of experimental values for two NaF-ZrF_4-UF_4 mixtures in contact with chromium. In order to present a numerical example of the calculations involved, the following parameters

---

[46]This statement is based on the important assumption that chemical equilibrium with respect to Eq. 1 is assumed to exist at every surface point within the loop. Concentration gradients within the salt normal to the circulation path are ignored.

[47]P. L. Gruzin and G. B. Fedorov, *Doklady Akad. Nauk S.S.S.R.* 105, 264 (1955).

[48]J. D. Redman, *ANP Quar. Prog. Rep. June 30, 1957,* ORNL-2340, p 132.

[49]L. G. Overholser, private communication to R. B. Evans.
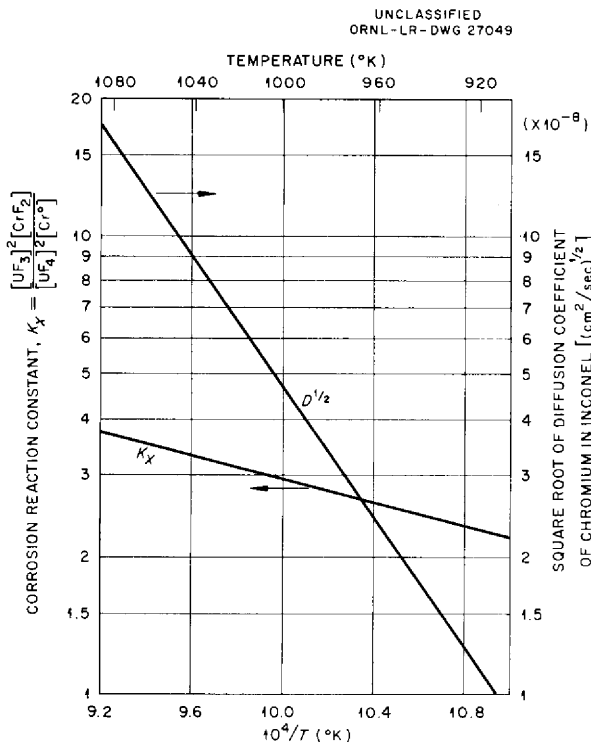
UNCLASSIFIED
ORNL–LR–DWG 27049

Fig. 2.2.16. Effect of Temperature on Parameters Which Control Rate of Chromium Migration in Inconel-Salt Systems.

and operating conditions, which are those of a typical experimental loop, were assumed:

Salt	NaF-ZrF$_4$-UF$_4$ (50-46-4 mole %)
Flow rate	1 fpm
Loop	Inconel tubing, 0.5 in. OD, 16 in. long, containing 16 wt % Cr
Maximum temperature	1060.8°K
Minimum temperature	933.3°K

In addition it was also necessary to make some simplifying assumptions regarding both concentration and temperature effects at certain loop positions and time. The reasons for this are brought out in the following section, in which the diffusional flow equations for applicable steady-state migration in loops are discussed.

Mass-Transport Equations for Steady-State Migration

Condition 2, given above, for steady-state migration implies that the over-all migration rate can

be written in terms of the diffusional flow which takes place in the metal; that is, it is assumed that the circulating rate of the salt does not contribute to the transport equation.

Condition 6 states that, for a unit area at any loop position, L, the chromium concentration at the surface remains constant with time. If it is assumed that all chromium diffusion through a unit area, A, into the wall is always normal to A, the following equation may be written to relate the chromium concentrations, C, time, t, the diffusion coefficient, D, and penetration distance, x:

$$(2) \quad C(x,t)_{cold\ zone} = C_{Inconel} +$$

$$+ (C_{surface} - C_{Inconel})\ erfc\ \frac{x}{2(Dt)^{1/2}}$$

and

$$(3) \quad C(x,t)_{hot\ zone} = C_{surface} +$$

$$+ (C_{Inconel} - C_{surface})\ erfc\ \frac{x}{2(Dt)^{1/2}} \ .$$

The related rate expression for both the cold and hot zones is

$$(4) \quad \frac{dM}{dt} = - DA\ \frac{\partial C}{\partial x}\bigg]_{surface}$$

$$= A\ \Delta C \left(\frac{D}{\pi t}\right)^{1/2} \ ,$$

where $\Delta C = C_{surface} - C_{Inconel}$. The signs of dM/dt, which is the weight of chromium diffusing per unit time (in grams per second), depend on ΔC; thus, a positive dM/dt means that chromium is diffusing into the wall. The cumulative amount which will have migrated across any unit area of surface from time zero to any time t is given by
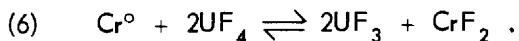
$$(5) \quad \Delta M = 2A\ \Delta C \left(\frac{Dt}{\pi}\right)^{1/2} = 2t\ \frac{dM}{dt} \ .$$

The chromium concentration at the tubing surface, that is,

$$C_{surface} = [Cr°]_{surface}\ \rho_{metal} \ ,$$

where C and ρ are in density units and $[Cr°]$ is expressed in terms of weight fraction of chromium

in the metal, is governed by the reaction

(6) $Cr^\circ + 2UF_4 \rightleftharpoons 2UF_3 + CrF_2$.

Thus,

(7) $K[Cr^\circ] = \dfrac{[UF_3]^2\,[CrF_2]}{[UF_4]^2}$.

The right-hand side of Eq. 7 is constant, according to steady-state condition 4(c). Therefore

$$K_{BP}[Cr^\circ]_{BP} = K_L[Cr^\circ]_L ,$$

where the subscript BP refers to balance point and L refers to a unit area at any loop position, or

(8) $\Delta C = \rho_{metal}\,[Cr^\circ]_{Inconel}\left(\dfrac{K_{BP}}{K_L} - 1\right)$.

The rate of diffusion as a function of time at any position L may then be obtained by combining Eqs. 4 and 8 to give

(9) $\left.\dfrac{dM}{dt}\right]_L = A\rho_{metal}\,[Cr^\circ]_{Inconel} \times$

$\times \left(\dfrac{K_{BP}}{K_L} - 1\right)\left(\dfrac{D}{\pi t}\right)^{1/2}$.

In order to obtain the over-all rate at which the chromium is being transferred, it is necessary to integrate the instantaneous rates over an entire hot or cold zone, as follows:

(10) $\dfrac{dM}{dt} = 2r\rho_{metal}\,[Cr^\circ]\left(\dfrac{\pi}{t}\right)^{1/2}$

$\displaystyle\int_{L_1}^{L_2}\left(\dfrac{K_{BP}}{K_L} - 1\right)D^{1/2}\,dL ,$

where r is the radius of the Inconel tube. If $T_L < T_{BP}$, $K_L < K_{BP}$, and $dM/dt > 1$, chromium is diffusing into the wall in the cold zone; the converse is true for the hot zone.

The integration indicated in Eq. 10 cannot be performed until the K_L and $D^{1/2}$ vs L relationships are known. Two important parameters are involved: (1) the wall temperature, which controls $D^{1/2}$, and (2) the metal-salt interface temperature, which controls K_L. These temperatures must be

available as a function of L in order to obtain over-all values of dM/dt.

Salt and Wall Temperature Relationship

When a loop is externally heated, the temperature of the circulating molten salt, T_s, will lag the loop wall temperature, T_w, with the temperature gradient being a function of the heat transfer coefficient and heat capacity of the salt. A heat balance on the simplest model of such a system is given by the equation

(11) $\dfrac{dT_s}{dt} + B(T_w - T_s) = 0$,

where

$B = \dfrac{2h}{\rho C_p r}$,

the quantities h, C_p, and ρ are the heat transfer coefficient, specific heat, and density of the salt, and r is the inner radius of the tubing.

An equation relating T_w, tubing length, L, velocity of circulating salt, u, and time, t, must be obtained in order to solve Eq. 11 under steady-state conditions. Actually all that must be assumed is the shape of the plot of T_w vs loop position. It is not at all unreasonable to assume that the equation of the plot is

(12) $T_w = T_{mean} + a \sin \omega t$,

where a is one-half the loop ΔT, that is, 0.5 (1060.8 − 933.3) °K, and ω is 2π times the flow velocity divided by the length of the loop.

The salt temperature, which may be obtained by combining Eqs. 11 and 12, is

$T_s = T_{mean} + \dfrac{Ba}{(B^2 + \omega^2)^{1/2}}\sin(\omega t - \phi)$,

where

$\phi = \tan^{-1}\dfrac{\omega}{B}$.

A plot of T_w and T_s is shown in Fig. 2.2.17. The physical properties of the salt, NaF-ZrF$_4$-UF$_4$ (50-46-4 mole %), give a value for B that is very nearly equal to the value of ω for the loop described above. Therefore ϕ was chosen to be 45 deg. A rotating vector representation of the T_w and T_s relationships is also shown in Fig. 2.2.17. After the graph was prepared, L was
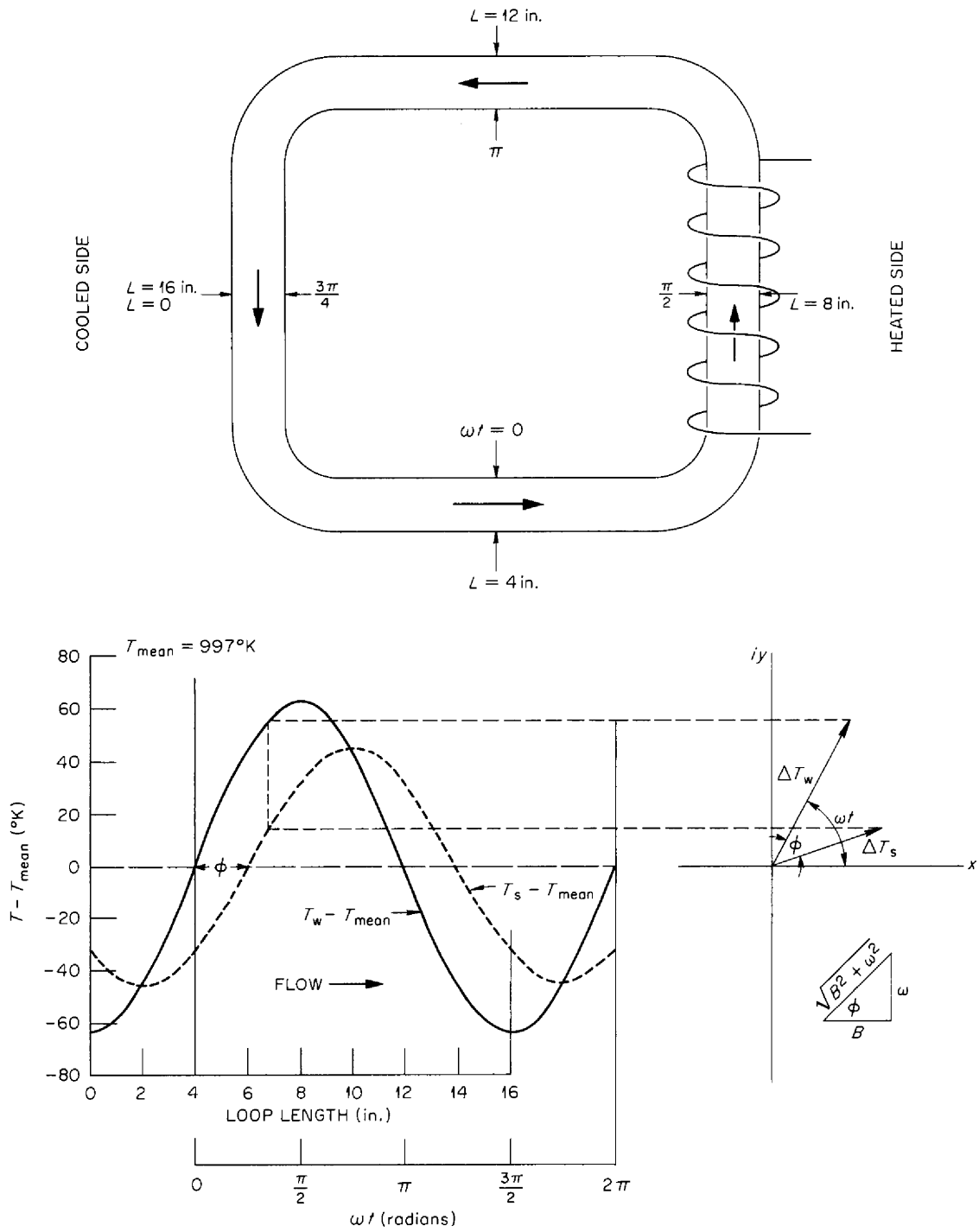
Fig. 2.2.17. Temperature-Time Relationships for Idealized Thermal-Convection Loop.

2.2.19. The curves on Fig. 2.2.19 are tentative; however, they strongly suggest that the amount of steady-state chromium migration within actual loops (similar to the type considered) will be very small.

ACTIVITIES IN ALLOYS

S. Langer

Measurements of the activities of the metallic components of container materials for fused-salt fuels have been made in order to study the effects of composition and temperature on the activities and thus on the corrosion resistance of container alloys. The activity of chromium in nickel-chromium alloys (Inconel) has been studied,[50] and data are presented here for the nickel-molybdenum system. In future work the chromium-molybdenum system is to be studied, as well as the ternary system nickel-molybdenum-chromium, which includes the INOR alloys developed by the ORNL Metallurgy Division.

Measurements of the activity of nickel in Ni-Mo alloys are being made by using the emf method described in the previous report.[51] The cell being used for the measurements is designed as shown in Fig. 2.2.20 to permit the tight gasketing required to maintain an inert atmosphere over the liquid metal bath in which the cell is immersed. The liquid metal bath was found to be necessary to prevent a large temperature gradient along the electrodes. A tin bath was unsatisfactory because a hard, sintered mass of oxide formed on the surface and frequently cracked the cells. Liquid bismuth baths are quite satisfactory, and the small amount of oxide that forms is not deleterious to the cell.

[50]M. B. Panish, *ANP Quar. Prog. Rep. Sept. 10, 1956,* ORNL-2157, p 100.

[51]S. Langer, *ANP Quar. Prog. Rep. Sept. 30, 1957,* ORNL-2387, p 130.

ORNL-LR-DWG 27052
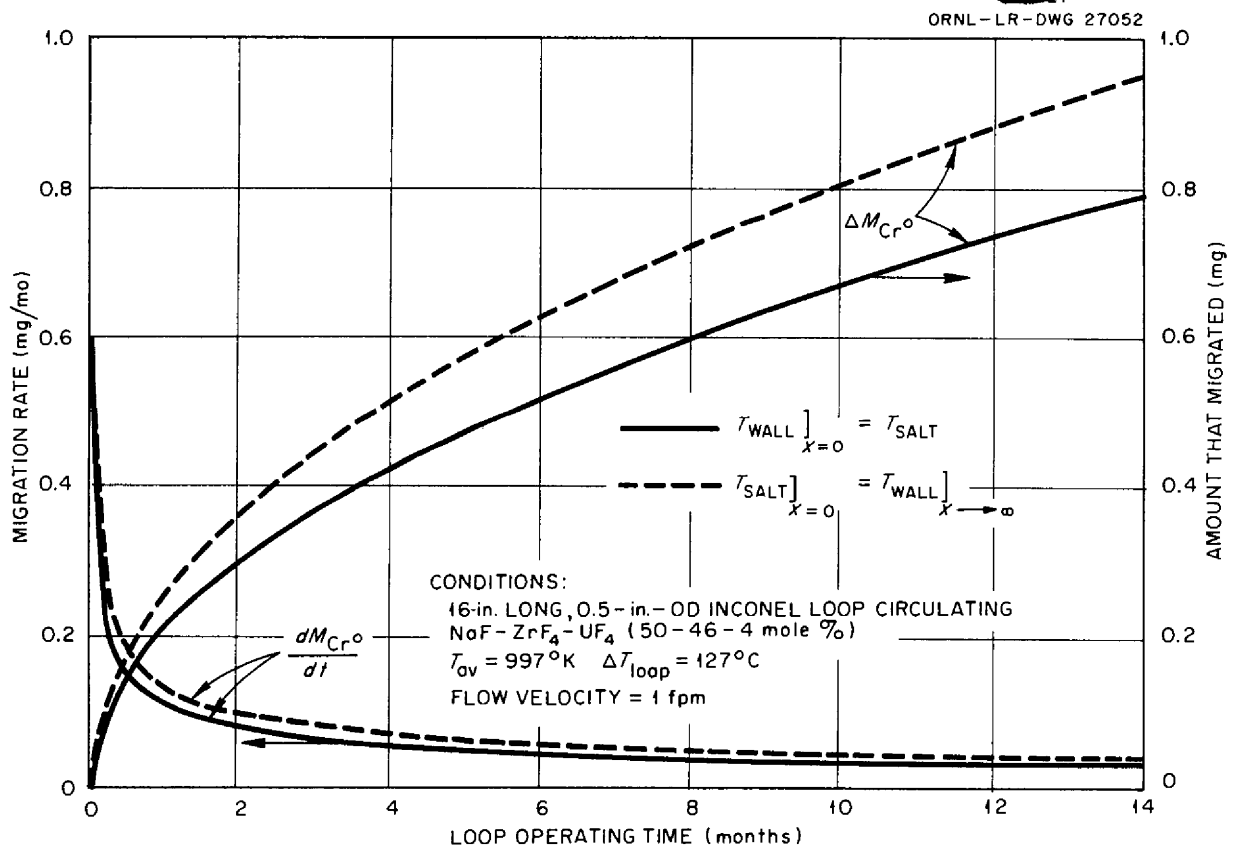
Fig. 2.2.19. Chromium Migration Characteristics for a Pre-equilibrated Thermal-Convection Loop.

THERMOCOUPLE WELL

TUNGSTEN-GLASS SEAL

TO HELIUM SUPPLY

SILVER-SOLDERED TUNGSTEN-NICKEL JOINT

CROSS SECTION OF CELL

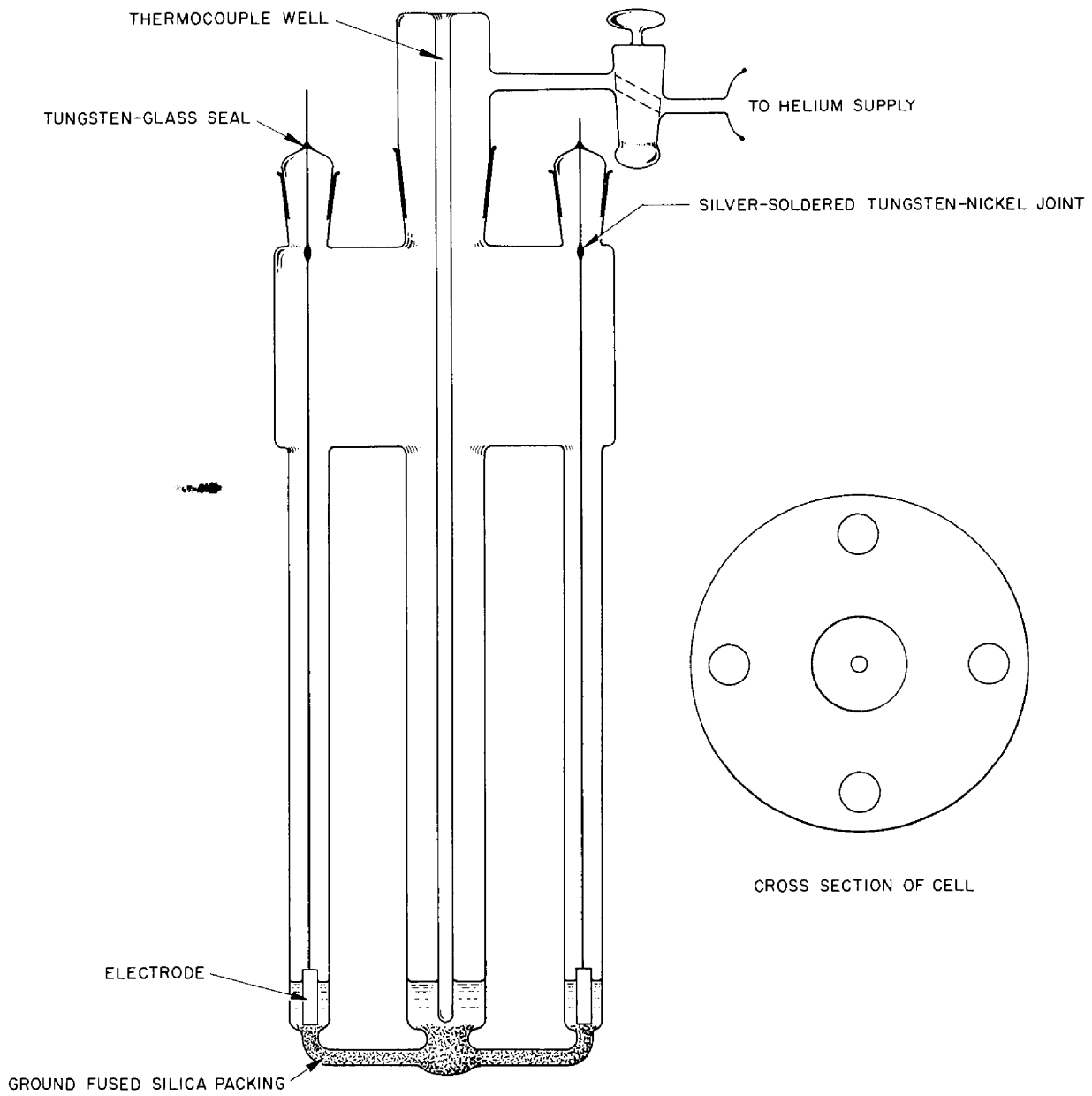ELECTRODE

GROUND FUSED SILICA PACKING

Fig. 2.2.20. **EMF Cell for Measuring Alloy Activities.**

Only preliminary data on two alloy compositions are available thus far. The activity of nickel in an alloy containing 90 mole % Ni is 0.70 at 800°C. This corresponds to an activity coefficient of 0.76. The behavior of this alloy in the cell appears to be quite reproducible. An alloy containing 80 mole % Ni has a nickel activity of about 0.32 at 800°C. The activity coefficient in this case is about 0.40. The data on this alloy have not yet been reproduced to within the desired precision.

The preliminary data seem to indicate large negative deviations from Raoult's law. From inspection of the nickel-molybdenum phase diagram,[52] this is to be expected. The 90 mole % Ni alloy is in the solid-solution region, and the rather large negative deviation should not be surprising in view of the proximity of the compound $MoNi_4$. The 80 mole % Ni alloy might have been expected to exhibit even greater deviation from ideality, since it is within the region of stability of the compound at 800°C.

It is expected that the precision and accuracy of the preliminary data will be improved by measurements now being made. Measurements are to be made of the activities of alloys containing as high a molybdenum content as is metallurgically feasible over a temperature range between 700 and 1000°C. Measurements over this temperature range will permit the determination of the temperature-dependent thermodynamic properties, and the data obtained at temperatures above 900°C will have additional interest, since the 900 to 1000°C temperature range is above the region of stability of both the compound $MoNi_4$ and the higher-molybdenum compound $MoNi_3$. In this region it would be expected that the activity of nickel would be more nearly ideal.

DISSIOLUTION OF STAINLESS STEEL FUEL ELEMENTS IN FLUORIDE MELTS

J. E. Eorgan   G. J. Nessle

The possibility of dissolving stainless steel fuel elements in molten fluorides, with the resultant advantage of adaptability to the present volatility process, made it desirable to do some exploratory experiments to determine the feasibility and general characteristics of such a

process. The choice of a solvent salt was based on the ability of the salt to dissolve or disintegrate a set minimum quantity of stainless steel fuel elements to yield a concentration of uranium in the molten salt which would be economically feasible for adaptation in the volatility process. From previous experience in handling various fluoride mixtures, the alkali fluoride compositions containing NaF, LiF, and KF seemed to be most promising. The composition chosen was NaF-LiF-KF (11.5-46.5-42 mole %), which combined relatively high solubilities of the structural metals nickel, chromium, and iron with a fairly low melting point (460°C).

For the first experiment, which was run to gain knowledge of the general characteristics of the dissolution process, a 2-kg batch of the chosen fluoride mixture was purified according to normal procedures in a copper-lined reactor vessel. The reactor vessel was equipped with copper thermocouple wells and dip lines, so that copper was the only metal that contacted the molten salt. After the purification and sampling steps, a type 347 stainless steel plate 4 in. square and 0.0625 in. thick, which weighed approximately 71 g, was suspended in the melt attached to a copper rod. The temperature was maintained at 650°C, and anhydrous HF was bubbled through the molten salt at approximately 1 liter/min. Hydrofluorination was continued for a period of 24 hr, and salt samples were taken every 4 hr. A sample of the stainless steel was submitted for analysis after the 24-hr period, and the following report of the analysis was received:

Component	Amount (wt %)
Ni	10.3
Cr	17.6
Fe	69.8
Nb	1.72

The results obtained from analyses of the seven salt samples are compared in Table 2.2.23 with the theoretical concentrations in the salt if the structural metals in the type 347 stainless steel plate had completely dissolved.

At the conclusion of the experiment the molten salt was transferred from the reactor vessel so that the copper liner could be examined. It was found by examination of the cooled melt and the

---

[52]American Society for Metals, *Metals Handbook*, 1948 ed., p 1230, American Society for Metals, Cleveland, 1948.

Table 2.2.23. Results of First Experimental Study of the Dissolution of Type 347 Stainless Steel in NaF-KF-LiF Eutectic by Hydrofluorination

Sample No.	Period of Hydrofluorination (hr)	Metal Concentrations in Salt Samples					
		Ni		Cr		Fe	
		ppm	g	ppm	g	ppm	g
Type 347 stainless steel*			7.3		12.5		49.6
1	0	40		30		280	
2	4	2955	5.9	720	1.4	9,620	19.2
3	8	3465	6.9	1280	2.5	10,795	21.6
4	12	3840	7.7	1850	3.6	12,375	24.7
5	16	3900	7.8	1410	2.8	9,620	19.2
6	20	3730	7.5	960	1.9	7,830	15.6
7	24	4005	8.0	1490	3.0	9,720	19.4

*Concentrations given are calculated values based on complete dissolution of sample in salt.

reactor vessel that the steel plate had completely dissolved or disintegrated and that some odd nodule-type salt formations had remained in the reactor, attached to the support rod and the dip leg at about the liquid level. These formations appeared to be water soluble, and no metal particles were visible. From the results given in Table 2.2.23, it seemed that the plate was completely dissolved at the end of 12 hr, since metal concentrations did not increase after this point. All the nickel was accounted for in the bulk of the transferable melt, but only half the iron and less than one-fourth the chromium could be found.

The first experiment established that dissolution of the steel plate was possible, and therefore a second experiment was run to investigate further the disposition of the structural metals in the molten mixture. The conditions of the first experiment were duplicated as closely as possible, but only three filter-stick salt samples were taken, on the assumption that dissolution of the steel plate would occur as it had in the first experiment. An attempt was made to obtain a closer material balance in order to give a better idea as to the disposition of the dissolved metal. At the completion of the experiment the salt batch was transferred from the reaction vessel into a tared receiver can

through a sintered nickel filter with 0.0015-in. pores.

The nodule type of formation occurred again on the steel plate support rod and the dip leg. A rough material balance is given below:

	Amount (g)
Type 347 stainless steel plate	71
Total salt charge	2000
Transferable salt	1657
Filter-stick samples (3)	67
Nontransferable salt left in reactor	347 (by difference)

Samples of each item were submitted for chemical analysis to determine the distribution of the nickel, chromium, and iron, and the results are presented in Table 2.2.24.

Accurate weights of the salt sections that made up sample 4 were difficult to obtain, because these nodules had to be broken off the support rods and the sides of the copper liner. The weights were sufficiently accurate, however, that by making some liberal assumptions a rough material balance was obtained. Samples 2 and 3 were assumed to be the most homogeneous samples as far as nickel concentration was concerned, and the analyses were in good agreement

Table 2.2.24. Results of Second Experimental Study of the Dissolution of Type 347 Stainless Steel
in NaF-KF-LiF Eutectic by Hydrofluorination

Sample No.	Sample Description	Metal Concentrations in Salt Samples					
		Ni		Cr		Fe	
		ppm	g	%	g	%	g
	Filter stick samples (67 g)						
1	Taken before hydrofluorination	2300*	4.6	0.025	0.5	0.058	1.1
2	Taken after 12 hr of hydrofluorination	3700	7.4	0.18	3.6	2.1*	41.8
3	Taken after 24 hr of hydrofluorination	3600	7.2	0.26	5.2	1.36	27.2
4	Nondule-type formations on support rod and dip leg (~347 g)	2300	0.7	3.25	9.0	9.6	26.4
5	Transferable material collected in receiver can (1657 g)	9100*	15.0	0.42	6.9	1.70	28.2

*Analyses were questionable but were not rechecked.

with those of similar samples from the first experiment. A rough material balance of the structural metals in the fluoride salt is given in Table 2.2.25, and fairly close agreement with theoretical values may be seen.

In order to determine the effect of uranium on the dissolution of type 347 stainless steel fuel elements in an alkali metal fluoride salt such as NaF-LiF-KF (11.5-46.5-42 mole %), two experiments were run in which the uranium-bearing salt NaF-LiF-KF-UF$_4$ (10.9-44.5-43.5-1.1 mole %) was used as the solvent. In a practical application the uranium would come from the fuel elements.

Table 2.2.25. Material Balance of Structural Metals
from the Dissolution of Type 347 Stainless Steel Plate
in NaF-LiF-KF Eutectic

Sample No.	Weight of Material Analyzed (g)	Metals Found in Salt (g)		
		Ni	Cr	Fe
3	1724	6.4	4.5	23.4
4	347	0.8	11.3	33.3
Totals	2071	7.2	15.8	56.7
Theoretical values for type 347 stainless steel	71	7.3	12.5	49.5

Of greatest concern in the dissolution process was the possibility of concentrating the uranium in the nontransferable, that is, high-melting, phase of the salt bath during dissolution of the steel fuel element. Previous experiments had shown that such phases could occur.

In the first of the two experiments, a steel plate 4 in. square and $\frac{1}{16}$ in. thick, which weighed 71 g, was dissolved in 2 kg of molten salt at 1200°F by bubbling HF gas through the bath at approximately 1 liter/min. The dissolution process was complete at the end of 12 hr, according to analytical results. At the end of 24 hr the melt was transferred through a sintered nickel filter into a storage can. Approximately 300 g of material remained in the reactor vessel as the nontransferable high-melting phase. The uranium analysis of the salt bath prior to dissolution of the stainless steel was 6.3%. The analysis of the transferable salt showed a uranium content of 6.5%, and the nontransferable salt contained 2.4% U. The chromium and iron tended to concentrate in the nontransferable phase. In general, therefore, the presence of uranium seemed to have little effect, if any, on the dissolution process, and the uranium showed no tendency to concentrate in the nontransferable phase.

In the second experiment the conditions described above were duplicated, except that a piece of stainless steel 4 × 12 × $\frac{1}{16}$ in., which

weighed 213 g, was used. In this case dissolution again seemed to be complete at the end of 12 hr, according to chemical analysis. Attempts to transfer the salt bath through a sintered nickel filter were fruitless, however, even though the salt temperature was raised to 1400°C in 50-deg increments. The filter was finally removed, and the salt was transferred through tubing. Approximately 740 g of salt remained in the reactor vessel. This nontransferable phase appeared to be crystalline after freezing and could be described as mushy at high temperature. The nickel again appeared to remain completely in solution, there being little difference in nickel concentration between the transferable and nontransferable phases. Small filter samples taken at 6-hr intervals prior to transfer of the bath gave nickel concentrations close to those found in the bulk phases. The iron and chromium again concentrated in the nontransferable phase and were present to a fair extent as metal crystals. The uranium analysis showed 6.5% in the original bath, 6.7% in the transferable phase, and 3.3% in the nontransferable phase.

In general it appears that the stainless steel concentration used in this experiment was too high, although the dissolution or disintegration process was not appreciably affected. If less stainless steel were used, a practical process could be evolved for removing the uranium from the steel and leaving a constant and nonaccumulative heel in the reactor vessel. This heel could be flushed out periodically with a dummy salt mixture if desired.

OXIDATION OF MIXTURES COMPOSED OF SODIUM AND POTASSIUM

E. E. Ketchen

A study of the oxidation of sodium and potassium mixtures under carefully controlled conditions has been made in an attempt to determine the effect of certain variables on the final composition of the mixed oxides. The variables studied include (1) the original composition of sodium-potassium mixture, (2) the temperature of oxidation, and (3) the temperature and time of equilibration following the oxidation.

For the first experiments, which were performed at 25 to 30°C, the equipment consisted of a glass capsule 6 in. long and 1 in. in diameter, with a sintered glass disk installed midway in the capsule. A similar capsule that was constructed of nickel was used at elevated temperatures. The oxidation was accomplished by the introduction of measured volumes of dry air. The oxides were separated from the bulk of the liquid metals by filtration, and the remaining liquid metals were removed by amalgamation.

The early runs, in which Na-K (50-50 mole %) was used, gave a value of 25 for the Na-to-K ratio in the mixed oxides formed at 30 to 35°C. No significant difference was found at 200°C if the oxides were removed immediately, but, if they were formed at 200°C and equilibrated for 40 hr at 400°C, the ratio was found to be less than 10.

The early experiments were not precise, and therefore a more thorough study of the oxidation was made at 30 to 35°C in an attempt to find conditions that would yield more precise results. The glass apparatus was modified to provide a larger surface for oxide formation, and all operations were carried out in a vacuum dry box in order to reduce contamination by water vapor. The oxidation of two compositions of the Na-K mixture was studied under the modified conditions, and the results are presented in Table 2.2.26.

It is evident from the lack of precision in the data that a close control of the variables involved is absolutely essential. It is apparent, however, that the necessary control is extremely difficult to accomplish. Traces of moisture, which is the most likely contaminant, should tend to reduce the Na-to-K ratio, and therefore the larger values are probably closest to the correct ratio. The lack of precision in these experiments makes it difficult to establish any quantitative effect of composition of the alkali metal mixture on the Na-to-K ratio in the mixed oxides. The data, however, show a significant decrease in the ratio upon an increase in the K content from 49 to 77 wt %.

Table 2.2.26. Composition of Oxides Formed by Oxidation of Sodium-Potassium Mixtures at 30 to 35°C

Composition of Na-K Mixtures (wt %)	Composition of Oxides			Composition of Na-K Mixtures (wt %)	Composition of Oxides		
	Na (mg)	K (mg)	Na-to-K Ratio		Na (mg)	K (mg)	Na-to-K Ratio
51-49	13.8	0.17	82	23-77	8.1	0.27	30
	6.7	0.089	75		7.4	0.23	32
	5.3	0.058	91		8.6	0.31	28
	4.1	0.085	48		4.7	0.21	22
	4.3	0.049	88		5.9	0.30	20
	11.6	0.13	89		4.4	0.31	14
	10.4	0.21	50		8.5	0.31	27
	8.5	0.15	56		8.1	0.31	26
	7.7	0.11	70		6.0	0.23	26
	4.0	0.24	17		5.4	0.19	28
	6.6	0.14	47		5.6	0.30	19
	21.0	0.37	57		4.9	0.36	14
			Av 64 ± 22		7.5	0.22	34
					18.0	0.48	37
							Av 25 ± 7

2.3. PHYSICAL PROPERTIES OF MOLTEN MATERIALS

F. F. Blankenship

SUMMARY OF ARE FUEL VAPOR-PRESSURE STUDIES

R. E. Moore

The vapor pressures of a number of fused salt mixtures in the NaF-ZrF_4 and NaF-ZrF_4-UF_4 systems were measured to obtain information needed for the selection of a fuel for the Aircraft Reactor Experiment. A quasi-static method of vapor pressure measurement, which originated with Rodebush and Dixon[1] and was later used by Fiock and Rodebush,[2] was chosen for this work because it appeared to be the most reliable method for use at the temperatures and pressure range (5–200 mm Hg) considered. The apparatus and technique have been described by Beusman.[3]

---

[1]W. H. Rodebush and A. L. Dixon, *Phys. Rev.* 26, 851 (1925).

[2]E. F. Fiock and W. H. Rodebush, *J. Am. Chem. Soc.* 48, 2522 (1926).

[3]C. Beusman, *Activities in the KCl-FeCl$_2$ and LiCl-FeCl$_2$ Systems*, ORNL-2323 (May 15, 1957).

The ZrF_4 used for vapor pressure measurements and for the preparation of purified mixtures was material which chemical analysis showed to be 98 to 99% pure. Uranium tetrafluoride was obtained from the Mallinckrodt Chemical Works. The NaF used was reagent-grade material. The NaF-ZrF_4 and NaF-ZrF_4-UF_4 mixtures were prepared by fusion under an inert atmosphere, followed in every case, except that of the composition 75 mole % ZrF_4–25 mole % NaF, by treatment with HF, H_2, and inert gas, in the order stated.

A summary of vapor pressure data for pure ZrF_4 and mixtures of ZrF_4 and NaF is given in Table 2.3.1, and a summary of the data for UF_4-bearing mixtures related to the ARE fuel or fuel concentrates is given in Table 2.3.2. References in the tables indicate the ANP progress report in which the data are reported. In some cases, as indicated, the data were refined or extended later.

Petrographic examinations[4] of samples distilled from binary mixtures containing more than 43

---

[4]Made by T. N. McVay, Consultant, ORNL.

Table 2.3.1. Vapor Pressures of NaF-ZrF₄ Mixtures and of ZrF₄

ZrF_4 Content (mole %)	Temperature Range (°C)	Constants for the Vapor Pressure Equation*		Reference
		A	*B*	
43	868–1034	7,289	7.34	ORNL-1609, p 106
47	795–994	7,206	7.62	ORNL-1649, p 99**
50	812–990	7,675	8.14	ORNL-1649, p 99**
57.8	732–906	8,250	9.00	ORNL-1609, p 106
75	754–844	9,369	10.57	ORNL-1771, p 129
100	713–839	10,936	12.11	ORNL-1375, p 147**

*The constants, A and B, are for the general equation

$$\log_{10} p \text{ (mm Hg)} = -\frac{A}{T(^\circ K)} + B \, .$$

**The data given were revised and extended from those given in the ANP quarterly progress report cited.

Table 2.3.2. Vapor Pressures of NaF-ZrF$_4$-UF$_4$ Mixtures

Mixture Number	Composition (mole %)			Temperature Range (°C)	Constants for the Vapor Pressure Equation*		Reference
	NaF	ZrF$_4$	UF$_4$		A	B	
27	40	50	4	807–968	7779	8.281	ORNL-1375, p 148**
30	50	46	4	807–979	7551	7.888	ORNL-1375, p 148**
33	50	25	25	848–1096	6906	6.844	ORNL-1515, p 159
39	65	15	20	1166–1266	6944	5.86	ORNL-1609, p 106
40	53	43	4	790–1012	7106	7.37	ORNL-1556, p 88**

*The constants, A and B, are for the general equation

$$\log_{10} p \ (\text{mm Hg}) = -\frac{A}{T(^\circ K)} + B \ .$$

**The data given were revised and extended from those given in the ANP quarterly progress report cited.

mole % ZrF$_4$ show them to be virtually pure ZrF$_4$. Thus the total pressures are approximately equivalent to the partial pressures of ZrF$_4$. As may be seen in Fig. 2.3.1, which is a plot of pressure vs composition at 912°C obtained from the data in Table 2.3.1, large negative deviations from ideal behavior occur. Thus it appears that complexing exists in the solution.

The actual ARE fuel composition, 53.09 mole % NaF–40.73 mole % ZrF$_4$–6.18 mole % UF$_4$, was determined by titration to criticality, and its vapor pressure was not measured. The vapor pressures of compositions in the neighborhood of the ARE fuel composition were low enough, however, that operational difficulties traceable to ZrF$_4$ vapor were neither expected nor encountered in the ARE.

Estimated vapor pressures for a number of other ZrF$_4$-bearing mixtures containing UF$_4$ were given in a recent report.[5] The composition given that is nearest to that of the actual ARE fuel contains 6.5 mole % UF$_4$–40 mole % ZrF$_4$. Its vapor pressure at the fuel outlet temperature (1522°F) is about 8 mm Hg.
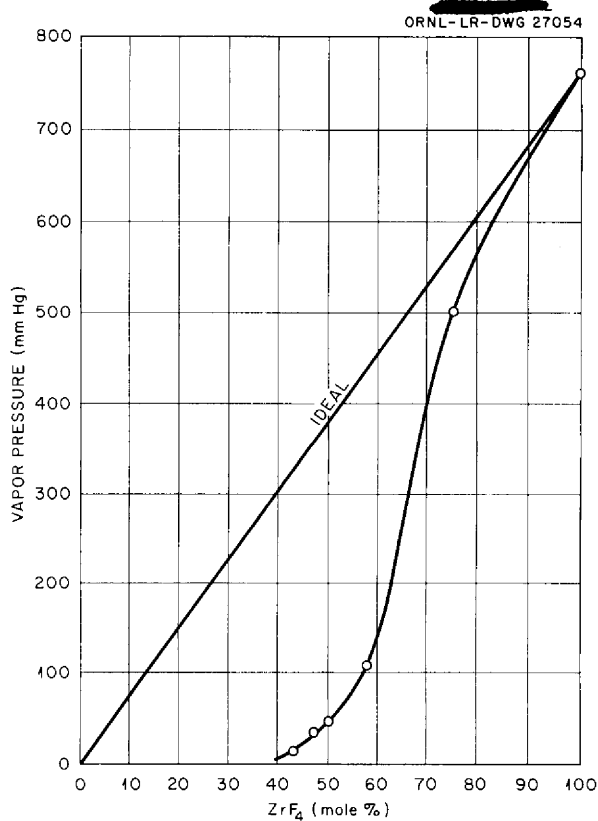
[5]S. Cantor, *ANP Quar. Prog. Rep. June 30, 1957,* ORNL-2340, p 158.

ORNL-LR-DWG 27054

Fig. 2.3.1. Vapor Pressures of NaF-ZrF$_4$ Mixtures at 912°C.

VAPOR PRESSURES OF MOLTEN FLUORIDE MIXTURES

S. Cantor

Vapor pressure studies have provided, as part of the search for optimum fuels, directly determinable physical property data, as well as a measure of the thermodynamic activities of components in fuel mixtures. The main objective of the studies was to obtain the vapor pressures of binary fuel solvents, such as the mixtures of ZrF_4 with alkali fluorides. It could be assumed that the addition of small amounts of fuel (2–4 mole % UF_4) to the solution would not markedly alter the solution structure and that the vapor pressure would change in accordance with Raoult's law.

As stated in the preceding section, a quasi-static method developed by Rodebush and Dixon was used to measure vapor pressures. The compositions to be studied were prepared by weighing and mixing the purified components in a dry box. The alkali fluorides were purified by fusing, slowly cooling the melt, and selecting clear crystal fragments. The commercially obtained ZrF_4 was further purified by vacuum sublimation of the best hafnium-free material. All other pure components and mixtures used were produced at the Laboratory.

It is important to note here that there was a a concurrent effort to measure vapor pressures being carried out at Battelle Memorial Institute

for which the transpiration or carrier-gas technique was used. The results of the BMI research are discussed here in relation to the work done at ORNL.

The binary systems studied in both laboratories, along with the references which most fully describe the results, are given in Table 2.3.3. In most cases it was necessary to measure the vapor pressure of the pure components in order to be able to calculate the activities. The references for these measurements are given in Table 2.3.4.

For the ZrF_4 systems, it was usually found that sharp decreases in ZrF_4 vapor pressures occurred as the alkali fluoride concentrations were increased. Also, there was a correlation between decreasing ZrF_4 vapor pressure and alkali cation size. The purpose of studying the $7NaF \cdot 6ZrF_4$-$7NaF \cdot 6UF_4$ system was to investigate the effect of partial substitution of UF_4 for ZrF_4 while maintaining a constant NaF concentration. The results clearly indicated that this substitution decreased the vapor pressure, but to a far less degree than increasing the amount of alkali fluoride.

For the compositions studied at ORNL, it was at first assumed that the measured pressures were due to ZrF_4 alone. Above about 40 mole % ZrF_4, this assumption, tested by sampling of the vapor, proved to be quite valid. At lower liquid-phase concentrations of ZrF_4, the probable formation of vapor-phase compounds made the assumption

Table 2.3.3. Binary Solvent Systems Whose Vapor Pressures Were Measured as Part of the ANP Program

System	Reference
LiF-ZrF_4	*Vapor Pressures of the Rubidium Fluoride—Zirconium Fluoride and Lithium Fluoride—Zirconium Fluoride Systems,* BMI-1199 (June 27, 1957)
NaF-ZrF_4	*Vapor Pressures of the Sodium Fluoride—Zirconium Fluoride System and Derived Information,* BMI-1064 (Jan. 9, 1956)
KF-ZrF_4	*ANP Quar. Prog. Rep. June 10, 1956,* ORNL-2106, p 111
RbF-ZrF_4	*Vapor Pressures of the Rubidium Fluoride—Zirconium Fluoride and Lithium Fluoride—Zirconium Fluoride Systems,* BMI-1199 (June 27, 1957)
$7NaF \cdot 6ZrF_4$-$7NaF \cdot 6UF_4$	*ANP Quar. Prog. Rep. Dec. 31, 1956,* ORNL-2221, p 146
NaF-BeF_2	*Vapor Pressure and Equilibrium Studies of the Sodium Fluoride— Beryllium Fluoride Systems,* BMI-1186 (May 27, 1957)

Table 2.3.4. References for Vapor Pressures of Pure Components

Compound	Reference
ZrF_4	*Vapor Pressures of the Sodium Fluoride—Zirconium Fluoride System and Derived Information,* BMI-1064, p 7 (Jan. 9, 1956)
UF_4	*ANP Quar. Prog. Rep. June 10, 1955,* ORNL-1896, p 65
BeF_2	*Vapor Pressure and Equilibrium Studies of the Sodium Fluoride—Beryllium Fluoride Systems,* BMI-1186, p 3 (May 27, 1957)
LiF, NaF, KF, RbF, CsF	*ANP Quar. Prog. Rep. March 31, 1957,* ORNL-2274, p 128
NaF	*Vapor Pressures of the Sodium Fluoride—Zirconium Fluoride System and Derived Information,* BMI-1064, p 7 (Jan. 9, 1956)
LiF, RbF	*Vapor Pressures of the Rubidium Fluoride—Zirconium Fluoride and Lithium Fluoride—Zirconium Fluoride Systems,* BMI-1199, p 3 (June 27, 1957)

poorer. The vapor compounds were first postulated by Sense[6] in order to explain apparent NaF partial pressures obtained in the NaF-ZrF_4 system. Vapor compounds also had to be postulated in the LiF-ZrF_4, RbF-ZrF_4, and NaF-BeF_2 systems if the thermodynamic stability of these systems was to be preserved. Because the vapor above the molten salt solutions under study at ORNL (RbF-ZrF_4, KF-ZrF_4, NaF-ZrF_4) was virtually all ZrF_4, it was still possible to calculate ZrF_4 activities[7,8] directly from total pressure measurements. These activities were then used to form the analytical expression

(1) $$\log \gamma_1 = AN_2^2 + BN_2^3 ,$$

where γ_1 is the activity coefficient of ZrF_4, N_2 is the mole fraction of alkali fluoride, and A and B are constants. This expression was used in the Gibbs-Duhem equation, in the form

(2) $$N_1 \, d \log \gamma_1 + N_2 \, d \log \gamma_2 = 0 ,$$

where N_1 is the mole fraction of ZrF_4 and γ_2 is the activity coefficient of the alkali fluoride.

Equation 2, in turn, was used to calculate alkali fluoride activities.[7,8] The alkali fluoride activities could be considered to be only approximate, because it was necessary to extrapolate Eq. 1 to $N_2 = 1$ in order to solve the Gibbs-Duhem equation. The results of these calculations showed that the alkali fluoride activity decreased sharply with increasing ZrF_4 concentration.

Once a large body of vapor pressure data was accumulated for molten mixtures of ZrF_4 and alkali fluorides, estimates of vapor pressures were made for a number of unmeasured compositions of ZrF_4-base fuels.[9] In these estimates, the vapor pressures of ZrF_4 were assumed to be linear functions of composition over the appropriate extrapolation or interpolation range. The vapor pressures of fuel mixtures composed of UF_4 and alkali fluorides were too small to measure by the methods used, but, with the vapor pressure known for each pure fluoride used in the melt, estimates of the upper limits of vapor pressure were compiled[9] by assuming that Raoult's law was obeyed by the alkali fluorides and that Henry's law was obeyed by UF_4.

Any continuation of vapor pressure investigations of fused fluorides of reactor significance should involve systems containing BeF_2. One

---

[6]K. A. Sense *et al., Vapor Pressures of the Sodium Fluoride—Zirconium Fluoride System and Derived Information,* BMI-1064 (Jan. 9, 1956).

[7]S. Cantor and S. D. Christian, *ANP Quar. Prog. Rep. Sept. 10, 1956,* ORNL-2157, p 108.

[8]S. Cantor, *ANP Quar. Prog. Rep. Dec. 31, 1956,* ORNL-2221, p 145.

[9]S. Cantor, *ANP Quar. Prog. Rep. June 30, 1957,* ORNL-2340, p 158.

such important system that is amenable to measurement by the methods now in use or under development is $LiF-BeF_2$. The determination of activities in BeF_2 systems presents a greater problem than for the corresponding ZrF_4 systems. The difficulty that arises is the inability to equate BeF_2 vapor pressures to total vapor pressures except at higher BeF_2 concentrations (75 mole % or more). In compositions below these higher concentrations, vapor compounds[10] start contributing sizably to the total pressure. Therefore, it will be necessary to obtain partial pressures of each component in order to calculate activities. At present, the carrier-gas technique is being developed to aid in measuring the partial pressures. The transpiration vapor pressures are not sufficient to be useful in obtaining the activities of the alkali fluorides in these mixtures. Recent evidence convincingly shows that there are appreciable quantities of dimeric and even trimeric molecules in the vapor of most alkali halides.[11] Since the vapor pressures obtained in the transpiration method are dependent on the molecular weight of the vapor, total pressures will still have to be measured in order to help obtain the partial pressures of the species involved.

A MASS SPECTROMETRIC STUDY OF SALT VAPORS

L. O. Gilpatrick   M. Blander

The vapors of some fused salts have been shown, as stated above (and in ref 12), to contain double and triple molecular species. An understanding of the fundamental nature of these associated species in the vapor is necessary for the interpretation of the vapor pressure data of fuel mixtures in terms of the activities of the volatile components. It is also necessary for the estimation of the volatility of components of fused salt mixtures. Polymer formation can cause components of salt mixtures to be even more volatile as part of an associated species than the pure component is, in some cases.

A molecular-beam mass spectrometric study, which continued the work of Rosenstock *et al.*,[13] was undertaken in order to develop a method of exploring the vapor-phase associations so that the occurrence of the phenomenon and its effects could be predicted. The mass spectrometer provides a measure of the ionized progeny of individual associated vapor species. With this technique, the individual vapor species which were the precusors of the observed ions can be inferred, and by control and measurement of the temperature of the vapor source the internal energy of vaporization and of association of the detectable species can be measured. The mass spectrometer is uniquely suited to measuring these energies of association.

Potassium chloride was chosen as a suitable material with which to develop the method, since prior studies of that compound had been reported.[3,11,13] It was incompletely studied by Rosenstock by using a hot filament as a source of ions in the mass spectrometer. This method yields only relative energies of vaporization of the various vapor species. The ion species observed were K^+ and KCl^+, which are derived from monomeric KCl, primarily, and K_2Cl^+, which is derived from a dimeric species, K_2Cl_2. The existence of these species agrees, in general, with the findings of Miller and Kusch[11] and of Beusman.[3]

The mass spectrometer used in this study was a 6-in.-radius 60-deg Nier-type machine with a metal envelope; it was evacuated by a mercury diffusion pump.[14] The accelerating voltage, 2000 v, was supplied by a well-regulated source capable of delivering a current of 2 ma. The ion-beam intensity was measured by a vibrating-reed electrometer. The output from the electrometer was recorded on a 0 to 10 mv strip-chart recorder, which produced a permanent record of the ion-beam intensities.

The effusion cell used to produce the molecular beam of salt molecules, as finally modified, is shown in Fig. 2.3.2. The cell was heated from the 110-v main by means of a voltage regulator and a variable autotransformer. This arrangement

[10]K. A. Sense, R. W. Stone, and R. B. Filbert, Jr., *Vapor Pressure and Equilibrium Studies of the Sodium Fluoride–Beryllium Fluoride System*, BMI-1186 (May 27, 1957).

[11]R. C. Miller and P. Kusch, *J. Chem. Phys.* 25, 860 (1956).

[12]S. A. Ochs, R. E. Cote, and P. Kusch, *J. Chem. Phys.* 21, 459 (1953).

[13]H. Rosenstock *et al.*, *Mass Spectra Studies of Silver Halides and Alkyl Halides*, paper No. 34 presented at the 4th Annual Meeting of the American Society for Testing Materials, Committee E-14 on Mass Spectrometry, Cincinnati, May 28, 1956.

[14]G. F. Wells, *Stable Isotope Research and Production Semiann. Prog. Rep. May 20, 1954*, ORNL-1732, p 27.
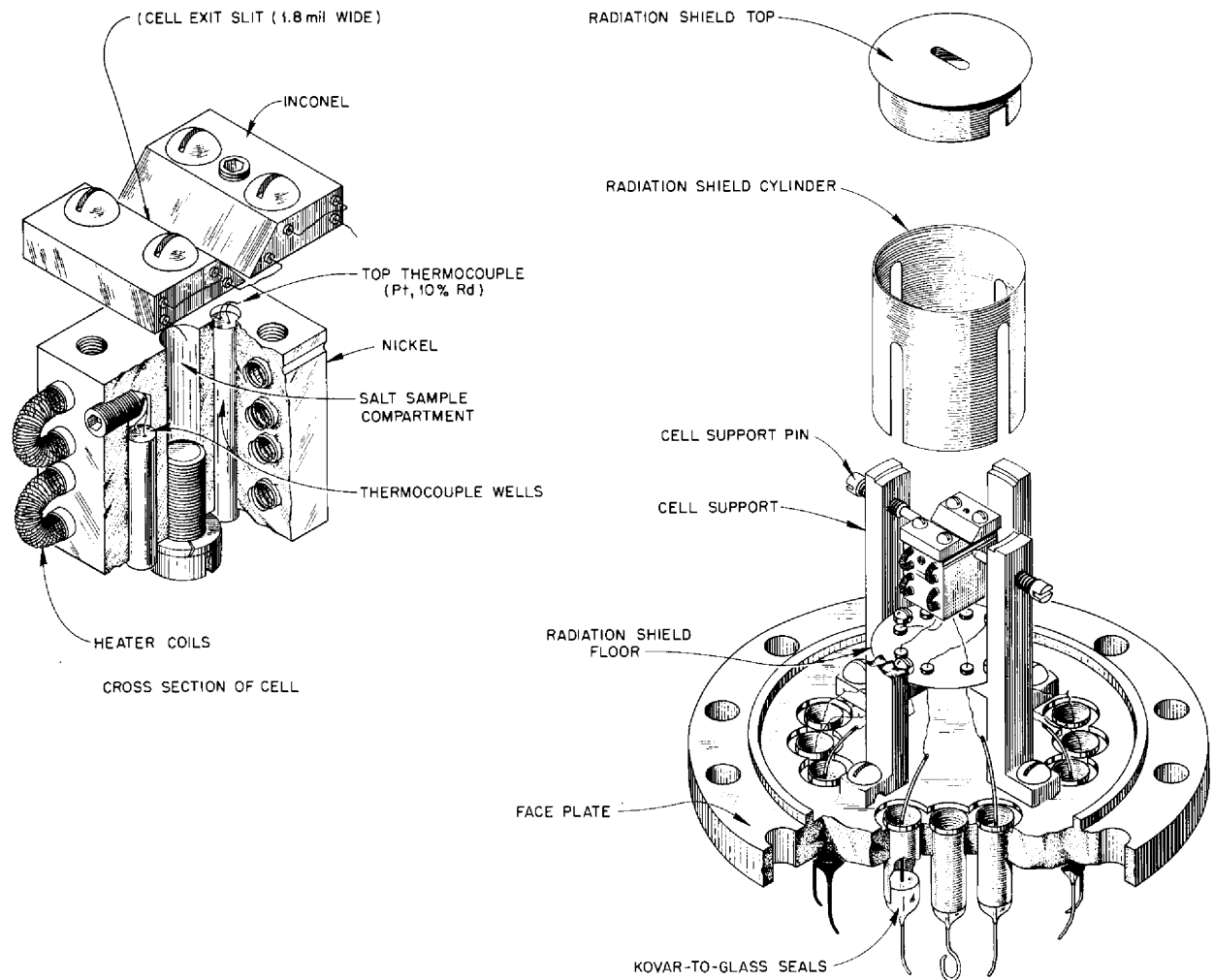
Fig. 2.3.2. Effusion Cell.

proved to be sufficiently stable as a source of heater voltage for temperatures to be maintained to within a few tenths of a degree for periods of 1 hr or more. Temperatures of the cell were measured by two platinum–platinum-rhodium thermocouples, one fixed in the cell body and the other fixed in one of the slits. These thermocouples were calibrated with U. S. Bureau of Standards thermocouples prior to use. The cell body and the cell slits were independently heated in the final equipment, and an attempt was made to keep the slits at a higher temperature than that of the cell, by at least 3°C, to prevent the deposition of salt on the slits. The lowest temperature, that is, the cell body temperature, was used in all calculations as the temperature most representative of the vapor temperature. The effusing stream of salt vapors was roughly collimated in order, primarily, to control the deposition of salt at unwanted locations in the source. Salt deposits upon insulators were an early source of electrical leakage and are a troublesome factor in this type of experiment. Only those molecules which are intercepted by the ionizing electron stream are

effective in forming ions, so narrow collimation of the molecular stream is not necessary.

The effusion cell was charged with reagent-grade potassium chloride which had been fused in platinum. Clear crystals of salt were chosen from the melt and loosely packed into the effusion cell. After the cell was assembled and the slits were adjusted to 2.5 mils with a feeler gage, it was mounted in the mass spectrometer and checked for electrical leakage and thermocouple response. The heaters were then adjusted to give the cell a temperature of 350 to 400°C, and the outer envelope of the mass spectrometer was raised to a temperature of 250°C. This bakeout-degassing operation lasted at least 16 hr and, in some cases, for a number of days, until the hydrocarbon background was reduced to a negligible level at the region of the lower mass position for potassium chloride (74).

The data were taken by raising the temperature of the cell in increments of 20 to 30 deg and making measurements until constant temperatures and mass intensities were observed. This time interval varied from more than $1\frac{1}{2}$ hr at the lower temperatures to less than 15 min at the higher temperatures. An attempt was made to take data from both an ascending and a descending sequence of temperatures; however, the salt capacity of the effusion cell was such that it showed signs of exhaustion before any complete total sequence could be measured.

If the pressure of the salt vapor is low enough so that the mean free path of the molecules is greater than the slit width of the effusion cell, the number of molecules of a given kind escaping from the slit should be a function only of the temperature. Also if the area of the slit is small compared with the inner surface area of the cell, the pressure of salt vapor in the cell should approach the equilibrium pressure at a given temperature. In this experiment the ratio of cell surface area to slit area was 800. The measured ion current, or mass spectrometer peak height, of any of the ionized progeny n_i' of the species i as a function of the temperature of the salt in the effusion area is given by

$$(1) \qquad \frac{\partial \ln n_i'}{\partial (1/T)} = -\frac{\Delta E_i}{R} ,$$

where E_i is the energy of vaporization of the species i, a quantity which cannot be obtained

directly by any other experimental method. The values of the absolute partial pressure of the species are not obtainable by this method because the ionization efficiencies for the production of the ionized progeny are not, in general, known.

If a salt species, KCl, forms a dimer, $(KCl)_2$, the following equilibrium obtains:

$$(2) \qquad (KCl)_2 \rightleftharpoons 2KCl$$
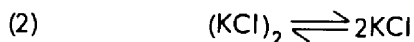
The equilibrium constant K is given by

$$(3) \qquad K = \frac{p_1^2}{p_2} ,$$

where p_1 is the partial pressure of the monomer and p_2 is that of the dimer. The standard free energy, $\Delta F°$, is given by

$$(4) \qquad \Delta F° = -RT \ln K \cong \Delta E° + RT - T \Delta S° .$$

The quantity $\Delta S°$, which can be estimated by the use of statistical mechanics, increases with an increase of mass.[15] The energy, $\Delta E°$, can be estimated for alkali halides by considering the ions as charged, polarizable spheres. This quantity can also be obtained from the experimental data by the relation

$$(5) \qquad \Delta E° = 2 \Delta E_1 - \Delta E_2 ,$$

where ΔE_1 and ΔE_2 can be calculated from the measurements by using Eq. 1. These energies are one of the two sets of factors that control the association, and, at present, they can be measured independently only by the method described here.

Several measurements were made on KCl prior to the use of heated slits, and none of the experiments were completely successful because of the formation of deposits to a greater or lesser degree at the exit slit. The deposits had the effect of reducing the intensity of the beam in an arbitrary and variable manner. A plot of the log of the peak heights of the observed KCl^+ and K_2Cl^+ species vs $1/T$, as obtained in one of these measurements, is shown in Fig. 2.3.3. The slopes of these lines, calculated by using Eq. 1, yield the energy of vaporization of the monomer (ΔE_1), and the dimer (ΔE_2), and, by using Eq. 5, the heat

---

[15]R. Fowler and E. Guggenheim, *Statistical Thermodynamics*, chap III, University Press, Cambridge, 1939.
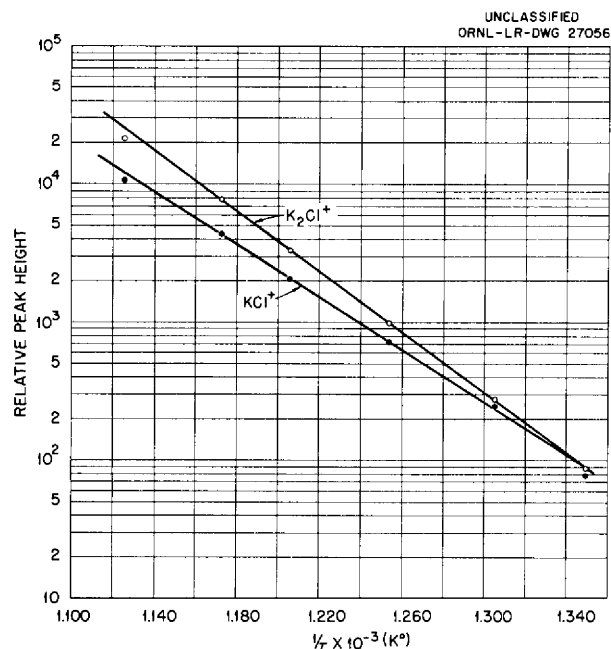
UNCLASSIFIED
ORNL-LR-DWG 27056

Fig. 2.3.3. Relative Intensities of Monomer and Dimer Species of KCl as a Function of Temperature. Data obtained from a mass spectrometric study of an effusing beam of KCl.

of association (ΔE^o) can be obtained. The values found, in kcal/mole, are:

$$\Delta E_1 = 42.5 ,$$

$$\Delta E_2 = 49.8 ,$$

$$\Delta E^o = 35.2 .$$

These values differ from the values of Beusman[3] and those of Miller and Kusch.[11] As mentioned earlier, this discrepancy may be due to the problem of salt deposition at the effusion slit. Such deposits have not been reported elsewhere, although they may be the source of the anomalous behavior observed in similar experiments on oxides.[16] The modified equipment, shown in Fig. 2.3.2, has not as yet produced satisfactory data.

SURFACE TENSIONS OF MOLTEN SALTS

S. Langer

The surface tension of a confined fluid has been shown to be important, in certain cases, in heat transfer[17] and in corrosion processes.[18] A study of the surface tension of molten fluoride mixtures was therefore initiated. The sessile-drop technique

was chosen for this study and has been described in previous reports in this series. The data obtained to date include fairly reliable measurements of the surface tension of the NaF-ZrF$_4$ mixture (53-47 mole %) at 600 and 700°C and preliminary data at 800°C. A summary of the data obtained by the sessile-drop technique is presented in Table 2.3.5 and compared with data obtained by Miles[19] by the maximum-bubble-pressure technique. A

Table 2.3.5. Surface Tension of NaF-ZrF$_4$ (53-47 Mole %) at Various Temperatures

Temperature (°C)	Surface Tension (dynes/cm)	
	Data of Miles	Author's Data
600	127*	127 ± 6
700	120	119 ± 4
800		138 ± 7**

*Average of three measurements corrected for more recent values of the density.

**The large loss of weight of the sessile drop during the course of the measurement renders this value highly inaccurate for NaF-ZrF$_4$ (53-47 mole %). It would apply perhaps to a melt containing about 30 mole % ZrF$_4$.

preliminary value of 180 dynes/cm has been obtained for the surface tension of pure molten UF$_4$ at 1050°C. This work was initiated in an effort to determine the effect of small amounts of UO$_2$ on the wetting properties of UF$_4$. Data obtained by Cohen and Jones[20] for NaF-ZrF$_4$-UF$_4$ (50-46-4 mole %) with a tensiometer are presented for comparison in Table 2.3.6. These tables summarize all the surface tension data on fuel mixtures and their components that are available thus far.

[16]M. G. Inghram and W. A. Chupka, *Chemical Bonds by Thermodynamic Methods*, paper No. 40 presented at the 4th Annual Meeting of the American Society for Testing Materials, Committee E-14 on Mass Spectrometry, Cincinnati, May 28, 1956.

[17]W. K. Stromquist and R. M. Boarts, *Effect of Wetting on Heat Transfer Characteristics of Liquid Metals. Third Quarterly Report*, ORO-60 (Jan. 31, 1952).

[18]J. W. Taylor, *J. Nuclear Energy* 2, 15 (1955).

[19]F. W. Miles, ANP *Quar. Prog. Rep. Sept. 10, 1956*, ORNL-2157, p 118.

[20]S. I. Cohen and T. N. Jones, ANP *Quar. Prog. Rep. June 10, 1953*, ORNL-1556, p 88.

Table 2.3.6. Data Obtained by Cohen and Jones[20] on the Surface Tension of $NaF \cdot ZrF_4 \cdot UF_4$ (50-46-4 Mole %) at Various Temperatures

Temperature (°C)	Surface Tension (dynes/cm)
530	157
630	132
730	115

In connection with these experiments, it should be noted that surface tension data are almost valueless without a knowledge of the density of the liquid. Miles[19] developed a method by which both the density and the surface tension can be obtained from the measurements involved in the maximum-bubble-pressure technique. While theoretically the density of a sessile drop can be obtained by weighing the drop and calculating its volume from its surface profile, in practice the method is subject to extremely large errors. Preliminary pycnometric density data on molten UF_4 and dilatometric measurements of solid UF_4 have yielded the interesting result that UF_4 melts with negligible expansion, if any.

Much of the knowledge of fused fluoride salts gathered in the past four years is still of a qualitative nature. During the course of these experiments, for example, it has become apparent that further information on the wetting behavior of fluoride salts is needed. The sessile-drop experiments on metal supporting surfaces and the maximum-bubble-pressure experiments have shown that truly clean hydrogen-fired surfaces are completely wetted by molten $NaF \cdot ZrF_4$ but that, if thin oxide films are allowed to form on the metal surface after hydrogen-firing, the films will prevent wetting until they are dissolved by the molten salt. These observations are difficult to reconcile with the lack of evidence of wetting in fuel purification vessels, where it has been consistently observed that the purification pots drain cleanly and that no residual film of salt (other than splattered droplets) is left on the walls. Visual observation studies[21] have tended to confirm this behavior, since the salt meniscus appears to be definitely convex, especially in melts containing BeF_2.

---

[21] R. J. Sheil, private communication to S. Langer.

2.4. PRODUCTION OF PURIFIED MIXTURES

G. J. Nessle   J. P. Blakely

PREPARATION OF FLUORIDE COMPOUNDS

B. J. Sturm   L. G. Overholser

Compounds not available commercially have been synthesized for use in ANP chemistry studies. Of particular interest were fluorides of the metals being considered as container materials for various fuels and the products of their reactions with constituents of proposed fuels. Many of these compounds had not been reported in the chemical literature. Corrosion products found in fuels have been identified by comparison of their x-ray diffraction patterns and optical crystallographic properties with those of synthesized compounds. Fluorides of the fission products have been prepared for use in the study of their effects on the fuel mixtures of interest.

Alkali-Metal Fluochromates

A series of bright green chromium fluoride complexes of the type $M_3^I Cr^{III} F_6$ were prepared in which M^I stands for an alkali metal or ammonium ion.[1] The purpose of preparing the alkali metal fluochromates was to obtain their crystallographic properties for comparison with those of unidentified phases.

Potassium hexafluochromate(III), K_3CrF_6, was prepared by slowly heating to 900°C a mixture of 3 moles of potassium bifluoride with one of hydrated chromic fluoride. Substitution of sodium bifluoride for the potassium bifluoride yielded Na_3CrF_6. Heating hydrated chromic fluoride with an excess of ammonium bifluoride to 250°C formed $(NH_4)_3CrF_6$. The compounds Li_3CrF_6, Rb_3CrF_6, and Cs_3CrF_6 were then obtained by reacting the alkali metal fluoride with either $(NH_4)_3CrF_6$ or a mixture of ammonium bifluoride and hydrated chromic fluoride.

Fusion of Li_3CrF_6 with Na_3CrF_6 gave the compound Li_2NaCrF_6. The ternary system K_3CrF_6-Li_3CrF_6-Na_3CrF_6 has a solid–solid-solution area bounded by the compounds K_2NaCrF_6, $K_3Na_3(CrF_6)_2$, and K_2LiCrF_6. The compositions of corrosion products that result from the action of NaF-KF-LiF-UF_4 or NaF-KF-LiF on chromium-containing alloys have always been within this solid-solution area.[2] The compound Rb_3CrF_6 was identified as the corrosion product that results from the attack of a chromium-containing alloy by an RbF-LiF composition.[3]

Other Double Fluorides

A new series of compounds of the type $M^{II}ZrF_6$ were formed by fusing ZrF_4 with fluorides of divalent transition metals. The compounds $CrZrF_6$, $MnZrF_6$, $FeZrF_6$, $CoZrF_6$, $NiZrF_6$, and $ZnZrF_6$ have been prepared.[4] The compounds $CuZrF_6$, $CdZrF_6$, and $PbZrF_6$ probably exist, but the products of fusions corresponding to these compositions have not yet been adequately studied. The compound $NiZrF_6$ was identified as the corrosion product that results from the action on a nickel container by the vapors resulting from the fusion of ammonium bifluoride with a fluozirconate composition.

Fusions of alkali-metal fluorides with transition-metal fluorides give a series of compounds. Except for lithium fluoride, which does not combine, the alakli metal fluorides form 1:1 compounds with manganese, cobalt, and nickel difluorides.[5] This is probably also true with chromous fluoride, but the results are confused by the contamination of the preparations by chromic-containing phases as a result of disproportionation of some of the chromous fluoride. The rubidium and cesium compounds were unknown before this work was begun, and very little information was available on the physical properties of the rest of these compounds.

Simple Inorganic Fluorides

Many different anhydrous fluorides were prepared. Moisture was removed from lithium, sodium, and potassium fluorides by heating in vacuum to

[1]B. J. Sturm and L. G. Overholser, *ANP Quar. Prog. Rep. Dec. 10, 1952*, ORNL-1439, p 115.

[2]B. J. Sturm and L. G. Overholser, *ANP Quar. Prog. Rep. Sept. 10, 1952*, ORNL-1375, p 122.

[3]B. J. Sturm and E. E. Ketchen, *ANP Quar. Prog. Rep. Sept. 10, 1954*, ORNL-1771, p 67.

[4]B. J. Sturm, *ANP Quar. Prog. Rep. Dec. 10, 1955*, ORNL-2012, p 91.

[5]B. J. Sturm and L. G. Overholser, *ANP Quar. Prog. Rep. June 10, 1953*, ORNL-1556, p 48.

around 500°C. Strontium, cadmium, cerium, praseodymium, neodymium, and samarium fluorides were precipitated by the addition of hydrofluoric acid to aqueous solutions of their salts.[6-8] Oven drying at around 200°C yielded essentially anhydrous material.

Yttrium fluoride, precipitated from aqueous solution, was treated with anhydrous hydrogen fluoride at an elevated temperature to ensure freedom from moisture. The hydrated ferric, nickelous, cuprous, and zinc fluorides were dehydrated by treating them in a similar manner.[7] Twenty hours of hydrofluorination followed by 4 hr of flushing with helium reduced the boron content of cupric fluoride to below 2 ppb, the spectroscopic limit of detection. The anhydrous fluorides prepared by treatment with hydrogen fluoride gas were usually flushed with purified helium gas to remove adsorbed hydrogen fluoride. The hydrated aluminum, chromic, and nickelous fluorides were reacted with ammonium fluoride or bifluoride at around 200°C to form the ammonium fluocomplex, which was decomposed at a higher temperature to form the anhydrous fluoride.[6]

Hydrofluorination of anhydrous ferric chloride at around 300°C and chromic chloride at around 600°C converted the chlorides to fluorides.[4,9] The hydrated nickelous, ferrous, and cobaltous chlorides were slowly heated to around 500°C during the passage of hydrogen fluoride to convert them to the anhydrous fluorides.[7,10] Silver carbonate was similarly converted into the fluoride at around 150°C, and ferrous oxalate was converted at around 600°C.[11] The tetrafluorides of thorium and uranium were freed of oxide and moisture by hydrofluorination at around 700°C.[9] Vanadium trifluoride was prepared by condensing hydrogen fluoride onto vanadium trioxide powder, heating to remove water and excess hydrogen fluoride, and rehydrofluorinating at 200°C.[10]

Chromous Fluoride

High-purity chromous fluoride was needed for studying the removal of chromium from container materials by fluoride fuels. Reaction of powdered chromium metal with hydrogen fluoride gas at about 800°C was found to be a poor method of preparing chromous fluoride, because a coating of the fluoride formed on the metal and prevented further reaction with the hydrogen fluoride. Grinding of the mixture exposed new metal surface to react with hydrogen fluoride, but three successive treatments failed to react all the metal. The product was also contaminated with chromic fluoride that resulted from the reaction

$$2CrF_2 + 2HF \longrightarrow 2CrF_3 + H_2$$
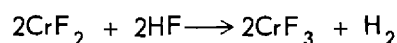
Hydrofluorination of chromous chloride at about 700°C yielded chromous fluoride that was contaminated by chromic fluoride, because of oxidation by hydrogen fluoride, and traces of unreacted chloride.[12] The chromic fluoride could be reduced by hydrogen.

A few kilograms of chromous fluoride were prepared by hydrogen reduction of chromic fluoride. The chromic fluoride was usually made by thermally decomposing ammonium fluochromate, which was made by fusing ammonium bifluoride with hydrated chromic fluoride. Usually the preparation of chromic fluoride and its reduction by hydrogen were combined into a single step in which ammonium fluochromate was placed in a nickel reaction vessel and the temperature was slowly raised to 700°C while a flow of hydrogen was maintained. Chromous fluoride prepared in this manner was usually contaminated with some opaque material. This was especially true of the product near the walls of the nickel reaction vessel. The chromous fluoride was further purified by fusing at 1100°C, recrystallizing, and manually separating the clear crystals from the opaque residue.

At first it was assumed that the opaque material resulted from reduction of some of the chromous fluoride to the free metal. Free metal could not be found by x-ray diffraction analysis, but gamma chromium nitride was identified in the opaque material. The following reactions are proposed

[6]E. E. Ketchen and B. J. Sturm, *ANP Quar. Prog. Rep. June 10, 1955,* ORNL-1896, p 76.

[7]B. J. Sturm, *ANP Quar. Prog. Rep. Dec. 10, 1953,* ORNL-1649, p 62.

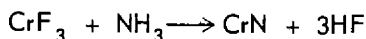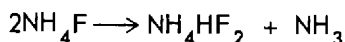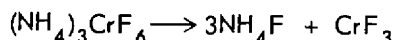[8]B. J. Sturm, *ANP Quar. Prog. Rep. March 10, 1956,* ORNL-2061, p 100.

[9]B. J. Sturm and E. E. Ketchen, *ANP Quar. Prog. Rep. March 10, 1955,* ORNL-1864, p 66.

[10]B. J. Sturm and L. G. Overholser, *ANP Quar. Prog. Rep. June 30, 1957,* ORNL-2340, p 164.

[11]L. G. Overholser and B. J. Sturm, *ANP Quar. Prog. Rep. Sept. 10, 1953,* ORNL-1609, p 70.

[12]B. J. Sturm and L. G. Overholser, *ANP Quar. Prog. Rep. Dec. 31, 1956,* ORNL-2221, p 153.

to explain the formation of chromium nitride:

$$(NH_4)_3CrF_6 \longrightarrow 3NH_4F + CrF_3$$

$$2NH_4F \longrightarrow NH_4HF_2 + NH_3$$

$$CrF_3 + NH_3 \longrightarrow CrN + 3HF$$

The formation of chromium nitride by the reaction of ammonia with chromic chloride was reported by Schwarzkopf and Kieffer.[13] It is reasonable to expect chromic fluoride and ammonia to react in the same way.

If chromic fluoride was not completely reduced to chromous fluoride, a phase was formed which had a composition intermediate between the compositions of chromic and chromous fluoride. The exact composition of this phase has not been established, but its optical properties and x-ray diffraction pattern have been determined.

SUMMARY OF EXPERIENCE IN THE PREPARATION OF FUEL FOR THE AIRCRAFT REACTOR EXPERIMENT

C. R. Croft   J. E. Eorgan
F. A. Doss   J. Truitt

The nuclear poisons, such as boron, cadmium, and certain of the rare earth elements, are not common contaminants of enriched uranium, sodium, and zirconium fluorides. Hafnium, which invariably contaminates zirconium and its compounds, can be reduced in concentration to acceptable limits (50 to 100 parts of Hf per million parts of Zr) on a commercial scale. Since the initial concentrations of these poisons were low and the parasitic capture of neutrons in the core structure would be considerable, purification processes were designed to minimize corrosion and to ensure the absence of slightly soluble oxides and oxyfluorides rather than to improve neutron economy.

The best-quality UF_4 available commonly contains small quantities of UO_2, UF_5, and UO_2F_2. The commercially available ZrF_4, even when prepared by hydrofluorination of $ZrCl_4$ and further refined by sublimation at low pressure, contains up to 2% excess oxides and oxyfluorides, up to 0.2% Cl^-, and Fe^{+++} to the extent of a few hundred parts per million. Both these tetrafluorides are readily hydrolyzed to oxides and oxyfluorides

[13]P. Schwarzkopf and R. Kieffer, *Refractory Hard Metals*, Macmillan, New York, 1953.

at elevated temperatures. Commercial NaF contains some sulfur, mostly as sulfate, and small amounts of water.

The fuel solvent, NaF-ZrF_4, and the fuel concentrate, $2NaF \cdot UF_4$, were prepared separately for the ARE, as required by the startup procedure. For testing of components and for heat transfer and metallurgical research, however, large quantities of the fuel mixture NaF-ZrF_4-UF_4 were prepared in various compositions. Such bulk production was carried out on a 250-lb-batch scale, but considerable production of special compositions in small batches on a 5-, 10-, and 50-lb experimental scale was required for many specific test programs. In general the fluoride mixtures were purified by the process described below, with only minor modifications for the small batches when specific requirements had to be met for specialized experiments.

Purification of Fuel Solvent

The equimolar NaF-ZrF_4 mixture required for the ARE was purified in 250-lb batches. The reaction vessel, in which the chemical processing was accomplished, and the receiver vessel, into which the purified mixture was ultimately transferred, were 13-in.-dia, vertical cylindrical containers, 48 and 24 in. long, respectively, that were fabricated of A-nickel by the Heliarc welding of $\frac{3}{8}$-in. plate. The top of the reactor vessel was pierced by a charging port consisting of a 4-in.-dia pipe which was capped well above the heated zone by a Teflon-gasketed flange. The tops of both the receiver and the reaction vessel were pierced by short risers which terminated in Swagelok fittings through which gas lines, thermowells, etc., of $\frac{3}{8}$-in. nickel tubing could be introduced. A transfer line of $\frac{3}{8}$-in. nickel tubing terminated near the bottom of the reactor vessel and near the top of the receiver; entry of this tube was effected through copper-gasketed flanges on 1-in.-dia tubes which pierced the tops of both vessels. This transfer line contained a filter of Micro Metallic sintered nickel and a sampler which collected a specimen of the liquid during transfer. Through one of the risers in the receiver a $\frac{3}{8}$-in. nickel tube extended to the receiver bottom; this tube, which was sealed outside the vessel, ultimately served as the means for transfer of the purified melt to the ARE. A schematic diagram of the reaction vessel—receiver assembly is shown in Fig. 2.4.1.

TEFLON GASKETED FLANGE

4-in.-DIA CHARGING PORT

$\frac{3}{8}$-in.-NICKEL TRANSFER LINE

FILTER

SAMPLER

REACTION VESSEL

RECEIVER VESSEL
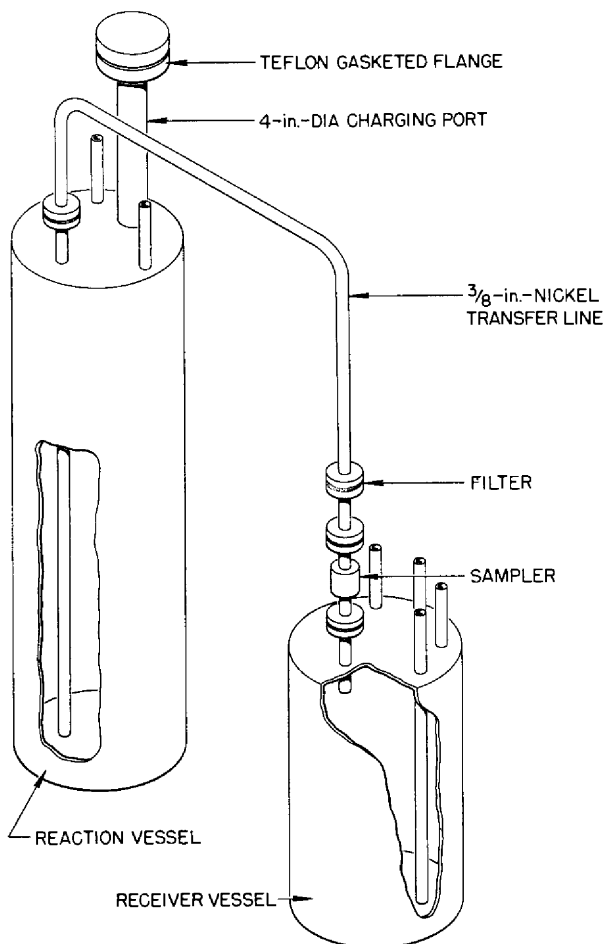
Fig. 2.4.1. Apparatus for Purification of Fluoride Mixtures.

This assembly was connected, through traps for collecting sublimed ZrF_4, to a manifold through which He, H_2, HF, or vacuum could be supplied to either vessel. By a combination of large tube furnaces, resistance heaters, and lagging, sections of the apparatus could be brought, independently, to controlled temperatures in excess of 800°C.

The raw materials in batches of the proper composition were blended and charged into the reaction vessel. The material was melted and heated to 700°C under an atmosphere of anhydrous HF to remove H_2O with a minimum of hydrolysis. The HF was then replaced with H_2 for a period of 1 hr, during which the temperature was raised to 800°C, to reduce U^{5+} and U^{6+} to U^{4+}, sulfur compounds to S^{--}, and extraneous oxidants (Fe^{+++}, for example) to lower valence states.

The hydrogen and all subsequent reagent gases were fed at about 3 liters/min to the reaction vessel through the receiver and the transfer line and, accordingly, bubbled up through the molten charge. The hydrogen was then replaced by anhydrous HF, which served, during a 2- to 3-hr period at 800°C, to volatilize H_2S and HCl and to convert oxides and oxyfluorides of uranium and zirconium to tetrafluorides, but at the expense of introduction of considerable NiF_2 into the melt through reaction of HF with the container. A final 24- to 30-hr treatment at 800°C with H_2 sufficed to reduce the NiF_2 and the contained FeF_2 to insoluble metals.

At the conclusion of the purification treatment, a pressure of helium above the salt in the reactor vessel forced the melt through the transfer line, filter, and sampler into the receiver. The metallic iron and nickel were left in the reactor vessel or on the sintered nickel filter.

The purified melt was permitted to freeze under an atmosphere of helium in the receiver vessel, and, by appropriate manipulation of connections and valves, the cold receiver was detached and removed to storage while the helium atmosphere was maintained over the contents.

Purification of Fuel Concentrate

The $2NaF \cdot UF_4$ mixtures were prepared by a very similar processing schedule in similar but smaller equipment. In order to avoid the possibility of criticality accidents, the fuel concentrate was prepared by using reactors and receivers 4 in. in diameter to limit batch sizes to about 30 lb.

Storage and Ultimate Transfer

The receiver vessels containing either fuel solvent or fuel concentrate were connected to manifolds that supplied pure helium at slightly more than atmospheric pressure and were stored in this manner at room temperature until used.

Transfer of the material for ultimate use was accomplished by forcing the remelted charge under helium pressure through the transfer line built into the receiver vessel. In this simple fashion, virtually quantitative transfer of the molten material could be accomplished. Transfer of up to 250 lb of solvent usually left less than 0.5 lb of solvent in the container.

PILOT-SCALE PURIFICATION OPERATIONS

C. R. Croft   J. Truitt

In the early stages of the ANP program, extensive small-scale experimentation was carried out in order to develop a suitable process and a flexible processing unit for the purification of fluoride mixtures. Small-scale units of 5- and 10-lb capacity were installed, and later, as demands grew, 50-lb units were added. Finally, six small units and three 50-lb units were in continuous use. Although bulk production was taken over by the 250-lb capacity units, demands for small, special batches continued to increase. During the active life of the ANP fluoride production program, 653 batches totaling approximately 11,500 lb of various fluoride compositions for use in phase equilibrium studies, physical property measurements, small-scale corrosion tests, and other experiments were processed in these pilot-scale units.

PRODUCTION-SCALE OPERATIONS

J. E. Eorgan

The ARE and the large-scale component testing program, as stated above, created demands for processed fluorides far beyond the capabilities of the small pilot-scale units, and therefore the 250-lb production units were installed to process fairly standard compositions in large quantities. The first production operation of this facility was the processing of the approximately 3300 lb of fuel solvent required for the ARE. Analyses of the 14 batches of fuel solvent processed for use in the ARE, as can be seen from the results given in Table 2.4.1, showed the purity of the finished material to be very satisfactory. Since this was the first operation of the production-scale units, the performance of the processing units during this period served as a basis for future production schedules.

Table 2.4.1. Results of Analyses of ARE Fuel Solvent

Batch No.	Chemical Analysis						Spectrographic Analysis (ppm)	
	Major Constituents (%)			Impurities (ppm)				
	Zr	F	Na	Fe	Cr	Ni	HF	B
1	43.3	45.0	9.76	30	<10	<10	240	0.2
2	43.9	45.2	11.0	45	<20	<20	55	0.2
3	43.9	45.5	10.6	60	<10	25	100	0.9
4	42.0	44.7	10.8	55	<20	45	80	0.9
5	44.1	44.9	11.0	90	<20	<20	60	0.6
6	43.6	44.7	10.5	35	<20	30	85	0.5
7	43.6	45.2	10.4	35	<20	30	70	0.5
8	43.4	44.6	10.4	35	<20	<20	108	0.1
9	43.1	44.6	10.6	35	<20	<20	67	1.0
10	43.8	44.6	10.6	45	<20	35	60	0.3
11	43.7	45.1	10.5	40	<20	35	71	0.4
12	43.7	44.8	10.7	30	<20	<20	39	0.3
13	44.1	44.5	10.3	40	<20	30	42	0.6
14	43.9	44.7	10.3	<20	<20	35	48	0.6

The efficiency, or production loss, of this process and facility, with regard to raw material usage vs quantity of final product, was very good. A material balance for the fuel-solvent production operation is given below:

	Weight (lb)
Raw fluorides used (NaF and ZrF$_4$)	3412
Net fluorides produced	3348
Net samples	5
Net heels left in reactor vessels	56
Total produced	3409
Net loss	3

On the basis of usable product, a production efficiency of 98% was obtained.

The production facility was normally run on a five-day-week, 24-hr-shift basis during the early stages of the component testing program. When demands from off-area consumers (such as Pratt & Whitney Aircraft) increased, the operation was placed on a continuous seven-day-week schedule. Maximum production on the seven-day-week schedule was reached at 1000 lb per week. Production on a five-day-week schedule averaged about 600 lb per week.

During the production operation of this facility, 322 batches totaling 80,000 lb of processed fluorides were produced. Since production usually exceeded demand, the facility operated on an average of eight months per year.

SERVICE OPERATIONS

F. A. Doss   J. Truitt
J. E. Eorgan   N. V. Smith

In conjunction with the accelerated component testing program, and the resulting acceleration in fluoride production, a facility was established for the efficient and accurate handling of the large amounts of fluorides and liquid metals used. The 250-lb batches could, in some cases, be used directly, but ordinarily these batches had to be reduced to quantities ranging from 1 to 50 lb to fit specific test programs. Complete analytical records and material balances were kept to avoid confusion in the interpretation of component test results. Responsibility was taken for the loading, sampling, and unloading of charge materials from component test equipment, including the high-temperature critical assemblies. During the course of the program, approximately 70,000 lb of processed fluorides and 35,000 lb of liquid metals were dispensed. In addition, some 200 storage cans used in dispensing processed fluorides to local and off-area consumers were maintained.

2.5. ANALYTICAL CHEMISTRY

J. C. White

DETECTION OF TRACES OF NaK IN AIR

A. S. Meyer, Jr.   J. P. Young

A study of sensitive methods for the detection of traces of alkali metals in air was carried out in order to provide a monitor for the exhaust air from the ART NaK-to-air radiators. The sensitivity requirement for a suitable detector was established on the basis of a tentative limit of a NaK leak which would correspond to the introduction of a total volume of 6 cm^3 of NaK per hour into the exhaust air stream. On the basis of the design flow rate of air in the radiator ducts, the instrument was required to respond to a concentration of NaK in air of 10 ppb by weight. Since it was also assumed that the inlet air could be contaminated with alkali metal compounds in concentrations comparable with those introduced by the radiator leaks, it was considered necessary that the detector be designed to monitor both the inlet and exhaust streams and to respond to an increment of 10 ppb of NaK across the radiators. Additional specifications for a suitable detector included a rapid response time and a high degree of reliability.

Methods of detection which were evaluated during the feasibility studies included chemical analyses, photometric smoke detection, emission spectrographic analysis, flame photometric analysis, surface-ionization detection, and resonance-radiation measurement. In addition, some consideration was given to a technique in which a material that could be readily detected by existing conventional methods of analysis would be added to the NaK. Radiometric techniques were not considered.

Existing chemical methods, emission spectrographic techniques, and smoke detection do not offer sufficient sensitivity for the detection of NaK at the 10-ppb concentration level. Although mass spectrographic techniques offer adequate sensitivity, they do not appear to be applicable to the proposed system because of the problems concerned in introducing representative, continuous samples of the alkali metal oxide suspensions through capillary leaks into the ionization chambers of the spectrometer. For the proposed differential measurement it would be necessary to maintain capillary leaks of equal rates for both inlet and exhaust air.

Although flame photometric measurements may be extended to ultimate sensitivities in the desired concentration range, such measurements might not be reliable because of the problem of maintaining a constant flame source by remote control. Experience with a Beckman flame photometer during operation of the ARE indicated that this problem imposes serious limitations to the application of this instrument. Additional complications can be predicted in the application of this technique to the proposed detector in that it would be necessary to maintain two flames at identical temperatures and to meter samples of the inlet and exhaust gases to these flames at constant rates.

The detection of alkali metals by means of a surface-ionization detector is based on the measurement of the current that is carried by positive ions which are formed when atoms of the alkali metals are brought into contact with a heated filament. This detector has been applied to the detection of sodium and NaK in helium.[1] Concentrations of 2 ppm of sodium and 9 ppm of NaK have been detected in this manner. It was suggested[2] that the surface-ionization detector might be used for air samples if an iridium filament were used. Under these conditions, detection limits of 1 to 10 ppm of NaK could be achieved. The calibration curves reported for the measurement of alkali metals in helium (current vs saturation temperature) are linear over only a very limited range of concentration, however, and this method would therefore not be readily applicable to the proposed differential measurement of concentration. This method was given some further consideration since it was thought that, because of the small size of the sensing elements, numerous elements could be placed in strategic locations to detect the larger concentrations of alkali metals which would be present in the immediate vicinity of the leak. The detection requires the measurement of relatively small direct currents, however, and the instrumentation for such a multiple installation of detectors might become prohibitive.

[1]H. S. McKown, *A Detector for Sodium Vapor — A Surface Ionization Sodium Detector*, K-996 (Feb. 16, 1953).

[2]J. R. Sites, private communication to A. S. Meyer, Jr.

The proposed resonance-absorption method is based on the measurement of the attenuation of a beam of sodium D light (589 mμ) on passage through sodium metal vapor. This method offers extreme sensitivity for the detection of sodium. Since the absorption coefficient for sodium vapor at the center of the resonance line is approximately 10^{-12} N, where N is the density of sodium in atoms per square centimeter, it was calculated that a concentration of 0.01 ppm of atomic sodium in air would be sufficient to reduce by 50% the intensity of a beam of sodium radiation that had traversed a 50-cm optical path. Inasmuch as compounds of sodium such as Na_2O do not absorb the resonance radiation, it is necessary to maintain the sample at a temperature sufficient to cause thermal dissociation of Na_2O to atomic sodium in order to obtain a measurable absorption of the resonance line.

On the basis of thermodynamic constants it was calculated that a concentration of Na_2O of 10 ppb could be quantitatively dissociated at temperatures as low as 800°C. Dissociation of comparable concentrations of K_2O, which can also be detected by the resonance-absorption method, is complete at approximately 600°C.[3]

A test model of an instrument designed to compare the absorption of samples of the inlet and exhaust air from the radiators was constructed. Detailed descriptions, including a photograph of the instrument, were given previously.[4] In this instrument a beam of sodium D light is divided into two pulsed beams of equal intensity by a 90-cycle mechanical chopper. After the beams are passed through heated absorption cells which contain samples of the inlet and exhaust air, the transmitted beams are recombined at a photomultiplier tube. A 90-cycle a-c signal, which is proportional to the difference in absorption between the inlet and exhaust air, is generated by the photomultiplier.

This instrument was tested by passing, through one of the tubes, samples of sodium in air which were prepared by mixing with the air stream helium that had been saturated with sodium vapor. A detection limit of approximately 100 ppb was noted. With minor modifications of the instrument,

which included the substitution of a Polaroid chopper and refinements of the 90-cycle tuned amplifier, the limit of detection was lowered to 60 ppb.[3] Additional modifications of the instrument were made to eliminate the continuous radiation of the heated cell walls from the photomultiplier tube and to provide means of exact alignment of the optical system. Details of these modifications were given previously.[5] Experimental work on the project was discontinued before the improved instrument could be tested.

It is believed that the studies which have been carried out have demonstrated the applicability of this method to the detection of the radiator leaks. The test model responded almost instantaneously to small increments in the concentration of the sodium in the air samples, and with refinements in the optical and electronic components its sensitivity could readily be increased to provide detection at the required concentration level. The double-beam system is known to offer high stability and reliability. With minor modifications, the instrument could be adapted to the detection of other alkali metals in air.

On the basis of these experiments, design criteria for a working model of the instrument were prepared.[3] Improvements to the test model would include: a rigidly mounted optical system to provide a multiple pass of the light beam through the sample; an electrodeless source lamp excited by radio frequencies to provide extended lamp life and a sharper line source; multilayer interference filters to isolate the resonance line more effectively; and a phase-sensitive amplifier to discriminate completely against frequencies of other than 90 cycles.

Although the feasibility of the proposed detector appears to have been demonstrated, much additional experimental work would be required to establish sampling techniques. Questions to be resolved include the selection of the best material for the construction of sampling ports and transfer lines, the determination of the optimum temperature and flow rates to minimize deposition of the alkali metals on the walls of the tubing, and the required recovery time of the assembly after exposure to the large concentrations of alkali metals which would be introduced by a major leak. A comparison of the transfer characteristics of K_2O and

[3]A. S. Meyer, Jr., and J. P. Young, *ANP Quar. Prog. Rep. June 30, 1957*, ORNL-2340, p 166.

[4]A. S. Meyer, Jr., and J. P. Young, *ANP Quar. Prog. Rep. March 31, 1957*, ORNL-2274, p 137.

[5]A. S. Meyer, Jr., and J. P. Young, *ANP Quar. Prog. Rep. Sept. 30, 1957*, ORNL-2387, p 148.

Na_2O should be undertaken in order to provide criteria for a choice of the element which could be monitored most efficiently.

A major test facility would be required in order to provide a means of simulating a NaK leak in an ART radiator. This facility could be used to establish criteria for the selection of sampling points which would assure complete mixing of the air for representative sampling and to determine the reliability of the instrument in the detection of small increments in the concentration of the alkali metal in the presence of large background concentrations.

Although the tests could be carried out with less extensive equipment if the alkali metal could be introduced to the air stream at an infinitesimal rate as a dilute solution, preliminary experiments[6] have indicated that the physical properties of the samples vary widely with the method of preparation. Accordingly, to carry out definitive tests of sampling procedures, the direct addition of NaK to the heated air stream would be essential. Tests carried out with water have indicated that for minimal rates of injection, as a jet, high pressures and minute orifices are required. In order to inject NaK at a rate consistent with a test facility of reasonable proportions, pressures in excess of 1000 psi and orifices 0.0001 to 0.0003 in. in diameter would be required. Orifices of this diameter can be drilled by anodic dissolution with a virtual electrode.[7] Orifices less than 0.0005 in. in diameter have been fabricated in nickel by this technique. Zirconium orifices would be more satisfactory, but electrolytic drilling of this material has not been successful.

These sampling difficulties could be largely resolved by adding to the NaK a volatile material which could be detected in small concentrations. Mercury has been suggested as an ideal additive, since it could be readily transferred and can be detected by resonance-absorption methods at operating temperatures. The addition of mercury would be contingent on the evaluation of its effect on the compatibility of NaK with structural materials and its effect on nuclear properties.

---

[6] A. S. Meyer, Jr., and J. P. Young, *ANP Quar. Prog. Rep. Dec. 31, 1956,* ORNL-2221, p 164.

[7] A. Uhlir, Jr., *Rev. Sci. Instr.* **26**, 965 (1955).

DETERMINATION OF OXYGEN IN FLUORIDE SALTS

A. S. Meyer, Jr.   G. Goldberg

The gas-measuring system of the apparatus[8] for the determination of oxygen in fluoride salts with $KBrF_4$ was calibrated by measuring the displacement of the manometer levels produced by the addition of measured volumes of oxygen. Discrete additions of oxygen were made by means of the apparatus shown in Fig. 2.5.1. By appropriate rotation of the three-way stopcock (S_8) the volume of oxygen in the sealed arm of the stopcock (0.281 cm^3) is connected with the Toepler pump. The oxygen is transferred to the measuring system by means of the Toepler pump in a manner analogous to its transfer from the reaction system when determinations are performed. The coefficient of variation of the calibration measurements was less than 2%.

The accuracy of the calibration was confirmed by determining the oxygen in 10-mg samples of Y_2O_3. Comparable precision was obtained in these measurements. Typical results of replicate determinations by this procedure are given in Table 2.5.1.

The range of the method is from a minimum of 5 μg of oxygen, as measured with the oil manometer, to a maximum of 100 mg, as measured by the mercury manometer. For quantities of oxygen in excess of 100 μg, the precision of the method would appear to be less than 5%.

---

[8] A. S. Meyer, Jr., and G. Goldberg, *ANP Quar. Prog. Rep. Sept. 30, 1957,* ORNL-2387, p 150.

Table 2.5.1. Determination of Oxygen in Samples of Y_2O_3 and YF_3

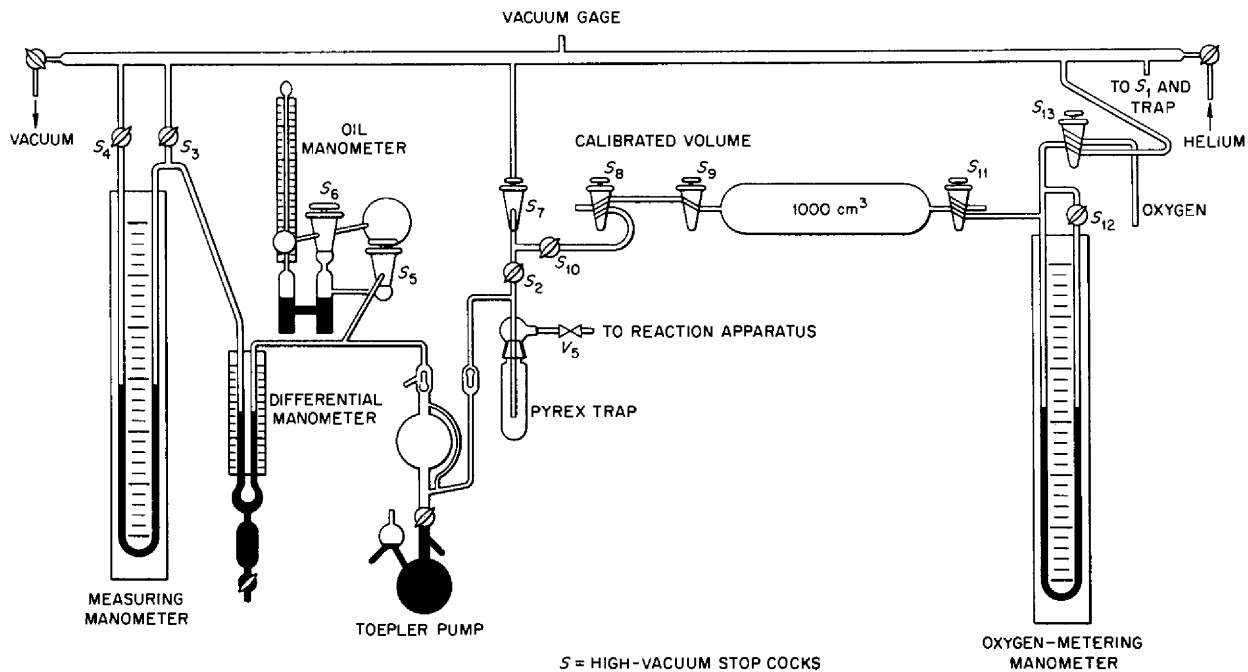| Sample Composition	Sample Weight (g)	Oxygen (mg)	
		Theoretical	Determined
Y_2O_3	0.0103	2.19	2.16
	0.0102	2.17	2.18
YF_3	1.00		0.58
	1.00		0.59

Fig. 2.5.1. Constant-Volume Manometer Calibrating Apparatus.

Part 3

METALLURGY

W. D. Manly

3.1. NICKEL-MOLYBDENUM ALLOY DEVELOPMENT STUDIES

MATERIAL DEVELOPMENT

H. Inouye   T. K. Roche
J. H. Coobs

The developmental work on nickel-molybdenum-base alloys for use as reactor structural materials in contact with the fused salt fuel NaF-KF-LiF-UF$_4$ (11.2-41-45.3-2.5 mole %, fuel 107) at normal operating temperatures of 1650°F and above has been terminated. Much of the technology and experience gained in this investigation will be of value to the Molten Salt Reactor program.

Status of Development

Based on the requirements for an ideal container material for fuel 107, the experimental nickel-molybdenum-base alloys have shown exceptional promise. The various alloys which have been studied fall into three general categories: solution-hardening, precipitation-hardening, and dispersion-hardening alloys. The solution-hardening alloys are represented by alloys INOR-1 and -8; the precipitation-hardening alloys by INOR-3, -4, -6, and -7; and the dispersion-hardening alloys by INOR-5 and -9. Preliminary data on the properties of the INOR alloys 1 through 8 were presented previously, along with the composition ranges of each alloy studied.[1] The data indicate that, of the three categories of alloys, the solid solution-hardening alloys most nearly meet the requirements. On this basis, the INOR-8 alloy was selected as having the best combination of properties, and much of the effort has been directed toward establishing the final composition and producing commercial quantities of the alloy. It is felt, however, that the full potential of alloys of the nickel-molybdenum system definitely has not yet been developed. For the immediate future, these alloys appear to be the only structural materials which show the possibility of bridging the gap between Inconel and the refractory metals niobium and molybdenum.

The most attractive feature of the nickel-base alloys containing 15 to 20% molybdenum as the principal alloying element is their versatility. From the studies of numerous alloy combinations and types, it has been determined that a particular property of interest can be improved, but usually at the expense of some other property. Inasmuch as the property variations are derived largely from additions of third, fourth, or fifth alloying elements, the principal properties of importance such as strength and corrosion resistance can be balanced to give an alloy composition which is best suited for a particular application. As the severity of the service conditions is increased (for example, higher temperatures and longer operating times), the freedom of modification becomes narrower, and thus many of the alloys are eliminated for various reasons. In short, for every temperature or application, there appears to be an optimum alloy composition.

For 1000 hr of operation, the alloys, as presently developed, appear to permit peak temperatures of 1650 to 1700°F at the metal-salt interface. This limitation has been tentatively set by the rapid increase of the corrosion tendency of the alloys containing chromium and the deterioration of strength above these temperatures.

The alloys that have been studied have been evaluated in terms of fabricability, mechanical properties, corrosion resistance, weldability, and aging characteristics. The results of these investigations are summarized below.

Fabricability. — Alloys which are solid solutions at the forging temperatures should present no unusual fabrication problems. Forging difficulties have been encountered with large heats of the INOR alloys, as reported previously,[1,2] but such difficulties have been associated with poor melting and forging techniques. It is anticipated that further fabrication problems will be those normally associated with developing reduction schedules for new materials.

A serious limitation in the production of tubing has been the tendency toward longitudinal splitting of alloys that contain over 0.10% carbon. This tendency has not been noted during hot-forging operations or during cold rolling of plate and sheet products.

---

[1]H. Inouye and T. K. Roche, *ANP Quar. Prog. Rep. March 31, 1957,* ORNL-2274, p 177.

[2]H. Inouye, T. K. Roche, and J. H. Coobs, *ANP Quar. Prog. Rep. June 30, 1957,* ORNL-2340, p 175.

Mechanical Properties. – The mechanical properties of the nickel-molybdenum alloys are described in detail in a subsequent section of this chapter. In general, the available data show that an increase of up to 200°F in operating temperature should be obtained by substituting INOR-8 for Inconel. Thus, operation at temperatures between 1650 and 1700°F with fuel 107 appears to be possible.

A correlation between microstructure and creep-rupture characteristics showed that the microstructures with grain-boundary networks of fine carbides had the best strength properties. Carbide precipitation studies showed that the desired microstructure could be obtained by using high annealing temperatures (2300°F). Improvements in the time to rupture and in ductility were made by minor additions of malleableizing elements and vacuum remelting of air melts.

Corrosion Resistance. – Within certain limitations, the corrosion-resistance characteristics of the nickel-molybdenum alloys approach the optimum for service in fused-salt, sodium, and air environments. The corrosion behavior of these alloys in fused salts and sodium is described in detail in a subsequent section of this chapter.

The oxidation rates of the nickel-molybdenum alloys have been found to vary from excessive to slight, depending upon the composition. The element having the largest effect is chromium, and its critical level at a temperature of 1800°F was determined to be 6%. Alloys containing less than 6% chromium show about 4 mils of oxidation in 170 hr, while those containing more than 6% show attack of less than 1 mil.

The extent of oxidation in 1000 hr at temperatures as high as 1750°F has been tolerable for all compositions studied. This conclusion is based upon the fact that approximately 75 loops have been operated without special coatings or protection. The probable maximum service temperatures in fuel 107, in sodium, and in air for alloys of current interest are given in Table 3.1.1.

Weldability. – The status of the development of techniques for welding these alloys has been reported in detail in reports in this series. It is felt that the weldability will not be a serious problem, since approximately 40 alloys of compositions representing various modifications of the nickel-molybdenum base material have been welded satisfactorily. Such welds have been in service for periods of up to 1000 hr at temperatures as high as 1850°F without evidence of deterioration. The incidence of poor weldability and cracking tendencies under restraint in various heats of the alloys has shown good correlation with evidence that those heats were not properly melted. The results of high-temperature ductility tests have been reported.[3]

[3]E. F. Nippes, W. F. Savage, and R. P. Meister, *Hot-Ductility of Nickel-Molybdenum Alloys*, Rensselaer Polytechnic Institute, Troy, N. Y., 1957.

Table 3.1.1. Maximum Permissible Interface Temperatures of Nickel-Molybdenum Alloys in Air, in Sodium, and in Fuel 107 for 1000 hr of Operation*

Alloy Composition (wt %)	Alloy Designation	Fuel 107	Sodium	Air
20 Mo–bal Ni	INOR-1	1850**	1650	1300
17 Mo–6 Fe–bal Ni		1800**	1650	1300
17 Mo–3 Nb–5 Fe–bal Ni	INOR-9	1800**	1650	1300
24 Mo–5 Cr–5 Fe–bal Ni	Hastelloy W	1800**	1650	1400
17 Mo–7 Cr–5 Fe–bal Ni	INOR-8	1700**	1650	1800
17 Mo–7 Cr–5 Fe–3 Nb–bal Ni	INOR-8 (modified)	1700**	1650	1800
17 Mo–10 Cr–bal Ni		1650	1650	1800

*Based on an allowable 4 mils of corrosion in 1000 hr.
**Estimates based on tests at 1650 or 1750°F.

Aging Characteristics. — Of the three elements, titanium, aluminum, and beryllium, which cause the basic nickel-molybdenum alloy to respond to an aging heat treatment, beryllium was found to be the most potent. Alloys containing beryllium in amounts as low as 0.25% exhibited strong aging tendencies at 1300°F. The aging response of alloys containing titanium and aluminum at 1300°F was significant, while at 1500°F these alloys either overaged in a short time or showed no effect.

Properties of INOR-8

It appears at this time that the alloy INOR-8, which is based on the Ni-Mo-Cr-Fe system, offers the best choice of properties for fulfilling the requirements of a structural material compatible with fused fluorides. The current optimum composition range of this alloy is: 15–18% Mo, 6–8% Cr, 4–5% Fe, 0.04–0.08% C, 0.8% (max) Mn, 0.5% (max) Si, bal Ni. The properties of this alloy were summarized and discussed previously.[1,4]

An investigation of the effect of varying composition on the mechanical properties of alloys of the INOR-8 type is under way. Eighteen alloys have been prepared and tested in creep rupture at a stress of 10,000 psi and a temperature of 1500°F in argon. Results of these tests, although incomplete, show that (1) increasing the molybdenum content is the most effective means of improving the creep properties, (2) increasing the chromium content from 5 to 7% without changing the molybdenum and iron content produces only a slight improvement in the creep properties, and (3) there is no obvious correlation of the time to rupture of the material with the total content of alloying elements in the nickel base.

Properties of INOR-9

Alloys designated INOR-9 have been studied to determine whether they may be suitable as possible substitutes for INOR-8. The base composition of these alloys is that of INOR-1 (a nickel-molybdenum binary alloy) with niobium and carbon added for strength. Since the alloys of this group do not contain elements that corrode in fuel 107, it is expected that a higher metal-salt interface temper-

ature would be permissible for INOR-9 than for INOR-8.

The heats of INOR-9 that are being investigated have the nominal composition 12–19% Mo, 3–5% Nb, 2–5% Fe, 0.06–0.30% C, bal Ni. The results obtained thus far show that (1) the maximum permissible niobium content for forgeability is about 7.5%, (2) the solid solubility of niobium up to 1700°F in the nickel-molybdenum base is 5%, (3) the creep strength is about equal to that of INOR-8, and (4) the oxidation rates of the INOR-9 alloys are slightly higher than those of Hastelloy B.

Phase Diagram Studies

An investigation is being conducted at the University of Tennessee (subcontract 582) for the purpose of establishing phase relationships and characteristic transformations in the binary nickel-molybdenum and ternary nickel-molybdenum-chromium systems. In the binary system, three secondary phases have been identified and their transformation temperatures have been determined, as stated previously.[1]

Solubility limits of molybdenum plus chromium in nickel are being determined, and identification of the phases observed is to be undertaken. The compositions studied range from 20 to 35% Mo and 3 to 15% Cr. Apparently the addition of chromium suppresses the formation of the beta phase (Ni_4Mo), inasmuch as it has not been observed in any of the ternary compositions.

Stress-Rupture Testing by New England Materials Laboratory

The production heats of INOR-1 through -6, which were prepared by the International Nickel Company, were stress-rupture tested at 1350, 1500, and 1650°F in air at the New England Materials Laboratory. A final report is being prepared in accordance with the terms of the contract. The data obtained on stress-rupture strengths of these alloys were summarized in a previous report.[4]

Status of Production Heats

A purchase order was placed with the International Nickel Company for the production of 4800-lb heats of six nickel-molybdenum-base alloys so that experience might be gained with this

[4]H. Inouye, T. K. Roche, and J. H. Coobs, *ANP Quar. Prog. Rep. Sept. 30, 1957*, ORNL-2387, p 161.

type of material. The alloy compositions are given below:

Alloy	Nominal Composition (wt %)
INOR-1	20 Mo—bal Ni
INOR-2	16 Mo—5 Cr—bal Ni
INOR-3	16 Mo—1 Al—1.5 Ti—bal Ni
INOR-4	16 Mo—2 Al—1.5 Ti—bal Ni
INOR-5	13 Mo—5 Cr—2 W—2 Nb—0.1 C—bal Ni
INOR-6	16 Mo—5 Cr—1 Al—1.5 Ti—bal Ni

In general, billet conversion of these alloys has been only moderately successful. Difficulties were encountered with cracking during the rolling of the titanium- and aluminum-bearing INOR alloys 4 and 6. INOR alloys 1, 2, and 5 were processed with considerably more success. Strength and weldability studies were conducted on the converted products received at ORNL. Recently, after some delay, the tube reducing of the tube shells was completed, and these shells are presently being redrawn to small-diameter seamless tubing. Currently, the International Nickel Company is engaged in the conversion of the remaining billet stock to items required for testing.

A 10,000-lb air-melted heat of INOR-8 was purchased from the Haynes Stellite Company to supply the immediate material needs of the various test programs. Casting and fabrication of the alloy by hot and cold working to bar, plate, sheet, and strip products was accomplished with little or no difficulty. Various shapes of this material have been received, including forged bar, hot-rolled plates, hot-rolled sheet, hot-rolled bar, six production-size extrusion billets, and rolled strip for the processing of Weldrawn tubing.

Recently, a review was made of the progress to date on Westinghouse Electric Corporation subcontract 1067, and the first periodic report on this developmental work was submitted to ORNL. In summary, three heats of the specified INOR-8 composition were induction-melted in air. Difficulties were encountered in forging castings of these heats because of internal flaws formed during cooling. Various changes in mold design and melting practice were made to overcome this, as described in detail previously.[4]

A sound 3-in.-dia forging from the initial high-carbon heat of INOR-8 prepared by Westinghouse was received for evaluation. The material was successfully worked by extrusion and by hot and cold rolling. Specimens were prepared for creep-rupture studies and for density and thermal expansion measurements. The density of the material, as determined by weighing a machined specimen, was found to be 8.795 g/cm^3. Thermal-expansion measurements were made from room temperature to 1832°F with the cooperation of the Ceramics Group of the ORNL Metallurgy Division. The data obtained are presented in Fig. 3.1.1. The coefficients of linear thermal expansion, α, based on the data of Fig. 3.1.1 are given below:

Temperature Range (°F)	Average α (in./in.·°F)
	$\times 10^{-5}$
212–752	0.75
752–1112	0.73
1112–1832	1.02
212–1832	0.87
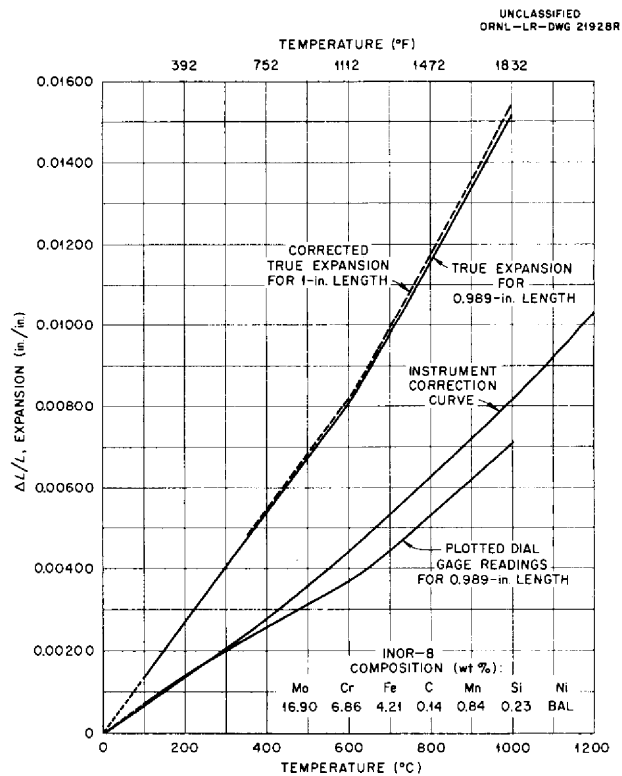
Fig. 3.1.1. Linear Thermal Expansion for 1-in. Length of INOR-8 as Determined with a Vacuum Dilatometer Direct-Reading Dial Gage. Sample used was only 0.989 in. long, and data were interpolated to values for a 1-in. length.

Creep-rupture tests on the air-melted and vacuum-remelted material, as shown previously,[4] indicated that definite improvements in time to rupture and in elongation were realized through vacuum remelting, but that the creep rate of the air-melted alloy was superior to that of the vacuum-remelted material.

Composite Tubing and Plate

In order to take advantage of the corrosion resistance of the nickel-molybdenum alloys in fuel 107 at temperatures exceeding 1650°F, it would be necessary to isolate the nickel-base alloy from the sodium through the use of composite tubing. Preliminary studies of INOR-8 and type 316 stainless steel diffusion couples show that an unknown phase or phases precipitate at the interface as a result of diffusion. The extent of the interface reaction is negligible after diffusion times of 500 hr at 1300°F. As expected, the severity of reaction increases rapidly as the temperature is increased to 1800°F. The precipitate is confined to the nickel-base side of the interface and occurs as a grain-boundary phase rather than as a continuous layer. Room-temperature tensile tests of composite sheet showed that strengthening occurred after diffusion heat treatments at 1300 and 1500°F. A weakening effect was observed in those specimens heat treated at 1650 and 1800°F. A minimum fracture ductility of 28% elongation was observed in the specimens heat treated at 1650°F.

The feasibility of fabricating composite tubing of Inconel and type 316 stainless steel was described previously.[1] It is anticipated that similar procedures can be applied to the fabrication of composites of INOR-8 and type 316 stainless steel.

MECHANICAL PROPERTIES INVESTIGATIONS

C. R. Kennedy[5]	J. R. Weir
R. W. Swindemann	J. W. Woods

Commercial nickel-base, molybdenum-containing alloys, such as Hastelloy B or W, have been considered for reactor applications because of their excellent resistance to chemical corrosion and their relatively high strength at elevated temperatures. Because such alloys showed promise as structural materials for a circulating-fuel reactor, an extensive investigation of the mechanical

properties of the Hastelloy alloys was carried out.[6] It was found that these alloys are not single-phase and that they suffer a serious loss of ductility as a result of the precipitation of a brittle beta phase in the reactor operating temperature range. These alloys also presented fabricational difficulties, particularly in the production of seamless tubing, and therefore it was considered that the best solution would be to change the alloy composition. Therefore, special alloys designed to retain the inherent advantages of the Hastelloys and to eliminate their objectionable characteristics were studied.

Screening tests were made of the creep-rupture properties of various experimental alloys exposed to fuel 107. For comparison, each alloy was tested with a stress of 8000 psi at 1500°F in two conditions: (1) annealed at 2000°F for 1 hr and (2) annealed at 2000°F for 1 hr and aged for 50 hr at 1300°F. Results of the creep-rupture tests, previously reported,[7-10] included data obtained for air-melted heats prepared by Battelle Memorial Institute, International Nickel Company, Westinghouse Electric Corporation, Superior Tube Company, and Haynes Stellite Company, as well as for vacuum-melted heats produced at ORNL.

Attempts were made to increase the strength of the nickel-molybdenum alloys by the addition of elements that form complex precipitates and by the addition of elements that are simple carbide formers. Additions of very small amounts (<1%) of aluminum and titanium did not seem to increase the strength, but did increase the elongation before fracture. Fabrication difficulties were encountered when additions of aluminum and titanium exceeded 1.5%. It was possible, however, to improve the creep characteristics by additions of carbide-forming elements, such as niobium and tungsten, without seriously compromising the other good characteristics. The BMI alloys

---

[5]On assignment from Pratt & Whitney Aircraft.

[6]C. R. Kennedy, D. A. Douglas, and W. D. Manly, *High Temperature Mechanical Properties of Hastelloy B and W*, ORNL-2402 (in press).

[7]C. R. Kennedy, *ANP Quar. Prog. Rep. Dec. 31, 1956,* ORNL-2221, p 249.

[8]J. W. Woods, *ANP Quar. Prog. Rep. March 31, 1957,* ORNL-2274, p 220.

[9]H. Inouye, T. K. Roche, and J. H. Coobs, *ANP Quar. Prog. Rep. June 30, 1957,* ORNL-2340, p 176.

[10]J. W. Woods and D. A. Douglas, *ANP Quar. Prog. Rep. Sept. 30, 1957,* ORNL-2387, p 171.

containing carbon in excess of 0.1% exhibited good high-strength properties, but they tended to fracture when subjected to tube-fabricating processes. Additional alloying elements, such as chromium (7%) and iron (4%), were found to improve the creep properties of the basic nickel-molybdenum binary alloy.

The Haynes Stellite INOR-8 (nominal composition, in wt %: 16 Mo—7 Cr—5 F—0.02 C—bal Ni) appears to be the best alloy produced to date. It has good corrosion resistance and fabricating characteristics, but, as a result of its low carbon content, the strength properties are only fair. It is considered to be feasible to substantially increase the strength of the alloy after the difficult fabrication processes are completed by adding more carbon through gas carburizing. Tests of specimens in which carbon was added by this means showed greatly improved strength properties.

A comparison of creep properties of untreated alloys and the same alloys after carburization with the properties of Hastelloy B are presented in Figs. 3.1.2, 3.1.3, and 3.1.4. It is evident that carburized INOR-8 becomes equivalent to Hastelloy B in creep strength at 1650°F.

Fig. 3.1.3. Creep Properties of Untreated INOR-8 and Carburized INOR-8 In Comparison with Those of Hastelloy B Exposed to Fuel 107 at 1650°F at a Stress of 5000 psi. (Secret with caption)
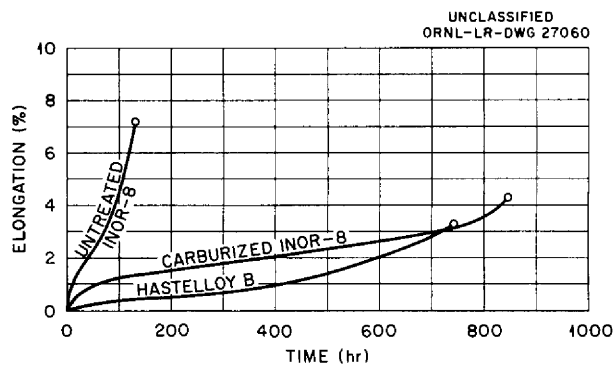
Fig. 3.1.4. Creep Properties of Untreated INOR-8 and Carburized INOR-8 in Comparison with Those of Hastelloy B Exposed to Fuel 107 at 1800°F at a Stress of 3000 psi. (Secret with caption)

CORROSION STUDIES

J. H. DeVan

J. R. DiStefano   R. S. Crouse

Two related series of tests have been made in order to evaluate the corrosion properties of nickel-molybdenum alloys in fused fluoride salts and in sodium. In the first series of tests, commercial alloys, such as Hastelloy B and Hastelloy W, were studied, while in the second series data were obtained on the corrosion properties of experimental nickel-molybdenum alloys, which from the standpoint of heat treatment and chemical properties are better adapted to reactor operation.

Fig. 3.1.2. Creep Properties of Untreated INOR-8 and Carburized INOR-8 in Comparison with Those of Hastelloy B Exposed to Fuel 107 at 1500°F at a Stress of 8000 psi. (Secret with caption)

Forced-circulation loops were used for most of the tests of the Hastelloys, but both thermal-convection and forced-circulation systems have been used to study the experimental alloys.

Forced-Circulation Loop Tests of Hastelloys

The results of forced-circulation loop tests of Hastelloy B with fuel 107 as the circulated fluid are summarized in Table 3.1.2. Further details of these tests were presented in previous reports.[11,12] While defects present in the as-received Hastelloy B tubing precluded comprehensive analyses of the test results, it was demonstrated in these tests that basic nickel-molybdenum alloy systems are compatible with alkali-metal fluorides at temperatures up to 1760°F.

The results of forced-circulation tests of Hastelloy B and Hastelloy W with sodium as the circulated

---

[11]J. H. DeVan, *ANP Quar. Prog. Rep. Sept. 10, 1956,* ORNL-2157, p 136.

[12]J. H. DeVan and R. S. Crouse, *ANP Quar. Prog. Rep. March 31, 1957,* ORNL-2274, p 147.

fluid are summarized in Table 3.1.3. A comparison of these results with the results for other classes of alloys tested in sodium is presented in Fig. 3.1.5, in which the weights of cold-zone deposits are indicated as a function of temperature. As may be seen, the Hastelloys and the nickel-base alloys, in general, are considerably more susceptible to mass transfer in sodium at temperatures above 1300°F than are either the austenitic or the ferritic stainless steels.

Forced-Circulation Loop Tests of Experimental Nickel-Molybdenum Alloys

Two forced-circulation loops constructed of experimental nickel-molybdenum alloys have been successfully operated for 1000 hr with fuel 107. The first of these loops, 7641-9, was discussed previously.[13] The loop was fabricated from an alloy containing 17% Mo–6% Fe–bal Ni and was

---

[13]J. H. DeVan and R. S. Crouse, *ANP Quar. Prog. Rep. Sept. 30, 1957,* ORNL-2387, p 176.

UNCLASSIFIED
ORNL–LR–DWG 27061

Fig. 3.1.5. Comparison of Results of 1000-hr Forced-Circulation Loop Tests of Various Alloys with Sodium. All loops contained oxide cold traps and were operated with a temperature drop of 300°F.

Table 3.1.2. Operating Conditions and Results of Forced-Circulation Loop Tests of
Hastelloy B with Fuel 107 as the Circulated Fluid

Loop Number	Period of Operation (hr)	Maximum Fuel-Wall Interface Temperature (°F)	Maximum Bulk Fuel Temperature (°F)	Fuel Temperature Differential (°F)	Reynolds Number	Flow Rate (fps)	As-Received Size and Condition of Tubing	Metallographic Results
7425-13A[a]	1000	1555	1505	200	10,000	3.2	Size: 0.5 in. OD, 0.035 in. wall; as-received specimens had surface pits to a depth of 1 mil	Small pits found along hot-leg surface to a depth of 1.5 mils; no cold-leg deposits or layers
7641-1B	1000	1767	1635	280	10,000	2.6	Size: 0.5 in. OD, 0.065 in. wall; inner surfaces of as-received tubing had pits in some areas to a depth of 5 mils	Many pits in hot leg to a depth of 4 mils; pits to a depth of 7 mils in vicinity of weld in cold leg; no cold-leg deposits or layers
7641-2B	1013	1710	1640	295	5,500	1.2	Size: 0.5 in. OD, 0.065 in. wall; tubing from same lot as that used for Loop 7641-1B	Many pits in hot leg to a depth of 4 mils; pits to a depth of 7 mils in cold leg; deposits of fine metal crystals in small area of cold leg up to 0.5 mil thick
7641-3B	407.5[b]	1750	1660	300	10,000	2.6	Same as loop 7641-1B	Many pits in hot and cold legs to a depth of 3 mils; no deposits or layers
7641-4E	180[c]	1710	1645	293	20,000	5.1	Size: $\frac{1}{4}$-in. sched-40 pipe; inner surfaces badly pitted and cracks present on both sides of longitudinal closure weld	Loop was shut down and repaired four times because of leaks; cleaning fills omitted on third and fourth runs; a silver-colored loosely adherent layer found throughout loop; layer consisted primarily of fuel, but contained approximately 10% Ni and 5% Mo

[a]Suffix letters designate number of loop shutdowns prior to termination.

[b]Terminated because of pump failure; tubing ruptured upon attempting to restart circulation.

[c]Terminated because of tube failure.

Table 3.1.3. Operating Conditions and Results of Forced-Circulation Loop Tests of Hastelloy B
and Hastelloy W with Sodium as the Circulated Fluid

Temperature differential: 300°F

Fluid flow rate: 2.5 gpm

Loop Number	Loop Material	Maximum Fluid Temperature (°F)	Operating Time (hr)	Maximum Hot-Leg Attack (mils)	Maximum Thickness of Cold-Leg Deposits (mils)	Total Weight of Cold-Leg Deposits (g)
7641-1	Hastelloy B	1500	1000	2	27	17.3
7641-2	Hastelloy B	1300	1000	2	3	0.45
7641-3	Hastelloy B	1500	2000	2	30	20.6
7641-4	Hastelloy W	1500	1000	1.50	22	20.6

operated with a maximum fluid-metal interface temperature of 1760°F. Attack occurred along the hot-leg surfaces in the form of intergranular voids and was limited to a maximum depth of 4 mils.

A second loop constructed of an alloy containing 17% Mo—10% Cr—bal Ni has now completed operation with a maximum fluid—metal interface temperature of 1850°F. Other operating conditions for the loop, 7641-10, are given below:

Maximum bulk fuel temperature	1750°F
Fuel temperature drop	300°F
Reynolds number	10,000
Flow rate	1.4 gpm
Ratio of heated section surface area to total loop volume	2.1 $in.^2/in.^3$

Extensive attack was found metallographically throughout the hot leg of the loop that reached, at the point of maximum wall temperature, to a depth of 23 mils. The attack was predominantly in the form of intergranular voids and was accompanied by removal of second-phase material from the grain matrix, as well as from the grain boundaries. Cold-leg sections showed little attack, but there was a thin metallic deposit over most of the exposed surface. The quantities of metal contaminants in fuel samples taken after the test were

comparable with those normally found in Inconel — fuel 30 systems tested at 1500°F. The chromium content of the fuel was approximately 685 ppm, and chromium was the impurity that was present in the largest quantity.

It is obvious on the basis of these test results that chromium additions in amounts of 10% or greater would limit the usefulness of nickel-molybdenum alloys in fuel 107 to temperatures below 1800°F. Thermal-convection loop test results appear to have established a satisfactory operating temperature of 1650°F, as discussed below.

Thermal-Convection Loop Tests of Experimental Nickel-Molybdenum Alloys

Approximately 50 thermal-convection loops fabricated from alloys representing numerous compositional variations of the 83% Ni—17% Mo base have been operated with fuel 107 for periods up to 1000 hr and temperatures up to 1650°F. The primary purpose of these tests was to evaluate the effect of specific alloying elements on the corrosion resistance of the base composition.

Most of the loops were operated with a maximum bulk fuel temperature of 1500°F and with a corresponding 1650°F metal-fluid interface temperature. The results of these tests were summarized in a previous report.[13] From the test data it has been

possible to stipulate approximate limits of alloy additions which can be permitted from the standpoint of corrosion penetration and resistance to thermal-gradient mass transfer. As would be expected, the limits are quite dependent on operating temperatures. A list of several promising compositions and their approximate temperature limitations for operation with fuel 107 were presented in Table 3.1.1. Operation at temperatures only 100°F lower than those shown has been found to reduce the corrosive attack for the same time period to a depth of 1 to 2 mils.

3.2. MECHANICAL PROPERTIES STUDIES

D. A. Douglas

C. R. Kennedy[1]   J. R. Weir

R. W. Swindemann   J. W. Woods

An extensive investigation has been under way during the past several years in which the mechanical properties of the various materials to be used in circulating-fuel aircraft reactors were evaluated under simulated service conditions. Particular attention has been given to obtaining design data and to studying the behavior of the materials under the various conditions of stress, temperature, and environment that will be encountered during operation of the reactor. Fairly complete design data were obtained for Inconel, the structural alloy chosen for the ART, for beryllium, the moderator material, and for various shielding materials. Basic information on the behavior of metals has also been obtained in order to be able to predict the safe operating life of various components under a variety of operating conditions.

DESIGN DATA

Inconel

Creep and stress-rupture data were obtained for Inconel in the temperature range of 1300 to 1650°F in argon, in sodium, and in the fuel mixture NaF-ZrF$_4$-UF$_4$ (50-46-4 mole %, fuel 30). The data for an argon atmosphere were used for comparison. Variables such as grain size, section thickness, and alloy consistency were investigated. It was found that in the fused-salt environment the fine-grained material is stronger than the coarse-grained metal at 1300°F but weaker at 1500°F and above. However, in argon and in sodium the fine-grained Inconel maintains its superiority over the coarse-grained material at temperatures up to 1650°F, where metallurgical instabilities begin to introduce adverse effects. A comparison of three heats of Inconel showed that quite wide variations in the properties of the alloy may be expected. There is not a large enough difference in the major alloying elements to account for the lack of uniformity; therefore it appears that the source of the difference is the variations of the minor additions or of the residual elements which are difficult to control in air melts.

[1]On assignment from Pratt & Whitney Aircraft.

Details of these investigations have been reported.[2]

Since the strength properties of Inconel make it only marginally useful at peak aircraft reactor operating temperatures, some thought has been given to a modification which would increase the strength without impairing the excellent fabricating characteristics. Carbon is a very potent strengthening agent because it disperses carbides throughout the matrix and in the grain boundaries, but, unfortunately, such a structure is difficult to draw into tubing. It was believed to be feasible, however, to fabricate the tubing and then add additional carbon through carburization. Several creep specimens were therefore pack-carburized and tested in fuel 30 and in argon. The results of these tests, as presented in Figs. 3.2.1, 3.2.2, and 3.2.3, show that a very marked improvement in creep properties was obtained.

[2]J. R. Weir, D. A. Douglas, and W. D. Manly, *Inconel as a Structural Material for a High-Temperature Fused-Salt Reactor,* ORNL-2264 (June 4, 1957).

UNCLASSIFIED
ORNL-LR-DWG 27062
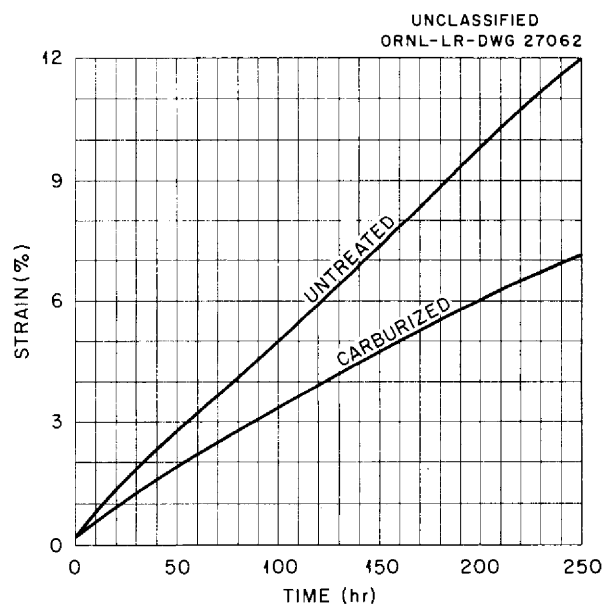
Fig. 3.2.1. Effect of Carburization on the Creep Properties of Inconel Tested in Fuel 30 at 1500°F and a Stress of 5000 psi. (Secret with caption)
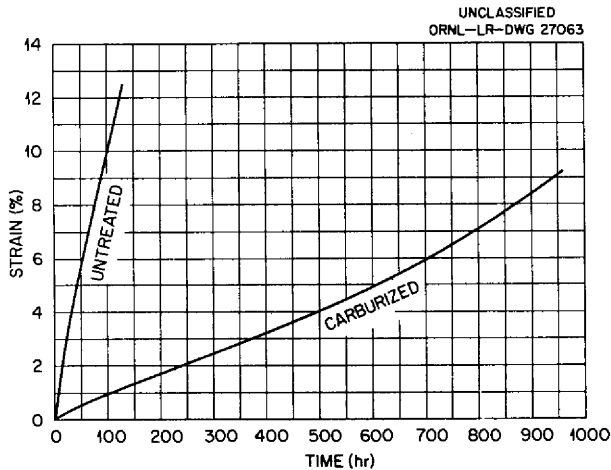
Fig. 3.2.2. Effect of Carburization on the Creep Properties of Inconel Tested in Fuel 30 at 1650°F and 3000 psi. (Secret with caption)
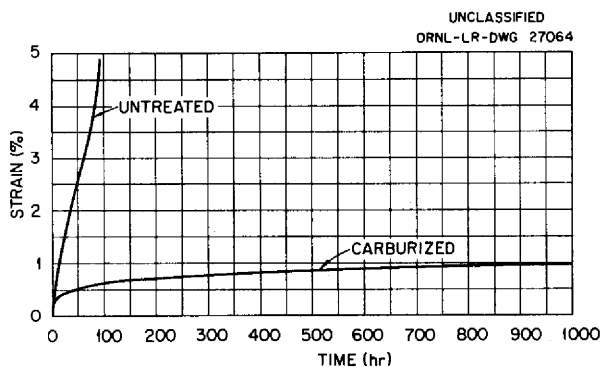
Fig. 3.2.3. Effect of Carburization on the Creep Properties of Inconel Tested in Fuel 30 at 1800°F and 1000 psi. (Secret with caption)

Recrystallized Inconel

A stable metallurgical microstructure is required in order to obtain optimum-strength properties in an alloy. Tests have demonstrated that metals which have been cold worked to various degrees may recrystallize under certain conditions of stress and temperature and that deleterious effects on the creep properties will result.[3] Since many reactor components are fabricated by pressure forming methods and are assembled by welding and brazing, portions of the structural metal will have experienced a variety of thermal treatments

prior to operation. Therefore a study was undertaken in order to establish the temperatures required for recrystallization after varying amounts of cold working and to determine the stable grain size achieved after high-temperature anneals.

The testing procedures used and illustrations of the grain sizes produced in recrystallized structures have been presented elsewhere.[4] It was noted in this study that the recrystallization temperature ranged from 1200 to 1650°F and was dependent on the amount of cold working and the time held at temperature. Fine-grained Inconel recrystallized at a temperature about 100°F lower than the temperature at which the coarse-grained material recrystallized for the same amount of prior deformation and time at temperature. The grain size that resulted from high-temperature treatments was found to be dependent on the degree of working prior to recrystallization up to a temperature of 1800°F. However, at 1900°F only very small differences in the final grain sizes could be seen regardless of the prior treatment.

Beryllium

Extensive mechanical tests of beryllium have been made in the temperature range of 800 to 1500°F by the Brush Beryllium Company under subcontract P.O. W34X-75581.[5] Also tests were made of samples trepanned from the actual beryllium moderator blocks prepared for the ART. The mechanical properties of the actual blocks were in excellent agreement with those obtained in the prior test program for material of like composition. Thus, it appears that data obtained in the test program can be reliably applied to large-scale production pressings.

EXTRAPOLATION OF TEST DATA

One of the problems associated with mechanical testing work is that there is frequent need for data under conditions outside the ranges of temperature or stress that have been explored. Thus, the first step in being able to anticipate the behavior of metals under service conditions is to develop a reliable method of interpolating and extrapolating

[3]J. R. Weir, Jr., *ANP Quar. Prog. Rep. Dec. 31, 1956,* ORNL-2221, p 244.

[4]D. A. Douglas and J. R. Weir, *Recrystallization and Grain Growth of Inconel,* ORNL-2406 (in press).

[5]R. G. O'Rourke *et al., Mechanical Properties of Reactor-Grade Beryllium at Elevated Temperatures,* COO-312 (Aug. 1956).

the available data. There has been much work done in this field, and there are several relationships which appear to have merit. The multitude of metallurgical variables involved in high-temperature deformation processes made it advisable, however, to derive empirical equations based on fairly specific data. Such equations are available for Inconel, and the method for using them and the limitations of the results are described in a topical report.[6]

THERMAL STRESS INVESTIGATIONS

The thermal cycles which occur in a reactor during its operation induce in the structural members corresponding stress and strain cycles. Thus for safe operation it is essential to know the effect of these strain cycles on the endurance of the structural materials. In order to obtain design data of this type, tests were conducted to determine the strain-cycle and stress-relaxation properties of Inconel. Important factors which have been investigated in conjunction with these tests are the effects of temperature, grain size, environment, specimen geometry, and cycle frequency. Testing devices were constructed for testing both tube and rod specimens. In order to gain a clear picture of the true influence of strain reversals, these rigs were designed to mechanically strain the specimens; whereas, under true operating conditions, the strains may be produced by thermal fluctuations. Supporting investigations in which thermally induced strain cycles are being studied are under way at the University of Alabama.

Strain-cycle tests in argon at 1300, 1500, and 1600°F were completed, and the data were presented previously.[7-9] Curves have been drawn which indicate the number of strain cycles to failure, N, as a function of plastic strain per cycle, ϵ_p. An empirical equation,

$$N^a \epsilon_p = C ,$$

has been formulated to relate the data, which fall on a straight line when plotted as log ϵ_p vs log N. Similar behavior was observed by Coffin[10] in his work on thermally induced cyclic strains in type 347 stainless steel.

At 1500 and 1600°F, fine-grained Inconel is superior to coarse-grained material; that is, the data indicate that fine-grained specimens endure a greater number of cycles at a given strain-cycle level before failure. At 1300°F, however, the difference in cycles to rupture between coarse- and fine-grained Inconel is negligible.

The influence of geometry is not great. Rod specimens appear to endure slightly more cycles before failure than tube specimens. However, this improvement may be attributed to a less sensitive method of detecting the initiation of failure in the case of rod specimens.

The effect of temperature on these properties is not appreciable over the temperature range studied. Specimens cycled at 1600°F exhibit only a slightly greater number of cycles to failure than specimens tested under comparable conditions at 1300 and 1500°F.

Tests have also been conducted on Inconel tubes in fuel 30 at 1500 and 1600°F. Results of these tests were presented in previous reports in this series.[9,11] The effect of fuel is to reduce the number of cycles to failure by 40 to 66% of the number of cycles in argon, depending on the plastic strain per cycle and the grain size.

Since the frequency of induced-strain cycles within a reactor will not be uniform, a program has been set up for determining the effect of frequency on the strain-cycle properties. Previously, all tests had been conducted with a 2-min/cycle period. Present investigations[9,11] are being conducted with a 30-min/cycle period on Inconel tube specimens at 1500°F, and there are indications that frequency may be an important factor. Specimens cycled at small strains and 30-min/cycle periods do not endure as many cycles as those cycled with the 2-min/cycle period. Further investigations will have to be completed before this effect can be entirely substantiated and understood.

[6]C. R. Kennedy and D. A. Douglas, *Use of a Rate Equation for the Extrapolation of Creep Data*, ORNL CF-57-8-119 (Aug. 20, 1957).

[7]C. R. Kennedy and D. A. Douglas, *Plastic Strain Absorption as a Criterion for High-Temperature Design*, ORNL-2360 (in press).

[8]J. R. Weir, Jr., *ANP Quar. Prog. Rep. Dec. 31, 1956*, ORNL-2221, p 246.

[9]C. R. Kennedy and D. A. Douglas, *ANP Quar. Prog. Rep. June 30, 1957*, ORNL-2340, p 190.

[10]L. F. Coffin, Jr., *Trans. Am. Soc. Mech. Engrs.* 76, 931–50 (1954).

[11]C. R. Kennedy and D. A. Douglas, *ANP Quar. Prog. Rep. Sept. 30, 1957*, ORNL-2387, p 182.

Results from the tests being made at the University of Alabama indicate that mechanical strain-cycle effects at 1300°F correlate well with thermally induced strain-cycle behavior at the same mean temperature.[11]

Additional tests were made in order to determine the effect of carburization, weld metal, and braze-metal coatings on the strain-cycle properties of Inconel tubes. Tests conducted on carburized Inconel tubes showed no change in strain-cycle characteristics as a result of the carburizing treatment.[11] A series of tests on all-weld-metal tubes was cancelled before completion, but the preliminary results[11] indicated that the welds were stronger in tension than the base metal at temperatures from 1400 to 1800°F. Several Inconel tube specimens coated with braze metal (92% Ni–3% Si–3% B–2% Fe) were tested in order to determine whether boron penetration of the base material would affect the strain-cycle properties. Rupture data from these tests at 1500°F were in good agreement with the design curve for coarse-grained Inconel at 1500°F. Consequently, it may be assumed that no detectable impairment of strain-cycle characteristics will be produced by the presence of a braze-metal coating.

A series of tests for evaluating the effect of prior strain cycling on the creep properties of Inconel was also conducted. The procedure and initial results were described previously.[11] In summary, the available data indicate that the creep strength and rupture life are significantly reduced by prior strain cycling and that, with increasing consumption of strain-cycle life, the creep-life expectancy is correspondingly reduced. The inference is that design calculations based on only one of these conditions would be optimistic for instances where both strain cycling and creep occurred.

Beryllium is the only other reactor material for which strain-cycle characteristics have been investigated. A series of tests was conducted at 1250°F on hot-pressed, reactor-grade beryllium, and the results were reported previously.[11] The test data revealed that beryllium, although much inferior to Inconel, nevertheless, does have ductility and is capable of withstanding cyclic strains at 1250°F.

Relaxation

Stresses induced by a thermal cycle in a constrained structural member usually undergo some degree of decay or relaxation if the temperature is sufficiently high This relaxation of stress occurs through a conversion, by creep, of the elastic strain into plastic strain. In order to establish the true plastic strain induced by a thermal loading, the relaxation characteristics of a material must be known and taken into consideration.

Relaxation tests of Inconel were completed for coarse- and fine-grained specimens at 1100, 1300, 1500, and 1650°F, and the test procedures, apparatus, and results have been described.[12] The data obtained in these tests indicate that, at temperatures greater than 1300°F, relaxation of stress occurs rapidly. The relaxation rate at these temperatures varies only when the initial strain is below the elastic limit. Moreover, induced plastic strains do not significantly increase the elastic limit, since recovery appears to be rapid at temperatures above 1300°F. Stresses are reduced to low residual values after a few minutes. Below 1300°F, however, relaxation occurs less rapidly. At 1100°F high initial strains produce work hardening, which results in larger elastic strains and higher stress values; these strains, in turn, relax slowly. The results also give indications of a grain-size effect. The relaxation rates of coarse-grained Inconel at all temperatures were lower than the rates for fine-grained material.

Fatigue

Under a subcontract to Battelle Memorial Institute, a program was initiated to investigate the effect of cyclic stresses imposed on a statically loaded system. The aim of this program was to define the stress conditions under which fatigue is the dominant failure mechanism and the stress conditions under which creep may be regarded as the controlling mechanism for failure. Preliminary tests for checking the performance of the apparatus and the reproducibility of results were satisfactorily completed. At present, tests are being conducted to determine the influence of stress-cycle frequency on the fatigue properties.

Biaxial Creep

Very little is known concerning the influence of stress distribution on deformation rates, and the

---

[12]C. R. Kennedy, D. A. Douglas, and W. D. Manly, *Relaxation Characteristics of Inconel at 1100 to 1650°F,* ORNL-2407 (in press).

fact that structures are normally subjected to multiaxial stresses emphasizes the need for additional research in this area. Therefore a program of tests is being conducted in which tubes are subjected to various ratios of axial and tangential stress and the resultant creep rates are measured. A considerable change in rupture life, ranging from 200 to 2000 hr, and significant variations of creep rates have been noted.[13] A considerable quantity of data must be accumulated before it will be possible to determine which of the various mechanical theories of failure describes the mechanism of fracture under these test conditions.

TESTS OF SHIELDING MATERIALS

Creep-rupture testing of an 80% Mg–20% Li alloy proposed as a neutron shielding material was completed. Data in addition to those presented previously[14] have been obtained at 200°F for specimens that were given a chemical surface

treatment[15] and are compared in Table 3.2.1 with data obtained for untreated specimens.

An alloy of very pure lead containing 0.06% copper has been proposed for use as a gamma-ray shielding material. Since no mechanical property data were available at a temperature of 230°F, the expected maximum operating temperature of the lead shield, a creep-rupture testing program was initiated to determine the strength of this alloy. A design criterion of a creep rate of 0.5% strain per year for a stress of 100 psi was established. The results of tests in air show that this alloy has a deformation rate of about 2% per year at 100 psi. Specimens tested at 50 and 20 psi showed deformation rates of 0.08% per year and 0.05% per year, respectively. A lead-lithium alloy was also investigated in the hope that its excellent room-temperature strength indicated good high-temperature strength. However, it was found that the lead-copper alloy has greater creep strength at 230°F than the lead-lithium alloy.[16]

[13]C. R. Kennedy and D. A. Douglas, *ANP Quar. Prog. Rep. Sept. 30, 1957*, ORNL-2387, p 185.

[14]J. R. Weir and C. W. Dollins, *ANP Quar. Prog. Rep. Sept. 10, 1956*, ORNL-2157, p 208.

[15]R. E. McDonald and C. F. Leitten, Jr., *ANP Quar. Prog. Rep. June 10, 1956*, ORNL-2106, p 173.

[16]D. H. Jansen, E. E. Hoffman, and D. M. Sheppard, *Lead-Lithium Shielding Alloy — Metallurgical Studies*, ORNL-2404 (in press).

Table 3.2.1. Results of Creep-Rupture Tests at 200°F of an 80% Mg–20% Li Alloy

Specimen Condition	Stress (psi)	Time to Indicated Strain (hr)					
		0.2%	0.5%	1%	2%	5%	10%
Treated	100	3579	6647				
	200	862	2284	3484			
Untreated	600	3.6	25	72	121	420	940
	800			0.5		1	71

3.3. WELDING AND BRAZING STUDIES

P. Patriarca

G. M. Slaughter   R. L. Heestand

PRODUCTION OF CAST RINGS OF BRAZING ALLOY

P. Patriarca   G. M. Slaughter

Difficulties were encountered by the York Corp. in the consistent brazing of radiator test units with sintered brazing-alloy rings obtained from Coast Metals, Inc.[1] Therefore a decision was made to use brazing-alloy rings cast in graphite molds for the fabrication of future units. Experiments have indicated that the cast rings are not so sensitive to the rate of temperature rise as are the sintered rings[2] and that the required consistent minimum brazing temperature is somewhat less.

Consequently, a production facility was set up by the Engineering and Mechanical Division for manufacturing approximately 3,000,000 rings according to the procedures previously developed by the Welding and Brazing Group of the Metallurgy Division.[3] Assistance was given by Metallurgy Division personnel in the determination and control of optimum ring dimensions and weights and in the establishment of systematic weight-control records. A production rate of approximately 60,000 to 70,000 rings per day was achieved, and a total of approximately 750,000 rings was manufactured prior to termination of production on September 6, 1957. A detailed description of the equipment and production procedures, including a cost estimate, is being prepared by the Engineering and Mechanical Division.[4]

FABRICATION OF THERMOCOUPLES FOR HIGH-TEMPERATURE SERVICE

P. Patriarca

The use of thermocouples in high-temperature fused-salt systems requires that a reliable thermocouple junction be made and that a leaktight seal be assured. It is also desired that the locations of the junctions of all thermocouples be at a consistent and known distance from the end cover.

The problem of sealing the junction end of four-wire Chromel-Alumel thermocouples which were housed in Inconel tubing and insulated with magnesium oxide was first approached by welding. A small Inconel plug was inserted into a hole which had been prepared by sand-blasting the magnesium oxide to the desired depth. The assembled components were then fused together, both with and without the addition of filler wire. The inadequacy of this and other similar procedures was apparent when radiographic inspection resulted in a rejection rate of approximately 20% as a result of cracks and pores in the weld zone.

High-temperature furnace-brazing procedures were then utilized in developing a suitable fabrication technique. In initial experiments the magnesium oxide was excavated for a short distance, the hole was filled with brazing alloy, and the unit was brazed. As was expected, this procedure resulted in excessive porosity and poor wetting of the 2%-aluminum-containing Alumel component of the thermocouple. Most test specimens leaked during vacuum testing; thus the seals would have been unsatisfactory for use in the corrosive fused salt environment. Further, the distance between the end of the seal and the thermocouple junction varied both in seals made by this method and in those made by the welding technique, and such variations could give significant errors in temperature measurements during service.

A method was consequently developed which satisfied the requirements as to both integrity of the seal and consistency in the distance between the end of the seal and the thermocouple junction. A schematic drawing that illustrates the thermocouple fabrication procedure is presented in Fig. 3.3.1, and the products of the various steps of the procedure are shown in Fig. 3.3.2.

[1]G. M. Slaughter, *ANP Quar. Prog. Rep. June 30, 1957,* ORNL-2340, p 223.

[2]G. M. Slaughter, *ANP Quar. Prog. Rep. March 31, 1957,* ORNL-2274, p 205.

[3]P. Patriarca and R. E. Clausing, *ANP Quar. Prog. Rep. Sept. 10, 1956,* ORNL-2157, p 200.

[4]W. S. Hornbaker, *Production of Fused Coast Metals No. 52 Alloy Brazing Rings,* ORNL-2424 (to be published).

BRAZING ALLOY RING OR POWDER (0.04 g)

EXCAVATED ∿ 1/8 in.

MAGNESIUM OXIDE INSULATION

THERMOCOUPLE WIRES, 2 CHROMEL AND 2 ALUMEL, 0.030-in. OD

INCONEL SHEATH, 0.254-in. OD 0.035-in. WALL, BORED WITH NO.12 DRILL TO TOP OF CAP

INCONEL COVER, 0.025-in. THICK, 3/16-in. DIA, PUNCHED

INCONEL CAP, 0.025-in. THICK, 11/64-in. DIA, PUNCHED AND DRILLED WITH NO.64 DRILL
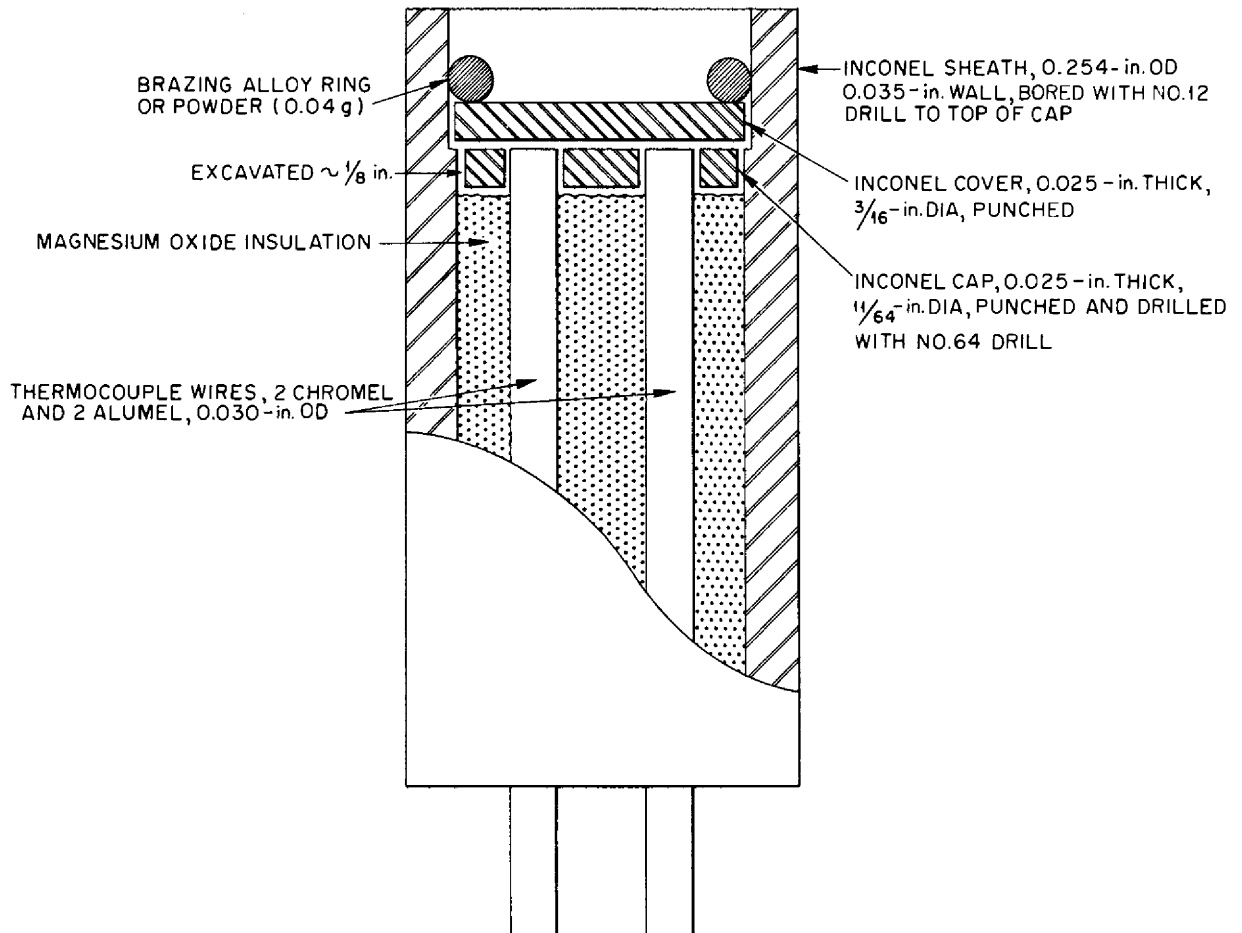
Fig. 3.3.1. Assembly Diagram of Thermocouple for High-Temperature Service.

After the magnesium oxide is excavated to the desired depth as illustrated, the four-hole Inconel disk is inserted into the hole, the thermocouple wires are cut off, a solid Inconel disk is placed on top, and the assembly is brazed in dry hydrogen at 1080°C. The brazing alloy can be preplaced either as powder or as a cast ring. If a cast ring is to be used, it is advisable to prime the ring to the joint with a slight amount of powder. Radiographic inspection can be used after manufacture to assure that high-quality joints are obtained.

FABRICATION OF ART HEAT EXCHANGERS

G. M. Slaughter

The fabrication of an experimental ART fuel-to-NaK heat exchanger by Black, Sivalls & Bryson, Inc., Tulsa, Oklahoma, was observed closely in order to assure the adequacy of the high-temperature brazing procedures utilized. The preplacement of Coast Metals brazing alloy No. 52 on the tube-to-header joints was closely examined before the unit was placed on the brazing fixture. Cast brazing-alloy rings, both circular and elliptical,
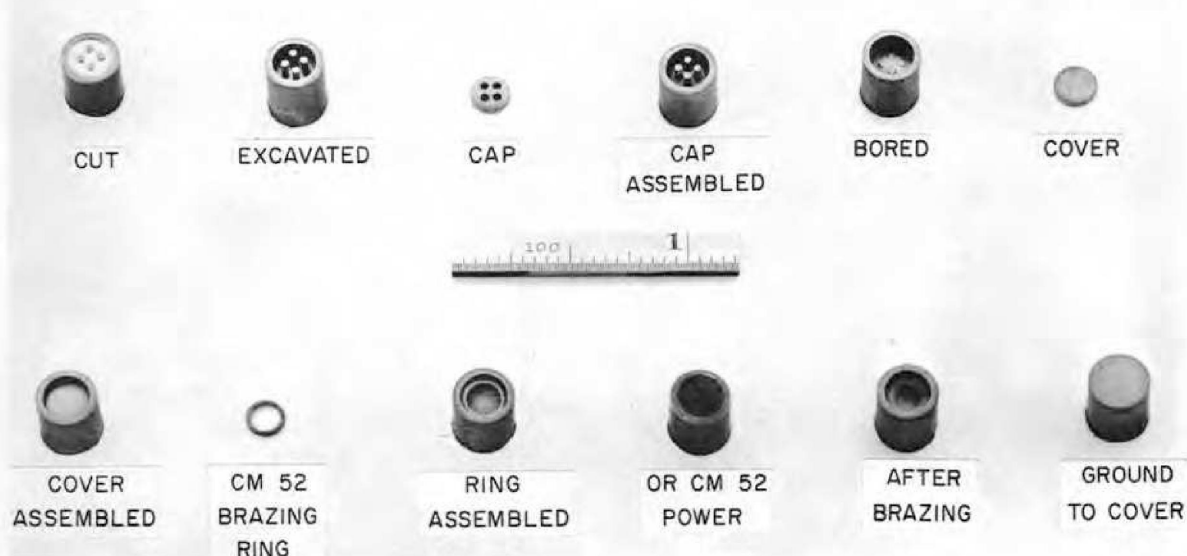
Fig. 3.3.2. Products of the Various Steps in the Preparation of Thermocouples for High-Temperature Service.

had been made in graphite molds at Black, Sivalls & Bryson, but there was considerable misfitting. In order to permit intimate contact between the rings and headers, many of the rings had to be removed and replaced by cemented half-rings. Additional brazing alloy in the form of slurry had to be applied to a large number of joints to connect the rings to the capillary joints. In a few instances, slurry had to be added to joints where the rings did not intimately contact the tubes.

The unit was placed on a large fixture, previously constructed at the York Corporation, that did not accurately match the contour of the heat exchanger; consequently, the extensive use of shims was required. This fixture was utilized for expediency, and one machined to greater accuracy was being constructed for brazing prototype units. The tube sheets of both headers were in the vertical position during brazing, with the axes of the tubes horizontal at the point of entrance to the header. Various measurements were made for determining the degree of distortion during brazing.

The unit was sealed in a retort and was brazed in a Lindberg furnace that had a working space approximately 6 ft wide, 8 ft deep, and 10 ft high. The maximum power rating of this furnace was 420 kw, and the recommended maximum working temperature was 2050°F. The hearth of the furnace was mounted on a flat car so that the retort could be located on the hearth while outside the furnace. The furnace temperature could be closely regulated with ten individual-zone controllers.

The atmosphere purification system for the furnace consisted of a BAC-150 activated-alumina Lectrodryer (closed cycle) and a Deoxo model D-1000-50 palladium catalyst. The inlet dewpoint to the retort was approximately −100°F throughout the brazing cycle.

Eight Chromel-Alumel thermocouples were attached to the assembly, job samples, and fixture, with two attached to each header of the heat exchanger. An approximate rate of temperature rise of 300°F/hr was employed, and $\frac{1}{2}$-hr temperature stabilization periods were used at approximately 1400 and 1600°F.

At the start of the soak period, the header thermocouples indicated temperatures that varied from 1900 to 1925°F. At the end of the 30-min soak period, the temperature variation recorded by

these four thermocouples was reduced to 5°F (1915–1920°F). The maximum temperature recorded by these thermocouples was 1925°F.

After removal of the heat exchanger from the retort, the brazes on both headers were examined. All visible joints, including those on the two job samples, had relatively good fillets, and the unit was, in general, clean and bright. The extent of runoff from one header was such, however, that the bottom row of tubes was solidly brazed to the bottom wedge of the header. More careful control of the brazing alloy preplacement procedures should reduce runoff, but it is felt that additional preventive measures should be studied.

In summary, it appeared that the gas purification and brazing equipment were adequate and that the general brazing procedures were well conducted. Previous experience had indicated that it might be more advisable from the standpoint of fillet reliability to have the units brazed with the tube sheets in the horizontal position (tube axes vertical). It is recognized, however, that this could only be accomplished in this case by brazing one end at a time and thereby introducing what could prove to be insurmountable distortion problems. It was recommended, therefore, that extra time and effort be devoted to the preplacement problem in an attempt to prevent runoff and to ensure reliable fillets.

ART FILL-AND-DRAIN TANK FABRICATION

R. L. Heestand

An investigation of optimum methods for fabricating the ART fill-and-drain tank tube-to-tube-sheet joints was completed. A description of the techniques used in the study was given previously.[5,6]

The optimum joint design consisted of trepanning the weld side of the tube sheet, as shown in Fig. 3.3.3. The trepanning serves to ensure good heat distribution by providing a uniform weld geometry and to minimize tube-sheet distortion and restraint in the vicinity of the weld joint. Test joints made initially by fusion welding showed some root cracks, but welds made with Inco No. 62

---

[5]E. A. Franco-Ferreira and G. M. Slaughter, *ANP Quar. Prog. Rep. March 31, 1957,* ORNL-2274, p 200.

[6]E. A. Franco-Ferreira, *ANP Quar. Prog. Rep. June 30, 1957,* ORNL-2340, p 225.

filler metal added to the joint were found to be free of root cracks.

In back-brazing the welded tube-to-tube-sheet joints, a unique heating problem existed in that the tube-sheet temperature continuously lagged behind the tube temperature throughout the brazing cycle because of the much greater thickness of the tube sheet. When Coast Metals brazing alloy No. 52 was applied by conventional means, the alloy would preferentially flow to the hottest member, and consequently there was poor flow on the tube sheet. The method of brazing-alloy preplacement shown in Fig. 3.3.3 and described
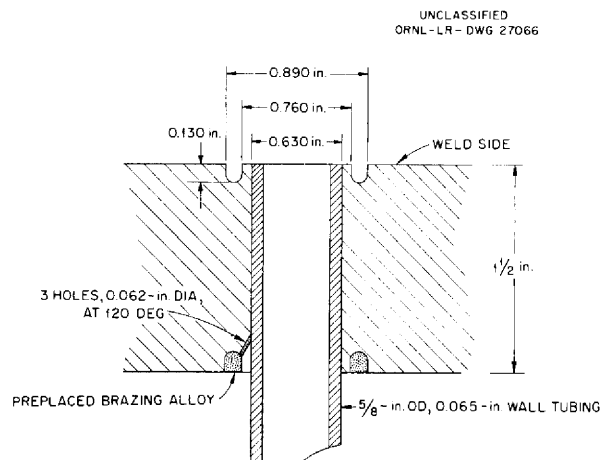
Fig. 3.3.3. Trepanned Joint Detail.

previously[6] removed the problem by allowing the brazing alloy to remain at the temperature of the tube sheet until the brazing temperature was reached. The trepanned sump on the braze side of the tube sheet then acted as an infinite reservoir from which the alloy flowed to fill the annulus between the tube and the tube sheet and to form a fillet where the tube met the tube-sheet surface. A typical joint of this type, cut so as to show one of the three sump holes, is shown in Fig. 3.3.4.

In order to further prove the techniques described above and to study the amount of distortion in the tubes which might be encountered in a typical braze cycle, a 66-tube Inconel sample that simulated a tube-sheet section was prepared. Brazing-alloy slurry (Coast Metals No. 52) was applied to

the braze side, and the tubes were then inserted and were welded with Inco No. 62 weld wire.
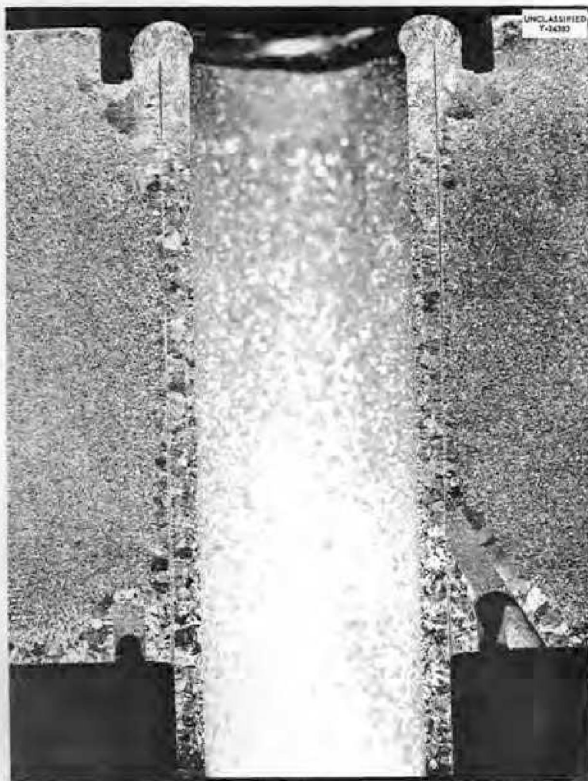
Fig. 3.3.4. Cross Section of a Typical Welded and Brazed Tube-to-Tube-Sheet Joint.

After brazing at 1920°F, no visual distortion was evident, and the complete fillets at all joints indicated a high degree of reliability. The weld side of the completed sample is shown in Fig. 3.3.5, and the braze side is shown in Figs. 3.3.6 and 3.3.7.

The utilization of brazing in the fabrication of this unit is unique, since high-temperature brazes are not normally used on tube sheets of this thickness. This method of alloy preplacement permits a high degree of reliability in both braze penetration and filleting, however, and it may well be applicable to tube-to-tube-sheet joints on other types of heat exchangers having components of similar size.

NIOBIUM WELDING

R. L. Heestand

Investigations of methods for welding niobium were started. Attempts are being made to produce ductile welds by the inert-arc fusion process and by the addition of filler metals.[7] Fusion welds manufactured manually at the Fansteel Metallurgical Corporation and fusion welds machine-made at ORNL have been examined metallographically. Although some differences in the sizes of the grains in the two welds were evident (Figs. 3.3.8 and 3.3.9), no other significant differences were apparent. Both types of fusion welds were tested in simple bend tests and found to be ductile. Experiments are also being carried out to determine differences in weldability of arc-cast and powder-metallurgy niobium. An inert-atmosphere dry box and fusion-welding techniques are being used for these experiments. Pure niobium wire and wire fabricated from arc-cast ingots of zirconium-niobium and zirconium-niobium-molybdenum alloys were prepared as filler metals for additional welding experiments. Welds fabricated by depositing niobium wire have large grains, and they have leaked in high-temperature service in liquid metals, even though they had passed room-temperature mass-spectrometer leak detection tests prior to operation. A cross section of a saddle weld made with niobium wire is shown in Fig. 3.3.10.

In the development of filler wires for welding niobium, the zirconium-niobium system was investigated because it was known that the 85% Zr–15% Nb alloy had satisfactory melting characteristics. Development studies pertaining to the transformation kinetics and fabrication of this alloy had been made by the Physical Metallurgy Group associated with the Homogeneous Reactor Project, and a prediction of the behavior of the alloy could be made. The studies had indicated that the zirconium-niobium alloy, with ternary additions to control age-hardening reactions, would be desirable because of its melting point, melting range, and transformation kinetics, and because of the possibility of solution of the niobium base metal in the weld metal.

Both butt welds and tubing saddle welds have been fabricated in an argon-atmosphere dry box (Fig. 3.3.11) by using the tungsten-arc process and zirconium-niobium filler wire. A typical butt weld in sheet niobium is shown in Fig. 3.3.12.

---

[7]R. L. Heestand and E. E. Hoffman, *Welding of Niobium Progress Report No. 1*, ORNL-2423 (to be published).
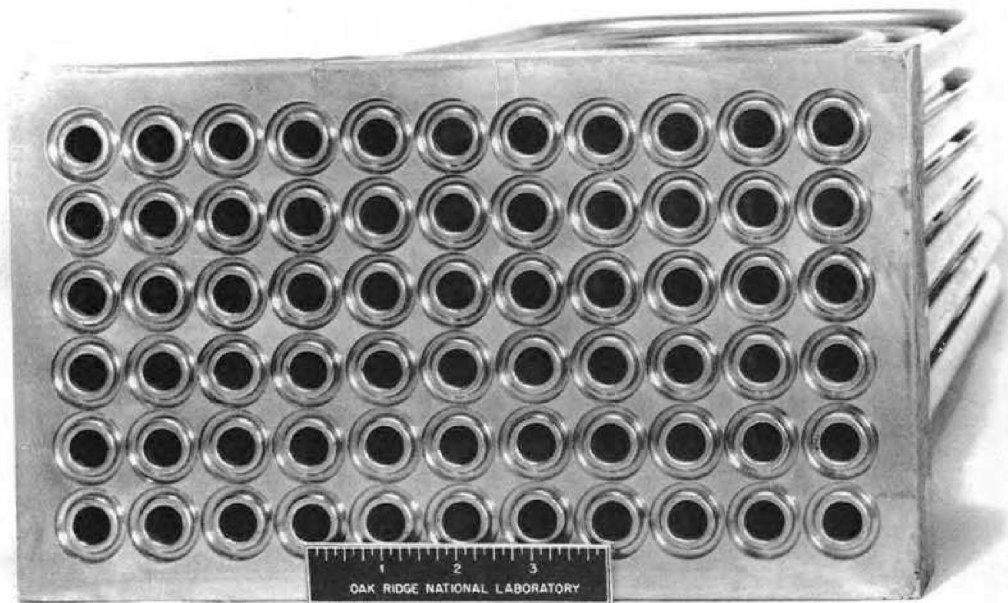
Fig. 3.3.5. Weld Side of Fill-and-Drain-Tank Sample.
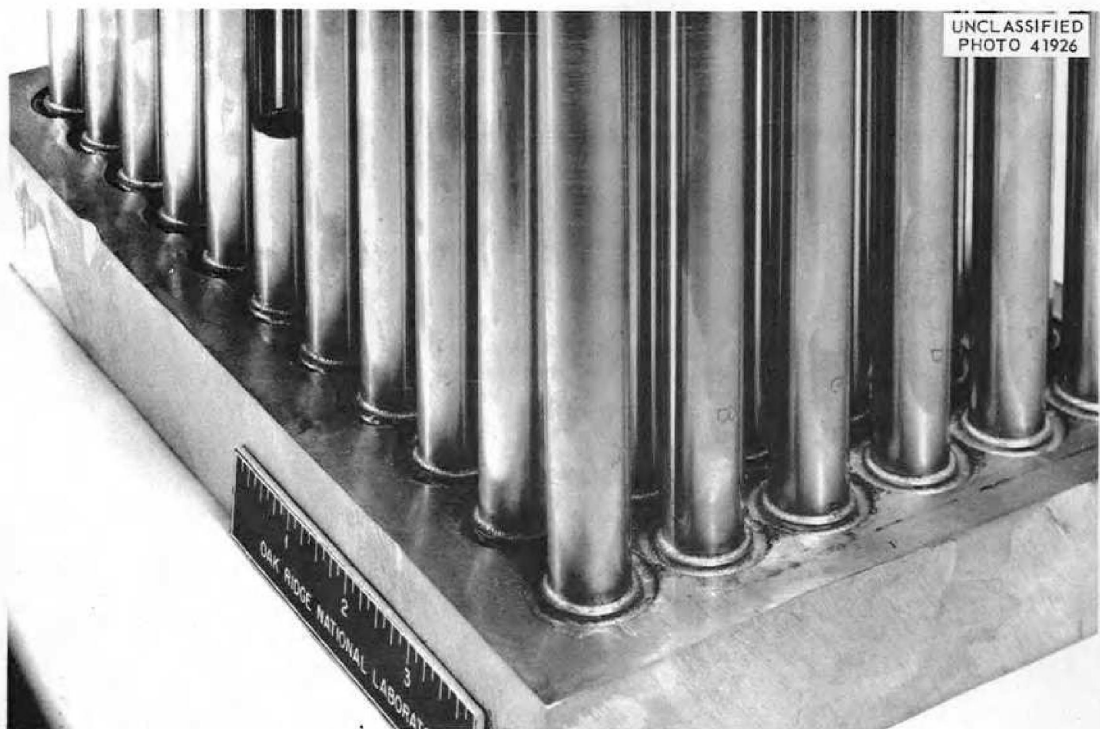
Fig. 3.3.6. Braze Side of Fill-and-Drain-Tank Sample Showing Filleting of Trepanned Braze Joint.
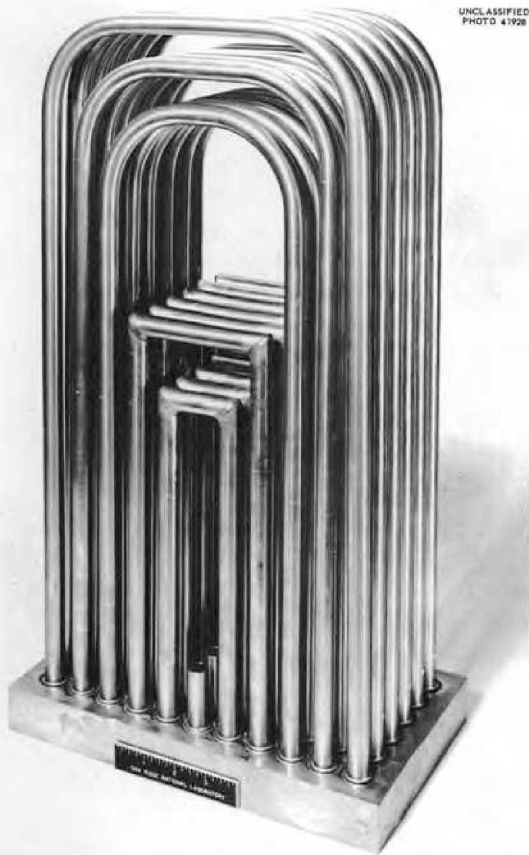
Fig. 3.3.7. Tube Side of Fill-and-Drain-Tank Sample.

The joint was spaced with a gap approximately 0.030 in. wide prior to welding. As may be seen in Fig. 3.3.12, the filler metal simulates a brazing alloy rather than an actual welding filler metal. The gap was penetrated, and wetting was observed on the side opposite to the welding area. Welds of this type have been found in free bend tests to be ductile when bent through a 90-deg angle. The major distortion was in the weld.

The more complicated saddle weld shown in Fig. 3.3.13 and in cross section in Fig. 3.3.14 was also fabricated with zirconium-niobium filler wire. In this case no joint spacing was used, and the alloy did not penetrate to the inside of the joint. It may be noted that the fine grain of the niobium base metal was retained. A saddle weld which was sectioned and crushed to demonstrate the ductility of the joint is shown in Fig. 3.3.15.

Similar butt welds and tubing saddle welds were fabricated with 80% Zr–15% Nb–5% Mo filler wire, and the ductility was found upon bending to be the same as for the 85% Zr–15% Nb wire. Deposition of the 80% Zr–15% Nb–5% Mo alloy is somewhat more difficult, however, because of a higher melting point. The 80% Zr–15% Nb–5% Mo alloy shows greater strength than the 85% Zr–15% Nb alloy. More complete investigations of alloys of the zirconium-niobium system are planned.
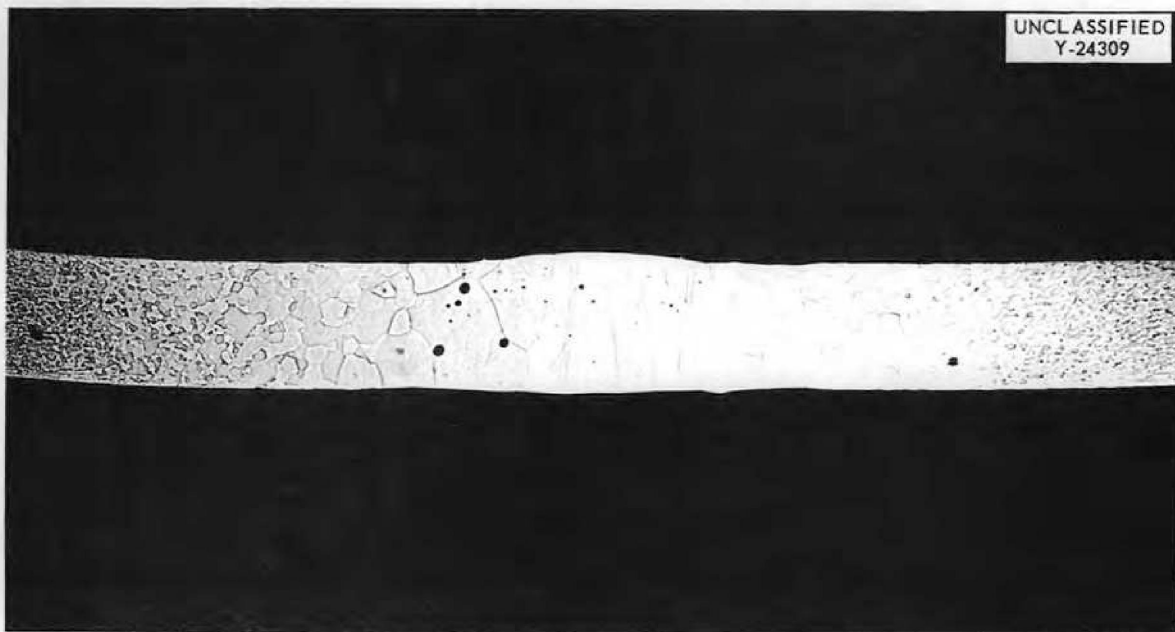
Fig. 3.3.8. Fusion Seam Weld Machine-Made in Niobium Tubing at ORNL. 22X.
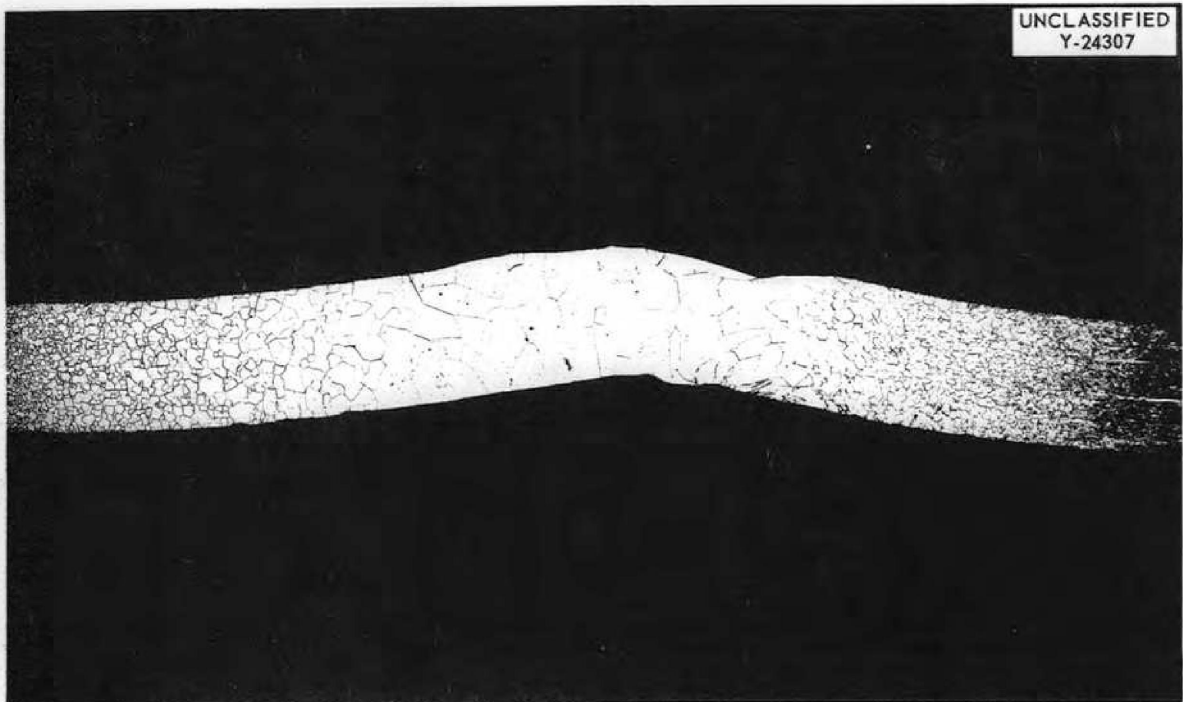
Fig. 3.3.9. Fusion Seam Weld Manually Made in Niobium Tubing at Fansteel Metallurgical Corporation. 22X.
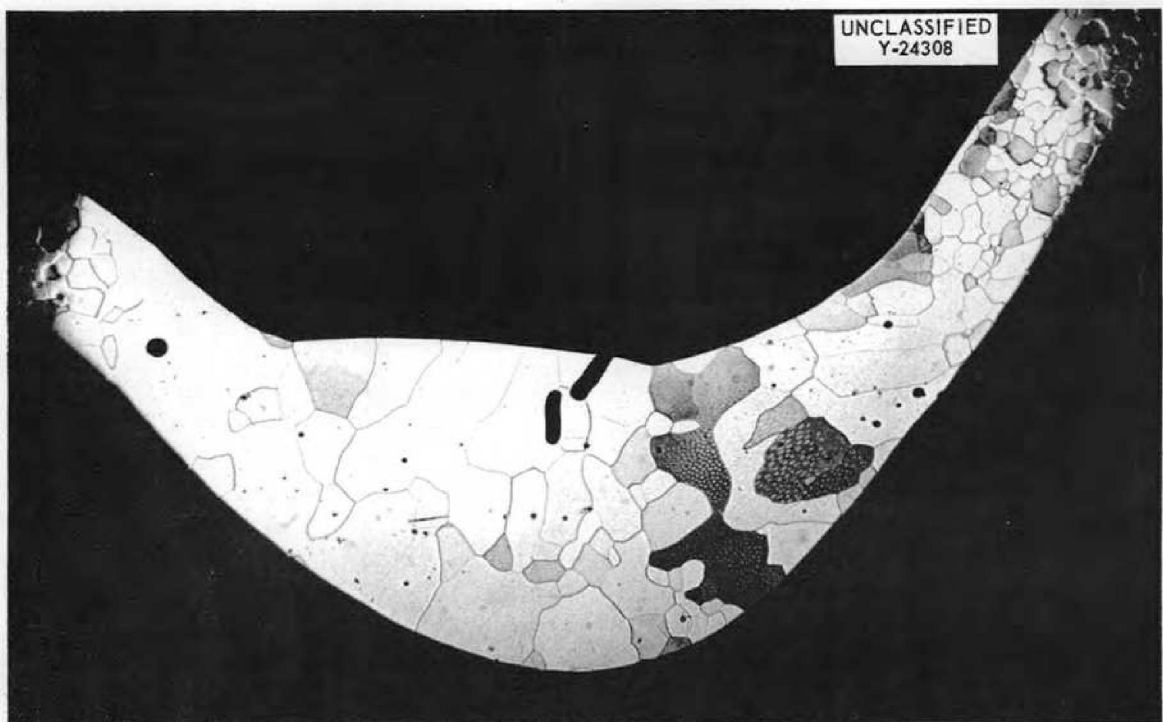
Fig. 3.3.10. Cross Section of Niobium Saddle Weld Made with Niobium Filler Wire. Weld made at ORNL by using inert-arc method. 22X.
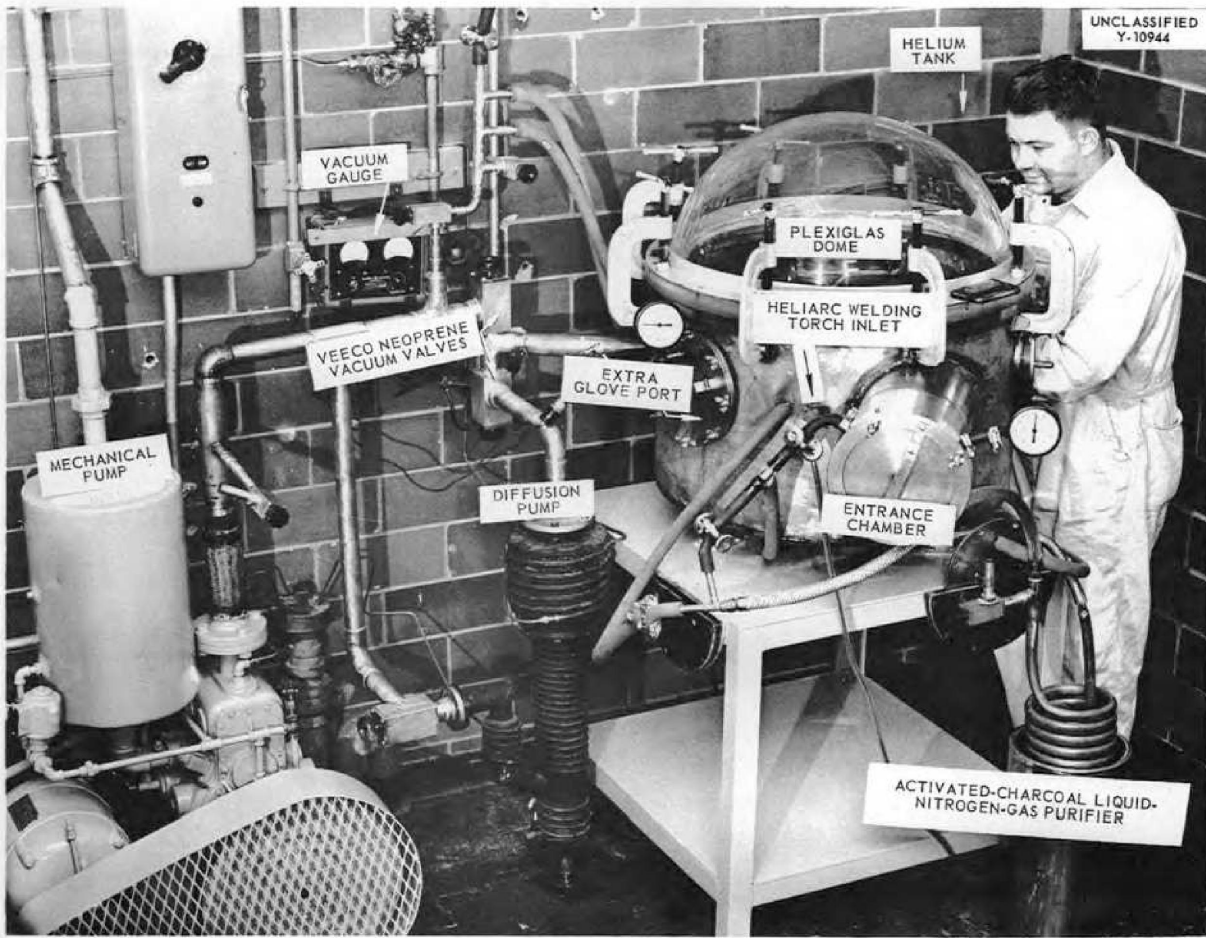
Fig. 3.3.11. Argon-Atmosphere Dry Box for Welding Niobium.
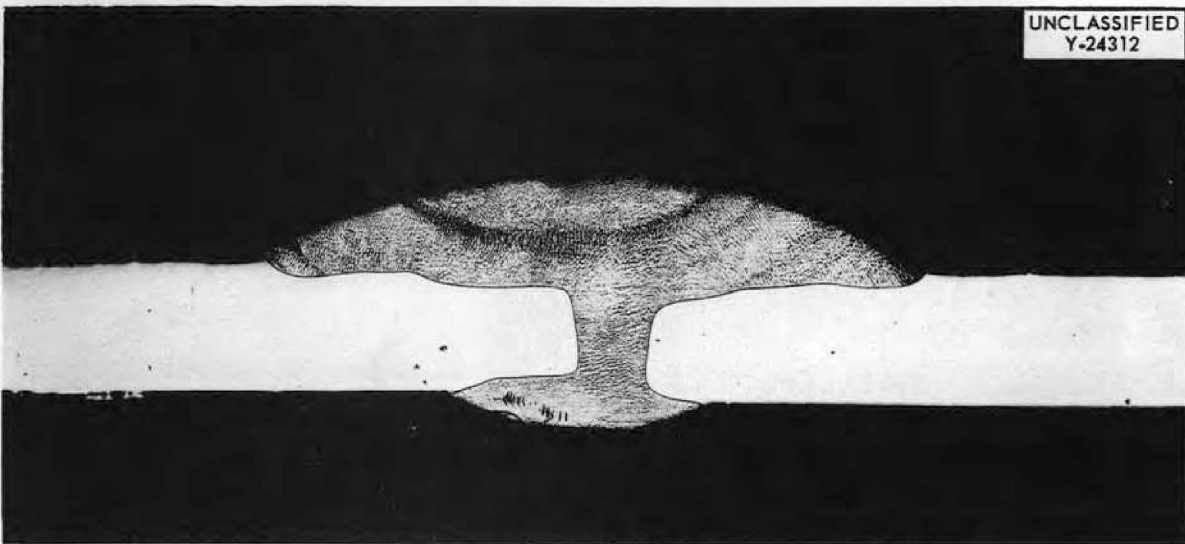
Fig. 3.3.12. Sheet Niobium Butt Weld Made by Using 85% Zr–15% Nb Filler Wire. 22X.

ONE INCH
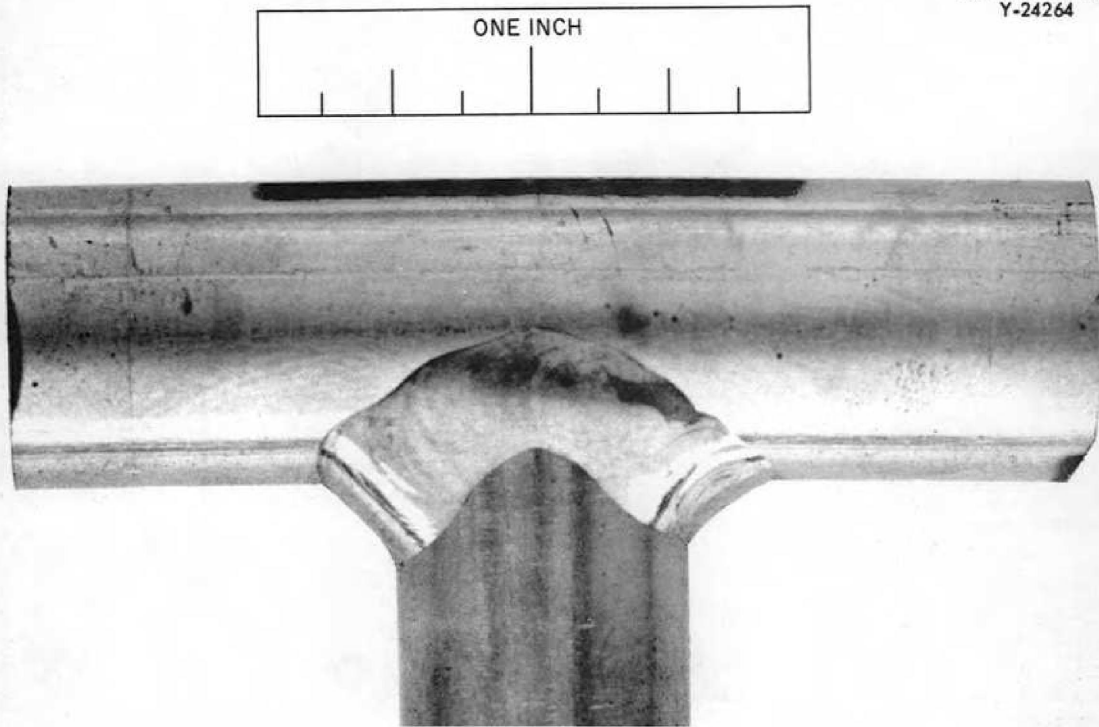
Fig. 3.3.13. Niobium Saddle Weld Made with 85% Zr−15% Nb Filler Wire. 3X.
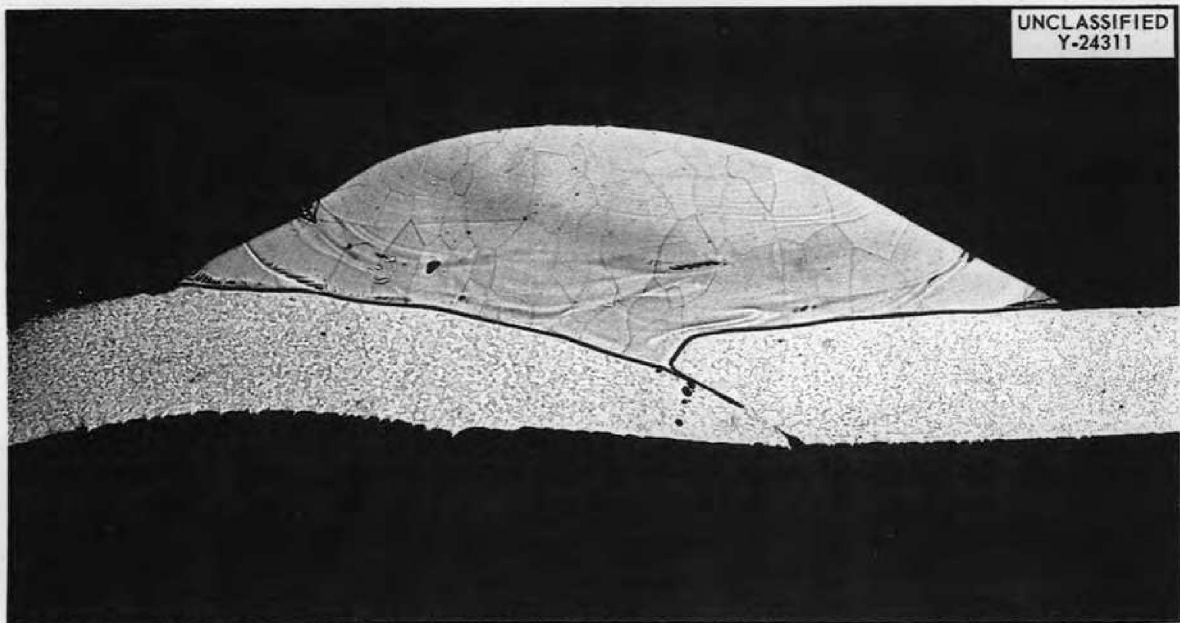
Fig. 3.3.14. Cross Section of Weld Shown in Fig. 3.3.13. 22X.

UNCLASSIFIED
Y-24267
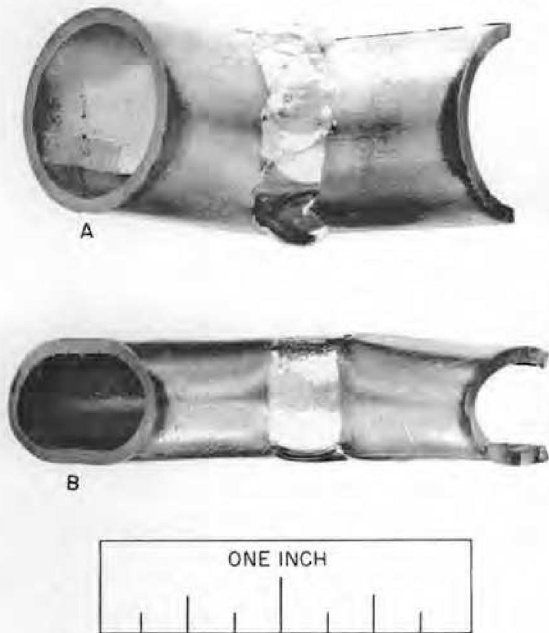
Fig. 3.3.15. Weld Shown in Fig. 3.3.13 as Sectioned and Crushed at Room Temperature To Show Ductility.

It has also been noted that impurities in the welding atmosphere, nitrogen and oxygen in particular, have embrittling effects on the weld metal and the base metal. Therefore the impurity tolerance of these elements will be investigated.

CARBURIZATION OF INCONEL TUBING

P. Patriarca   G. M. Slaughter

Means for obtaining fine grain structure in Inconel heat exchanger tubing after brazing have been extensively investigated. The influence of brazing temperature, time at temperature, and prior cold working were discussed in recent previous reports in this series.

Experiments have now been conducted with carburized tubes to study the effect of carburization on the grain size. An as-welded joint is shown in Fig. 3.3.16, and a joint that was brazed at 1080°C for 30 min is shown in Fig. 3.3.17. It may be seen that the carbides were distributed in the as-welded structure and that they went into solution and reprecipitated during the brazing cycle. The fine-grained structure evident in the as-brazed tubing indicates that the carbides were beneficial in preventing grain growth. Extensive

UNCLASSIFIED
Y-23809
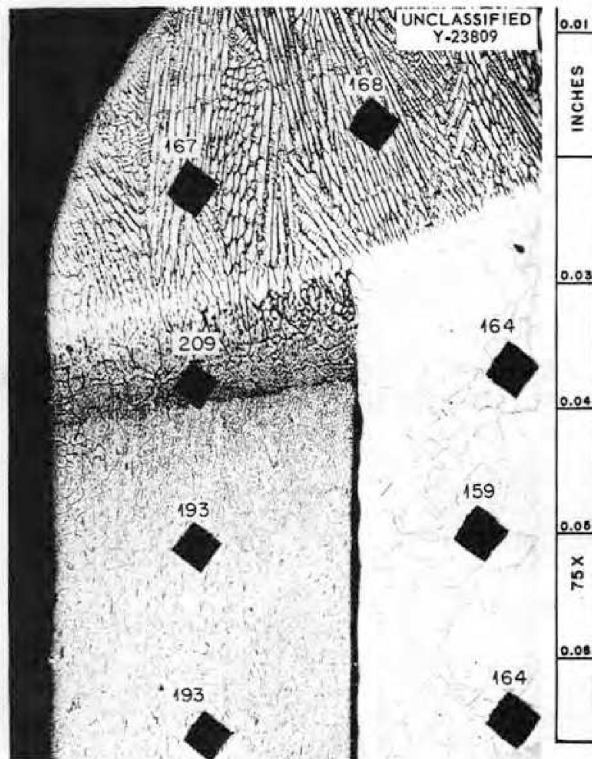
Fig. 3.3.16. As-Welded Tube-to-Header Joint Made with Carburized Inconel Tubing. Hardness numbers are in DPH units. Etchant: glyceria regia. 75X. Reduced 12.5%.

grain growth would have occurred in conventional Inconel subjected to the same brazing cycle. No significant changes in the hardness of the tubing as a result of the brazing cycle can be noted. The weld possessed a hardness approaching that of the uncarburized header material, since considerable dilution of the header material occurred.

Sections taken near brazed fillets on carburized and uncarburized tubes are compared in Figs. 3.3.18 and 3.3.19. The stabilization of the grain size as a result of carburization is evident. The influence of carburization on mechanical properties, corrosion, and other fabrication properties has not yet been determined.

WELDING AND BRAZING PROCEDURES

P. Patriarca   G. M. Slaughter

The following welding procedures, which were developed for internal use, are now being prepared for AEC publication:
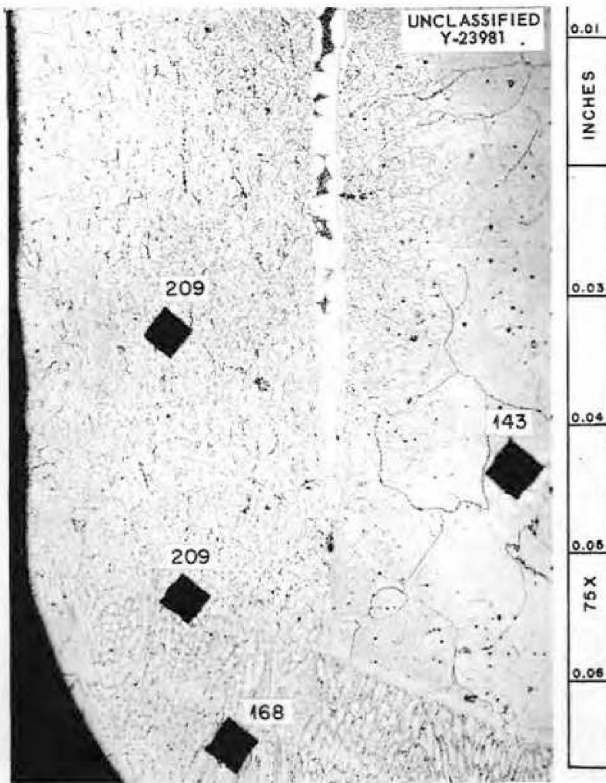
Fig. 3.3.17. **As-Brazed Tube-to-Header Joint Made with Carburized Inconel Tubing.** Hardness numbers are in DPH units. Etchant: glyceria regia. 75X. Reduced 11%.

Fig. 3.3.18. Section Taken near Brazed Fillet To Show Small Grain Size of Carburized Tubing.
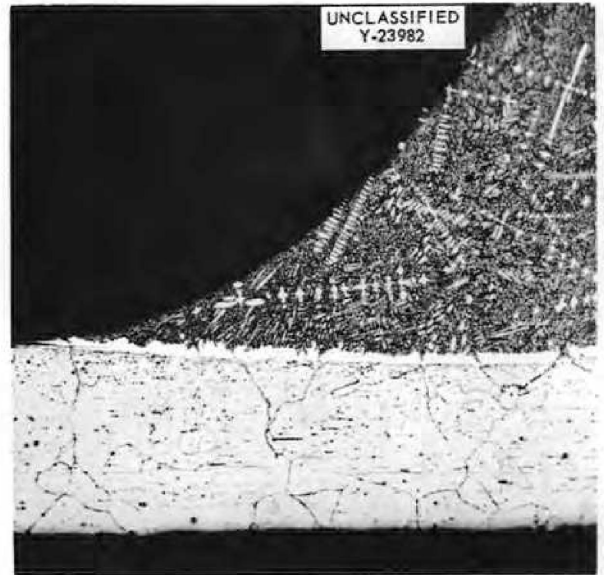
Fig. 3.3.19. Section Taken near Brazed Fillet To Show Large Grain Size of Uncarburized Tubing.

1. Procedure Specification PS-1 for D-C Inert-Arc Welding of Inconel Pipe, Plate, and Fittings.

2. Procedure Specification PS-2 for D-C Inert-Arc Welding of Inconel Tubing for High-Corrosion Applications.

3. Procedure Specification PS-8 for D-C Inert-Arc Welding of Nickel and Low-Carbon Nickel Pipe, Plate, and Fittings.

4. Procedure Specification PS-9 for D-C Inert-Arc Welding of Nickel and Low-Carbon Nickel Pipe, Plate, and Fittings to Inconel Pipe, Plate, and Fittings.

5. Procedure Specification PS-12 for Metal Arc-Welding of Inconel Plate.

6. Procedure Specification PS-14 for D-C Inert-Arc Welding of Inconel Pipe, Plate, and Fittings to Types 304, 316, 321, and 347 Stainless Steel Pipe, Plate, and Fittings.

7. Procedure Specification PS-15 for D-C Inert-Arc Welding of Hastelloy B and Hastelloy C Pipe, Plate, and Fittings.

8. Procedure Specification PS-18 for D-C Inert-Arc Welding of Hastelloy B and Hastelloy C Tubing for High-Corrosion Applications.

The corresponding Operator's Qualification Test Specifications have also been developed and are being prepared for AEC publication.

Summary reports have been published on (1) the development of high-temperature brazing alloys and their corrosion and oxidation resistance,[8] (2) the

fabrication of radiators and heat exchangers,[9,10] and (3) the developmental work on the bonding of cermet valve components to metals.[11]

[8]E. E. Hoffman *et al., An Evaluation of the Corrosion and Oxidation Resistance of High-Temperature Brazing Alloys,* ORNL-1934,(Oct. 23, 1956).

[9]P. Patriarca *et al., Fabrication of Heat Exchangers and Radiators for High Temperature Reactor Applications,* ORNL-1955 (June 14, 1956).

[10]P. Patriarca, G. M. Slaughter, and W. D. Manly, *Welding J. (N.Y.)* 36, 1172 (1957).

[11]P. Patriarca and G. M. Slaughter, "Bonding of Cermet Valve Components to Metals," *Welding J. (N.Y.)* (In press).

3.4. CORROSION AND MASS TRANSFER STUDIES

GENERAL CORROSION INVESTIGATIONS

E. E. Hoffman

W. H. Cook   D. H. Jansen

Brazing Alloys in Fuel Mixtures

D. H. Jansen

The Handy & Harman brazing alloys No. 91 (91.25% Ni–4.5% Si–2.9% B) and No. 93 (93.25% Ni–3.5% Si–1.9% B) in button form were subjected to 100-hr corrosion tests in the fuel mixture NaF-ZrF$_4$-UF$_4$ (53.5-40-6.5 mole %, fuel 44) in a see-saw apparatus at a hot-zone temperature of 1500°F. Both alloys showed good resistance to the fuel. Minor constituents of the alloys were leached to a depth of 1 to 2 mils, as shown in Fig. 3.4.1. Nickel, because of its comparative inertness to the fuel, was used for the test containers. Weight losses of the alloy specimens varied from 0.03 to 0.06%.

Brazing Alloys in Lithium

D. H. Jansen

Iron-base brazing alloys, as they become available, are subjected to corrosion screening tests in lithium. The more abundant high-nickel-content brazing alloys cannot be used in lithium because of their limited corrosion resistance. Recently, an 86% Fe–5% Si–5% Cu–4% B brazing alloy was corrosion tested for 100 hr in lithium under dynamic (seesaw apparatus) and static (capsule) conditions at 1500°F. The specimens tested were brazed type 347 stainless steel tube-to-header joints.

Under static conditions, the brazing alloy was leached of minor constituents to a depth of 4 mils, and there was some subsurface void formation in the depleted region, as shown in Fig. 3.4.2. The attack of the alloy tested in the seesaw apparatus was similar but of greater magnitude. Subsurface voids were present to a depth of 10 mils in one area. The weight losses of the specimens tested
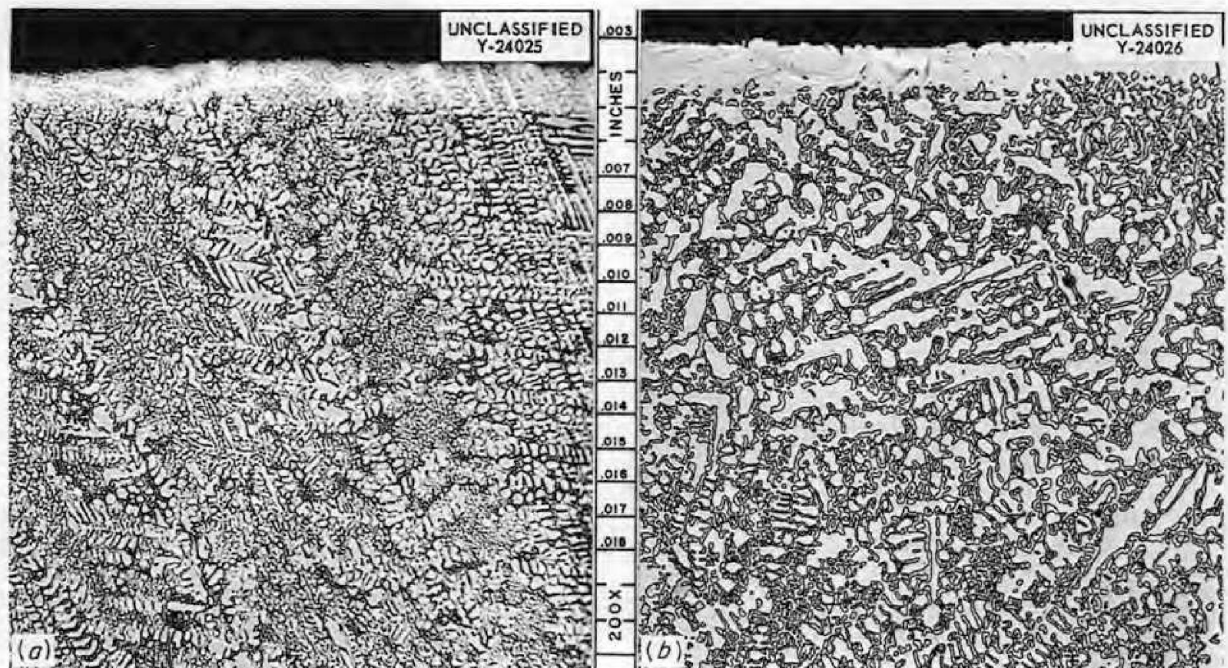
Fig. 3.4.1. Handy & Harman Brazing Alloys Nos. 91 (*a*) and 93 (*b*) After Exposure to NaF-ZrF$_4$-UF$_4$ (53.5-40-6.5 Mole %, Fuel 44) for 100 hr in Seesaw Apparatus at a Hot-Zone Temperature of 1500°F. Etchant: 10% oxalic acid. 200X. Reduced 10%. (Secret with caption)
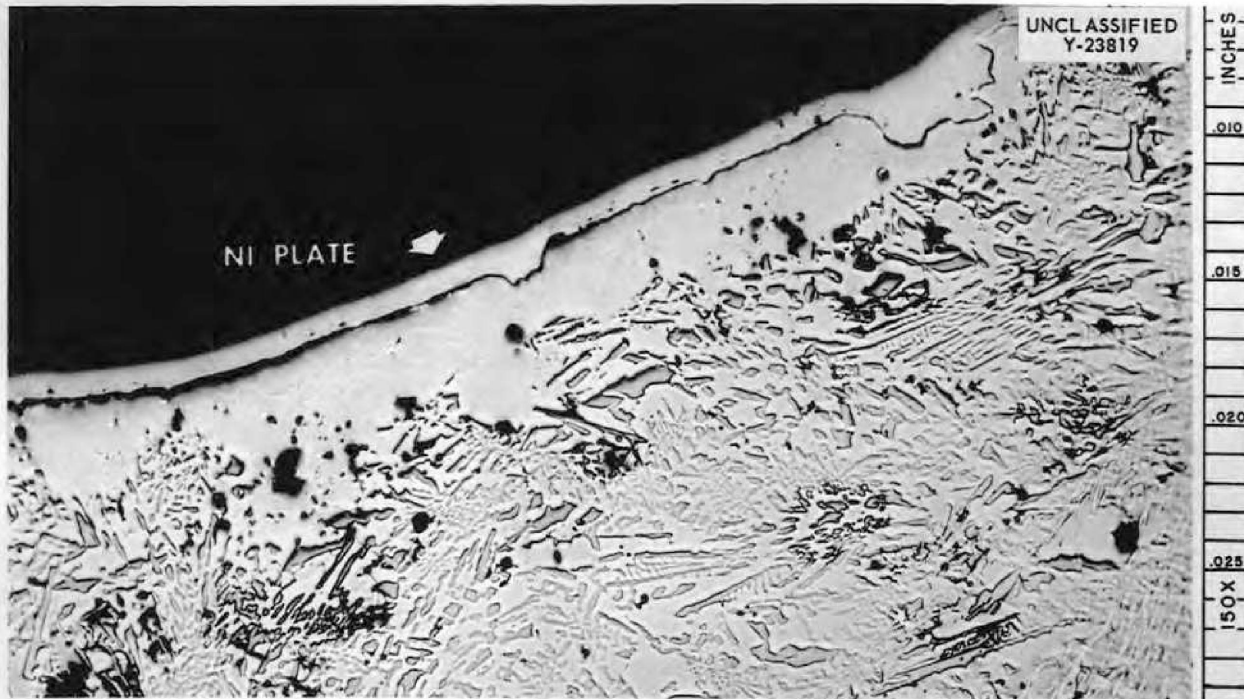
Fig. 3.4.2. Brazing Alloy of 86% Fe–5% Si–5% Cu–4% B on Type 347 Stainless Steel Tube-to-Header Joint After Exposure to Static Lithium at 1500°F for 100 hr. Specimen nickel plated to preserve the edge during metallographic polishing. As polished. 150X. (Secret with caption)

in the seesaw apparatus were five times as great as the weight losses that occurred during the static tests.

Inconel Welded with Nitrogen Shield Gas

D. H. Jansen

In connection with the initiation of a procedure for substituting nitrogen for helium as a shield gas in the welding of Inconel, corrosion tests were conducted on Inconel and Inconel–type 347 stainless steel welds made by using nitrogen as the shield gas. It was desired to determine whether the presence of nitrogen during welding would produce a weldment with different corrosion characteristics than those of an ordinary Heliarc weld on Inconel or on Inconel–type 347 stainless steel.

The corrosion specimens were exposed to fuel 44 and to NaK (56-44 wt %) for 500 hr in a seesaw apparatus at a hot-zone temperature of 1500°F. Upon completion of the tests, metallographic examination showed no attack on the welds exposed to NaK. The attack on the welds tested in fuel

44 was the same as that found previously on Heliarc welds tested under the same conditions. The only significant attack found on the welds made in the presence of nitrogen was to a depth of 2 mils on the Inconel–type 347 stainless steel weld, as shown in Fig. 3.4.3.

Cermet-Metal Joints in NaF-ZrF$_4$-UF$_4$ and in Sodium

W. H. Cook

Several methods were developed by the Welding and Brazing Group for joining cermets to metals,[1] as was required primarily for joining specific cermet disks and seats to Inconel for the production of the fuel dump valves for the ART. In order to evaluate the joints, the specimens described in Table 3.4.1 were corrosion tested for 100 hr in NaF-ZrF$_4$-UF$_4$ (50-46-4 mole %, fuel 30) in a seesaw apparatus with a hot-zone temperature of

---

[1]G. M. Slaughter, P. Patriarca, and W. D. Manly, *Bonding of Cermet Valve Components to Metals*, ORNL-2322 (in press).
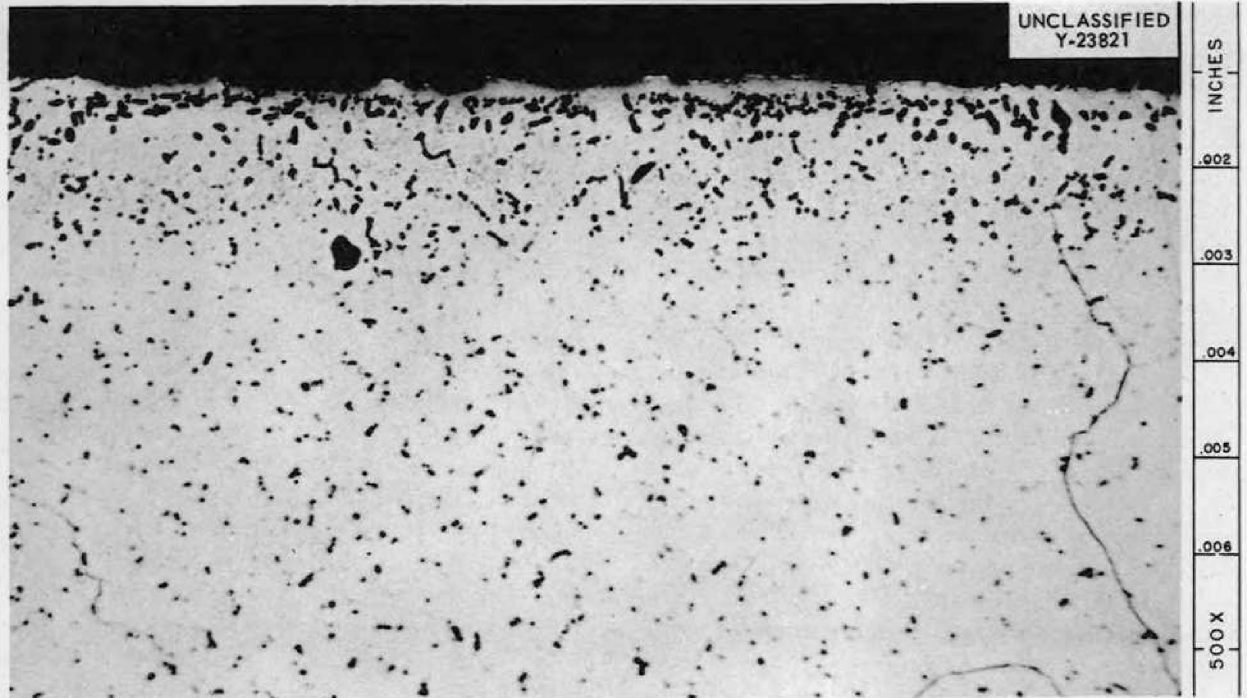
Fig. 3.4.3. Inconel–Type 347 Stainless Steel Weld Made in the Presence of Nitrogen and Tested in NaF-ZrF$_4$-UF$_4$ (53.5-40-6.5 Mole %, Fuel 44) for 500 hr in Seesaw Apparatus at a Hot-Zone Temperature of 1500°F. Etchant: 10% oxalic acid. 500X. (Secret with caption)

Table 3.4.1. Cermet-Inconel Joints Fabricated for Testing in Fuel 30

Joint No.	Cermet	Buffer	Type of Join
1	K151A (80% TiC–20% Ni)	Nickel	High-temperature fusion
2	K162B (70% TiC–25% Ni–5% Mo)	Nickel	High-temperature fusion
3	K94 (88% WC–12% Co)	Nickel	Brazed with copper
4	K94	Nickel	Brazed with Coast Metals alloy 50 (93% Ni–3.5% Si–2.5% B–1% Fe)
5	K138A (81% TiC–19% Co)	Mallory 1000 (90% W–6% Ni–4% Cu)	Brazed with a 60% Pd–40% Ni alloy
6	KM (89% WTiC$_2$–11% Co)	Mallory 1000	Brazed with a 60% Pd–40% Ni alloy

1500°F. None of the cermet-metal joints were attacked, with the possible exception of the joint which consisted of K94 brazed to nickel with Coast Metals alloy No. 50. Attack on this specimen was doubtful, and it will be tested again.

In these joints, nickel or Mallory 1000 was used to buffer the stresses developed by differences in thermal expansion between the cermet and the structural metal, Inconel. The high-temperature-fusion joints between cermets and nickel were made without brazing material, while the nickel was joined to Inconel by the conventional brazing techniques used in valve fabrication.

Specimens of joints 1, 2, and 4 were also tested in sodium for 100 hr at 1500°F in a seesaw apparatus. Results of metallographic examination and comparisons with untested specimens showed that these joints were not attacked. Joints 3, 5, and 6 were not tested because it was known that the brazing materials used were not corrosion resistant to sodium under these conditions.

Postoperative Examination of Prototype ART Control Rod

W. H. Cook

The ART prototype control rod used in a 3000-hr test of the control rod drive system was disassembled and examined. (A discussion of the test may be found in Chap 1.3 of this report.) The rod consisted of a column of porous cylinders of rare-earth oxides in stagnant, molten sodium in an Inconel thimble. The test conditions simulated those expected during ART operation, except that heat was applied externally. In the ART the control rod would be the heat source.

The 23 cylinders of rare-earth oxides (45–49.5% Sm_2O_3, 22.5–27% Gd_2O_3, balance other rare-earth oxides; apparent porosity, 46.3%) were, nominally, $1\frac{1}{4}$ in. OD, $\frac{3}{4}$ in. ID, and 1 in. long. They were contained in a thin-walled Inconel thimble, which was raised and lowered inside a second thimble of molten sodium. Holes in the inner thimble allowed the sodium to contact the ceramic cylinders.[2]

The ceramic cylinders may be seen in Fig. 3.4.4 as they appeared before the test and in Fig. 3.4.5 as they appeared after the test. The white material on the as-tested cylinders is residual sodium that

reacted with the room atmosphere after disassembly. The broken pieces (cylinders 12 through 23, as shown in Fig. 3.4.5) were subjected to 1171 thermal cycles from a maximum of 1630 ± 20°F to a minimum of 880°F (+30°F or –20°F) during the first 1800 hr of the test. This excessive temperature change was inadvertently caused by faulty temperature measuring and recording equipment. The actual temperatures given above were found by calibrating the faulty equipment with properly operating equipment. During the final 1200 hr of the 3000-hr test, cylinders 12 through 23 were subjected to 609 more cycles from a maximum of 1140 ± 30°F to a minimum of 790 ± 80°F; that is, they were subjected to the simulated ART conditions. Cylinders 1 through 11 were never subjected to a temperature change of more than 550°F.

All the thermal cycling was accomplished by raising and lowering the control rod from the fully in and fully out positions. Approximately 20 min was required for temperatures to reach equilibrium after a change of control-rod position. It is believed that cylinders 12 through 23 broke because of the excessive temperature cycling during the first 1800 hr of the test when the temperature changes required to reach equilibrium were about 500 to 800°F.

The results of this test indicate that these rare-earth cylinders can withstand thermal cycles, under the conditions described, of 550 to 650°F from 1650 ± 30°F. The most serious fault of these cylinders appears to be spalling of the type exhibited by cylinders 2, 6, and 9. At the base of each of the shallow holes caused by spalling, there was a small amount of particulate material. X-ray examinations of the particles showed the standard pattern of the rare-earth oxides and an additional, as yet unidentified, pattern.

The sodium that cooled the control rod during the test was examined spectrographically, and the quantities of rare earths found ranged from <0.7 to <0.3 ppm. The samples were taken by draining the sodium before disassembly of the rod. Since the analyses indicate that the rare-earth content of the sodium was negligible, it may be assumed that the breaking and spalling of the cylinders occurred without detectable fragmentation or powdering. The thin-walled Inconel thimble held the broken pieces in place, and thus the control rod was operable despite the breakage and,

---

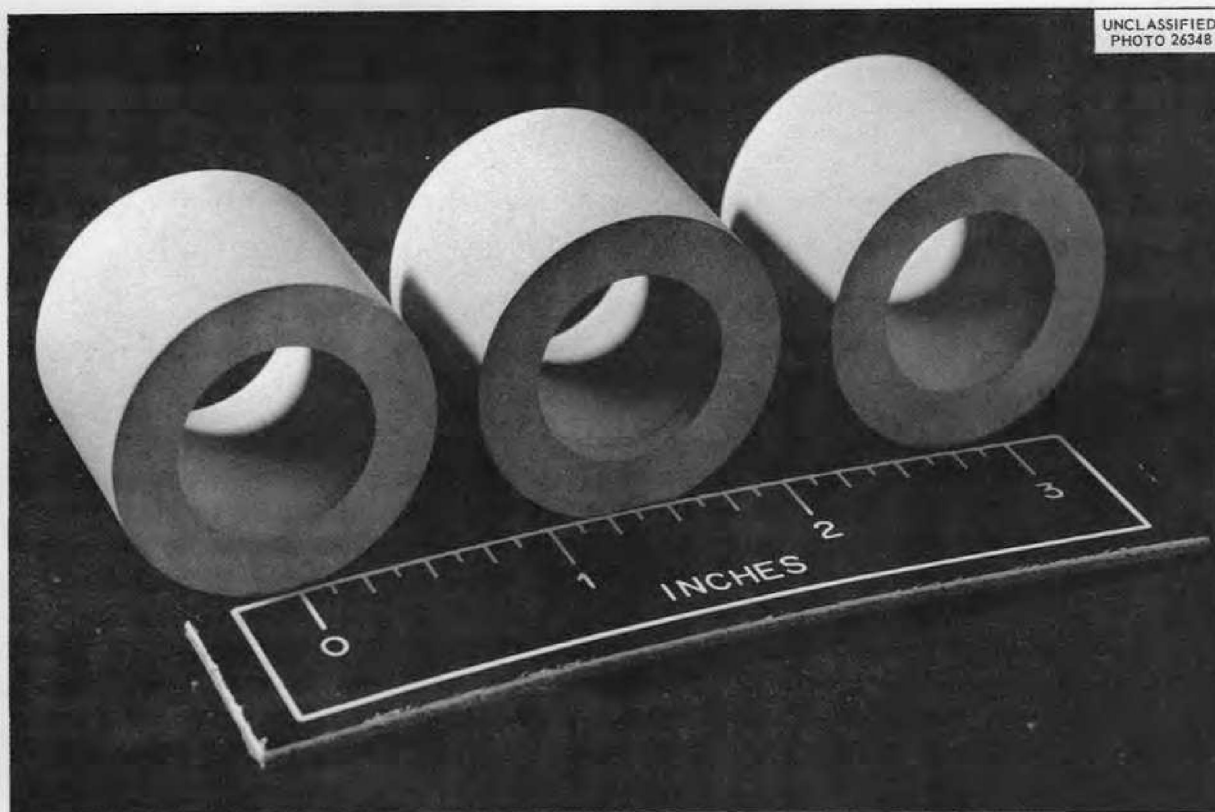[2]S. C. Shuford, *ANP Quar. Prog. Rep. June 10, 1956,* ORNL-2106, p 41.

Fig. 3.4.4. Rare-Earth-Oxide Compacts for ART Control Rod. (Confidential with caption)

in nuclear operation, would have performed its control function, because there was no change in the location of the cylinders.

CORROSION IN DYNAMIC SYSTEMS

Lithium in Niobium Thermal-Convection Loops

E. E. Hoffman   L. R. Trotter

The results of previous static tests and recently conducted seesaw-furnace tests[3] of niobium in contact with lithium at elevated temperatures have indicated that niobium has excellent corrosion resistance to lithium. In order to study these materials in a dynamic system, four thermal-convection loops constructed of sintered niobium were recently tested. In these tests the operating periods ranged from 23 to 500 hr, and hot-leg temperatures of 1500 and 1600°F were used. The

details of these tests are available in a separate report.[4]

In several of the thermal-convection loops, unusually heavy grain-boundary penetration of the niobium occurred. This type of penetration had not been detected in previous tests and was found only after the specimens had been polished and allowed to stand in air for several days. The presence of lithium was detected by heavy grain-boundary stains that were the result of the reaction of the lithium in the grain boundaries with the atmosphere. The lithium penetration extended completely through the hot-leg tube wall (0.020 in. thick) in three loops that were operated in a vacuum chamber. The heaviest attack occurred in the weld areas. Metallographic examination showed no lithium penetration of cold-leg sections of the loops. The presence of lithium in the hot-leg tube

---

[3]E. E. Hoffman, *ANP Quar. Prog. Rep. Sept. 30, 1957,* ORNL-2387, p 215.

[4]E. E. Hoffman and L. R. Trotter, *Columbium-Lithium Thermal Convection Loop Corrosion Tests,* ORNL CF-57-12-2 (to be issued).

173
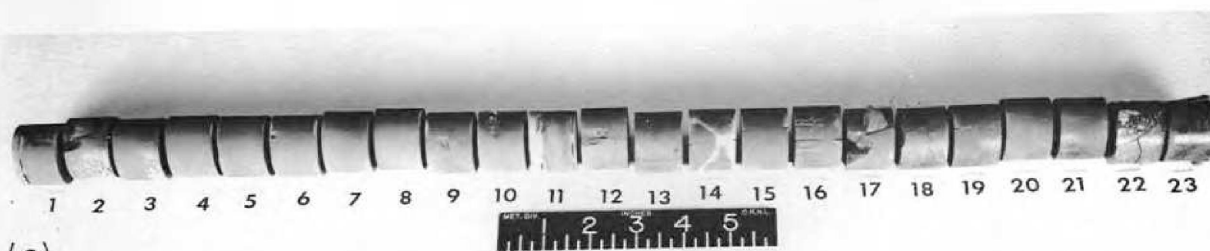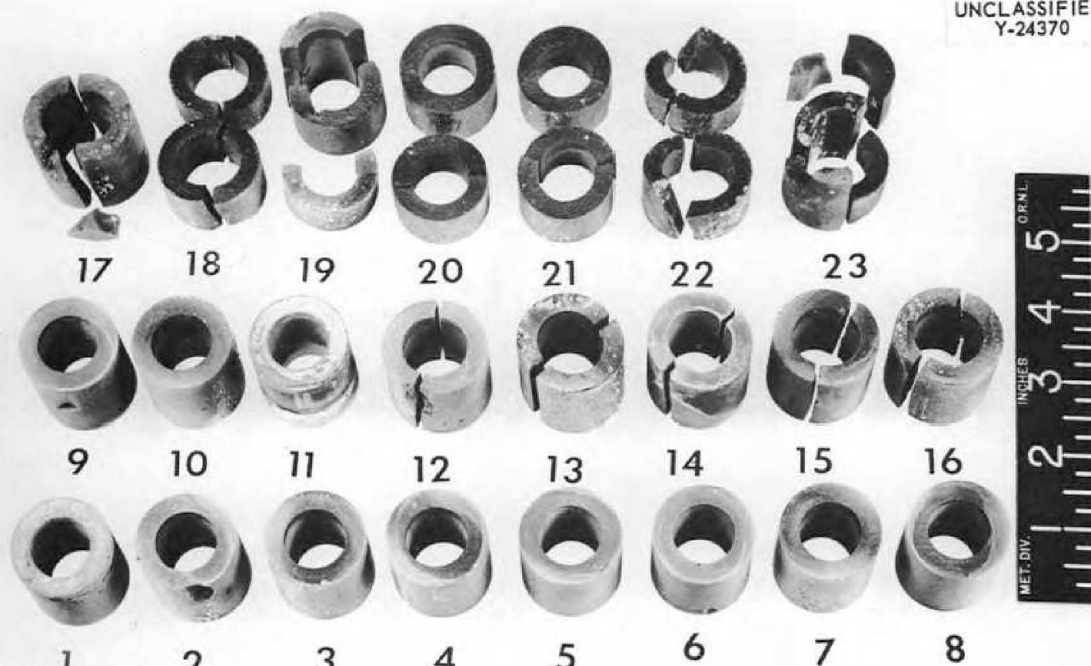
Fig. 3.4.5. Rare-Earth-Oxide Ceramic Cylinders After Exposure for 3000 hr to Molten Sodium in the ART Proto-type Control Rod Drive System Tests. (a) Cylinders shown in their arrangement in the control rod. (b) Individual cylinders showing most damaged regions. (Secret with caption)

walls was also confirmed by chemical analyses of various layers machined from the tube wall. A lithium concentration gradient was found, with the concentration of lithium being greatest in layers near the inner surface. The hot-leg tube walls that had been penetrated by the lithium cracked severely when bent, in contrast to cold-leg tube wall specimens which were quite ductile after the tests. It is thought at present that the lithium penetration may be due to grain-boundary impurities, probably carbides, and experiments are planned in which various grades of niobium will be tested to determine what factors control grain-boundary penetration.

Niobium loops are presently being fabricated by Heliarc welding in an inert-atmosphere chamber. A high-temperature brazing alloy containing 85% Zr–15% Nb is used as the filler rod. Static corrosion tests have shown that this brazing alloy has excellent corrosion resistance to lithium at 1700°F; the static tests were of 100 hr duration.

Lithium in Niobium Forced-Circulation Loops

J. H. DeVan   R. S. Crouse

A forced-circulation loop is being designed for studying lithium-niobium systems under the following conditions:

Lithium flow rate	1–2 gpm
Reynolds number	15,000
Maximum fluid temperature	1500–1800°F
Temperature differential	200–400°F

The niobium tubing of the loop is to be protected from air oxidation by a continuous outer sheath or cladding of type 310 stainless steel. Either indirect resistance heating with Nichrome-wound clamshell elements or induction heating may be used with the clad tubing. A preliminary loop design that includes clamshell heaters is shown in Fig. 3.4.6. An annulus filled with sodium is provided around both the hot and cold legs in order to obtain a much higher power density per unit length with the available clamshell heaters than could be obtained with heating units placed around the relatively small-diameter niobium tubing. Use of the sodium annulus also alleviates the thermal stress problems associated with bonding the niobium to the stainless steel cladding.

Although it is presently planned to utilize clad tubing for all portions of the loop, the portions external to the annular sections could be protected with a dry box or other sealed compartment if necessary. Procurement of the niobium tubing, both clad and unclad, has been initiated, and delivery is expected within six to eight months. While awaiting shipment of this tubing, various mechanical features of the loop design will be studied by using an all-stainless-steel prototype.

DEVELOPMENTAL STUDIES OF INCONEL SYSTEMS

J. H. DeVan   R. S. Crouse

Inconel Exposed to Fused Fluorides

From early studies of the compatibility of structural alloys with fused fluoride salt mixtures, it was found that nickel-base systems were the most corrosion resistant of the many types of alloys investigated. Consideration of the additional requirements of a structural alloy in a high-temperature reactor system indicated that Inconel would be the most suitable of the then available materials. Following this selection extensive

ORNL-LR-DWG 27067

Fig. 3.4.6. Niobium-Lithium Forced-Circulation Loop.

corrosion tests were conducted in order to ascertain the specific corrosion rates of Inconel in fused fluoride salt mixtures under the various conditions of reactor operation. The results of such experiments both in- and out-of-pile have appeared in previous reports in this series, as well as in several topical reports.[5-7] These

[5]G. M. Adamson *et al., Interim Report on High Temperature Corrosion With Fluoride Mixtures,* ORNL-2337 (in publication).

[6]G. M. Adamson *et al., Corrosion by Zirconium-Base Fluorides,* ORNL-2338 (in publication).

[7]W. D. Manly *et al., Aircraft Reactor Experiment — Metallurgical Aspects,* ORNL-2349 (Dec. 20, 1957).

studies were concluded about a year ago, at which time sufficient information had been obtained to effectively program the operation of the ETU and the ART with respect to expected corrosion rates.

Inconel Exposed to Sodium and to NaK

The utilization of Inconel as the primary construction material for the ART and the ARE required a determination of the corrosion properties of this alloy in sodium and in NaK over the temperature range from 1000 to 1500°F. Such corrosion data, which were obtained in both thermal-convection and forced-circulation loop experiments, have been reported in detail in previous reports in this series. The primary result of the experiments was an illustration of the very strong temperature dependence of the mass transfer that occurs in Inconel systems exposed to sodium and to NaK.

The mass transfer that occurred in a 1000-hr period was found to be quite minor at temperatures below 1300°F, but at higher temperatures noticeable metallic deposits that were rich in nickel were formed in the cold-leg regions of forced-circulation systems. The effects of temperature gradient and flow rate on mass transfer were also found to be significant at temperatures above 1300°F. The rate of mass transfer showed almost linear correspondence with these variables over the ranges studied. The level of oxide impurities in sodium and in NaK, evaluated in Inconel systems, was also of some importance, but the effect on the rate of corrosion was not so significant as it has been found to be at lower temperatures in iron-base systems.

3.5. MATERIALS FABRICATION RESEARCH

NIOBIUM FABRICATION

H. Inouye   D. O. Hobson
J. H. Coobs

Recrystallization of Niobium

J. P. Page

Specimens of niobium which had been subjected to various recrystallization treatments were analyzed by x-ray and metallographic techniques, and the times and temperatures necessary for the initiation and completion of recrystallization were determined. In addition a study was made of the effects of recovery and recrystallization on the room-temperature properties of niobium. Except for the larger grain size of the recrystallized arc-cast material, no significant differences were found between arc-cast and powder-metallurgy niobium. A topical report describing the complete investigation of the recrystallization of niobium has been published.[1]

Fabrication of Niobium Loops

A preliminary design has been prepared, as described in the previous chapter of this report (Chap. 3.4), for a forced-circulation loop that is to be fabricated of niobium tubing and is to be operated with lithium as the circulated fluid. The principal problems that will be associated with the construction and operation of such loops will be material procurement, oxidation protection of the niobium, and welding. The development work under way on the welding of niobium was described in Chap. 3.3 of this report. Purchase orders have been initiated for the procurement of 0.500-in.-OD × 0.035-in.-wall tubing, 1¼-in.-OD × 0.035-in.-wall tubing, and plate, but the finished material will probably not be received for several months. Alternative plans for meeting the material requirements include the purchase of forged ingots to be processed into tubing and of arc-cast billets to be extruded to tube blanks. Since the proposed loops will be exposed along part of their length to air, it will be necessary to provide some sort of cladding that will protect the niobium tubing from exposure. It will be possible to clad much of the tubing with

[1]J. P. Page, *The Annealing Behavior of Cold-Rolled Niobium,* ORNL-2372 (Sept. 19, 1957).

stainless steel, but, because of their irregular shapes, the electromagnetic pump, the surge tank, and some bends would be difficult to clad by using ordinary cladding methods. Therefore other means are being sought for protectively cladding irregular surfaces and shapes fabricated of niobium. In the initial studies, several of the high-temperature, nickel-base brazing alloys are being applied to niobium specimens, which are then subjected to oxidation tests. The braze metal is applied by flame spraying, and it is then sintered in helium at a temperature just above its melting point. Oxidation tests are presently being made in a horizontal tube furnace at 1700°F in static air, but, since the specimens must be removed from the furnace and cooled before they are weighed, long-time oxidation tests of up to 1000 hr will be run in vertical-tube oxidation furnaces that do not require thermal cycling of the specimens during weighing.

The results of some of the initial oxidation tests of niobium specimens coated with Wall Colmonoy Nicrobraz or Coast Metals alloys No. 52 or 53 are compared with the results of similar tests of type 310 stainless steel in Fig. 3.5.1. The sharp rise in the curve for the sample coated with Nicrobraz is the result of the failure of the cladding at two corners of the specimen. The niobium, upon exposure to air, oxidized at a very rapid rate, with the results shown in Fig. 3.5.2. The cladding was unable to prevent the oxide from spreading and was rolled back upon itself. A second test of a Nicrobraz-coated sample, in which the coating did not fail, showed the Nicrobraz to have oxidation resistance comparable with that of the Coast Metals alloys. Tests will also be made of niobium specimens that have been copper-plated and then aluminized. Several attempts have been made to fabricate such specimens, but each attempt has failed because impure sintering atmospheres prevented bonding between the copper and the aluminum.

Consolidation of Niobium Pellets

An experimental quantity of niobium pellets produced by the Electro Metallurgical Company was consolidated into a rod by extrusion. After being stripped from the stainless steel can in which it was extruded, the rod was cold-swaged to a reduction of 97%, without annealing. On the
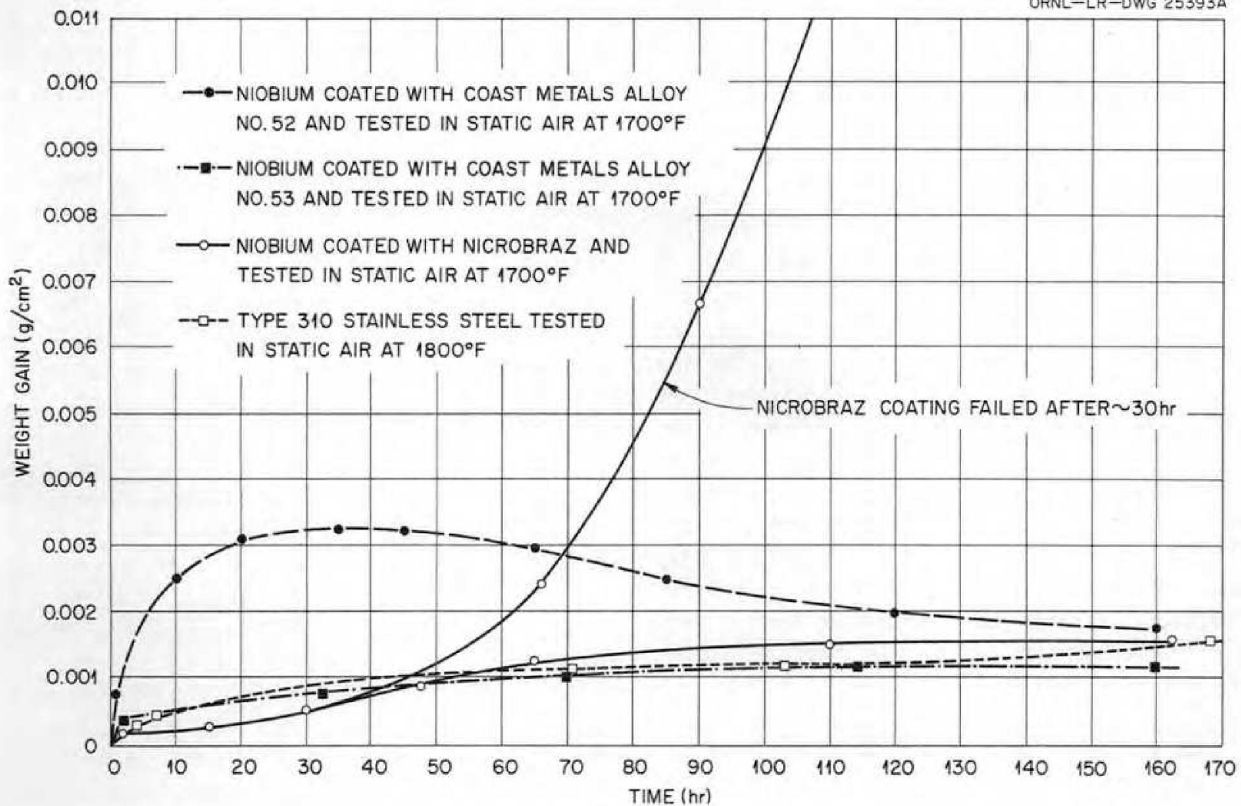
Fig. 3.5.1. Oxidation of Niobium Coated with Various Brazing Materials.
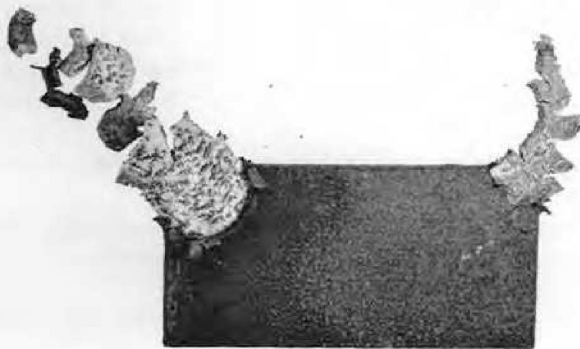

UNCLASSIFIED
Y-24413

Fig. 3.5.2. Nicrobraz-Coated Niobium Specimen After 137 hr of Exposure to Static Air at 1700°F. (Secret with caption)

basis of this experiment, five tube-blank extrusions of the pellets were processed. Mild steel cans were used for compacting and preheating the pellets. The mild steel was removed after extrusion by using a pickling solution. The extruded blanks were then vacuum-annealed and sent to the Superior Tube Company for redrawing. However, the tube blanks failed during reduction because of severe splitting in the joints between pellets. Therefore no further attempts will be made to use this technique for the production of niobium tubing.

YTTRIUM METAL PRODUCTION

T. Hikido[2]   J. H. Coobs

Experimental studies of the production of high-purity yttrium metal were continued. In the process being developed,[3] lithium is used to reduce a

----

[2]On assignment from the U.S. Air Force.

[3]T. Hikido, R. E. McDonald, and J. H. Coobs, ANP Quar. Prog. Rep. Sept. 30, 1957, ORNL-2387, p 228.

mixture of YF_3-MgF_2-LiF to produce an yttrium-magnesium alloy.

Two additional experimental runs were completed, runs L-5 and -6. In run L-5, 693 g of alloy was produced for a yield of 67%. Difficulty was encountered in achieving satisfactory operating temperatures in run L-6, however, because of inadequate insulation, and a very poor yield of alloy resulted.

Several lots of the Y-Mg alloy obtained in these and previous runs were vacuum-distilled to remove the magnesium and the excess lithium. The resulting sponge was then arc-melted under an argon atmosphere with a tungsten electrode. The results of chemical analyses of these melts are presented in Table 3.5.1.

Sample L-5A, which was melted as a finger casting, was cold-swaged to a cylindrical shape and then vacuum-annealed at 1000°C for $\frac{1}{2}$ hr. After surface folds were removed by machining, the

Table 3.5.1. Chemical Analysis of Arc-Melted
Yttrium Sponge

Sample Number	Impurities Found (ppm)			
	Oxygen	Nitrogen	Lithium	Magnesium
L-2A	1700		<10	970
L-2B	1400	50		65
L-4A	1900	170	<1	360
L-4B	1800	250	2	69
L-5A	1000	150	<2	480

sample was cold-swaged 37%, as shown in Fig. 3.5.3. The sample was then cold-worked from 0.41 in. to 0.09 in. in diameter, with the use of intermediate vacuum anneals. The amount of cold work between anneals was over 30%. However, it was subsequently discovered that some cracks had developed during the initial 37% cold-swaging operation.

Equipment for vacuum-distilling larger quantities of alloy (approximately 4–5 lb) is presently being constructed. In the next alloy-reduction experiment, the transfer of molten fluorides into the reaction retort will be tried. Heretofore the fluoride charge has been cast into nickel containers and then crushed to granular particles in an inert-atmosphere dry box. The charge was loaded into stainless steel transfer flasks, which were coupled to the reaction retort through a Jamesbury vacuum valve system. It is hoped that the transfer of molten charge material will reduce contamination by eliminating some of the handling steps.

SHIELDING MATERIALS DEVELOPMENT

J. H. Coobs

A shield plug assembly was devised to protect the fuel pump motors of the ART from reactor radiation. The plug was made up of three layers assembled into an Inconel container. The layers were a dense gamma-ray shield composed of tungsten carbide bonded with Hastelloy C, a thermal shield of low-density zirconia, and a neutron shield composed of boron carbide dispersed in copper. The developmental work leading to the final components and the fabrication of a full-size

UNCLASSIFIED
Y-23975

Fig. 3.5.3. Cast Yttrium Sponge from Run L-5 After 37% Reduction by Cold-Swaging. (Confidential with caption)

assembly are described in a separate report.[4] In addition, a report is being prepared on the developmental work that led to the selection of the particular materials used for the neutron shield of the ART.

TUBULAR CONTROL ROD PRODUCTION

J. H. Coobs

The feasibility study of the extrusion of control rods was continued. Tensile bars cut from two of the successful extrusions described previously[5] were tested at room temperature and at 1500°F, and elongations of 2 and 5% were obtained, as compared with elongations of less than 0.1% for the specimens tested previously.

CERAMIC INVESTIGATIONS

L. M. Doney

Development of High-Density BeO Bodies

R. L. Hamner

Developmental work was initiated at the request of GE-ANP on high-density BeO bodies for use as moderating material. Very fine particles of BeO are being obtained by the controlled calcination of $BeSO_4$. Heating at 950°C for 1 hr in an oxidizing atmosphere produced a mass of fluffy, white agglomerates, which were broken down in a ball mill prior to pressing. The surface area of this material was 20 to 26 m^2/g.

Cylindrical specimens were hot-pressed at 200 psi and temperatures of 1325, 1425, and 1525°C. The densities obtained were 91, 92, and 96% of theoretical, respectively. The high sinterability of this powder is indicated by the fact that, in order to obtain comparable densities with commercial grades of BeO powder, it is necessary to use temperatures 400°C higher.

Extrusion of Magnesia and Beryllia Insulators

C. E. Curtis

Rods of magnesium oxide and of beryllium oxide were extruded to provide rod insulators with four

---

[4]J. P. Page and J. H. Coobs, *The Shield Plug Assembly for the ART Fuel Pumps,* ORNL-2353 (in press).

[5]M. R. D'Amore, *ANP Quar. Prog. Rep. June 30, 1957,* ORNL-2340, p 242.

longitudinal holes as required in thermocouple assemblies. The magnesium oxide rods were approximately 0.370 or 0.490 in. in diameter, and the beryllium oxide rods were approximately 0.242 in. in diameter. Both types of rods were fired at 1400°C for 4 hr. The beryllium oxide rods will be swaged in the tube assembly.

Production of Metal Hydrides

R. A. Potter

Preparations are being made for hydriding dense yttrium metal when it becomes available. Reactor-grade zirconium, which is available and which responds to hydrogen in much the same manner as yttrium does, is being used in developing the hydriding processes.

In the method being tested currently, an air-evacuated, sealed nickel capsule is used through which the hydrogen must diffuse before coming into contact with the metal specimen. The sealed nickel capsule eliminates the necessity of maintaining a rather elaborate gas-cleaning train and also provides a simple method whereby the hydrided metal can be kept from contact with the atmosphere until it is to be clad.

In a typical experiment, a machined, $\frac{1}{2}$- by 3-in., zirconium metal rod is placed inside a length of $\frac{3}{4}$-in.-dia, 20-mil-wall nickel tubing with molybdenum spacers at both ends to prevent contact between the nickel and the sample. End caps are welded in place on the tubing, and the assembly is evacuated with a vacuum pump connected to a $\frac{1}{4}$-in.-dia nickel tube welded into one end cap. The small tube is then forged closed, and the sealed assembly is heated in a hydrogen atmosphere at temperatures ranging from 1475 to 1850°F and at pressures from 1 to 2 atm.

Four such encapsulated samples have been treated under different pressure, temperature, and time conditions. They were fired in a vacuum to the peak temperature, hydrogen was allowed to flow through the retort as the temperature was dropped to a lower level, and a static pressure was maintained throughout a soak period. In some instances, the samples were refired in an attempt to increase the hydrogen content. The firing conditions and the results for the four samples are presented in Table 3.5.2.

Table 3.5.2. Conditions and Results of Hydriding Experiments on Four Zirconium Samples

Sample Number	Number of Firing Cycles	Maximum Temperature During Vacuum Heating ($^\circ$F)	Minimum Soak Temperature ($^\circ$F)	Total Time at Minimum Soak Temperature (hr)	Hydrogen Pressure (psig)	Hydrogen Content of Sample (wt %)
1	1	1700	1650	3	3	0.2
2	2	1850	1605	2	3	0.2
3	3	1830	1605	5	15	0.7
4	6	1830	1475	8	15	1.1

3.6. METALLOGRAPHIC EXAMINATIONS OF ENGINEERING TEST COMPONENTS AFTER SERVICE

ART PROTOTYPE TEST RADIATOR NO. 1

R. J. Gray   J. E. Van Cleve, Jr.

Test radiator No. 1 failed immediately after reaching full power in its first controlled thermal cycle. The NaK outlet temperature for the radiator remained approximately constant during the transition, and the inlet temperature was increased from 1350 to 1500°F at a rate of 50°F/min. The radiator operated for a total time of 870 hr with the NaK inlet temperature above 1000°F. The total number of thermal cycles before the radiator failed was $9\frac{1}{2}$. The examination of the point of failure was described in the previous report,[1] and the investigation of fin-to-tube joint braze integrity, mass transfer, corrosion, and other items of interest are described here.

---

[1]R. J. Gray and J. E. Van Cleve, Jr., *ANP Quar. Rep. Sept. 30, 1957*, ORNL-2387, p 232.

Sixteen samples were removed from the radiator at the positions shown schematically in Fig. 3.6.1 (see Fig. 3.6.10, this report, for photograph of a radiator with areas numbered as indicated in Fig. 3.6.1). The samples were sectioned to expose two opposing joint areas on each tube and then were mounted in plastic material. The samples were then ground and polished, and the joint areas were examined at a magnification of 50. In Table 3.6.1, the results of the analyses of fin-to-tube joint braze integrity and the degree of oxidation of the fin collar are presented and compared with results for other radiators previously examined.

Incomplete melting of the braze-alloy rings was noted in several instances; a typical sample is shown in Fig. 3.6.2. A partially melted ring which did not flow over the fin collar to protect the copper core is shown in Fig. 3.6.3. A crack in the stainless steel cladding on the fin may

FLOW
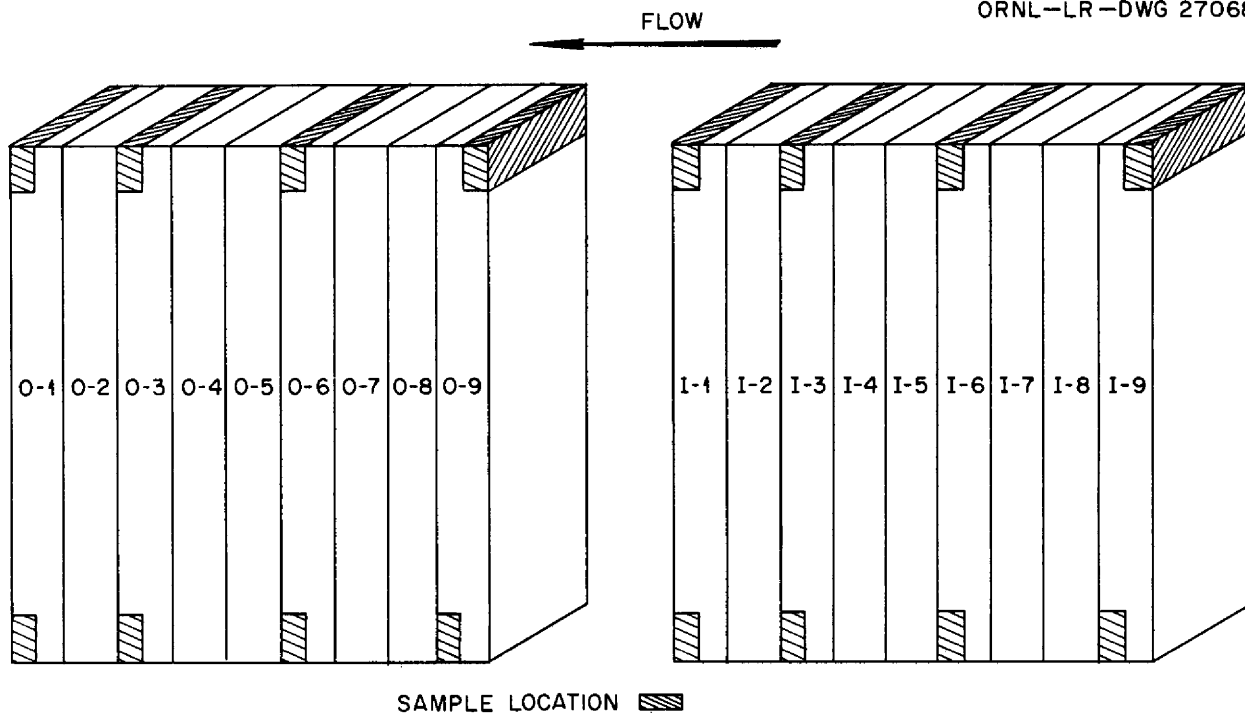
SAMPLE LOCATION

Fig. 3.6.1. Diagram of Radiator Showing Locations at Which Samples Were Taken for Evaluation of Fin-to-Tube Joint Braze Integrity.

Table 3.6.1. Fin-to-Tube Joint Braze Integrity and Degree of Oxidation of Fin Collars

	Radiator Designation					
	ART Prototype No. 1	York No. 3	York No. 4	York No. 5	York No. 9	PWA No. 2
Number of hours of service in the temperature range 1000 to 1600°F	870	361	1356	1265	1283	1199
Number of joint areas examined	2440	2684	2757	3105	2608	3210
Percentage of joint areas having 75 to 100% adherence	41.1	90.4	60.7	38.4	44.6	100
Percentage of joint areas having 50 to 74% adherence	8.2	5.9	18.8	9.6	21.2	
Percentage of joint areas having 25 to 49% adherence	3.1	1.1	5.5	7.0	9.4	
Percentage of joint areas having 0 to 24% adherence	47.6	2.6	15.0	45.0	24.8	
Percentage of joint areas having nonoxidized copper fins	10.2	84.5	61.9	29.0	23.5	100
Percentage of joing areas having slightly oxidized copper fins	43.1	7.5	19.5	13.6	8.5	
Percentage of joint areas having heavily oxidized copper fins	46.7	8.0	18.6	57.4	68.0	
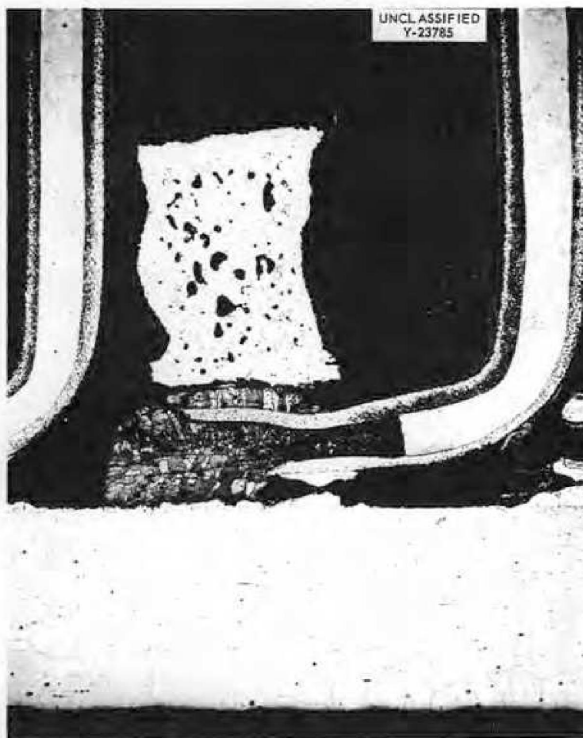
Fig. 3.6.2. Typical Partially Melted Braze Ring. Etchant: 10% oxalic acid. 50X.

also be seen at the point of maximum bending. A similar crack in the cladding of another fin is shown in Fig. 3.6.4. The thickness variations of the stainless steel cladding indicate that the bending operation may have caused the crack in the cladding before the radiator was placed in operation.

The inside and outside diameters and the wall thicknesses of the tubes were measured at various intervals between the header and fin matrix during the polishing process. Variations in the outside diameter and in the wall thickness were noted in several instances, but all the differences could be directly attributed to damage by the fire that resulted from the NaK leak. There was no variation of the inside diameter that was sufficient to indicate the presence of a stress high enough to produce plastic flow in the tubes.

The tube failure which permitted the NaK leak could have been the result of at least three things: reaction with an insulating material, damage to the tube during fit-up and brazing, and the presence of stringers across the tube wall. Intergranular voids of the type that would have indicated deleterious effects of strain
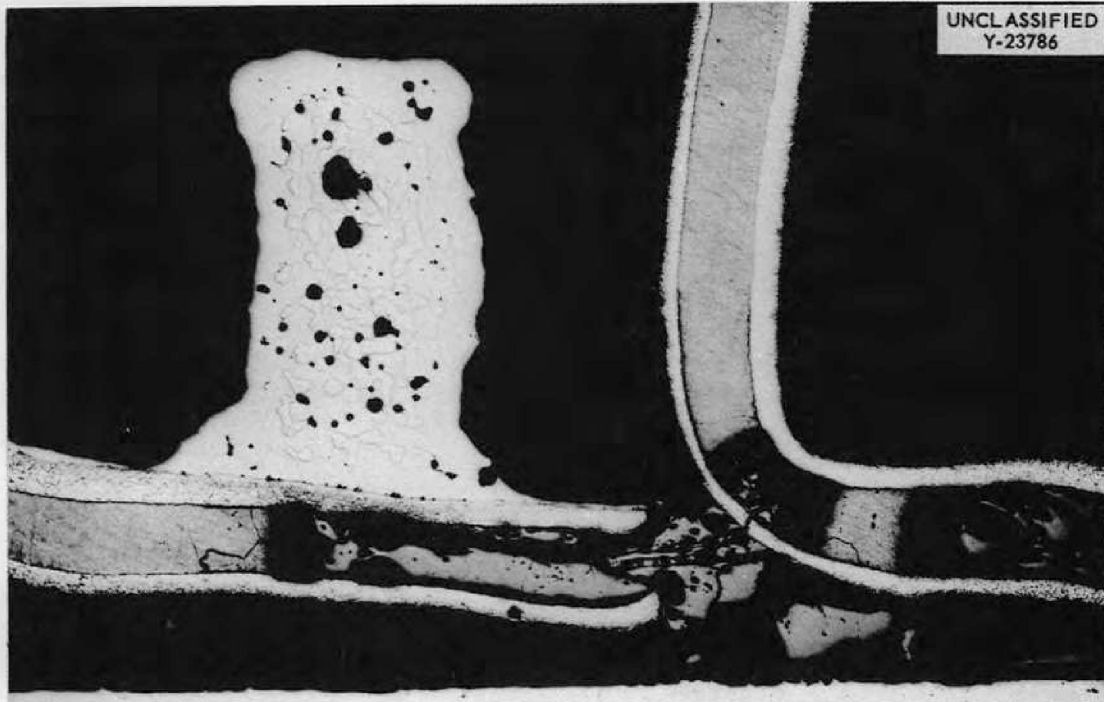
Fig. 3.6.3. Braze Ring That Did Not Melt Sufficiently To Protect the Fin Collar. Note crack in stainless steel cladding of fin at the bend. Unetched. 50X.
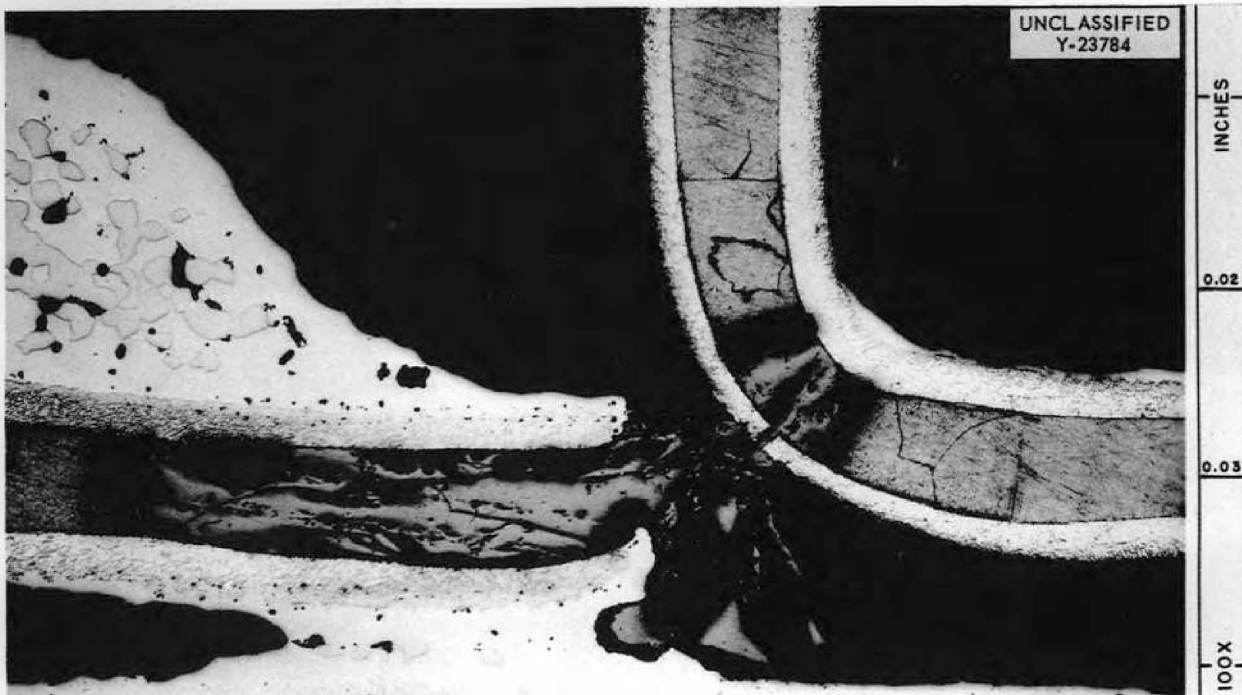
Fig. 3.6.4. Stainless-Steel-Clad Copper Fin That Was Found To Have a Crack at the Point of Maximum Bending. Unetched. 100X.

cycling or creep were not found. Since no signs of incipient failure were found, the exact cause of the tube rupture cannot be stated. The fin-to-tube brazed joints were poor, but they were not so bad as in some previously operated York radiators. A job sample that was turned down because of poor flow of the brazing alloy is shown in Fig. 3.6.5. As may be seen, most of the brazing alloy rings are only partially melted, and, in some instances, there is no evidence of flow.

Corrosion and mass transfer were negligible because of the relatively short operating time. The surface of a tube that was exposed to NaK in the hottest area is shown in Fig. 3.6.6. As may be seen, the maximum corrosion consists only of a general roughening of the surface. The area of maximum mass transfer is shown in Fig. 3.6.7. The tube shown was removed from the coolest zone of the radiator. The maximum thickness of the deposited material is 0.004 in.

Short slits, similar to those shown in Fig. 3.6.10, were made through the fins between each tube at both the top and bottom of the radiator prior to operation. These slits averaged ten fins in depth and left a considerable amount of unprotected copper exposed to the air stream. Eight samples were therefore removed from the radiator in order to investigate the oxidation of the copper. The positions at which these samples were taken are shown in Fig. 3.6.8. The maximum copper oxidation was found near the NaK inlet header. The maximum depth of oxidation was 0.027 in., and the average in the area of maximum oxidation was 0.021 in. The average depth of oxidation found in the cooler outlet region was 0.007 in.

The fin that was most severely oxidized is shown in Fig. 3.6.9. As may be seen, the stainless steel cladding flared out because of the increase in volume that resulted from oxidation of the copper.
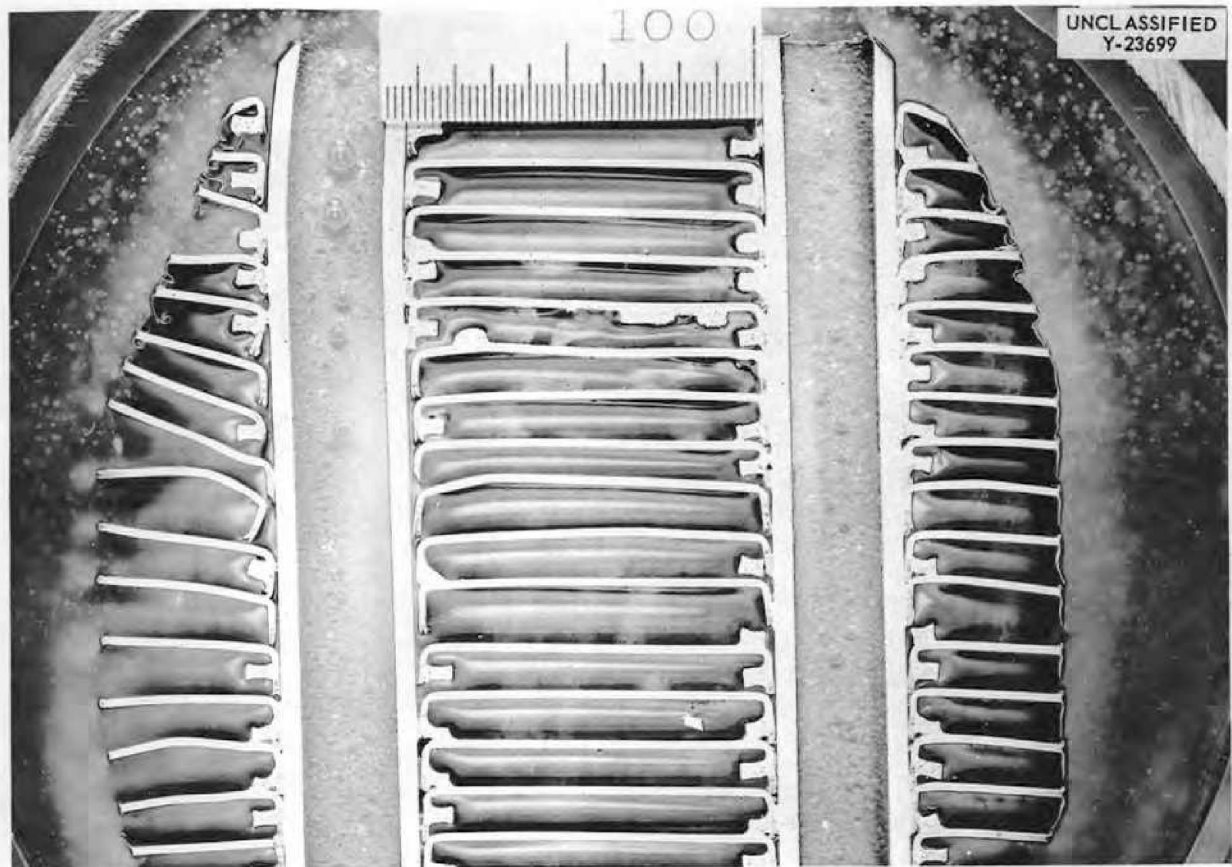
Fig. 3.6.5. **Typical Brazed Joint Job Sample.** Note partially melted and unmelted brazing-alloy rings.
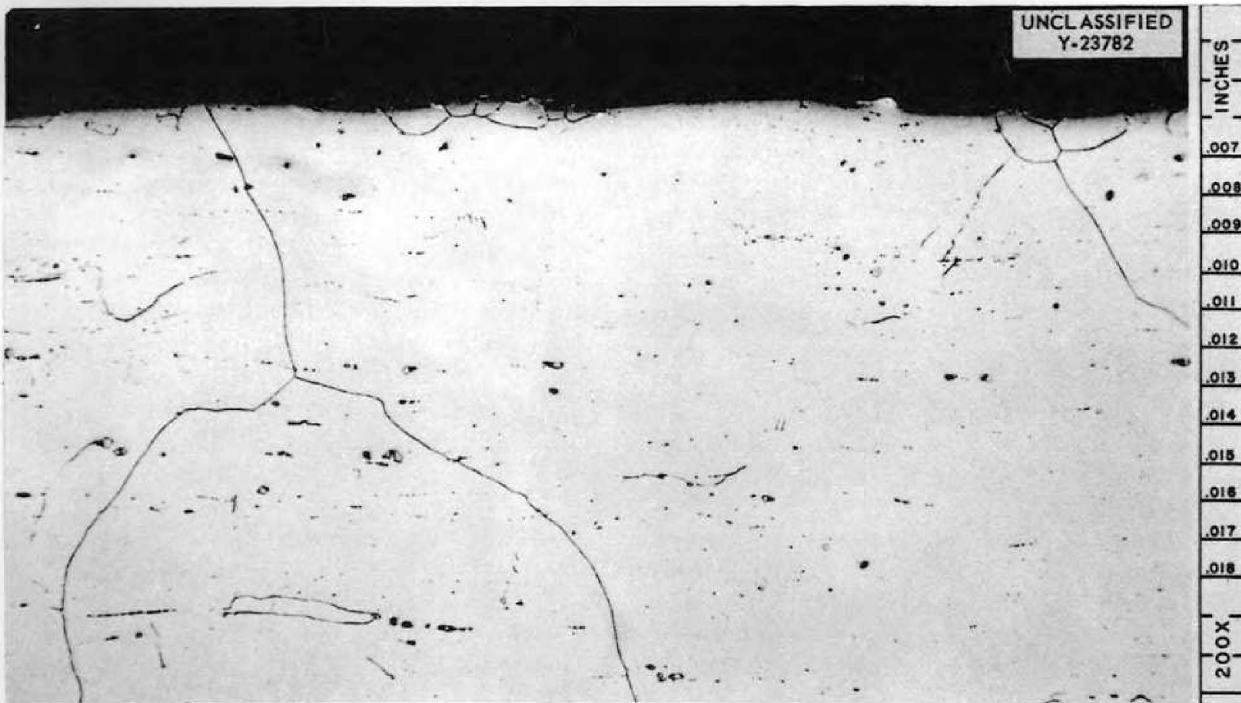
Fig. 3.6.6. Area of Maximum Corrosion of ART Prototype Radiator No. 1. Note general roughening of surface. Etchant: 10% oxalic acid. 200X. (Secret with caption)
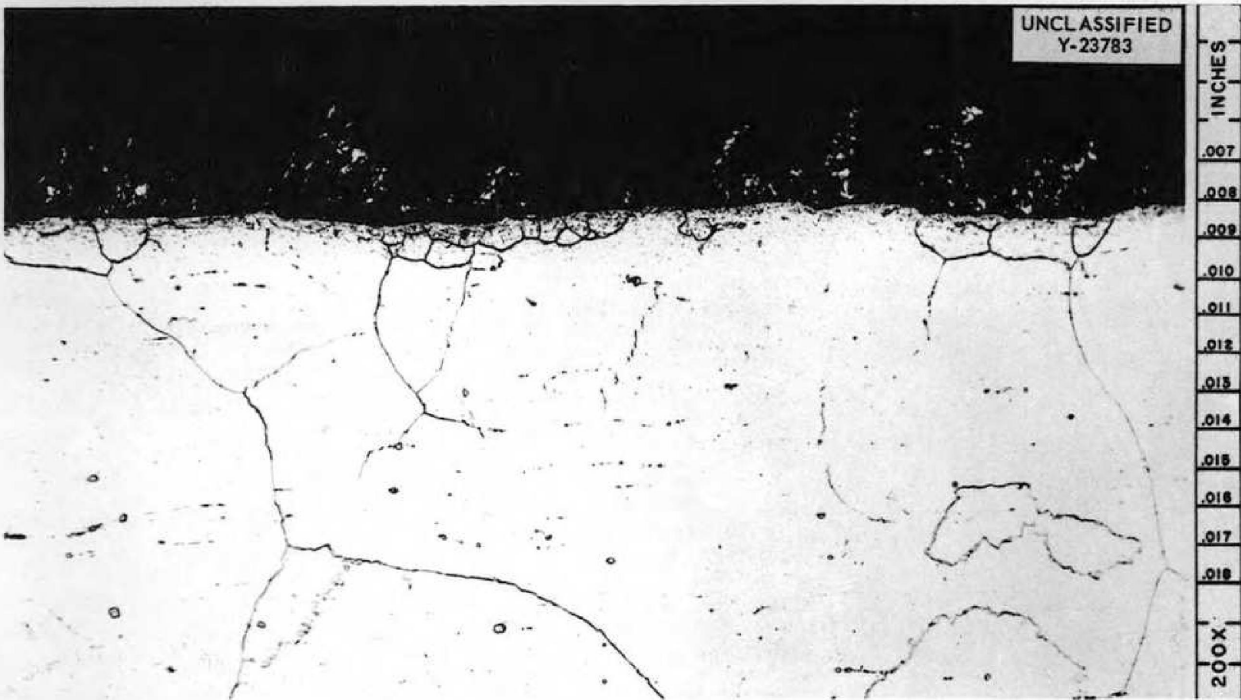
Fig. 3.6.7. Area of Maximum Mass Transfer in ART Prototype Radiator No. 1. Etchant: 10% oxalic acid. 200X. (Secret with caption)
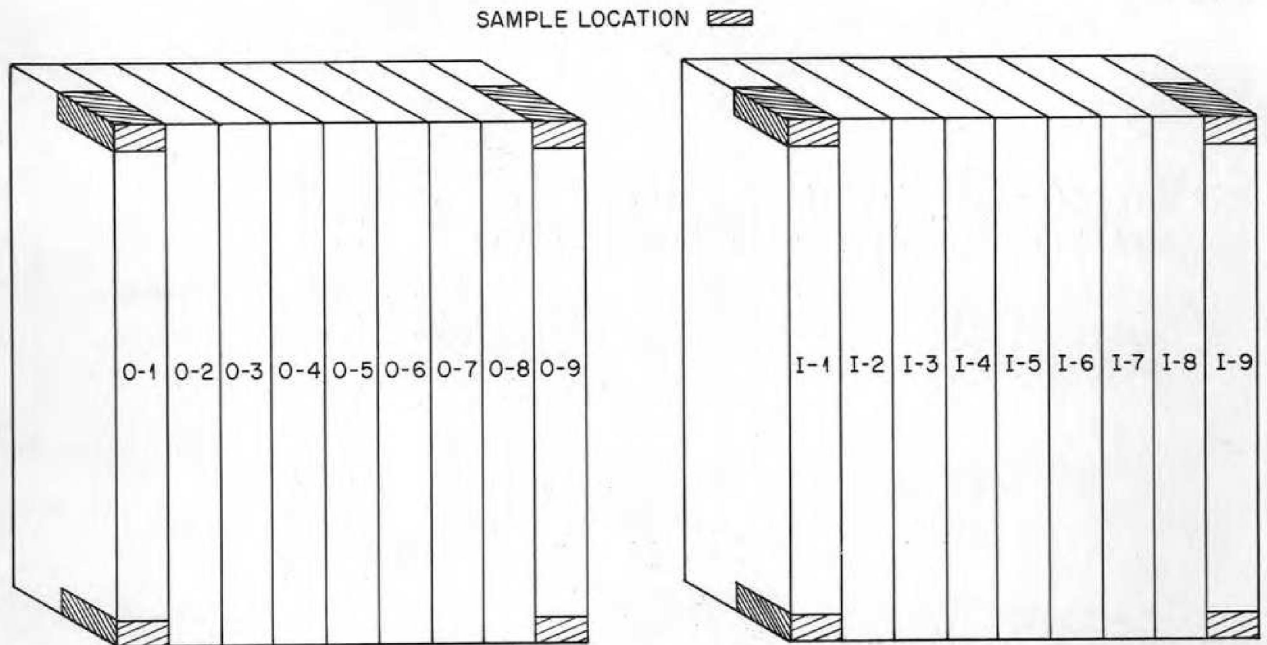
SAMPLE LOCATION

Fig. 3.6.8. Diagram of Radiator Showing Locations at Which Samples Were Taken for Evaluation of Fin Oxidation.

Fig. 3.6.9. Stainless-Steel-Clad Copper Fin with Unprotected Edge Showing Oxidation That Occurred During Operation of ART Prototype Radiator No. 1. Unetched. 150X. Reduced 24.5%. (Secret with caption)

ART PROTOTYPE TEST RADIATOR NO. 2

R. J. Gray   J. E. Van Cleve, Jr.

Test radiator No. 2 failed during the temperature-differential phase of the 182nd thermal cycle. The failure and the fire that resulted because of gross leakage of NaK to air were confined to the tubes between the NaK inlet header and the fin matrix. The operating history of the radiator is summarized below:

Total hours at 1200°F or above	862
Total hours of operation with a temperature differential	431
Total hours at design temperature differential	310
Number of successful thermal cycles	181

The radiator was prepared for examination in the same manner as that used previously for examination of test radiator No. 1. The cleaned radiator is shown in Fig. 3.6.10 prior to sectioning for examination. The failed tubes were found in sections I-8 and I-7. Each section contains 20 tubes arranged in a four-by-five matrix. Twelve
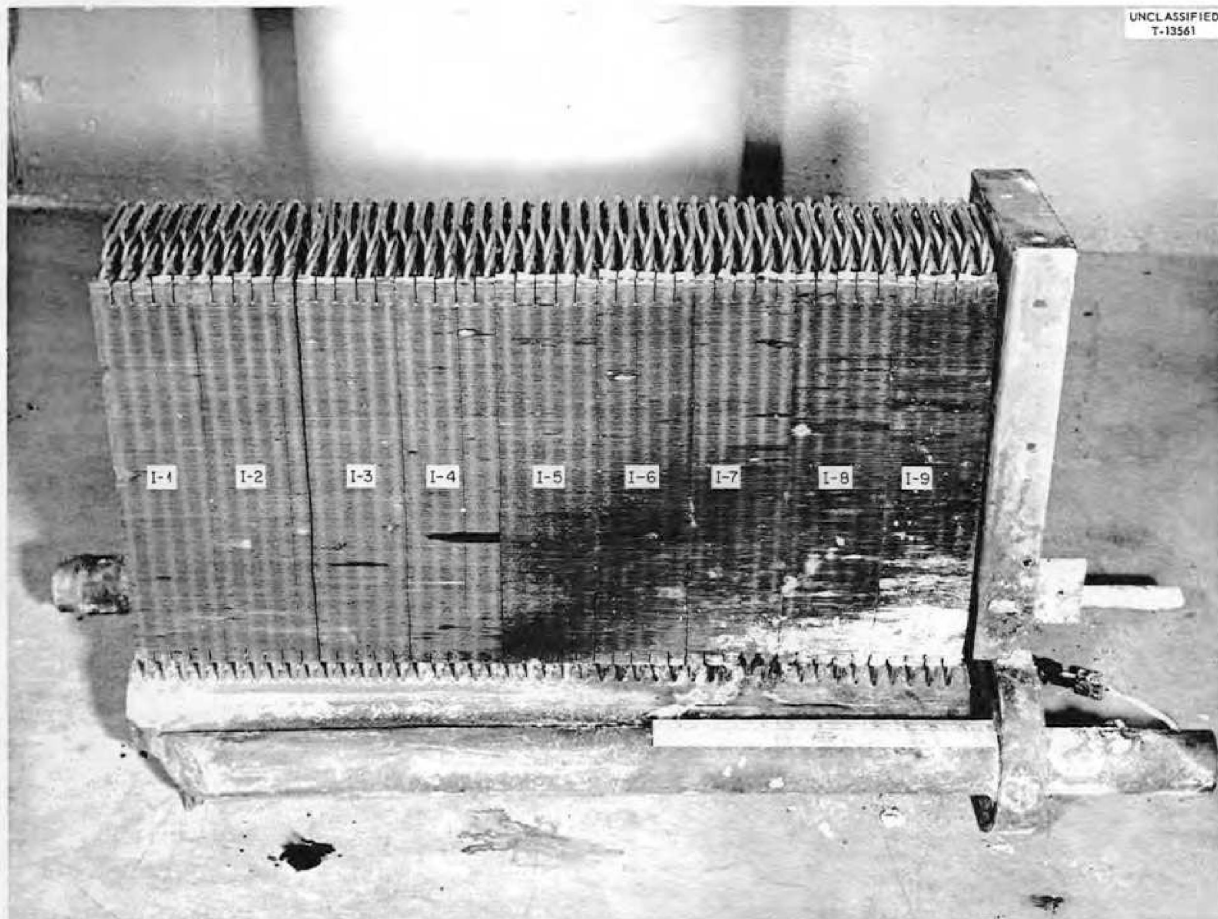
Fig. 3.6.10. ART Prototype Test Radiator No. 2 After It Had Been Cleaned. (────── with caption)

of the 40 tubes in the two sections were found to have perforations.

The two sections that contained the damaged tubes are shown in Figs. 3.6.11 and 3.6.12. In the most severely damaged section, I-7, ten of the 20 tubes were found to be damaged. All 40 of the tubes in the two sections were examined for evidence of incipient failure. The microstructure that was typical of 39 of the 40 tubes is shown in Fig. 3.6.13. As may be seen, there is no evidence of incipient failure. The microstructure of the one tube that showed signs of incipient failure is shown in Figs. 3.6.14, 3.6.15, and 3.6.16.

Although only one of the 40 tubes examined showed evidence of incipient failure, it is felt that this evidence is reliable and that the original failure occurred in this tube. The other tubes were probably ruptured by the fire that occurred because of the leakage of NaK.

Similar incipient failure has also been found in creep test specimens. The microstructure of a specimen that was tested in argon at 1500°F and a stress of 3000 psi is shown in Fig. 3.6.17; the tube ruptured after 374 hr of testing. Note the fissures at the grain boundaries and the striking similarity to Figs. 3.6.14 and 3.6.15.
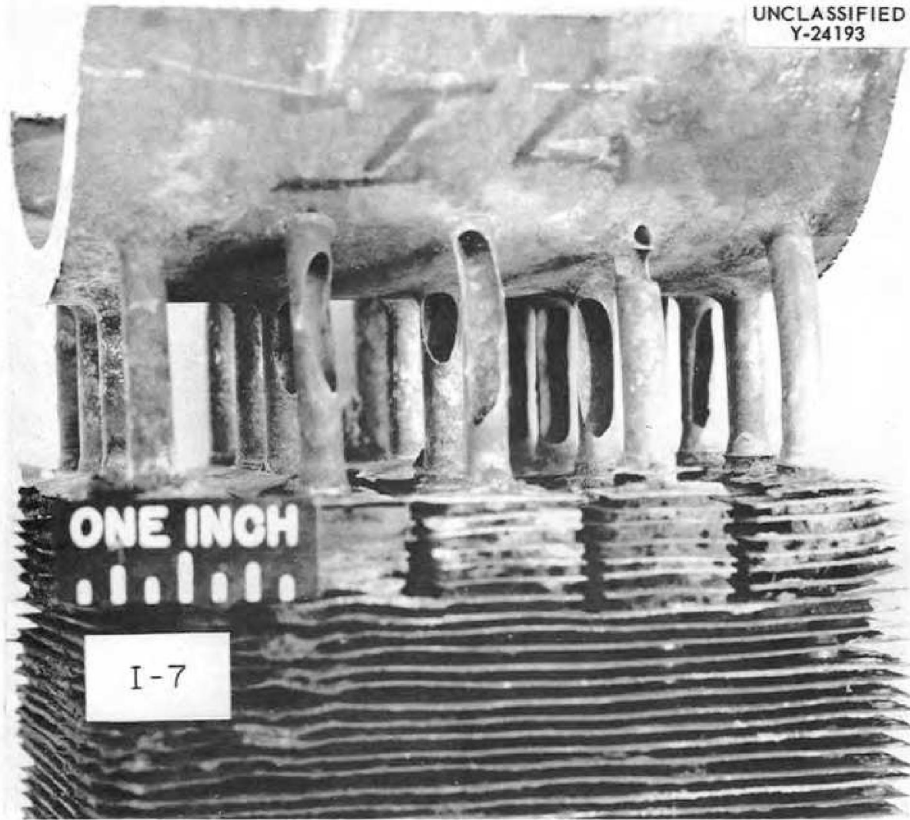
Fig. 3.6.11. Fire Damage in Section I-7.

Fig. 3.6.12. Fire Damage in Section I-8.
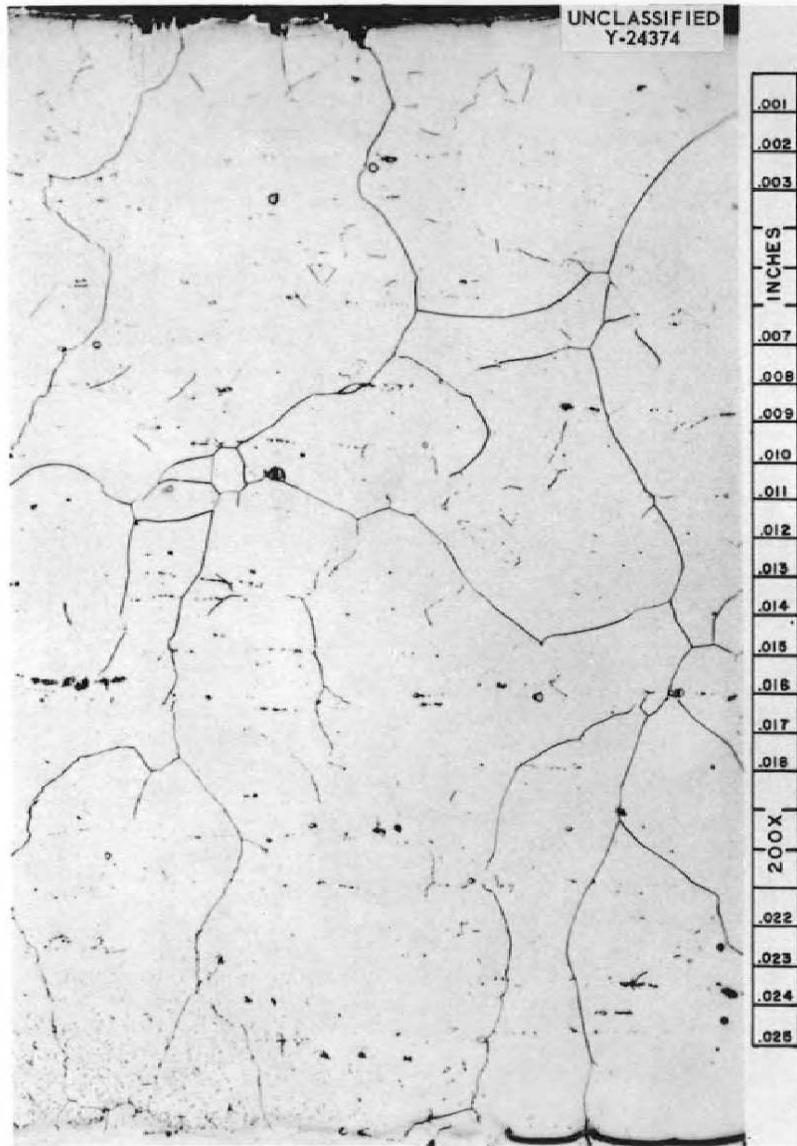
Fig. 3.6.13. Typical Microstructure Found in 39 of the 40 Tubes Examined. Etchant: 10% oxalic acid. 200X.
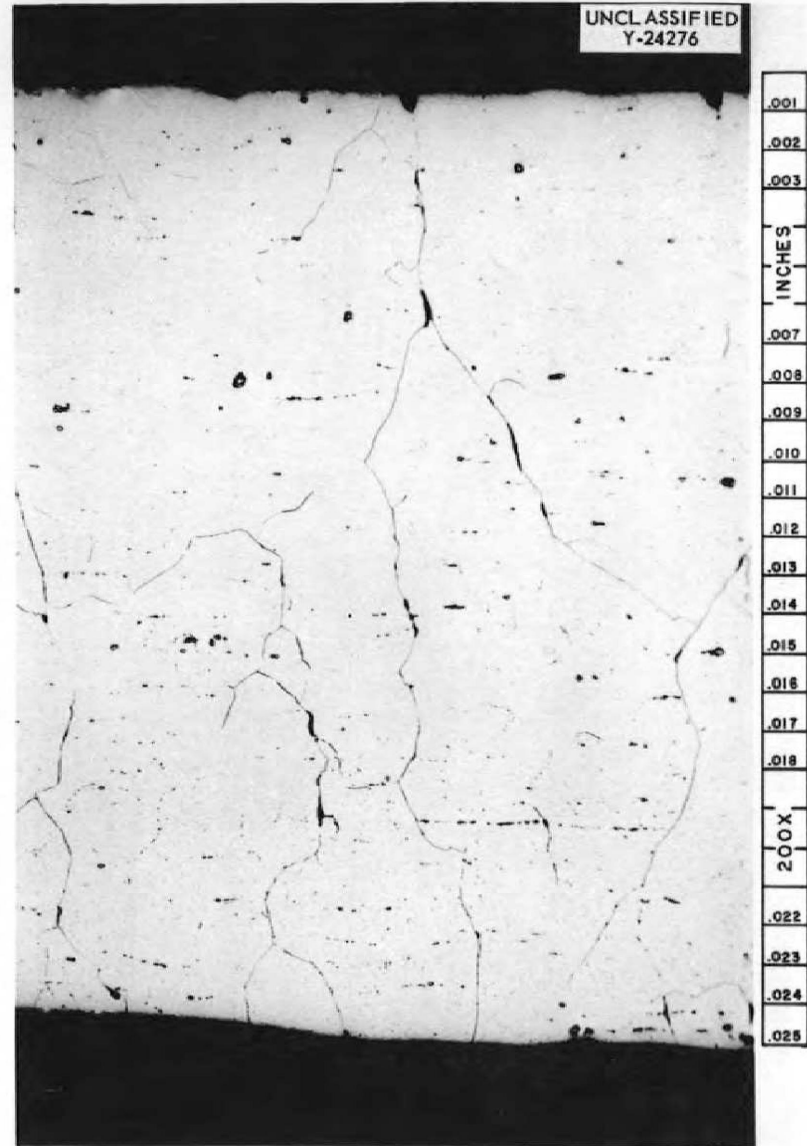
Fig. 3.6.14. Microstructure Indicative of Incipient Failure in a Tube That Ruptured. Etchant: 10% oxalic acid. 200X.
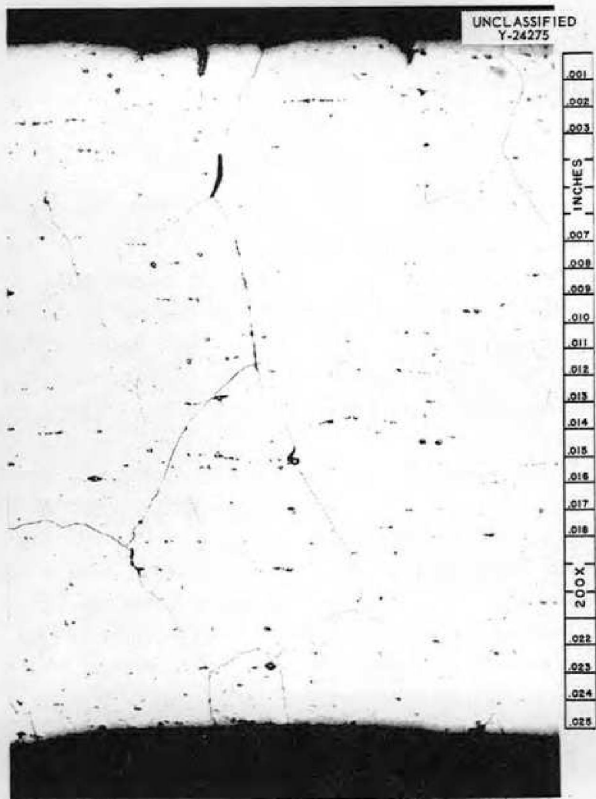
Fig. 3.6.15. Another Area of the Tube Shown in Fig. 3.6.14. Etchant: 10% oxalic acid. 200X. Reduced 30%.
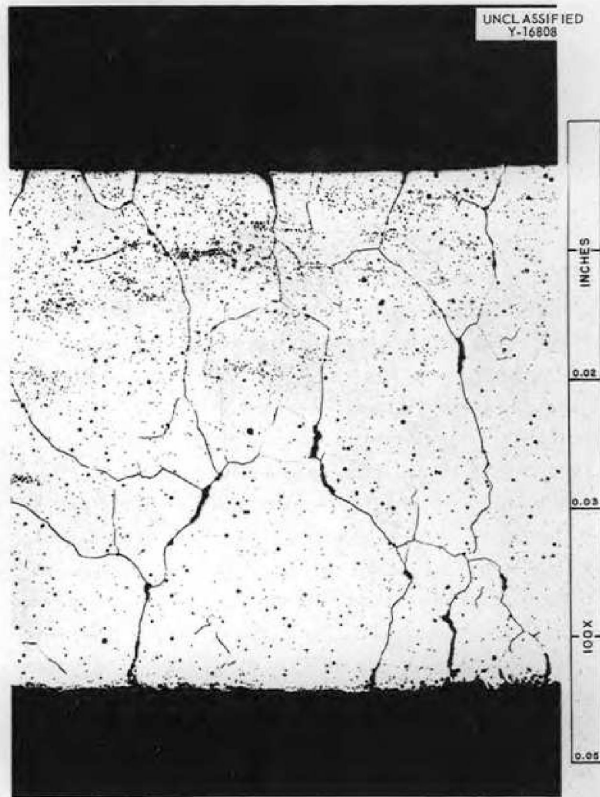
Fig. 3.6.17. Microstructure of Inconel Creep-Test Specimen Showing Incipient Fissures at Grain Boundaries. 100X. Reduced 33%.
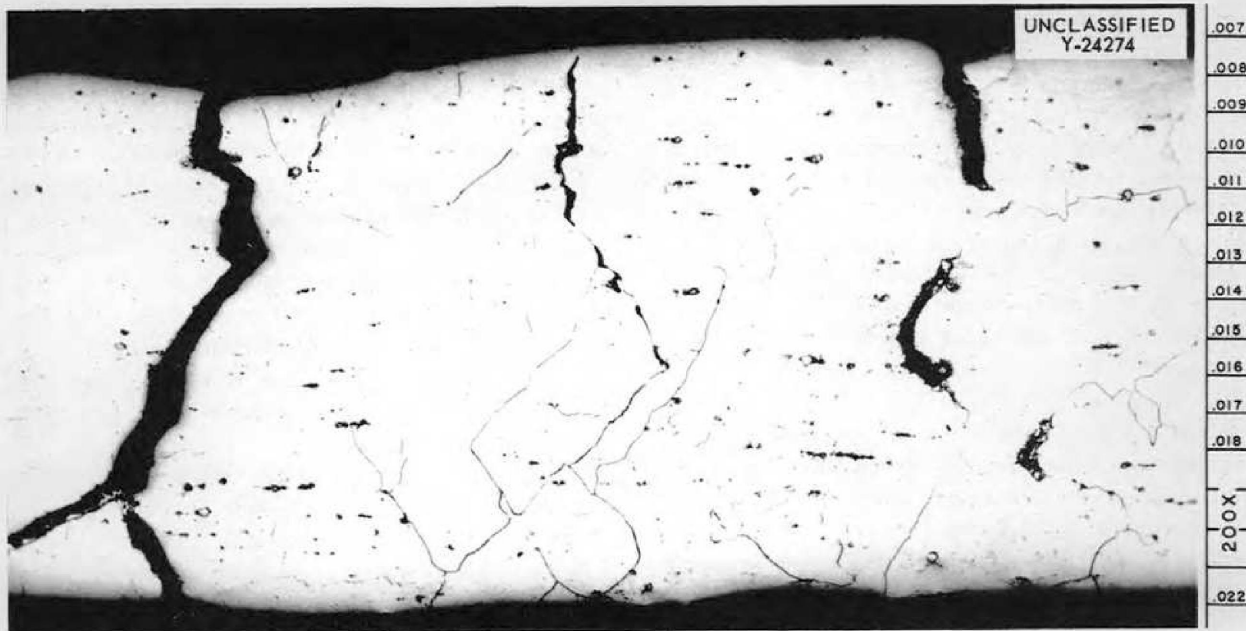
Fig. 3.6.16. Microstructure Closer to the Hole in Tube Shown in Figs. 3.6.14 and 3.6.15. Etchant: 10% oxalic acid. 200X.

191

3.7. NONDESTRUCTIVE TESTING

R. B. Oliver

EDDY-CURRENT THICKNESS MEASUREMENTS

R. B. Oliver
R. A. Nance   J. W. Allen

The inherent accuracy of the new eddy-current thickness gage[1] was increased by the substitution of drift-free transistor oscillators for the variable-frequency signal generator previously employed. Although transistors are sensitive to thermal changes, they have a high degree of frequency stability if a uniform temperature is maintained.

The study of eddy-current cladding-thickness determinations has been continued, with particular emphasis on alleviating the problems encountered with the probe coils currently in use. These coils are contained in commercially procured, high-permeability, low-loss cup cores, approximately $\frac{1}{2}$ in. in diameter. The electromagnetic field produced by the coil investigates an area $\frac{1}{2}$ in. in diameter, which is much larger than the area of minimum cladding thickness sought. Since the eddy-current reading is a function of the area and of the minimum cladding thickness, it is difficult to obtain a true evaluation of the cladding thickness with this coil. Some cladding-thickness measurements have been satisfactory, but the error in a number of cases has been excessive. Smaller probe coils are being fabricated to remedy this problem. The accuracy of the determination will increase as the area of the field of the coil approaches the area of minimum cladding thickness. It is also difficult to locate the exact area of minimum cladding for metallographic examination because of the asymmetrical nature of the electromagnetic field produced by the present probe coils. Therefore the small cup cores are being constructed to produce symmetrical fields in addition to decreasing the size of the field.

A study has been initiated to determine the feasibility of measuring the thickness of hot-dipped aluminum coatings on aluminized steel. Preliminary tests indicate that a nominal coating thickness of 0.001 in. can be measured to within 0.0002 in.

---

[1]R. B. Oliver, J. W. Allen, and R. A. Nance, *ANP Quar. Prog. Rep. Sept. 30, 1957*, ORNL-2387, p 247.

REMOTE X-RAY VIEWING

R. B. Oliver   J. W. Allen

A closed-circuit television system (RCA model ITV-6) for direct x-ray imaging has been installed in the Nondestructive Test Laboratory, and the initial adjustment and alignment have been accomplished. Preliminary studies have been made on the system to evaluate it for practical inspection use.

The system consists of a conventional industrial-type Vidicon camera and television monitor connected in a closed video circuit. The conventional light-sensitive Vidicon camera tube was replaced with an x-ray-sensitive tube having a selenium target (photoconductive receptor) approximately ten times thicker. The thicker target allows greater absorption of x rays and thus greater x-ray sensitivity.

The technique for use of this system is similar to that used in conventional radiography. The object to be examined is placed near the photoconductive face of the Vidicon tube, and the source of x radiation is placed at some distance from the object. The system is, therefore, subject to the same geometrical considerations as those of the conventional radiographic method. An inherent image magnification of approximately 12 diameters is obtained, since the $\frac{1}{2}$- by $\frac{3}{4}$-in. roster scanned on the Vidicon target is reproduced as a 6- by 9-in. roster on the kinescope.

Preliminary studies of the sensitivity and resolution of the system have been encouraging. The exposure and contrast sensitivity, although not so great as those attained with film, are adequate for many applications. Since the exposure of the photoconductive target is continuous rather than accumulative, as it is with a photo-emulsion, it is inherently less sensitive than film. The greatest area of usefulness of the system appears to be in the inspection of thin sections through which high-intensity radiation can reach the photoconductive target.

A very high degree of resolution is attainable with this system in comparison with other types of direct or remote x-ray image-viewing systems; the resolution is not limited by a mosaic of fluorescing crystals, as is the case with a

fluorescent screen. The system will clearly resolve the x-ray image of a 500-mesh screen, and thus it is possible that resolution in excess of 500 lines per inch may be achieved. The inherent magnification appears to improve the resolution of fine detail, as illustrated in Fig. 3.7.1, which is a photograph of the television screen showing the x-ray image of a small point-contact semiconductor diode. This image, although trivial, illustrates the desirability of high-resolution image magnification. The wire of the diode is less than 0.005 in. in diameter and terminates on a germanium wafer at the lower extremity, the assembly being contained in a glass envelope (light-gray area). In another test, a fine crack in a $\frac{1}{4}$-in.-dia, 0.025-in.-wall INOR-8 tube was readily observed; the crack was less than $\frac{1}{4}$-in. long.

It is expected that the detection of small defects in small-diameter tubing will be improved by rotating the tube during observation. The evaluation of this technique and the contrast sensitivity on small-diameter tubing has been hampered by the lack of suitable remotely controlled mechanical equipment. Accordingly, an existing skew-roll feed mechanism is being modified to accommodate the x-ray Vidicon system. This mechanism will permit evaluation of the method for the inspection of tubing to proceed quickly and effectively.

MATERIALS INSPECTION
R. W. McClung
Tubing

Approximately 13,000 ft of small-diameter CX-900 Inconel tubing was inspected during the last quarter by the immersed-ultrasound and the

UNCLASSIFIED
PHOTO 42833

Fig. 3.7.1. Radiograph of a Semiconductor Diode ($\frac{3}{16}$-in.-dia, $\frac{5}{16}$-in.-long) Made by Photographing the Monitor Screen of the X-Ray-Sensitive Television System.

encircling-coil eddy-current techniques; the rejection rate was about 5%. The total length of the tubing inspected for the ANP program was about 120,000 ft.

Pipe

Approximately 1500 ft of Inconel pipe in sizes varying from $\frac{1}{8}$-in. sched-40 up to $3\frac{1}{2}$-in. sched-40 was inspected by the immersed-ultrasound method; the rejection rate was less than 5%. About 450 ft of $3\frac{1}{2}$-in. sched-40 pipe was also inspected by the resonance-ultrasound method in order to accurately determine the wall thickness throughout each length. The total inspected length of pipe has been approximately 8250 ft.

Plate

The immersed-ultrasound technique was used during the last quarter to inspect approximately 375 ft^2 of Inconel plate in thicknesses varying from $\frac{1}{2}$ to 1 in. This brought the total inspected quantity up to about 1500 ft^2. The rejection rate has averaged 1% or less and has varied according to the location of the defects and the possibility of their removal when the plates were cut to size.

Hastelloy B Tubing

A special lot of Hastelloy B tubing was fabricated by the Republic Steel Corp., Cleveland, Ohio, in order to determine their potentiality as suppliers of this type of material. The tubing was of three sizes, $\frac{1}{4}$-in., $\frac{5}{16}$-in., and $\frac{3}{8}$-in. OD, but the wall thickness of each size of tubing was 0.030 in. It was known that a few gross flaws were present, and therefore the prime interest was in the remainder of the tubing. In general, it was found to be among the best of the Hastelloy B tubing inspected to date. The quality of the larger diameter tubing seemed to be better than that of the $\frac{1}{4}$-in.-OD tubing. Among the rejectable conditions noted were cracks alongside the weld bead of the $\frac{1}{4}$-in.-OD tubing shown in Fig. 3.7.2. The excessive weld penetration found in the $\frac{3}{8}$-in.-OD tubing shown in Fig. 3.7.3 was also considered to be undesirable. Pores found on the inner surface of the $\frac{5}{16}$-in.-OD tubing are shown in Fig. 3.7.4.
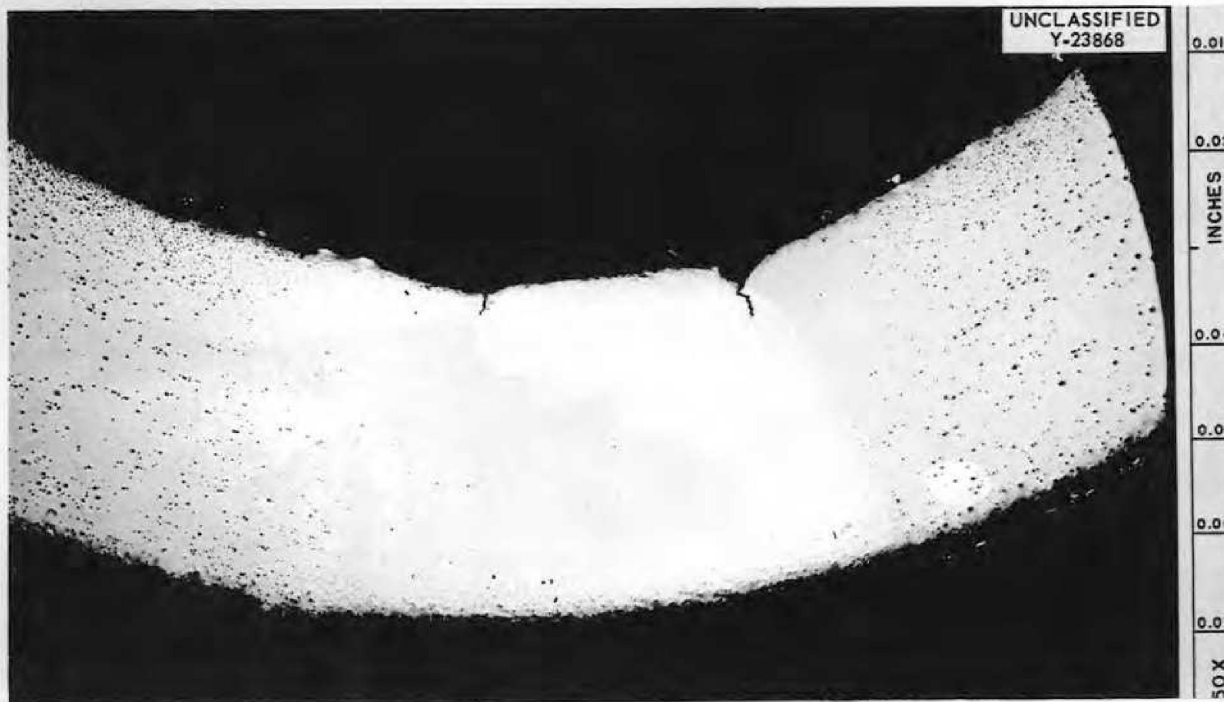
Fig. 3.7.2. Weldrawn Hastelloy B Tubing Showing Cracks at the Root of the Weld Bead. Unetched. 50X.
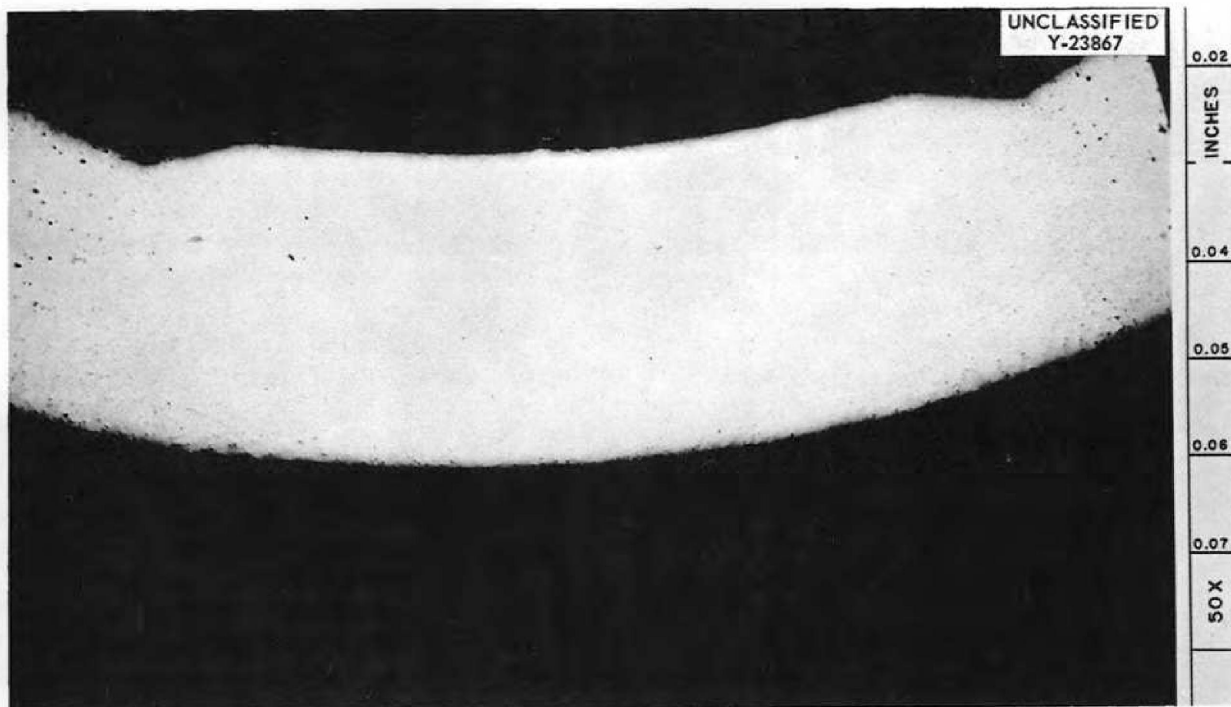
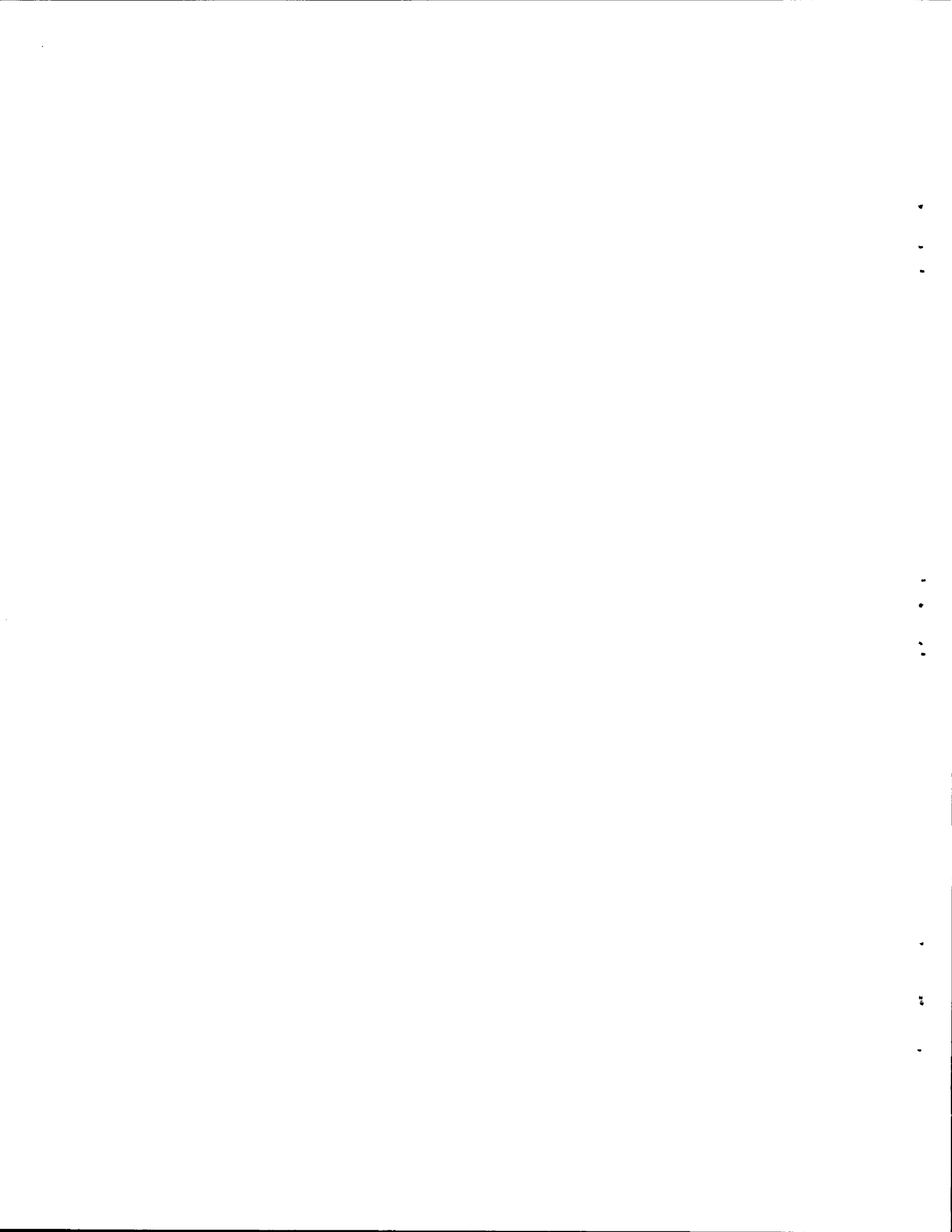Fig. 3.7.3. Weldrawn Hastelloy B Tubing Showing the Results of Excessive Penetration of the Weld Bead. Unetched. 50X.
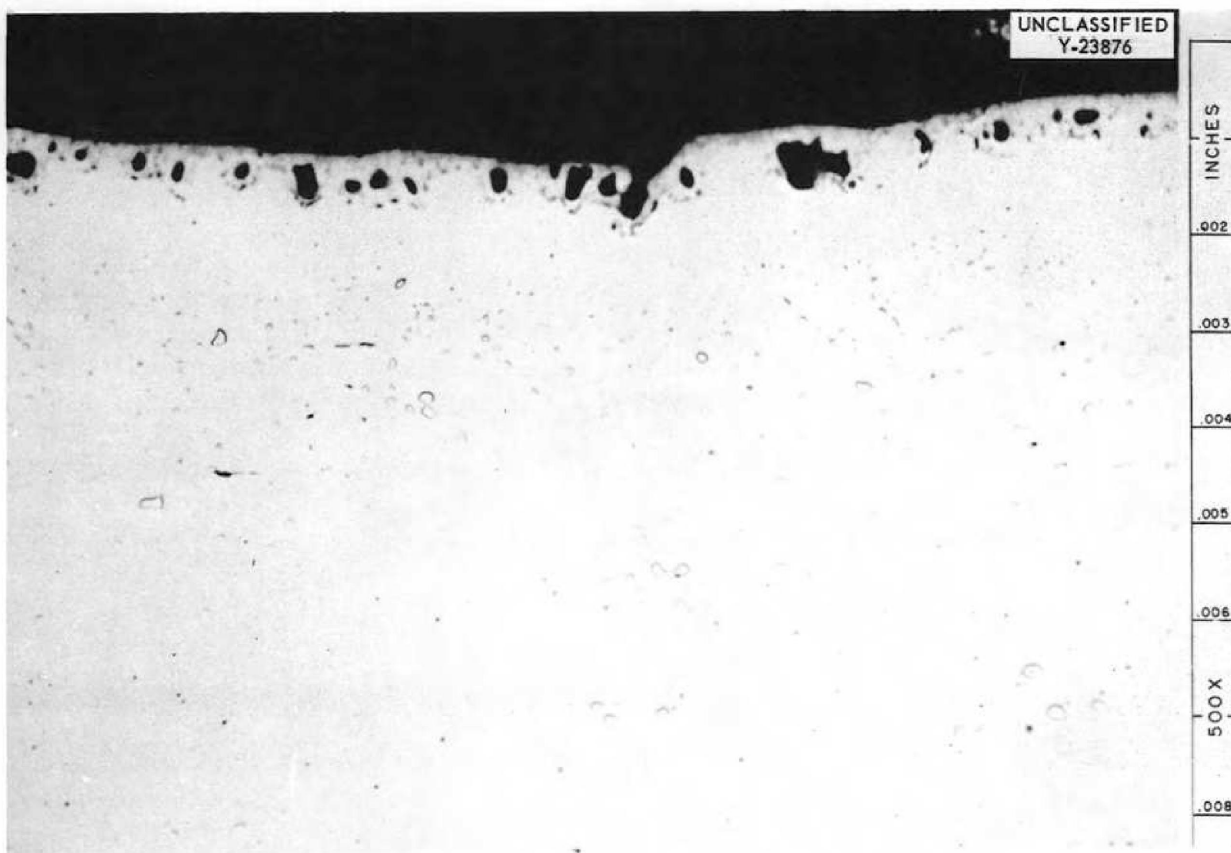
Fig. 3.7.4. Microsection of Weldrawn Hastelloy B Tubing Showing Pores on the Inner Surface. Unetched. 500X.

195

Part 4

RADIATION DAMAGE

G. W. Keilholtz

4.1. RADIATION DAMAGE

G. W. Keilholtz

EXAMINATION OF IRRADIATED COMPONENTS AND MATERIALS

A. E. Richt

N. A. Carter   W. B. Parsley
C. Ellis   E. D. Sims
E. J. Manthos   R. M. Wallace

MTR In-Pile Loops

Examinations of the four forced-circulation loops that were operated in the MTR with fused fluoride fuels as the circulated fluids have been completed.[1] The impeller housings from loops Nos. 4, 5, and 6, which were the last items to be examined, were opened on the remotely operated lathe. The results of the examination of the impeller from loop No. 3 were described previously.[2] The impellers could not be removed from the housings because of a shoulder on the pump shaft, and therefore only the front faces of the impellers could be examined. No evidences of fuel were found in the front halves of the impellers from loops Nos. 4 and 5; however, there was a fuel deposit in the bottom of the housing of the impeller from loop No. 6. As may be seen in Figs. 4.1.1, 4.1.2, and 4.1.3, the

teeth of the impellers from loops Nos. 4, 5, and 6 showed no evidences of erosion. The impeller housing cover plates and the forward halves of the impellers from loops Nos. 4, 5, and 6 are shown in Figs. 4.1.4 through 4.1.9. The fuel deposit that may be seen in Fig. 4.1.9 at the bottom of the housing of the impeller from loop No. 6 is shown again in Fig. 4.1.10 at a higher magnification. No metallographic specimens were taken from any of these impellers.

Fig. 4.1.2. Teeth of Impeller from Pump Used in MTR In-Pile Loop No. 5. 4X. Reduced 11%.

Fig. 4.1.3. Teeth of Impeller from Pump Used in MTR In-Pile Loop No. 6. 4X. Reduced 11%.

---

[1]For descriptions of these loops and the conditions under which they were operated, see Part 1 of previous reports in this series.

[2]A. E. Richt et al., ANP Quar. Prog. Rep. Dec. 31, 1956, ORNL-2221, p 290.

Fig. 4.1.1. Teeth of Impeller from Pump Used in MTR In-Pile Loop No. 4. 4X. Reduced 11%.

Moderator Materials

Disassembly and examination of the capsules irradiated in the second exposure in the MTR of the high-temperature moderator-materials testing assembly were completed, except for further metallographic examination of the molybdenum capsule that contained zirconium hydride. Three capsules were irradiated: one was beryllium oxide encased in Inconel; another was graphite encased in nickel; and the third was zirconium hydride encased in molybdenum. The results of the examination of the BeO-containing capsule were described previously;[3] the examinations of the other two capsules are described here.

[3]A. E. Richt *et al.*, *ANP Quar. Prog. Rep. Sept. 30, 1957*, ORNL-2387, p 257.

Fig. 4.1.4. Cover Plate of Housing for Impeller of Pump Used in MTR In-Pile Loop No. 4. $\frac{1}{2}$X.
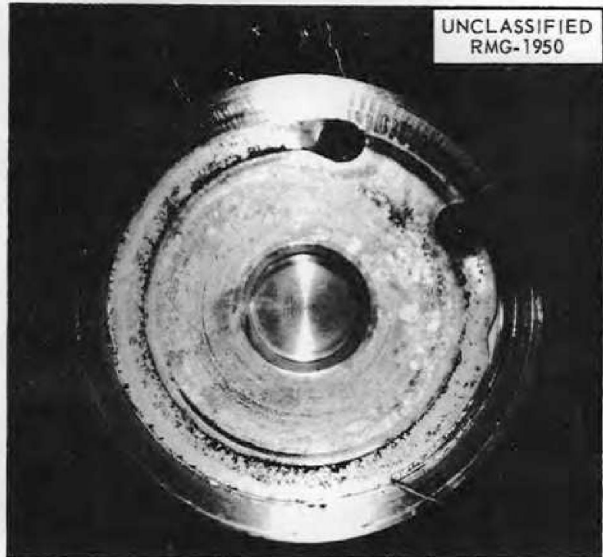
Fig. 4.1.6. Cover Plate of Housing for Impeller of Pump Used in MTR In-Pile Loop No. 5. $\frac{1}{2}$X.
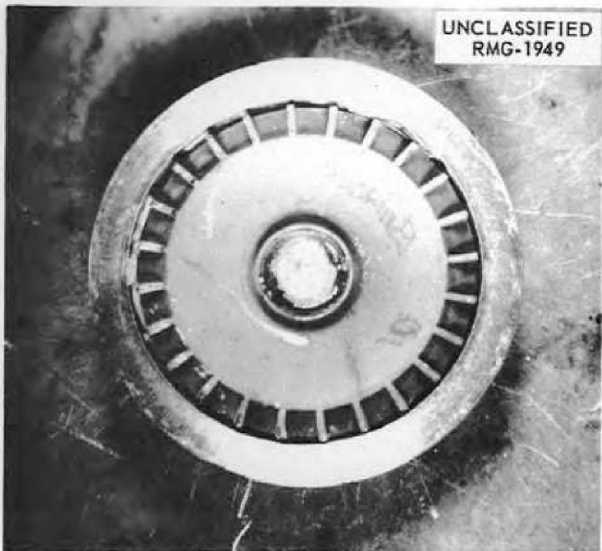
Fig. 4.1.5. Forward Face of Impeller from Pump Used in MTR In-Pile Loop No. 4. $\frac{1}{2}$X.

Fig. 4.1.7. Forward Face of Impeller from Pump Used in MTR In-Pile Loop No. 5. $\frac{1}{2}$X.

The nickel jacket of the graphite-containing capsule was removed by milling the jacket longitudinally and then peeling it from the graphite slug. No cracking or flaking of the graphite slug was visible after the jacket was removed. The diameters of the four graphite slugs were found to be 1.2498, 1.2505, 1.2502, and 1.2502 in., which compared favorably with the original slug diameter of 1.251 in. Metallographic examination of the nickel jacket revealed that no reaction between the

Fig. 4.1.10. Fuel Deposit Indicated by Arrow in Fig. 4.1.9 at a Higher Magnification. 4X.

Fig. 4.1.8. Cover Plate of Housing for Impeller of Pump Used in MTR In-Pile Loop No. 6. $\frac{1}{2}$X.

Fig. 4.1.9. Forward Face of Impeller from Pump Used in MTR In-Pile Loop No. 6. $\frac{1}{2}$X.

graphite and the nickel had occurred, as shown in Fig. 4.1.11. The outer surface showed void formation to a depth of 8 mils. The small cracks on the inner surface of the jacket were probably formed while the sample was being handled during cutting and mounting. The Inconel jacket from the BeO-containing capsule examined previously likewise did not react with the moderator material, as may be seen in Fig. 4.1.12.

The zirconium hydride capsule was sectioned on the remote lathe and milling machine. During sectioning of the capsule, the molybdenum jacket separated from the zirconium hydride slug; thus, it appears that there was little or no bonding between the jacket and the slug. Zirconium hydride chips were collected during machining and submitted for chemical analysis.

The zirconium hydride in the brazed end of the capsule was damaged, as shown in Fig. 4.1.13. The remainder of the slug was undamaged and appeared to be structurally intact. A control capsule showed similar damage of the zirconium hydride at the brazed end; thus, it appears that the damage was the result of poor fabrication techniques rather than irradiation. The molybdenum jacket was very brittle and broke easily. There was no evidence, however, of reaction with the zirconium hydride on the inner surface of the molybdenum, as shown in Fig. 4.1.14.

A section of the control capsule with the molybdenum jacket and the zirconium hydride slug intact and a section of the irradiated zirconium
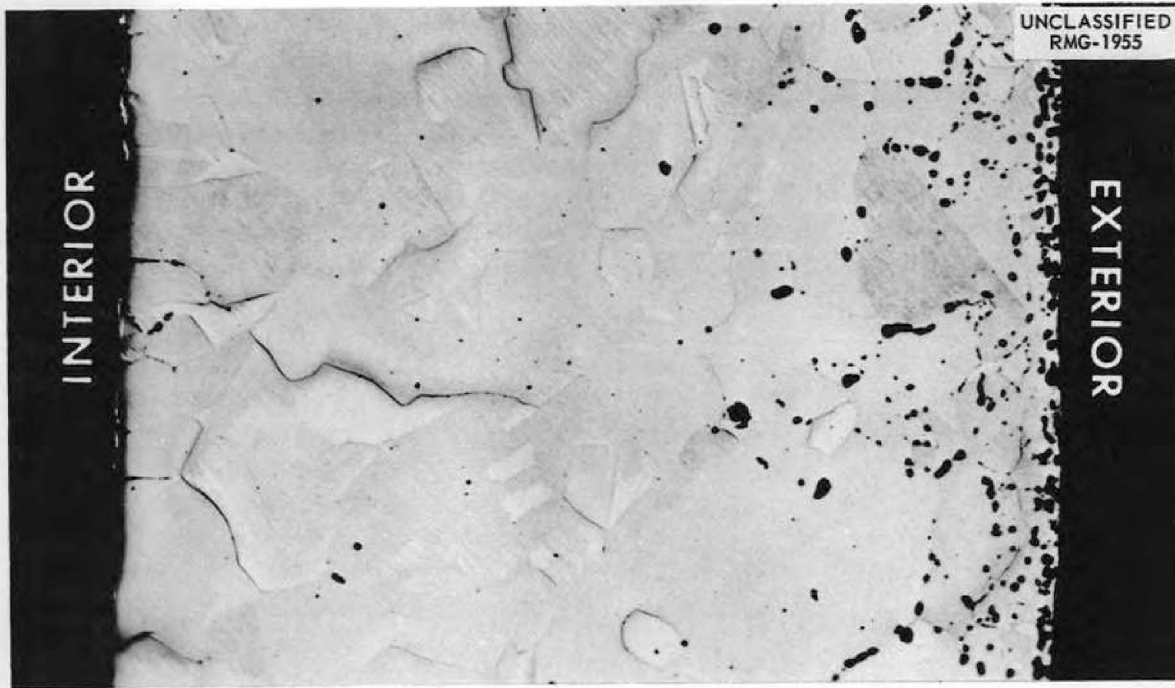
Fig. 4.1.11. Nickel Jacket from Graphite-Containing Capsule Which Was Irradiated in the MTR. 250X.
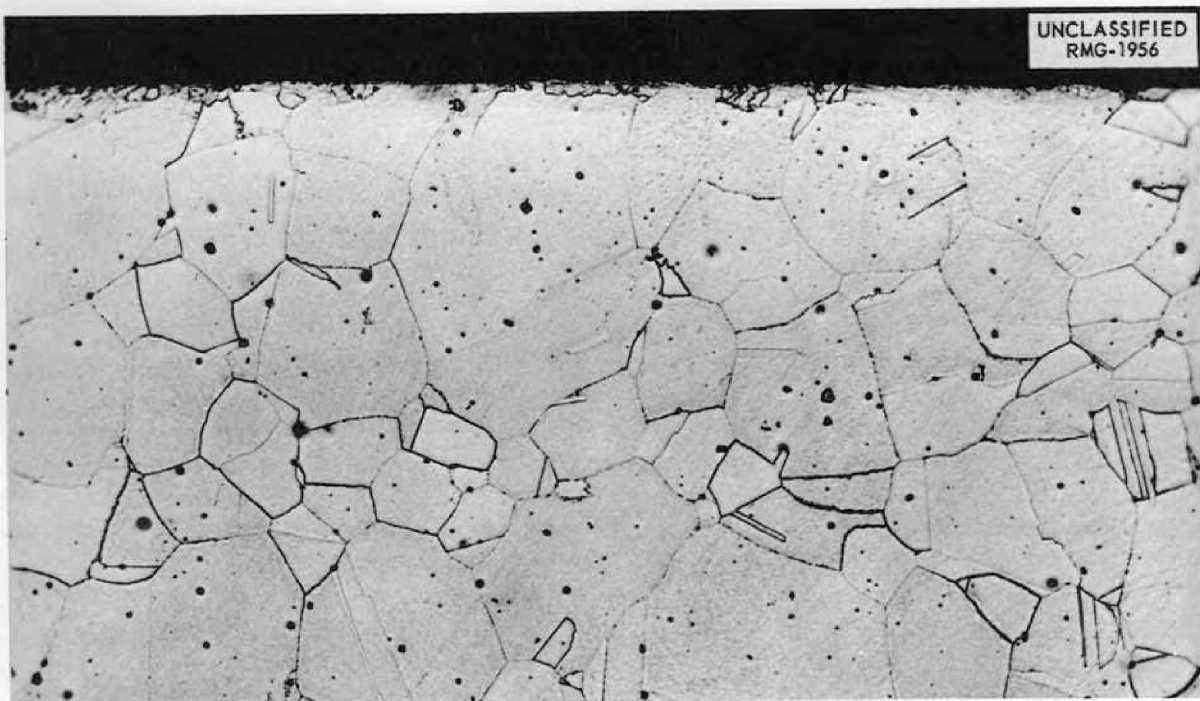

Fig. 4.1.12. Inner Surface of Inconel Jacket Removed from the BeO-Containing Capsule That Was Irradiated in the MTR. 250X.

hydride slug are being examined metallographically. The irradiated and the control samples appear to be similar, except that the needlelike phase is coarser in the control slug than in the irradiated slug, and, in contrast to those in the irradiated

UNCLASSIFIED
RMG-1957

Fig. 4.1.13. Zirconium Hydride Slug Showing Damage Found at Brazed End of Capsule Upon Removal of Molybdenum Jacket After Irradiation in the MTR. This damage was caused by poor fabrication techniques rather than irradiation. 4X. Reduced 17%.

slug, the needles in the control slug are in bundles in the matrix rather than being distributed uniformly. In both samples there is a third phase interspersed among the needles, as shown in Figs. 4.1.15 through 4.1.18. The control sample was anodized to enhance the contrast between the two phases. Attempts to anodize the irradiated sample have been only partially successful.

Direct comparisons of the structures of the irradiated and unirradiated specimens cannot be made because the unirradiated specimen was overheated during the brazing cycle. It is not known at this time whether the structural differences evident in Figs. 4.1.15 through 4.1.18 are the result of irradiation or of variations during fabrication; further, they may possibly be normal structural variations.

Complex reactions were found to have occurred at the interface of the zirconium hydride and the iron layer used between the zirconium hydride and the molybdenum jacket, and at the interface of the iron and the molybdenum. The control capsule exhibited three distinct reaction zones, as may be seen in Fig. 4.1.19. The irradiated specimen appeared to have only two reaction zones, as shown in Fig. 4.1.20. Further metallographic

UNCLASSIFIED
RMG-1964

Fig. 4.1.14. Interior Surface of Molybdenum Jacket Removed from an Irradiated Zirconium Hydride—Containing Capsule. Specimen nickel-plated for edge preservation. 250X.
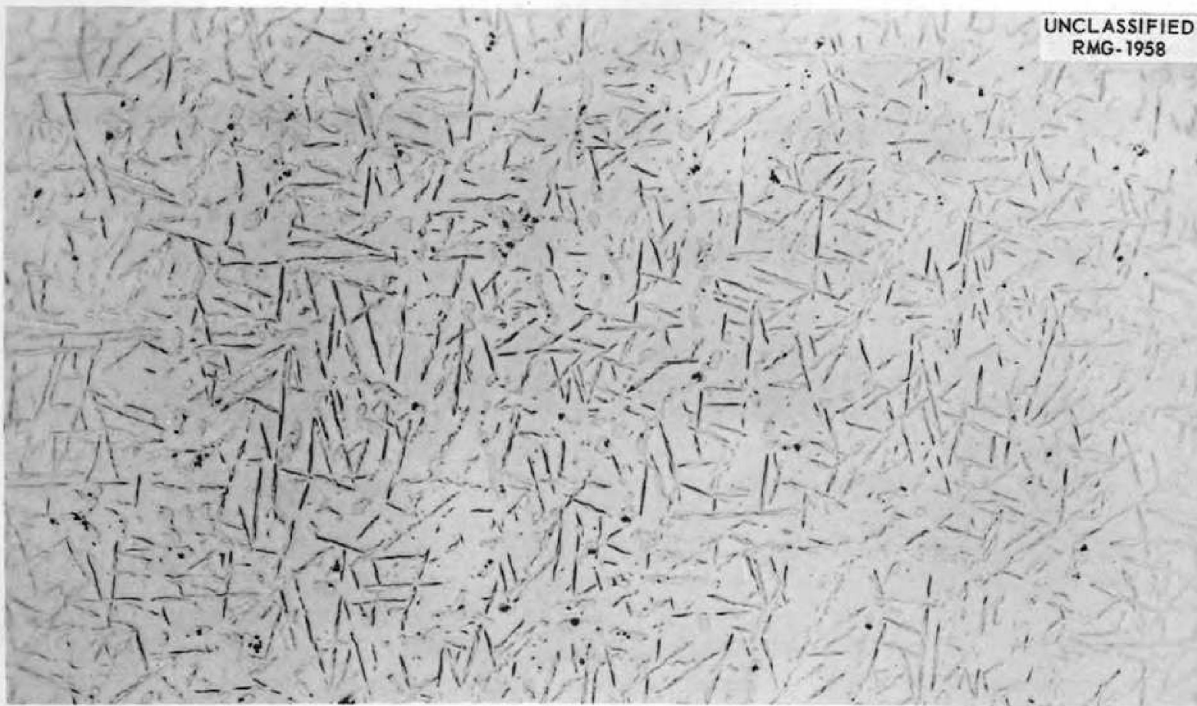
Fig. 4.1.15. Structure of Irradiated Zirconium Hydride, as Polished. 250X.
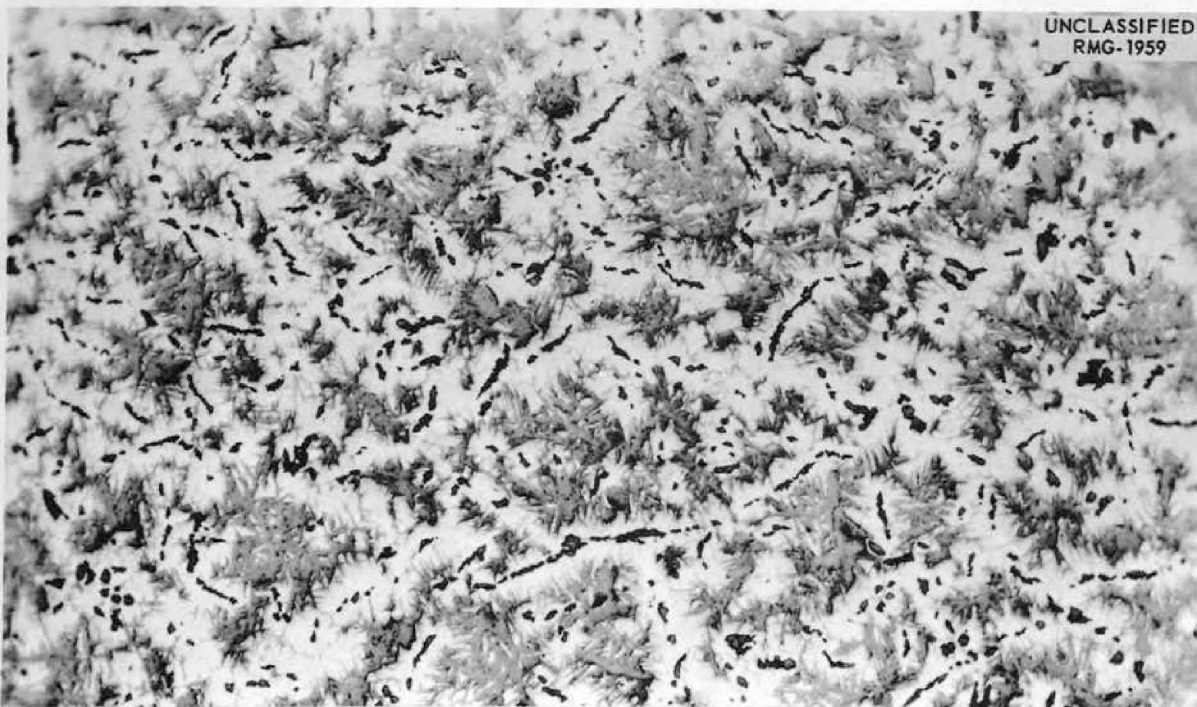

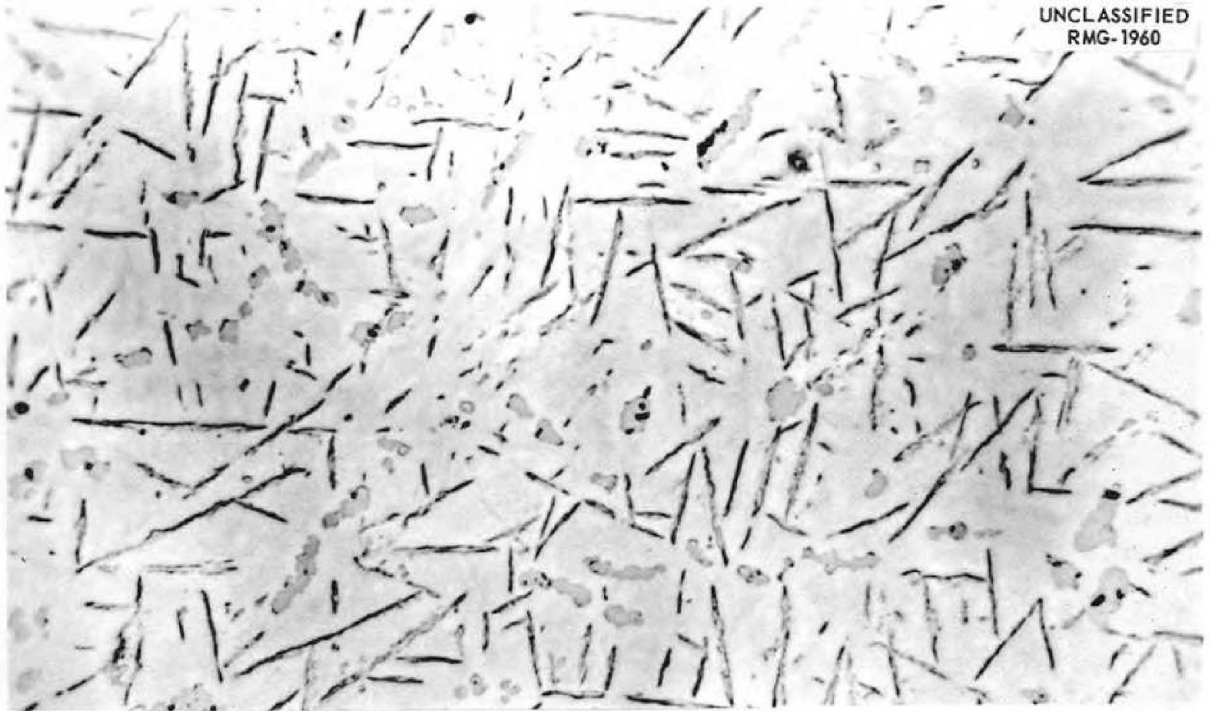Fig. 4.1.16. Structure of Unirradiated Zirconium Hydride, as Anodized. 250X.

Fig. 4.1.17. Structure of Irradiated Zirconium Hydride Shown at a Higher Magnification Than That Used for Fig. 4.1.15. 500X.
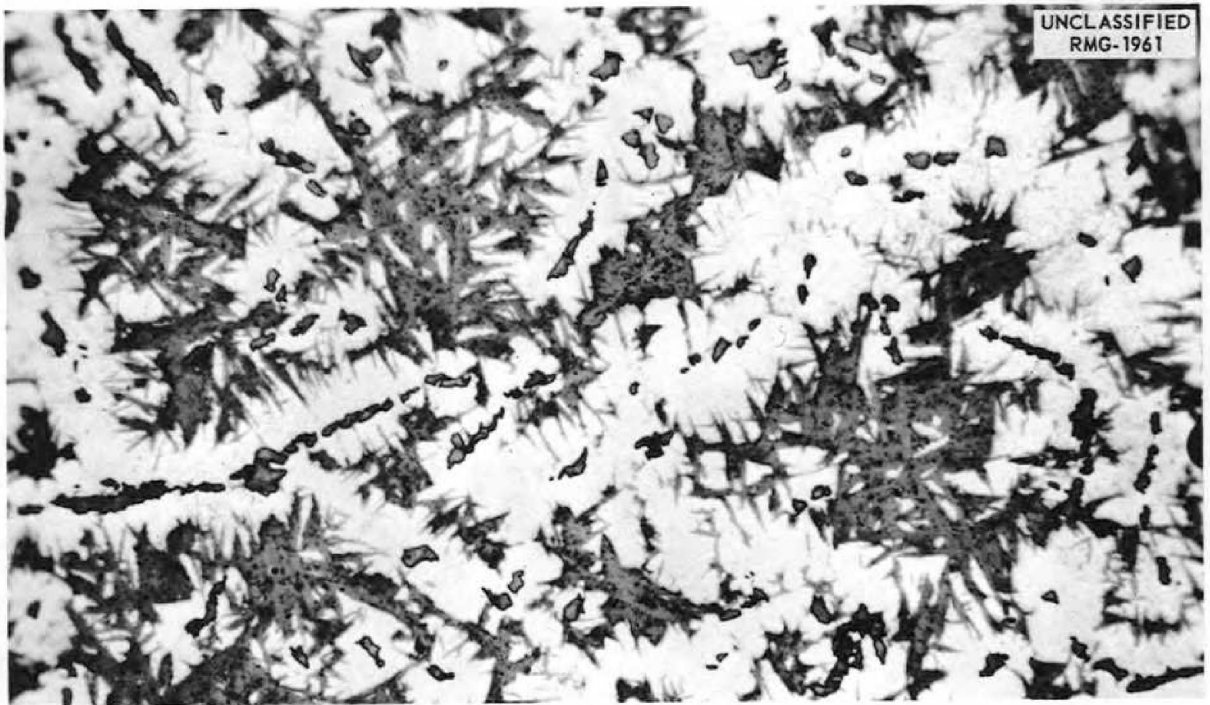

Fig. 4.1.18. Structure of Unirradiated Zirconium Hydride Shown at a Higher Magnification Than That Used for Fig. 4.1.16. 500X.
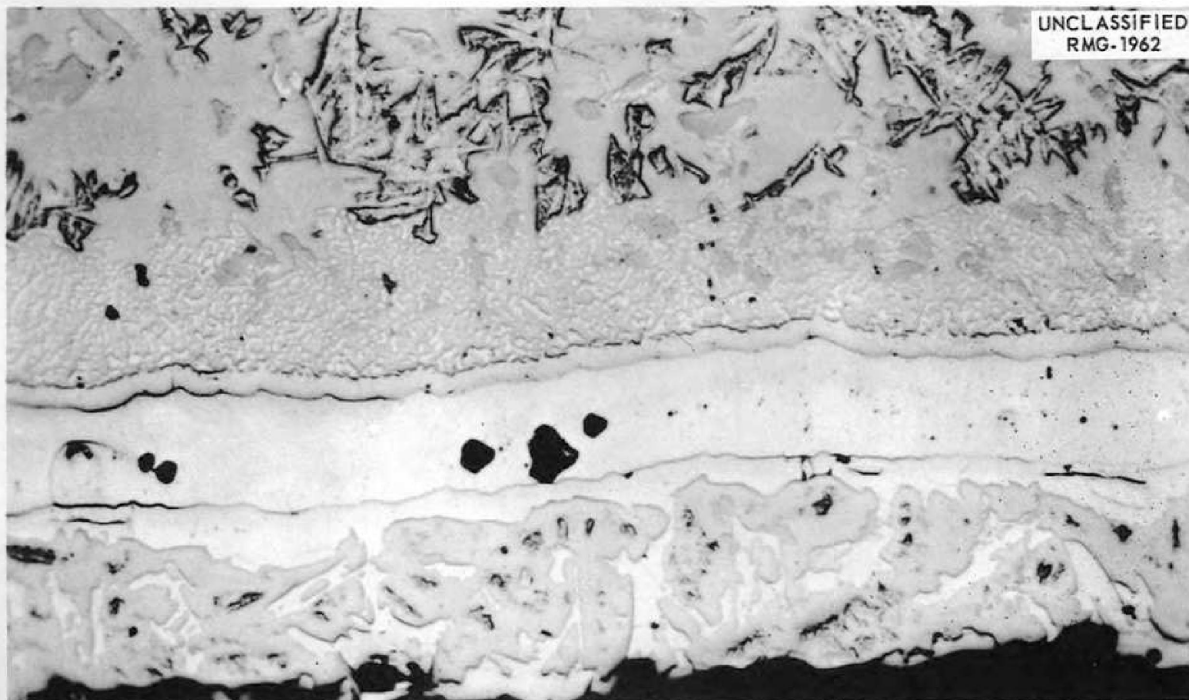
205

Fig. 4.1.19. Zirconium Hydride—Iron and Iron-Molybdenum Interfaces of Unirradiated Capsule. As polished. 500X.
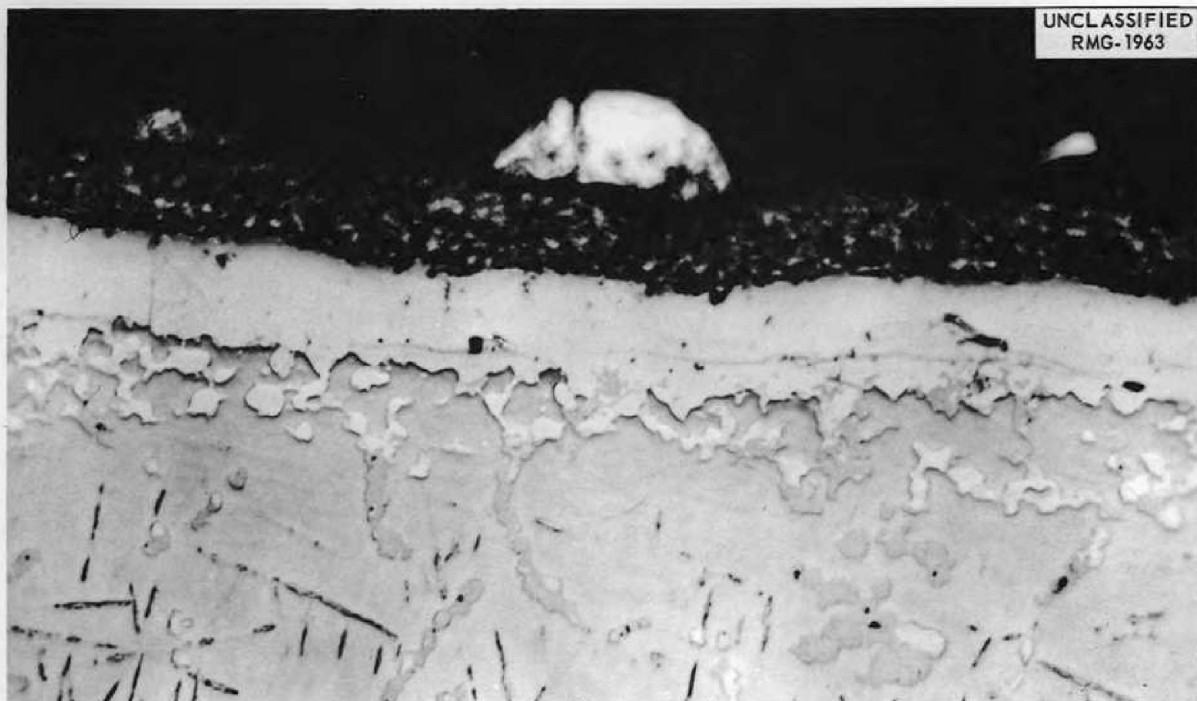
Fig. 4.1.20. Zirconium Hydride—Iron and Iron-Molybdenum Interfaces of Irradiated Capsule. As polished. 500X.

examinations of both specimens are being carried out in an attempt to determine the cause of the structural variations observed in the zirconium hydride matrix.

CREEP AND STRESS-RUPTURE TESTS OF INCONEL

J. C. Wilson

| W. E. Brundage | N. E. Hinkle |
| W. W. Davis | J. C. Zukas |

MTR Experiments

The out-of-pile test was completed that corresponded to the MTR tube-burst tests conducted previously.[4] The apparatus for the out-of-pile test as well as the operating conditions duplicated those of the in-pile test except for the absence of radiation. Seven of the eight out-of-pile specimens ruptured before the test was discontinued at the end of a 304-hr period. The times to rupture, as shown in Table 4.1.1, were two to five times

longer than in the MTR tests, but the times were still of the order of a factor of 4 shorter than in tests conducted by the Metallurgy Division.[5]

As may be seen from the data in Table 4.1.1, the strain at fracture in the out-of-pile specimens was greater than that in the corresponding in-pile specimens. The in-pile apparatus was disassembled and the specimens were checked for fracture location. Metallographic examination of both out-of-pile and in-pile specimens will be carried out in order to establish any differences in the mode of fracture.

The thermocouple wires used in the out-of-pile test were brittle after the test. In order to determine whether a change in thermocouple characteristics accompanied the loss of ductility, tests on the constancy of thermocouple calibration were carried out in helium in an Inconel tube. The thermocouples were located in air and in helium.

[4]J. C. Wilson *et al., ANP Quar. Prog. Rep. June 30, 1957,* ORNL-2340, p 268.

[5]J. R. Weir, Jr., D. A. Douglas, and W. D. Manly, *Inconel as a Structural Material for a High-Temperature Fused-Salt Reactor,* ORNL-2264 (June 4, 1957).

Table 4.1.1. Rupture Life and Elongation of Inconel as Measured in In-Pile and Out-of-Pile Tube-Burst Tests

Tube Wall Thickness* (in.)	Specimen Number	Stress (psi)	Type of Test	Time to Rupture (hr)	Elongation (%)
0.030	21	3000	In-pile**	78	0.8
	22	3000	In-pile	78	0.7
	33	3000	Out-of-pile	144	4
	29	3000	Out-of-pile	304	3.1
	20	4000	In-pile	17	1.1
	16	4000	In-pile	33	0.75
	27	4000	Out-of-pile	78	4.4
	31	4000	Out-of-pile	100	5
	17	5000	In-pile	13	1.2
	24	5000	In-pile	19	1
	30	5000	Out-of-pile	55	5
	25	5000	Out-of-pile	103	5.2
0.050	1	4000	In-pile	23	0.85
	3	4000	In-pile	29	0.96
	36	4000	Out-of-pile	105	7.6
	34	4000	Out-of-pile	115	7.6

*Original inside diameter = 0.51000 $\pm$ 0.00025 in.

**Fast flux = 2×10^{13} neutrons/cm^2·sec (above 1 Mev).

Also a test is being made of some of the fused-quartz insulation used in the in-pile and out-of-pile tests. Preliminary information indicates that errors of the order of 100°F (below true temperature) in thermocouple readings may occur after 250 hr for Chromel-Alumel thermocouples. Iron-constantan couples are affected to a lesser extent in the opposite direction. In a test without the fused-quartz insulation, no disparity between thermocouples located in air and in helium was found after 500 hr at temperatures of 1500°F and above, and a single tube-burst specimen (at a stress of 4000 psi) in the helium side of the apparatus ruptured at a period corresponding with the values obtained in the Metallurgy Division. This suggests that the fused-quartz insulation supplies a reducing atmosphere that affects the calibration of the Chromel-Alumel couples so that the specimens may be at a higher temperature than the thermocouples indicate.

Thus it appears that part of the reason for the reduced times to rupture observed in the in-pile and out-of-pile tests is the loss of calibration of the thermocouples. Unless radiation changed the rate of deterioration of the thermocouples, it is still not clear why such large ductility changes were observed.

LITR Experiments

In the most recent LITR test, an Inconel tube stressed at 2000 psi and exposed to the fused salt fuel $NaF-ZrF_4-UF_4$ (62.5-12.5-25 mole %) has been in hole HB-3 for over 620 hr without rupture, in contrast to tubes tested previously which failed after 100 hr or less. Postirradiation examination of the tubes previously tested revealed a leak in one of the Swagelok fittings on the pressure side of one of the specimens and a defective high-pressure seal on the thermocouples of another specimen. In the apparatus being used at present there are no Swagelok fittings, and all seals were checked at double the operating pressure. A pure cobalt foil was inserted inside the specimen tube to measure directly the flux depression.

A tube-burst specimen (0.010 in. wall thickness) pressurized to a stress of 3000 psi with helium was subjected to thermal cycling between 1100 and 1500°F in air, out-of-pile. A joint brazed with Coast Metals alloy No. 52, near the specimen but at a temperature approximately 100°F lower than

that of the test section, was temperature-cycled over 4000 times in 1000 hr without failure, but the test section finally ruptured. The results of this test indicate that cyclic stresses are not the cause of the cracks that have been found in brazed joints in the in-pile rigs.

Three tube-burst specimens tested previously in hole HB-3 of the LITR at a constant stress of 2000 psi at 1500°F, with both sides in helium, were examined. One ruptured after 1050 hr, and showed an increase of 1.1% in inside diameter. A second ruptured at 1650 hr, and the inside diameter increased about 0.9%. The third specimen had not failed when the test was terminated at 1675 hr, but it showed an increase of about 0.9% in inside diameter. A fourth specimen, stressed at 1000 psi at 1500°F for 1675 hr in the reactor, also did not rupture, but it showed an increase of 0.56% in inside diameter. The test sections are now being examined metallographically. The low ductility, as in the case of the MTR tests, cannot be accounted for at this time.

ORR Experiments

The design of a facility for mounting experiments on the pool face of the Oak Ridge Research Reactor was completed. The facility is to be installed before the reactor goes critical. Experiment cans and locking devices for the cans were designed. Apparatus for conducting flux and gamma-heating surveys was also designed.

LITR VERTICAL FUSED-SALT LOOP

W. E. Browning   R. P. Shields
J. E. Lee

Disassembly of the vertical in-pile loop which circulated fused-salt fuel for 235 hr in the LITR was completed, and various parts are being examined and analyzed. One-inch lengths of fuel tube were cut from each thermocouple location, and other fuel and metal samples were taken from the pump region. Particular attention was given to the pump bearing. As stated in the previous report,[6] the lower bearing was locked and the bearing just below the motor was difficult to turn. These bearings were separated from the housing and shaft, and the grease seals were removed.

[6]W. E. Browning *et al.*, *ANP Quar. Prog. Rep. Sept. 30, 1957*, ORNL-2387, p 270.

The grease has decomposed and become waxlike, and it had been pushed to the side away from the ball bearings. Samples of this damaged lubricant were taken to be analyzed for fission-gas decay products and for analysis by the California Research Corporation. An attempt is being made to degrease and decontaminate the bearings so they can be cut apart and examined.

An induction furnace (Fig. 4.1.21) has been set up for melting salt samples from the Inconel fuel-tube specimens. The melt-out chamber is glass,

and it can be evacuated and filled with helium to prevent contamination of the salt by the atmosphere. When the Inconel tube walls are heated quickly, the salt slides out as a solid pellet. Tests with un-irradiated samples have shown this system to be satisfactory. Salt samples from irradiated tubing will be analyzed chemically, and the tube samples will be examined metallographically in order to evaluate the corrosion of the loop that occurred during the test.

MTR STATIC CORROSION TESTS

W. E. Browning   H. L. Hemphill

Three capsules containing fused-salt fuels which had been irradiated in the MTR were dismantled and examined metallographically. The results of the examinations are presented in Table 4.1.2. The Inconel capsule showed the expected corrosion attack. The two Hastelloy B capsules were found to have thin films on the surfaces that were exposed to the fuel. Tests are under way to identify the film and to study the mechanism of its deposition. Corrosion of these capsules was negligible.

Two more Hastelloy B capsules containing NaF-KF-LiF-UF$_4$ fuel were withdrawn from the MTR. One of these had been irradiated for 2496 hr at 1250°F and at an initial power density of 6000 w/cm^3. There was no indication of failure when the capsule was withdrawn.

IRRADIATION OF MODERATOR MATERIALS FOR USE AT HIGH TEMPERATURES

W. E. Browning   R. P. Shields

Apparatus for testing beryllium, beryllium oxide, and yttrium hydride at high gamma-heating densities

16 in.

INSTRUMENT

VACUUM

He

ALL PYREX MELT-OUT ASSEMBLY INSTALLED BEHIND SHIELDING

TAPERED QUARTZ SLEEVE

TUBING SAMPLE

INDUCTION HEATER

PLATINUM CRUCIBLE
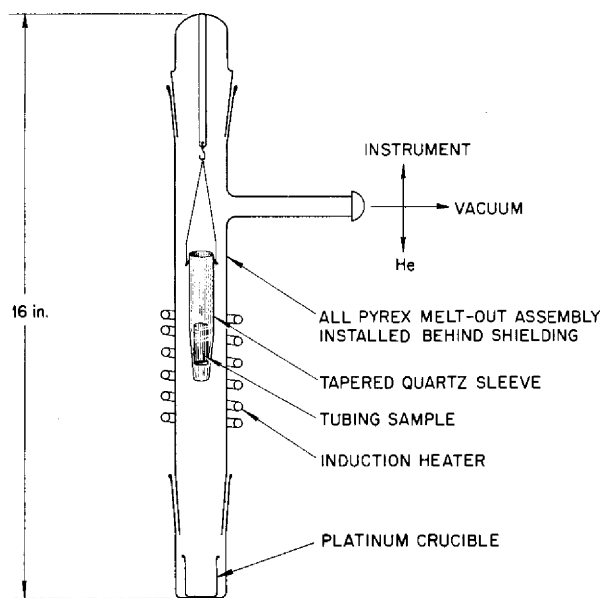
Fig. 4.1.21. Induction Furnace for Removing Fluoride Fuel from Inconel Tubing.

Table 4.1.2. Results of MTR Static Corrosion Tests at 1500°F and at a Power Density of 6000 w/cm^3

Capsule Number	Container Material	Fuel	Duration of Exposure (hr)	Metallographic Results
331	Inconel	NaF-ZrF$_4$-UF$_4$ (53.5-40-6.5 mole %)	304	1 to 2 mils of penetration
364	Hastelloy B	LiF-NaF-KF-UF$_4$ (44.3-11.8-38.2-5.77 mole %)	138	Film deposited; penetration negligible
335	Hastelloy B	LiF-NaF-KF-UF$_4$ (44.3-11.8-38.2-5.77 mole %)	119	Film deposited; penetration negligible

in the ETR is being prepared. Those moderator materials are to be irradiated with neutrons and gamma rays in the ETR where the heating rate will be 25 w/g. A temperature of about 1450°F will be monitored by a thermocouple on each side of the capsule and by one inside a well in one piece of each type of specimen.

All specimens for the test, except the BeO, have been fabricated and then encapsulated in Inconel. Capsules for the BeO were completed and the BeO specimens are complete except for final checks. Extra beryllium specimens and capsules were made and encapsulated. A thin molybdenum foil was wrapped around each pellet, and a disk was cut to cover the end of each pellet. One set of the completed beryllium specimens will be heat cycled by the Metallurgy Division, which fabricated all the specimens. The heat-cycled specimens will be examined to determine the compatibility of the metals at high temperature.

A reactor-core filler block has been procured from the factory which manufactured the parts for the ETR, and it has been modified for this experiment. Details of the gas system for conducting heat from the specimens to the capsule walls are being worked out with ETR personnel.

IRRADIATION EFFECTS IN PHOTOCONDUCTIVE DETECTORS

J. C. Pigg   R. A. Zingaro

An initial investigation has been completed of the effects of neutron and gamma radiation on chemically deposited thin films of lead sulfide, which are highly sensitive to infrared radiation and have a wide variety of commercial and military applications. The polycrystalline structure of the films and the relatively high and localized concontration of impurities make the behavior of these films very complex; therefore, the results of this study are of practical interest. Irradiation has been found to cause additional crystalline imperfections, and the effects are reflected in changes in the electrical and photoconducting properties of this semiconductor. The results of the initial experiments are described here.

The samples used were chemically deposited PbS cells, supplied by the Eastman Kodak Company, and were of the type previously described by Woods.[7] One set of contacts, which were prepared by evaporation techniques and which were

[7]J. F. Woods, *Phys. Rev.* **106**, 235 (1957).

used in making resistivity measurements, were located at the center of the sensitive area. The configuration is shown in Fig. 4.1.22. The thicknesses of samples 38 and 40 were 0.86 and 0.85 μ, respectively, and samples 5, 22, and 26 were assumed to be 0.5 μ thick.
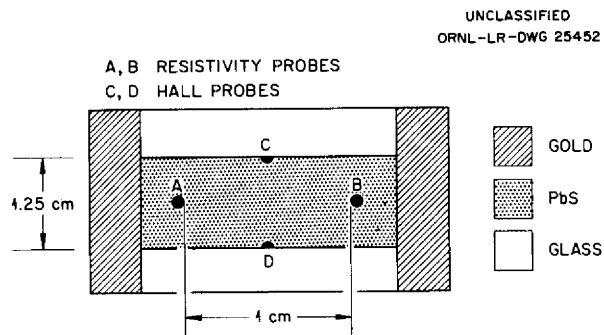

UNCLASSIFIED
ORNL-LR-DWG 25452

A,B RESISTIVITY PROBES
C,D HALL PROBES

GOLD
PbS
GLASS

Fig. 4.1.22. Configuration of Lead Sulfide Sample Cells.

Measurements were made at a temperature of 24.5 ± 0.5°C. All voltages were amplified by an Applied Physics Corp. vibrating-reed electrometer, but the actual readings were taken on a Rubicon Co. potentiometer. Resistances were computed from the relation between the direct current and the voltage. All resistances measured were of the order of 10^5 ohms. During all electrical measurements the cell was sealed from light. Thus all reported values represent dark-current measurements.

The magnetic field for Hall-voltage measurements was furnished by a 9000-gauss permanent magnet; therefore it was not possible to reverse the magnetic field. Instead, the sample was rotated through 180 deg in the field, and readings were taken with the current flowing in both the forward and reverse directions during each orientation. The Hall voltages were calculated from the difference of the averages of a number of readings made with the cell in each orientation. The Hall measurements could not be made with a precision of better than ±5%. The maximum error in all other electrical measurements was about 0.5%. The other significant sources of error in these experiments were the fluctuations in room temperature (±0.5°C) and in humidity.

Changes in the photosensitivity of the cells were followed by measuring the signal output when a

cell was subjected to radiation in the 5000- to 25,000-Å region. A Cary model 14R spectrophotometer supplied the monochromator, light chopping, and amplification systems. The cell was mounted at the monochromator exit, and the signal from the cell was fed directly into the preamplifier input. This circuitry proved to be very satisfactory, since the preamplifier system is designed for use with an identical type of PbS detector, which actually forms part of the instrument. Absolute wavelength-response curves could not be obtained with such an arrangement, since the slit-width drive could not operate to compensate for the variable energy output of the light source.

Neutron irradiations were carried out in the ORNL Graphite Reactor. The samples were placed in a boron carbide container so that slow-neutron bombardment would be essentially eliminated. The fast-neutron flux was taken to be 8×10^{11} neutrons/cm^2·sec. Gamma irradiations were carried out in the ORNL "gamma garden," which utilizes a cobalt source. The flux density was taken to be 2.65×10^6 r/hr, which is equivalent to about 10^{12} photons/cm^2·sec.

A set of values observed for the four cells on which electrical measurements were made is given in Table 4.1.3. The values of the Hall coefficient, R_H, are in good agreement with those reported by Woods,[7] Lawrence,[8] and Lummis and Petritz.[9] By assuming a film thickness of 0.5 μ, values of R_H from +105 to +245 were calculated for the cells studied by Lummis and Petritz on the basis of their data. The resistivity values are, in general,

lower than those reported by Woods, who gave 25.9 to 38.3 ohm-cm as the resistivity of his sample. However, resistivity values calculated from the data of Lummis and Petritz varied from 15 to 36 ohm-cm. The agreement of these values within a rather wide range indicates the variance which is to be expected for thin films of this type.

A plot of the resistivities of PbS cells 26 and 40 as functions of neutron irradiation is presented in Fig. 4.1.23, A. An initial drop in resistivity may be seen for both cells that is followed by a gradual rise as the neutron dose is increased. The change in resistivity of cell 40 with time, following neutron irradiation is shown in Fig. 4.1.23, B. There was a rapid decrease in resistivity during the first 24 hr, and it is to be noted that the resistivity continued to fall with time until, after the tenth day of annealing, it had reached an apparent equilibrium value which was below the resistivity of the cell prior to irradiation. The five measurements made during the tenth to twenty-first days gave an average value for the resistivity of cell 40 of 13.7 ± 0.2 ohm-cm, which is 17% below the initial resistivity of this film, 16.4 ohm-cm. The data for cell 40 are plotted on a larger scale in Fig. 4.1.24 for clarity.

The change in resistivity of the PbS cell after neutron irradiation followed simple, first-order kinetic relations, as may be seen in Fig. 4.1.25. The half-life of the annealing process, determined graphically, was 11 hr, which gave a value of 0.063 hr^{-1} for the specific rate constant. Thus the value of the resistivity following neutron irradiation may be expressed as

$$(1) \qquad \rho = \rho_0 \, e^{-0.063 \, t} \, ,$$

where ρ is the value of the resistivity t hr after the value ρ_0 is measured.

[8]*Ibid.*, p 238. Woods' values of R_H run from +121 to +133, and Lawrence reports values of +130 and +160.

[9]F. L. Lummis and R. L. Petritz, *Phys. Rev.* 105, 502 (1957).

Table 4.1.3. Properties of Chemically Deposited Lead Sulfide Cells at Room Temperature in the Dark

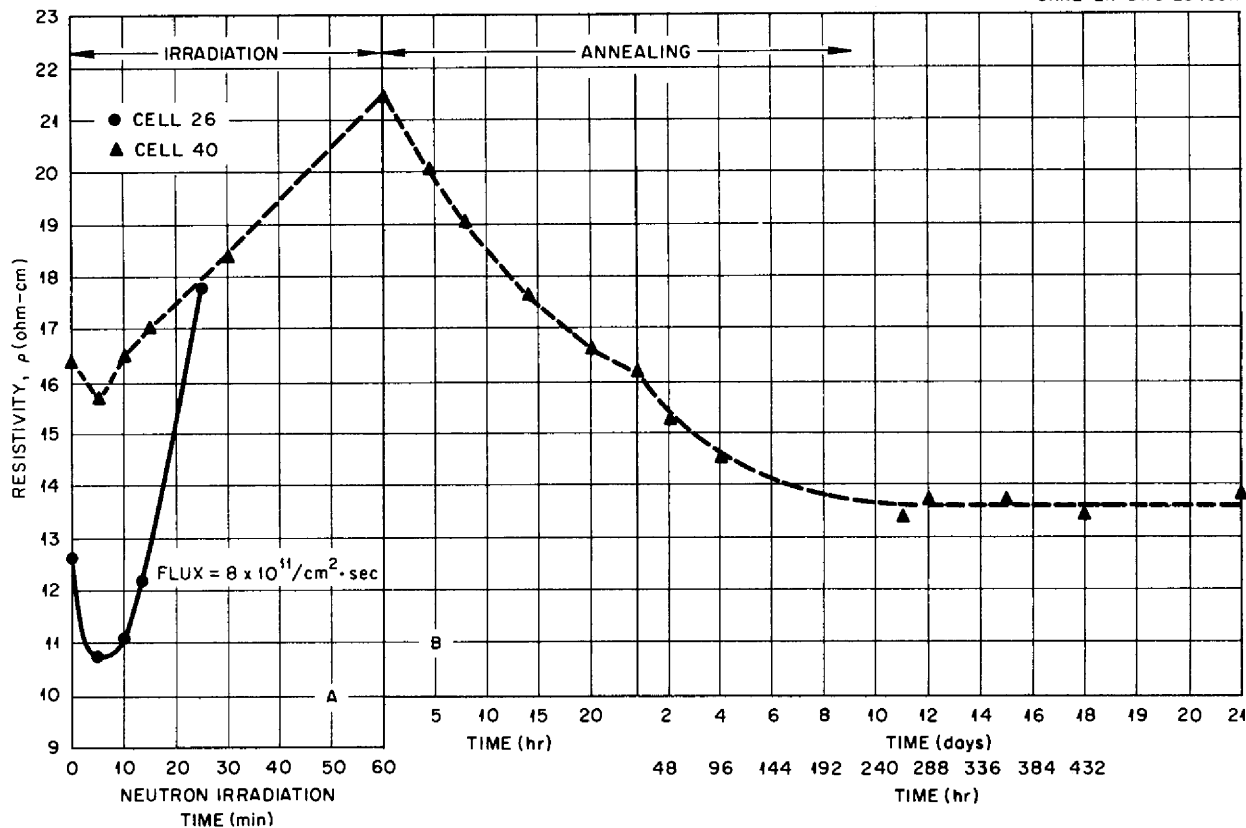| Cell	Hall Coefficient, R_H (cm^3/coulomb)	Resistivity, ρ (ohm-cm)	Carrier Concentration, n (cm^{-3})	Carrier Mobility, μ_H (cm^2/v·sec)
			$\times 10^{16}$	
22	+261	29.4	2.8	8.9
26	+132	12.6	5.6	10.5
38	+163	14.7	4.5	11.1
40	+190	16.4	3.9	11.6

Fig. 4.1.23. Effect on Resistivity of PbS Cells of Neutron Irradiation Followed by Annealing.

The percentage changes in the Hall coefficient, carrier concentration, and carrier mobility of cell 40 are given in Table 4.1.4. Since the Hall coefficient changed a maximum of less than 5% during irradiation, which is within the limit of experimental error, it is concluded that this property, as well as the carrier concentration, remained unchanged by irradiation. The carrier mobility, which is directly dependent on the Hall coefficient and inversely proportional to the resistivity, showed an increase as the resistivity decreased initially, and then decreased when the resistivity increased. The changes in these properties one to three weeks after neutron irradiation, as shown in Table 4.1.5, were significant, and all the values showed definite trends toward limiting values. The measured values for these properties 18 and

Table 4.1.4. Changes in Electrical Properties of Chemically Deposited PbS Cell 40 During Neutron Irradiation

Total Fast-Neutron Dose (neutrons/cm^2)	Percentage Changes* in		
	Hall Coefficient	Carrier Concentration	Carrier Mobility
2.4×10^{14}	+1	3	+5
4.8×10^{14}	+5	5	+4
7.2×10^{14}	−1	0	−4
1.4×10^{15}	−1	0	−11

*Based on values measured prior to irradiation.
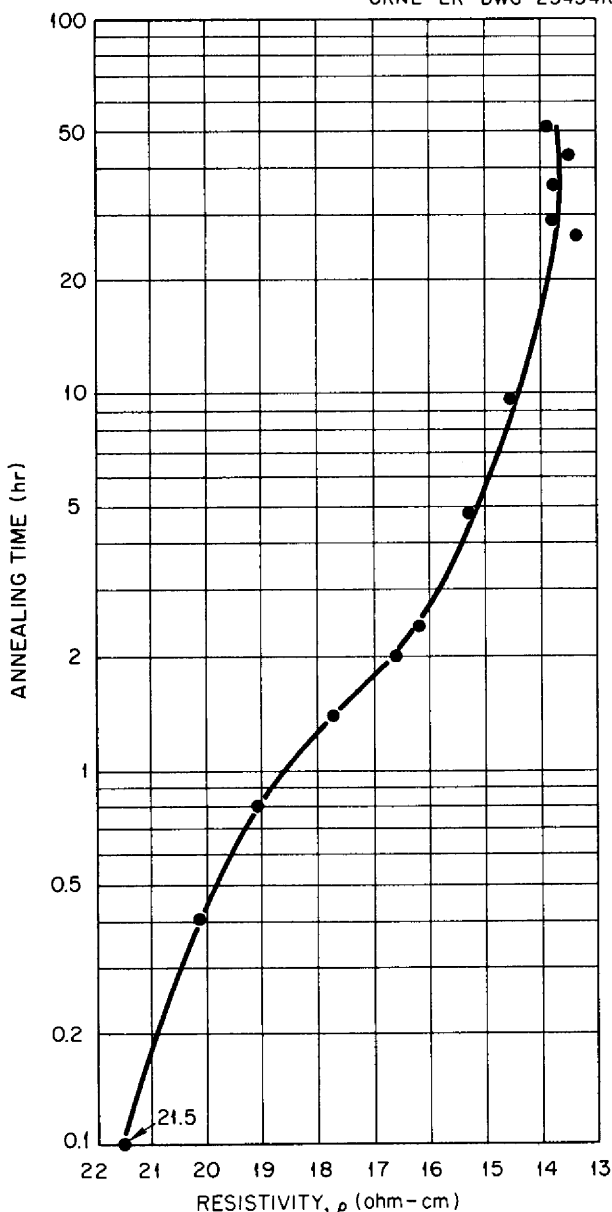
Fig. 4.1.24. Change in Resistivity of Chemically Deposited PbS Cell 40 Following Neutron Irradiation.

Fig. 4.1.25. Change in Resistivity with Time of Neutron-Irradiated Cell 40 and Gamma Irradiated Cell 38.

21 days after irradiation were, for the Hall coefficient, 181 and 195 cm^3/coulomb, respectively; for the carrier concentration, 4.1 and 3.7 cm^{-3}; and for the carrier mobility, 13.4 and 14.0 cm^2/v·sec. The Hall coefficient and the carrier concentration reached about the same values after 21 days that they had before irradiation (see Table 4.1.3), but the carrier mobility showed a significant increase. Data for the period im-

mediately following irradiation are not given because the resistivity was recorded automatically during that period and the Hall voltage could not be measured automatically by the method being used. It is apparent, however, that at some time during the first few days of the annealing period there was a decrease in the Hall voltage and a concurrent increase in carrier mobility followed by a gradual return of these properties to their initial values. The annealing mechanism led to a permanent net decrease in resistivity, while only a

Table 4.1.5. Changes in Electrical Properties of
Chemically Deposited PbS Cell 40 After Neutron
Irradiation to a Total Dose of
2.9×10^{15} Neutrons/cm^2

Days After Neutron Irradiation	Percentage Changes in		
	Hall Coefficient	Carrier Concentration	Carrier Mobility
7	−21	+20	+7.8
11	−18	+18	−0.9
12	−13	−13	+34
15	+9	−8	+29
18	−5	+5	+15
21	+2	−5	+20

temporary change took place in the carrier con-
centration and in the Hall coefficient.

The effect of irradiation on the photoconduc-
tivity of the PbS film (cell 26) was also examined,
and the results are shown in Fig. 4.1.26. Neutron
irradiation brought about a significant decrease in
the photoconducting properties of the material,
and the decrease was proportional to the total
neutron dose. The curves of Fig. 4.1.26 should
not necessarily be interpreted as indicating that
the change in sensitivity was also a function of
the wavelength of the exciting radiation. Thus
curve *a* shows that the cell no longer responded to
radiation of 24,000 Å after 30 min of irradiation,
but that it still responded to shorter wavelengths
(curves *b, c,* and *d*). This was primarily the
result of the light source emitting much more
intense radiation at the shorter wavelengths. An
examination of the data (Table 4.1.6) indicates,
however, that the neutron irradiation effects were
not uniform throughout the wavelength region ex-
amined and that they became more marked at longer
wavelengths. A more quantitative study of a sys-
tem which would provide uniform light intensity
at all wavelengths is necessary before the effect
at longer wavelengths can be considered to be
real. It is of interest to note that restoration of
the initial level of photosensitivity did not occur
even after three weeks of annealing. Indeed, the
signal output after this time was only about one-
half to one-third the original value, and it appeared
to be stabilized at the lower level.
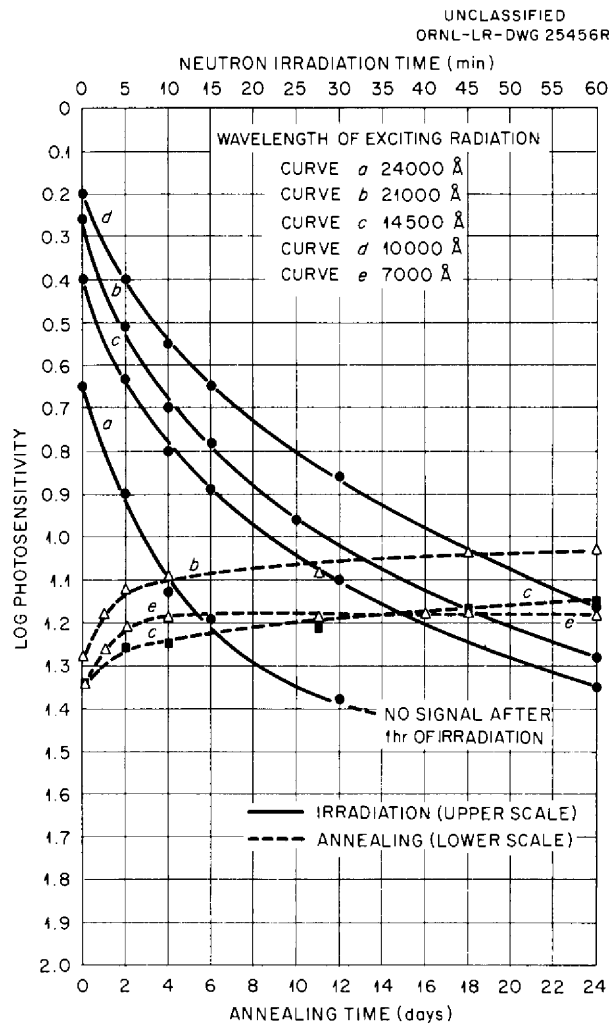
Fig. 4.1.26. Effect of Neutron Irradiation on Photo-
conductivity of Chemically Deposited PbS Films (Cell
26).

The changes in resistivity, Hall coefficient,
carrier concentration, and carrier mobility produced
by gamma irradiation are plotted as the various
curves of Fig. 4.1.27. The effects during and im-
mediately following irradiation were fairly clean
cut, but it is apparent that the long-term annealing
effects following long periods of irradiation were
very complex.

An increase in resistivity during gamma irradia-
tion (plot A-I) was clearly demonstrated. Cell 38
showed a threefold increase in resistivity after
receiving a dose of 5×10^6 r and a fourfold in-
crease after a dose of 10×10^6 r. After a dose of

Table 4.1.6. Absolute Decrease in Signal Output of PbS Detector (Cell 26) at Various Wavelengths as a Function of Neutron Irradiation

Wavelength of Exciting Radiation ($\overset{\circ}{A}$)	$(S_0 - S_n)^*$				
	At $n = 5$	At $n = 10$	At $n = 15$	At $n = 30$	At $n = 60$
24,000	0.25	0.48	0.54	0.73	
20,000	0.25	0.44	0.52	0.70	1.02
16,000	0.26	0.43	0.52	0.72	
10,000	0.20	0.35	0.45	0.66	0.95
7,000	0.19	0.35	0.46	0.67	0.94

*S_0 is the absolute signal output prior to irradiation, and S_n is the absolute signal output after n min of neutron irradiation.

21×10^6 r, cell 22 showed an increase in resistivity from 29.4 to 352 ohm-cm. During the time immediately following irradiation (plot A-II), the resistivity showed a gradual decrease. The lower curve, which demonstrates this change following a 2-hr irradiation, suggests that the resistivity reached a limiting value after about 24 hr; the actual values of the last four measurements were 41.2, 40.4, 37.8, and 39.7 ohm-cm. The tendency of the cell to reach an apparent equilibrium state if the total irradiation did not exceed a certain maximum was also indicated by the changes in the photoconducting properties, as will be discussed later. Nineteen days after a dose of 10×10^6 r, however, the resistivity was (plot A-III) still undergoing large fluctuations.

If the change in resistivity of sample 28 following a total gamma irradiation of 5×10^6 r is plotted as a function of time as in Fig. 4.1.25, application of the first-order kinetic law gives the following relationship for the change in resistivity following a total gamma irradiation which does not exceed the "tolerance" for the cell:

$$(2) \qquad \rho = \rho_0\, e^{-0.041\, t} .$$

The half-life of the annealing process was 17 hr.

Further examination of Fig. 4.1.27 shows that there were over-all increases in the Hall coefficient (plot B-I) and concurrent drops in carrier concentration and mobility (plot C-I) during gamma irradiation of cells 22 and 38, but that the changes were quite irregular. For instance, the data for cell 22 show a small decrease from 261 to 247 in R_H

during the initial 2 hr of irradiation, a threefold increase during the second 2-hr period of irradiation, and an eightfold increase when the accumulated dose reached 21×10^6 r. Similarly, the data for cell 38 show a fourfold increase during the initial 2-hr period of irradiation, but a slight decrease during the second 2-hr period. These irregular patterns are, of course, reflected in the changes in the carrier concentration and mobility, which depend upon R_H.

The long-range annealing effects (plots A-III, B-III, and C-III) were so irregular that they will be mentioned only briefly. It is clear that no equilibrium condition had been reached 19 days after irradiation. There was a trend toward lower values for the resistivity and Hall coefficient, but it is not possible to predict, on the basis of the data obtained thus far, at what time an equilibrium state would be reached and what these values would be at equilibrium. The carrier concentration and mobility fluctuated so widely that no definite trend is indicated by the data.

The previously mentioned ability of these cells to recover from the effects produced by gamma irradiation is demonstrated in Fig. 4.1.28. As may be noted, the cells lost their sensitivity rapidly as they accumulated progressively greater doses of radiation. Examination of curves a, b, and c for cell 22 shows that this cell was still sensitive after receiving an accumulated irradiation of 10.4×10^6 r, and after receiving 20.8×10^6 r it still gave a reasonably good signal at 1.5 and 1.0 μ, although no signal was obtained at 1.8 μ.
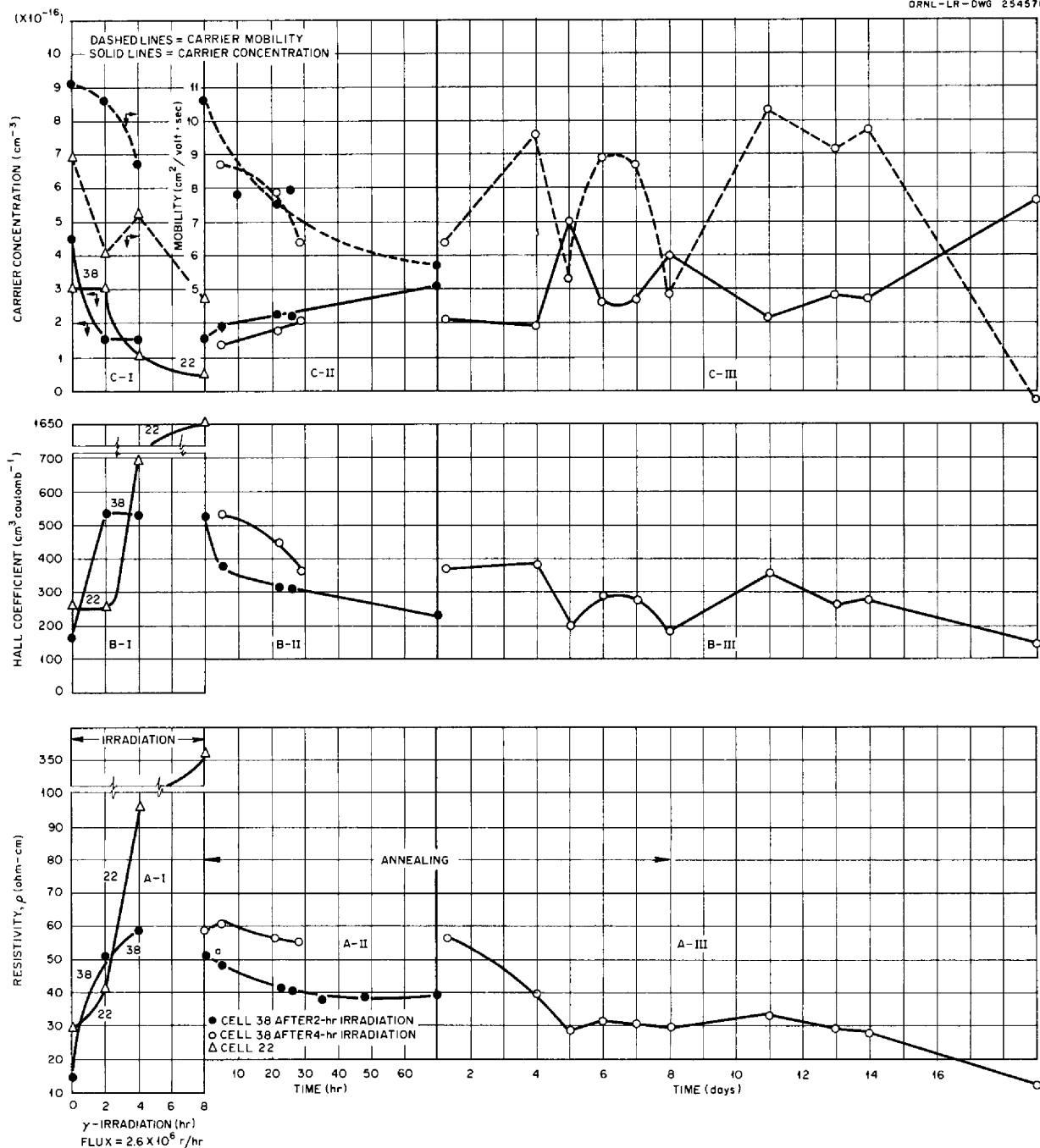
215

Fig. 4.1.27. Effect of Gamma Irradiation on Electrical Properties of Chemically Deposited PbS Films.
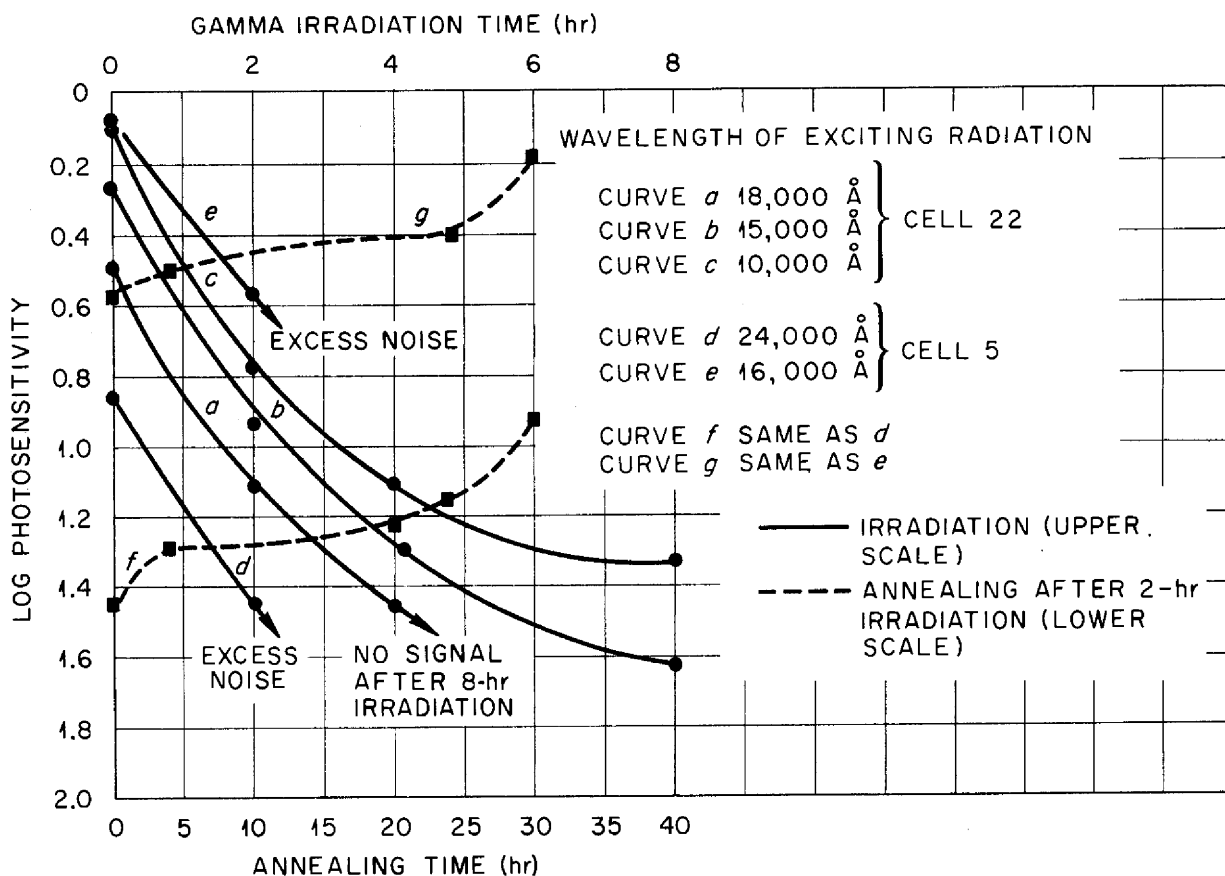
Fig. 4.1.28. Effect of Gamma Irradiation on the Photoconductivity of Chemically Deposited PbS Films.

Further examination revealed that after irradiation to an accumulated dose of 2.6×10^6 r, cell 5 (curves d and e) showed a considerable drop in photoresponse, but, after annealing at room temperature for 30 hr (curves f and g), the sensitivity returned almost to the initial value. After being subjected to another gamma irradiation of equal intensity, however, cell 5 had completely lost its light sensitivity. The photosensitivity of cell 5 was measured daily for three weeks following irradiation, and it had not recovered any of its valuable photoconducting properties. The loss in photosensitivity appears to have been the result of a very large increase in the noise level of this cell after irradiation. In order to check this, the cell was scanned on the Cary spectrometer in the usual manner, except that the light source was turned off. Instead of the recorder showing no response under these conditions, as is normally

the case prior to irradiation, a very erratic and appreciable noise signal was recorded. This observation is, at best, qualitative, but clearly indicative.

A consideration of the effects of gamma irradiation on these thin films of chemically deposited PbS reveals a fundamental property. In brief, these cells appear to have a fixed tolerance for gamma irradiation. If the total dose is maintained below this tolerance, the physical changes effected in the matrix can effectively be annealed out, and the cell will revert to its original state. If the total irradiation exceeds this tolerance, either the cell will be permanently damaged or the annealing rate will be extremely slow. Which of these latter possibilities is actually operative has not yet been definitely established by these studies.

The possibility that fracture of the PbS film of cell 5 may have occurred was considered. The

217

film was examined under a magnification of 1000, and no visible change in the smooth continuity of the layer was found. Electron diffraction studies should be made, however, before this possibility is eliminated.

The problem of establishing a gamma tolerance for these cells is complicated by the rather individual nature of the cells. Even in this preliminary investigation a difference of 400% was observed in the sensitivity of two of these samples prior to gamma irradiation.

The PbS cells used in this study were supplied by the Eastman Kodak Company and the Bureau of Ships, United States Navy.

IRRADIATION EFFECTS IN SEMICONDUCTOR BARRIERS

J. C. Pigg

C. C. Robinson   O. E. Schow

The program of study of irradiation effects in semiconductor barriers is rather specialized and was initiated at a time when a large, jumbled body of information had already been accumulated. Since reports of current progress are necessarily isolated bits of information that appear out of context to the over-all picture of the development, each report, in order to be clear, must include the background information and thinking for each bit of data. Such a survey introduction to each report tends, however, to obscure the current achievements. It has been decided, therefore, to present at this time a survey of the pertinent work and to summarize the concepts on which the current work is based. Subsequent reports will present program developments.

There are many groups engaged in studying radiation effects in semiconductor components, and, since the motivations and objectives of the investigations vary, the data accumulated and the conclusions drawn seem to be contradictory. Therefore statements describing motivation, objectives, and experimental details can frequently remove contradictions in the data and in the conclusions. The purpose of the ORNL program is to contribute to an understanding of the effects of irradiation on semiconductor barriers in terms of

---

[10]W. Shockley, *Electrons and Holes in Semiconductors, with Applications to Transistor Electronics,* Van Nostrand, New York, 1950.

fundamental processes. Such knowledge is applicable both to the development of semiconductor devices with reduced sensitivity to radiation fields and to a better understanding of the barrier mechanism.

Semiconductor Materials

A semiconductor is a material whose electrical conductivity has an energy of activation.[10] When the electrons are all in their lowest energy state, the valence band is full and the conduction band is empty (Fig. 4.1.29). In such a condition the electrons cannot be accelerated by an electric field, and hence no conduction can occur. If ϵ_g is so large that electrons cannot be excited across the forbidden band at normal temperatures, the material is an insulator. If ϵ_g is zero, the material is a conductor; if ϵ_g is such that electrons can be thermally excited across the forbidden band, the material is a semiconductor. Such conduction is a property of the material itself and as such is called intrinsic semiconduction.
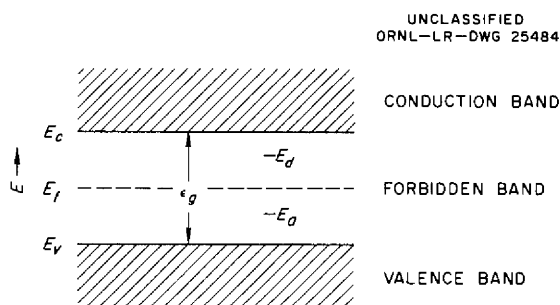

Fig. 4.1.29.   Schematic Band Picture of a Semiconductor.

When impurities are present in the crystal, such impurities may contribute energy levels which lie in the forbidden band. If such impurity atoms have more valence electrons than are necessary to satisfy the bonding conditions of the crystal, the electron may be excited from its ground state E_d to the conduction band — such atoms are called donors. Similarly an impurity atom having less than the number of electrons required to satisfy the bonding conditions may accept electrons from the valence band and leave a hole — such impurity atoms are called acceptors. For germanium and silicon, impurities from atoms listed in column V of the periodic table act as donors, while impurities

from atoms listed in column III act as acceptors. Conduction by such carriers is called extrinsic semiconduction. It can be seen from Fig. 4.1.29 that the activation energy for extrinsic conduction is smaller than that for intrinsic conduction.

If an excess of donor atoms is present, the conduction will .occur by electrons (negative carriers) in the conduction band — such a material is said to be n-type. If an excess of acceptor impurities is present, the conduction will occur by holes (positive carriers) in the valence band — such material is said to be p-type.

The conductivity σ of a semiconductor is given by[10]

$$(1) \qquad \sigma = ne\mu_n + pe\mu_p ,$$

where

n = electron concentration,
p = hole concentration,
e = electronic charge,
μ_n = electron mobility,
μ_p = hole mobility.

If one type of carrier predominates, the expression for intrinsic conductivity, Eq. 1, is modified by dropping the term corresponding to the minority carrier.

The concentration and sign of the majority carrier can be obtained from Hall measurements. When a current is established in a sample which has been placed in a magnetic field, the motion of charged carriers will be perturbed by the Lorentz force acting on the moving charges. A.voltage will be established across the sample perpendicular to the magnetic field and the current. The sign of this voltage gives the sign of the majority carrier. The magnitude of this voltage is inversely proportional to the carrier concentration. The relation of the quantities, together with appropriate constants needed to convert the units, is

$$(2) \qquad n = 7.38 \times 10^{18} \frac{HI}{(\pm V)t} ,$$

where

H = magnetic field, in oersteds,
I = current, in amperes,
t = thickness of sample perpendicular to both H and I, in cm,
V = Hall voltage, positive for holes, negative for electrons, in volts,
n = concentration of n- or p-type carriers.

If n and σ are known, the mobility of an extrinsic semiconductor may be determined from the extrinsic expression for conductivity:

$$\sigma = ne\mu .$$

Since electrons obey Fermi-Dirac statistics they will be distributed throughout the available energy states according to the Fermi function:

$$f = \frac{1}{e^{(E-E_f)/kT} + 1} ,$$

where

T = absolute temperature,
k = the Boltzmann constant,
E = the energy under consideration,
E_f = the Fermi energy,

which can be shown to be the chemical potential of the carriers. When E_f lies at the middle of the forbidden band, the electrical properties are those which would be seen if E_d and E_a were absent. Thus the material exhibits intrinsic behavior when the Fermi level is at the middle of the forbidden band. When the Fermi level lies above the middle, the sample is n-type; when it lies below the middle of the band, the sample is p-type. If E_f lies close (within a few times kT) to either the valence band or the conduction band, the sample is said to be degenerate. If E_f lies several times kT from these bands, the sample is said to be nondegenerate. For nondegenerate samples, Bose-Einstein statistics can be used to calculate carrier concentrations.

It can readily be seen that both n- and p-type conduction occurs simultaneously in intrinsic material. In extrinsic material, conduction is normally due to one type of carrier. However, minority carriers can be produced in significant quantities by photoelectric effects or by injection at a barrier. Injection of minority carriers by forward-biased barriers accounts for the high forward currents in diodes and for emitter action in a transistor.

In the case of the transistor, the injected minority carriers drift across the base of the unit to the collector. The current amplification, α, of the transistor is determined by the ratio of the collector current to the emitter current. The injected carriers constitute a departure from equilibrium, and their concentration decays at a rate $1/\tau$, where τ denotes the lifetime of the minority carrier. In order for a minority carrier to decay,

219

there must be a transition between the valence band and the conduction band.[11,12] These transitions tend to occur via an intermediate step that involves energy levels or trapping centers which lie in the forbidden band: for example, E_d and E_a as in Fig. 4.1.29. Consequently the lifetime decreases as the densities of these energy levels increase.

When a semiconductor is placed in a radiation field, there are three major ways in which the radiation field can induce permanent changes in the material. Capture of thermal neutrons produces isotopes which decay to leave substitutional impurities in the crystal lattice. Elastic collisions from energetic neutrons produce disorder in the form of interstitials and vacancies, as well as small regions of disorder. Gamma photons produce Compton electrons, which in turn can produce interstitial-vacancy pairs. The results of all these interactions is to produce new levels in the forbidden band.

In germanium the center of density of the radiation-induced levels lies below the middle of the forbidden band. The Fermi level will thus shift toward this center of density, and conductivity behavior such as that illustrated in Fig. 4.1.30(a) will be observed.[13] The conductivity of n-type material will decrease as the Fermi level falls until the sample becomes p-type. After the sample becomes p-type, the Fermi level will move toward the equilibrium position and the conductivity will saturate. The latter half of the curve also illustrates the behavior of high-density p-type material. Low-density p-type material in which the Fermi level is below the saturation position will exhibit a drop in conductivity such as that illustrated in Fig. 4.1.30(a).

The initial rate at which carriers are removed from n-type germanium is 3.2 carriers per incident fast neutron,[14] 0.02 carrier per incident thermal

Fig. 4.1.30. Comparisons of Effect of Radiation on the Behavior of Bulk Germanium and Silicon with the Effect on the Behavior of Germanium and Silicon Diodes.

neutron,[15] 0.0015 carrier per incident 1-Mev photon.[16] For p-type material, the rate of carrier change by fast neutrons depends upon the initial concentration,[17] but it is less than that for n-type material.

Both n- and p-type silicon become intrinsic under fast-neutron bombardment.[18] The initial rate of carrier removal is about 5 carriers per incident neutron. The behavior of the conductivity of

[11] R. N. Hall, *Phys. Rev.* 87, 387 (1952).

[12] W. Shockley and W. T. Reed, Jr., *Phys. Rev.* 87, 835 (1952).

[13] J. C. Pigg and C. C. Robinson, *Elec. Mfg.* 59(4), 116 (1957).

[14] J. W. Cleland et al., *Phys. Rev.* 83, 312—19 (1951).

[15] J. W. Cleland, K. Lark-Horovitz, and J. C. Pigg, *Phys. Quar. Prog. Rep. March 15, 1950*, ORNL-694, p 56.

[16] J. W. Cleland, J. H. Crawford, Jr., and D. K. Holmes, *Phys. Rev.* 102, 722—24 (1956).

[17] J. W. Cleland, J. H. Crawford, Jr., and J. C. Pigg, *Phys. Rev.* 99, 1170—81 (1955).

[18] J. W. Cleland et al., *Phys. Solids Institute Quar. Prog. Rep. April 30, 1951*, ORNL-1095, p 35.

silicon under bombardment is illustrated by Fig. 4.1.30(*d*). The acceptor and donor levels both fall at about the middle of the forbidden band, and hence the Fermi level moves to this position.

Semiconductor Devices

Irradiation-induced changes in carrier concentration, lifetime, mobility, and trap density all contribute to the change in the operating behavior of a semiconductor device. Units which depend upon the existence of a *p-n* junction will, obviously, be destroyed when all the material becomes of the same type. The limiting conditions on the operation of such a device in a radiation field are thus those imposed by the radiation-induced changes in the bulk of the semiconductor. The interim behavior, prior to complete breakdown, can also be indicated by the change in properties of the bulk material.

The properties involved in the case of a diode may be illustrated by means of the equivalent circuit shown in Fig. 4.1.31. There is a leakage path over the surface of the unit, a base resistance that results from the bulk resistance of the semiconductor, and a barrier which can be assumed to obey the diode equation

$$I = I_0(e^{qV/kT} - 1) \, ,$$

where *V* is the applied voltage[19] and *q* is the electronic charge. Both R_b and R_L (Fig. 4.1.31) may be functions of voltage or current, but, for present purposes, they will be considered to be ohmic.

With the use of the equivalent circuit of Fig. 4.1.31 and the present knowledge of the behavior of the electrical properties of semiconductors subjected to a radiation field, as discussed above, the changes in the current-voltage characteristic of a germanium *p-n* junction that can be expected as a result of irradiation may be described. In the forward direction, the leakage resistance can be ignored for a practical diode. The unit can be considered as a barrier in series with the base resistance. Curve *a* of Fig. 4.1.32 illustrates the current-voltage relationship which could be expected to exist for a pure barrier. In a practical unit, however, the current is limited by the base resistance, and a characteristic such as

Fig. 4.1.31. Diode Equivalent Circuit.

curve *b* is obtained. Upon irradiation the semiconducting material is changed.[20] Carriers are removed from the *n*-type material, and the Fermi level in that region is lowered. In the *p*-type material, the Fermi level moves toward some equilibrium position which depends upon the temperature of the unit during exposure. In any case, the Fermi level does not move so far in the *p*-type material as in the *n*-type material. Hence the barrier will be lower and there will be a corresponding increase in I_0. The resistance of the *n*-type base, however, will increase because of the decrease in carrier concentration and the decrease in the lifetime of injected minority

[19]H. C. Torrey and C. A. Whitmer, *Crystal Rectifiers*, chap. 4, McGraw-Hill, New York, 1948.

[20]J. C. Pigg, *Solid State Semiann. Prog. Rep. Aug. 31, 1953*, ORNL-1606, p 79.
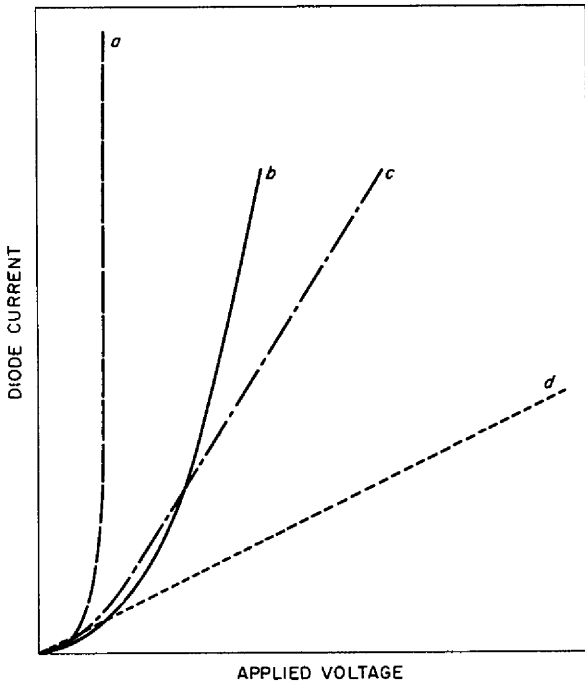
Fig. 4.1.32. Behavior of the Forward Current-Voltage Characteristic of a Semiconductor Device.

carriers. At low voltages, high current can be expected for a given voltage. At higher voltages, where the current is limited by the base resistance, a lower current can be expected. The new current-voltage characteristic will have the appearance of curve c of Fig. 4.1.32. Under prolonged exposure both sides of the barrier will tend toward the same ultimate carrier concentration, and hence the sample will tend toward ohmic behavior.

The base resistance can be neglected in the consideration of the reverse characteristic curve. The current through the unit is composed of two parts, the diode current, I_d, and the leakage current, I_L:

$$I_d = I_0(1 - e^{-qV/kt}) \ ,$$

and

$$I_L = \frac{V}{R_L} \ .$$

As discussed in the case of the forward characteristic, irradiation will result in an increase in an increase in I_0. The behavior of R_L depends

upon the type of semiconductor, the initial treatment of the surface, and the chemical environment of the surface. The n-type germanium base units irradiated to date have exhibited an increase in R_L with exposure. Hence a change in the reverse characteristic from that shown as curve a in Fig. 4.1.33 to that shown in curve b in Fig. 4.1.33 can be expected.
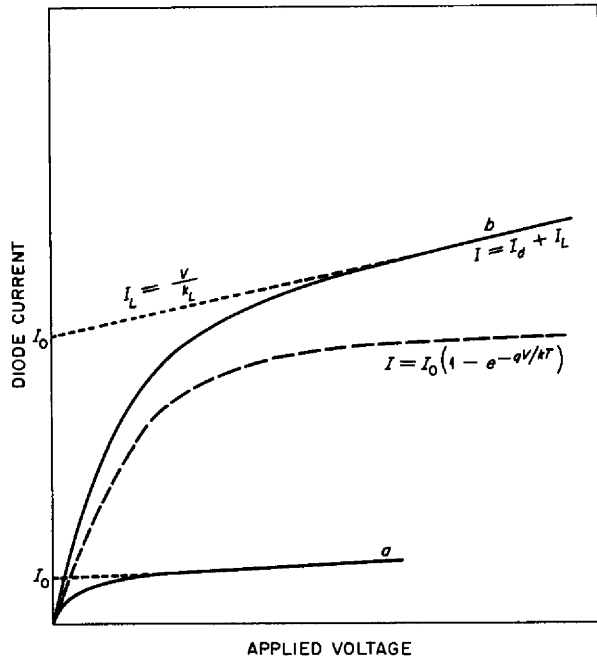
Fig. 4.1.33. Behavior of the Reverse Current-Voltage Characteristic of a Semiconductor Device.

The expression for I_0 is given by Shockley[10] as:

$$I_0 = I_{ps} + I_{ns} \ ,$$

where

$$I_{ps} = Aqp\left(\frac{D_p}{\tau_p}\right)^{1/2} \ ,$$

$$I_{ns} = Aqp\left(\frac{D_n}{\tau_n}\right)^{1/2} \ ,$$

A is the area of the junction, q is the electronic charge, p and n are the densities of the holes and electrons, respectively, D is the diffusion constant, and τ is the lifetime of the indicated carrier.

The expression for I_0 has been modified by Pell to include an additional term to account for charge generation in the barrier region.[21] This added term varies inversely with lifetime and barrier height. It has been shown that the minority-carrier lifetime is extremely sensitive to energetic irradiation;[22] hence, the increase in I_0 with irradiation is expected to be larger than that anticipated on the basis of the change in carrier concentration alone. This large expected change is in agreement with experimental observations.

The forward (F) and reverse (R) currents at 1-v bias, as a function of neutron exposure, were illustrated in Fig. 4.1.30, parts (b), (c), (e), and (f) for germanium and silicon rectifiers. The germanium point contact behaves as illustrated by part (b).[23] The current in the forward direction drops to a minimum as the bulk conductivity becomes intrinsic. As the bulk material becomes p-type and the conductivity increases, the forward current increases. The reverse current increases monotonically as the barrier is destroyed, and the sample becomes ohmic as the Fermi level comes to the same position in the forbidden band throughout the sample.

The silicon junction diode compares with bulk silicon in a similar manner.[24] The forward current drops as the bulk resistance increases. The reverse current increases as the barrier is destroyed. Eventually the sample becomes intrinsic for both directions of bias.

The characteristic behavior of a silicon point contact is somewhat different,[25] as is shown in Fig. 4.1.30(e). The forward current behaves in the same manner as for the other diodes shown in Fig. 4.1.30. The reverse characteristic, however, shows no strong effect as a result of a barrier being destroyed. Such behavior can be understood if it is postulated that the region around the contact behaves not as p-type but essentially as intrinsic material; that is, the barrier would be

i-n instead of p-n. Such an i-n barrier would rectify, but not so well as the p-n barrier. The barrier would be destroyed as the bulk silicon became intrinsic. During this time, the reverse current would also decrease toward the intrinsic level. Such a barrier would be unipolar, that is, it would conduct by one type of carrier; hence it would be more efficient at high frequencies, as has been observed. The point-contact silicon diode is the most satisfactory for high-frequency applications: for example, 3-cm mixer applications.

Since transistor action involves the interaction of two such barriers, with one barrier biased in the forward direction and the other in the reverse direction, all the properties involved in diode changes apply simultaneously. The collector cutoff current will increase as the I_0 of the collector barrier increases. The slope of the collector characteristic will change as the leakage resistance across the surface of the base changes. The emitter current-voltage characteristic will behave in a manner similar to the behavior of the forward diode characteristic.

Sah *et al.*,[26] in considering both the diffusion and charge-generation components of the emitter current, express the current amplification, α, as

$$\alpha = \frac{\operatorname{sech}(W_b/L_b)}{1 + \dfrac{J_{rg} + J_d'}{J_d \tanh(W_b/L_b)}}$$

where L_b is the minority-carrier diffusion length in the base, W_b is the base width, J_d is the injected current density flowing into the base, J_d' is the injected current density flowing into the emitter, and J_{rg} is the current component resulting from recombination and generation in the emitter barrier. The recombination-generation current density for forward bias is shown to be

$$J_{rg} = 2\,\frac{kT}{qE}\,\frac{qnl}{2\tau_0}\,e^{qV/2kT}\,,$$

where E is the electric field at the junction, V is the voltage across the emitter barrier, and τ_0 is the minority-carrier lifetime in the base. While the diffusion component is inversely proportional to the square root of the minority-carrier lifetime,

[21]E. M. Pell, *J. Appl. Phy.* **26**, 658 (1955).

[22]J. C. Pigg *et al.*, *ANP Quar. Prog. Rep. March 31, 1957*, ORNL-2274, p 265.

[23]J. H. Crawford, K. Lark-Horovitz, and J. C. Pigg, *Phys. Quar. Prog. Rep. March 15, 1950*, ORNL-694, p 64.

[24]J. C. Pigg and C. C. Robinson, *Solid State Semiann. Prog. Rep. Aug. 30, 1956*, ORNL-2188, p 19, Fig. 12.

[25]J. C. Pigg, *Solid State Quar. Prog. Rep. Feb. 10, 1953*, ORNL-1506, p 47.

[26]C. T. Sah, R. N. Noyce, and W. Shockley, *Proc. Inst. Radio Engrs.* **45**, 1228 (1957).

the charge-recombination-generation component is inversely proportional to the first power. Hence J_{rg} will increase faster than J_d as τ decreases.

At low damage levels, where $L_b \ll W_b$, the relative importance of the charge-recombination-generation current with respect to the diffusion current varies with the applied bias. When the emitter bias is approximately equal to or greater than the barrier height, the diffusion current predominates. At bias voltages that are small compared with the barrier height, the charge-generation current predominates.

The diffusion length is connected with the lifetime by the relation

$$L = (D\tau)^{1/2} .$$

Where L_b becomes comparable with W_b, the factor sech (W_b/L_b) takes control and decreases α rapidly.

In the range where $L_b \ll W_b$, tanh (W_b/L_b) is a rapidly varying function compared with sech (W_b/L_b). The change in α with irradiation would

then be expected to be governed by the following condition:

$$L_b \text{ (initial)} \gg W_b$$

and

$$J_d \gg J_{rg}, J_{d'} .$$

In the early stages of irradiation tanh (W_b/L_b) changes rapidly and there is an initial increase in α. However, as the irradiation progresses the concentration of radiation-induced levels increases, and J_{rg} increases faster than J_d. When $L_b \approx W_b$, tanh (W_b/L_b) saturates, but in this range sech (W_b/L_b) decreases rapidly. Hence changes in both J_{rg} and sech (W_b/L_b) tend to decrease the value of α. Such behavior has been experimentally observed[27] (Fig. 4.1.34). For units with W_b and L_b of the same order of magnitude, such as low-frequency power devices, this initial increase in α may not be observed[28] (Fig. 4.1.35).

---

[27]J. C. Pigg and J. W. Cleland, *Solid State Quar. Prog. Rep. Feb. 10, 1953*, ORNL-1506, p 48, Fig. 28.

[28]J. C. Pigg and C. C. Robinson, *Solid State Semiann. Prog. Rep. Feb. 29, 1956*, ORNL-2051, p 63, Fig. 54.
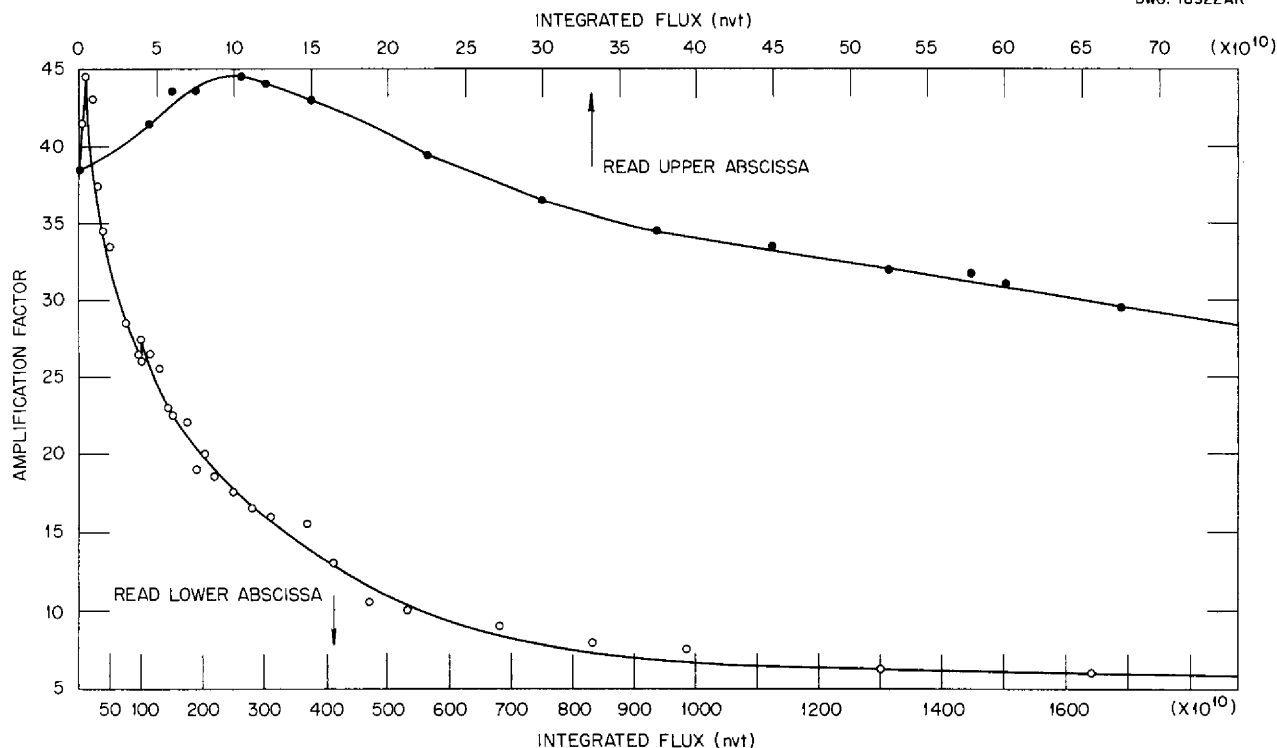
Fig. 4.1.34. Power Supply for Rectifier Experiment.
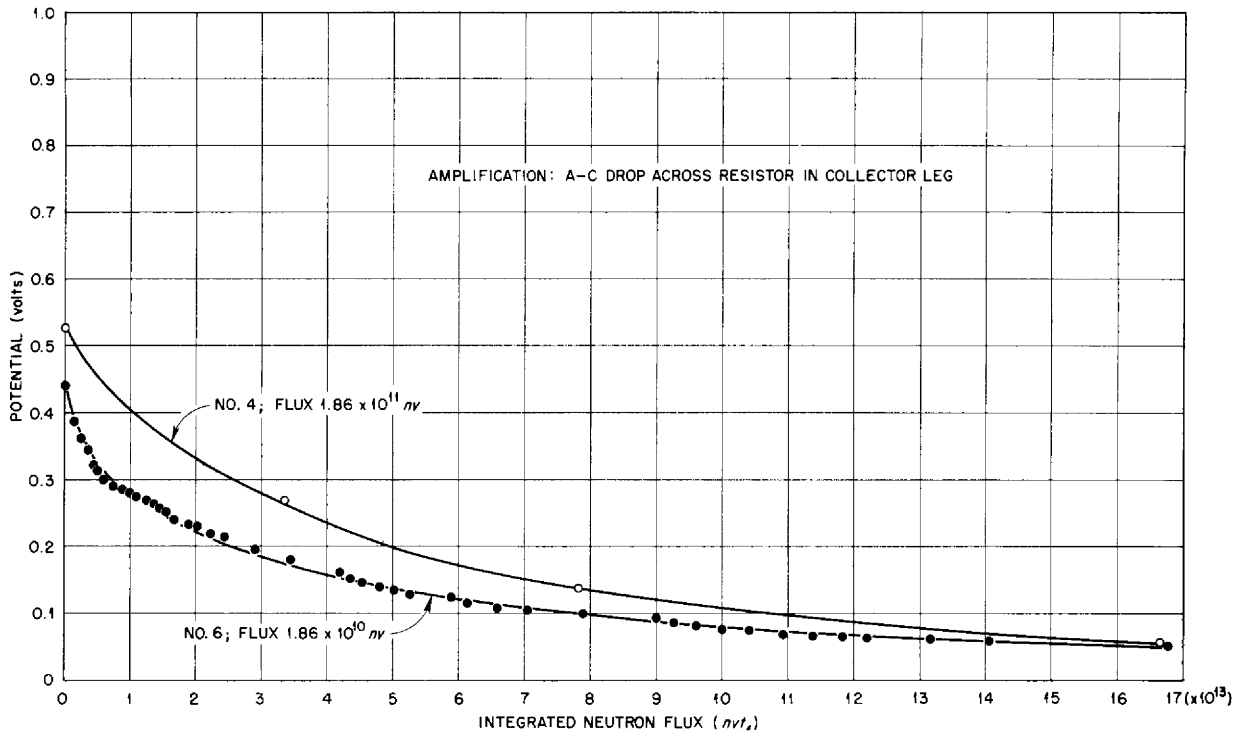
Fig. 4.1.35. Changes in Amplification of Two Minneapolis-Honeywell H-2 Power Transistors as a Function of Integrated Fost-Neutron Exposure.

In high-frequency units having a very thin base region, much greater stability should be expected. When $W_b/L_b \ll 1$,

$$\text{sech } (W_b/L_b) \approx 1 \text{ and tanh } (W_b/L_b) \approx - (W_b/L_b) \ .$$

In the denominator J_{rg} varies with $1/\tau$ and J_d tanh (W_b/L_b) varies as $1/\tau$. The collector current, as a function of irradiation for various emitter currents of a surface-barrier transistor, is shown[29] in Fig. 4.1.36. The unit is changed very little by irradiation to an integrated flux of 10^{14} neutrons/cm^2.

The value of I_{co}, the collector cutoff current, behaves like the value of the reverse characteristic. The I_0 increases rapidly because of the increasing saturation diffusion current and the increasing contribution of the charge-recombination-generation current. Because of the J_{rg} component, I_0 does not saturate. The leakage component can become the predominant term if surface changes occur.

[29]J. C. Pigg and C. C. Robinson, *Solid State Semiann. Prog. Rep. Aug. 30, 1956*, ORNL-2188, p 19, Fig. 11.
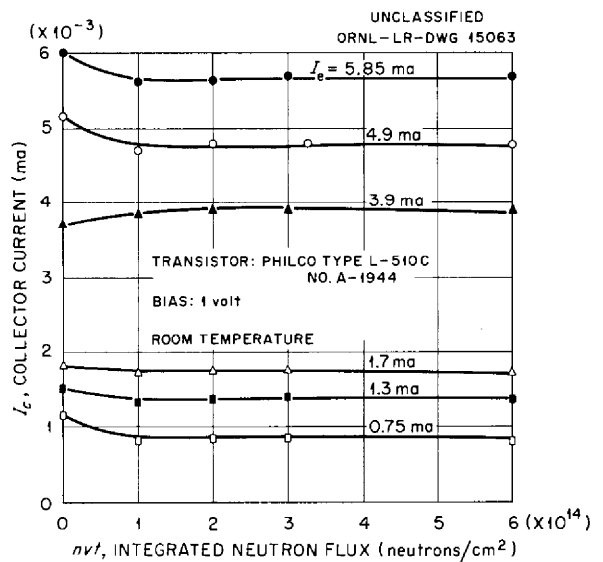
Fig. 4.1.36. Changes in Collector Currents of a Philco L5106 Surface-Barrier Transistor os a Function of Irradiation.

This will be determined by the type of material and surface treatment of the unit under consideration.

The transistor characteristics will change in the manner illustrated[30] in Fig. 4.1.37. Prior to irradiation there is a family of curves, I_c, with a cutoff I_{co}; subsequent to irradiation, the cutoff current increases to I'_{co}. If surface damage occurred, the slope would increase as illustrated. Because of the decrease in minority-carrier lifetime, α diminishes, as is indicated by the decreased separation of the curves. Although the I_0 of the barrier increases, a smaller part of the emitter curve reaches the collector, and the increased base resistance, in the case of silicon or n-type germanium, results in a lower value for I'_c. The curves will continue to collapse until the sample tends toward ohmic behavior.

The current state of the knowledge of the effect of radiation on semiconductor devices, such as transistors and diodes, is sufficient for qualitative understanding of the observed behavior; that is, the observed changes can be explained in terms of predictable physical changes in the crystal structure of the unit. In principle, it should also be possible to quantitatively describe the behavior, but techniques for determining the pertinent parameters for a completed unit have not yet been developed.

---

[30]G. L. Keister and H. V. Stewart, *Proc. Inst. Radio Engrs.* 45, 931 (1957).
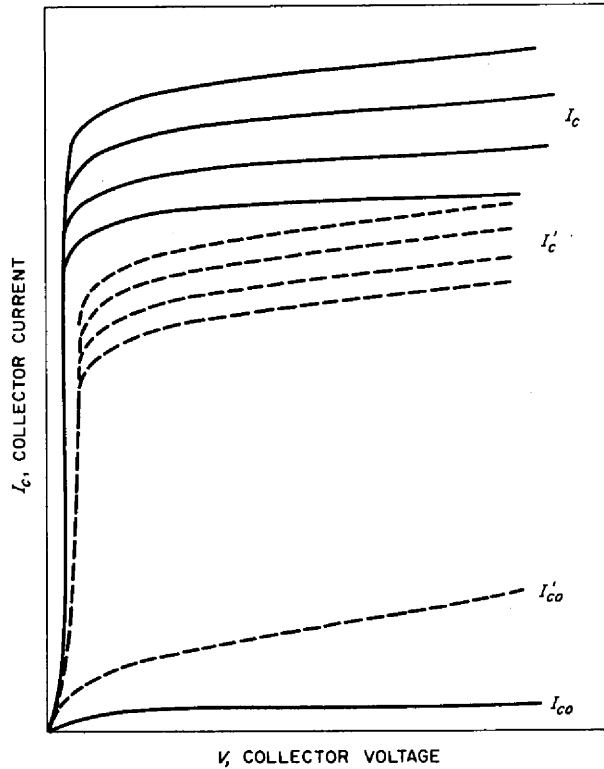
Fig. 4.1.37. Collector Voltage vs Collector Current.

226

Part 5

SHIELDING

E. P. Blizard

5.1. SHIELDING THEORY

EFFECT OF ANISOTROPIC SCATTERING ON THE NEUTRON FLUX IN AIR

C. D. Zerby

For many calculations[1] of fluxes and dose rates resulting from air-scattered neutrons, isotropic scattering in the center-of-mass system is assumed. The question naturally arises as to the validity of this assumption. In order to obtain some insight into the problem, the Monte Carlo code used previously[1] for calculating the fluxes and dose rates of multiply scattered neutrons was altered to include an anisotropic scattering cross section proportional to $(1 + a \cos \theta)$ in the center-of-mass system. Thus, the differential cross section is given by

$$(1) \qquad \frac{d\sigma}{d\Omega} = K(1 + a \cos \theta) \ .$$

The value of the constant K was chosen to make the integral of the differential cross section equal to the total cross section. The value of a is arbitrary and constant over the whole energy range.

The cases investigated were for a point monodirectional beam of neutrons in an infinite volume of air. The beam angle with respect to the source detector axis, θ, and the value of a were the only parameters varied. The constants of the problem were:

Source energy, E_0	5 Mev
Separation distance, g	50 ft
Air density, ρ	0.00125 g/cm^3

Three problems were solved for each value of θ, corresponding to the values of a of 0, 0.3, and 0.7. By expressing the value obtained from the calculation as a function of a, that is, $\Phi(a)$, the ratio of $\Phi(a)$ to $\Phi(0)$ was obtained. This ratio then represents the factorial change which would be expected in the results of a calculation in which isotropic scattering was assumed if anisotropy were to be introduced.

[1]For example, see C. D. Zerby, *A Monte Carlo Calculation of Air-Scattered Neutrons*, ORNL-2277 (April 23, 1957).

The resulting ratios of the total number flux, energy flux, and dose rate are presented as a function of beam angle of emission in Figs. 5.1.1, 5.1.2, and 5.1.3. It may be observed that in each case the ratio is less than 1 for beam angles greater than 10 deg, which indicates that the results obtained by using isotropic scattering in the center-of-mass system are, in general, conservative.

It was found from the calculations in which isotropic scattering in the center-of-mass system was used that the equation which fits the neutron flux data best is[2]

$$(2) \qquad \Phi_N(0) = \frac{\Sigma_s(E_0)}{4\pi g} \frac{\pi - \theta}{\sin \theta} \ ,$$

[2]J. Hilgeman, F. L. Keller, and C. D. Zerby, *Monte Carlo Calculations of Fluxes and Dose Rates Resulting from Neutrons Multiply Scattered in Air*, ORNL-2375 (to be published).
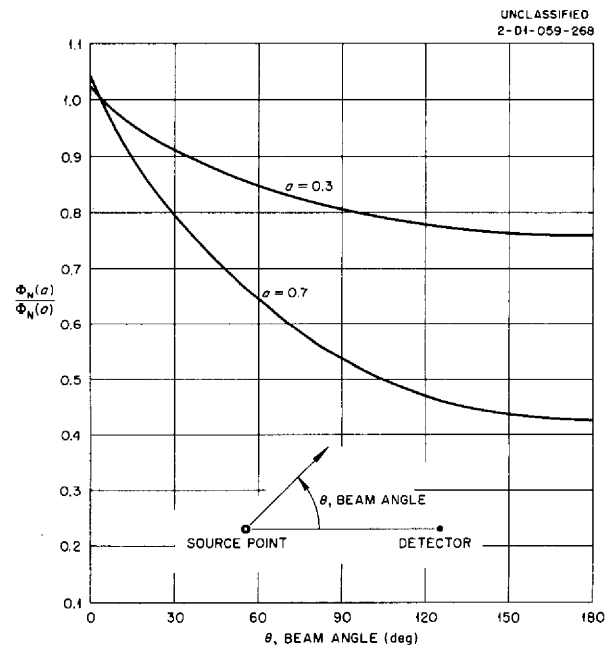
Fig. 5.1.1. Ratio of the Total Neutron Flux in Air with Anisotropic Scattering to That Obtained with Isotropic Scattering. Detector 50 ft from a monodirectional beam of 5-Mev neutrons. Air density = 0.00125 g/cm^3.
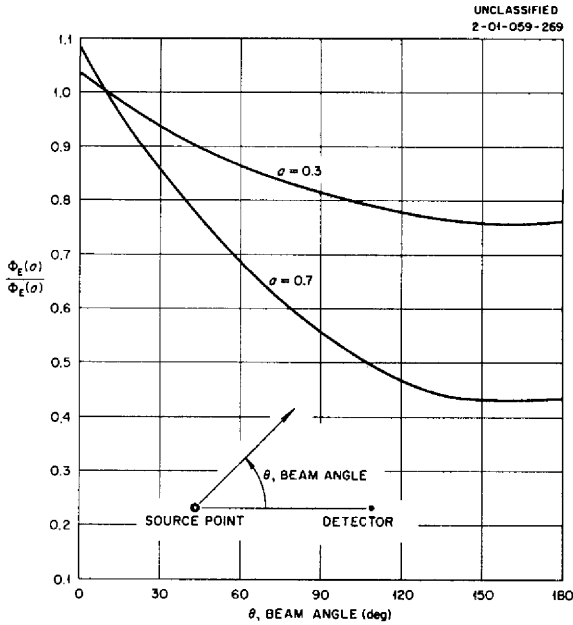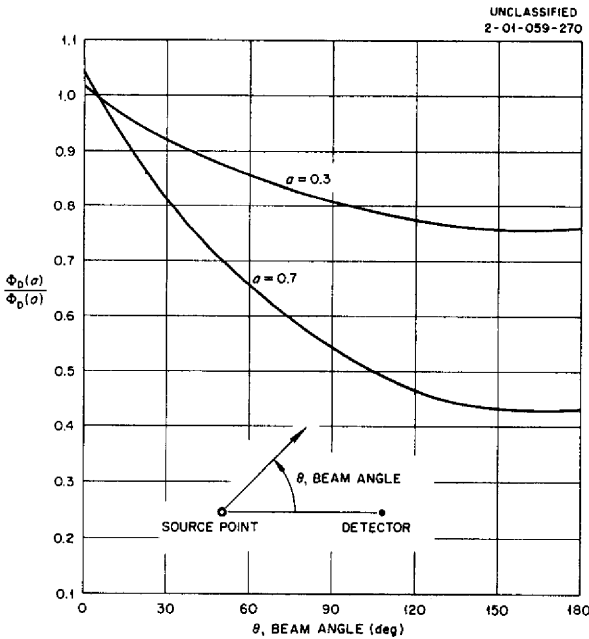
Fig. 5.1.2. Ratio of the Total Neutron Energy Flux in Air with Anisotropic Scattering to That Obtained with Isotropic Scattering. Detector 50 ft from a monodirectional beam of 5-Mev neutrons. Air density = 0.00125 g/cm³.

**Fig. 5.1.3. Ratio of the Total Neutron Dose Rate in Air with Anisotropic Scattering to That Obtained with Isotropic Scattering.** Detector 50 ft from a monodirectional beam of 5-Mev neutrons. Air density = 0.00125 g/cm³.

where

$\Phi_N(0)$ = neutron flux per source neutron,

$\Sigma_s(E_0)$ = macroscopic scattering cross section at the source energy,

g = separation distance.

Equation 2 was also found to fit the neutron flux calculated for singly scattered neutrons on the assumptions of isotropic scattering in the laboratory system and no attenuation on either leg.

A similar expression fits the calculated total dose rate, $\Phi_D(0)$, per source neutron. This equation is

$$(3) \qquad \Phi_D(0) = \frac{C(E_0)}{1.2} \frac{\Sigma_s(E_0)}{4\pi g} \frac{\pi - \theta}{\sin \theta} ,$$

where $C(E_0)$ is the flux-to-dose-rate conversion factor at the source energy.

Since such a simple approach was so effective in providing a fit for the data for isotropic scattering in the center-of-mass system, a similar set of equations for the cases of anisotropic scattering was investigated. The assumption that the differential scattering cross section given in Eq. 1 was effective in the laboratory system and a calculation of the singly scattered flux in which attenuation on both legs was neglected yielded the following equation:

$$(4) \qquad \Phi_N(a) = \Phi_N(0) \left(1 - a \frac{\sin \theta}{\pi - \theta}\right) ,$$

where $\Phi_N(0)$ is as given in Eq. 2. From Eq. 4 and a similar equation for $\Phi_D(a)$, it is seen that

$$(5) \qquad \frac{\Phi_N(a)}{\Phi_N(0)} = \frac{\Phi_D(a)}{\Phi_D(0)} = \left(1 - a \frac{\sin \theta}{\pi - \theta}\right) .$$

Values of these ratios calculated with the use of Eq. 5 are compared with results obtained in Monte Carlo calculations in Tables 5.1.1 and 5.1.2. As may be observed, the results of the Monte Carlo calculation when anisotropic scattering is considered are not fitted by the values obtained with the use of Eq. 5 as closely as would be desired. In fact, it is obvious from a qualitative analysis that Eq. 4 should become less accurate the more anisotropic the scattering. This is borne out in the tables.

Table 5.1.1. Ratio of the Total Neutron Flux in Air
with Anisotropic Scattering to That Obtained
with Isotropic Scattering

θ (deg)	Formula	Monte Carlo	Error of Formula (%)
		$a = 0.3$	
2	0.997	1.008	− 1.1
30	0.943	0.911	+ 3.5
90	0.809	0.806	+ 0.3
130	0.737	0.769	− 4.2
180	0.700	0.760	− 7.9
		$a = 0.7$	
2	0.992	1.020	− 2.7
30	0.866	0.796	+ 8.8
90	0.554	0.537	+ 3.2
130	0.386	0.453	−14.8
180	0.300	0.425	−29.4

Table 5.1.2. Ratio of the Total Dose Rate in Air
with Anisotropic Scattering to That Obtained
with Isotropic Scattering

θ (deg)	Formula	Monte Carlo	Error of Formula (%)
		$a = 0.3$	
2	0.997	1.011	− 1.4
30	0.943	0.920	+ 2.5
90	0.809	0.810	− 0.2
130	0.737	0.768	− 4.0
180	0.700	0.761	− 8.0
		$a = 0.7$	
2	0.992	1.026	− 3.3
30	0.866	0.815	+ 6.1
90	0.554	0.545	+ 1.7
130	0.386	0.449	−14.0
180	0.300	0.430	−30.2

BREMSSTRAHLUNG SPECTRA IN SODIUM IODIDE AND IN AIR[3]

C. D. Zerby   H. S. Moran

In order to provide some information on the production of secondary electromagnetic radiation in materials, a calculation was set up on the Oracle to determine the spectra of bremsstrahlung radiation resulting from the degradation of electrons. The results of calculations for two materials, sodium iodide and air, are shown in Figs. 5.1.4 and 5.1.5.

[3]Presented in more detail in a report by C. D. Zerby and H. S. Moran, *Bremsstrahlung Spectra in NaI and Air*, ORNL-2425 (Feb. 25, 1958).
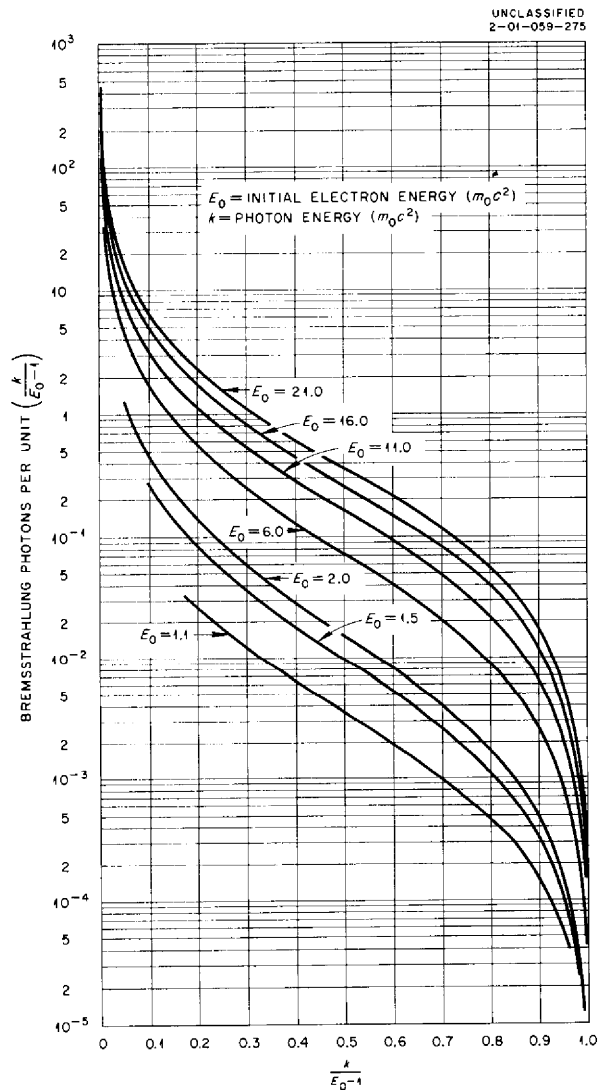
Fig. 5.1.4. Bremsstrahlung Spectrum in Sodium Iodide.
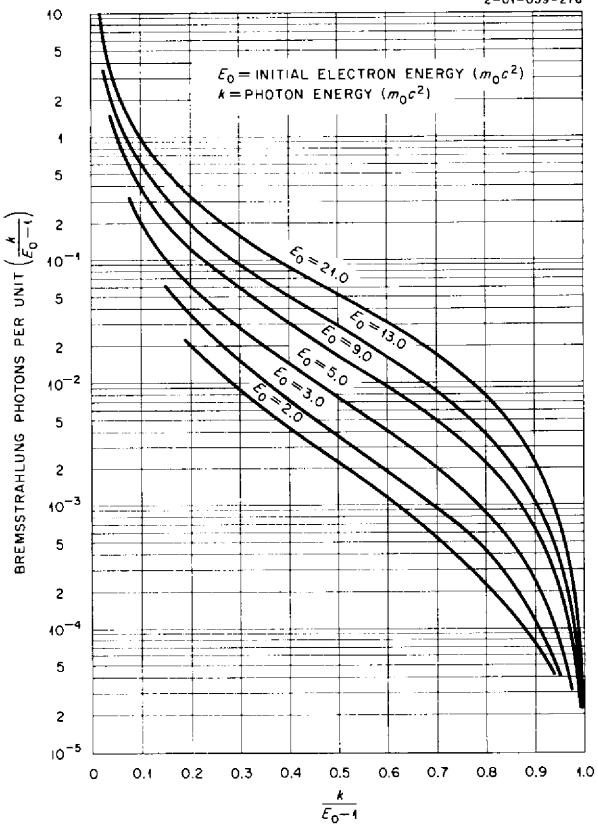
Fig. 5.1.5. Bremsstrahlung Spectrum in Air.

In the calculation, the degradation of the electrons was assumed to occur only by inelastic collisions with the bound electrons of the medium and by radiative collisions with nuclei. It was also assumed that the initial electron energy was sufficiently low for the energy degradation by inelastic collisions to predominate. For the cases presented in Figs. 5.1.4 and 5.1.5 the last assumption is certainly true.[4]

The energy loss per centimeter of path length (stopping power) for an electron making inelastic collisions is given by the equation[5]

$$(1) \quad -\frac{dE}{dx} = \frac{2\pi r_0^2 NZ}{\beta^2} \left\{ \ln \frac{\beta^2(E-1)}{2I^2(1-\beta^2)} - \left(2\sqrt{1-\beta^2} - 1 + \beta^2\right) \ln 2 + 1 - \beta^2 + \frac{1}{8}\left(1 - \sqrt{1-\beta^2}\right)^2 \right\},$$

where

E = total relativistic electron energy $(m_0 c^2)$,

I = mean excitation potential $(m_0 c^2)$,

$\beta^2 = (v/c)^2 = (E^2 - 1)/E^2$,

r_0 = classical electron radius (cm),

N = atomic density (cm^{-3}),

Z = charge number.

The Born-approximation cross section for the production of light (bremsstrahlung radiation) by an electron in the field of a nucleus without screening is given by[6]

$$(2) \quad \Phi^a(E,k) = \frac{r_0^2 Z^2}{137} \frac{N}{k} \frac{p_1}{p} \left\{ \frac{4}{3} - 2EE_1 \frac{p_1^2 + p^2}{p_1^2 p^2} + \left(\frac{\epsilon E_1}{p^3} + \frac{\epsilon_1 E}{p_1^3} - \frac{\epsilon_1 \epsilon}{pp_1}\right) + L\left[\frac{8}{3}\frac{EE_1}{pp_1} + \frac{k^2}{p^3 p_1^3}\left(E^2 E_1^2 + p^2 p_1^2\right) + \frac{k}{2pp_1}\left(\frac{EE_1 + p^2}{p^3}\epsilon - \frac{EE_1 + p_1^2}{p_1^3}\epsilon_1 + \frac{2kEE_1}{p_1^2 p^2}\right)\right] \right\},$$

[4]W. Heitler, *The Quantum Theory of Radiation*, 3d ed., p 252, Clarendon Press, Oxford, 1954.

[5]H. A. Bethe and J. Ashkin, *Experimental Nuclear Physics* (ed. by E. Segrè), p 254, Wiley, New York, 1953.

[6]W. Heitler, *The Quantum Theory of Radiation*, 3d ed., p 245, Clarendon Press, Oxford, 1954.

where the following relations are used:

$$(3) \begin{cases} L = 2 \ln \left(\dfrac{EE_1 + pp_1 - 1}{k} \right) , \\[2mm] \epsilon = 2 \ln (E + p) , \\[2mm] \epsilon_1 = 2 \ln (E_1 + p_1) , \\[2mm] E_1 = E - k , \\[2mm] p^2 = E^2 - 1 , \\[2mm] p_1^2 = E_1^2 - 1 . \end{cases}$$

As may be seen from Eq. 3, Eq. 2 is simply a function of E and k, where E has the same definition as in Eq. 1 and k is the photon energy expressed in units of $m_0 c^2$. The expression $\Phi^a(E,k) \, dk$ is the electron cross section (cm^{-1}) for producing a photon in the interval k to $k + dk$.

When the electron screening of the nucleus is taken into account and Eq. 2 is reduced to the relativistic case, $E \gg m_0 c^2$, the following equation[7] is obtained:

$$(4) \quad \Phi^b(E,k) = \frac{r_0^2 Z^2 N}{137} \frac{4}{k} \times$$

$$\times \left\{ \left[1 + \left(\frac{E - k}{E} \right)^2 \right] \left[\frac{\phi_1(\gamma)}{4} - \frac{1}{3} \ln Z \right] - \frac{2}{3} \left(\frac{E - k}{E} \right) \left[\frac{\phi_2(\gamma)}{4} - \frac{1}{3} \ln Z \right] \right\} ,$$

where γ is given by [8]

$$(5) \qquad \gamma = 100 \, \frac{k}{E(E - k) Z^{1/3}} .$$

The functions $\phi_1(\gamma)$ and $\phi_2(\gamma)$ are presented graphically by Bethe and Ashkin;[9] however, they are well represented with less than 0.3% error by the empirical relations

[7]H. A. Bethe and J. Ashkin, *Experimental Nuclear Physics* (ed. by E. Segrè), p 260, Wiley, New York, 1953.

[8]*Ibid.*, p 259.

[9]*Ibid.*, p 262.

$$(6) \quad \phi_1(\gamma) = 5.089 e^{-0.6587\gamma} + 15.661 e^{-0.0481\gamma} ,$$

$$(7) \quad \phi_2(\gamma) = \phi_1(\gamma) - 0.595 e^{-3.04\gamma} .$$

The quantity γ measures the effect of screening. For $y \gg 1$ the screening can be neglected; however, for $y = 0$ the screening is complete. Although Bethe and Ashkin give a series of equations similar to Eq. 4 that are valid for various ranges of y, the use of Eqs. 6 and 7 in Eq. 4 makes Eq. 4 valid for all values of y.

With the use of Eqs. 1, 2, and 4, the total bremsstrahlung spectra from an electron slowing down in a compound is given by

$$(8) \quad K(E_0, k_0) \, dk_0 = \int_{k+1}^{E_0} \frac{\sum_j \Phi_j(E,k) \, dE}{\sum_j \left(-\dfrac{dE}{dx} \right)_j} \, dk_0 ,$$

where $K(E_0, k_0) \, dk_0$ is the number of photons produced by an electron slowing down from energy E_0 in the interval k_0 to $k_0 + dk_0$. The subscript j refers to the jth element of the compound. The quantity $\Phi(E,k)$ is obtained from Eq. 2 or Eq. 4, depending on which is appropriate in the course of integration.

Equation 8 was solved on the Oracle to provide the data presented in Figs. 5.1.4 and 5.1.5. For convenience, the results are presented as the number of photons per unit $(k/E_0) - 1$ as a function of $(k/E_0) - 1$. The integral under the curve represents the total number of photons released.

A CALCULATION OF GAMMA-RAY DOSE RATES FROM NEUTRON CAPTURE IN AIR

F. L. Keller   C. D. Zerby
W. W. Dunn[10]

Experiments at the TSF and elsewhere have indicated that the gamma rays which are produced by the capture of neutrons in air may become a major contribution to the dose rate inside the crew compartment of a heavily divided aircraft shield. Very little quantitative work has been done, however, on the problem of determining at a point in air the gamma-ray dose rate which results from these air-capture gamma rays.

[10]On assignment from USAF.

The problem may be idealized to that of determining the air-capture gamma-ray dose rate and angular distribution at a detector located an arbitrary distance from a point source of monoenergetic neutrons where both the source and detector are considered to be embedded in an infinite volume of air. The calculation should include the contributions from captures which take place during the slowing-down process as well as contributions from captures which occur during the diffusion at thermal energy. A portion of the results of a parameter study of this problem by the Monte Carlo technique for both point isotropic and line-beam sources is presented here. The complete results will be published in a separate report.[11]

Calculational Method

The Monte Carlo machine code which was used for this problem was a modification of the Monte Carlo code which was used to calculate neutron scattering in air.[12] This original code was completely described in the report cited; therefore, the discussion here will be limited to a very brief description of the general features of the code as modified to perform the present problem.

The total cross sections for oxygen and nitrogen were taken from BNL-325[13] and were considered to be identical with the scattering cross sections, except for the absorption cross section of nitrogen. The absorption cross section of oxygen is extremely small and was neglected. The absorption cross section of nitrogen is made up of the (n,p) and (n,γ) cross sections, which were taken to be 1.70 barns and 0.08 barn, respectively, at 0.025 ev and were assumed to have a $1/v$ dependence. The scattering probability was taken as isotropic in the center-of-mass system.

The source was taken to be either a point isotropic source of monoenergetic neutrons of energy E_n or a point source which emitted a monoenergetic line beam of neutrons of energy E_n at an angle θ_0 with respect to the source-detector axis. The space about the detector was

divided into a number of solid-angle intervals, and estimates of the angular distribution of the dose rate at the detector were made.

The neutron histories were generated in exactly the same manner as described in the report on air scattering.[12] At each neutron collision, the probability of capture was determined, and a statistical estimate was made of the capture gamma-ray dose-rate contribution at the detector from that collision. The neutron was then allowed to scatter randomly and to continue with a reduced weighting. The neutrons were degraded in energy at each scattering by the standard elastic-scattering relations until the neutron energy reached 0.025 ev. After the neutron energy was degraded to 0.025 ev, the neutron was permitted to scatter and diffuse without further energy loss. A neutron history was terminated if the neutron weight after the *l*th collision was less than about 1/600th of its original weight or if the collision occurred at a distance greater than 32 mean free paths from the detector position. This enabled a 0.025-ev neutron to make approximately 45 collisions before its history was terminated. For higher source energies the average number of collisions was, of course, greater.

The capture gamma rays were assumed to be emitted isotropically from the collision point, and an exponential buildup factor was used in the dose-rate calculation. The spectrum of capture gamma rays which was used in the dose-rate determination was from the recent work of Bartholomew and Campion.[14] The dose-rate contributions were stored in appropriate solid-angle intervals at the detector under the assumption that all gamma rays from a given event entered the detector in the solid-angle interval which contained the radius vector from the detector to the collision point. All the results were normalized to one neutron per second leaving the source, and all the results reported here were from calculations which used 500 neutron case histories. It should be pointed out that because the method of statistical estimation was employed, the results were relatively insensitive to the number of neutron histories used.

[11] W. W. Dunn, F. L. Keller, and C. D. Zerby, *A Calculation of Gamma-Ray Dose Rates from Neutron Capture in Air*, ORNL-2462 (unpublished).

[12] C. D. Zerby, *A Monte Carlo Calculation of Air-Scattered Neutrons*, ORNL-2277 (April 23, 1957).

[13] D. J. Hughes and J. A. Harvey, *Neutron Cross Sections*, BNL-325 (July 1, 1955).

[14] G. A. Bartholomew and P. J. Campion, *Can. J. Phys.* **35**, 1347 (1957).

The result of the Monte Carlo calculation was checked against the result obtained from the neutron flux given by the direct solution to the transport equation for the case of a point isotropic source of 0.025-ev neutrons located a distance of 15 m from the detector. The assumptions involved in both calculations were the same except that the Monte Carlo calculation took the neutron-scattering probability to be isotropic in the center-of-mass system, whereas the transport equation treated the scattering as isotropic in the laboratory system. This would be expected to lead to a slightly lower value for the Monte Carlo result. The comparison showed that the Monte Carlo result was about 10% smaller than the result from the check calculation. Hence, the results reported here are believed to be good to about 10 to 20%. It is interesting to note that the dose-rate contribution from the flux given by the nonasymptotic part of the solution to the transport equation was about 30% of the total dose rate in the above case.

Results for Point Isotropic Sources ·

A series of calculations were performed for point isotropic neutron sources with energies of 0.025, 0.1, 1.0, 100, and 10,000 ev and a source-detector separation distance of about 50 ft. The air density was taken to be 0.001205 g/cm^3, which corresponds to approximately sea-level conditions. A plot of the total gamma-ray dose rate vs the neutron source energy is shown in Fig. 5.1.6. It may be

noted that the dose rate varies with the neutron source energy approximately as $E^{-1/3}$.

In these calculations, each gamma-ray dose-rate contribution at the detector was also stored with respect to the energy, at capture, of the neutron which gave rise to the contribution. Figures 5.1.7, 5.1.8, and 5.1.9 show histograms of the dose rate plotted as a function of neutron capture energy for several of the cases run in this study. It may be seen that, for relatively low neutron source energies, a large part of the gamma-ray dose rate at the detector comes from neutrons which are captured at energies that are within a factor of α
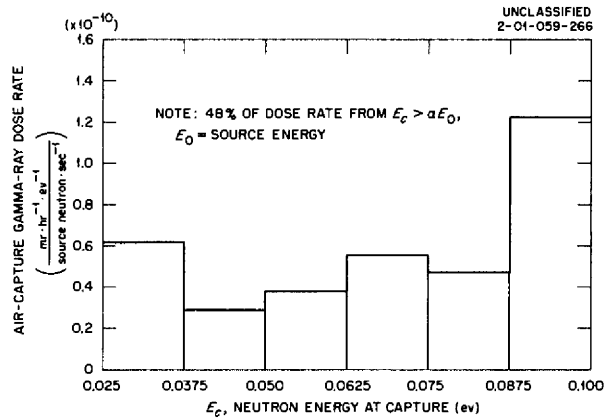
Fig. 5.1.7. Air Capture Gamma-Ray Dose Rate 50 ft from a Point Isotropic Neutron Source as a Function of E_c for $E_0 = 0.1$ ev.
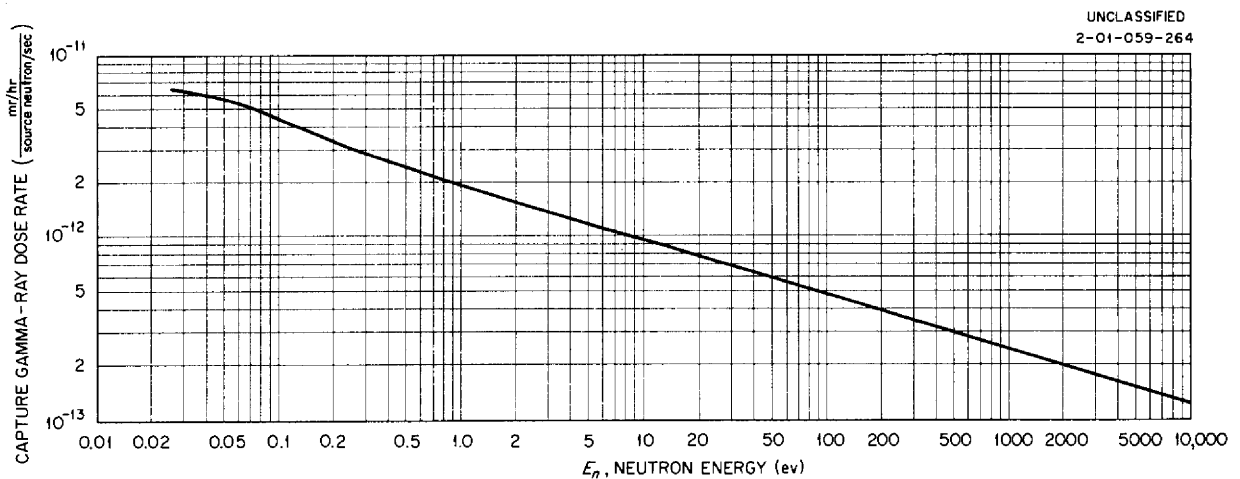

Fig. 5.1.6. Air Capture Gamma-Ray Dose Rate at a Detector 50 ft from a Point Isotropic Monoenergetic Neutron Source.
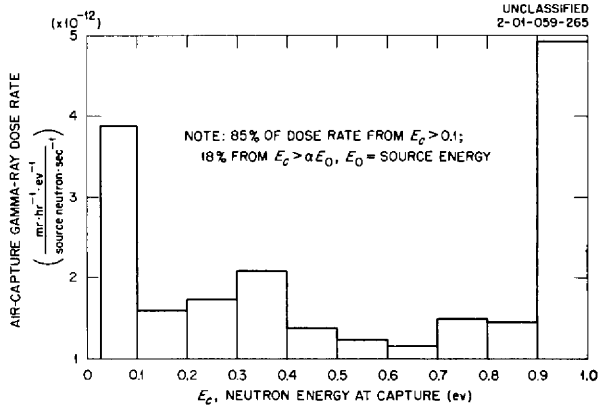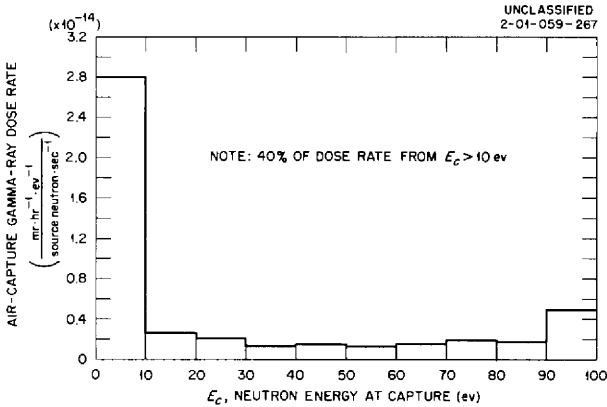
NOTE: 85% OF DOSE RATE FROM $E_c > 0.1$;
18% FROM $E_c > \alpha E_0$, E_0 = SOURCE ENERGY

E_c, NEUTRON ENERGY AT CAPTURE (ev)

Fig. 5.1.8. Air-Capture Gamma-Ray Dose Rate 50 ft from a Point Isotropic Neutron Source as a Function of E_c for $E_0 = 1.0$ ev.

NOTE: 40% OF DOSE RATE FROM $E_c > 10$ ev

E_c, NEUTRON ENERGY AT CAPTURE (ev)

Fig. 5.1.9. Air-Capture Gamma-Ray Dose Rate 50 ft from a Point Isotropic Neutron Source as a Function of E_c for $E_0 = 100$ ev.

of the source energy, where $\alpha = [(A - 1)/(A + 1)]^2$ and A is the average mass number for air. This fact throws considerable doubt on calculations of the air-capture gamma-ray dose rate which use the results of the standard age-diffusion equation for the neutron flux, since these results are known to break down for neutron energies which are within a factor of α of the source energy.

Results for Line-Beam Sources

Figure 5.1.10 shows the results for a series of problems which was run for line-beam neutron sources. The gamma-ray dose rate at the detector is shown plotted as a function of the angle of emission of the beam for various monoenergetic

sources. The source-detector separation distance was 65 ft, and the air density was again taken as 0.001205 g/cm³. The curves are relatively flat over the region from 30 to 180 deg, and they become flatter as the source energy is increased, as would be expected.

$E_n = 0.025$ ev

$E_n = 1.0$ ev

$E_n = 10.0$ ev

$E_n = 1000$ ev

θ_0, ANGLE OF EMISSION (deg)
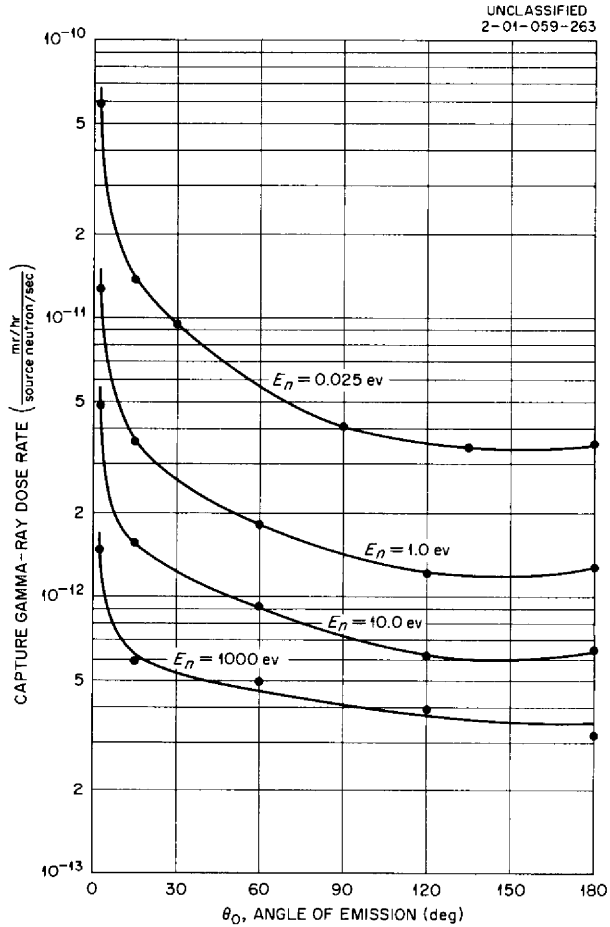
Fig. 5.1.10. Air-Capture Gamma-Ray Dose Rate of a Detector 65 ft from a Line-Beam Neutron Source Emitted at Various Angles from the Source-Detector Axis.

Since most aircraft reactor shields are designed so that most of the neutron leakage is from the rear of the shield, the curves of Fig. 5.1.10 indicate that a knowledge of the exact surface angular distribution of these low-energy neutrons is relatively unimportant. The important thing is to have a knowledge of the spectrum and total number of low-energy leakage neutrons. Because of the

extreme difficulty in making accurate experimental determinations of low-energy neutron spectra, it will probably be necessary to generate this information by Monte Carlo techniques. Additional results, including angular distributions of the dose rate and results for other separation

distances, and a more detailed discussion of these calculations will be found in the complete report.[15]

[15]W. W. Dunn, F. L. Keller, and C. D. Zerby, *A Calculation of Gamma-Ray Dose Rates from Neutron Capture in Air*, ORNL-2462 (unpublished).

5.2. LID TANK SHIELDING FACILITY

W. Zobel

PRATT & WHITNEY SERIES OF ADVANCED SHIELDING MATERIALS STUDIES

E. A. Warman[1]

A second group of tests of advanced shielding materials[2] was performed in the Lid Tank Shielding Facility (LTSF) in order to obtain information required in the Pratt & Whitney shield design effort (LTSF exp. 70). The purpose of these tests was to determine the feasibility of using various materials in the shield of a fast-neutron reactor intended for possible aircraft-propulsion application.

The materials tested were lithium hydride, depleted uranium, and borated water, with particular emphasis being placed on a study of the production of secondary gamma rays in the uranium. In most of the tests, these materials were used in combination with nickel and stainless steel. The configurations tested are described in Table 5.2.1, and the physical properties of the materials used are presented in Table 5.2.2.

The components in configurations 36 through 42 and 90 and 91 were installed dry in the LTSF configuration tank, which is a steel tank with $\frac{5}{8}$-in.-thick walls. The tank has a $\frac{3}{8}$-in.-thick aluminum window on the source side; an unavoidable 1.6-cm space between the aluminum window and the source plate was filled with air contained in a plastic bag. The borated water used in configurations 36 through 42 and 90 and 91 was contained in an aluminum tank with $\frac{1}{8}$-in.-thick walls. This tank was 31 in. long. Configurations 43 through 49 and 79 through 86 were submerged in borated water in the configuration tank.

Gamma-ray dose-rate measurements were taken beyond each configuration, and fast-neutron and thermal-neutron measurements were made beyond all configurations, except configurations 85, 86, 90, and 91. No neutron measurements were made beyond configuration 86, and only thermal-neutron measurements were made beyond configurations

85, 90, and 91. The fast-neutron and gamma-ray data represent instrument response measurements converted to ergs/g·hr·w of tissue dose as calibrated with known sources. The thermal-neutron data are instrument response measurements normalized to cadmium-difference gold-foil fluxes. The fluxes were corrected for flux depression by the 2-mil-thick foils and for self-absorption and self-shielding. The instrumentation used in these tests was the same as that described previously.[3] The measurements made beyond all the configurations are presented here, along with a brief discussion; the data have not yet been analyzed.

Configurations OB, 43, 45, 48, 81, and 82. — Gamma-ray dose-rate measurements taken beyond configuration 81, as shown in Fig. 5.2.1, indicate the effect of substituting 1 in. of stainless steel for 1 in. of borated water in configuration OB, which consisted entirely of borated water. The dose rate was decreased by about 27%.

In configuration 43, 2 in. of nickel was inserted in front of the stainless steel of configuration 81. This resulted in a decrease in the gamma-ray dose rate of about 55% from that of configuration 81 at a distance of 40 cm from the source plate and a decrease of about 42% at a distance of 160 cm. The change in slope of the dose-rate curve possibly indicates a "harder" spectrum of gamma rays.

In configuration 82, a $1\frac{1}{2}$-in.-thick slab of depleted uranium was placed behind the stainless steel of configuration 43. The slope of the gamma-ray curve was changed, and the curve itself was lowered considerably. The gamma-ray dose rate at 40 cm from the source plate was lowered approximately 70% and at 160 cm it was lowered about 92%. The change in the slope of the curve indicates a "softer" gamma-ray spectrum. The measured reduction and the change in slope also indicate a reduction in the contribution of primary gamma rays from the source plate.

The effect of inserting 1 ft of borated water in front of the uranium in configuration 82 is shown by gamma-ray measurements beyond configuration 48. The dose rate was decreased by 80% at a

---

[1]On assignment from Pratt & Whitney Aircraft.

[2]The first group of tests was described by W. Zobel *et al., ANP Quar. Prog. Rep. June 30, 1957*, ORNL-2340, p 285, and by E. A. Warman, *ANP Quar. Prog. Rep. Sept. 30, 1957*, ORNL-2387, p 300.

[3]D. R. Otis, *ANP Quar. Prog. Rep. Dec. 31, 1956*, ORNL-2221, p 331.

Table 5.2.1. Description of Configurations Tested in Pratt & Whitney Series

Configuration Number	Description of Configuration	Location of Probe,[a] z_0 (cm)	Unavoidable[b] Gap Within Configuration
OB	Borated water ($B\text{-}H_2O$) in configuration tank	2.6^c	
36	2 in. of Ni + 1 in. of stainless steel + 2 ft of LiH + $B\text{-}H_2O$ in an Al tank	77.4	3.4 cm of air
37	2 in. of Ni + 1 in. of stainless steel + 3 in. of depleted U + 2 ft of LiH + $B\text{-}H_2O$ in an Al tank	85.6	4.0 cm of air
38	2 in. of Ni + 1 in. of stainless steel + 2 ft of LiH + 3 in. of depleted U + $B\text{-}H_2O$ in an Al tank	85.2	3.6 cm of air
39	2 in. of Ni + 1 in. of stainless steel + 2 ft of LiH + $1\frac{1}{2}$ in. of depleted U + $B\text{-}H_2O$ in an Al tank	81.4	3.6 cm of air
40	2 in. of Ni + 1 in. of stainless steel + 1 ft of LiH + 3 in. of depleted U + 1 ft of LiH + $B\text{-}H_2O$ in an Al tank	85.6	4.0 cm of air
41	2 in. of Ni + 1 in. of stainless steel + 1 ft of LiH + $1\frac{1}{2}$ in. of depleted U + 1 ft of LiH + $B\text{-}H_2O$ in an Al tank	81.4	3.6 cm of air
42	2 in. of Ni + 1 in. of stainless steel + 1 ft of LiH + $1\frac{1}{2}$ in. of depleted U + 1 ft of LiH + $1\frac{1}{2}$ in. of depleted U + $B\text{-}H_2O$ in an Al tank	85.0	3.4 cm of air
43	2 in. of Ni + 1 in. of stainless steel + $B\text{-}H_2O$	12.8	2.6 cm of $B\text{-}H_2O$
44	2 in. of Ni + 1 in. of stainless steel + 3 in. of depleted U + $B\text{-}H_2O$	21.0	3.2 cm of $B\text{-}H_2O$
45	2 in. of Ni + 1 in. of stainless steel + 2 ft of $B\text{-}H_2O$ + $1\frac{1}{2}$ in. of depleted U + $B\text{-}H_2O$	75.8	0.8 cm of $B\text{-}H_2O$
46	2 in. of Ni + 1 in. of stainless steel + 2 ft of $B\text{-}H_2O$ + 3 in. of depleted U + $B\text{-}H_2O$	81.8	3.0 cm of $B\text{-}H_2O$
47	2 in. of Ni + 1 in. of stainless steel + 1 ft of $B\text{-}H_2O$ + 3 in. of depleted U + $B\text{-}H_2O$	51.8	3.5 cm of $B\text{-}H_2O$
48	2 in. of Ni + 1 in. of stainless steel + 1 ft of $B\text{-}H_2O$ + $1\frac{1}{2}$ in. of depleted U + $B\text{-}H_2O$	46.0	1.5 cm of $B\text{-}H_2O$
49	2 in. of Ni + 1 in. of stainless steel + 1 ft of $B\text{-}H_2O$ + $1\frac{1}{2}$ in. of depleted U + 1 ft of $B\text{-}H_2O$ + $1\frac{1}{2}$ in. of depleted U + $B\text{-}H_2O$	81.0	2.2 cm of $B\text{-}H_2O$
79	2 in. of Ni + 1 in. of stainless steel + $\frac{1}{2}$ in. of boral + 3 in. of depleted U + $B\text{-}H_2O$	23.1	4.0 cm of $B\text{-}H_2O$
80	2 in. of Ni + 1 in. of stainless steel + $\frac{1}{2}$ in. of boral + 3 in. of depleted U + $\frac{1}{2}$ in. of boral + $B\text{-}H_2O$	25.0	4.7 cm of $B\text{-}H_2O$
81	1 in. of stainless steel + $B\text{-}H_2O$	6.6	1.5 cm of $B\text{-}H_2O$

Table 5.2.1 (continued)

Configuration Number	Description of Configuration	Location of Probe,[a] z_0 (cm)	Unavoidable[b] Gap Within Configuration
82	2 in. of Ni + 1 in. of stainless steel + $1\frac{1}{2}$ in. of depleted U + B-H$_2$O	16.8	2.8 cm of B-H$_2$O
83	2 in. of Ni + 1 in. of stainless steel + 3 in. of B-H$_2$O + 3 in. of depleted U + B-H$_2$O	27.6	2.1 cm of B-H$_2$O
84	2 in. of Ni + 1 in. of stainless steel + 6 in. of B-H$_2$O + 3 in. of depleted U + B-H$_2$O	35.4	2.4 cm of B-H$_2$O
85	2 in. of Ni + 1 in. of stainless steel + 30 in. of B-H$_2$O + 3 in. of depleted U + B-H$_2$O	97.0	3.0 cm of B-H$_2$O
86	2 in. of Ni + 1 in. of stainless steel + 18 in. of B-H$_2$O + 3 in. of depleted U + B-H$_2$O	65.6	2.0 cm of B-H$_2$O
90	2 in. of Ni + 1 in. of stainless steel + 2 ft of LiH + $4\frac{1}{2}$ in. of depleted U + B-H$_2$O in an Al tank	88.0	2.5 cm of air
91	2 in. of Ni + 1 in. of stainless steel + 1 ft of LiH + $4\frac{1}{2}$ in. of depleted U + 1 ft of LiH + B-H$_2$O in an Al tank	88.2	2.7 cm of air

[a]Actual distance from source plate to back of solid configuration; that is, the borated water at the back of the configuration is not included.

[b]Includes the 1-cm recession of the aluminum window in the configuration tank.

[c]Probe inside the configuration tank at the aluminum window.

Table 5.2.2. Physical Properties of Materials Used for LTSF Mockup Tests
of Advanced Shielding Materials (Pratt & Whitney Series)

Material	Actual Thickness per Slab (cm)	Description
Type 347 stainless steel	2.54	5-ft × 5-ft × 1-in. slab; composition, 58.35 wt % Fe—18.0 wt % Cr—10.3 wt % Ni —2.0 wt % Mn—1.0 wt % Si—0.08 wt % C—0.04 wt % P—0.03 wt % S; density, 7.8 g/cm^3
Nickel	2.54	Metallic slab, 64 × 66 × 1 in.
Uranium	3.81	Metallic slab, 52 × 55$\frac{5}{16}$ × $1\frac{1}{2}$ in., depleted to 0.24% U^{235}
Lithium hydride	32.0	5 × 5 × 1-ft slab encased in aluminum cans ($\frac{1}{4}$-in.-thick walls); composition, 95 wt % LiH—5 wt % unaccounted for (probably oxygen and hydrogen); density, 0.75 g/cm^3
Boral	1.3	48 × 48 × $\frac{1}{2}$-in. slab with 0.05-in.-thick Al cladding; composition, 80 wt % Al—15.7 wt % B—4.3 wt % C; density, 2.60 g/cm^3
Borated water		Composition, 1.34 wt % natural boron; density, 1.05 g/cm^3 at 20°C
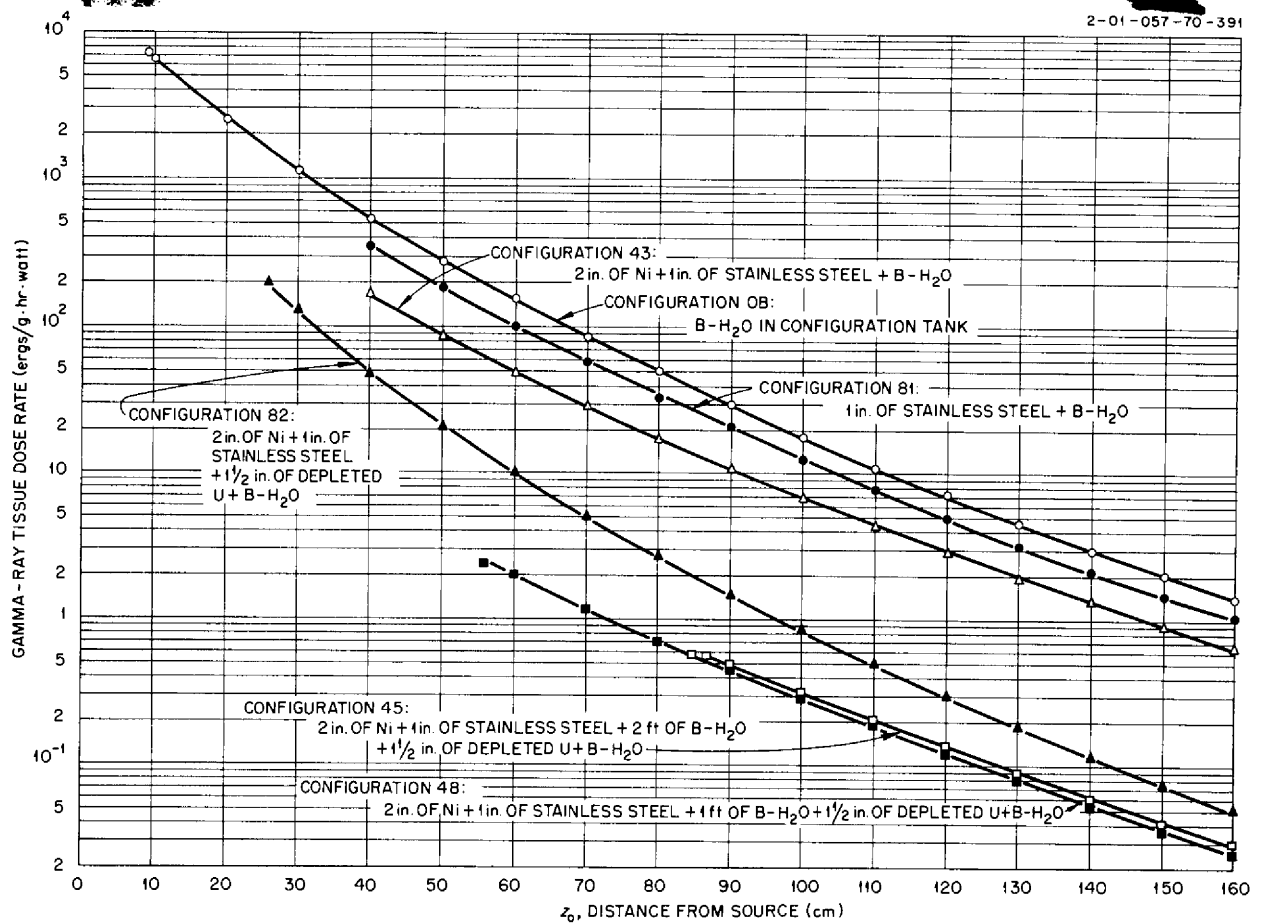
Fig. 5.2.1. Gamma-Ray Tissue Dose Rates Beyond Configurations 43, 45, 48, 81, and 82.

distance of 60 cm from the source plate and by 50% at 160 cm. The change in the slope of the curve indicates a harder spectrum. The difference between the curves for configurations 82 and 48 is believed to be almost entirely due to the reduction in secondary gamma-ray production in the uranium. The cause of this reduction is, of course, the decrease in the thermal- and fast-neutron fluxes incident on the uranium.

The borated water space of configuration 48 was increased to 2 ft in configuration 45. The resulting gamma-ray curve appears to be raised slightly. This, however, may be attributable to experimental error.

Corresponding thermal-neutron flux and fast-neutron dose-rate measurements for the configurations discussed above are shown in Figs. 5.2.2 and 5.2.3.

Configurations 82, 44, 79, and 80. — Configuration 44 represents configuration 82 with a second $1\frac{1}{2}$-in.-thick slab of uranium added to it. The degradation of the higher energy gamma rays in the added uranium resulted in a softened emergent gamma-ray spectrum, as is evidenced by the change in the slope of the curve of the data plotted in Fig. 5.2.4.

In configuration 79, a $\frac{1}{2}$-in.-thick boral curtain was placed on the source-plate side of the 3 in. of uranium in configuration 44. The gamma-ray dose-rate curve was lowered by approximately 20%. This decrease is believed to be due almost entirely to a reduction in the number of secondary gamma rays resulting from (n,γ) captures in the uranium. The reduction, of course, results from the reduction in the neutron flux incident on the
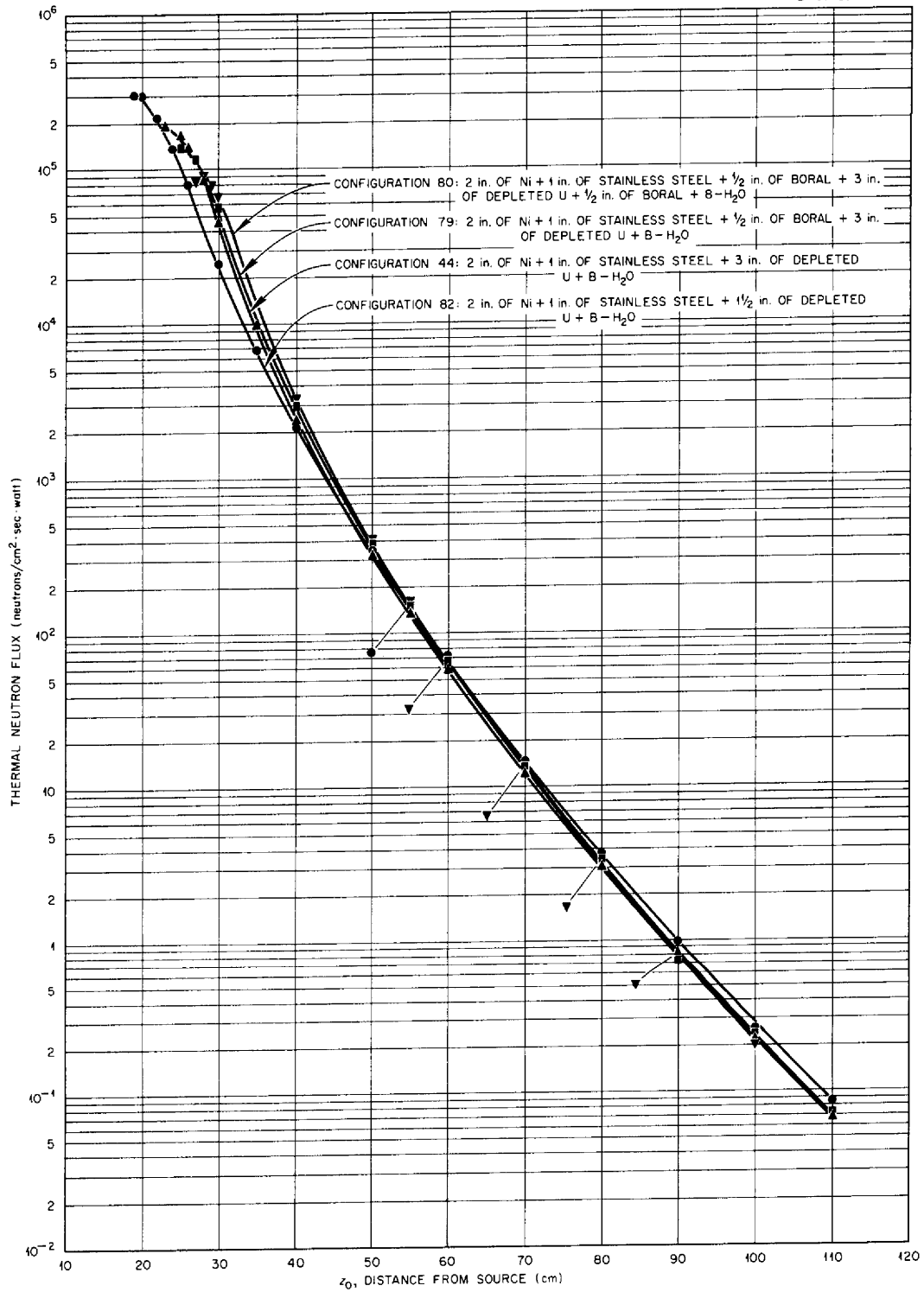
241
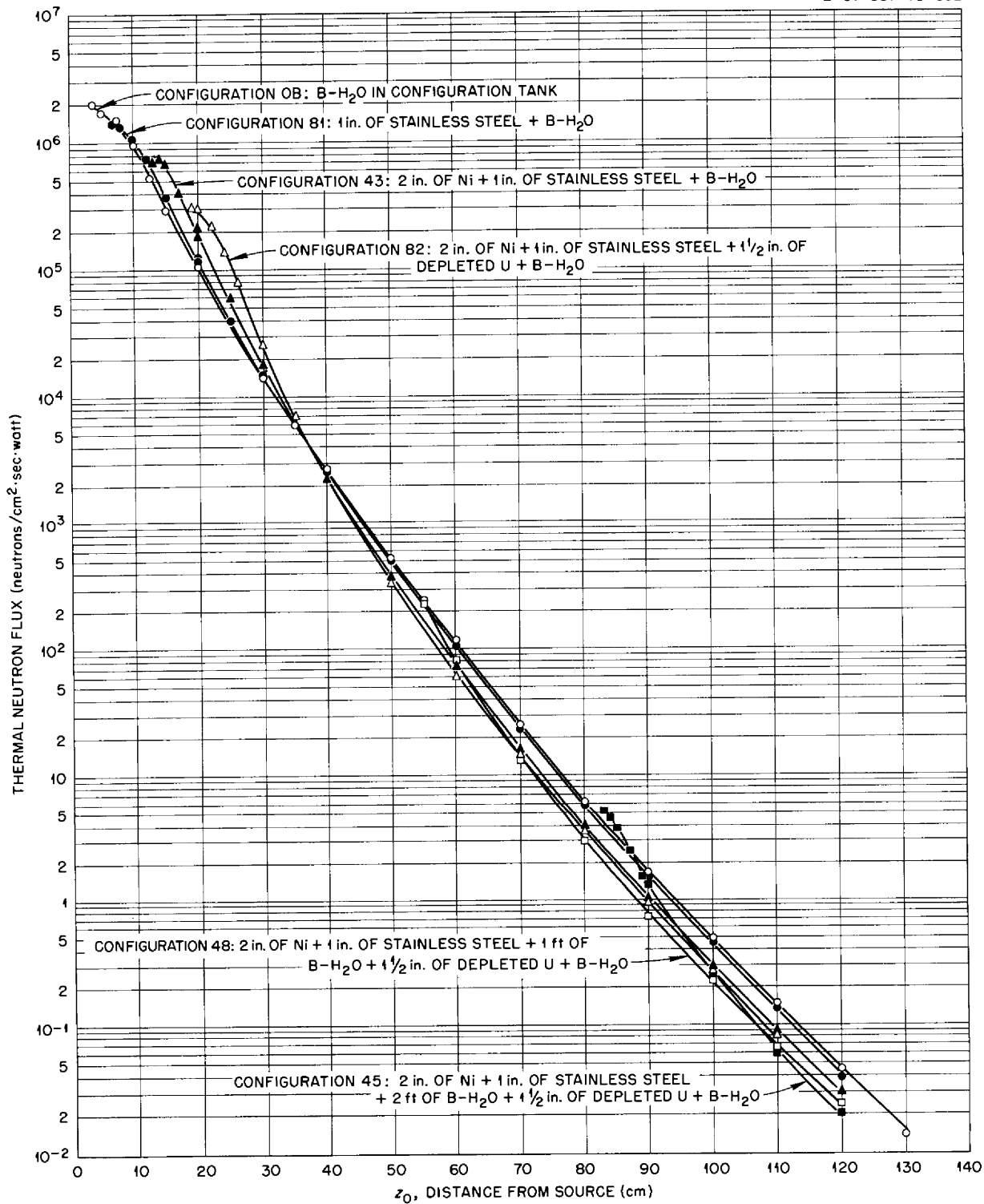
Fig. 5.2.2. Thermal-Neutron Fluxes Beyond Configurations 43, 45, 48, 81, and 82.
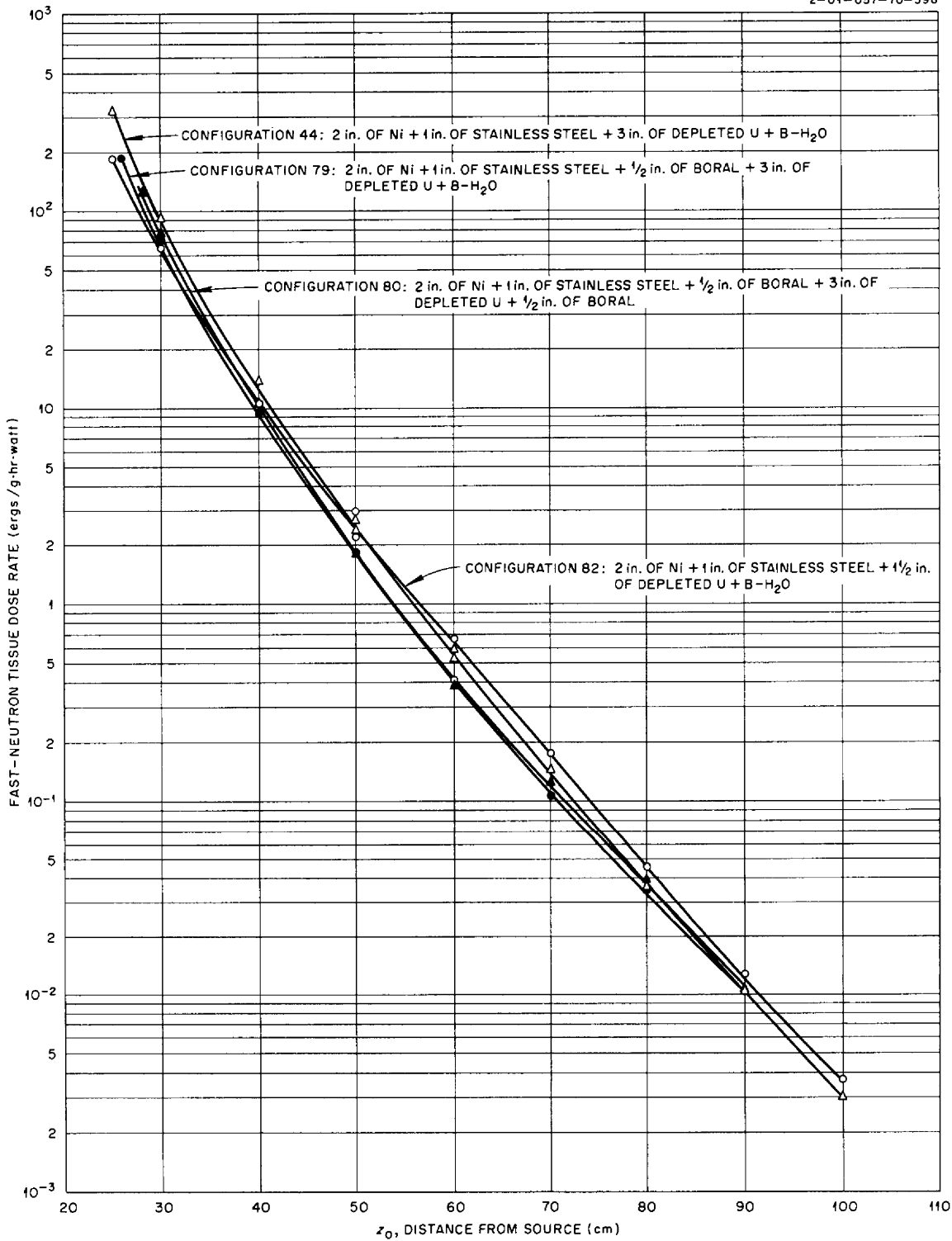
Fig. 5.2.3. Fast-Neutron Tissue Dose Rates Beyond Configurations 43, 45, 48, 81, and 82.

2-01-057-70-394
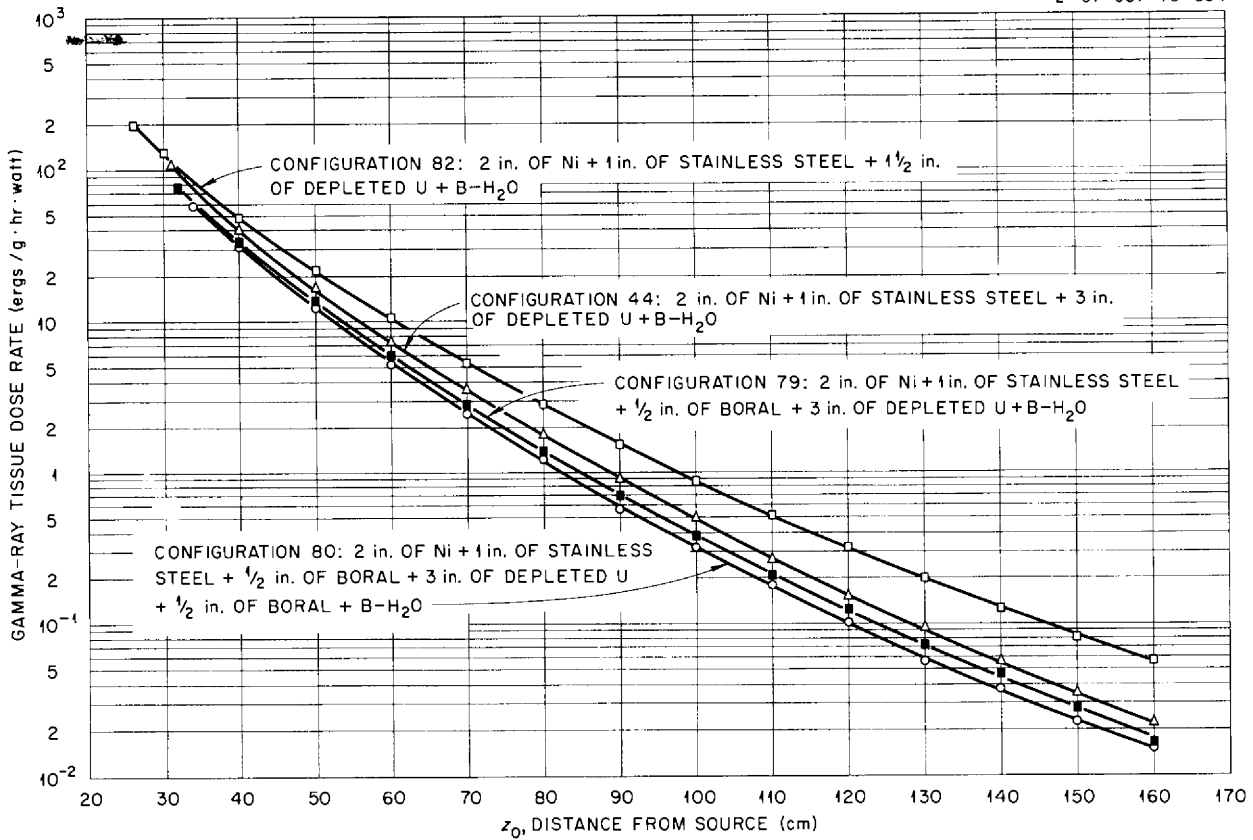
Fig. 5.2.4. Gamma-Ray Tissue Dose Rates Beyond Configurations 44, 79, 80, and 82.

uranium, that is, from the absorption of neutrons in the boral.

In configuration 80, a second $\frac{1}{2}$-in.-thick boral curtain was placed behind the 3 in. of uranium in configuration 79. The gamma-ray dose rate was almost unchanged at a distance of 34 cm from the source, but it was lowered approximately 16% at 160 cm. The change in the slope of the curve is possibly due to the reduction of secondary gamma-ray production in the borated water backing.

The neutron measurements beyond configurations 44, 79, 80, and 82 are shown in Figs. 5.2.5 and 5.2.6.

Configurations 43, 44, 46, and 49. — Gamma-ray dose-rate measurements beyond configuration 44 illustrate the effect of adding 3 in. of uranium to configuration 43. The gamma-ray dose rate beyond configuration 44 was lowered about 80% from that beyond configuration 43 in the forward region and

by about a factor of 30 in the region farther from the source plate, as shown in Fig. 5.2.7. The radical change in the slope of the curve points out the much softer energy spectrum of gamma rays being detected.

Configuration 46 was similar to configuration 44 except that 2 ft of borated water was inserted in front of the 3 in. of uranium. The resulting decrease in the gamma-ray dose rate is believed to be due principally to the reduction in secondary gamma-ray production in the uranium. If this is assumed to be true, the difference between dose rates beyond the two configurations can be taken to be the approximate secondary gamma-ray contribution to the dose rate beyond configuration 44.

In configuration 49, the borated water spacing of configuration 46 was broken up into two equal parts, the second section dividing the uranium in half. This lamination proved to be a more
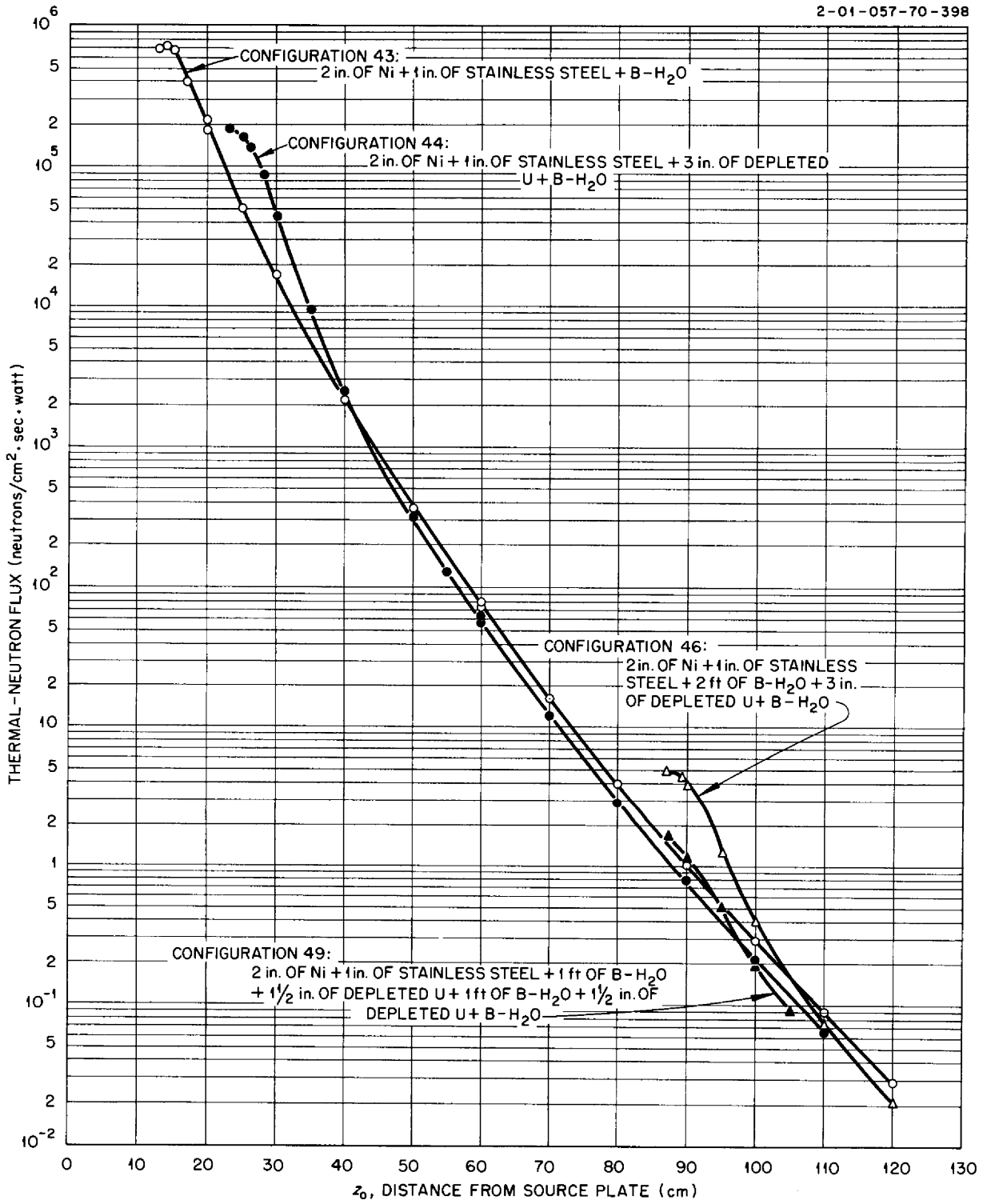
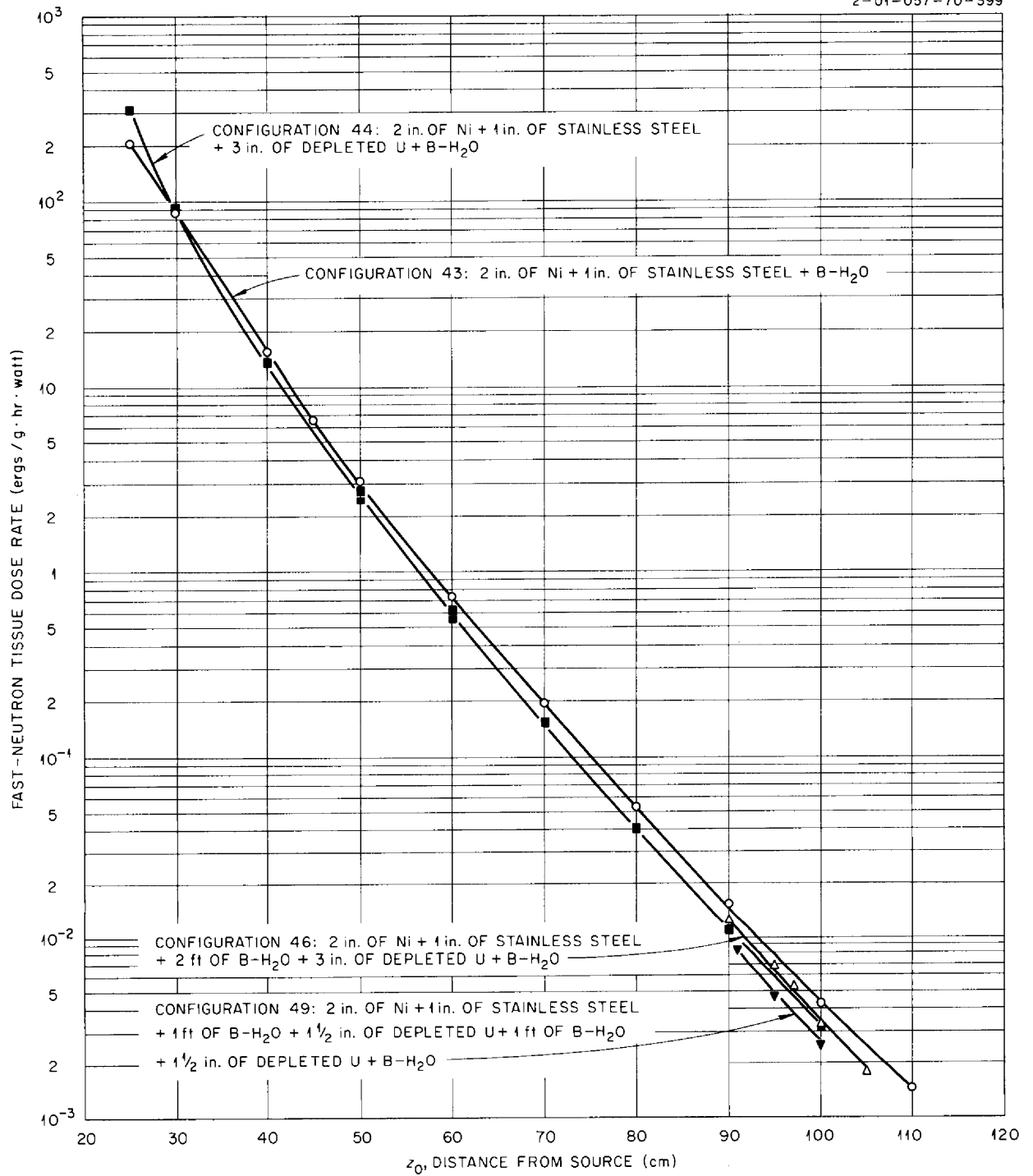Fig. 5.2.5. Thermal-Neutron Fluxes Beyond Configurations 44, 79, 80, and 82.

Fig. 5.2.6. Fast-Neutron Tissue Dose Rates Beyond Configurations 44, 79, 80, and 82.
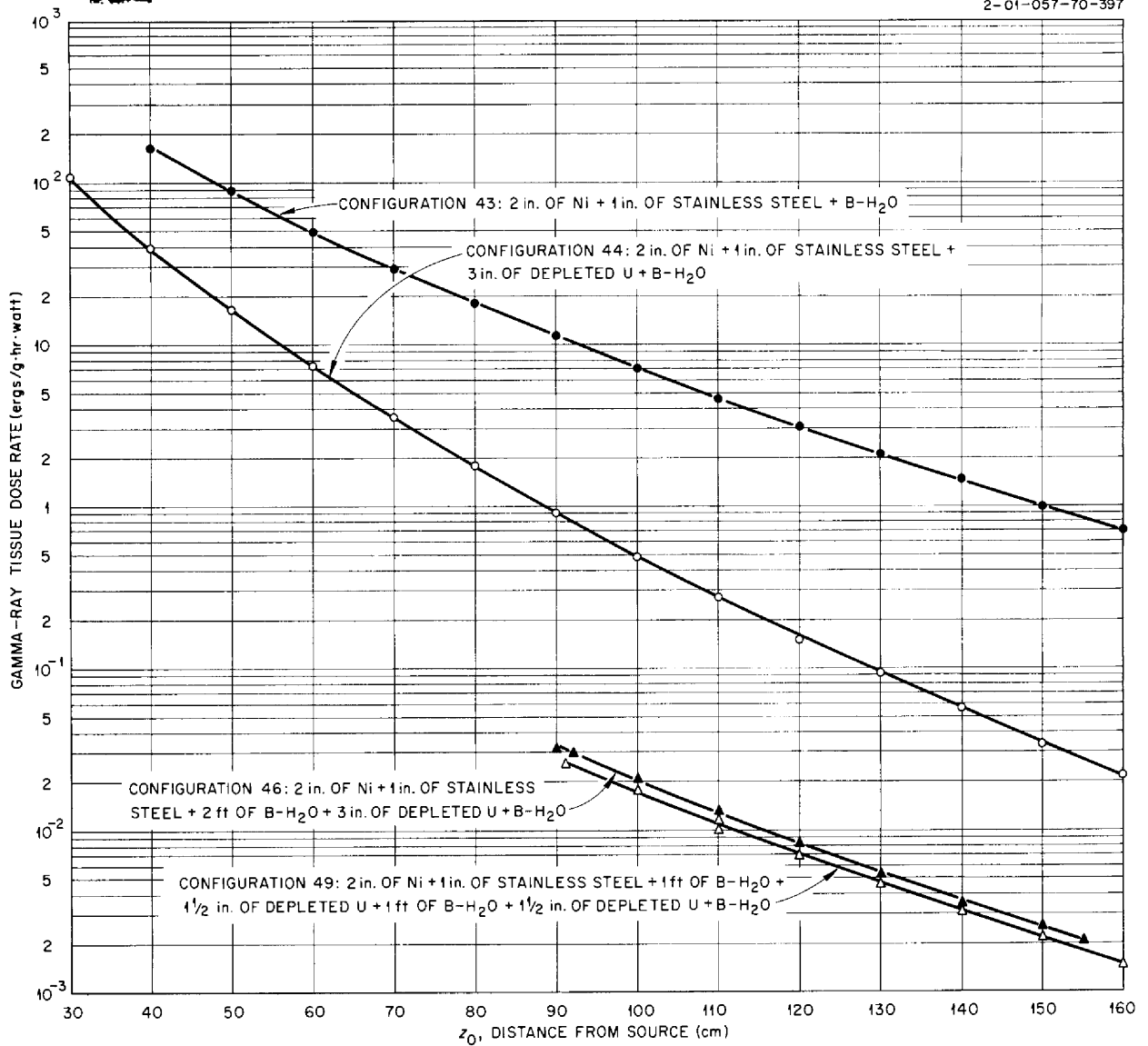
Fig. 5.2.7. Gamma-Ray Tissue Dose Rates Beyond Configurations 43, 44, 46, and 49.

effective gamma-ray shield, the dose rate being reduced about 14%.

The thermal-neutron and fast-neutron measurements beyond configurations 43, 44, 46, and 49 are presented in Figs. 5.2.8 and 5.2.9.

Configurations 44, 46, 47, 83, 84, 85, and 86. — One series of configurations was tested in order to investigate the production of secondary gamma rays in 3 in. of depleted uranium as a function of the amount of borated water preceding it. The results are shown in Fig. 5.2.10.

In going from configuration 44, which contained only the unavoidable amounts of borated water between the solid sections of the configuration, to configuration 83, which contained 3 in. of borated water between the stainless steel and the uranium, the gamma-ray dose rate was reduced by about 55%. The slope of the curve was changed only slightly. A combination of two phenomena is believed to be the cause of this reduction. The first, and probably the most important, is that the production of (n,γ) capture gamma rays in the

Fig. 5.2.8. Thermal-Neutron Fluxes Beyond Configurations 43, 44, 46, and 49.

Fig. 5.2.9. Fast-Neutron Tissue Dose Rates Beyond Configurations 43, 44, 46, and 49.
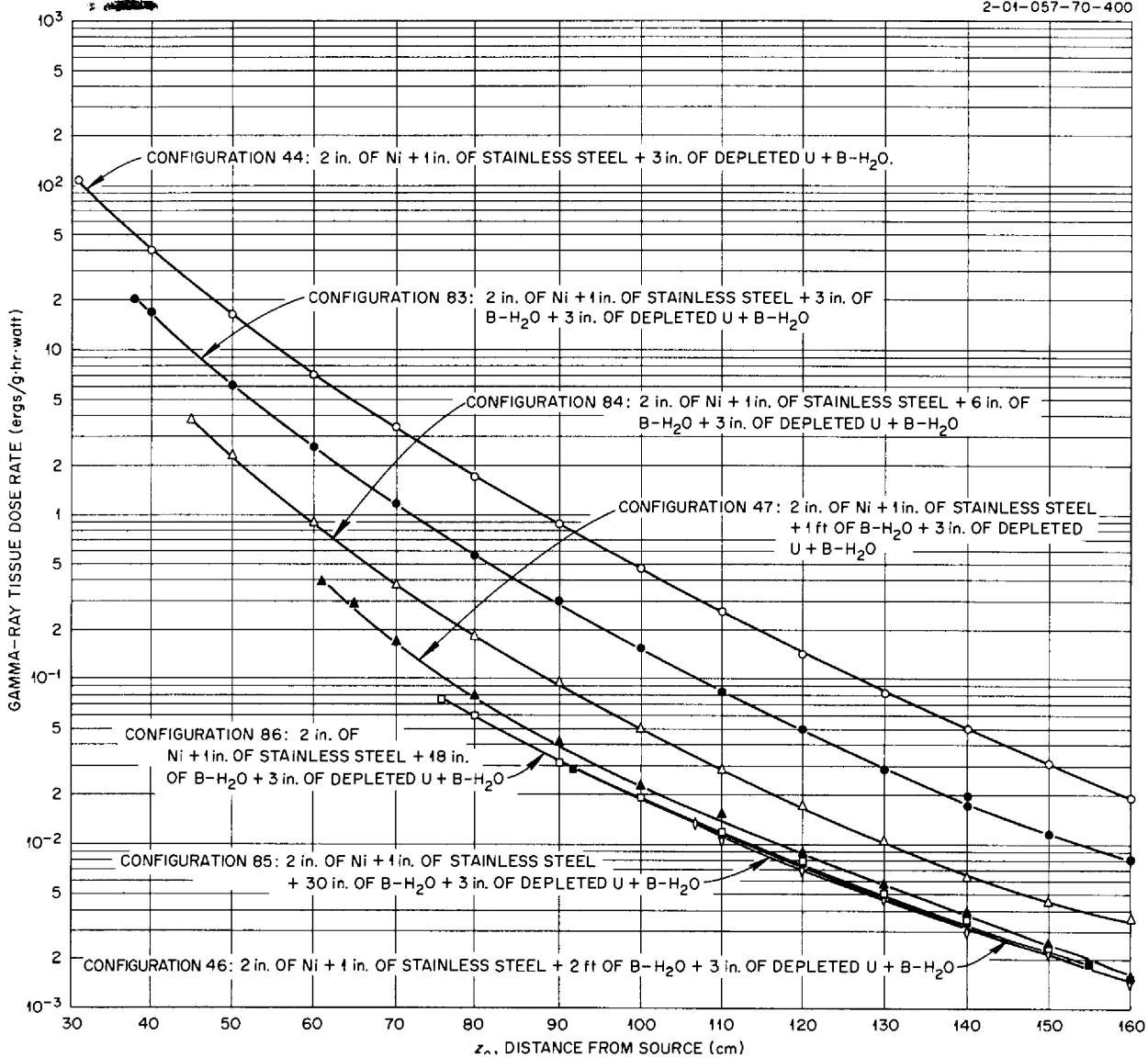
Fig. 5.2.10. Gamma-Ray Tissue Dose Rates Beyond Configurations 44, 46, 47, 83, 84, 85, and 86.

uranium was greatly reduced by the reduction of the incident thermal-neutron flux by the 3 in. of borated water. The second effect is that fissions in the uranium slab caused by intermediate and fast neutrons were largely eliminated by the additional neutron shielding.

In configuration 84, the borated water within the configuration was increased to 6 in., and the additional 3 in. lowered the gamma-ray dose rate by approximately 57% more. This was caused by a further reduction in the secondary contribution. Configuration 47 had 1 ft of borated water in front

of the uranium, and a further reduction in the gamma-ray dose rate of about 55% was effected, which again is attributable to the reduction of the number of secondary gamma rays produced in the uranium.

There was 18 in. of borated water in configuration 86. The gamma-ray dose-rate curve was lowered about 25% from that beyond configuration 47 and had a slightly different slope, possibly indicating a harder spectrum. In configuration 46, in which the amount of borated water was increased to 24 in., the gamma-ray dose-rate curve

was again lowered slightly in the forward region, but, owing to the change in slope, it was raised slightly in the regions farther from the source. It might be concluded that the curve for configuration 46 represents only gamma rays from the source plate; that is, secondary gamma rays produced in the uranium this far out in the borated water are negligible.

Configuration 85 contained 30 in. of borated water, which resulted in a further slight reduction in the gamma-ray dose rate, but this reduction is sufficiently within experimental error as to be inconclusive.

Thermal- and fast-neutron measurements beyond configurations 44, 46, 47, 83, and 84 are shown in Figs. 5.2.11 and 5.2.12, respectively. Thermal-neutron measurements beyond configuration 85 are shown in Fig. 5.2.11, but no fast-neutron measurements were made for this configuration. Neither thermal- nor fast-neutron measurements were made for configuration 86.

Configurations 36, 39, 41, and 43. − A comparison of configurations 43 and 36 shows the effect of adding 2 ft of lithium hydride to the nickel−stainless steel region. There are, however, two other differences between these configurations. The use of the aluminum-canned lithium hydride introduced a $\frac{1}{4}$-in. thickness of aluminum in configuration 36 on each side of the lithium hydride. Also, the solid components in configuration 36 were dry and were backed by borated water in an aluminum tank, which introduced an additional $\frac{1}{8}$-in. thickness of aluminum in configuration 36 just behind the lithium hydride. Between the solid components in configuration 36 there were distributed air gaps totaling 3.4 cm, while in configuration 43 there were distributed borated water gaps totaling 2.6 cm. The use of lithium hydride increased the gamma-ray dose rate, as shown in Fig. 5.2.13. The fact that the gaps were occupied by air rather than borated water probably accounted for some of the increase because of the slightly higher thermal-neutron flux incident on the nickel, stainless steel, and lithium hydride. The decreased density in the region of the shield occupied by the lithium hydride (from 1.05 g/cm^3 for borated water to 0.75 g/cm^3 for lithium hydride) no doubt accounted for a considerable portion of the increase.

The thermal-neutron flux beyond configuration 36 was lowered from that beyond configuration 43 by

about 53% at 83 cm from the source plate and by about 70% at 110 cm (see Fig. 5.2.14). This reduction in flux and change in slope shows the relative attenuation effectiveness of lithium hydride and borated water. This rather large reduction in the thermal-neutron flux is accompanied by a 70% reduction in the fast-neutron dose rate. The obvious advantages of using lithium hydride as a shielding material are illustrated by its good neutron attenuation properties, with only a slight increase in the gamma-ray dose rate, and relatively light weight.

In configuration 39, a $1\frac{1}{2}$-in.-thick slab of depleted uranium was placed behind the 2 ft of lithium hydride in configuration 36. The addition of the uranium resulted in a reduction of the gamma-ray dose rate by about a factor of 20 (see Fig. 5.2.13). This is about the attenuation to be expected for gamma rays of 2 or of 7 Mev, and is not far from that to be expected for intermediate energies. Hence it is unlikely that neutron-induced gamma rays in the uranium are a significant contribution to the gamma-ray dose with the uranium in place.

The slope of the thermal-neutron flux curve for configuration 39 was drastically changed from that for configuration 36 as shown in Fig. 5.2.14. The flux was increased by about a factor of 4 at 88 cm from the source plate but only by about 20% at 100 cm. The curves would probably cross at greater distances. This change might be attributed to the fact that the uranium is a strong inelastic scatterer, and thus it enhances the softer flux near the slab at the expense of that which would penetrate to greater distances. The fast-neutron data for these configurations (Fig. 5.2.15) indicate that the addition of the uranium behind the lithium hydride caused an increase in the fast-neutron dose rate next to the slab, but the data cannot be accurately extrapolated to indicate the situation farther back.

In configuration 41, the $1\frac{1}{2}$-in.-thick slab of uranium was positioned between two 1-ft slabs of lithium hydride. The gamma-ray dose rates were approximately the same as those behind configuration 39 (Fig. 5.2.13), but the thermal-neutron fluxes were reduced considerably (Fig. 5.2.14).

Configurations 38, 39, 40, 41, 90, and 91. − In configuration 38, a second $1\frac{1}{2}$-in. slab of uranium was added to configuration 39, with a resulting
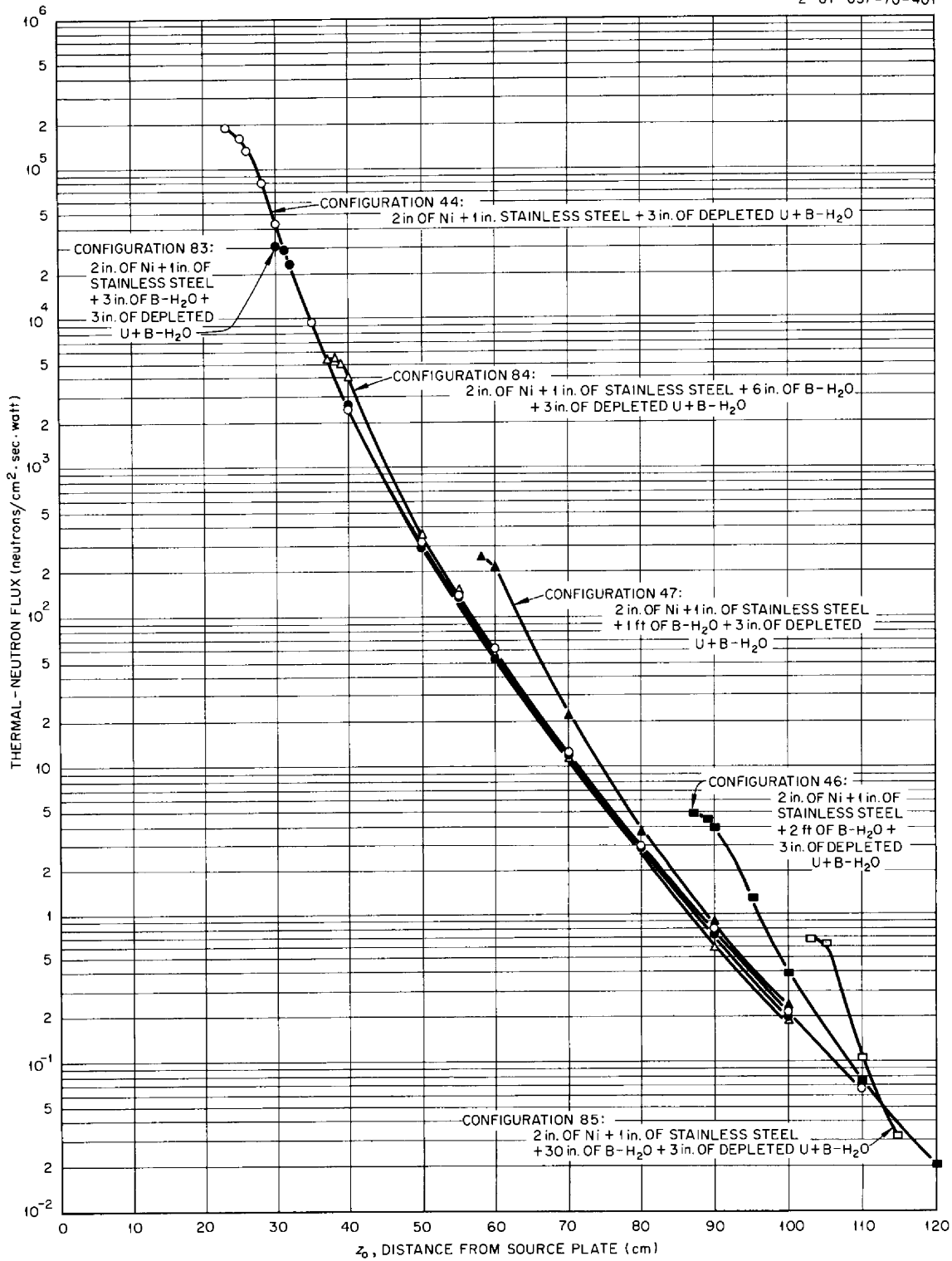
251

2-01-057-70-401

Fig. 5.2.11. Thermal-Neutron Fluxes Beyond Configurations 44, 46, 47, 83, 84, and 85.
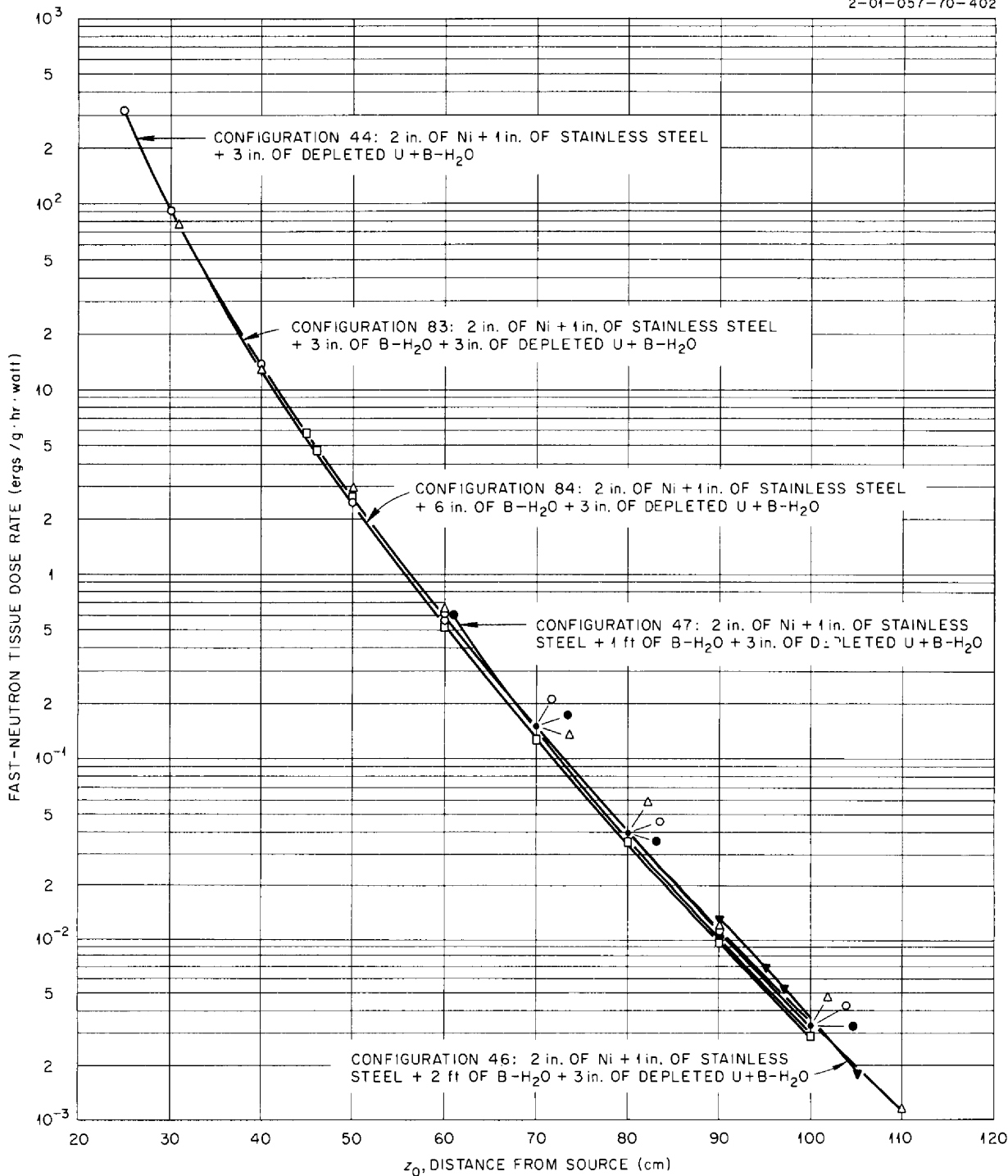
2-01-057-70-402

Fig. 5.2.12. Fast-Neutron Tissue Dose Rates Beyond Configurations 44, 46, 47, 83, and 84.
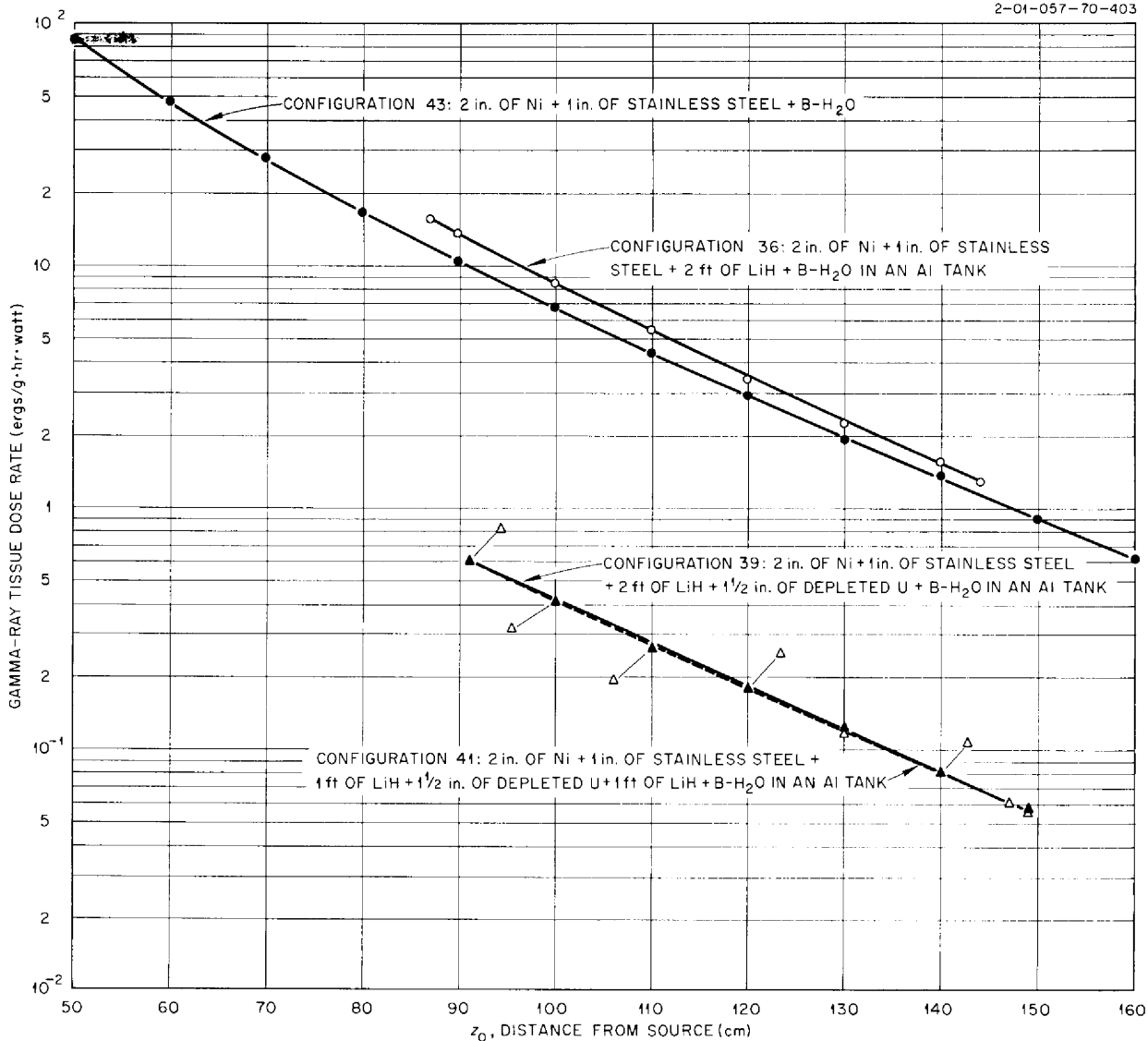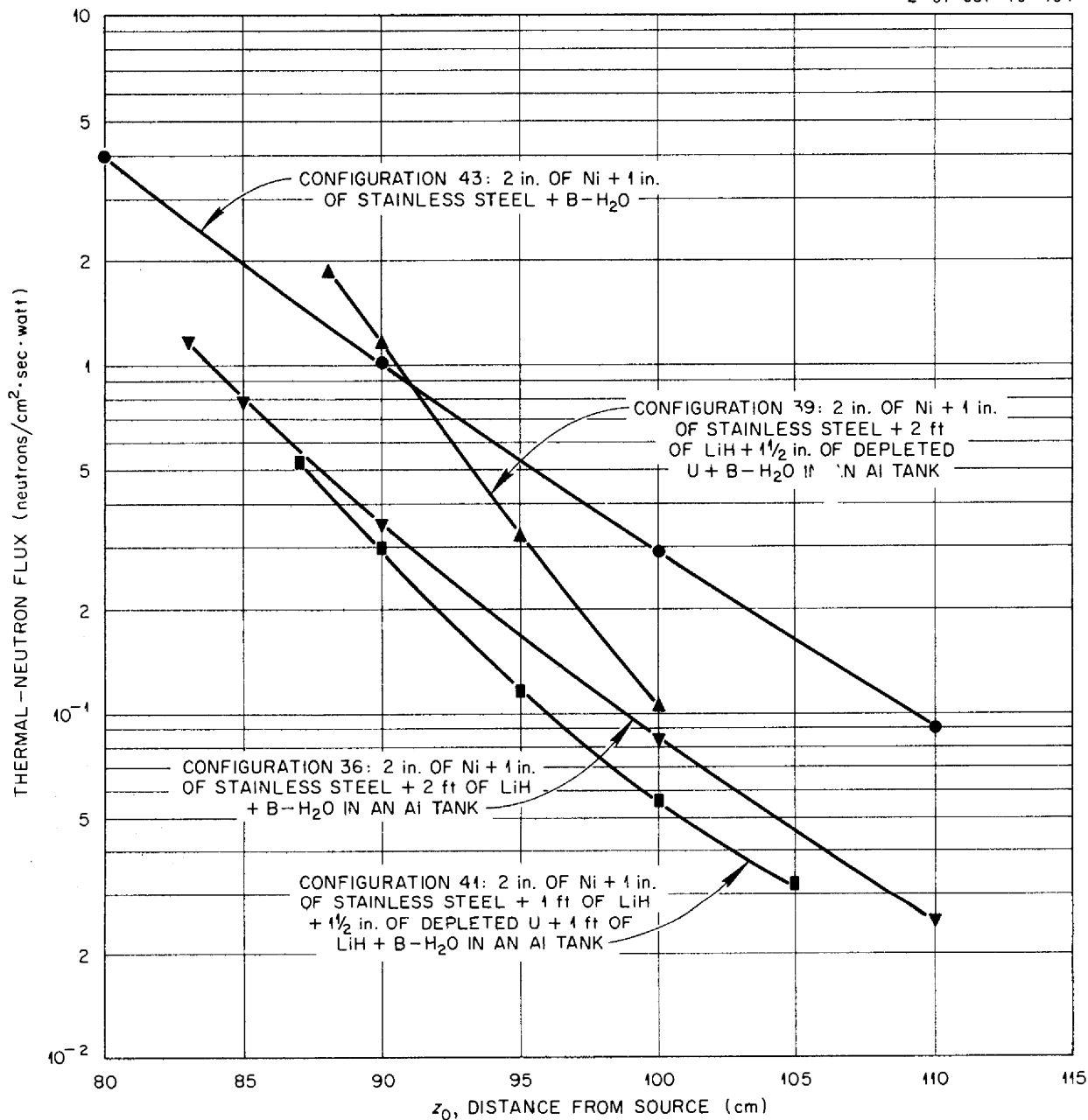
Fig. 5.2.13. Gamma-Ray Dose Rates Beyond Configurations 36, 39, 41, and 43.

lowering of the gamma-ray dose rate by about a factor of 18 (Fig. 5.2.16). This large reduction again indicates negligible secondary gamma-ray production in the uranium. The thermal-neutron curve for configuration 38 was raised over that for configuration 39 in the forward region (Fig. 5.2.17) because of the replacement of borated water with the uranium. The fast-neutron dose rate (Fig. 5.2.18) was lowered about 15%.

The 3 in. of uranium in configuration 38 was repositioned between the two lithium hydride slabs to form configuration 40. Unlike configuration 41, in which $1\frac{1}{2}$ in. of uranium was positioned between the lithium hydride layers, the gamma-ray dose rate in this case was increased by about 80% (Fig. 5.2.16). This increase might be principally attributable to the production of secondary gamma rays in the uranium.

The depleted uranium gamma-ray shield was increased to a thickness of $4\frac{1}{2}$ in. in configurations 90 and 91. Configuration 90 represented the addition of another $1\frac{1}{2}$-in. slab of uranium

2-01-057-70-404

Fig. 5.2.14. Thermal-Neutron Fluxes Beyond Configurations 36, 39, 41, and 43.

2-01-057-70-405
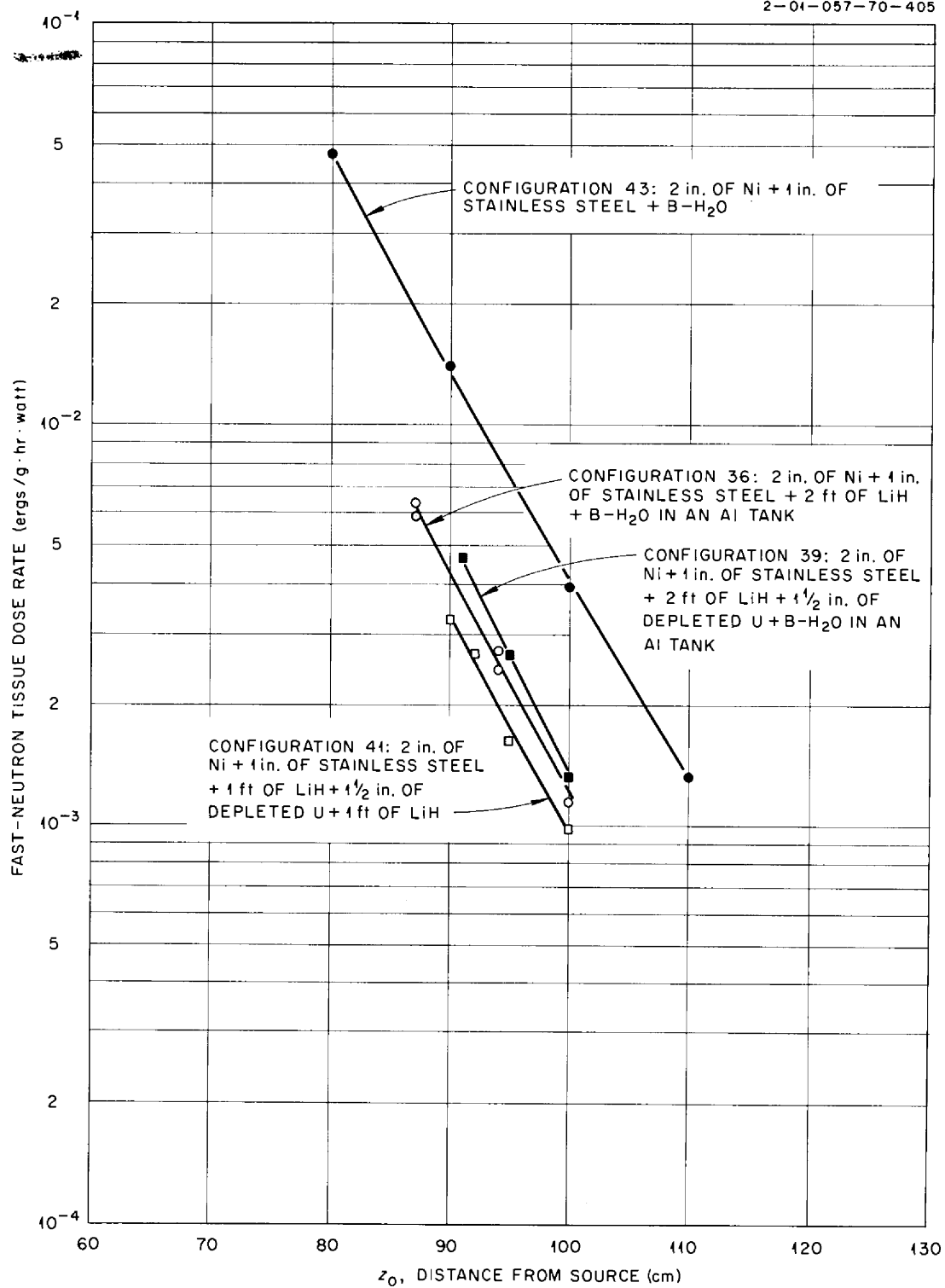
Fig. 5.2.15. Fast-Neutron Tissue Dose Rates Beyond Configurations 36, 39, 41, and 43.
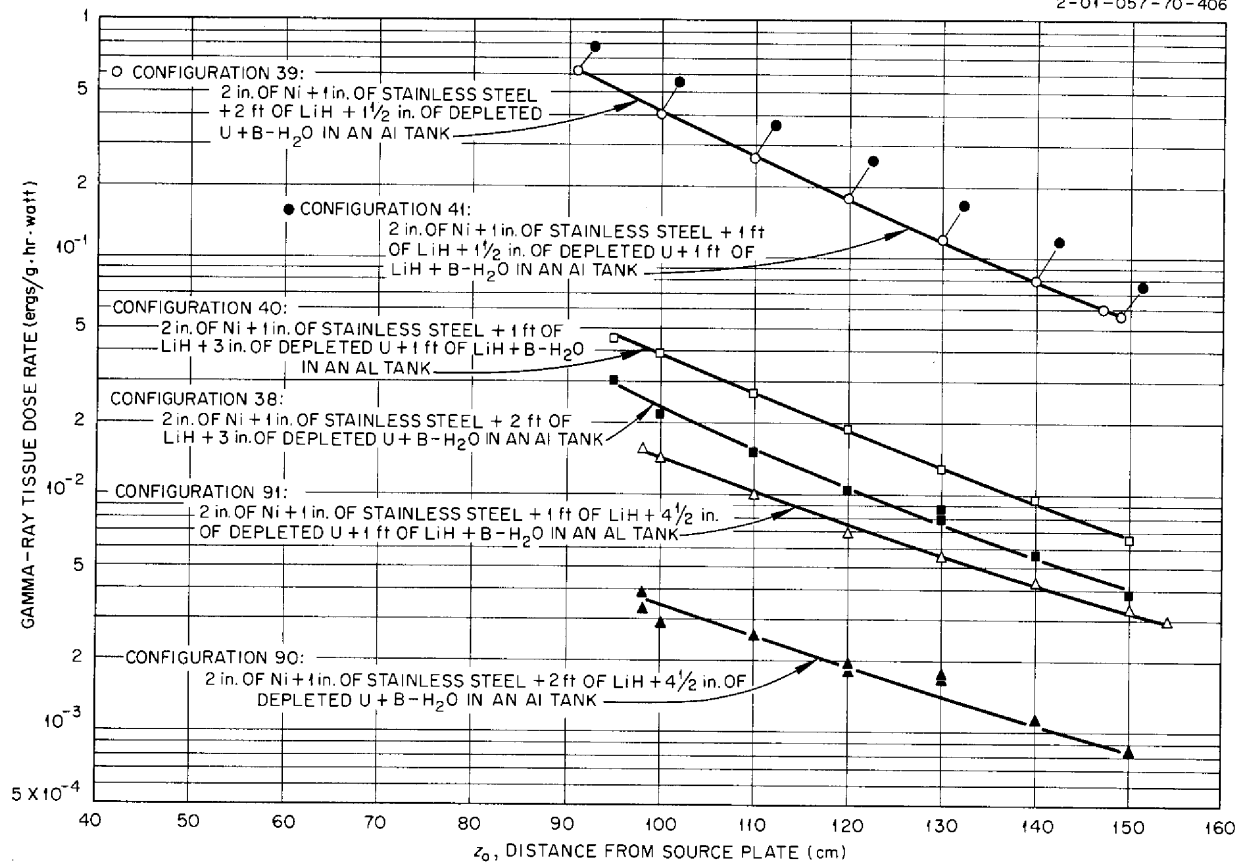
2-01-057-70-406

Fig. 5.2.16. Gamma-Ray Tissue Dose Rates Beyond Configurations 38, 39, 40, 41, 90, and 91.

to configuration 38, and the gamma-ray dose rate beyond configuration 90 was considerably lower than that beyond configuration 38 (Fig. 5.2.16). The slope of the curve was changed slightly, the dose rate for configuration 90 being a factor of 7 lower in the forward region but only a factor of 5 lower in the region farther from the source plate. The thermal-neutron flux curve (Fig. 5.2.17) was shifted by the additional uranium.

In configuration 91, the $4\frac{1}{2}$ in. of uranium was positioned between the two 1-ft-thick slabs of lithium hydride. As was the case when configuration 40 was compared with configuration 38, the gamma-ray dose rate beyond configuration 90 was raised by roughly a factor of 4 over that beyond configuration 91 (see Fig. 5.2.16). This increase is also believed to be due to an increase in the production of secondary gamma rays in the uranium caused by the greater neutron flux incident on

the uranium. The accompanying decrease in the thermal-neutron flux measured behind the configuration (Fig. 5.2.17) tends to justify at least a part of this assumption. No fast-neutron data were obtained for configurations 90 or 91. It should be pointed out that the statistics on the data for this group of configurations were much poorer than those for other data included in this report.

Configurations 36, 37, 38, 40, and 42. – In configuration 37, a 3-in.-thick slab of depleted uranium was placed between the stainless steel and the 2-ft-thick lithium hydride neutron shield. The gamma-ray dose rate beyond the configuration (Fig. 5.2.19) was about a factor of 9 below that beyond configuration 36, in which there was no uranium. This substantial decrease is believed to be largely the result of the increased attenuation of primary gamma rays. A comparison of the data for configurations 37 and 38 indicates
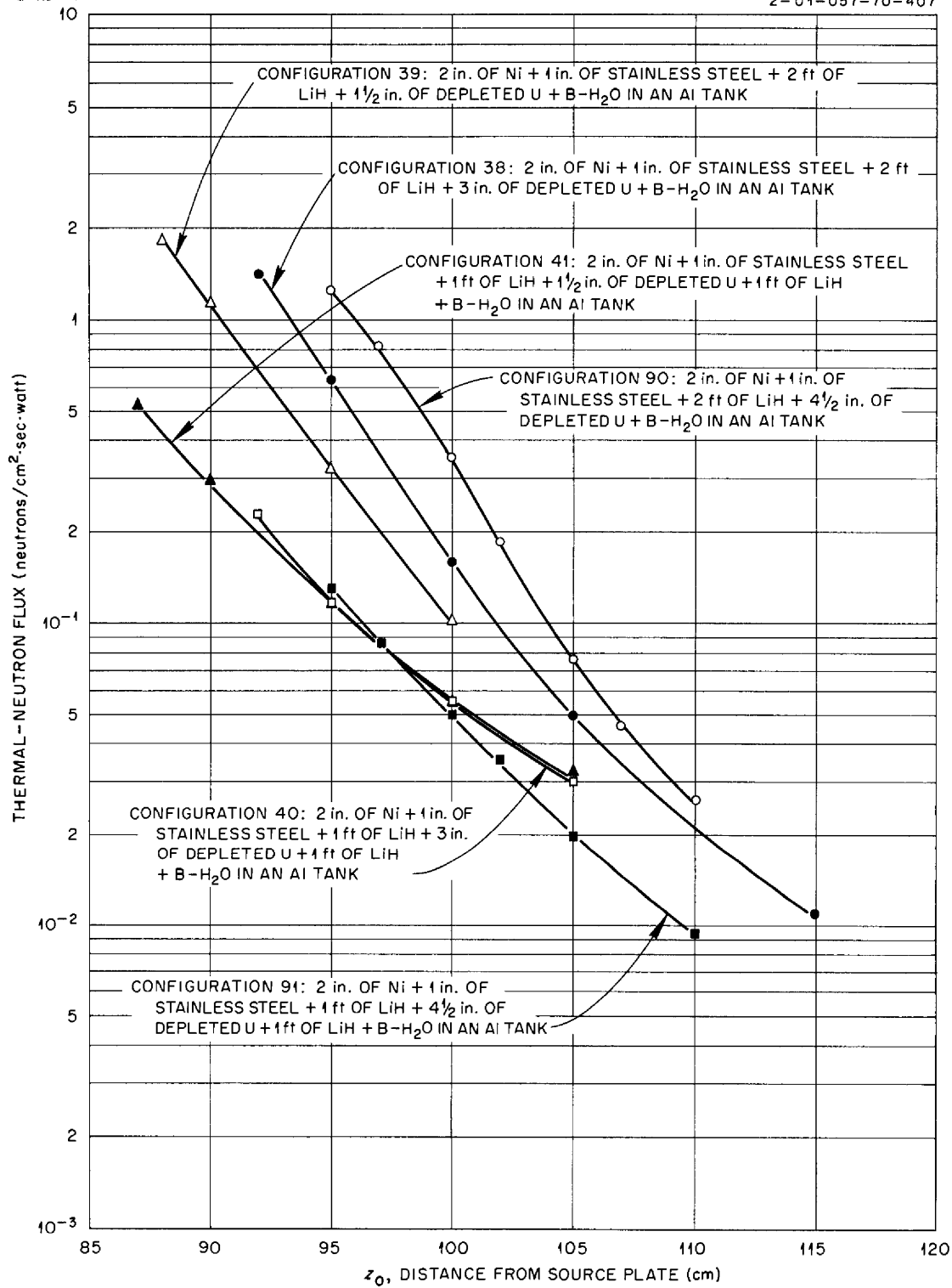
257

Fig. 5.2.17. Thermal-Neutron Fluxes Beyond Configurations 38, 39, 40, 41, 90, and 91.
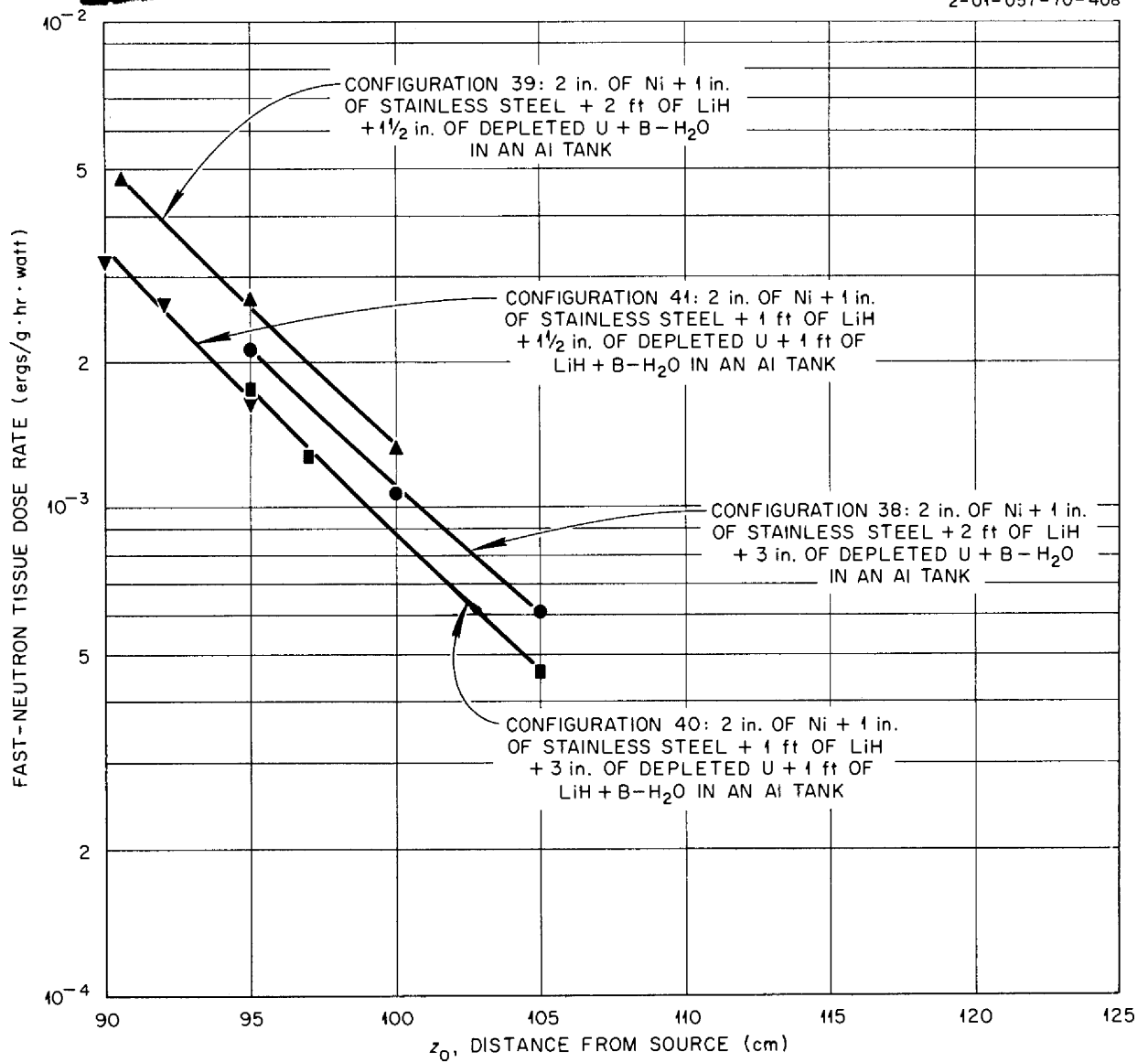
2-01-057-70-408

Fig. 5.2.18. Fast-Neutron Tissue Dose Rates Beyond Configurations 38, 39, 40, and 41.

that the large difference in the gamma-ray dose rate between these configurations is essentially the contribution of secondary gamma rays from the uranium to the total measured dose beyond configuration 37.

Configuration 42 represents a repositioning of configuration 38 so that both the uranium and the lithium hydride components are broken up into two separate layers. The slope of the gamma-ray dose-rate curve (Fig. 5.2.19) was changed by this repositioning. The dose rates were identical for both configurations at 95 cm from the source plate, but the dose rate for configuration 42 was lower by about 15% at 140 cm. The change in the slope of the curve possibly indicates softening of the spectrum as a result of the increased degradation of primary gamma rays. A comparison of configuration 42 with configuration 40, in which only the lithium hydride is separated into two layers, shows that the dose rate beyond configuration 42 is about 45% lower. This decrease is
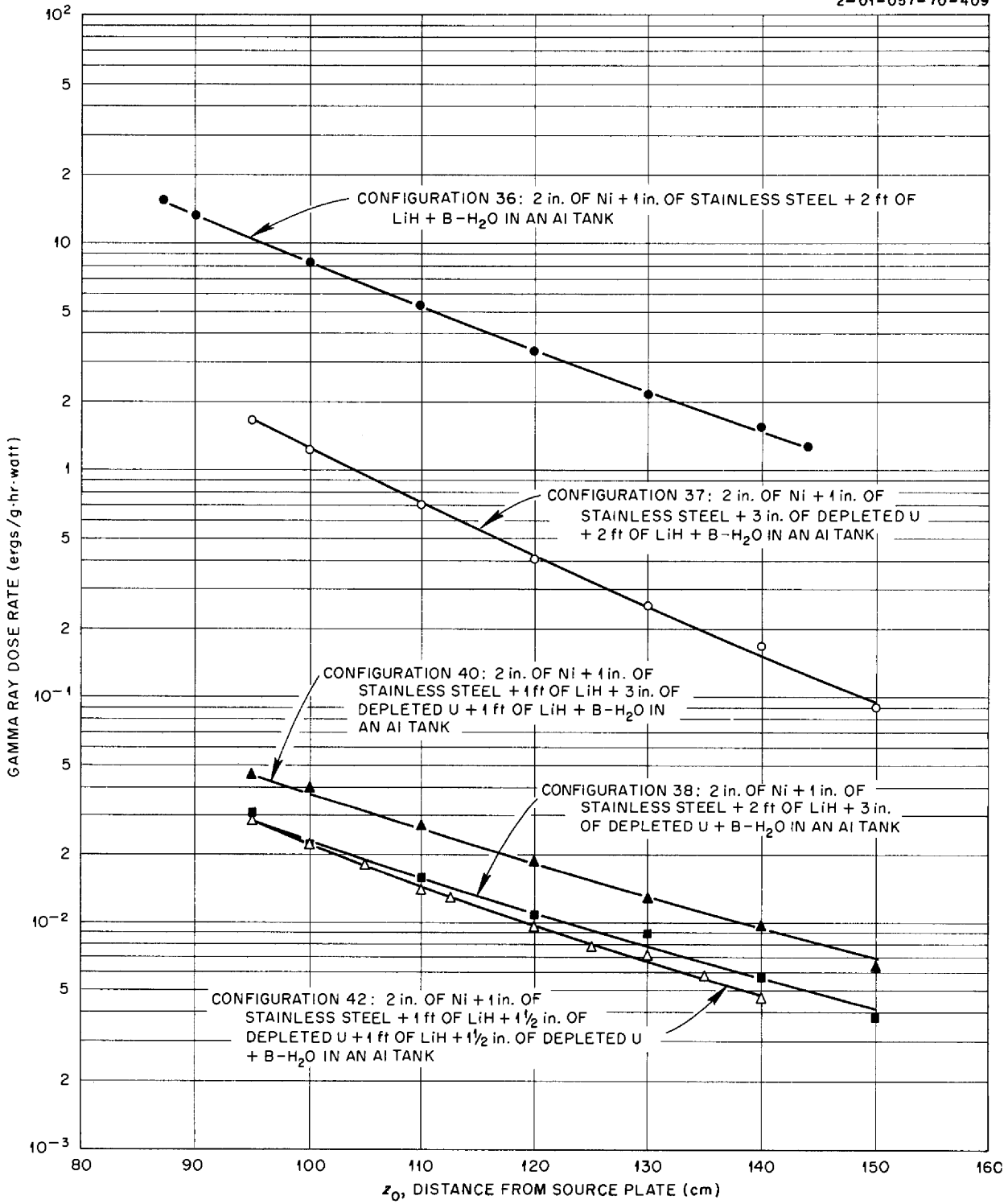
Fig. 5.2.19. Gamma-Ray Dose Rates Beyond Configurations 36, 37, 38, 40, and 42.

believed to be due principally to a reduction in the production of secondary gamma rays in the second $1\frac{1}{2}$-in.-thick slab of uranium.

Thermal-neutron and fast-neutron measurements beyond configurations 37 and 42 are compared with corresponding measurements beyond configurations 36, 38, and 40 in Figs. 5.2.20 and 5.2.21, respectively.

GENERAL ELECTRIC COMPANY SERIES OF ADVANCED SHIELDING MATERIALS STUDIES

D. W. Cady[4]   J. M. Miller

In addition to the series of tests described in the preceding paper, the production of secondary

[4]On assignment from Wright Air Development Center.

2-01-057-70-410
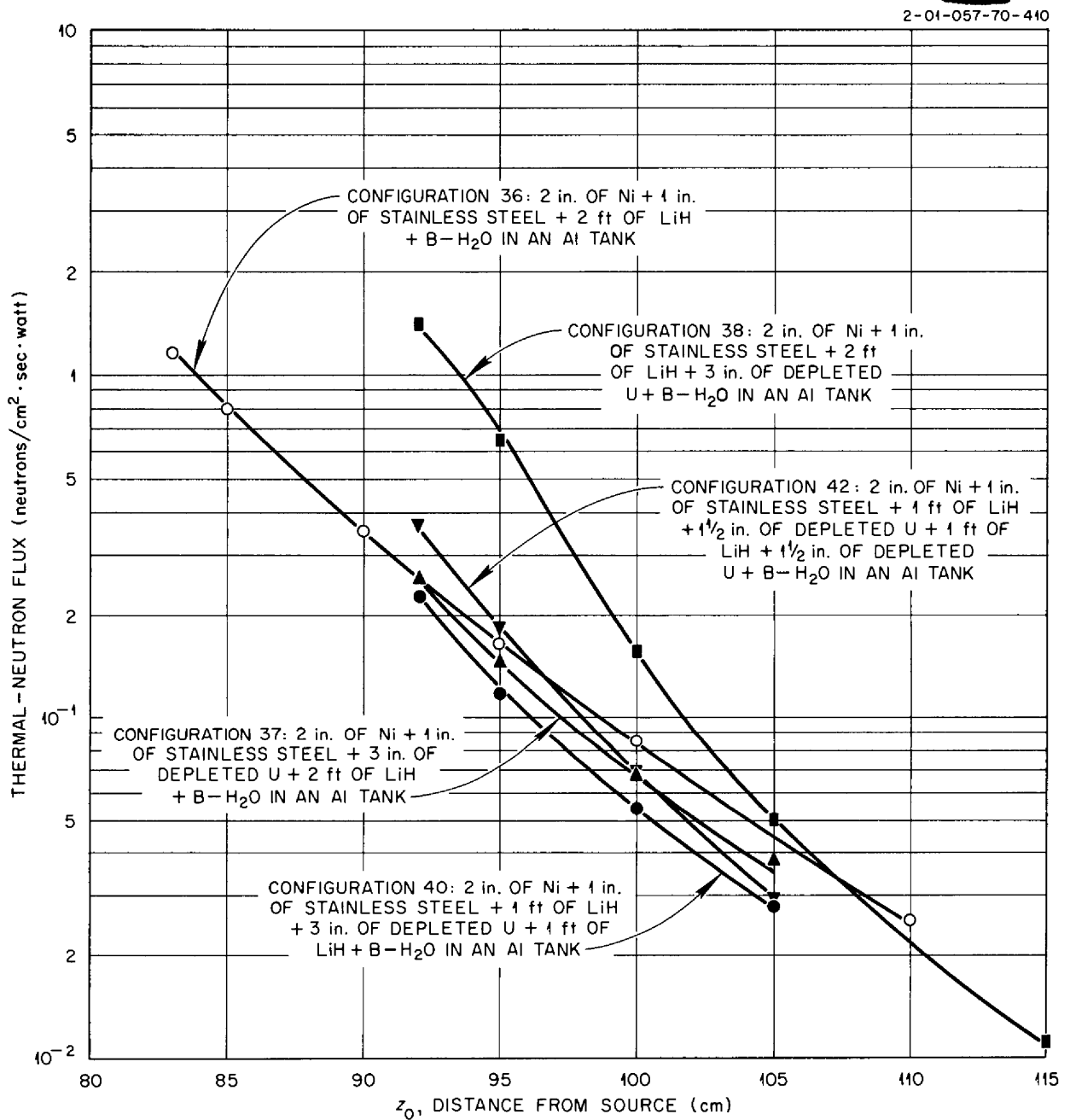
Fig. 5.2.20. Thermal-Neutron Fluxes Beyond Configurations 36, 37, 38, 40, and 42.
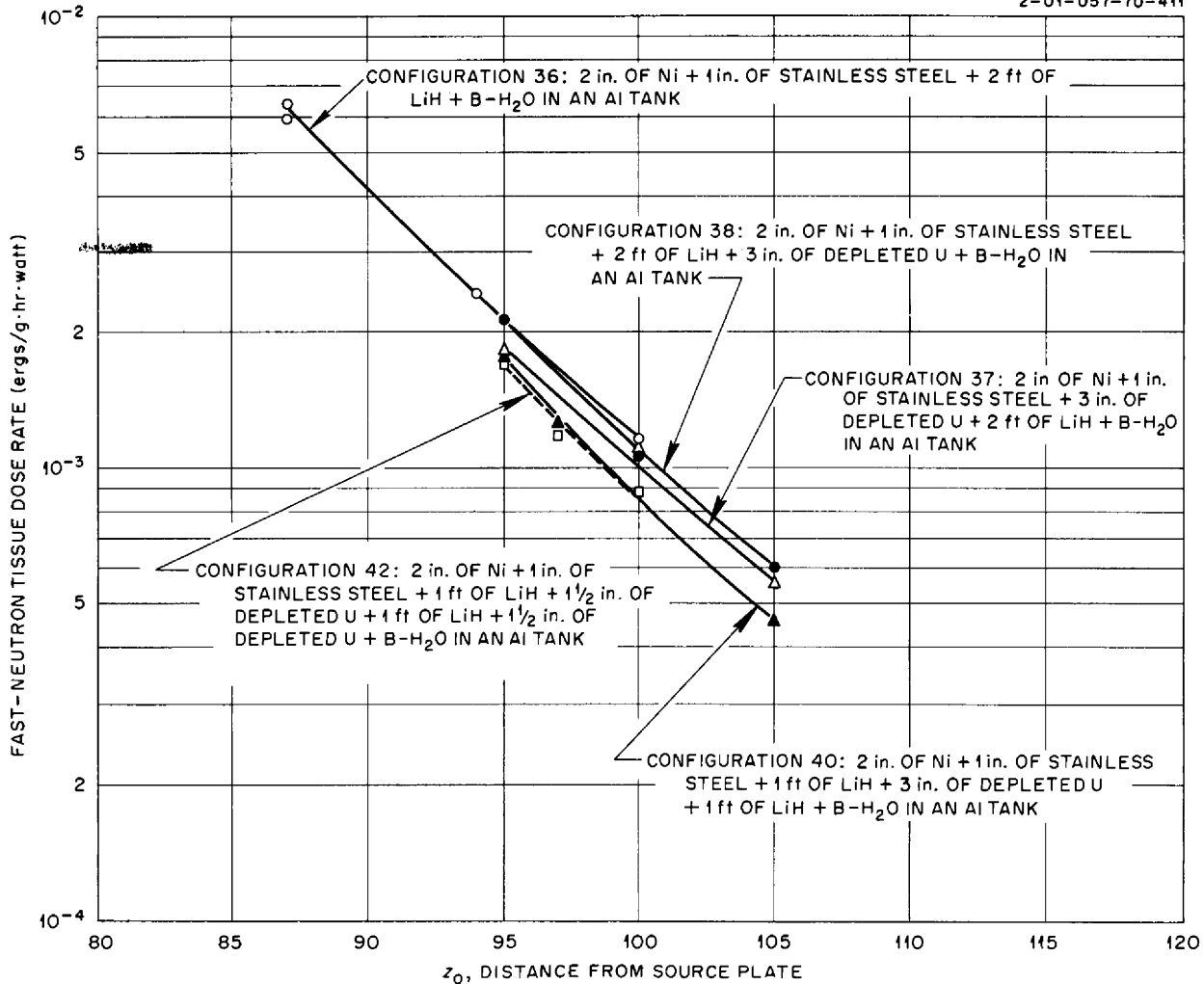
Fig. 5.2.21. Fast-Neutron Tissue Dose Rates Beyond Configurations 36, 37, 38, 40, and 42.

gamma rays in Hevimet, stainless steel, and depleted uranium is being studied in a series of tests designed by the General Electric Company to support their ANP effort. This experiment is essentially a continuation of an earlier experiment, No. 69, which was described previously.[5] In general, the configurations used in this series consist of an oil layer adjacent to the source plate followed by a 4-in.-thick beryllium layer, a gamma-ray shield of one of the three materials being studied, and a 12-in.-thick lithium hydride

neutron shield. All the configurations are submerged in oil, and measurements of the gamma-ray dose rate are made in the oil at various distances beyond the lithium hydride. Thermal-neutron flux measurements are made beyond a few configurations. The effect of inserting boral within several of the configurations is also being studied. The configurations tested thus far are described in Table 5.2.3, and the physical properties of the various materials used in the configurations are presented in Table 5.2.4.

The first group of tests in this series was designed for a determination of the effectiveness of an oil layer preceding the configuration in reducing the secondary gamma-ray production within the

---

[5] R. W. Peelle *et al.*, *ANP Quar. Prog. Reps. June 10, 1956*, ORNL-2106, p 269; *Sept. 10, 1956*, ORNL-2157, p 278; *Dec. 31, 1956*, ORNL-2221, p 335.

Table 5.2.3. Description of Configurations Tested in GE Series

Configuration Number	Description of Configuration	Location of Probe, z_0 (cm)	Unavoidable Oil Gap Within Configuration (cm)
1-A	2.9 cm of oil + 4 in. of Be + 2 in. of Hevimet + 12 in. of LiH + oil	55.2	3.4
1-B	12.9 cm of oil + 4 in. of Be + 2 in. of Hevimet + 12 in. of LiH + oil	66.0	3.2
1-C	22.9 cm of oil + 4 in. of Be + 2 in. of Hevimet + 12 in. of LiH + oil	74.6	1.8
1-D	32.9 cm of oil + 4 in. of Be + 2 in. of Hevimet + 12 in. of LiH + oil	85.0	2.2
1-E	40.6 cm of oil + 4 in. of Be + 2 in. of Hevimet + 12 in. of LiH + oil	92.0	0.5
1-F	1 cm of oil + 4 in. of Be + $\frac{1}{2}$ in. of boral + 2 in. of Hevimet + 12 in. of LiH + oil	56.2	3.1
1-G	1 cm of oil + 4 in. of Be + $\frac{1}{2}$ in. of boral + 2 in. of Hevimet + $\frac{1}{2}$ in. of boral + 12 in. of LiH + oil	58.0	3.6
2-A	1.0 cm of oil + 4 in. of Be + 4 in. of stainless steel + 12 in. of LiH + oil	58.0	2.3
2-B	11.0 cm of oil + 4 in. of Be + 4 in. of stainless steel + 12 in. of LiH + oil	67.6	2.9
2-C	21.0 cm of oil + 4 in. of Be + 4 in. of stainless steel + 12 in. of LiH + oil	77.2	2.5
2-D	31.0 cm of oil + 4 in. of Be + 4 in. of stainless steel + 12 in. of LiH + oil	87.2	2.5
2-E	37.2 cm of oil + 4 in. of Be + 4 in. of stainless steel + 12 in. of LiH + oil	93.6	0.7
2-F	1.0 cm of oil + 4 in. of Be + $\frac{1}{2}$ in. of boral + 4 in. of stainless steel + 12 in. of LiH + oil	59.8	2.9
2-G	1.0 cm of oil + 4 in. of Be + $\frac{1}{2}$ in. of boral + 4 in. of stainless steel + $\frac{1}{2}$ in. of boral + 12 in. of LiH + oil	61.0	2.8
2-H	9.7 cm of oil + 4 in. of Be + $\frac{1}{2}$ in. of boral + 4 in. of stainless steel + 12 in. of LiH + oil	68.4	2.8
2-I	11.2 cm of oil + 4 in. of Be + 4 in. of stainless steel + $\frac{1}{2}$ in. of boral + 12 in. of LiH + oil	69.4	2.3
2-J	9.7 cm of oil + 4 in. of Be + $\frac{1}{2}$ in. of boral + 4 in. of stainless steel + $\frac{1}{2}$ in. of boral + 12 in. of LiH + oil	69.4	2.5
2-K	27.8 cm of oil + 4 in. of Be + $\frac{1}{2}$ in. of boral + 4 in. of stainless steel + 12 in. of LiH + oil	84.6	0.9
2-L	1.0 cm of oil + 4 in. of Be + 8.7 cm of oil + $\frac{1}{2}$ in. of boral + 4 in. of stainless steel + 12 in. of LiH + oil	68.4	2.8

Table 5.2.3 (continued)

Configuration Number	Description of Configuration	Location of Probe, z_0 (cm)	Unavoidable Oil Gap Within Configuration (cm)
2-M	1.0 cm of oil + 4 in. of Be + $\frac{1}{2}$ in. of boral + 8.7 cm of oil + 4 in. of stainless steel + 12 in. of LiH + oil	68.4	2.8
3-A	4.2 cm of oil + 4 in. of Be + $1\frac{1}{2}$ in. of depleted U + 12 in. of LiH + oil	53.4	1.9
3-B	13.8 cm of oil + 4 in. of Be + $1\frac{1}{2}$ in. of depleted U + 12 in. of LiH + oil	62.8	1.7
3-C	24.2 cm of oil + 4 in. of Be + $1\frac{1}{2}$ in. of depleted U + 12 in. of LiH + oil	73.4	1.9
3-D	33.2 cm of oil + 4 in. of Be + $1\frac{1}{2}$ in. of depleted U + 12 in. of LiH + oil	82.2	1.7
3-E	40.8 cm of oil + 4 in. of Be + $1\frac{1}{2}$ in. of depleted U + 12 in. of LiH + oil	89.8	1.7
3-F	1.0 cm of oil + 4 in. of Be + $\frac{1}{2}$ in. of boral + $1\frac{1}{2}$ in. of depleted U + 12 in. of LiH + oil	51.8	1.2
3-G	1.0 cm of oil + 4 in. of Be + $\frac{1}{2}$ in. of boral + $1\frac{1}{2}$ in. of depleted U + $\frac{1}{2}$ in. of boral + 12 in. of LiH + oil	53.8	1.9
4-A	1.0 cm of oil + 4 in. of stainless steel + oil	15.8	2.0
4-B	11.0 cm of oil + 4 in. of stainless steel + oil	26.4	2.6
4-C	21.0 cm of oil + 4 in. of stainless steel + oil	35.2	1.4
4-D	31.0 cm of oil + 4 in. of stainless steel + oil	44.8	1.0
4-E	41.0 cm of oil + 4 in. of stainless steel + oil	56.0	2.2
4-F	51.0 cm of oil + 4 in. of stainless steel + oil	65.2	1.4
4-G	61.0 cm of oil + 4 in. of stainless steel + oil	75.4	1.6
4-H	71.0 cm of oil + 4 in. of stainless steel + oil	86.2	2.4
5-A	1.0 cm of oil + 4 in. of Be + 12 in. of LiH + oil	46.0	0.5

gamma-ray shield. Figure 5.2.22 shows that increasing the thickness of the oil layer preceding a beryllium–Hevimet–lithium hydride shield (configurations 1-A through 1-E) from 2.9 to 12.9 cm reduced the gamma-ray dose rate beyond the shield approximately 35%. Increasing the thickness of the oil layer another 10 cm decreased the gamma-ray dose rate an additional 16%. Oil layers greater than 22.9 cm appeared to have no further effect. This information can be used to determine the optimum thickness of the oil layer for the contemplated reactor-shield configuration. The oil

layers had approximately the same effect in tests of similar configurations with stainless steel (configurations 2-A through 2-E) and with depleted uranium (configurations 3-A through 3-E), as shown in Figs. 5.2.23 and 5.2.24.

In all the tests described above an attempt was made to increase the thickness of the oil layer in 10-cm increments. The fact that the configuration tank used to hold the shield components had a 1-cm recess in the tank wall adjacent to the source plate (see preceding section) made it impossible to obtain an oil layer smaller than

Table 5.2.4. Physical Properties of Materials Used for LTSF Mockup Tests
of Advanced Shielding Materials (G-E Series)

| Material	Actual Thickness per Slab (cm)	Description
Transformer oil		Specific gravity, 0.88 at 15.6°C; nominal composition, 86.5 wt % C—12.5 wt % H
Beryllium	10.16	48 × 49 × 4-in. metallic slabs
Hevimet	6.35	5-ft × 5-ft × 2-in. slabs made from smaller pieces held together with 5-ft × 5-ft × $\frac{1}{4}$-in. Al sheet; composition, 90 wt % W—6 wt % Ni—4 wt % Cu; density of Hevimet, 16.9 to 17.2 g/cm^3
Type 347 stainless steel	2.54	See Table 5.2.2
Uranium	3.81	See Table 5.2.2
Lithium hydride	32	See Table 5.2.2
Boral	1.3	See Table 5.2.2
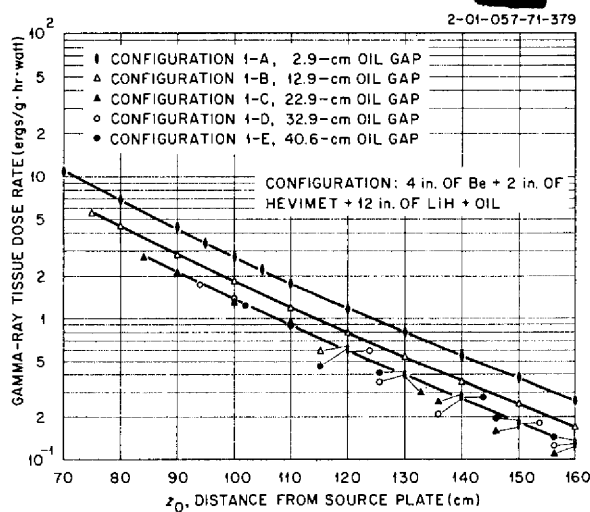
Fig. 5.2.22. Gamma-Ray Tissue Dose Rates Beyond Configurations 1-A Through 1-E: Effect of Increasing the Thickness of the Oil Gap Preceding Shields Containing Hevimet.

1 cm, as is evident in configuration 2-A. Moreover, the design specifications set by GE for the experiment required that the centers of the gamma-ray shields in configurations 1-A, 2-A, and 3-A be equidistant from the source plate. Since the gamma-ray shields used in configurations 1-A and 3-A were thinner than the gamma-ray shield used in configuration 2-A, the oil layers preceding these configurations were necessarily thicker.

A cross plot of the data presented in Figs. 5.2.22 through 5.2.24 is shown in Fig. 5.2.25, which presents the gamma-ray dose rate at 100 cm from the source plate as a function of the distance between the source plate and the center of the gamma-ray shield for each of the three tests. This cross plot indicates that the minimum thickness of the oil layer preceding the beryllium for the lowest gamma-ray dose is approximately 20 cm.

In several configurations $\frac{1}{2}$-in.-thick sheets of boral were placed adjacent to or near the gamma-ray shield. The purpose of these tests was to

2—01—057—71—380
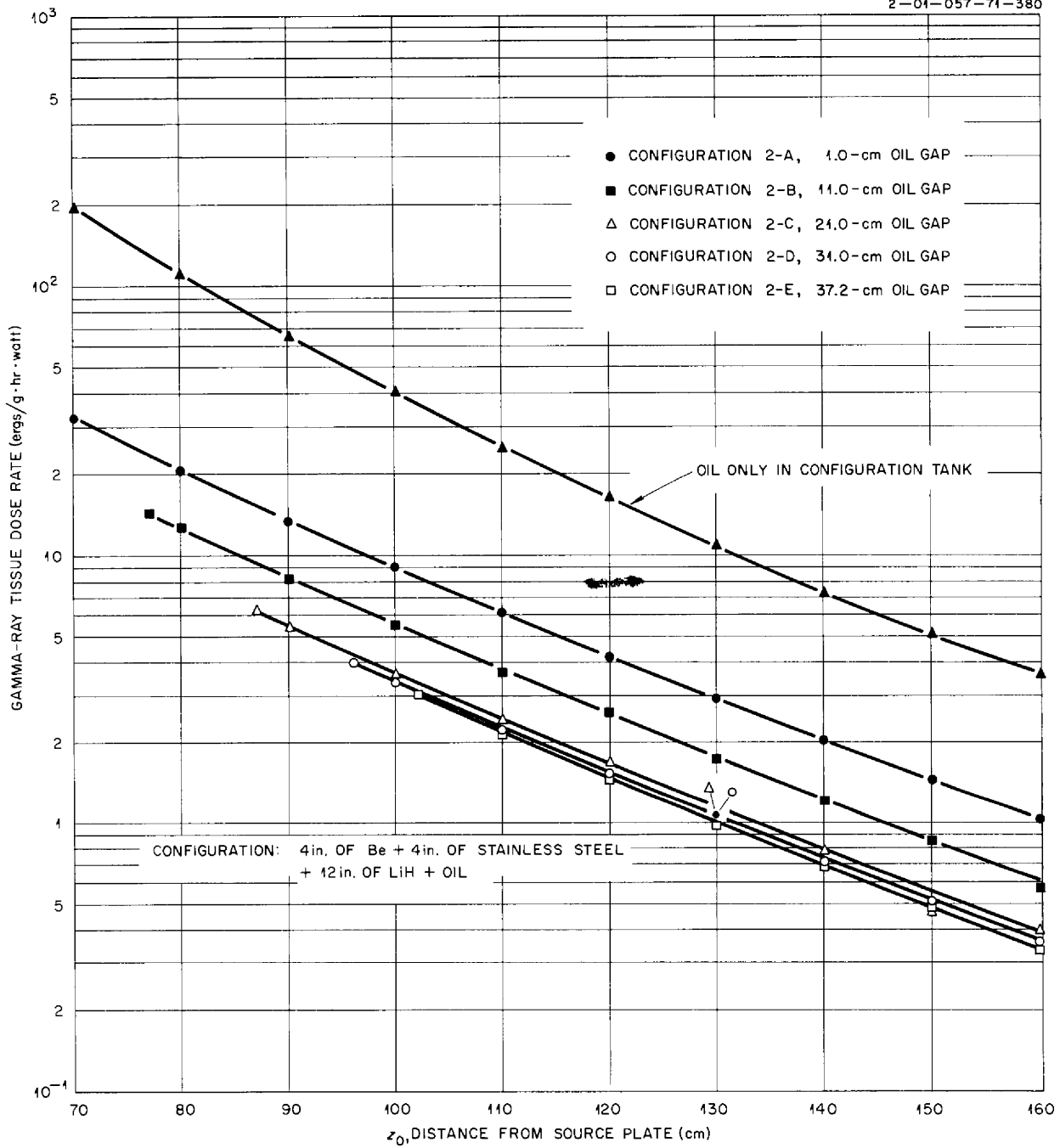
Fig. 5.2.23. Gamma-Ray Tissue Dose Rates Beyond Configurations 2-A Through 2-E: Effect of Increasing the Thickness of the Oil Gap Preceding Shields Containing Stainless Steel.
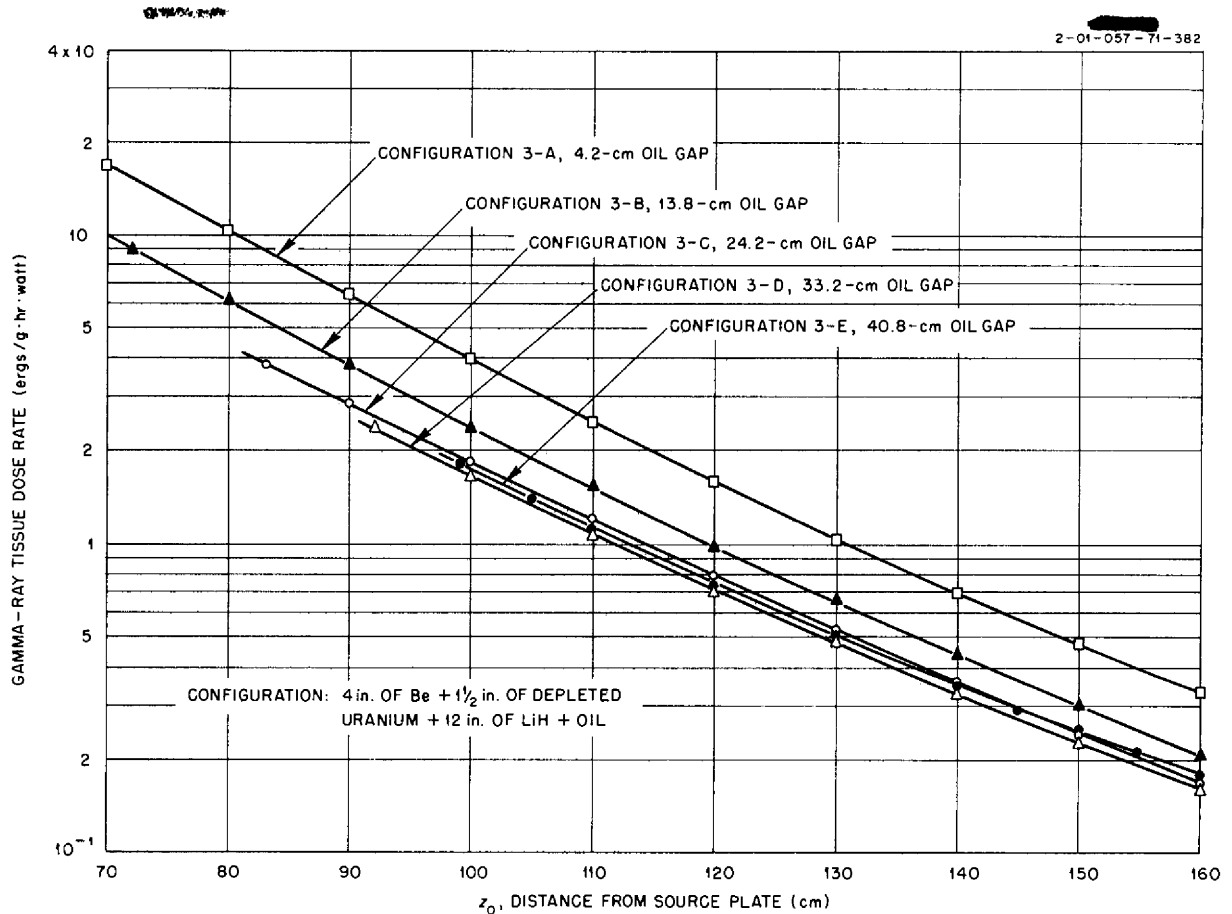
Fig. 5.2.24. Gamma-Ray Tissue Dose Rates Beyond Configurations 3-A Through 3-E: Effect of Increasing the Thickness of the Oil Gap Preceding Shields Containing Depleted Uranium.

determine the effectiveness of boral in reducing the secondary gamma-ray production in the gamma-ray shield. In configurations 1-F, 2-F, and 3-F, a single sheet of boral was placed immediately in front of the gamma-ray shield, while in configurations 1-G, 2-G, and 3-G the boral was positioned both before and after the shield. The measurements (Fig. 5.2.26) showed that placing the boral in front of the Hevimet reduced the dose rate beyond the shield approximately 31%. Positioning a second boral sheet behind the Hevimet produced a further slight reduction, which may be within experimental error. Placing the boral in front of the stainless steel reduced the dose rate beyond the shield approximately 47% (Fig. 5.2.27). The second boral sheet behind the stainless steel again produced a further slight reduction. In

configurations with depleted uranium, the addition of the boral sheet in front of the uranium reduced the gamma-ray dose rate 51% at a distance 70 cm from the source but only 39% at a distance of 160 cm (Fig. 5.2.28). A second boral sheet placed behind the gamma-ray shield again reduced the dose rate only slightly.

Several other tests were performed with variations of the configurations containing stainless steel, the results of which are plotted in Fig. 5.2.29. In configurations preceded by an approximately 9-cm-thick oil layer (configurations 2-H and 2-J), the addition of a second boral sheet behind the stainless steel reduced the gamma-ray dose rate about 10%. It is felt that no particular significance can be attached to the 10% reduction
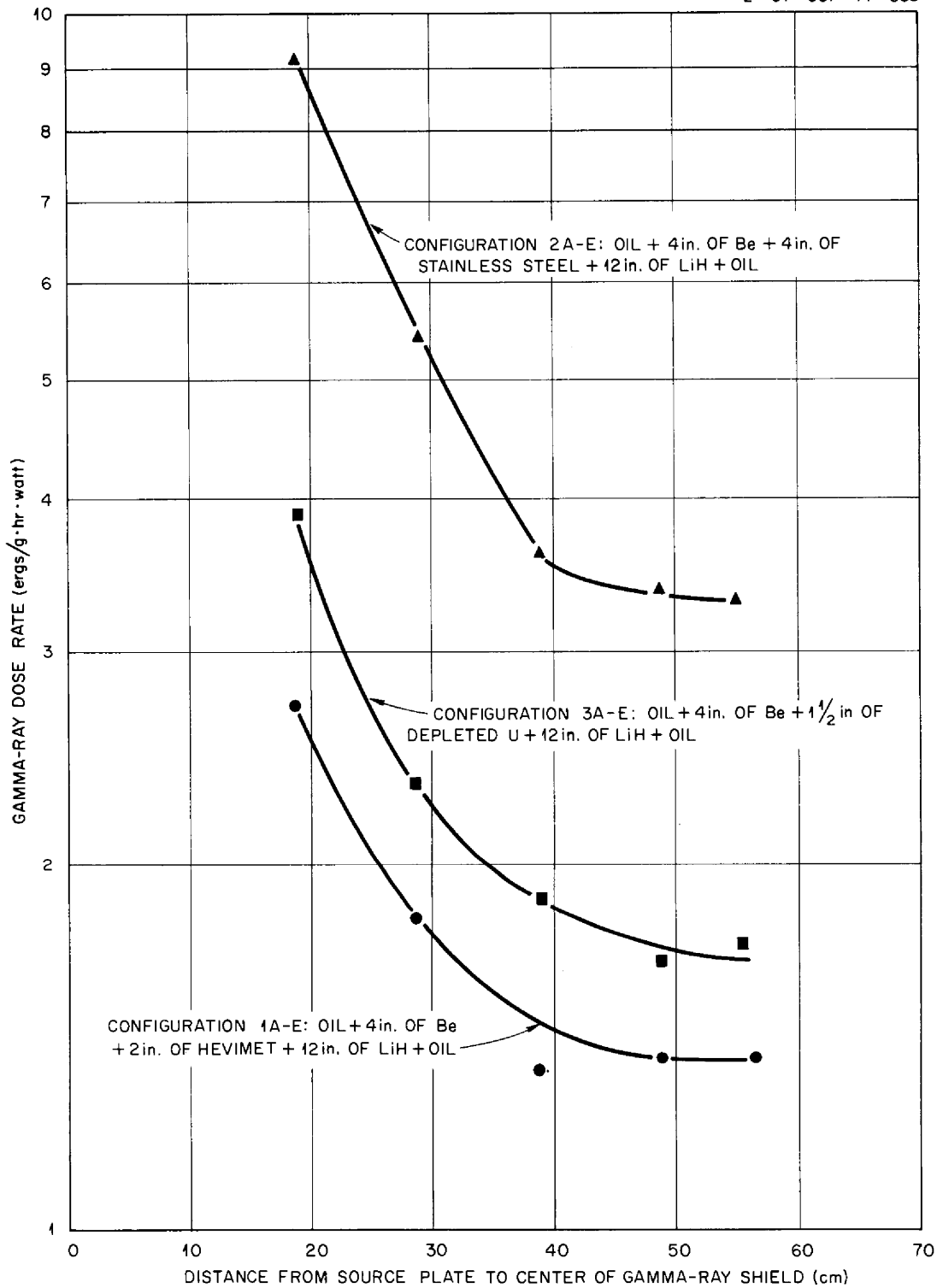
Fig. 5.2.25. Gamma-Ray Tissue Dose Rates 100 cm from the Source Plate as a Function of the Distance Between the Source Plate and the Center of the Gamma-Ray Shield (Configurations 1-A Through 1-E, 2-A Through 2-E, and 3-A Through 3-E).
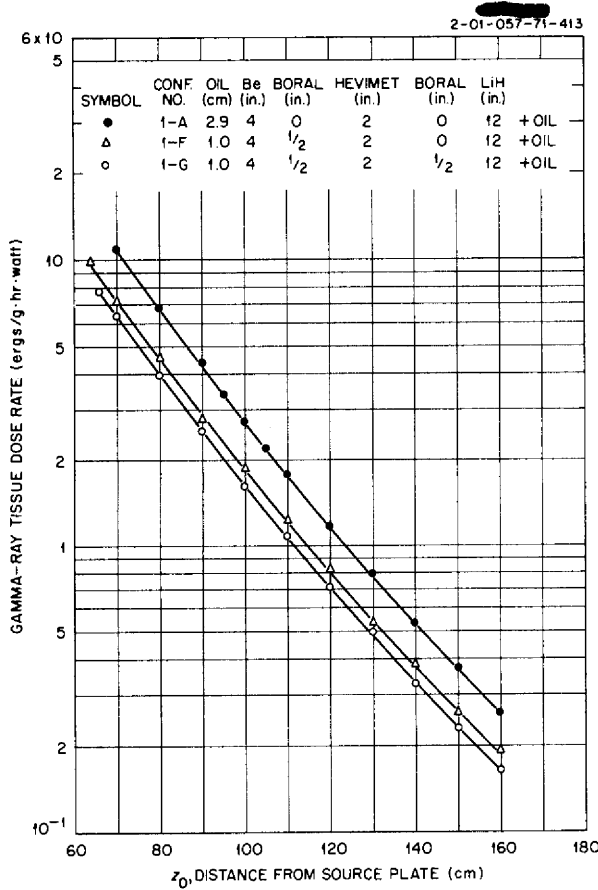
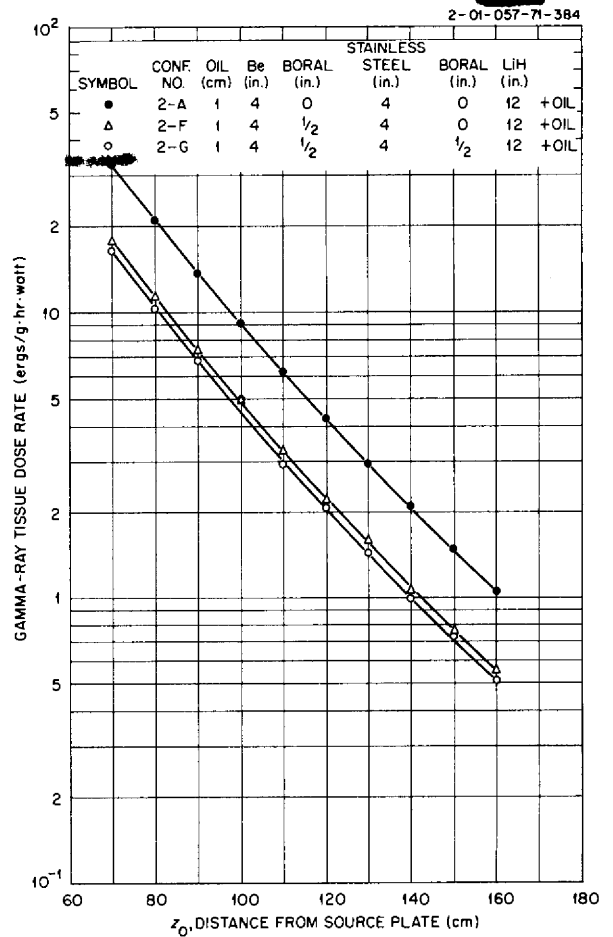| SYMBOL	CONF. NO.	OIL (cm)	Be (in.)	BORAL (in.)	HEVIMET (in.)	BORAL (in.)	LiH (in.)	
●	1-A	2.9	4	0	2	0	12	+OIL
Δ	1-F	1.0	4	½	2	0	12	+OIL
○	1-G	1.0	4	½	2	½	12	+OIL

Fig. 5.2.26. Gamma-Ray Tissue Dose Rates Beyond Configurations 1-A, 1-F, and 1-G: Effect of Inserting Boral Within Configurations Containing Hevimet.

in dose rate because the magnitude of experimental errors may account for this variation.

A comparison of measurements beyond configurations 2-F (from Fig. 5.2.27) and 2-K and 2-H (from Fig. 5.2.29), which contain a single sheet of boral immediately in front of the stainless steel, shows that increasing the thickness of the oil layer adjacent to the source plate from 1.0 to 9.7 cm reduced the gamma-ray dose rate approximately 29%. Increasing the oil layer from 9.7 to 27.8 cm reduced the gamma-ray dose rate only 10%, which, again, may be within experimental error. This appears to indicate that, for configurations with boral in front of stainless steel, increasing the thickness of the oil layer preceding the configuration to more than 10 cm does not effectively reduce the dose rate beyond the shield.

SYMBOL	CONF. NO.	OIL (cm)	Be (in.)	BORAL (in.)	STAINLESS STEEL (in.)	BORAL (in.)	LiH (in.)	
●	2-A	1	4	0	4	0	12	+OIL
Δ	2-F	1	4	½	4	0	12	+OIL
○	2-G	1	4	½	4	½	12	+OIL

Fig. 5.2.27. Gamma-Ray Tissue Dose Rates Beyond Configurations 2-A, 2-F, and 2-G: Effect of Inserting Boral Within Configurations Containing Stainless Steel.

The results of this test are to be compared with measurements beyond similar configurations in which no boral was used (configurations 2-B and 2-D in Fig. 5.2.23), in which cases increasing the thickness of the oil layer preceding the configurations from 11 to 31 cm reduced the dose rate approximately 38%.

A comparison of configurations 2-H and 2-I, based on the assumption that the thicknesses of the oil layers preceding the two configurations are essentially the same, shows the effect of placing a boral sheet in front of the stainless steel rather than behind it. The dose rate beyond configuration 2-H is approximately 28% lower than that behind configuration 2-I. A comparison of

configurations 2-I and 2-J shows the effect of using boral both in front of the stainless steel and behind it, rather than just behind it. The resulting decrease in the dose rate was about 35%.
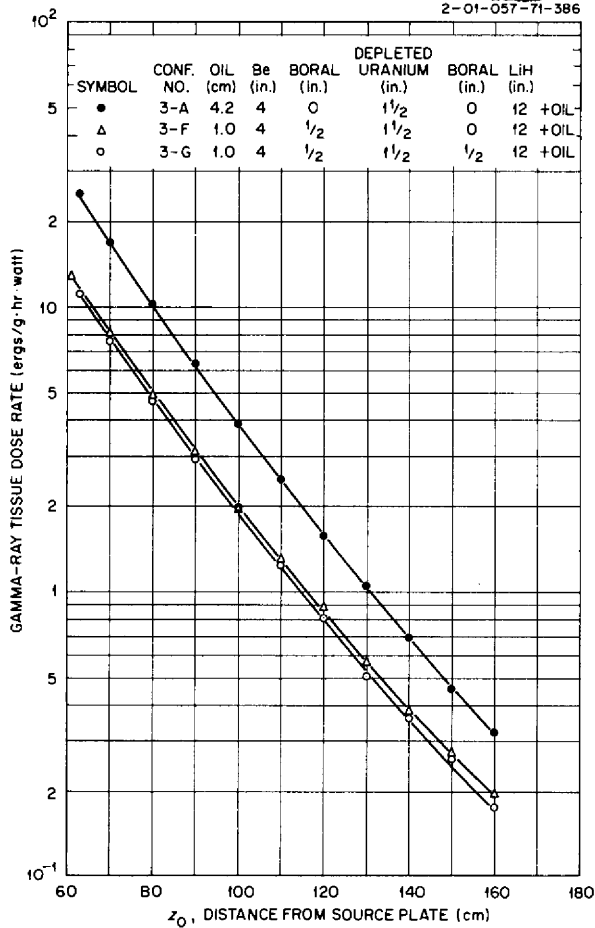

Fig. 5.2.28. Gamma-Ray Tissue Dose Rates Beyond Configurations 3-A, 3-F, and 3-G: Effect of Inserting Boral Within Configurations Containing Depleted Uranium.

Configurations 2-L and 2-M were tested to determine whether an oil layer within the configuration is best located in front of or behind a boral sheet preceding the stainless steel gamma-ray shield. The measurements show that the dose rates beyond the two configurations are the same, and apparently indicate that most of the neutrons which cause capture gamma rays in the steel are thermalized in the beryllium rather than the oil.

In order to determine the effectiveness of oil in reducing the secondary gamma-ray production in a gamma-ray shield when no beryllium, boral, or lithium hydride is present, a group of tests was run in which a 4-in.-thick stainless steel slab was moved in the oil from a position close to the source plate to a position 71 cm from the source plate. As the stainless steel was moved away from the source, the dose rate at a point 100 cm from the source (see Fig. 5.2.30) varied from 17 ergs/g·hr·w for a 1-cm-thick oil layer to approximately 3.5 ergs/g·hr·w for a 31-cm-thick oil layer, which represents an 80% reduction. Greater thicknesses of oil did not reduce the dose rate further.

A test was also carried out to determine the attenuation of the gamma-ray dose rate by 4 in. of beryllium and 12 in. of lithium hydride. A plot of the results (Fig. 5.2.31) shows that the beryllium and lithium hydride reduced the dose rate about 40% at a distance 70 cm from the source and about 10% at a distance of 160 cm.

The effect on the thermal-neutron flux of inserting one or two $\frac{1}{2}$-in.-thick boral sheets within the configurations was also studied. From the plots in Figs. 5.2.32, 5.2.33, and 5.2.34 it appears that placing a boral sheet both before and after the gamma-ray shield is no more effective in reducing the flux than placing a single sheet in front of the shield only.

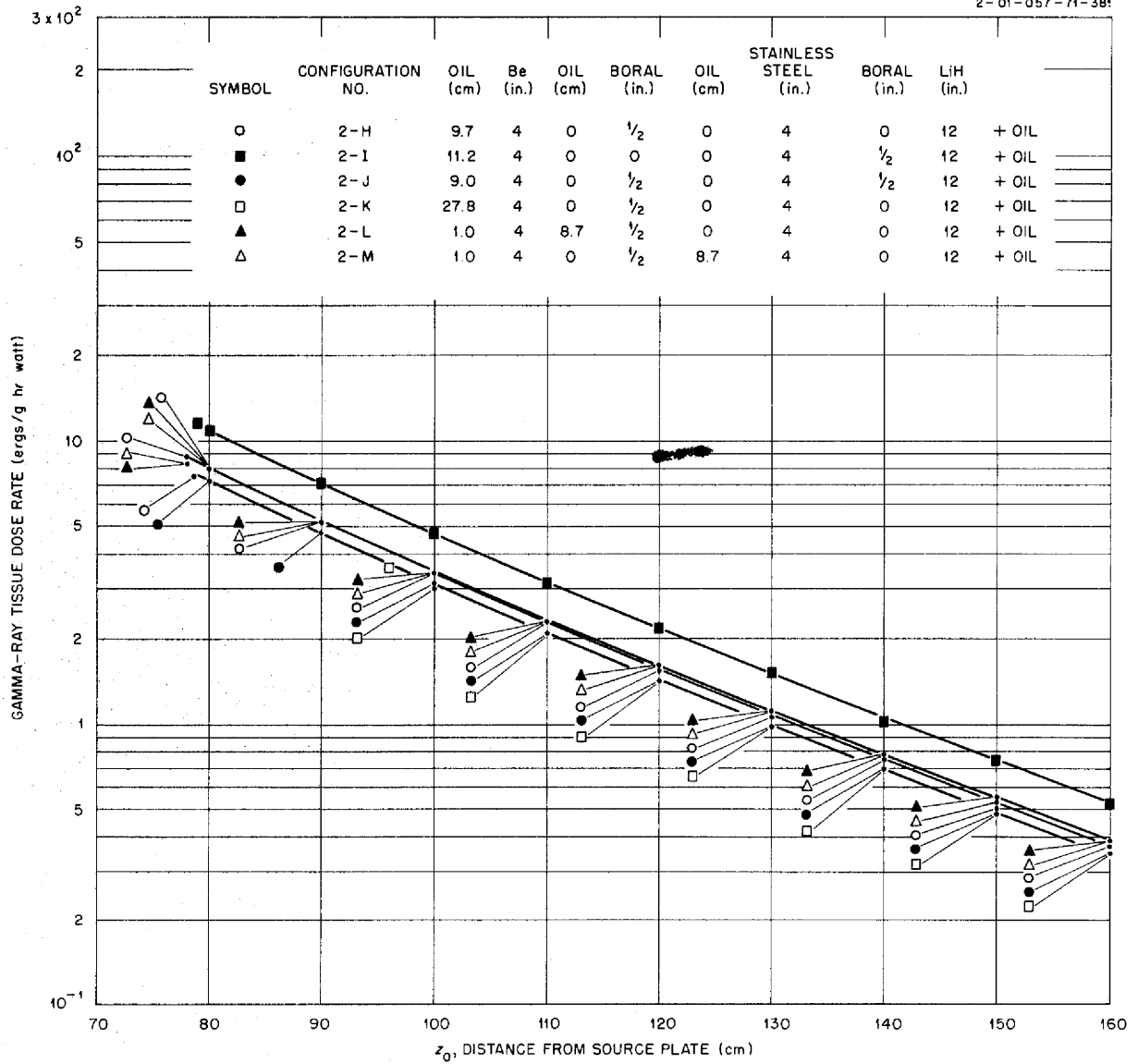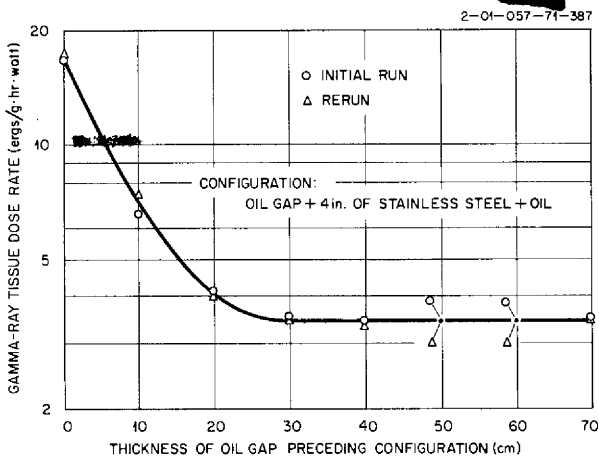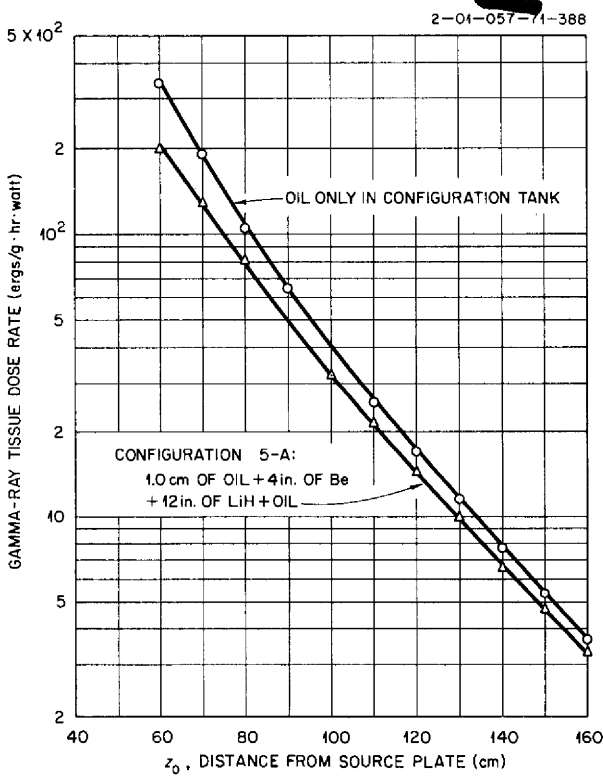Other configurations will be tested in this series.

Fig. 5.2.29. Gamma-Ray Tissue Dose Rates Beyond Configurations 2-H Through 2-M: Effect of Inserting Boral and Oil Gaps Within Configurations Containing Stainless Steel.

271

Fig. 5.2.30. Gamma-Ray Tissue Dose Rates 100 cm from the Source Plate as a Function of the Thickness of the Oil Gap Preceding Stainless Steel (Configurations 4-A Through 4-H).


Fig. 5.2.31. Gamma-Ray Tissue Dose Rates Beyond Configuration 5-A: Effect of Oil, Beryllium, and Lithium Hydride Components When Gamma-Ray Shield Is Omitted.
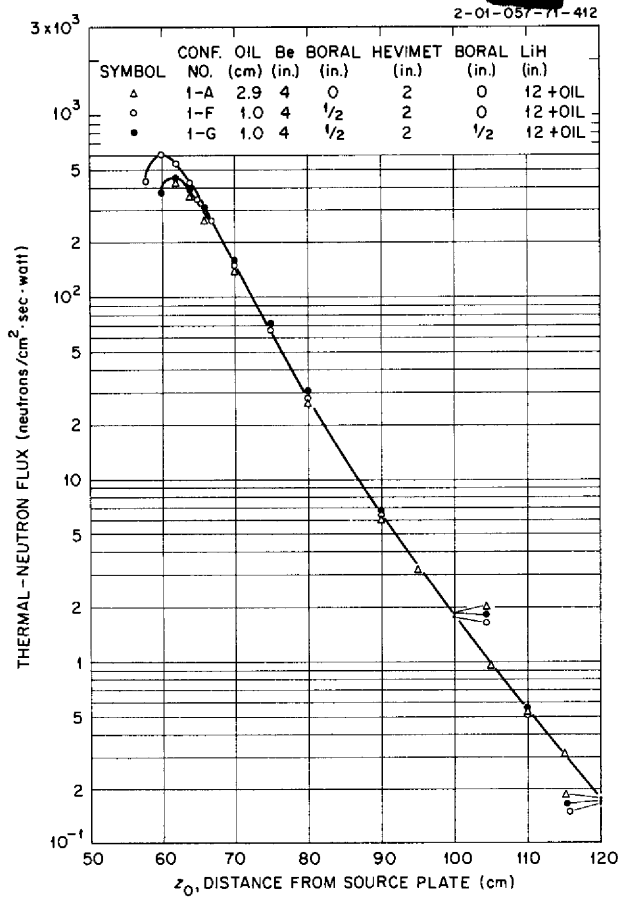
Fig. 5.2.32. Thermal-Neutron Fluxes Beyond Configurations 1-A, 1-F, and 1-G: Effect of Inserting Boral Within Configurations Containing Hevimet.
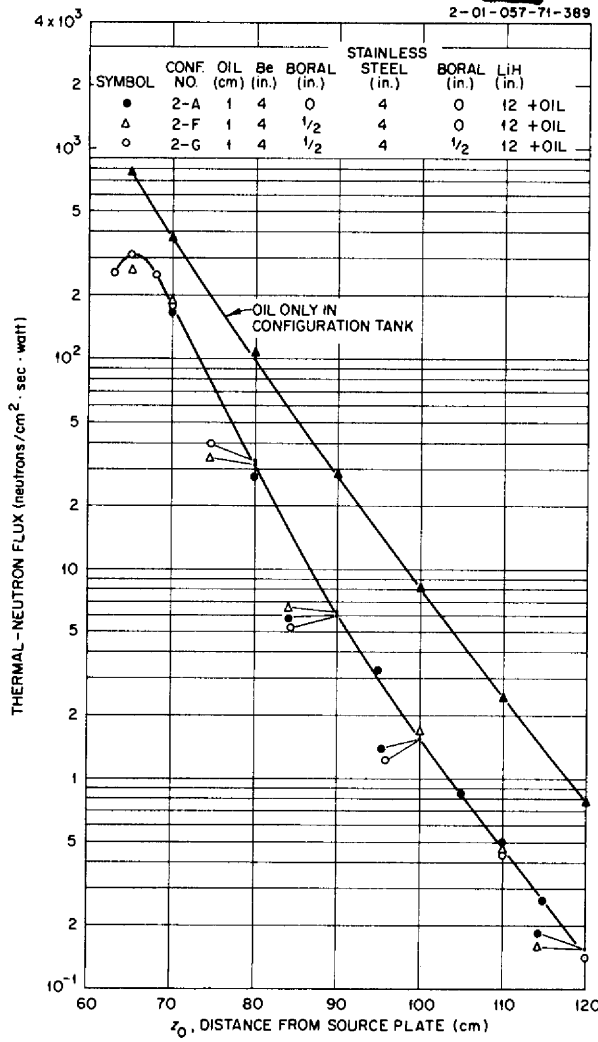
Fig. 5.2.33. Thermal-Neutron Fluxes Beyond Configurations 2-A, 2-F, and 2-G: Effect of Inserting Boral Within Configurations Containing Stainless Steel.
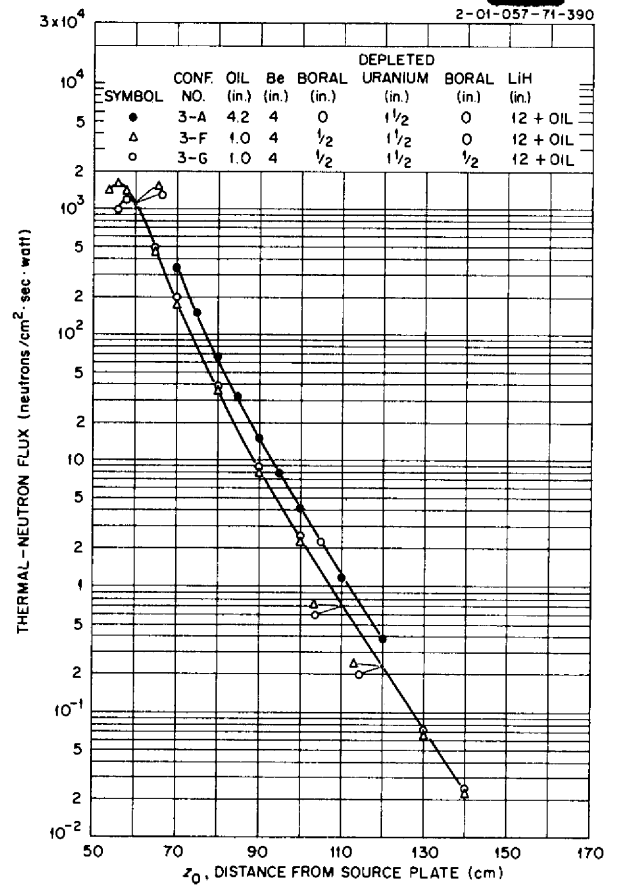
Fig. 5.2.34. Thermal-Neutron Fluxes Beyond Configurations 3-A, 3-F, and 3-G: Effect of Inserting Boral Within Configurations Containing Depleted Uranium.

5.3. TOWER SHIELDING REACTOR II

C. E. Clifford   L. B. Holland

MECHANICAL DESIGN[1]

The design of the core of the Tower Shielding Reactor II (TSR-II) has been modified slightly to provide more clearance for the thermal expansion that will occur when the reactor is operating at a power of 5 Mw. In earlier layouts[2] it was planned to place the lead-boral shield adjacent to the aluminum pressure tank. In order to ensure that the tank is not heated above a safe level by gamma-ray heating in the lead and neutron heating in the boral, it will be separated from the shield by a $\frac{1}{4}$-in.-thick layer of water, as shown in Fig. 5.3.1. The lower portion of the lead-boral shield will be hemispherical, and it will be suspended from a ring on the tank wall at the horizontal midplane of the core. With this arrangement there will be sufficient room for the shield to expand downward with heating. Radial expansion at the midplane will also be permitted. When the reactor is rotated about a horizontal axis, the shield will be restrained from moving by keys on the hemisphere which will engage slots in the support ring. In order to minimize fission gamma-ray leakage through the break in the midplane, the lead shield will be divided so that an extension of the interface will not intersect any of the fuel region.

The annular fuel elements and the lower central fuel elements will be mounted on the central cylinder. Each fuel element will be fixed at the top and guided at the lower end to permit some growth. These annular fuel elements will be removable remotely from above. The lower central fuel elements will be bolted to the cylinder so that they cannot be removed while the annular elements are in place. This is to prevent the possibility of lifting the lower central fuel elements into the midplane of the core region with the annular elements in place.

CONTROL MECHANISM

A full-scale mockup of the control mechanism has been designed, as shown in Fig. 5.3.2. It

will have a 2.5-in. stroke, and the method of operation will be the same as that for the prototype, which was described previously.[3] Normally the spring will hold the control plate against the fuel. Water will flow through the mechanism until the flow area around the piston is closed by the traveling nut. The pressure will build up in the cylinder, and the control plate can then follow the traveling nut to control the reactor. Interrupting the water flow will scram the mechanism.

NUCLEAR CALCULATIONS[4]

The preliminary nuclear calculations[5] were performed for a TSR-II design in which there was a water reflector exterior to the core, as shown in Fig. 5.3.3. By a modification of the 3G3R Oracle code, this reflector was represented as a boundary condition, so that the internal water reflector could be divided into two regions for control studies. A recent further modification of the 3G3R code provides a means of representing the several layers of the external reflector (see Fig. 5.3.1) as a set of boundary conditions.

The two outermost regions of the spherical reflector can be removed at one time. These two regions are assumed to be arranged in their exact geometry with a critical core region inside. The values of α are then solved for in the following equations:

$$(\phi_1 + 2J_1)\,\alpha_{11} = \phi_1 - 2J_1 \ ,$$

$$(\phi_1 + 2J_1)\,\alpha_{12} + (\phi_2 + 2J_2)\,\alpha_{22} = \phi_2 - 2J_2 \ ,$$

where

α_{11} = number of fast neutrons incident on the reflector that are returned as fast neutrons,

α_{12} = number of fast neutrons incident on the reflector that are returned as thermal neutrons,

---

[1] The engineering design work for the TSR-II is being performed by the ORNL Engineering Department.

[2] C. E. Clifford and L. B. Holland, *ANP Quar. Prog. Rep. March 31, 1957*, ORNL-2274, p 294; *June 30, 1957*, ORNL-2340, p 323; *Sept. 30, 1957*, ORNL-2387, p 304.

[3] C. E. Clifford and L. B. Holland, *ANP Quar. Prog. Rep. June 30, 1957*, ORNL-2340, p 328.

[4] The nuclear calculations for the TSR-II are being performed by M. E. LaVerne.

[5] C. E. Clifford and L. B. Holland, *ANP Quar. Prog. Rep. March 31, 1957*, ORNL-2274, p 294.
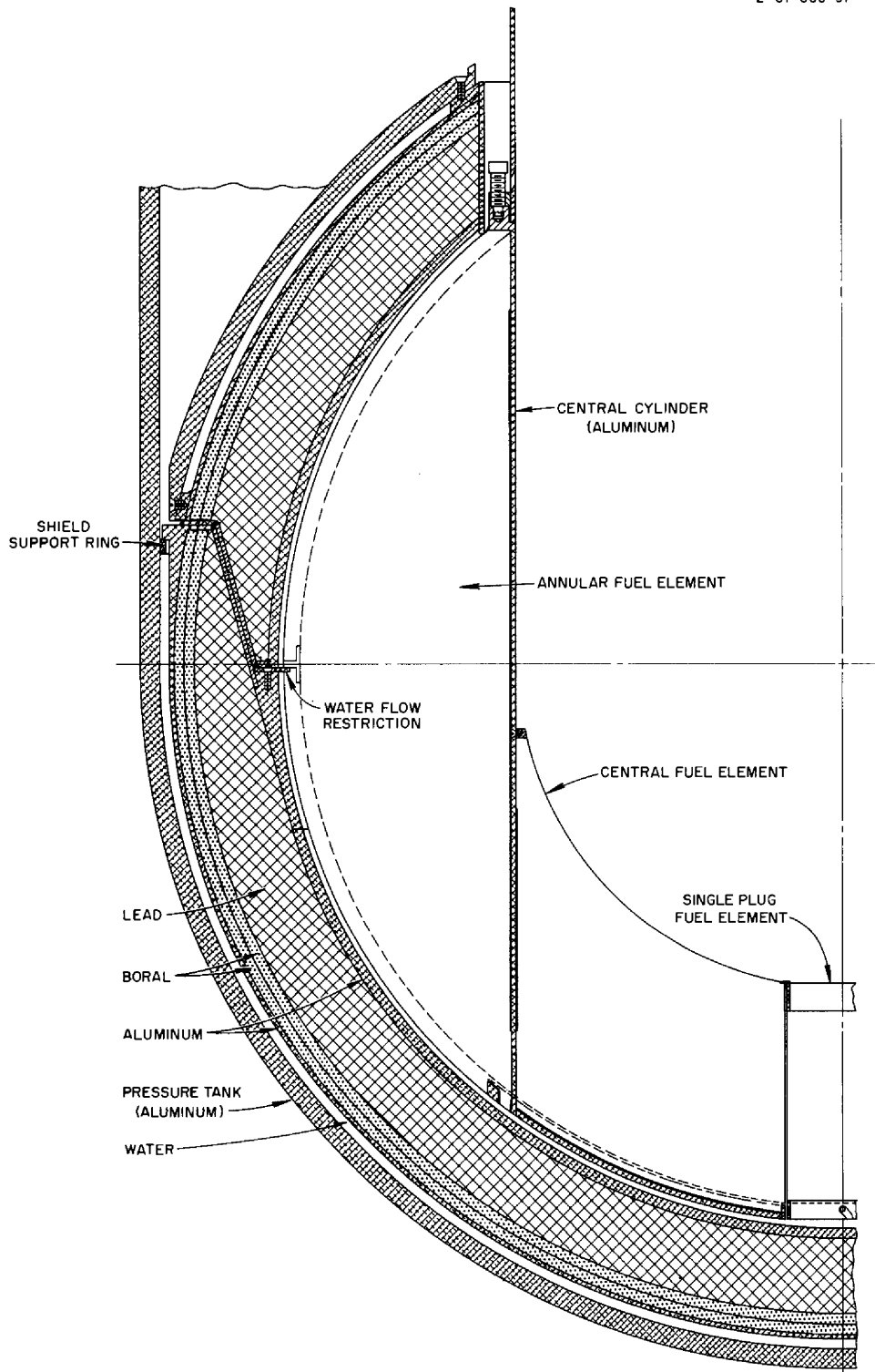
CENTRAL CYLINDER
(ALUMINUM)

ANNULAR FUEL ELEMENT

SHIELD
SUPPORT RING

CENTRAL FUEL ELEMENT

WATER FLOW
RESTRICTION

SINGLE PLUG
FUEL ELEMENT

LEAD

BORAL

ALUMINUM

PRESSURE TANK
(ALUMINUM)

WATER

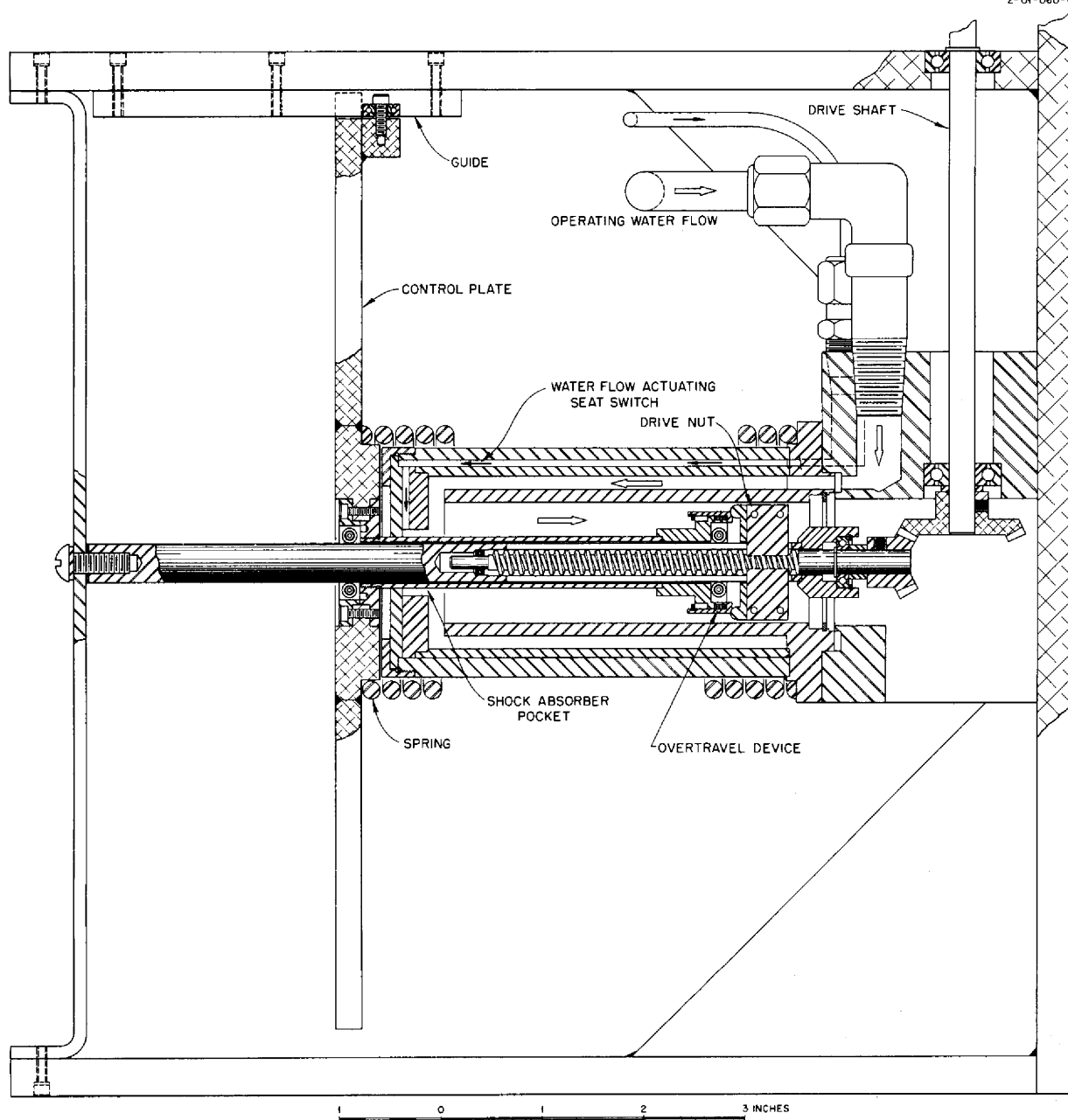Fig. 5.3.1. Suspension System for TSR-II Fuel Elements and Lead-Boral Shield Section.

Fig. 5.3.2. Experimental Mockup of the Control Mechanism for the TSR-II.

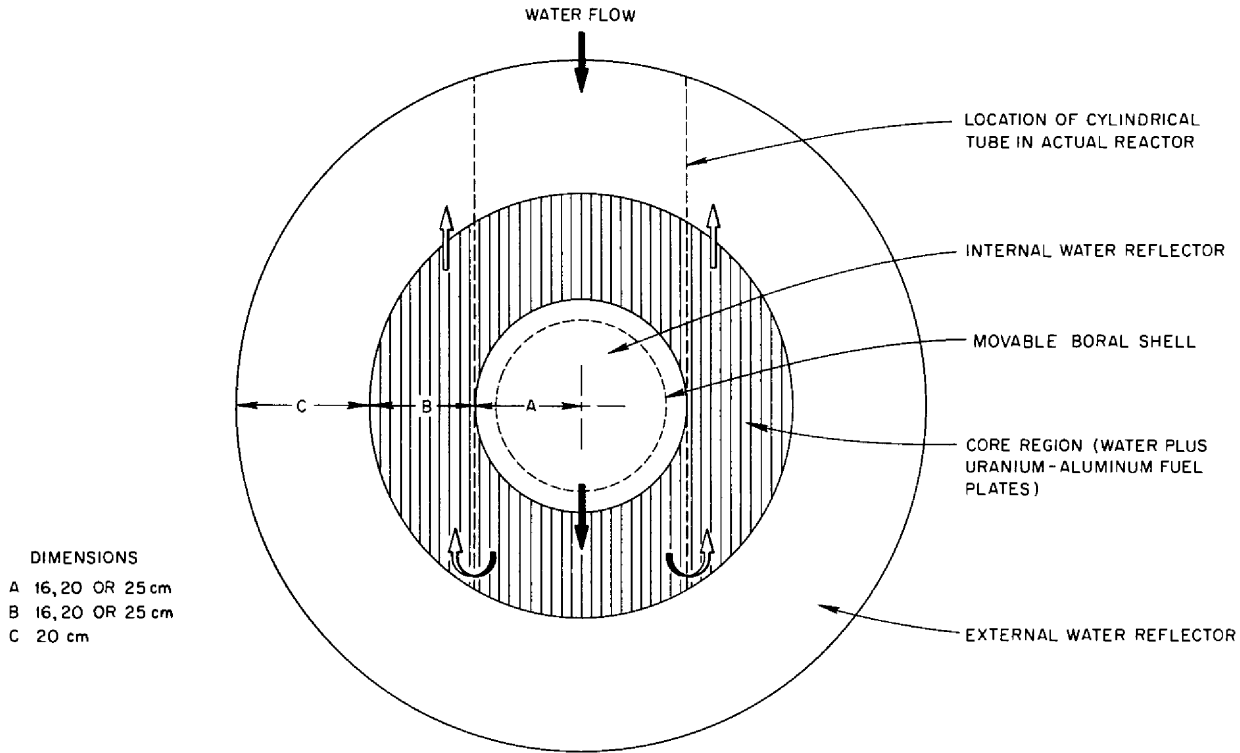**Fig. 5.3.3. Vertical Section of the Reactor Core Model Used in the Nucleor Parameter Study for the TSR-II.**

a_{22} = number of thermal neutrons incident on reflector that are returned,

ϕ_1 = fast-neutron flux,

ϕ_2 = thermal-neutron flux,

J_1 = fast-neutron current,

J_2 = thermal-neutron current.

The values of a can be obtained by running two cases, one of which has a black shell placed between the core and the reflector to eliminate the thermal current. The values obtained for a are independent of the ratio ϕ_1/ϕ_2.

Two additional terms can be derived, as follows:

$$\frac{2J_1}{\phi_1} = \frac{1 - a_{11}}{1 + a_{11}} = \frac{1}{\beta_{51}},$$

$$\frac{2J_2}{\phi_2} = \frac{1 - a_{22}}{1 + a_{22}} - \frac{a_{12}}{(1 + a_{11})(1 + a_{22})} \frac{\phi_1}{\phi_2}$$

$$= \frac{1}{\beta_{52}}.$$

The β terms, which are not independent of the ratio ϕ_1/ϕ_2, are input numbers of the 3G3R Oracle code and represent boundary conditions. Thus a new reactor configuration can be studied which has three regions and boundary conditions that represent two additional regions that have been removed. This can be repeated to remove several regions.

This procedure was used to strip off four outer regions of the TSR-II and represent them as boundary conditions, the four regions being a 20-cm-thick water reflector, a $\frac{1}{2}$-in.-thick boral shell, the 2-in.-thick lead region, and an aluminum-water region. With these boundary conditions, calculations were performed to obtain the critical mass and the amount of reactivity available for control in a reactor having a 17.5-in.-dia internal reflector and a 5.5-in.-thick core region which were separated by a $\frac{1}{4}$-in.-thick shell of aluminum and water. From these calculations it was found that a thermally black control shell which could move away from the core in the internal reflector region could control 12% in k. Since the control

plates actually will cover only one-half this area, their total worth could be 6% in *k*.

From the information now available, it is possible to estimate the total amount of excess reactivity required to compensate for the following effects:

Xenon buildup[6] (for 10 hr of operation at 5 Mw)   0.8%

Temperature rise (estimated from Bulk   0.7%
  Shielding Reactor data)

Shield changes   1.0%

Control   0.5%

    Total   3.0%

Two other items should be included in such a list: (1) burnup of fuel and (2) possible errors in fuel loading as a result of errors in the calculation of the critical mass or fabrication of the fuel plates. In order to provide for these two factors, calculations of the critical mass were made for the condition of a critical reactor with a solid control shell 1.6 cm from the fuel. Thus, when the control plates are against the fuel, the reactor is 3% subcritical, and, when the reactor is just critical with the control plates 1.6 cm from the fuel, an additional 3% in reactivity can be obtained to compensate for temperature rise, etc. by moving the plates farther from the fuel. Fixed boron-loaded plates can be mounted 1.6 cm from the fuel in the areas not covered by the movable control plates. The fixed control plates can be adjusted either way to provide a 3% change in reactivity at the time of the initial critical experiment and subsequently as required by fuel burnup, depending, of course, on the amount and direction of the initial adjustment.

The relative fast- and thermal-neutron flux distributions in the internal reflector and core region for the above operating condition are shown in Fig. 5.3.4 and Table 5.3.1. The average normalized fluxes and currents are shown in Table 5.3.2.

Nuclear calculations are being continued to determine the temperature coefficient of reactivity and the reactivity worth of voids in the core and internal reflector. This information will be used to study the kinetic behavior of the reactor and its control system. A kinetic analysis of the water system is presently being set up for study.

---

[6]Calculated on the basis of data given by H. K. Clark and J. C. English, *Xenon Tables*, DP-200 (May 1957).
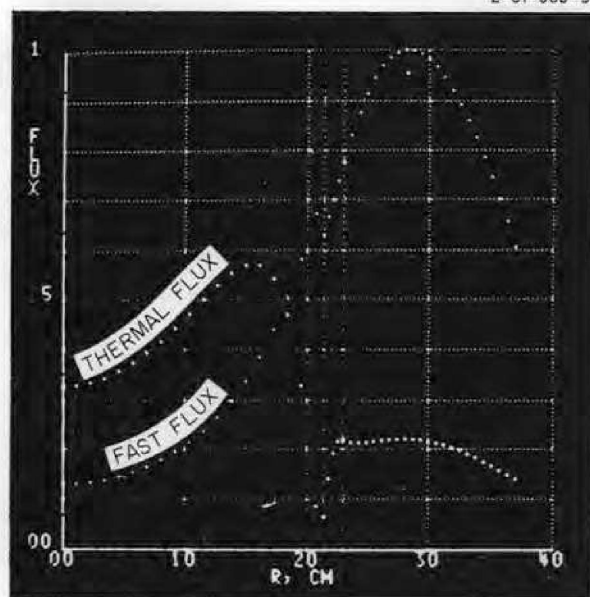
Fig. 5.3.4. Neutron Flux in the TSR-II with a Thermally Black Control Shell in the Internal Water Reflector 1.6 cm from the Core-Reflector Interface.

The calculated critical mass for the reactor is 8.2 kg of U^{235}. Since the fuel element development was based on a loading of 8 kg, no additional developmental work will be required for fuel plate fabrication. Additional checks on the critical mass calculations will include a calculation with a multigroup, multiregion reactor code, probably the Cornpone code on the Oracle computer, and a simple experiment at the Critical Experiments Facility.

The proposed critical assembly will not be an exact mockup of the TSR-II, but it will utilize the TSR-II dummy aluminum fuel elements. The fuel will be contained in a water solution that will fill the spaces between the aluminum plates. Two experiments will be performed, each with a different fuel concentration, from which the critical mass can be deduced. In order to check the validity of the method, a dummy aluminum element has been fabricated for use in the Bulk Shielding Reactor. This element is sealed, top and bottom, at the end of the fuel regions so that fuel, in solution, can be placed in the element; the reactivity worth of the solution element can then be compared with that of a regular element which contains an equivalent amount of U^{235}.

Table 5.3.1. Calculated Fast-Neutron and Thermal-Neutron Flux Distributions
in a TSR-II Configuration with a Control Shell 1.6 cm from the Fuel

Distance from Center Along a Radius (cm)	Fast-Neutron Flux	Thermal-Neutron Flux
1.15	0.1317	0.3302
2.31	0.1344	0.3357
3.46	0.1389	0.3448
4.61	0.1454	0.3575
5.77	0.1540	0.3739
6.92	0.1649	0.3939
8.08	0.1784	0.4173
9.23	0.1949	0.4436
10.38	0.2147	0.4723
11.54	0.2384	0.5020
12.69	0.2666	0.5307
13.84	0.2999	0.5554
14.10	0.3394	0.5711
16.15	0.3860	0.5705
17.30	0.4409	0.5424
18.46	0.5058	0.4705
19.61	0.5823	0.3304
20.76	0.6725	0.0865
20.76–21.40*		
21.40	0.6332	0.0685
21.80	0.6661	0.1417
22.20	0.7011	0.1913
22.60	0.7381	0.2177
23.00**	0.7774	0.2209
23.64	0.8318	0.2152
24.27	0.8773	0.2140
24.91	0.9147	0.2150
25.55	0.9448	0.2171
26.18	0.9680	0.2192
26.81	0.9847	0.2210
27.45	0.9952	0.2222
28.09	1.0000	0.2224
28.73	0.9992	0.2218
29.36	0.9931	0.2202
30.00	0.9821	0.2175
30.64	0.9663	0.2140
31.27	0.9460	0.2095
31.91	0.9215	0.2041
32.55	0.8931	0.1979
33.18	0.8611	0.1911
33.82	0.8257	0.1835
34.45	0.7872	0.1755
35.10	0.7458	0.1671
35.73	0.7019	0.1585
36.36	0.6556	0.1499
37.00	0.6071	0.1417

*Position of $\frac{1}{4}$-in.-thick control shell.

**At reflector-core interface.

Table 5.3.2. Average Normalized Fluxes and Currents
in TSR-II Configuration with a Control
Shell 1.6 cm from the Fuel

Region	Fast Neutrons	Thermal Neutrons
Average Normalized Flux		
Internal reflector, inside control shell	0.4068	0.4505
Internal reflector, outside control shell	0.7046	0.1759
Core	0.8674	0.1962
Net Current		
Outer core boundary	0.1003	0.0030

WATER COOLING AND PURIFICATION SYSTEM

The design and specifications for the water system are 95% complete. The lump sum contract for the installation is to be let the last week of February 1958 and the work is scheduled to be completed in September. Earlier estimates had indicated that the work could be completed by July 1.

A flow diagram of the water system, along with tentative locations of the pressure- and temperature-measuring elements, is shown in Fig. 5.3.5. The main components of this system will be:

1. a 60-hp circulating pump capable of delivering 1000 gpm when the reactor is operating at a 200-ft altitude,
2. a venturi nozzle for measuring water flow,
3. the reactor, which will operate up to a 5-Mw heat output,
4. a two-cell, air-cooled heat exchanger capable of removing 17,065,000 Btu/hr from water entering at 160°F and leaving at 125.8°F when the ambient air temperature is 75°F,
5. a 1500-gal detention tank.

There will also be the following auxiliary units of the flow system:

1. a main bypass valve for reduced flow when the reactor is operating in the power range from 5 kw to 5 Mw;
2. a 5-hp d-c emergency circulating pump which will operate continuously and which is required for removing afterheat following any emergency shutdown that may occur while the radiator is operating at 5 Mw and for circulating the water while the reactor is operating at a power below 5 kw;
3. a water-level control system which will consist of a 250-gal level tank, compressed gas to remove water from the system, and a fill pump which will take water from the pool and put it into the system;
4. a 40-kw heater to prevent water lines from freezing when the reactor is not operating (the air cooler will be supplied with louvers and additional heaters);
5. a mixed-bed demineralizer which will bypass the detention tank with a flow of 40 gpm and which can also be used to keep the reactor pool water clean;
6. a Tracerlab fission break monitor which will give an alarm if iodine activation, which would indicate a rupture in a fuel element, is noted in the reactor outlet water.

EXTENSION OF GAMMA-RAY-HEATING CALCULATION FOR THE TSR-II

W. W. Dunn[7]   D. K. Trubey

In the previous computation[8] of the gamma-ray heating in the TSR-II, two assumptions were made concerning the angular and energy dependence of the gamma-ray flux at the core-shield interface. The first assumption was that the collided energy spectrum was represented by the NDA differential energy spectrum after passage through one mean free path of water,[9] and the second was that the collided and uncollided fluxes were isotropic at the core-shield interface. In order to check the validity of these assumptions, an additional calculation has now been completed by using the Bowman-Trubey Monte Carlo data on the gamma-ray penetration of lead shields[10] in order to compute the heating in the first $\frac{1}{8}$ in. of lead in the shield, that is, the lead adjacent to the core. This first lead interval was chosen as

[7]On assignment from U.S. Air Force.

[8]W. W. Dunn and D. K. Trubey, *ANP Quar. Prog. Rep. Sept. 30, 1957*, ORNL-2387, p 307–316, esp 312.

[9]H. Goldstein and J. E. Wilkins, *Calculations of the Penetrations of Gamma Rays. Final Report*, NYO-3075 (June 30, 1954).

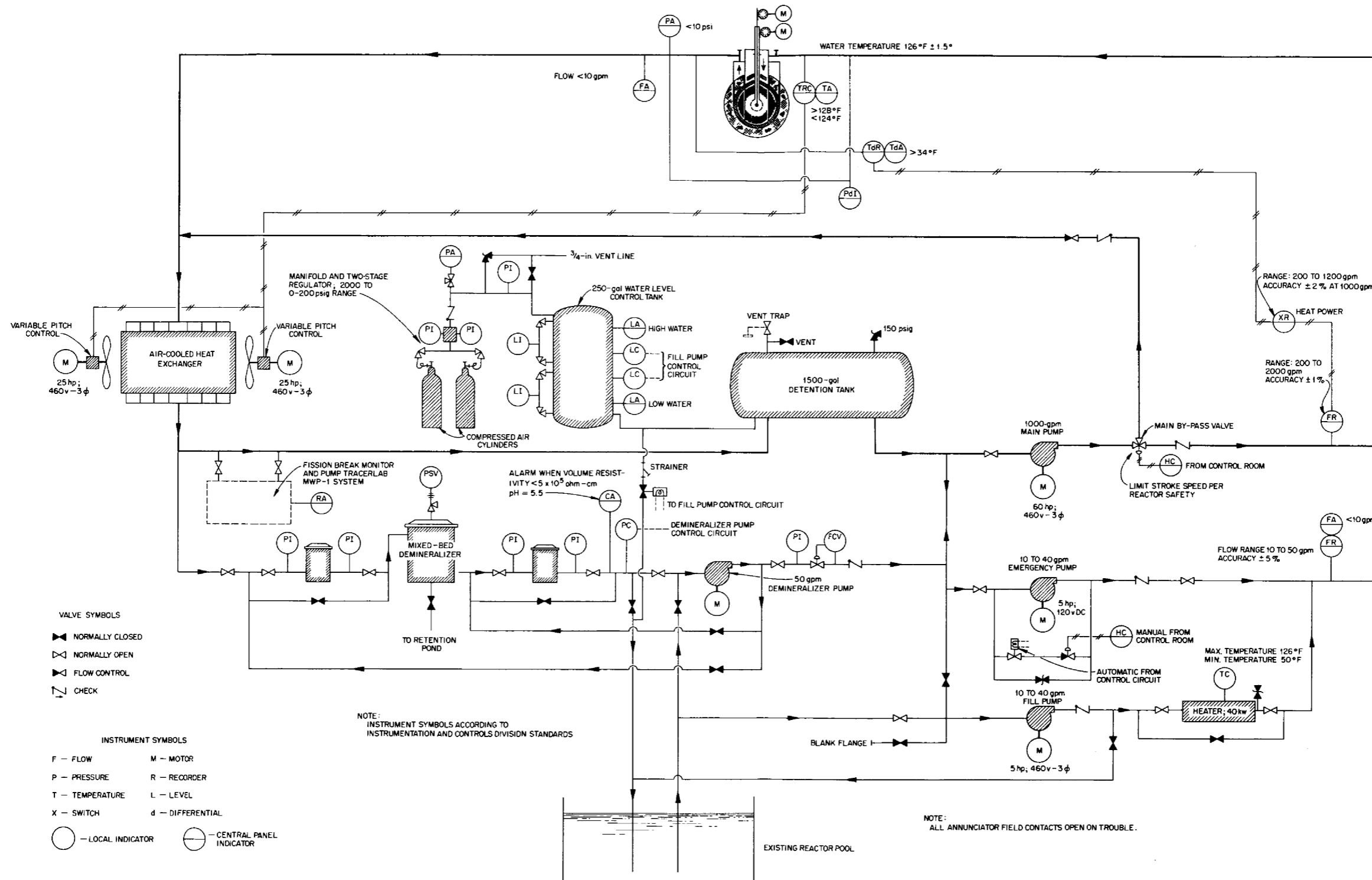[10]L. A. Bowman and D. K. Trubey, *ANP Quar. Prog. Rep. Sept. 30, 1957*, ORNL-2387, p 320.

PA <10 psi

WATER TEMPERATURE 126°F ± 1.5°

FLOW <10 gpm

FA

TRC TA >128°F <124°F

ToR TdΔ >34°F

PdI

RANGE: 200 TO 1200 gpm
ACCURACY ± 2% AT 1000 gpm

XR HEAT POWER

RANGE: 200 TO 2000 gpm
ACCURACY ± 1%

FR

MANIFOLD AND TWO-STAGE REGULATOR; 2000 TO 0-200 psig RANGE

PA

PI

³/₄-in. VENT LINE

250-gal WATER LEVEL CONTROL TANK

VENT TRAP

150 psig

VENT

VARIABLE PITCH CONTROL

AIR-COOLED HEAT EXCHANGER

VARIABLE PITCH CONTROL

25 hp;
460 v - 3 φ

25 hp;
460 v - 3 φ

PI PI

PI PI

LA HIGH WATER

LC FILL PUMP CONTROL CIRCUIT

LC

LI

LI

LA LOW WATER

1500-gal DETENTION TANK

1000-gpm MAIN PUMP

MAIN BY-PASS VALVE

HC FROM CONTROL ROOM

LIMIT STROKE SPEED PER REACTOR SAFETY

COMPRESSED AIR CYLINDERS

FISSION BREAK MONITOR AND PUMP TRACERLAB MWP-1 SYSTEM

PSV

STRAINER

ALARM WHEN VOLUME RESISTIVITY < 5 × 10⁵ ohm-cm
pH = 5.5

CA

TO FILL PUMP CONTROL CIRCUIT

DEMINERALIZER PUMP CONTROL CIRCUIT

60 hp;
460 v - 3 φ

FA <10 gpm

FR

RA

PI PI

MIXED-BED DEMINERALIZER

PI PI

PC

PI FCV

10 TO 40 gpm EMERGENCY PUMP

FLOW RANGE 10 TO 50 gpm
ACCURACY ± 5%

VALVE SYMBOLS

▶◀ NORMALLY CLOSED

▷◁ NORMALLY OPEN

▶◁ FLOW CONTROL

↖◁ CHECK

TO RETENTION POND

50 gpm DEMINERALIZER PUMP

M

5 hp;
120 v DC

HC MANUAL FROM CONTROL ROOM

AUTOMATIC FROM CONTROL CIRCUIT

MAX. TEMPERATURE 126°F
MIN. TEMPERATURE 50°F

TC

INSTRUMENT SYMBOLS

F — FLOW   M — MOTOR
P — PRESSURE   R — RECORDER
T — TEMPERATURE L — LEVEL
X — SWITCH   d — DIFFERENTIAL

○ — LOCAL INDICATOR

⬭ — CENTRAL PANEL INDICATOR

NOTE:
INSTRUMENT SYMBOLS ACCORDING TO
INSTRUMENTATION AND CONTROLS DIVISION STANDARDS

BLANK FLANGE

10 TO 40 gpm FILL PUMP

5 hp; 460 v - 3 φ

HEATER; 40 kw

NOTE:
ALL ANNUNCIATOR FIELD CONTACTS OPEN ON TROUBLE.

EXISTING REACTOR POOL

Fig. 5.3.5. Cooling Water Flowsheet for the TSR-II.

the check point, since a large part of the gamma-ray heating occurs within it, and, in addition, it is in the interval in which the Bowman-Trubey results could be most accurately and readily utilized.

The Bowman-Trubey results yielded the gamma-ray heating, in percentage of the initial energy, E_0, as a function of the angle of incidence, θ, on the lead after passage through a varying number of mean free paths of water. Data were available for initial energy groups of 1, 3, 6, and 10 Mev and for incident angles of 0, 60, 70.5, and 75.5 deg. For this calculation the source gamma rays were considered to be isotropic in the source planes, and the core source-shell regions and the source gamma-ray energies were grouped exactly as was done for the previous calculation.

The Bowman-Trubey results were first cross-plotted to produce plots of $g(\theta)$, the percentage of initial energy E_0 deposited in the first $\frac{1}{8}$ in. of lead, as a function of the angle of incidence of the gamma rays. This was done for various mean free paths of water preceding the lead. A typical plot is shown in Fig. 5.3.6. It is to be noted that the resulting curves have shapes identical to those produced in the previous calculation when $f(\theta)$, the percentage of initial energy deposited, was plotted for various depths of penetration into the shield as a function of incident angle. It was possible to compare $f(\theta)$ and $g(\theta)$ at 0.05 mean free path of material penetrated, and that comparison is also shown in Fig. 5.3.6. Since the minimum energy of the Bowman-Trubey data was 1 Mev, the Monte Carlo code was used to produce data at 0.5 Mev for use in this calculation.

The normalized gamma-ray flux, $A(E_0, \text{shell})$, for each E_0 from each source shell was found from the following expression, which incorporates the usual transformation from a spherical-shell source to an equivalent infinite plane source (neglecting the back plane):

$$(1) \quad \frac{1}{2}\left[\frac{r}{r_0} \; S(E_0, \text{shell}) \; \phi(r) \, \Sigma_f t\right]$$

$$= \int_0^{\pi/2} A(E_0, \text{shell}) \sin\theta \, d\theta \; ,$$
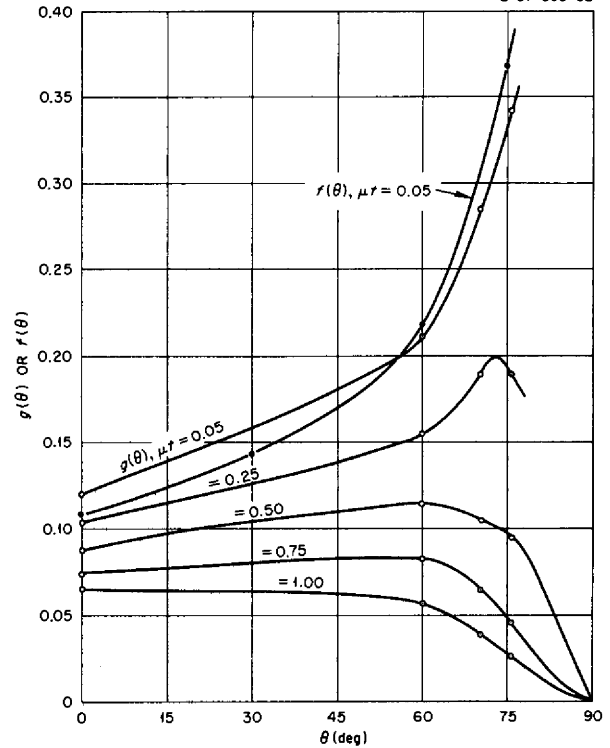
Fig. 5.3.6. Per Cent of Energy Absorbed in Pb₁ as a Function of the Incident Angle for Various Source Planes; $E = 4$ Mev.

where

$r =$ distance from center of core to spherical source shell, cm,

$r_0 =$ distance from center of core (or center of internal water reflector) to core-shield interface, cm,

$S(E_0, \text{shell}) =$ source term for each shell, number of gamma rays of energy E_0 generated per square centimeter per fission per second,

$\phi(r) =$ thermal-neutron flux in the source shell at point r,

$\Sigma_f =$ macroscopic fission cross section of U^{235},

$t =$ shell thickness, cm.

With $g(\theta)$ and $A(E_0, \text{shell})$ for each value of E_0, and θ in each source shell, the gamma-ray heating in the first $\frac{1}{8}$-in. lead interval was found by

summing over E_0 and the source shell the numerically integrated expression:

(2) $H(E_0)$

$$= \int_\theta g(\theta)(E_0, \text{shell}) \, A(E_0, \text{shell}) \, \sin\theta \cos\theta \, d\theta \ ,$$

where the $\cos\theta$ is required for the flux-to-current conversion. Table 5.3.3 presents the result of the summation of Eq. 2 compared with the results obtained in steps 1 and 2 of the previous calculations.[8] The heating estimated by step 1 was determined by multiplying the heating at the core-shield interface, as a function of initial energy group, by the ratio of the lead to core energy absorption coefficients for that energy group.

Table 5.3.3. Heating in the First $\frac{1}{8}$-in.-Thick Layer
of Lead in the TSR-II Shield Calculated
by Various Methods

Calculation	Heating (watts/cm^2·Mw)
Previous calculation	
Step 1	0.548
Step 2	0.445
Present calculation	0.215

It may be seen that the result from step 1 of the previous calculation represents the extreme maximum limiting case, since it was assumed that the flux was the same in the $\frac{1}{8}$-in. lead interval as in the core. It is expected that step 2 of the previous calculation also gave an overestimate of the true heating for several reasons. First, the NDA buildup factors assumed an infinite medium and did not take into account the reduction in the low-energy fluxes at the core-shield interface, which in turn would reduce the heating. This total flux reduction, which is not reflected in the tabulated results, is of the order of 20% for the 1.0-Mev fluxes[11] and would be much greater for the lower energies and less for the higher energies. Second, the collided fluxes which were obtained from the point kernel and

_____

[11]Unpublished results of the Bowman-Trubey calculation.

buildup factors at the core-shield interface were assumed to be in such a direction as to penetrate the shield, and this would not be entirely true in the actual case, especially at low energies. Other small effects which would contribute to an overestimate were: the assumption of nearly isotropic distribution for the collided fluxes, which would overestimate the heating in the first lead interval and underestimate the heating in the succeeding layers if the collided flux were more peaked in the forward direction, as is probably the case; and the assumption of the differential energy spectrum for water to represent the core, which would overestimate the low-energy group, since the effect of the aluminum and uranium would be to reduce the low-energy spectrum.

The present calculation by necessity required considerable interpolation to perform the necessary cross-plotting, and for this reason there is an uncertainty in the results. The neglect of the source gamma rays in the source planes directed away from the shield is probably the one source of error which lowers the calculated result. While this calculation avoids many of the errors inherent in step 2 of the previous calculation, the use of the transformation from a spherical shell source to an infinite plane source does introduce some error, since the medium is not infinite and homogeneous.

In conclusion, it can be stated that the original assumptions on energy spectra and angular dependence in the previous calculation (step 2) give a reasonably conservative estimate of the heating in the first lead interval. Since the heating in this interval is most dependent on the low-energy spectrum, it would be expected that the overestimation caused by the energy-spectra assumption would be decreased in succeeding lead layers, and hence there is the prospect of improvement with penetration into the shield. The angular-distribution assumption gives an overestimation in the initial layer, and, if the collided flux is more peaked in the forward direction, it tends to underestimate the heating deep in the shield. No further refinements of these calculations are contemplated, since the heating is considered to be sufficiently defined for purposes of construction.

5.4. TOWER SHIELDING FACILITY

C. E. Clifford

STUDY OF GAMMA RAYS PRODUCED BY NEUTRON INTERACTIONS IN AIR

V. R. Cain   F. J. Muckenthaler

During the past few years a large number of measurements have been made of gamma-ray dose rates inside crew shields for several shielding configurations. Dose-rate measurements of this type, however, give very little information as to the original energy of the gamma rays entering the crew compartment and still less as to their origin. Gamma-ray dose rate measurements in the crew shields have indicated an intensity greater than that expected from the scattering of gamma rays alone. Therefore, consideration has been given to the possibility of secondary gamma-ray production from neutrons leaving the reactor shield. Interactions of neutrons in air include inelastic scattering, as well as elastic scattering, and thermal-neutron capture. Calculations of gamma-ray intensities from inelastically scattered neutrons are somewhat difficult because neither the scattering cross section nor the energy distribution of gamma rays for this interaction is well known. The fact that the neutron energy spectrum leaving a shield is difficult to measure further complicates the problem. Measurements for determining the inelastic-scattering cross section for neutrons in air would be very difficult to make at the TSF. An experiment was performed, however, in which gamma-ray spectral measurements were made from which it is hoped that the order of magnitude of the dose rate to be expected from inelastic scattering can be deduced.

Experimental Configuration

In order to detect the high-energy gamma rays resulting from neutron interactions with the air, it was necessary to eliminate, where possible, other sources of high-energy gamma rays. Since the number of gamma rays born in the reactor was many orders of magnitude larger than the number born in the air, the reactor had to be well shielded from the detector. This was accomplished by submerging the reactor in the handling pool 8 ft below the surface of the ground and thus interposing approximately 40 ft of earth as shielding.

As shown in Fig. 5.4.1, the experimental configuration included an 8-in.-dia by 10-ft-long air-filled collimator attached to one face of the reactor so that a beam of radiation was emitted into the air at an angle of 60 deg from the horizontal. The axis of the collimator passed through the center of the face of the reactor. A partially shielded sodium iodide crystal (3 by 3 in.) mounted on a DuMont 6363 phototube was located approximately 1 ft above ground level at a horizontal distance of 52 ft from the reactor. The crystal was enclosed in a cavity surrounded by an 8-in. thickness of lead and at least 4 ft of concrete. On the side of the detector shield facing the reactor, a 4-in.-wide collimator slit extended through the shield to the detector position. The floor of the slit slanted 10 deg upward from the detector position so that no direct radiation from the ground would be admitted. The crystal and phototube were mounted so that the axis of the phototube was at an angle of 45 deg from the horizontal to ensure maximum sensitivity.

The collimator slit, which was 5 ft long and 5 ft deep at the deepest point (at the detector position), was filled with borated water contained in a 4-in. by 4-ft by 4-ft plastic bag. The borated water prevented neutrons from reaching the detector and also reduced the number of capture gamma rays produced in the concrete walls of the collimator. In addition, a $\frac{3}{16}$-in.-thick sheet of boron-impregnated Plexiglas (hereafter referred to as boron Plexiglas) was placed over the outside of the collimator slit. (The boron Plexiglas used in this experiment is Plexiglas impregnated with boron carbide to a density of 0.55 g of boron per cubic centimeter.) The effectiveness of this neutron shielding was verified by a series of measurements with a BF_3 chamber and a fast-neutron dosimeter placed in the detector cavity. The measurements indicated that there was no detectable neutron flux in the cavity.

The reactor and its collimator could be rotated about the vertical axis of the reactor. The measure of this rotation is indicated by the angle θ, which is the angle between a vertical plane including the reactor center and the detector center and a vertical plane including the reactor
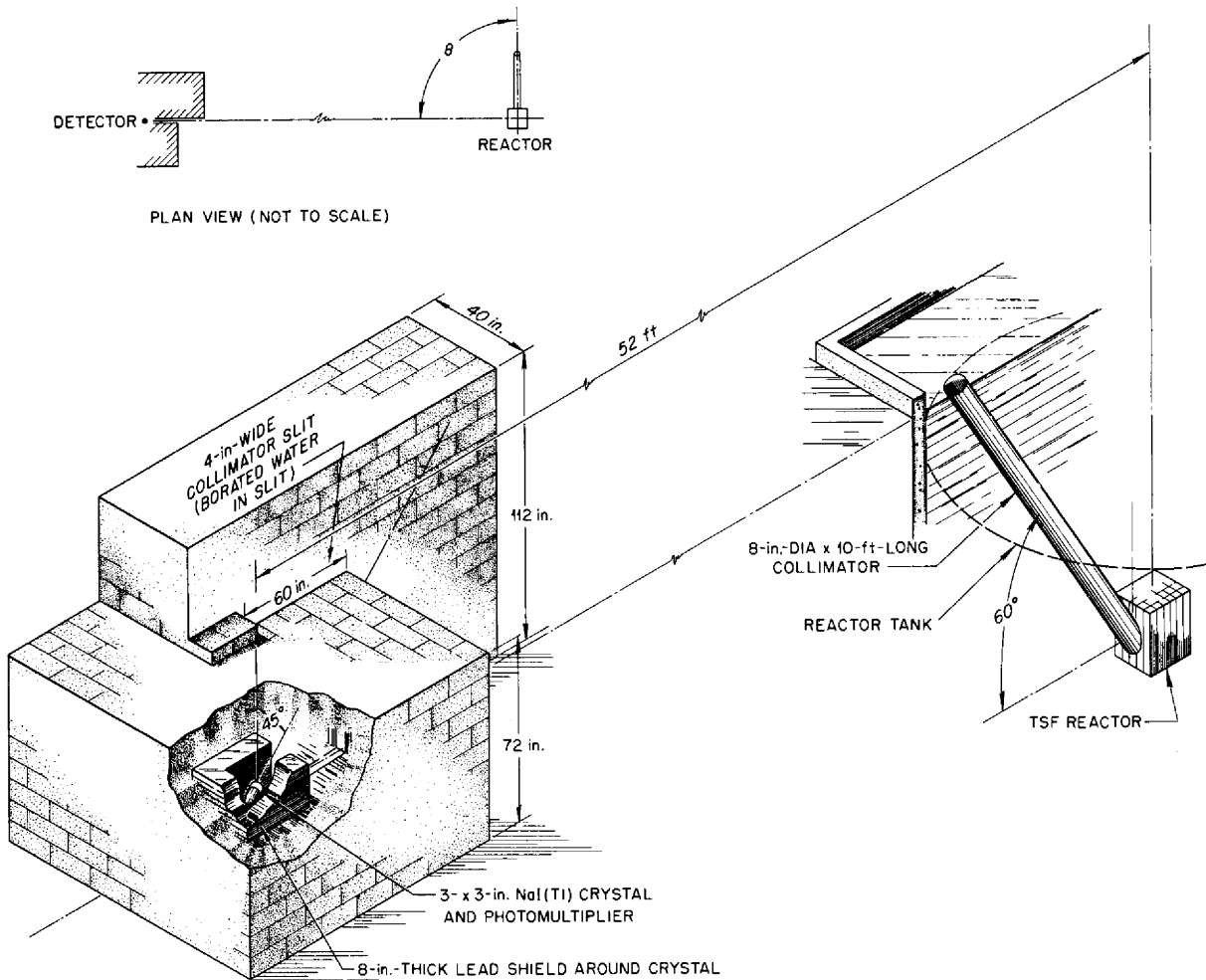
Fig. 5.4.1. Configuration for the Measurement of the Spectra of Gamma Rays Resulting from Neutron Interactions in Air.

center and the axis of the reactor collimator. However, most of the measurements were taken with θ = 0 deg, and for this geometry the intersection of the detector lines of sight with the cone of radiation from the reactor is depicted in Fig. 5.4.2. It can be seen that the detector solid angle easily includes all the radiation cone near the ground level, but the fraction of the cone included in the solid angle decreases as the distance from the reactor is increased.

Other than the measurements with θ = 0 deg, measurements were actually made for only one other value of θ, that is, θ = 90 deg, θ being measured in the clockwise direction from the reactor-detector axis. For the measurement taken

with this beam angle, additional concrete shielding was placed above and in front of the detector collimator to reduce the number of primary gamma rays scattering from the reactor beam that would enter the detector collimator and be scattered into the detector.

Determination of Detector Response

As mentioned above, the detector consisted of a 3- by 3-in. sodium iodide crystal mounted on a DuMont 6363 phototube. Pulses from the tube were sorted by two 20-channel analyzers connected in series, and the pulse-height output was calibrated with respect to energy against the 1.12-Mev Zn^{65} gamma ray.
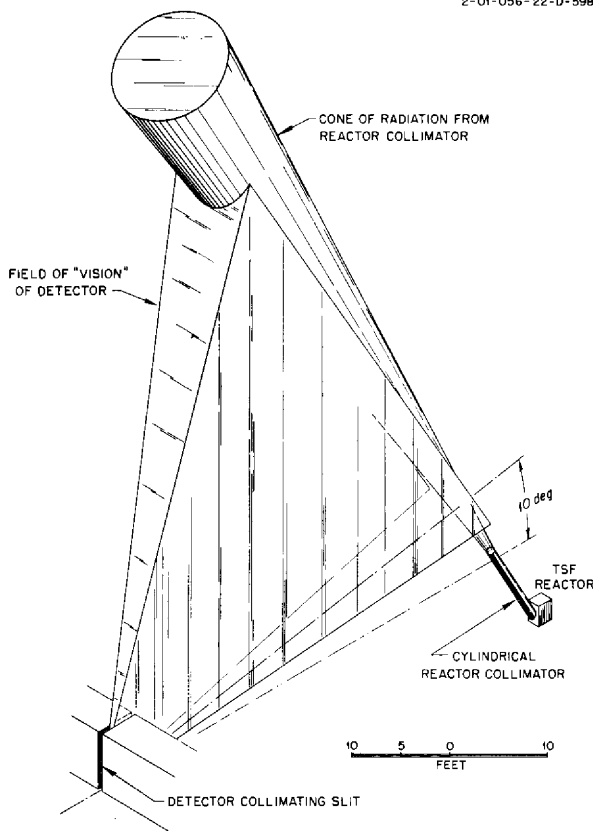
Fig. 5.4.2. Geometric Relationships When $\theta = 0$ deg: TSF Experiment To Measure the Spectro of Gamma Rays Resulting from Neutron Interactions in Air.

Fig. 5.4.3. Response of Detector to 4.4-Mev C^{12*} Gamma Rays. Top curve represents response of NaI crystal to gamma rays produced at Van de Graaff accelerator. Lower curve represents response to Po-Be gamma rays filtered through a B-H_2O-filled collimator.

In order to better understand the effect that the borated water in the collimator might have on the gamma-ray spectrum, a polonium-beryllium source was placed outside the collimator and the pulse-height spectrum of the 4.4-Mev gamma ray from the $Be^9(\alpha,n)C^{12*}$ reaction was observed. The resulting spectrum was compared, as shown in Fig. 5.4.3, with the spectral response of this type of crystal to 4.4-Mev gamma rays produced at the Van de Graaff accelerator with the $N^{15}(p,\alpha)C^{12*}$ reaction when no collimator was used.[1] It can be seen that the borated water caused a significant reduction in the magnitude of the peak corresponding to the 4.4-Mev gamma ray and that the Compton scattering was increased substantially.

---

[1]P. R. Bell, private communication.

Experimental Results and Discussion

The top curve in Fig. 5.4.4 represents the total gamma-ray pulse-height spectrum resulting from neutron interactions in air measured in the geometry described above when $\theta = 0$ deg. This spectrum presumably consists of gamma rays resulting from the capture of thermal neutrons in the nitrogen of the air plus those from other sources. The highest energy gamma ray from thermal-neutron capture by
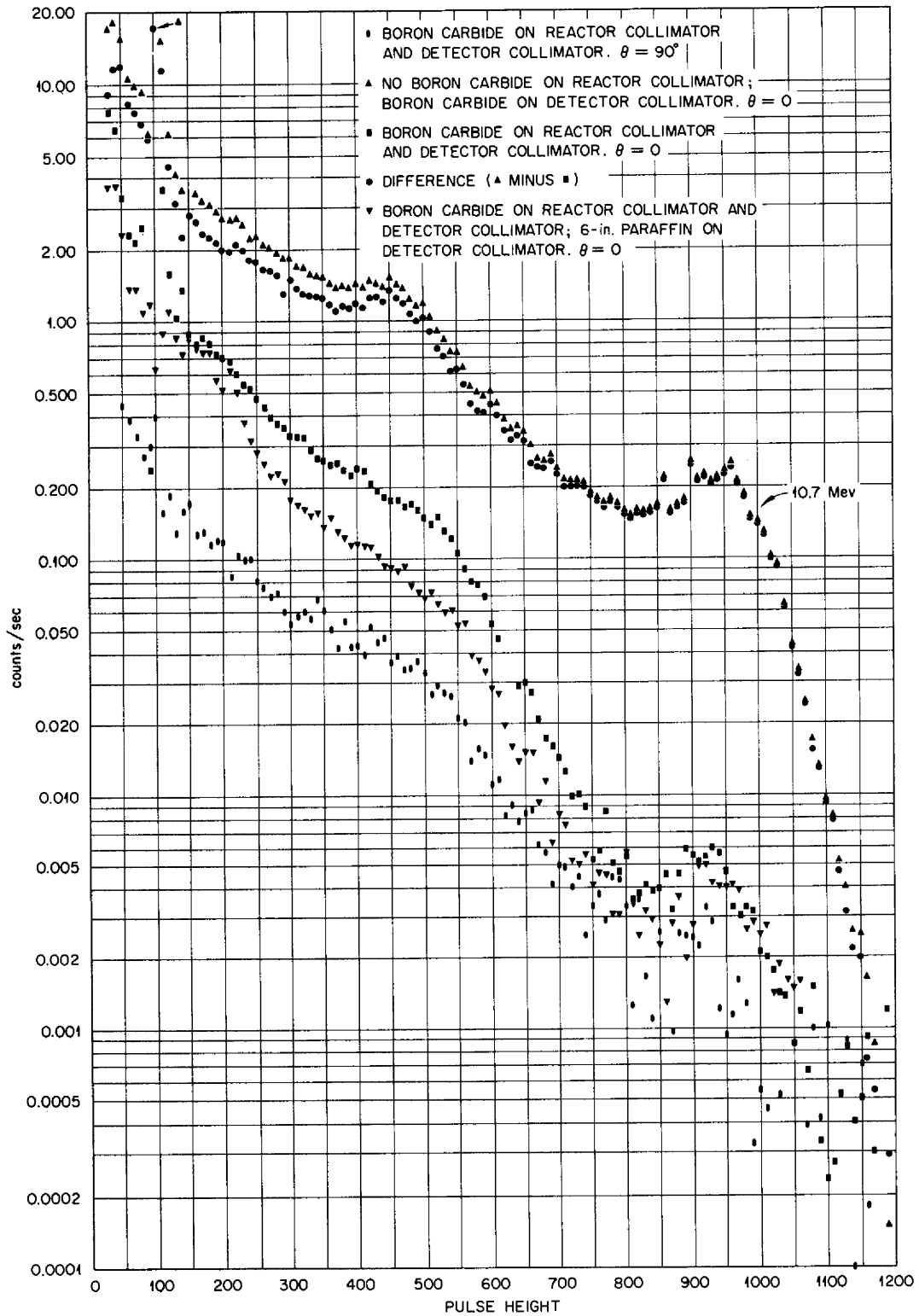
Fig. 5.4.4. Total Pulse-Height Spectra of Gamma Rays Resulting from Neutron Interactions in Air.

N^{14} which is known to have been observed[2] is at 10.8 Mev, and this can be identified in the curve at a pulse-height setting of 1000. The two peaks that occur at pulse-height settings of 960 and 920 are typical of high-energy gamma-ray responses in a 3- by 3-in. sodium iodide crystal. The higher peaks that correspond to pulse-height settings of 900 and 860 are caused by improperly operating channels in the analyzer. Some of the high counting rates below a setting of 150 were due to the detection of Zn^{65} gamma rays from portions of the calibrating source which had been left in the borated water of the collimator; low-energy Compton-scattered gamma rays also contributed.

Unfortunately, it was not possible in the experiment to isolate the gamma rays contributed .by thermal-neutron captures from those contributed by inelastically scattered fast neutrons. It was possible, however, to reduce the effect of the capture-gamma-ray contribution by blacking out most of the thermal neutrons so that a difference spectrum could be obtained which could then be used to determine the approximate contribution from inelastically scattered neutrons. In order to obtain measurements with a reduced capture-gamma-ray contribution, the upper end of the reactor collimator was covered with boron Plexiglas. The resulting gamma-ray spectrum is shown in the third curve from the top in Fig. 5.4.4. It can be seen that the 10.8-Mev capture-gamma-ray peak was reduced in intensity by a factor of 40. However, the portion of the curve that corresponds to lower pulse-height settings was not reduced by the same factor, which indicates that this portion of the spectrum not only represented gamma rays which originated from thermal-neutron capture but also represented gamma rays from another source. This other source is presumably inelastically scattered fast neutrons that were unaffected by the boron Plexiglas on the reactor collimator. If this curve is subtracted from the top curve in the figure, which represents the total capture-gamma-ray contribution plus the contribution from inelastically scattered neutrons, the difference curve would represent the spectrum of capture gamma rays from low-energy neutrons which were eliminated by the boron Plexiglas on the reactor collimator. This difference curve, which is also plotted in Fig.

---

[2]G. A. Bartholomew and P. J. Campion, *Can. J. Phys.* 35, 1347 (1957).

5.4.4, shows very little fine structure; however, the energy-level distribution in N^{15} is such that it is possible for gamma rays of the order of 15 different energies ranging from 3.5 to 10.8 Mev to be emitted, and these would be smeared by scattering in air and in the borated water and by interactions in the crystal itself. Several energy levels from 5.2 to 5.6 Mev are responsible for about one-fourth of the gamma rays from thermal-neutron capture in nitrogen, and this difference curve does seem to indicate a prominent peak at about 4.5 to 5 Mev. Determination of the actual capture-gamma-ray spectrum, however, can only be done by what is known as the "subtraction" method, and an analysis of this type is yet to be performed. The peak observed in this difference curve at a pulse-height setting of about 100 is the result of a shift in gain during the foreground and background runs which brought about improper subtraction of the Zn^{65} gamma rays. (While the reactor collimator was covered with boron Plexiglas, one series of measurements was made with the reactor collimator rotated to $\theta = 90$ deg. The results of these measurements are included in Fig. 5.4.4, but no attempt has yet been made to interpret the data.)

If it is assumed that the 10.8-Mev peak obtained in the measurements in which boron Plexiglas was used on the reactor collimator is due only to thermal-neutron capture in nitrogen, this peak can be normalized with the same peak in the capture-gamma-ray difference curve. The difference between these two curves, shown in the lower curve in Fig. 5.4.5, was thought to be due to gamma rays resulting from inelastically scattered fast neutrons. The large number of high-energy gamma rays (>2.25 Mev), however, indicated the possibility that a significant contribution to this inelastic-scattering spectrum might be the result of neutron interactions in the concrete walls of the collimator. (For example, silicon capture gamma rays have very high energies.) In order to resolve this question, additional measurements were made in which the intensities of the neutrons and gamma rays entering the collimator slit were changed through the use of lead and several thicknesses of paraffin placed over and in front of the slit.

Data obtained when $4\frac{1}{2}$ in. of paraffin, 9 in. of paraffin, and/or 4 in. of lead was placed over the collimator slit and boron Plexiglas covered the reactor collimator are given in Fig. 5.4.6. For these measurements the gain of the amplifier was
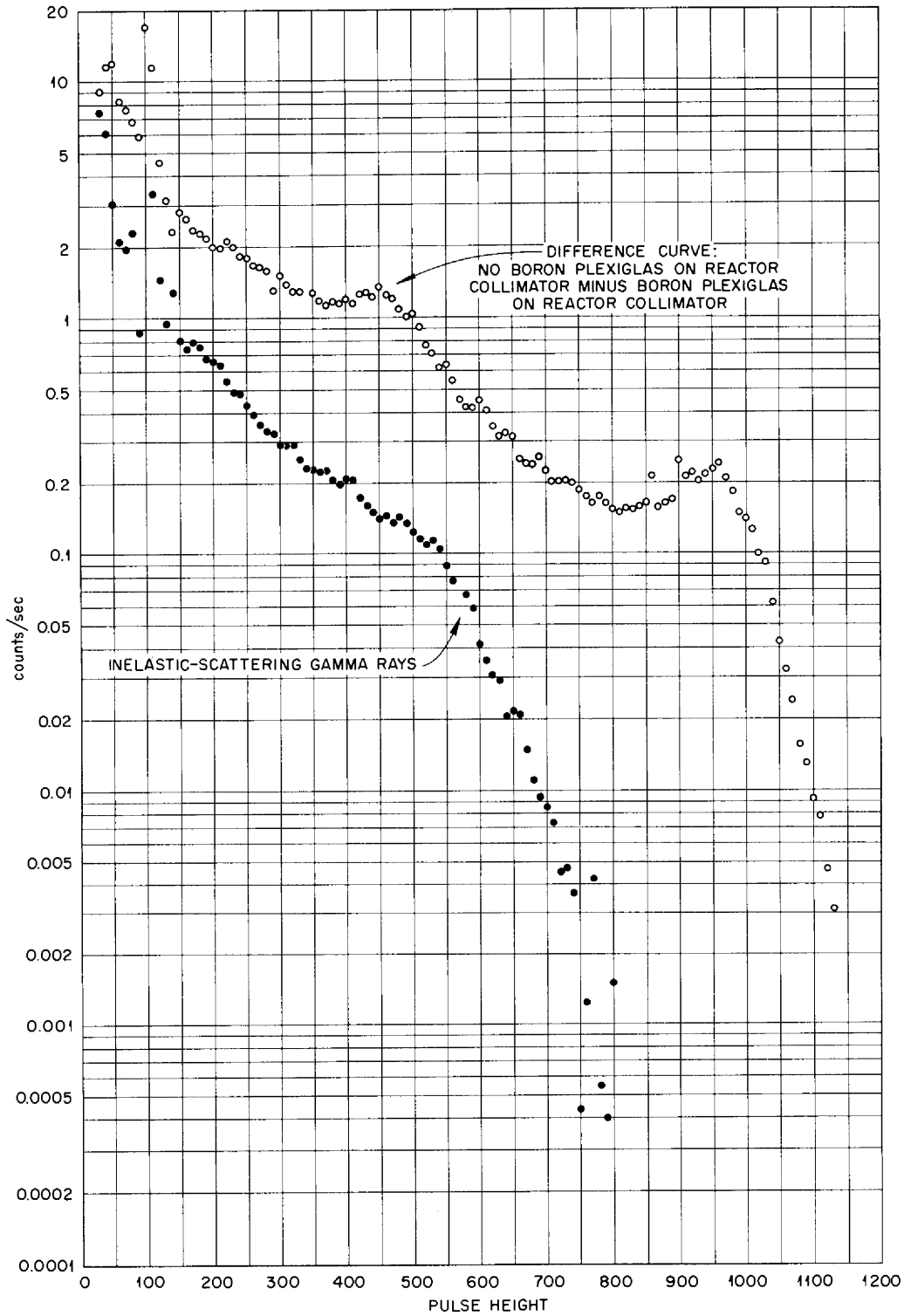
Fig. 5.4.5. Pulse-Height Spectra of Capture and Inelastic-Scattering Gamma Rays Resulting from Neutron Interactions in Air.
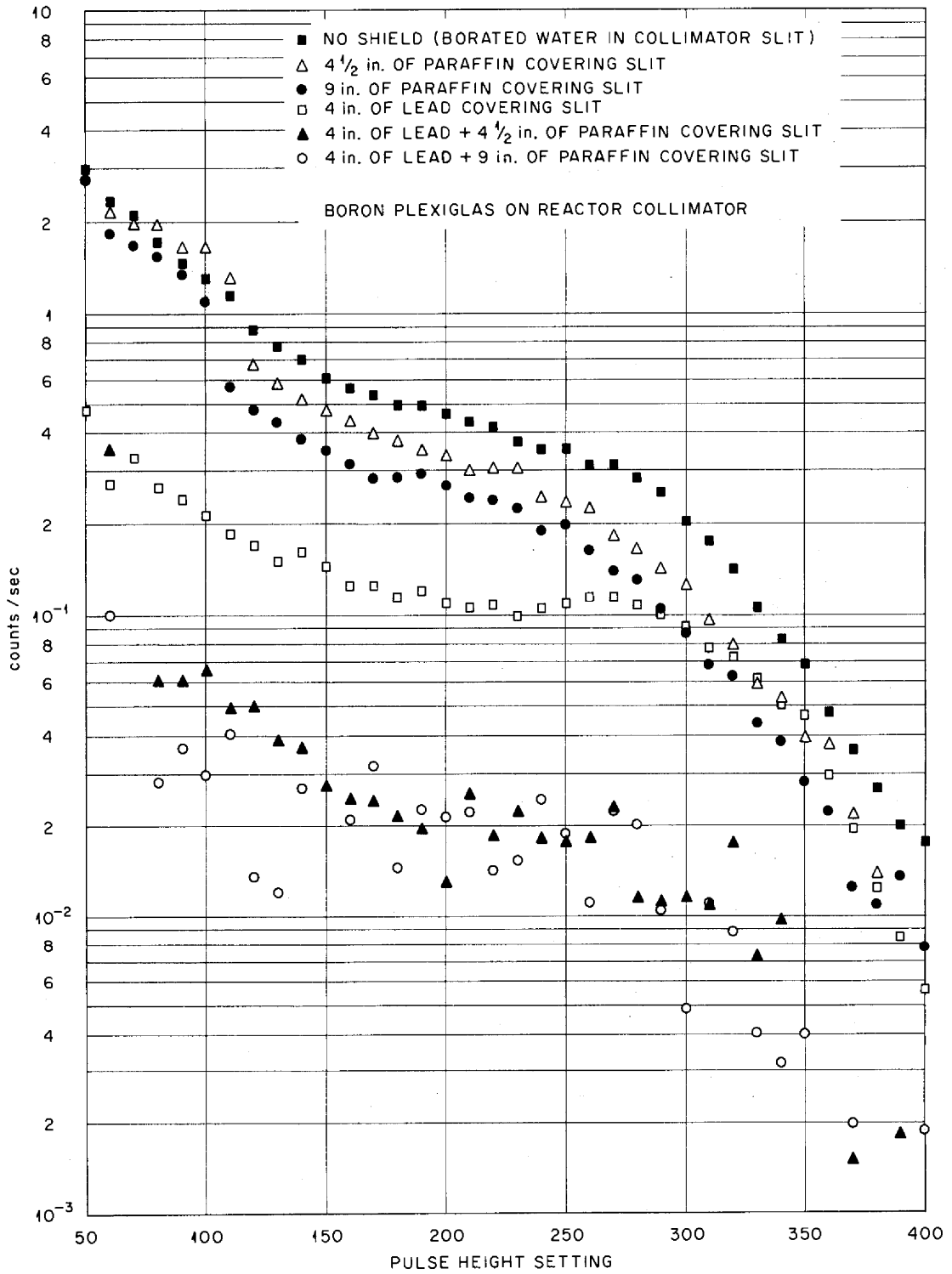
UNCLASSIFIED
2—01—056—22—670

Fig. 5.4.6. Pulse-Height Spectra of Gamma Rays Resulting from Neutron Interactions in Air: Effect of Various Shields Covering the Collimator Slit (θ = 0 deg).

reduced so that a pulse-height setting of 100 corresponded to about 2.25 Mev. If a relaxation length of about 30 cm for gamma rays in paraffin is 'assumed, the reduction in the gamma-ray intensity was that to be expected for the two paraffin thicknesses (a factor of 1.8 for $4\frac{1}{2}$ in. of paraffin) if the gamma rays were coming from outside the slit. A comparable reduction was found when 6 in. of paraffin covered the collimator slit (see Fig. 5.4.4). Had these gamma rays resulted from neutron interactions in the detector collimator slit, however, the gamma-ray intensity would have been reduced much more (about a factor of 7 when $4\frac{1}{2}$ in. of paraffin was added).

When 4 in. of lead covered the slit, the counting rate decreased only a factor of 5 below 4 or 5 Mev and only a factor of 2 above this energy. This large contribution above 5 Mev appeared to be due to neutron captures in the lead. This was verified by placing $4\frac{1}{2}$ in. of paraffin on the lead, which further reduced the counting rate a factor of about 10. A 9-in. thickness of paraffin was also placed on the lead, as shown in Fig. 5.4.4, but the additional $4\frac{1}{2}$ in. did not effect a further reduction in the gamma-ray intensity, since the first $4\frac{1}{2}$ in. was sufficient to attenuate the neutrons. It should be pointed out that the measurements in which both lead and paraffin were used were very near background.

Since the gamma rays at the detector could be greatly reduced by using lead and paraffin but were not reduced by the paraffin alone more than was expected for gamma rays formed outside the collimator, it was concluded that these gamma rays were the result of interactions in air and not from thermal-neutron capture in the detector collimator. It is assumed here that the source was almost entirely inelastically scattered neutrons; however, contributions from other sources, such as multiply scattered gamma rays, may be included. Theoretical calculations of probable gamma-ray spectra from inelastic scattering of neutrons in N^{14}, thermal-neutron capture, and scattered primary gamma rays are being made.

Thermal-Neutron Flux Measurements

Thermal-neutron flux measurements in the air around the reactor were made with a bare single-barreled BF_3 counter to facilitate calculations of the air capture gamma-ray intensities; the calculations will be made for the same configurations for which the gamma-ray spectra given above were measured. It should be emphasized that these measurements give a count rate that is proportional to the neutron density. The calibration procedure used essentially multiplies the neutron density by the thermal-neutron velocity (2200 m/sec), and the result is the "effective" thermal-neutron flux. This has only to be multiplied by the capture cross section at 2200 m/sec to obtain the capture rate in a $1/v$ absorber.

For the thermal-neutron flux measurements the counter was suspended at a fixed point in air and the reactor and its collimator were rotated about the reactor vertical centerline, as shown in Fig. 5.4.7. The counter position fell along the center-line of the beam when the beam was in the vertical
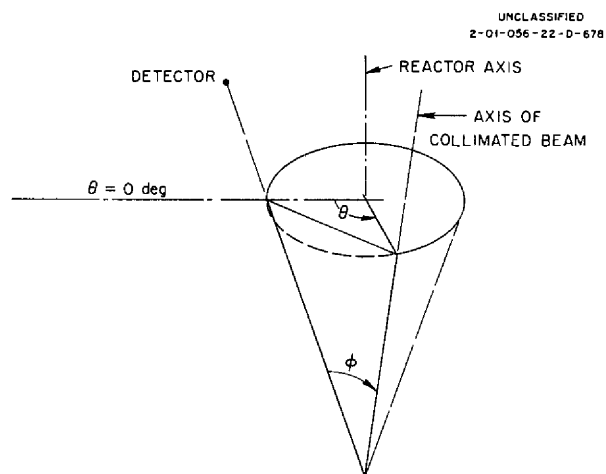
Fig. 5.4.7. Geometry for Measurement of the Thermal-Neutron Flux in Air.

plane defined by $\theta = 0$ deg. Measurements were taken both with and without a boron Plexiglas cover on the reactor collimator. The resulting effective thermal-neutron fluxes, with and without the collimator cover, are plotted as a function of ϕ, the angle between the axis of the beam and a line through the center of the reactor and detector, in Figs. 5.4.8 and 5.4.9 for several separation distances, r, measured from the reactor center to the detector center. The same information is given as a function of r for $\phi = 0$, 15, 30, and 60 deg in Figs. 5.4.10, 5.4.11, 5.4.12, and 5.4.13, respectively. The curves of Fig. 5.4.9 have been fitted with an expression of the form $e^{-r/\lambda}/r^2$, and
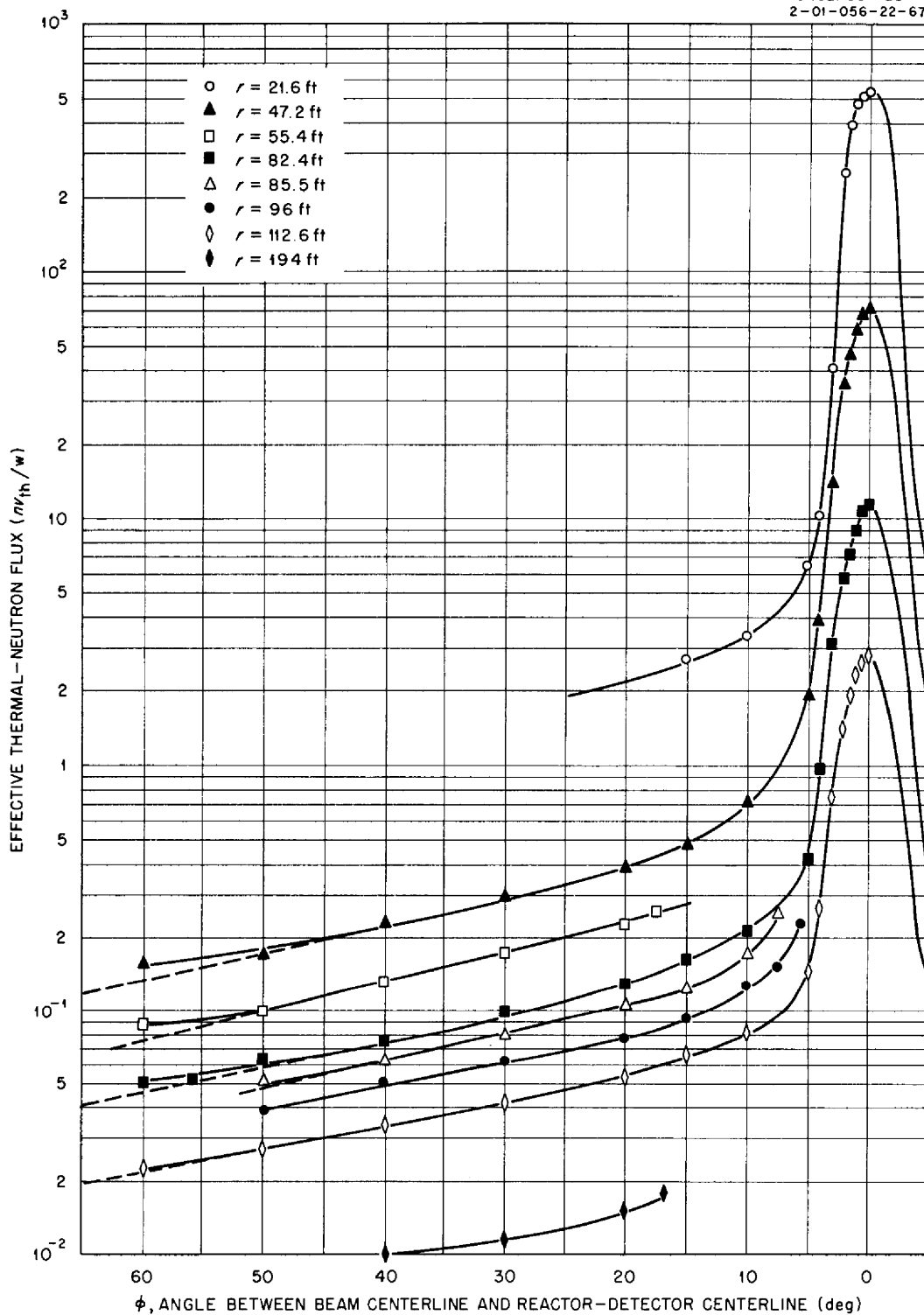
UNCLASSIFIED
2-01-056-22-671

Fig. 5.4.8.   Effective Thermal-Neutron Flux at Various Distances *r* as a Function of the Angle ϕ: No Boron Plexiglas on Reactor Collimator.
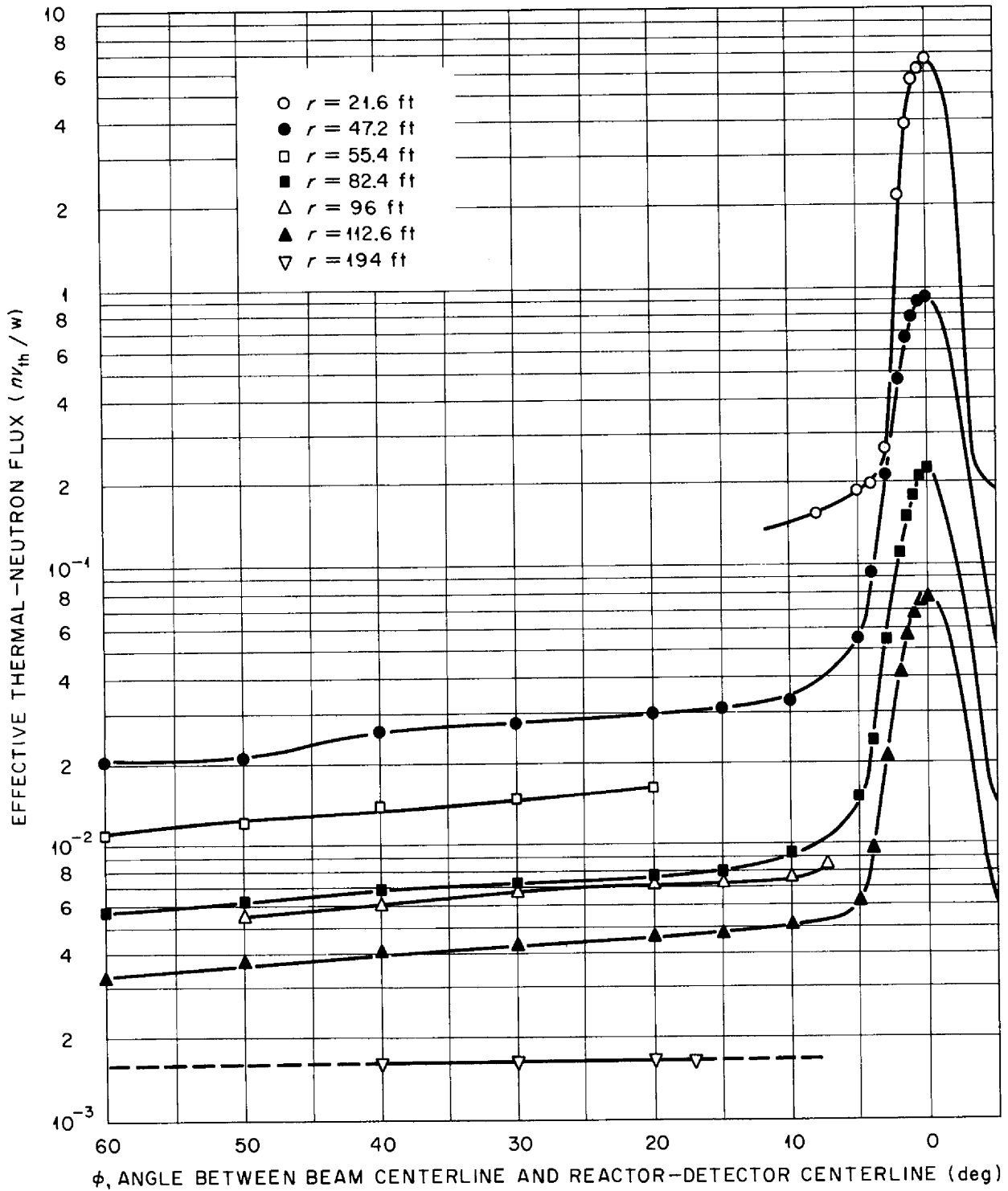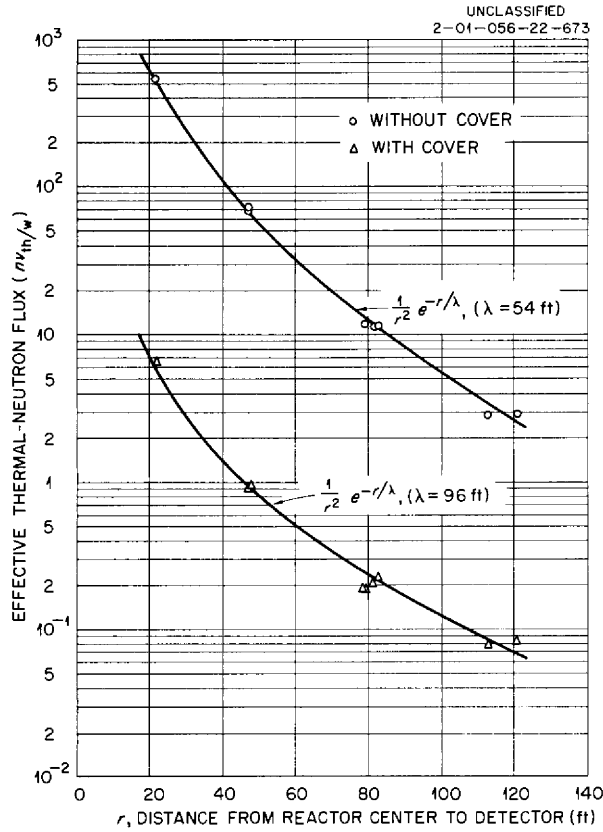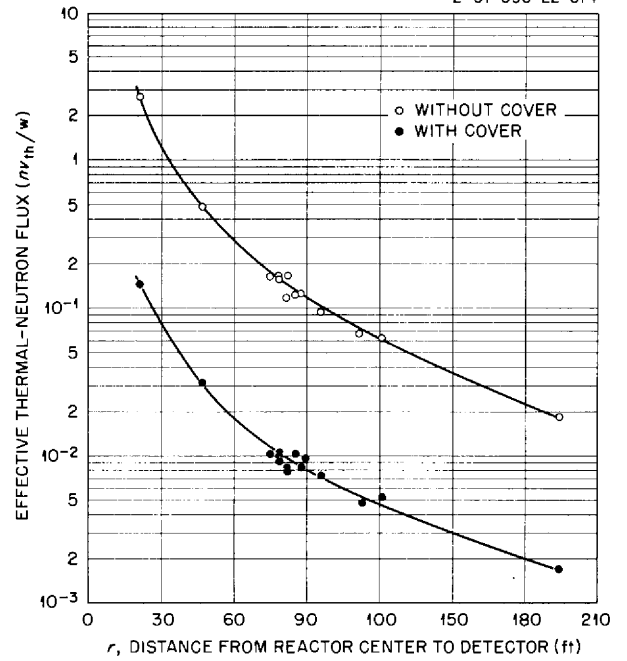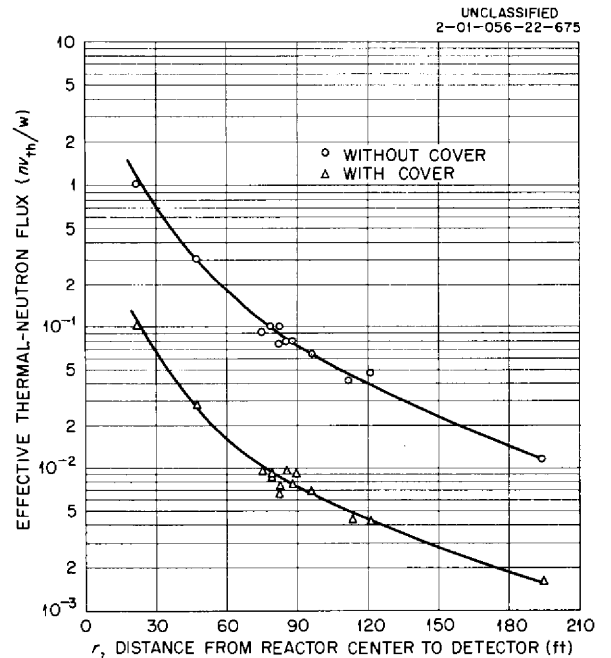
Fig. 5.4.9.   Effective Thermal-Neutron Flux at Various Distances *r* as a Function of the Angle φ: Boron Plexiglas on Reactor Collimator.

$\frac{1}{r^2} e^{-r/\lambda}$, ($\lambda = 54$ ft)

$\frac{1}{r^2} e^{-r/\lambda}$, ($\lambda = 96$ ft)

Fig. 5.4.10. Effective Thermal-Neutron Flux as a Function of the Distance r for $\phi = 0$ deg: With and Without Boron Plexiglas on Reactor Collimator.

relaxation lengths of 54 and 96 ft, respectively, were obtained without and with the cover. These expressions are probably not valid for distances greater than 120 ft (for which measurements were not obtained), because a larger fraction of the neutrons that contribute to the counts started from the reactor with energies higher than thermal. For this same reason, the curves of Figs. 5.4.11 through 5.4.13 cannot be fitted with a simple expression.

In addition to the measurements described in the preceding paragraph, a series of measurements was also made along short vertical lines at fixed horizontal distances from the reactor as the reactor and its collimator were rotated. These vertical lines were centered above and below the beam axis defined by $\theta = 0$ deg and served to show that the neutron beam was symmetrical about its axis.

Fig. 5.4.11. Effective Thermal-Neutron Flux as a Function of the Distance r for $\phi = 15$ deg: With and Without Boron Plexiglas on Reactor Collimator.

Fig. 5.4.12. Effective Thermal-Neutron Flux as a Function of the Distance r for $\phi = 30$ deg: With and Without Boron Plexiglas on Reactor Collimator.

295
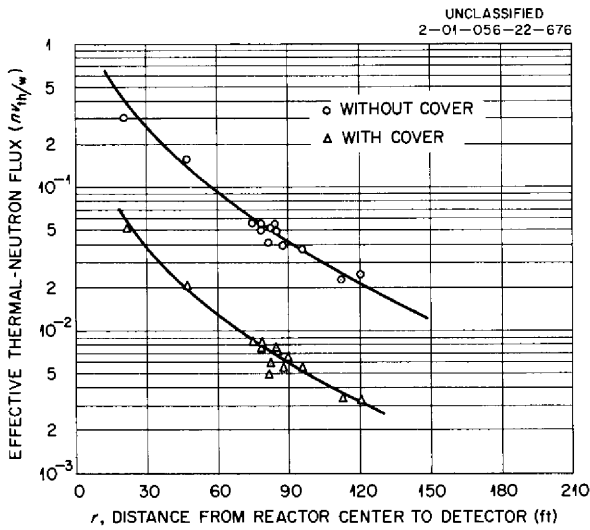
Fig. 5.4.13. Effective Thermal-Neutron Flux as a Function of the Distance *r* for $\phi = 60$ deg: With and Without Boron Plexiglas on Reactor Collimator.

It also indicates that the ground did not perturb the flux appreciably in the air volume seen by the gamma-ray spectrometer.

A measure of the relative importance of thermal neutrons from the source and higher energy neutrons from the source which have been slowed down in air may be obtained by taking, for a given position in space, the ratio of the measurements

for which a boron Plexiglas cover was used to those for which no cover was used. This ratio is plotted in Fig. 5.4.14 as a function of distance from the reactor for angles of $\phi = 0$, 15, 30, and 60 deg. The higher energy neutrons become more important as the ratio decreases.
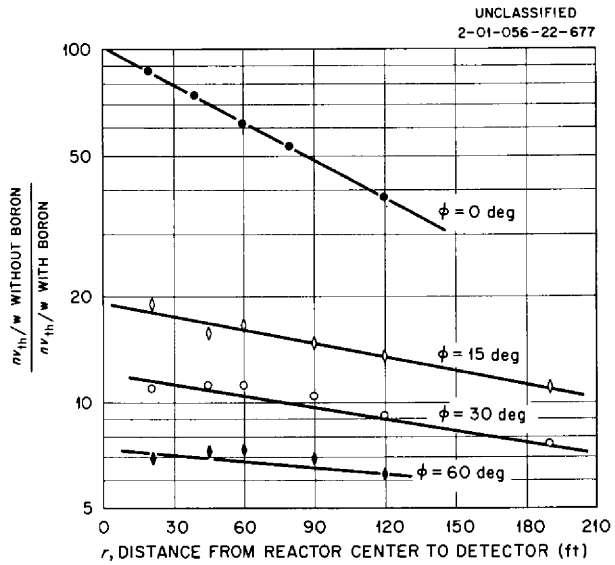
Fig. 5.4.14. Ratio of the Effective Thermal-Neutron Fluxes With and Without Boron Plexiglas on the Reactor Collimator as a Function of the Distance *r* for Various Angles ϕ.

INTERNAL DISTRIBUTION

1. R. G. Affel
2. J. W. Allen
3. C. J. Barton
4. M. Bender
5. D. S. Billington
6. F. F. Blankenship
7. E. P. Blizard
8. C. J. Borkowski
9. W. F. Boudreau
10. G. E. Boyd
11. M. A. Bredig
12. E. J. Breeding
13. W. E. Browning
14. F. R. Bruce
15. A. D. Callihan
16. D. W. Cardwell
17. C. E. Center (K-25)
18. R. A. Charpie
19. R. L. Clark
20. C. E. Clifford
21. J. H. Coobs
22. W. B. Cottrell
23. R. S. Crouse
24. F. L. Culler
25. D. R. Cuneo
26. J. H. DeVan
27. L. M. Doney
28. D. A. Douglas
29. W. K. Eister
30. L. B. Emlet (K-25)
31. D. E. Ferguson
32. A. P. Fraas
33. J. H. Frye
34. W. T. Furgerson
35. R. J. Gray
36. A. T. Gresky
37. W. R. Grimes
38. A. G. Grindell
39. E. Guth
40. C. S. Harrill
41. M. R. Hill
42. E. E. Hoffman
43. W. H. Hoffman
44. A. Hollaender
45. A. S. Householder

46. J. T. Howe
47. W. H. Jordan
48. G. W. Keilholtz
49. C. P. Keim
50. F. L. Keller
51. M. T. Kelley
52. F. Kertesz
53. J. J. Keyes
54-55. J. A. Lane
56. R. B. Lindauer
57. R. S. Livingston
58. R. N. Lyon
59. H. G. MacPherson
60. R. E. MacPherson
61. F. C. Maienschein
62. W. D. Manly
63. E. R. Mann
64. L. A. Mann
65. W. B. McDonald
66. J. R. McNally
67. F. R. McQuilkin
68. R. V. Meghreblian
69. R. P. Milford
70. A. J. Miller
71. R. E. Moore
72. J. G. Morgan
73. K. Z. Morgan
74. E. J. Murphy
75. J. P. Murray (Y-12)
76. M. L. Nelson
77. G. J. Nessle
78. L. G. Overholser
79. P. Patriarca
80. S. K. Penny
81. A. M. Perry
82. D. Phillips
83. J. C. Pigg
84. P. M. Reyling
85. A. E. Richt
86. M. T. Robinson
87. H. W. Savage
88. A. W. Savolainen
89. R. D. Schultheiss
90. D. Scott
91. J. L. Scott

92. R. D. Shipley
93. A. Simon
94. O. Sisman
95. J. Sites
96. M. J. Skinner
97. A. H. Snell
98. C. D. Susano
99. J. A. Swartout
100. E. H. Taylor
101. R. E. Thoma
102. D. B. Trauger
103. D. K. Trubey
104. G. M. Watson

105. A. M. Weinberg
106. J. C. White
107. G. D. Whitman
108. E. P. Wigner (consultant)
109. G. C. Williams
110. J. C. Wilson
111. C. E. Winters
112. W. Zobel
113–115. ORNL – Y-12 Technical Library,
Document Reference Section
116–122. Laboratory Records Department
123. Laboratory Records, ORNL R.C.
124–126. Central Research Library

EXTERNAL DISTRIBUTION

127–129. Air Force Ballistic Missile Division
130–131. AFPR, Boeing, Seattle
132. AFPR, Boeing, Wichita
133. AFPR, Curtiss Wright, Clifton
134. AFPR, Douglas, Long Beach
135–137. AFPR, Douglas, Santa Monica
138. AFPR, Lockheed, Burbank
139–140. AFPR, Lockheed, Marietta
141. AFPR, North American, Canoga Park
142. AFPR, North American, Downey
143–144. Air Force Special Weapons Center
145. Air Materiel Command
146. Air Research and Development Command (RDGN)
147. Air Research and Development Command (RDTAPS)
148–161. Air Research and Development Command (RDZPSP)
162. Air Technical Intelligence Center
163–165. ANP Project Office, Convair, Fort Worth
166. Albuquerque Operations Office
167. Argonne National Laboratory
168. Armed Forces Special Weapons Project, Sandia
169. Armed Forces Special Weapons Project, Washington
170. Assistant Secretary of the Air Force, R&D
171–176. Atomic Energy Commission, Washington
177. Atomics International
178. Battelle Memorial Institute
179–180. Bettis Plant (WAPD)
181. Bureau of Aeronautics
182. Bureau of Aeronautics General Representative
183. BAR, Aerojet-General, Azusa
184. BAR, Convair, San Diego
185. BAR, Glenn L. Martin, Baltimore
186. BAR, Grumann Aircraft, Bethpage
187. Bureau of Yards and Docks
188. Chicago Operations Office

Reports previously issued in this series are as follows:

ORNL-528	Period Ending November 30, 1949
ORNL-629	Period Ending February 28, 1950
ORNL-768	Period Ending May 31, 1950
ORNL-858	Period Ending August 31, 1950
ORNL-919	Period Ending December 10, 1950
ANP-60	Period Ending March 10, 1951
ANP-65	Period Ending June 10, 1951
ORNL-1154	Period Ending September 10, 1951
ORNL-1170	Period Ending December 10, 1951
ORNL-1227	Period Ending March 10, 1952
ORNL-1294	Period Ending June 10, 1952
ORNL-1375	Period Ending September 10, 1952
ORNL-1439	Period Ending December 10, 1952
ORNL-1515	Period Ending March 10, 1953
ORNL-1556	Period Ending June 10, 1953
ORNL-1609	Period Ending September 10, 1953
ORNL-1649	Period Ending December 10, 1953
ORNL-1692	Period Ending March 10, 1954
ORNL-1729	Period Ending June 10, 1954
ORNL-1771	Period Ending September 10, 1954
ORNL-1816	Period Ending December 10, 1954
ORNL-1864	Period Ending March 10, 1955
ORNL-1896	Period Ending June 10, 1955
ORNL-1947	Period Ending September 10, 1955
ORNL-2012	Period Ending December 10, 1955
ORNL-2061	Period Ending March 10, 1956
ORNL-2106	Period Ending June 10, 1956
ORNL-2157	Period Ending September 10, 1956
ORNL-2221	Period Ending December 31, 1956
ORNL-2274	Period Ending March 31, 1957
ORNL-2340	Period Ending June 30, 1957
ORNL-2387	Period Ending September 30, 1957